

Energy, Environment, and Sustainability  
Series Editor: Avinash Kumar Agarwal

Gautam Kalghatgi  
Avinash Kumar Agarwal  
Felix Leach  
Kelly Senecal *Editors*

# Engines and Fuels for Future Transport



 Springer

# **Energy, Environment, and Sustainability**

## **Series Editor**

Avinash Kumar Agarwal, Department of Mechanical Engineering, Indian Institute of Technology Kanpur, Kanpur, Uttar Pradesh, India

## **AIMS AND SCOPE**

This books series publishes cutting edge monographs and professional books focused on all aspects of energy and environmental sustainability, especially as it relates to energy concerns. The Series is published in partnership with the International Society for Energy, Environment, and Sustainability. The books in these series are edited or authored by top researchers and professional across the globe. The series aims at publishing state-of-the-art research and development in areas including, but not limited to:

- Renewable Energy
- Alternative Fuels
- Engines and Locomotives
- Combustion and Propulsion
- Fossil Fuels
- Carbon Capture
- Control and Automation for Energy
- Environmental Pollution
- Waste Management
- Transportation Sustainability

## **Review Process**

The proposal for each volume is reviewed by the main editor and/or the advisory board. The chapters in each volume are individually reviewed single blind by expert reviewers (at least four reviews per chapter) and the main editor.

**Ethics Statement** for this series can be found in the Springer standard guidelines here <https://www.springer.com/us/authors-editors/journal-author/journal-author-helpdesk/before-you-start/before-you-start/1330#c14214>

More information about this series at <https://link.springer.com/bookseries/15901>

Gautam Kalghatgi · Avinash Kumar Agarwal ·  
Felix Leach · Kelly Senecal  
Editors

# Engines and Fuels for Future Transport

 Springer



*Editors*

Gautam Kalghatgi  
Oxford, UK

Felix Leach  
Department of Engineering Science  
University of Oxford  
Oxford, UK

Avinash Kumar Agarwal  
Department of Mechanical Engineering  
Indian Institute of Technology Kanpur  
Kanpur, India

Kelly Senecal  
Convergent Science  
Madison, WI, USA

ISSN 2522-8366

ISSN 2522-8374 (electronic)

Energy, Environment, and Sustainability

ISBN 978-981-16-8716-7

ISBN 978-981-16-8717-4 (eBook)

<https://doi.org/10.1007/978-981-16-8717-4>

© The Editor(s) (if applicable) and The Author(s), under exclusive license to Springer Nature Singapore Pte Ltd. 2022, corrected publication 2022

This work is subject to copyright. All rights are solely and exclusively licensed by the Publisher, whether the whole or part of the material is concerned, specifically the rights of translation, reprinting, reuse of illustrations, recitation, broadcasting, reproduction on microfilms or in any other physical way, and transmission or information storage and retrieval, electronic adaptation, computer software, or by similar or dissimilar methodology now known or hereafter developed.

The use of general descriptive names, registered names, trademarks, service marks, etc. in this publication does not imply, even in the absence of a specific statement, that such names are exempt from the relevant protective laws and regulations and therefore free for general use.

The publisher, the authors and the editors are safe to assume that the advice and information in this book are believed to be true and accurate at the date of publication. Neither the publisher nor the authors or the editors give a warranty, expressed or implied, with respect to the material contained herein or for any errors or omissions that may have been made. The publisher remains neutral with regard to jurisdictional claims in published maps and institutional affiliations.

This Springer imprint is published by the registered company Springer Nature Singapore Pte Ltd.

The registered company address is: 152 Beach Road, #21-01/04 Gateway East, Singapore 189721, Singapore

# Preface

Transport and mobility are central to modern societies. Transport accounts for around 20% of global primary energy use and contributes around 23% of global CO<sub>2</sub> emissions but 14% of greenhouse gas (GHG) emissions if other gases such as methane and nitrous oxide are taken into account. Incidentally, this is the same share of GHG emissions as from livestock farming for meat and dairy. There are around 1.3 billion light-duty vehicles (LDVs) in the world, with this number expected to go up to 1.7 billion by 2040 because of growth in the developing countries. However, LDVs account for only around 45% global transport energy demand which is very large; the world uses over 11 billion liters of liquid fuel each day. Currently, around 99.7% of all transport runs on combustion engines and 95% of transport energy comes from petroleum-based liquid fuels. The alternatives to the current transport energy system such as battery electric vehicles start from a very low base and face very significant barriers to unlimited and fast growth. Hence, internal combustion engines (ICEs) will continue to play a very central role in running global transport and need to be continuously improved in terms of efficiency and emissions.

This book has fifteen chapters addressing various issues important to ICEs, and we hope it will be useful to interested professionals and students.

The International Society for Energy, Environment and Sustainability (ISEES) was founded at the Indian Institute of Technology Kanpur (IIT Kanpur), India, in January 2014 to spread knowledge/awareness and catalyze research activities in the fields of energy, environment, sustainability, and combustion. Society's goal is to contribute to the development of clean, affordable, and secure energy resources and a sustainable environment for society, spread knowledge in the areas mentioned above, and create awareness of the environmental challenges the world is facing today. The unique way adopted by ISEES was to break the conventional silos of specializations (engineering, science, environment, agriculture, biotechnology, materials, fuels, etc.) to tackle the problems related to energy, environment, and sustainability in a holistic manner. This is quite evident by the participation of experts from all fields to resolve these issues. ISEES is involved in various activities such as conducting workshops, seminars, and conferences in the domains of its interests. Society also recognizes

the outstanding works of young scientists, professionals, and engineers for their contributions in these fields by conferring them awards under various categories.

The Fifth International Conference on ‘Sustainable Energy and Environmental Challenges’ (V-SEEC) was organized under the auspices of ISEES from December 19 to 21, 2020, in virtual mode due to restrictions on travel because of the ongoing COVID-19 pandemic situation. This conference provided a platform for discussions between eminent scientists and engineers from various countries, including India, Spain, Austria, Bangladesh, Mexico, USA, Malaysia, China, UK, Netherlands, Germany, Israel, and Saudi Arabia. At this conference, eminent international speakers presented their views on energy, combustion, emissions, and alternative energy resources for sustainable development and a cleaner environment. The conference presented two high-voltage plenary talks by Dr. V. K. Saraswat, Honorable Member, NITI Ayog, on ‘Technologies for Energy Security and Sustainability’ and Prof. Sandeep Verma, Secretary, SERB, on ‘New and Equitable R&D Funding Opportunities at SERB.’

The conference included nine technical sessions on topics related to energy and environmental sustainability. Each session had 6–7 eminent scientists from all over the world, who shared their opinion and discussed the trends for the future. The technical sessions in the conference included emerging contaminants: monitoring and degradation challenges; advanced engine technologies and alternative transportation fuels; future fuels for sustainable transport; sustainable bioprocessing for biofuel/non-biofuel production by carbon emission reduction; future of solar energy; desalination and wastewater treatment by membrane technology; biotechnology in sustainable development; emerging solutions for environmental applications, and challenges and opportunities for electric vehicle adoption. Five hundred plus participants and speakers from all over the world attended this three days conference.

The conference concluded with a high-voltage panel discussion on ‘Challenges and Opportunities for Electric Vehicle Adoption,’ where the panelists were Prof. Gautam Kalghatgi (University of Oxford), Prof. Ashok Jhunjhunwala (IIT Madras), Dr. Kelly Senecal (Convergent Science), Dr. Amir Abdul Manan (Saudi Aramco), and Dr. Sayan Biswas (University of Minnesota, USA). Prof. Avinash K. Agarwal, ISEES, moderated the panel discussion. This conference laid out the roadmap for technology development, opportunities, and challenges in energy, environment, and sustainability domain. All these topics are very relevant for the country and the world in the present context. We acknowledge the support received from various agencies and organizations for the successful conduct of the Fifth ISEES conference V-SEEC, where these books germinated. We want to acknowledge SERB (special thanks to Dr. Sandeep Verma, Secretary) and our publishing partner Springer (special thanks to Ms. Swati Meherishi).

The editors would like to express their sincere gratitude to the authors from all over the world for submitting their high-quality work. We would like to express our gratitude to the reviewers, who reviewed various chapters of this monograph and provided their valuable suggestions to improve the manuscripts.

Oxford, UK  
Kanpur, India  
Oxford, UK  
Madison, USA

Gautam Kalghatgi  
Avinash Kumar Agarwal  
Felix Leach  
Kelly Senecal

# Contents

<b>1</b>	<b>Introduction to Engines and Fuels for Future Transport</b> .....	<b>1</b>
	Gautam Kalghatgi, Avinash Kumar Agarwal, Kelly Senecal, and Felix Leach	
<b>2</b>	<b>Sustainable Transportation</b> .....	<b>7</b>
	Carl Hergart	
<b>3</b>	<b>A Review of Emissions Control Technologies for On-Road Vehicles</b> .....	<b>39</b>
	Ameya Joshi	
<b>4</b>	<b>Opposed-Piston Engine Potential: Low CO<sub>2</sub> and Criteria Emissions</b> .....	<b>57</b>
	Laurence J. Fromm, Fabien Redon, and Ashwin Salvi	
<b>5</b>	<b>An Overview of Hybrid Electric Vehicle Technology</b> .....	<b>73</b>
	Nirendra Nath Mustafi	
<b>6</b>	<b>Life-Cycle Analysis for the Automotive Sector</b> .....	<b>103</b>
	Graham Conway	
<b>7</b>	<b>Pre-chamber Combustors: An Enabling Technology for High Efficiency, Low CO<sub>2</sub> Engine Operation</b> .....	<b>133</b>
	Michael Bunce, Hugh Blaxill, Nathan Peters, Sai Krishna Pothuraju Subramanyam, Adrian Cooper, and Mike Bassett	
<b>8</b>	<b>A Pathway to Ultra-Lean IC Engine Combustion: The Narrow Throat Pre-chamber</b> .....	<b>175</b>
	Manuel Alejandro Echeverri Marquez, Ponnya Hlaing, Priybrat Sharma, Emre Cenker, Jihad Badra, Amer Amer, James W. G. Turner, Hong Im, Gaetano Magnotti, and Bengt Johansson	

<b>9</b>	<b>On the Use of Active Pre-chambers and Bio-hybrid Fuels in Internal Combustion Engines</b> .....	<b>205</b>
	Patrick Burkardt, Maximilian Fleischmann, Tim Wegmann, Marco Braun, Julian Knöll, Leif Schumacher, Florian vom Lehn, Bastian Lehrheuer, Matthias Meinke, Heinz Pitsch, Reinhold Kneer, Wolfgang Schröder, and Stefan Pischinger	
<b>10</b>	<b>The Use of Ammonia as a Fuel for Combustion Engines</b> .....	<b>233</b>
	Dong Han, Yusen Liu, and Zhen Huang	
<b>11</b>	<b>Ammonia as Fuel for Transportation to Mitigate Zero Carbon Impact</b> .....	<b>257</b>
	Christine Mounaïm-Rousselle, Pierre Bréquigny, Agustin Valera Medina, Elena Boulet, David Emberson, and Terese Løvås	
<b>12</b>	<b>Methanol as a Fuel for Internal Combustion Engines</b> .....	<b>281</b>
	Chuntao Liu, Zhiqiang Li, Yiqiang Pei, and Yanzhao An	
<b>13</b>	<b>Technologies for Knock Mitigation in SI Engines—A Review</b> .....	<b>325</b>
	Cinzia Tornatore, Luca Marchitto, and Gerardo Valentino	
<b>14</b>	<b>Explicit Equations for Designing Surrogate Gasoline Formulations Containing Toluene, n-Heptane and Iso-pentane</b> ....	<b>351</b>
	Roger F. Cracknell, Jack Scrutton, and Sandro Gail	
<b>15</b>	<b>Prediction of Ignition Modes in Shock Tubes Relevant to Engine Conditions</b> .....	<b>369</b>
	Minh Bau Luong and Hong G. Im	
	<b>Correction to: The Use of Ammonia as a Fuel for Combustion Engines</b> .....	<b>C1</b>
	Dong Han, Yusen Liu, and Zhen Huang	

# Editors and Contributors

## About the Editors



**Gautam Kalghatgi** worked for 31 years at Shell Research in the UK followed by 8 years in Saudi Aramco before retiring in June 2018. He has been Visiting Professor at the Oxford University; Imperial College, London; KTH Stockholm; TU Eindhoven, and Sheffield University. He is Fellow of the Royal Academy of Engineering, SAE, I.Mech.E., and the Combustion Institute and Honorary Fellow of the International Society for Energy Environment and Sustainability (ISEES). He is on the International Board of Directors of the Combustion Institute and on the editorial boards of several journals. He has published around 140 papers and a book, ‘Fuel/Engine Interactions,’ on combustion, fuels and engine research and on transport energy. This work is cited widely with a current H index of 56 on Google Scholar. He has received many awards for his work including the 2021 ASME Internal Combustion Engines Award, Huw Edwards Award of the Institute of Physics, SAE Horning Award, and the Sugden Award of the Combustion Institute. He has a B.Tech. from IIT Bombay (1972) and a Ph.D. from Bristol University (1975) in Aeronautical Engineering. His Ph.D. project was on supersonic jet impingement. He did postdoctoral research on turbulent combustion at Southampton University (1975–1979) before joining Shell.



**Prof. Avinash Kumar Agarwal** joined IIT Kanpur in 2001. He worked at the Engine Research Center, UW@Madison, the USA as a Post-Doctoral Fellow (1999–2001). His interests are IC engines, combustion, alternate and conventional fuels, lubricating oil tribology, optical diagnostics, laser ignition, HCCI, emissions, and particulate control, 1D and 3D Simulations of engine processes, and large-bore engines. Prof. Agarwal has published 435+ peerreviewed international journal and conference papers, 70 edited books, 92 books chapters, and 12200+ Scopus and 19000+ Google Scholar citations. He is the associate principal editor of FUEL. He has edited “Handbook of Combustion” (5 Volumes; 3168 pages), published by Wiley VCH, Germany. Prof. Agarwal is a Fellow of SAE (2012), Fellow of ASME (2013), Fellow of ISEES (2015), Fellow of INAE (2015), Fellow of NASI (2018), Fellow of Royal Society of Chemistry (2018), and a Fellow of American Association of Advancement in Science (2020). He is the recipient of several prestigious awards such as Clarivate Analytics India Citation Award-2017 in Engineering and Technology, NASI-Reliance Industries Platinum Jubilee Award-2012; INAE Silver Jubilee Young Engineer Award-2012; Dr. C. V. Raman Young Teachers Award: 2011; SAE Ralph R. Teetor Educational Award-2008; INSA Young Scientist Award-2007; UICT Young Scientist Award-2007; INAE Young Engineer Award-2005. Prof. Agarwal received Prestigious CSIR Shanti Swarup Bhatnagar Award-2016 in Engineering Sciences. Prof. Agarwal is conferred upon Sir J C Bose National Fellowship (2019) by SERB for his outstanding contributions. Prof. Agarwal was a highly cited researcher (2018) and was in the top ten HCR from India among 4000 HCR researchers globally in 22 fields of inquiry.





**Felix Leach** is Associate Professor of Engineering Science at the University of Oxford, a post held jointly with that of Fellow and Tutor in Engineering Science at Keble College. His research interests are in emissions and efficiency of thermal propulsion systems and air quality. He has had a particular focus on particulate emissions from gasoline direct injection engines and developing a fundamental understanding of NO<sub>x</sub> emissions from diesel engines. He has spent over a decade working in close collaboration with industry using world-leading measurement capabilities to help develop a clean engine for the twenty-first century. In addition to his work on thermal propulsion systems, he has a significant engagement with public policy on emissions from vehicles and their interaction with air quality. He has run projects with Oxford City Council and Oxford Bus Company measuring emissions from in-service buses. He also runs projects measuring and understanding air quality in Oxford and the impact of various vehicle restrictions on air quality. He founded the annual Oxford Air Quality Meeting which draws together experts in vehicle emissions, air quality measurement, public health, and policy. Recently, he co-authored the book *Racing Toward Zero: The Untold Story of Driving Green*, available now from SAE. He holds M.Eng. and D.Phil. degrees in Engineering Science from the University of Oxford and is Chartered Engineer and Member of the Institution of Mechanical Engineers, Fellow of the Higher Education Academy, and Member of the Society of Automotive Engineers.



**Dr. Kelly Senecal** is Co-founder and Owner of Convergent Science, a computational fluid dynamics (CFD) software company headquartered in Madison, Wisconsin. He is Visiting Professor at the University of Oxford, Adjunct Professor at the University of Wisconsin-Madison, and Co-founder and Director of the Computational Chemistry Consortium (C3). He is one of the original developers of CONVERGE, an industry-leading CFD solver. He is Fellow of the Society of Automotive Engineers (SAE), Member of the executive committee of the American Society of Mechanical Engineers (ASME), ICE Division, Member of the board of advisors for the Central States Section of the Combustion Institute, and 2019 Recipient of the ASME Internal

Combustion Engine Award. Recently, he co-authored the book *Racing Toward Zero: The Untold Story of Driving Green*, available now from SAE.

## Contributors

**Avinash Kumar Agarwal** Engine Research Laboratory, Department of Mechanical Engineering, Indian Institute of Technology Kanpur, Kanpur, India

**Amer Amer** Transport Technologies Division, R&DC, Saudi Aramco, Dhahran, Eastern Province, Saudi Arabia

**Yanzhao An** State Key Laboratory of Engines, Tianjin University, Tianjin, China

**Jihad Badra** Transport Technologies Division, R&DC, Saudi Aramco, Dhahran, Eastern Province, Saudi Arabia

**Mike Bassett** MAHLE Powertrain Ltd., Northampton, UK

**Hugh Blaxill** MAHLE Powertrain LLC, Plymouth, MI, USA

**Elena Boulet** College of Physical Sciences and Engineering, Cardiff University, Cardiff, UK

**Marco Braun** Chair of Fluid Mechanics and Institute of Aerodynamics, RWTH Aachen University, Willnerstr. 5a, Aachen, Germany

**Pierre Bréquigny** Univ. Orléans, INSA-CVL, PRISME, Orléans, France

**Michael Bunce** MAHLE Powertrain LLC, Plymouth, MI, USA

**Patrick Burkardt** Chair of Fluid Mechanics and Institute of Aerodynamics, RWTH Aachen University, Willnerstr. 5a, Aachen, Germany

**Emre Cenker** Transport Technologies Division, R&DC, Saudi Aramco, Dhahran, Eastern Province, Saudi Arabia

**Graham Conway** Southwest Research Institute, San Antonio, TX, USA

**Adrian Cooper** MAHLE Powertrain Ltd., Northampton, UK

**Roger F. Cracknell** Shell Global Solutions (UK), Shell Centre, London, United Kingdom

**David Emberso** Department of Energy and Process Engineering, Norway University of Science and Technology, Trondheim, Torgarden, Norway

**Maximilian Fleischmann** Institute for Combustion Engines, RWTH Aachen University, Forckenbeckstr. 4, Aachen, Germany

**Laurence J. Fromm** Achates Power, Inc., San Diego, CA, USA

**Sandro Gail** Shell Global Solutions GmbH, Hamburg, Germany

**Dong Han** Shanghai Jiao Tong University, Shanghai, China

**Carl Hergart** Leyland Trucks Ltd., Leyland, Lancashire, UK

**Ponnya Hlaing** Clean Combustion Research Centre, King Abdullah University of Science and Technology, Thuwal, Saudi Arabia

**Zhen Huang** Shanghai Jiao Tong University, Shanghai, China

**Hong Im** Clean Combustion Research Centre, King Abdullah University of Science and Technology, Thuwal, Saudi Arabia

**Bengt Johansson** Combustion Engine Research Center (CERC), Chalmers University of Technology, Gothenburg, Sweden

**Ameya Joshi** Emerging Technologies & Regulations, Environmental Technologies, Corning Inc., Corning, NY, USA

**Gautam Kalghatgi** Oxford, UK

**Reinhold Kneer** Institute of Heat and Mass Transfer, RWTH Aachen University, Aachen, Germany

**Julian Knöll** Chair of Fluid Mechanics and Institute of Aerodynamics, RWTH Aachen University, Wüllnerstr. 5a, Aachen, Germany

**Felix Leach** Department of Engineering Science, University of Oxford, Oxford, UK

**Florian vom Lehn** Institute for Combustion Technology, RWTH Aachen University, Templergraben 64, Aachen, Germany

**Bastian Lehrheuer** Institute for Combustion Engines, RWTH Aachen University, Aachen, Germany

**Zhiqiang Li** State Key Laboratory of Engines, Tianjin University, Tianjin, China

**Chuntao Liu** State Key Laboratory of Engines, Tianjin University, Tianjin, China

**Yusen Liu** Shanghai Jiao Tong University, Shanghai, China

**Terese Løvås** Department of Energy and Process Engineering, Norway University of Science and Technology, Trondheim, Torgarden, Norway

**Minh Bau Luong** Clean Combustion Research Center, King Abdullah University of Science and Technology, Thuwal, Saudi Arabia

**Gaetano Magnotti** Clean Combustion Research Centre, King Abdullah University of Science and Technology, Thuwal, Saudi Arabia

**Luca Marchitto** STEMS, Italian National Research Council, Napoli, Italy

**Manuel Alejandro Echeverri Marquez** Clean Combustion Research Centre, King Abdullah University of Science and Technology, Thuwal, Saudi Arabia

**Agustin Valera Medina** College of Physical Sciences and Engineering, Cardiff University, Cardiff, UK

**Matthias Meinke** Chair of Fluid Mechanics and Institute of Aerodynamics, RWTH Aachen University, Aachen, Germany

**Christine Mounaïm-Rousselle** Univ. Orléans, INSA-CVL, PRISME, Orléans, France

**Nirendra Nath Mustafi** Department of Mechanical Engineering, Rajshahi University of Engineering & Technology, Rajshahi, Bangladesh

**Yiqiang Pei** State Key Laboratory of Engines, Tianjin University, Tianjin, China

**Nathan Peters** MAHLE Powertrain LLC, Plymouth, MI, USA

**Stefan Pischinger** Institute for Combustion Engines, RWTH Aachen University, Aachen, Germany

**Heinz Pitsch** Institute for Combustion Technology, RWTH Aachen University, Aachen, Germany

**Fabien Redon** Achates Power, Inc., San Diego, CA, USA

**Ashwin Salvi** Achates Power, Inc., San Diego, CA, USA

**Wolfgang Schröder** Chair of Fluid Mechanics and Institute of Aerodynamics, RWTH Aachen University, Wüllnerstr. 5a, Aachen, Germany; JARA Center for Simulation and Data, RWTH Aachen University, Seffenter Weg 23, Aachen, Germany

**Leif Schumacher** Institute of Heat and Mass Transfer, RWTH Aachen University, Augustinerbach 6, Aachen, Germany

**Jack Scrutton** Shell Global Solutions (UK), Shell Centre, London, United Kingdom; University of Bath, Claverton Down, Bath, United Kingdom

**Kelly Senecal** Convergent Science Inc., Madison, WI, USA

**Priybrat Sharma** Clean Combustion Research Centre, King Abdullah University of Science and Technology, Thuwal, Saudi Arabia

**Sai Krishna Pothuraju Subramanyam** MAHLE Powertrain LLC, Plymouth, MI, USA

**Cinzia Tornatore** STEMS, Italian National Research Council, Napoli, Italy

**James W. G. Turner** Clean Combustion Research Centre, King Abdullah University of Science and Technology, Thuwal, Saudi Arabia

**Gerardo Valentino** STEMS, Italian National Research Council, Napoli, Italy

**Tim Wegmann** Chair of Fluid Mechanics and Institute of Aerodynamics, RWTH Aachen University, Willnerstr. 5a, Aachen, Germany

# Chapter 1

## Introduction to Engines and Fuels for Future Transport



Gautam Kalghatgi , Avinash Kumar Agarwal , Kelly Senecal,  
and Felix Leach 

**Abstract** Global transport is almost entirely powered by internal combustion engines (ICEs) and petroleum-derived liquid fuels. Currently, there are many efforts to move transport away from this energy system to reduce its carbon footprint. In addition, tailpipe emissions from ICEs have to meet increasingly stringent standards. However, all the alternatives, such as battery electric vehicles (BEVs), start from a very low base and face very serious barriers to unlimited and fast expansion and cannot completely displace ICEs for several decades to come. Hence it is also important to continue to improve ICEs to ensure the sustainability of transport. This volume considers some of these approaches, sustainable fuels, and methodologies like life cycle analysis (LCA) needed to assess the true impact of alternative approaches to power transport. This first chapter provides brief descriptions of the fourteen chapters that follow.

**Keywords** Internal combustion engines · Fuels · Life cycle analysis · Hybrid engines · Methanol · Ammonia

Modern societies depend critically on transport and mobility. Currently, internal combustion engines (ICEs) power 99.8% of global transport, and petroleum-based liquid fuels account for around 95% of global transport energy. The demand for global transport energy is extremely large, with the *daily* demand for liquid fuels is around 11.5 billion litres (Kalghatgi 2014, 2018). Currently, the world has around 1.3 billion light-duty vehicles (LDVs) and 380 million heavy-duty vehicles (HDVs), but

---

G. Kalghatgi (✉)  
Oxford, UK

A. K. Agarwal  
Engine Research Laboratory, Department of Mechanical Engineering, Indian Institute of  
Technology Kanpur, Kanpur 208016, India

K. Senecal  
Convergent Science Inc., Madison, WI, USA

F. Leach  
Department of Engineering Science, University of Oxford, Oxford, UK

© The Author(s), under exclusive license to Springer Nature Singapore Pte Ltd. 2022  
G. Kalghatgi et al. (eds.), *Engines and Fuels for Future Transport*, Energy, Environment,  
and Sustainability, [https://doi.org/10.1007/978-981-16-8717-4\\_1](https://doi.org/10.1007/978-981-16-8717-4_1)

LDVs account for only about 45% of global transport energy (Kalghatgi 2014, 2018). In the next 20–30 years, the worldwide demand for transport is expected to increase primarily in the non-OECD countries. There are great efforts and many initiatives to reduce the carbon footprint of transport and tailpipe emissions that have to meet increasingly stringent standards. Transport energy is expected, on current trends, to still come substantially (>80–90% by 2040) from petroleum-based fuels because alternatives such as electric vehicles and sustainable fuels start from a negligible base and cannot grow fast enough or without constraints (Kalghatgi 2014, 2018). There is also significant scope for improving the efficiency and environmental impact of ICEs (Leach et al. 2020; Kalghatgi 2015b). Indeed, the sustainability of the global transport sector cannot be ensured without improving internal combustion engines, though alternatives such as battery electric vehicles (BEVs) will undoubtedly increase (Kalghatgi 2014, 2015a, b, 2018; Senecal and Leach 2021; Leach et al. 2020). All available technologies have to be sensibly deployed and continuously improved to maintain the sustainability of transport—the future is eclectic (Senecal and Leach 2021). It is also important that all the technologies need to be assessed honestly on a life cycle basis to ensure that the claimed benefits are actually delivered, and the greenhouse gas (GHG) emissions and health impacts are not simply displaced elsewhere, from where the vehicle is used.

This book has fourteen other chapters, apart from this one, mostly authoritative reviews from experts in the field, addressing various aspects of developments in this field. This chapter gives a brief overview of these chapters.

The second chapter—“**Sustainable Transport**”—discusses many of these themes and makes a case for a fact-driven, decisive approach, keeping multiple options open. It calls for a diverse mix of low-carbon technologies to be pursued rather than betting on a single technology like battery electric vehicles—an eclectic future.

Minimising the tailpipe emissions is as important as reducing the GHG impact of transport. Indeed, vehicles have to meet increasingly stringent emissions regulations to be allowed to operate. The third chapter, “**A Review of Emissions Control Technologies for On-Road Vehicles**”, addresses this essential aspect of vehicle and engine technology. It makes the interesting point that attention is shifting to other emissions sources such as brake and tire wear, signalling that the battle against tailpipe emissions is nearly won.

Opposed Piston (OP) engines offer the prospect of very high efficiency and near-zero levels of criteria emissions with conventional after-treatment system configurations. The fourth chapter, “**Opposed-Piston Engine Renaissance: Low CO<sub>2</sub> and Criteria Emissions**”, provides an overview of OP engine design characteristics and summarises actual test results for heavy-duty diesel engines while using conventional underfloor after-treatment systems (DOC/DPF/SCR/ASC). The results show peak brake thermal efficiency greater than 49%; engine-out soot 75% lower than a benchmark 15L four-stroke conventional engine; tailpipe NO<sub>x</sub> 96% lower than 2020 EPA regulations; 65% lower than California’s 2027 ultra-low NO<sub>x</sub> regulation (on the FTP cycle).

The fifth chapter, “**An Overview of Hybrid Electric Vehicle Technology**”, reviews another extremely important approach to improving the sustainability of

transport through partial electrification, promising improvements in fuel consumption and emission rates with a performance comparable to the conventional vehicles. The performance of a hybrid electric vehicle (HEV) depends on the powertrain type, components configuration and energy management strategy (EMS). This chapter presents an overview of essential components used in HEVs, including the energy storage system (i.e. the battery, super-capacitor, and fuel cell), electric motors, and DC-DC/DC-AC converters and their size/capacity optimisation. It also discusses emissions of HEVs under actual operating conditions and key issues and challenges of HEV technology.

The sixth chapter, “**Life-Cycle Analysis for the Automotive Sector**”, addresses an extremely important aspect that regulators and policy makers currently ignore in choosing the optimum technology to minimise GHG emissions. For instance, for battery electric vehicles (BEVs), mining for raw materials and then manufacturing them into vehicle and powertrain components create embedded emissions. Production of fuel or electricity generates emissions, and the vehicle end-of-life also impacts total emissions depending on scrappage or recycling processes. To accurately account for these stages, a life-cycle analysis (LCA) is required. The chapter reviews several LCA studies and identifies commonly used assumptions, variations on assumptions, and their impact on conclusions. Finally, a set of recommendations for future LCA work is presented.

The seventh chapter, “**Pre-chamber Combustors: An Enabling Technology for High Efficiency, Low CO<sub>2</sub> Engine Operation**”, discusses a promising approach to ignite dilute/ lean mixtures in engines to improve efficiency. It examines applications and benefits of pre-chambers, including knock reduction in high specific output downsized engines and lean limit extension in high-efficiency engines. Fundamental barriers to pre-chamber engine adoption are discussed. Amongst the topics addressed: pre-chamber geometry optimisation that spans the full engine map, in-pre-chamber mixture preparation, low load and idle stability and ensuring sufficient spark retard for catalyst light-off. Pre-chamber engines can also be ideal platforms for future fuels, including low carbon fuels such as hydrogen with highly specific operating requirements. The role of the pre-chamber engine in future transport and its potential for facilitating significant decarbonisation of the sector is discussed.

The eighth chapter, “**Pathway to Ultra-Lean IC Engine Combustion: Narrow Throat Pre-chamber**”, continues with this theme. A narrow throat pre-chamber as an ignition source allows extending the lean limit through a robust multi reactive jet ignition and in-cylinder turbulence generation. Metal engine studies coupled with optical engine studies involving high-speed visualisation and laser diagnostics offer a better understanding of this combustion mode. This chapter evaluates and summarises recent advances in pre-chamber combustion research.

The ninth chapter, “**Active Pre-chamber with Bio-Hybrid Fuels**”, describes a research study using the bio-hybrid fuels such as ethyl acetate in an active pre-chamber system. Single-cylinder engine experiments are coupled with optical diagnostics and numerical modelling to understand the combustion process. Additional optical experiments on a rapid compression machine provide insights into the ignition inside the pre-chamber and the subsequent combustion in the main chamber.



Ammonia is being studied as a carbon-free fuel for internal combustion engines. Ammonia has a higher volumetric energy density than gasoline and is easier to produce, store, and transport than other carbon-free fuels. However, ammonia-fueled applications exhibit lower efficiency and stability than conventional-fueled systems due to ammonia's lower flame speed and combustion temperatures. Chapter 10, "**The Use of Ammonia as a Fuel for Combustion Engines**" and Chap. 11, "**Ammonia as Fuel for Transportation to Mitigate Zero Carbon Impact**", both review previous and ongoing studies, exploring the potential of ammonia as an ICE fuel. The literature where ammonia has been used on its own or with other fuels in SI, CI and HCCI engines is reviewed. The strategies to overcome the shortcomings of ammonia as an engine fuel are discussed.

Chapter 12, "**Methanol as Fuel for Internal Combustion Engine**", is a comprehensive review of methanol as an ICE fuel. It covers the production of methanol and the well-to-wheel GHG emissions of different approaches to producing methanol. It reviews the history of methanol engines, stretching back over 100 years, and using methanol on its own and with other fuels in ICE. The advantages and disadvantages of methanol as an engine fuel are discussed, and the need for road testing in practical modern engines is identified.

Chapter 13, "**Technologies for Knock Mitigation in SI Engines—A Review**", reviews the literature on strategies used to overcome knock, which limits SI engine efficiency. Optimised combustion chamber geometry shapes and combinations of methodologies have been proposed for a reduced combustion time, water injection, cooled exhaust gas recirculation, and changes in the engine cooling systems have been applied to enhance end gas cooling, are some of the methods used to mitigate knock. The use of knock resistant fuels such as alcohols are also discussed.

Knock onset is determined by chemical kinetics of the fuel-air mixture ahead of the flame front as it is subjected to increasing pressure and temperature during the engine cycle. Reliable chemical kinetic models greatly assist the prediction of knock onset. However, practical fuels are too complex for such models to be developed, and simple surrogates, which can be more accurately modelled but are good substitutes for actual gasoline, are needed. Chapter 14, "**Explicit Equations for Designing Surrogate Gasoline Formulations Containing Toluene, n-heptane and iso-pentane**", describes the development of one such surrogate.

Finally, Chap. 15, "**Prediction of Ignition Modes in Shock Tubes Relevant to Engine Conditions**" describes a theoretical approach to the prediction of ignition modes in shock tubes. This is relevant to understanding pre-ignition in SI engines which can lead to very high knock intensities in downsized, turbocharged SI engines and limits this approach to improving SI engine efficiency.

We hope readers interested in transport, mobility, internal combustion engines, and new fuels find this collection of mostly review articles a useful resource.

## References

- Kalghatgi GT (2014) The outlook for fuels for internal combustion engines. *Int J Engine Res* 15:383–398
- Kalghatgi G (2015a) Petroleum-based fuels for transport. *J Automotive Safety Energy* 6(1):1–16. <https://doi.org/10.3969/j.issn.1674-8484.2015.01.001>
- Kalghatgi GT (2015b) Development of fuel/engine systems—the way forward to sustainable transport. *Engineering* 5:510–518
- Kalghatgi GT (2018) Is it really the end of internal combustion engines and petroleum in transport? *Appl Energy* 225:965–974
- Leach F, Kalghatgi G, Stone R, Miles P (2020) The scope for improving the efficiency and environmental impact of internal combustion engines. *Transp Eng* 1. <https://doi.org/10.1016/j.treng.2020.100005>
- Senecal K, Leach F (2021) Racing toward zero: the untold story of driving green. SAE International

# Chapter 2

## Sustainable Transportation



Carl Hergart

**Abstract** The past century has seen a remarkable rise in personal mobility and heavy goods transport. The development of the internal combustion engine has played a pivotal role in this development. Significant progress has been made in improving engine efficiency and reducing emissions. However, further improvements are necessary in order to meet local zero emission regulation as well as global climate goals. A rapid transition to renewable energy sources is key, enabling clean electricity generation and widespread deployment of sustainable fuels. Every country has a role to play. Developing nations must learn to become less dependent on fossil fuels as they grow their economies and industrialized nations must continue their sustainability journey and quickly transfer critical knowledge and lessons learned. Technologies should be assessed in terms of their life cycle impact and not simply their tailpipe emissions. As we consider the wide range of disparate applications across the transportation sector, we would be wise to embrace a fact-driven approach, keeping multiple options open and to build on past successes. Rather than betting it all on a single technology, a diverse mix of low-carbon technologies should be pursued.

**Keywords** Sustainability · Life cycle assessment · Internal combustion engines · Battery electric vehicles · Fuel cells · Hybrids

### 2.1 Setting the Scene

This book discusses a range of technologies relevant to transportation, including recent developments in combustion, alternative fuels and electrification. The purpose of this chapter is to provide some background and context for these topics and offer a perspective on sustainable transportation.

---

C. Hergart (✉)  
Leyland Trucks Ltd., Leyland, Lancashire, UK  
e-mail: [Carl.Hergart@Leyland-Trucks.co.uk](mailto:Carl.Hergart@Leyland-Trucks.co.uk)

© The Author(s), under exclusive license to Springer Nature Singapore Pte Ltd. 2022  
G. Kalghatgi et al. (eds.), *Engines and Fuels for Future Transport*, Energy, Environment,  
and Sustainability, [https://doi.org/10.1007/978-981-16-8717-4\\_2](https://doi.org/10.1007/978-981-16-8717-4_2)

### **2.1.1 Brief History**

The history of transportation is as old as our need to explore the world around us. Early human migration some 100,000 years ago prompted the need for a robust means of transportation. Shoes, rafts, dugout canoes and the domestication of the horse were all important early developments prior to the groundbreaking invention of the wheel around 3500–4000 years BC (Anthony 2010). As we learned to master transportation on land and over the seas, doing so quickly and conveniently became important. Instead of pulling carts and wagons by hand or using horses and oxen, we started looking for some sort of machine. Such a contraption emerged in 1712 when Thomas Newcomen successfully demonstrated continuous power transmission of his atmospheric (steam) engine (Morris 2012). The subsequent improvement by James Watt in 1776 laid the foundation for the industrial revolution. Steam engines were initially adopted by ships and became fundamental to the birth of the railways.

Towards the latter half of the nineteenth century, as means to motorize coaches and carriages were explored, the steam engine and the electric motor were obvious candidates. However, by then another interesting technology had started to gain momentum: the internal combustion engine. It offered higher power density and efficiency than steam and better range than electric. While the new technology relied on a fuel less abundant at the time than coal and electricity, it was ultimately deemed the best choice to power the rapidly growing automotive industry.

Mass industrialization quickly followed when Henry Ford brought together the concepts of the moving assembly line, overhead conveyers and a unified production plant. From its introduction in 1908 until 1927, over 15 million Model T's were sold and significantly increased the mobility of society as a whole (Floyd 1955). As the market matured, customers started to place increasing emphasis on form to go along with the function, demanding variety and annual model updates. With Ford initially being reluctant to broaden its portfolio beyond the Model T, General Motors, with their slogan “a car for every purse and purpose” rapidly gained market share. In his excellent book (Sloan 1980) Alfred Sloan gives a first-hand detailed account of the early growth of the automotive industry, establishing many of the foundational pillars we take for granted today, such as financing, trade-ins, dealer networks, overseas operations and organized research and development.

The growing number of vehicles drove the need for a supporting infrastructure, including roads, fueling stations and a service network. The early cars drove almost exclusively on dirt or gravel roads. Today, there are about 250 million vehicles just in the United States, supported by over 4 million miles of paved road and about 150,000 fueling stations (U.S. 2020; Outlet and Survey 2018). Of the roughly 1.5 billion vehicles on the roads today worldwide, 99% of them are powered by internal combustion engines consuming around 50 million barrels of oil equivalent (BOE) every day (International Energy Agency 2021).

### **2.1.2 Environmental Impact**

The environmental impact of the early transportation solutions was not immediately apparent, but already in the 1870s concerns were raised about the noxious smoke produced by steam locomotives. The very first underground railway, the City and South London Railway, actually prohibited the use of steam power, favoring electric locomotives (Duffy 2010).

In the 1940s a phenomenon referred to as smog started appearing in Southern California and Pennsylvania, causing stinging eyes and respiratory irritation. Haagen-Smit showed that the smog resulted from a photochemical reaction of unburned hydrocarbons, ground-level ozone and nitrogen oxides ( $\text{NO}_x$ ), originating from vehicle exhaust and industrial power generation (Haagen-Smit 1952). This groundbreaking discovery eventually led to the first vehicle emissions control system, positive crankcase ventilation, being introduced in 1961 in the State of California. Six years later the California Air Resources Board (CARB) was created and the Environmental Protection Agency (EPA) followed in 1970. In Europe, the European Economic Community (EEC) established rules, initially considerably less stringent than those in the United States, introduced in stages by engine displacement.

As regulations tightened, it became clear that the engine tuning required to meet the new emissions standards would incur an unacceptable fuel consumption penalty. This led to the invention of the catalytic converter, which was introduced on gasoline vehicles starting in 1975. The ensuing 35 years would see significant further emissions reduction resulting from several major developments including electronic engine control, advanced fuel injection systems, exhaust gas recirculation, sophisticated aftertreatment and combustion optimization. At the same time fuels became cleaner and better adapted to the engine. For example, gasoline fuels came to incorporate additives to inhibit engine knock and the amount of sulfur was limited in diesel fuel to ensure the durability of aftertreatment systems.

These efforts have been very effective in reducing the criteria pollutants  $\text{NO}_x$ , hydrocarbons (HC), carbon monoxide (CO) and particulate matter (PM), significantly improving the air quality in cities across the world. However, another issue has come to dominate the environmental debate: global warming.

### **2.1.3 Global Warming**

Global warming or the ‘Greenhouse effect’, as it is sometimes referred to, is a naturally occurring phenomenon resulting from certain gases in the atmosphere absorbing and emitting infrared radiation. These so-called Greenhouse Gases (GHGs) include water vapor ( $\text{H}_2\text{O}$ ), carbon dioxide ( $\text{CO}_2$ ), methane ( $\text{CH}_4$ ), nitrous oxide ( $\text{N}_2\text{O}$ ), and ozone ( $\text{O}_3$ ), as well as manufactured halocarbons, such as chlorofluorocarbons (CFCs). Their ability to absorb and emit infrared radiation goes back to their polyatomic structure, which gives them a dipole property and a vibration spectrum in

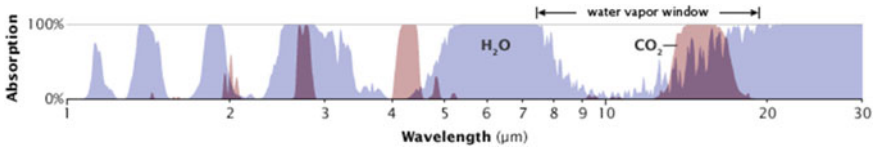


**Fig. 2.1** Absorption spectrum of water vapor and carbon dioxide (Lindsay 2009)

the infrared. Diatomic molecules such as oxygen and nitrogen—while vastly more abundant than the GHGs—do not absorb radiation in the infrared and consequently do not contribute to global warming. Without the greenhouse effect, Earth would be approximately 35 degrees Celsius cooler and unable to sustain life as we know it. Hence, the GHGs can be thought of as a kind of ‘thermostat’ that keeps us alive. Ozone also provides the benefit of absorbing the high-energy ultraviolet radiation from the sun, thus acting as an effective and life-saving sun screen.

In order to understand the significance of carbon dioxide in the global warming discussion it is important to recognize that Earth’s temperature is governed by a delicate balance between the incoming radiation from the sun, reflection by clouds and particles in the atmosphere, reflection from the surface of Earth and absorption by particles and molecules in the atmosphere (both incoming and outgoing). Any disturbance to the system, such as increased reflection through particles in the atmosphere or elevated absorption from gases in the atmosphere, will change the equilibrium and will result in a different temperature on Earth (Lindsay 2009). Figure 2.1 shows the absorption spectrum of water vapor and carbon dioxide, where 100% absorption means no radiation is getting through. Conversely, areas of low absorption are referred to as ‘atmospheric windows’, through which radiation can escape into space. We note that water is the dominant molecule in absorbing electromagnetic radiation in the infrared and is therefore mostly responsible for the heat being trapped in Earth’s atmosphere. However, it is the 12–15  $\mu\text{m}$  region in the infrared that is key to our understanding of the impact of  $\text{CO}_2$ . This is an area of the spectrum where water vapor does not absorb a lot of radiation, thus elevating the importance of  $\text{CO}_2$ . Moreover, this particular wavelength range happens to overlap with the peak of Earth’s surface radiation. Hence, elevated levels of  $\text{CO}_2$  effectively close this ‘water vapor window’ through which heat otherwise would escape.

Ice cores found in Vostok have allowed scientists to establish a correlation between  $\text{CO}_2$  and temperature, dating back some 800,000 years (Lüthi et al. 2008), see Fig. 2.2. Until around 1950, through multiple ice ages and times of warmer climate, the  $\text{CO}_2$  levels never exceeded 300 ppm. Since then, a sharp increase has been observed and as of August 2020 the atmospheric concentration of  $\text{CO}_2$  was 410 ppm (Lindsey 2020). It is generally accepted that this recent spike in  $\text{CO}_2$  has its origin in human activity and specifically the amount of  $\text{CO}_2$  released into the atmosphere.

Most of the  $\text{CO}_2$  is generated by the energy sector, whereas transportation is responsible for approximately 23% of the annual output (BP Energy Outlook 2020). When it comes to GHGs, the transportation contribution is even less, 14% (United States Environment Protection Agency (EPA) 2020). Hence, it is important to note

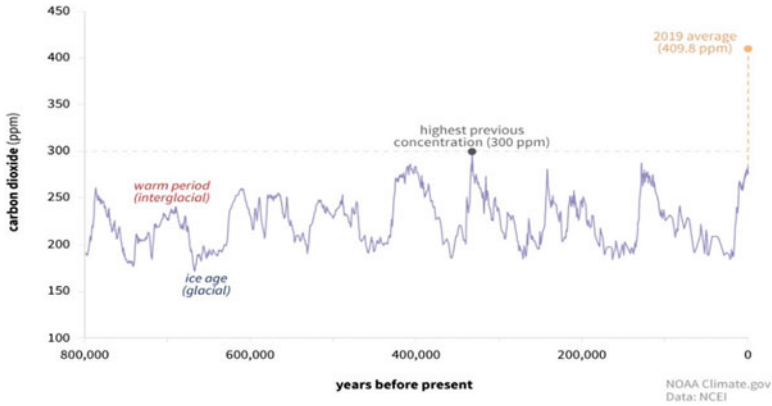


Fig. 2.2 Atmospheric CO<sub>2</sub> concentration measured at high resolution using preserved air samples from ice cores (Lindsey 2020)

that while CO<sub>2</sub> generated from vehicles indeed plays a significant role, it cannot alone solve the global warming problem. The goal of reducing CO<sub>2</sub> from transportation happens to be very well aligned with the objective of improving vehicle efficiency. The next section will review ways in which this can be accomplished.

## 2.2 Vehicle Efficiency Technologies

This book discusses a range of engine and powertrain technologies aimed at improving efficiency and sustainability. Regardless of the technology, there are a number of generic efficiency building blocks that are beneficial. This section will provide an overview of the key ones.

As seen in Fig. 2.3 (Stanton 2013), which shows the energy losses occurring in a

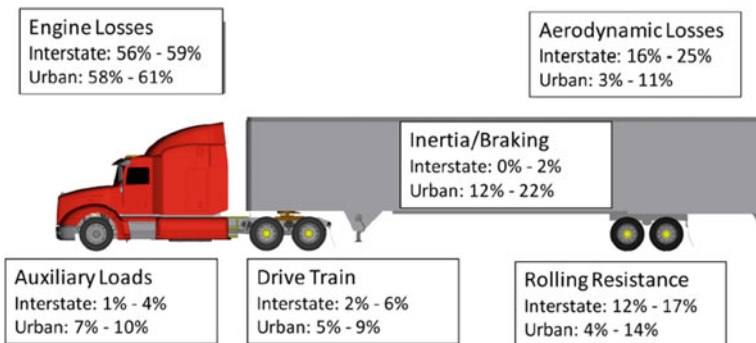


Fig. 2.3 Vehicle energy loss during long-haul and urban operation (Stanton 2013)

typical heavy-duty truck, aerodynamic losses account for 16–25% of the total energy loss during highway driving. Today’s trucks have come a long way in reducing drag thanks to technologies such as cab extenders, aerodynamic bumpers, tandem fairings, vented mud flaps, chassis skirts, side fairings and wheel well covers, just to name a few.

Rolling resistance is responsible for another 12–17% during highway operation. One of the most rapidly growing technologies adopted by fuel economy minded fleets today is tire pressure monitoring or inflation systems. Auxiliary loads, responsible for up to 10% of the total energy loss during urban operation, include air conditioning, power steering, cooling and lighting. Ways of reducing these losses will be discussed later when discussing mild hybridization. The overall energy required to move the vehicle is also heavily dependent on its weight. New materials enable lighter structures, but care has to be exercised in order not to sacrifice structural integrity and durability.

Another new and interesting way to reduce the vehicle energy requirement is to leverage connectivity and automation. Current examples include predictive cruise control for heavy-duty trucks, where GPS<sup>1</sup>-based terrain information is used to control vehicle set speed, such that fuel consumption is minimized. Over-The-Air (OTA) software updates are also being deployed across the industry to ensure vehicles have the latest controls and calibrations updates for optimal safety, reliability and efficiency. Vehicle platooning is yet another example, where two or more trucks are connected wirelessly, enabling optimization of the following distance through synchronization of braking and steering systems.

By leveraging Vehicle-to-X (V2X) connectivity, where ‘X’ can include things like traffic information, weather and infrastructure information (e.g. bridge heights and weight limits), vehicles can be ‘eco-routed’ in a way that minimizes overall energy use. The information generated from V2X can also be used to reduce the volume of trucks carrying empty or below capacity loads, as discussed by Hvolby et al. (2019).

With increased reliance on connectivity comes more stringent requirements for cyber security. New regulation is being introduced to reflect this as part of the UNECE Cyber Security regulation (United Nations Economic and Social Council 2020).

Whereas many of these technologies have been commercialized and are readily available, they are not universally adopted. In their 2019 annual fleet fuel study, the North American Council for Freight Efficiency (NACFE) concluded that truck fleets adopting efficiency improving technologies and practices achieved 14% better fuel economy than a ‘Business as Usual’ scenario (North American Council for Freight Efficiency 2019).

Figure 2.3 also shows that most of the vehicle losses occur in the powertrain (engine and drivetrain) and we will devote the next sub-sections to an introduction of the traditional powertrain topology featuring an internal combustion engine as well as alternative ones relying on full- or partial electrification.

---

<sup>1</sup> The Global Positioning System enables localization by triangulating information from satellites.



### 2.2.1 Internal Combustion Engine Powertrains

As mentioned in the introduction, the vast majority of vehicles on the roads today are powered by Internal Combustion Engines (ICE). The task of optimizing engine performance and efficiency is one of maximizing the yield from the chemical energy stored in the fuel. This requires a fundamental understanding of where the losses occur. Figure 2.4 shows a Sankey diagram of the energy flow in a heavy-duty truck equipped with a diesel engine during highway cruising. We note that 20–25% of the energy available in the fuel goes out with the exhaust flow. Part of this energy is used to drive a turbocharger and provides heat for the aftertreatment. The remainder is oftentimes referred to as ‘waste heat’ and presents an interesting opportunity to improve overall efficiency as will be discussed further below.

10–15% is lost through heat transfer during the combustion process. Insulating the combustion chamber, valves, ports and exhaust pipe have all been explored with various degree of success. The vision of an adiabatic engine remains elusive in spite of extensive research, as reported in Hergart et al. (2005).

**Waste Heat Recovery.** Two widely explored ways of recovering waste heat energy are turbocompounding and the Rankine bottoming cycle. Turbocompounding, as the name implies, involves “compounding” the power to the crankshaft by adding turbine shaft power to the power transferred through the pistons. The compounding power can come from an independent downstream power turbine or from the turbocharger turbine (Aghaali and Ångström 2015). Depending on the application and load cycle, turbocompounding can provide significant fuel economy improvement. However, the technology adds complexity and cost and thus represents a challenging business case for many applications. It is important to recognize that turbocompounding is not a drop-in solution. The engine turbocharger has to be re-matched to provide the

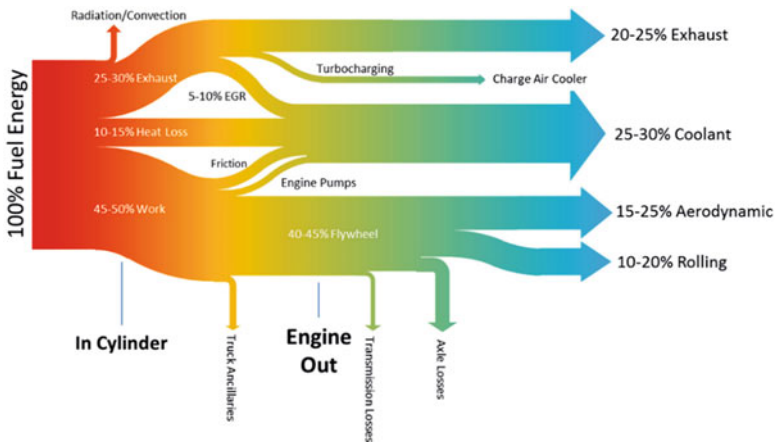


Fig. 2.4 Energy flow in a diesel engine during highway operation

required air flow and the combustion process has to be recalibrated to the new boost pressures. As the amount of energy extracted from the power turbine increases, the power of the reciprocating part of the engine typically goes down.

With the Rankine cycle, a working fluid undergoes a thermodynamic cycle, going from liquid to vapor and back to liquid, using exhaust waste heat and engine coolant. When the working fluid is an organic compound, the cycle is often referred to as the Organic Rankine Cycle (ORC), as opposed to the steam cycle used to describe the process when using water. ORC can provide up to 4% fuel economy improvement over a typical load cycle depending on how many waste sources are used.<sup>2</sup> Current industry developments are focused on reducing cost and complexity, providing attractive payback periods for customers adopting the technology (Xu et al. 2019).

**Engine Efficiency.** As shown in Fig. 2.4, 45–50% of the energy contained within the fuel can be used towards the propulsion of the vehicle. This represents the typical peak Brake Thermal Efficiency (BTE) of a modern diesel engine.<sup>3</sup> For gasoline engines, the BTE number is lower, primarily owing to the throttling losses associated with maintaining a stoichiometric fuel-air mixture and to a lesser extent due to the lower in-cylinder specific heat ratio and lower compression ratios required to prevent knock. Gasoline Direct Injection (GDI) has emerged as a means to increase the efficiency of gasoline engines, as discussed by Kalghatgi (2019) and Leach et al. (2020). Regardless of the fuel, increasing the brake thermal efficiency of the engine is of primary interest owing to its impact on the Total Cost of Ownership (TCO) for the vehicle operator and its direct impact on reducing CO<sub>2</sub> emissions.

The design of today's combustion chambers is the result of a century worth of practical experience enhanced by sophisticated high-fidelity simulations, optimizing parameters such as piston bowl shape, injector- and port geometry. Improvements in material properties have enabled friction reduction, increases in peak cylinder pressure and turbocharger speeds, ultimately increasing efficiency while complying with ever more stringent emissions standards. Figure 2.5 shows how the peak Brake Thermal Efficiency (BTE) of diesel engines in commercial trucks has evolved since 1960. The slight dip in efficiency around 2002 is attributed to the introduction of Exhaust Gas Recirculation (EGR), which required increasing the engine back pressure. Modern truck engines are almost 50% more efficient than their predecessors. Still, there is appetite for more. The U.S. Department of Energy established a goal of 55% BTE for the SuperTruck II program (Meijer and Grover 2020), which is also indicated in Fig. 2.5 with the dashed line. Focus areas for additional efficiency gains include improved combustion efficiency, e.g. through the use of Miller-cycle, increased turbocharger efficiency and reduced friction and parasitic losses.

---

<sup>2</sup> Potential energy sources for an Organic Rankine Cycle based waste heat recovery system include engine exhaust, EGR, engine coolant and charge air coolers.

<sup>3</sup> It is not unusual for large ship diesel engines, operating at constant speed and load, to achieve in excess of 50% BTE.

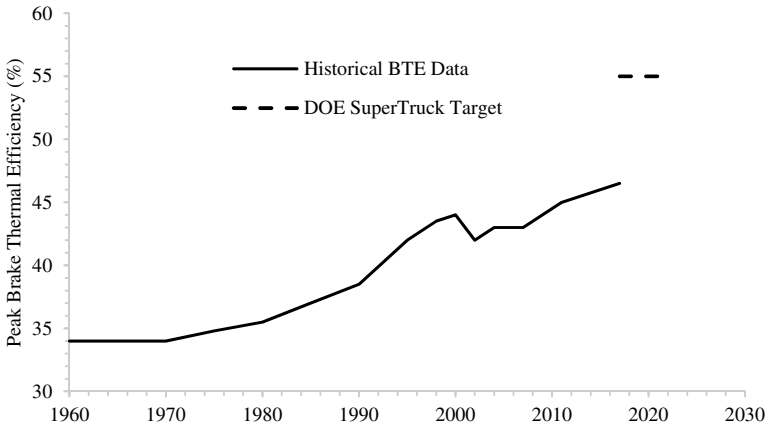


**Fig. 2.5** Historical evolution of peak engine Brake Thermal Efficiency (BTE) in heavy-duty truck engines along with the Department of Energy SuperTruck II target

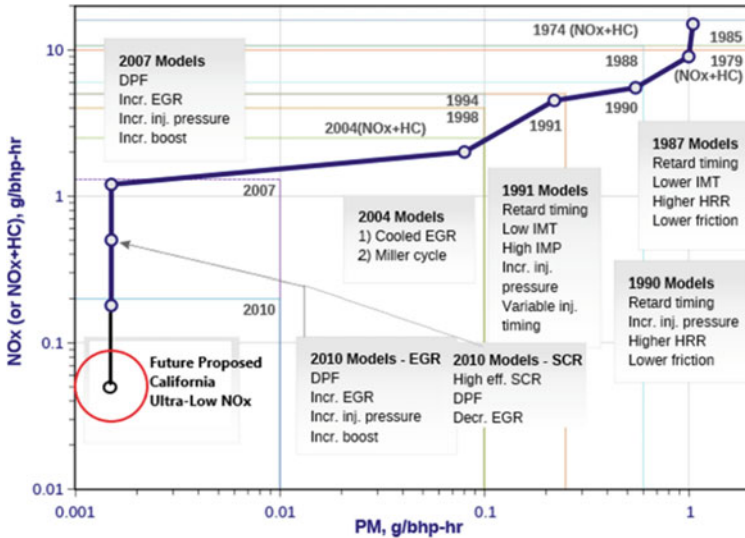


**Fig. 2.6** Evolution of Heavy-Duty on-road NO<sub>x</sub> and PM emissions in North America

**ICE Emissions Reduction.** The significant rise in efficiency has been accompanied by a remarkable reduction in criteria emissions.<sup>4</sup> Figure 2.6 shows the evolution of engine tailpipe Nitrogen Oxides (NO<sub>x</sub>) and Particulate Matter (PM) standards for Heavy-Duty diesel engines in North America over the past 50 years, along with the major key enabling technologies. From 1985 until 2002, Heavy-Duty on-road

<sup>4</sup> The criteria pollutants are carbon monoxide (CO), lead (Pb), nitrogen dioxide (NO<sub>2</sub>), ozone (O<sub>3</sub>), particulate matter (PM), and sulfur dioxide (SO<sub>2</sub>).

emissions standards in North America were largely achieved by optimizing and calibrating in-cylinder performance parameters. In 2002–2004 EGR was introduced and 2007 saw the widespread adoption of aftertreatment systems. Over the last three decades  $\text{NO}_x$  and particulates have been reduced by over two orders of magnitude. The mass of particulates originating from the combustion process is now less than that produced through tire wear and in some instances the exhaust from an engine is cleaner than the air coming into the engine (Reitz et al. 2020). Meanwhile, the efforts to reduce engine emissions continue unabated. California has proposed a new Ultra-Low  $\text{NO}_x$  rule to be phased in starting in 2024 (California Air Resources Board 2020) and the European Commission is considering more stringent legislation for Euro VII in the 2025–27 timeframe (ACEA 2020a).

Advanced aftertreatment will continue to play a key role in enabling these regulations to be met without negatively impacting efficiency and  $\text{CO}_2$ . Modern diesel engines are equipped with a system consisting of a Diesel Oxidation Catalyst (DOC), a Diesel Particulate Filter (DPF), a Selective Catalytic Reduction (SCR) catalyst and an Ammonia Slip Catalyst (ASC). These components have to be designed in such a way as to optimize the overall system efficiency, while meeting prevailing emissions standards. With future emissions regulation placing an increasing emphasis on low temperature performance during warm-up and low-load duty cycles, aftertreatment thermal management will become more challenging.

**Fuels.** It goes without saying that the type of fuel used in the engine has a major impact on the emissions. The vast majority of ICEs on the roads today use either gasoline or diesel, both being fossil fuels and thus contributing to global  $\text{CO}_2$  emissions. Natural gas has the potential to reduce  $\text{CO}_2$  by about 20% compared to diesel, but typically adds cost to the vehicle and struggles to meet the performance requirements. Biofuel and e-fuels represent two interesting options to reduce the carbon footprint of ICEs. While the respective chemistries involved in making them are fundamentally different, the common denominator is that  $\text{CO}_2$  is consumed in the production process.<sup>5</sup> In the case of biofuels, the  $\text{CO}_2$  is consumed by a plant or algae, whereas e-fuels rely on carbon capture. Both classes of fuels produce  $\text{CO}_2$  when they are burned and consequently give back the  $\text{CO}_2$  consumed during the production, thus making them overall carbon neutral. It is of particular interest to produce fuels that are sufficiently similar in their thermodynamic properties that they can be used as a drop-in replacement for either gasoline or diesel. As such, these fuels provide a tremendous opportunity to reduce the carbon footprint of the existing vehicle fleet. Hydrotreated Vegetable Oil (HVO) represents an excellent alternative available today to reduce the carbon intensity of diesel by a factor of 10 (Emission and Factors 2021). The challenge is that cheap renewable energy is not readily available, which is limiting the supply of these fuels.

There are also fuels that do not contain any carbon, such as hydrogen and ammonia. Both are subject to active research with hydrogen getting most of the attention currently. As an ICE fuel, hydrogen has proven to be quite competitive from an

---

<sup>5</sup> Assumes renewable energy is used in the production process.

efficiency perspective (Verhelst 2014) and the  $\text{NO}_x$  produced in the combustion process can be controlled through standard aftertreatment technologies. Most of the hydrogen discussion these days, though, revolves around fuel cells, owing to their potential for higher efficiency than hydrogen-powered ICEs.

Whereas hydrogen has the highest gravimetric energy density out of any fuel, its volumetric energy density is orders of magnitudes lower than gasoline and diesel. Because of this, fuel tanks need to store the hydrogen compressed, cryogenically or through the use of chemical or adsorptive bonds to solids or liquids—all very expensive methods.

It is also relevant to consider how the hydrogen is made. The three main production methods are coal gasification, steam methane reforming (SMR) and water electrolysis. Different “colors” are used as a terminology to distinguish between these methods (Senecal and Leach 2021). Brown or grey hydrogen is the result of coal gasification or SMR<sup>6</sup> and represents the vast majority (around 95%) of current global production, whereas green hydrogen is generated through water electrolysis using renewable energy. The color designation of the hydrogen is highly relevant when assessing the overall life cycle impact of hydrogen-based technologies. Regardless of the production method, the hydrogen itself is effectively the same, although certain methods may introduce undesired impurities.

**ICE powertrain integration.** In order to obtain optimum performance and efficiency, the internal combustion engine has to be properly integrated with the overall powertrain. Transmission and axle ratios have to be selected in such a way that overall performance requirements are met while maximizing the amount of time the engine spends operating in its most efficient region.

Powertrain downspeeding is an effective means to improving efficiency. However, whereas both axles and transmission clearly benefit from downspeeding, the situation is a bit more complicated in an engine. In a downspeed engine, the combustion takes place within a shorter crank angle window, which gets the overall process closer to the ideal thermodynamic constant volume cycle. The turbocharger also tends to operate more efficiently at reduced speeds. On the other hand, in order to maintain power output, a downspeed engine has to develop higher torque, which is typically accompanied by increased cylinder pressures and thermal loads. The core engine design and overall powertrain configuration become very important in the ability to benefit from downspeeding.

### 2.2.2 *Electric Powertrains*

A range of powertrains involving some level of electrification are receiving plenty of attention in recent years partly driven by the need to operate vehicles in zero emission

---

<sup>6</sup> SMR production of hydrogen can be made carbon neutral by capturing the  $\text{CO}_2$  produced. Hydrogen obtained this way is referred to as ‘blue hydrogen’.

mode within geofenced areas (Bannon 2030). In the following we will provide a brief overview of the following technologies:

- Mild hybrid
- Full hybrid
- Battery Electric
- Fuel Cell.

With regards to hybrids, the discussion will revolve around combinations of electric motors and internal combustion engines.

**Mild Hybrid.** A mild hybrid offers an interesting intermediate step between the conventional ICE powertrains and all-electric ones. A key attribute of the mild hybrid is the ability to power accessories, such as power steering, air conditioning compressor and water pump more efficiently by decoupling their operation from the engine. As electric propulsion is not the chief purpose of a mild hybrid, the motor can be kept small and compact and there is no need for a large battery pack. A key design decision for the mild hybrid is the position of the electric motor. Figure 2.7 shows the five major configurations in which to place the electric motor/generator.

The choice of configuration becomes a trade-off between cost, efficiency and feature capabilities. Table 2.1 summarizes some of the key attributes associated with

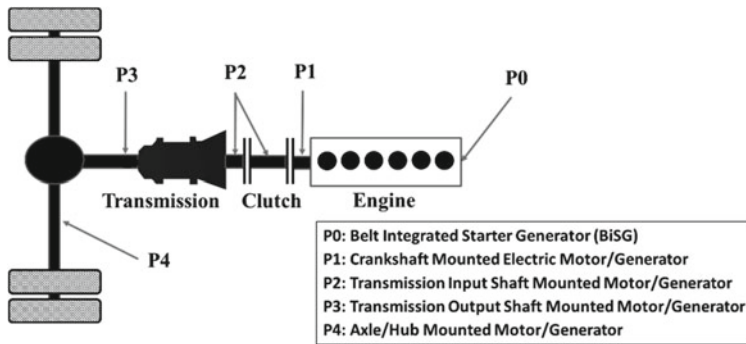


Fig. 2.7 Mild hybrid powertrain topologies

Table 2.1 Mild hybrid configurations and features

Topology	Stop/Start	Accessory electrification	Regen. braking	Torque assist	Engine-off coasting	All-electric propulsion	Torque vectoring
P0	●	●	●	●			
P1	●	●	●	●			
P2	●	●	●	●	●	●	
P3	●	●	●	●	●	●	●
P4	●	●	●	●	●	●	●

each concept. A P0 Belt integrated Starter Generator (BiSG) is a common and cost effective mild hybrid topology owing to its relatively minor impact on the existing vehicle architecture. However, it has limitations in the amount of fuel savings it offers and is not capable of engine-off coasting or all-electric propulsion.

Another attractive feature of a mild hybrid is the potential to provide thermal management to engine aftertreatment devices, which has become a highly relevant topic in light of the stringent regulation being imposed in Europe and North America, as discussed previously.

**Full Hybrid.** In a full hybrid, the electric motor takes on a more prominent role in the vehicle system by serving as tractive power source in addition to fulfilling all the tasks of the mild hybrid. As a consequence, full hybrids require much larger battery packs and electric motors. There are three main architectures: series, parallel and power-split, as shown in Fig. 2.8. All architectures are shown with an ICE below, but this can in principle be replaced by any type of primary energy converter. The choice of architecture depends on the application and comes with its own set of attributes. In a series hybrid the ICE is not directly connected to the drivetrain, but its output power is converted to electrical power used to charge the batteries via a generator. The energy in the batteries is used to power the electric motor, providing tractive power to turn the wheels. The decoupling of the ICE from the driveline allows the engine to operate at a more constant speed and load, which is beneficial from an efficiency and emissions standpoint and also avoids load transients. Furthermore, the engine can be switched off entirely, enabling all-electric operation. A series hybrid is sometimes referred to as a range-extender, since the ICE is effectively used to replenish the energy used by the batteries to power the electric motor. Because all traction power is provided by the batteries and the electric motor, these have to be sized accordingly, typically leading to a fairly large and expensive design. Furthermore, there is obviously an energy loss associated with converting mechanical energy into electrical and back to mechanical.

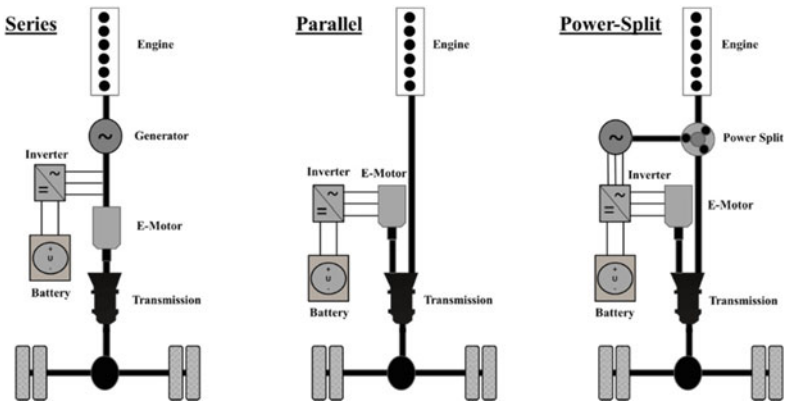


Fig. 2.8 Full hybrid architectures (left to right): Series, parallel and power-split

In a parallel hybrid, both the ICE and the electric motor are directly connected to the drivetrain and combine to provide the necessary traction power. This allows a level of powertrain optimization, such that, for example, the ICE is the primary power source during sustained highway driving, whereas the electric motor provides power during stop-and-go situations at low speeds. By splitting the duties of providing traction power, the power sources can be downsized. A smaller battery pack and electric motor typically translate into reduced overall cost and weight for a parallel hybrid than its series counterpart.

It is also possible to combine the two architectures into a series-parallel, or power-split hybrid, which aims to capitalize on the respective benefits of the series and the parallel. During low-speed, highly transient operation, the vehicle acts like a series hybrid, gradually transitioning to a parallel configuration during highway operation. This leads to increased complexity in the design and powertrain control and also requires a larger battery pack than the parallel hybrid.

A vehicle featuring the ability to charge the batteries from an external power source is called a Plug-In Hybrid Electric Vehicle (PHEV).

**Battery Electric Vehicle.** A battery electric vehicle relies solely on the electric power source for tractive power. The key components of an all-electric powertrain are the battery pack, electric motor, inverter and potentially a transmission depending on the application. The battery pack has to be sized to provide the desired range and have proper controls and thermal management to achieve adequate cycle life.

The voltage level is primarily dictated by the amount of power required, since the maximum current is effectively limited by the cost and weight of connectors and wires as well as the ability to route the cables. Higher current levels are also associated with winding losses.

A key architectural decision relative to all-electric powertrains is where to place the electric motor. There are broadly speaking three possibilities: Central Drive, e-axle and hub motors, as shown in Fig. 2.9. There are pros and cons associated with each. The central drive configuration retains the conventional driveline and axles and provides easy transmission packaging. An integrated e-axle benefits from a direct connection between motor, transmission and wheel ends, not requiring a bevel gear to connect a driveline to the rear axle. Consequently, e-axes have the potential of being

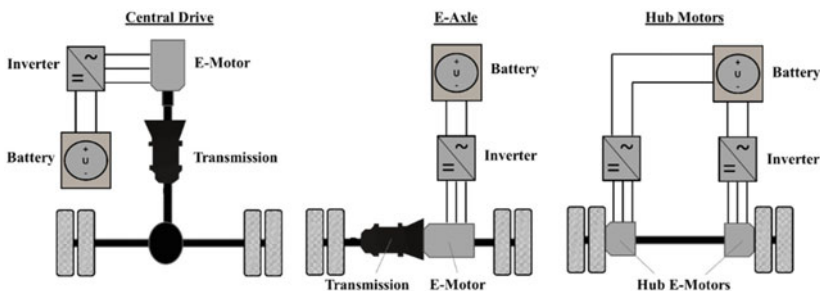


Fig. 2.9 Battery electric powertrain topologies (left to right): Central drive, e-axle and hub motors



a little bit more efficient than the central drive topology. However, challenges include un-sprung masses, vibration, hose- and wire flexing and packaging (especially when a gearbox is necessary). Hub motors are advantageous in terms of efficiency and also allow torque vectoring, but typically add cost.

Another key design decision is whether or not to connect a transmission to the electric motor. While less speed sensitive than diesel engines, the efficiency of electric motors does vary with speed and there are limits to their operation. The e-motor ratio defines the ratio between maximum and nominal motor speed. Depending on this ratio and the application requirements, a 1–4 speed transmission may be necessary. The most common motor types are Permanent Magnet Synchronous Machines (PMSM), Induction Magnet (IM), Synchro Reluctance (SynRel), and External Excited Synchro Machine (EESM). Of these the PMSM and the EESM typically offer the highest efficiency and power density, whereas the other types are more attractive in terms of cost.

**Battery Technology.** Choosing a battery starts with a clear understanding of the application. The amount of packaging space available determines the amount of capacity that can be accommodated for a given cell chemistry and form factor. The mission and duty cycle govern the necessary charge and discharge rates, which in turn have an impact on the amount of cooling required. The rate at which a battery is charged or discharged is characterized by the C-rate, defined as the battery power delivered divided by its energy capacity. Hence, a 10 kWh battery delivering 20 kW is being discharged at a C-rate of  $2\text{h}^{-1}$ . High C-rate capability ( $\sim 10$ ) is important in mild hybrid applications featuring stop-start. The need for high power density is also the reason for lead acid batteries being used in conventional vehicles to power e.g. the starter motor and the ignition system. Conversely, battery electric vehicle batteries are typically designed for C-rates between 0.5 and 1.

The lithium-ion battery has established itself as the dominant cell chemistry in battery electric vehicles. There is a wide range of different types, distinguished primarily by the type of material used for the cathode.<sup>7</sup> Figure 2.10 shows the trade-off between power and energy density for a range of different Li-ion battery types (Thelen and Bubna 2018). Nickel-Cobalt-Aluminum (NCA) and Nickel-Manganese-Cobalt Oxide (NMC) batteries have the highest energy density and are most common among battery electric passenger cars. Lithium-Titanate-Oxide (LTO) and Lithium-Manganese-Oxide (LMO) with their relatively high specific power are better suited for hybrid applications. There are several active efforts to increase the energy density, e.g. the Battery-500 consortium managed by PNNL, which aims to achieve 500 Wh/kg (Pacific Northwest National Laboratories 2021). Future chemistries (Li-Air, Al-Air, Zinc-Air) are expected to significantly improve specific energy and help the BEV/PHEV adoption, but currently suffer from limitations of the air cathode cycle life. Sodium-ion batteries are also being explored given concerns about the availability and cost of lithium (Fang et al. 2020). The use of solid-state electrolytes offers the potential for improved safety, energy density and faster charging capability.

---

<sup>7</sup> There are exceptions, such as the Lithium Titanate Oxide (LTO) battery, which is named after its anode material.

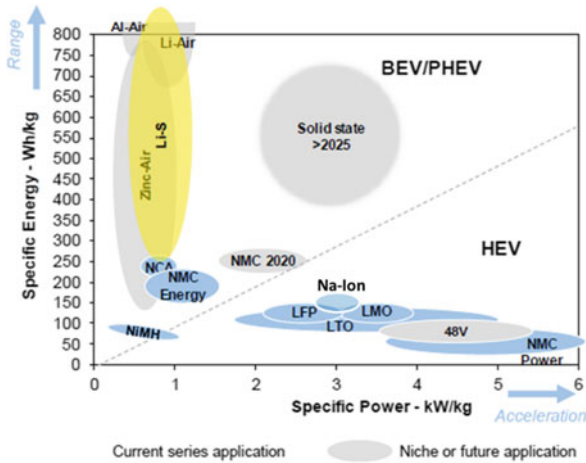


Fig. 2.10 Battery power vs. energy trade-off (Thelen and Bubna 2018)

However, the manufacturing is more complex and involve more hazardous materials (Advanced Propulsion Centre 2021a).

Battery cells, which typically have a voltage of 2–4 V each, are combined into modules and subsequently to packs. There are three main ways in which the cells are combined into modules: cylindrical, prismatic and pouch types. The choice effectively comes down to a trade-off between space utilization and thermal management. Cylindrical cells provides poor space utilization, but lend themselves to relatively straightforward thermal management. Prismatic cells make optimal use of the available space, but are more challenging to cool and are also less forgiving to cell swelling. Pouch cells are very flexible and provide excellent cell space utilization. However, they typically require some sort of support structure. Of the three types, pouch cells also suffer from the highest amount of swelling, which has to be taken into account in the thermal management and cell packaging.

Battery cost remains a major challenge. However, as seen in Fig. 2.11, significant progress has been made in recent years with further improvements expected as the installed capacity continues to grow.

**Fuel Cell Electric Vehicle (FCEV).** Similar to Battery Electric Vehicles (BEVs), Fuel Cell Electric Vehicles (FCEVs) rely on electricity to drive a motor, which provides propulsion power to the wheels. In that sense, the prior discussion on powertrain topology for BEVs applies here as well. However, unlike BEVs, FCEVs generate the electricity on-board and requires a continuous flow of reactants to sustain

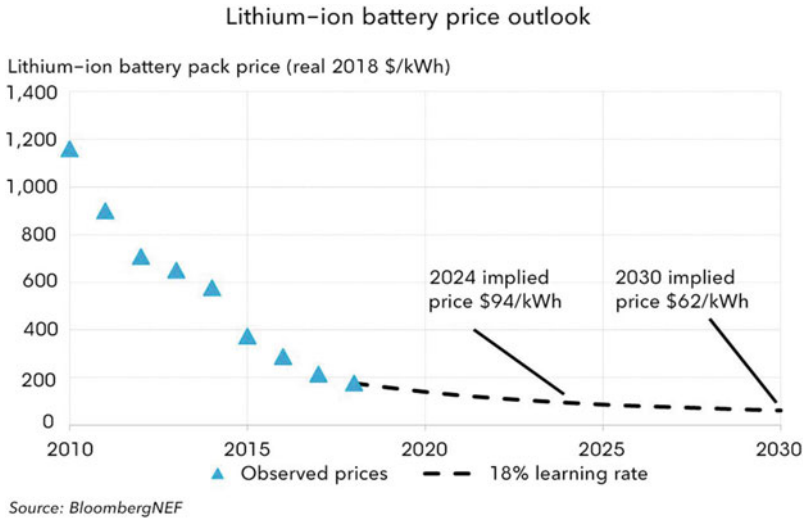


**Fig. 2.11** Li-ion battery pack price outlook (BloombergNEF 2018)

the operation. FCEVs therefore do not need nearly the amount of battery capacity that BEVs do.<sup>8</sup> This gives them an advantage in weight and fueling times.<sup>9</sup>

There are a number of different types of fuel cells, but they all feature an anode, a cathode and an electrolyte allowing charged ions to flow between the electrodes. In all but one (the solid oxide fuel cell), an oxidation reaction—assisted by a catalyst—occurs at the anode, generating positively charged ions and negatively charged electrons. The positively charged ions travel through the electrolyte, which is a semipermeable membrane that acts as an electrical insulator (O’Hayre et al. 2016). The electrolyte does not allow the electrons to go through, instead routing them through an electrical circuit from anode to cathode, thereby producing electricity. The type of electrolyte is used to classify the different kinds of fuel cells. The most commonly used fuel cell for automotive applications is the Polymer Electrolyte Membrane (PEM), also referred to as the Proton Exchange Membrane (PEM) type. Figure 2.12 shows a schematic of a PEM Fuel Cell (PEMFC) system. The heart of the fuel cell is the Membrane Electrode Assembly (MEA), which includes the membrane (electrolyte), the catalyst layers (electrodes), and Gas Diffusion Layers (GDLs). The latter facilitate transport of the reactants, i.e. hydrogen for the anode and oxygen for the cathode, into the catalyst layers. Because each MEA only produces a rather modest voltage, typically less than 1 V, several MEAs are connected in series to produce a fuel cell stack. Each MEA is separated by so-called Bipolar Plates (BPP) made of metal, carbon or composites, providing electrical conduction between cells and

<sup>8</sup> The presence of a battery is important in providing adequate transient response for the FCEV, since the fuel cell itself is limited in this respect.

<sup>9</sup> The time it takes to fill up a FCEV is comparable to that of an ICEV, whereas BEVs are an order of magnitude higher. However, proper pre-cooling of the hydrogen is required.

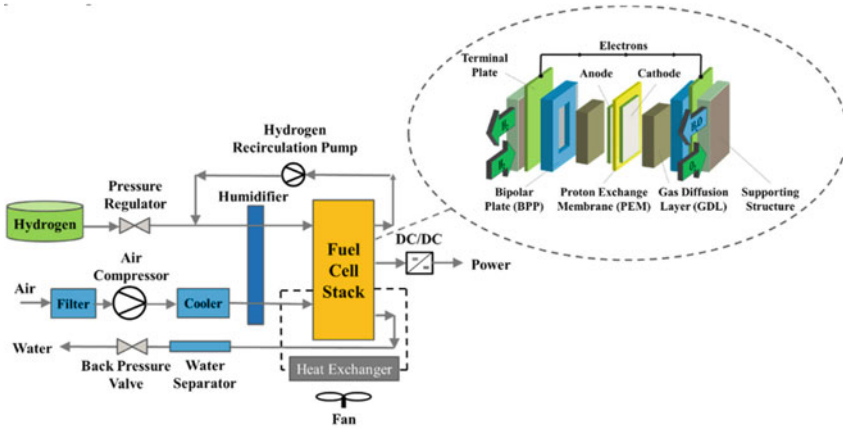


Fig. 2.12 Fuel cell system and stack schematic

strengthening the stack structure. Gaskets are also important parts of a fuel cell in order to prevent gas leaks.

In order to make the system work several other components are required, as shown in Fig. 2.12. These include, filters, valves, pumps, fans, compressors, humidifiers, controllers and DC/DC converters. Of the energy present in the hydrogen, roughly a third is lost to heat, which highlights the need for proper stack cooling. Another 5% or so is lost through membrane purging and leakage, such that the average stack efficiency is typically around 60%. The coolant pump and the air compressor consume about 5% of this, resulting in an overall system efficiency of around 55% (Sens et al. 2021). Efforts to improve the efficiency include reducing the electrochemical losses through optimized BPPs and GDLs and lowering power consumption of the system components. Increasing the operating temperature also have the potential to boost efficiency.<sup>10</sup> As a result of these developments, the efficiency is likely to improve in the future with some sources predicting 70% overall system efficiency in the next 15 years (Advanced Propulsion Centre 2021b).

Other major focus areas in the fuel cell research and development is to reduce cost and improve durability. The stack accounts for approximately 2/3 of the fuel cell system cost (excluding the hydrogen storage system) and efforts are underway to reduce the amount of Platinum Group Metals (PGM) used in the catalyst layers, finding cheaper materials for the BPPs and innovative GDL designs. However, the biggest potential lies in achieving economies of scale and optimized manufacturing. The worldwide number of fuel cell vehicles was about 23,000 in 2019, triple the figure in 2017 (International Energy Agency 2020). Continued growth will be necessary in order to sustain the cost reduction trend. This is of course also predicated by the

<sup>10</sup> Temperature control is very important for the fuel cell stack. The operating temperature for a PEMFC is the range of 50–100 °C, whereas it can be up to 1000 °C for a solid oxide fuel cell.

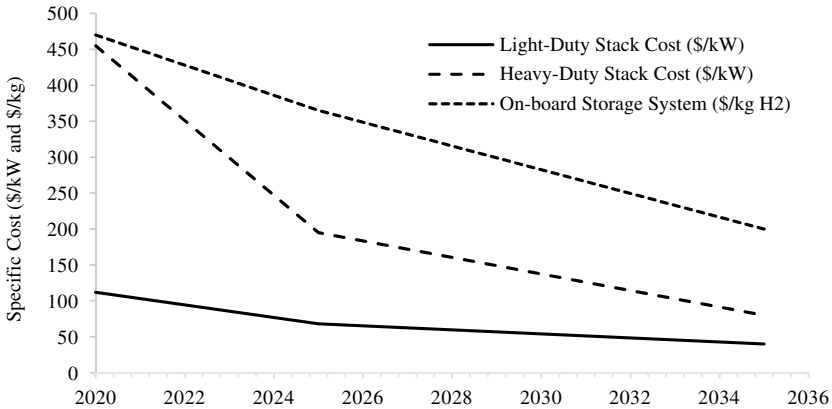


**Fig. 2.13** Key fuel cell component cost projections (Advanced Propulsion Centre 2021b)

availability of extensive hydrogen fueling infrastructure and competitive fuel prices (\$2/kg desirable vs. today's ~ \$14–16/kg).

Figure 2.13 shows the cost trends for light- and heavy-duty fuel cell costs along with the on-board storage. Hitting these targets will be essential in order to begin to rival the Total Cost of Ownership (TCO) of a vehicle powered by an internal combustion engine.

The durability of a fuel cell is impacted by the duty cycle, the thermal management and the design of the stack. In particular, catalyst aging leading to a reduction in active surface area can result in voltage loss over time. Impurities in the hydrogen may also impact catalyst performance and work is ongoing to reduce the sensitivity of the catalysts to such mechanisms. The current stack durability of 5,000 and 15,000 h, respectively for light- and heavy-duty applications will need to be further improved in order for the technology to gain widespread adoption.

## 2.3 The Way Forward

As the previous sections have shown, the history of transportation has been marked by significant progress, but also unintended consequences. Time and again, the transportation industry has responded to the challenges put forth by coming up with innovative solutions to further improve efficiency and reduce the environmental impact. As humanity faces its perhaps biggest challenge yet, posed by climate change, it is more important than ever for scientists and engineers across multiple disciplines to develop sustainable transport solutions and for policies to be guided by hard facts. Before entering into a discussion on potential solutions, it is useful to first clearly state the problem we are trying to solve. It can broadly be summarized as follows:

The amount of greenhouse gases added to the atmosphere needs to be reduced and eventually eliminated, such that we limit the temperature rise in the atmosphere and thus prevent anthropogenic climate change. Preferred transport solutions minimize greenhouse gases over the entire product life cycle and provide intermittent zero vehicle emission capability as required in geofenced areas while sustaining continued economic growth.

As a problem statement, it serves the purpose, but it lacks specificity. In order to be able to develop an effective strategy, we need to know the answers to questions like:

- By how much do we need to reduce GHGs? What areas need zero emission operation?
- How do we assess technologies in light of their GHG impact?
- How should the responsibility be divided among industry sectors and countries?
- Are the solutions we propose realistic, i.e. do they support continued economic growth and can they be achieved in time?
- By when do we need to have the solutions in place?

The objective of this section is to provide suggestions to these questions, positioning us to make some recommendations on the way forward towards a more sustainable future.

### ***2.3.1 The Carbon Budget***

To date 195 nations have signed onto the Paris Agreement (United Nations 2015), setting out a goal to limit global warming in this century to well below 2, preferably 1.5 degrees Celsius, compared to pre-industrial levels. The 1.5 degree figure was derived by the Intergovernmental Panel on Climate Change (IPCC), which stated that “with global warming of 1.5 degrees Celsius there would be increased risks to health, livelihood, food security, water supply, human security, and economic growth” (IPCC 2018). As we have seen from the opening section of this chapter, atmospheric temperature is intimately linked to the amount of GHGs. Specifically, the amount of additional CO<sub>2</sub> we can allow to go into the atmosphere prior to exceeding the previously discussed temperature target is referred to as the *carbon budget*. Estimates vary in the literature, but generally range between 200 and 600 billion tons of CO<sub>2</sub> equivalent. At the current rate of about 35 Billion tons of CO<sub>2</sub> being emitted annually, along with another 15 Billion tons coming from other GHG emissions (Ritchie and Roser 2020), it is clear that the carbon budget will be exhausted in the relative near term unless the global output is quickly reduced. This is confirmed by various atmospheric models, taking into account things like deforestation as well as biological and anthropogenic CO<sub>2</sub> emissions. Even the most optimistic scenarios only predict another 20 years until the carbon budget is exhausted (Hausfather 2018).

### 2.3.2 Carbon Intensity and Life Cycle Analysis

Any climate policy must be based on a good understanding of the sources of greenhouse gas emissions and what their relative contributions are. Carbon footprint is a commonly used term to characterize the amount of CO<sub>2</sub> directly or indirectly produced from human activities. As it pertains to transportation, carbon intensity is a good measure, defined as:

$$\text{Carbon Intensity} = \frac{\text{Carbon Dioxide Produced (g)}}{\text{Energy Consumed (kWh)}} \quad (2.1)$$

When considering the carbon intensity resulting from the various technologies we have discussed previously, it is important to look beyond the emissions generated during the use phase and consider the impact over the entire life cycle of the vehicle. Such a concept is referred to as a Life Cycle Assessment (LCA), and represents an ISO 14040/44 method to calculate the environmental impacts of products, covering the entire life cycle from cradle to grave, starting at the extracting and refining of raw materials and ending with the recycling of components and material. Figure 2.14 illustrates the different phases of LCA.

The amount of CO<sub>2</sub> generated in each stage varies significantly depending on the specific technology. Unfortunately, most of the debate today tends to revolve around the energy production, Well-To-Tank (WTW) and product use phase, Tank-To-Wheel (TTW). This is also reflected in the tailpipe focused CO<sub>2</sub> regulations being introduced in Europe and North America. And while the emissions originating from these phases are significant, dominant in many cases, disregarding the contributions from other stages of the life cycle results in a skewed picture and may in fact lead to the wrong conclusions. In a study commissioned by FVV, the German Research Association for Internal Combustion Engines, Bothe and Steinfort reviewed over 80 publications on LCA and concluded that there were not enough comprehensive studies that take all stages of the product life cycle into account (Bothe and

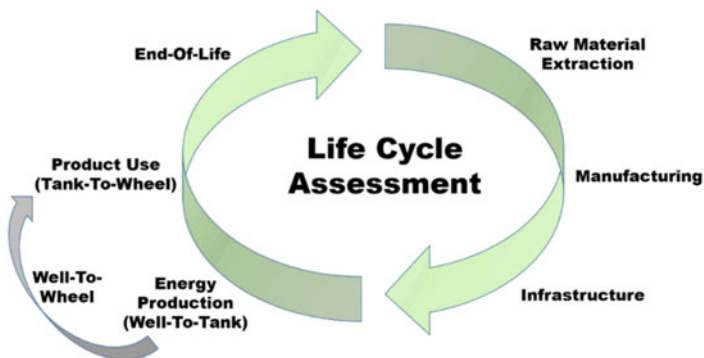


Fig. 2.14 Vehicle Life Cycle Assessment (LCA)

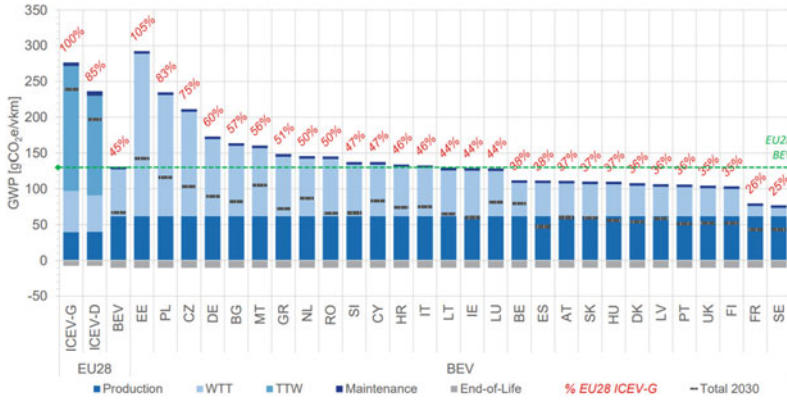
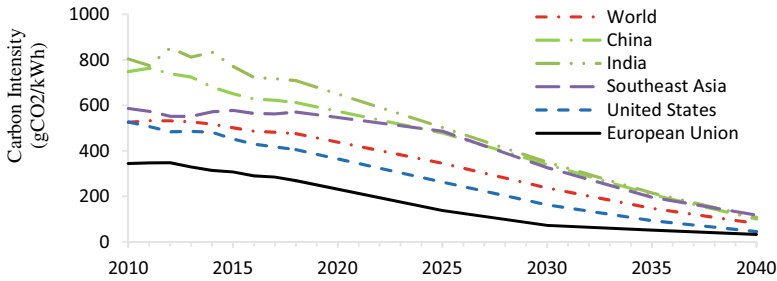


Fig. 2.15 Ricardo LCA analysis for European Commission (Ricardo 2020)

Steinfort 2020). Most of the literature reviewed centers around the ‘Well-to-Wheel’ (WTW) phases, which as discussed is only a subset of LCA. In particular, few studies focus on end-of-life emissions, and scarcer still are papers discussing the emissions related to the expanded infrastructure needs associated with new technologies. The FVV report compared a conventional diesel Internal Combustion Engine Vehicle (ICEV), a Battery Electric Vehicle (BEV), and a Fuel Cell Electric Vehicle (FCEV), concluding that lifecycle CO<sub>2</sub> emissions are similar across the three technologies. In a Ricardo report commissioned by the European Commission, Hill et al. (Ricardo 2020) noted that most studies tend to focus on passenger cars with relatively few covering commercial truck applications. Figure 2.15 compares the respective life cycle CO<sub>2</sub> emissions<sup>11</sup> from ICEVs burning gasoline and diesel against Battery Electric Vehicles (BEVs) using electricity from the various EU28 countries. The study suggests that in general, the BEV produces the lowest lifecycle CO<sub>2</sub> emissions, as a result of the considerably lower TTW contribution. However, in Poland the BEV is only marginally better than diesel and in Estonia it is worse. We also note that the BEVs are generally associated with the highest production stage CO<sub>2</sub> emissions. In fact, half of the BEV lifecycle CO<sub>2</sub> emissions may occur in the production phase. This contribution obviously grows with reduced vehicle Full Useful Life (FUL), as the emissions get spread across a lower mileage. Approximately half of the CO<sub>2</sub> generated during the BEV production phase is associated with the battery (Ricardo 2020). As noted by Amarakoon et al. (2013), the production of the cathode and electrolyte are particularly resource and manufacturing intensive. In an extensive Life Cycle-Impact Assessment (LCIA), they also concluded that the upstream materials extraction, processing and production of lithium-ion battery production has a non-negligible impact in terms of eutrophication potential (fertilization of surface waters through ammonia), ozone depletion (through production of aluminum for cathode material), ecological toxicity (freshwater contamination through use of steel

<sup>11</sup> Lifetime vehicle mileage of 225,000 km was assumed in this study.





**Fig. 2.16** Electricity grid average carbon intensity projections for various regions in the world (data compiled from Ritchie and Roser (2020))

in battery housing), and cancer and non-cancer hazard impact categories. End-of-Life material recovery is essential, since the extraction and processing of virgin materials are key contributors to these life cycle impacts. In particular, the extraction of lithium from salars<sup>12</sup> in Chile has received some attention in light of the potential impact on water supply and drought. Furthermore, mining of cobalt has raised ethical concerns, as more than half of the world's supply is extracted in the Democratic Republic of Congo, where child labor is still an issue (Posner 2020). The annual global production of cobalt increased by 60% over the last 10 years (U.S. 2020) and is destined for further growth as a result of accelerated adoption of BEVs.

With regards to fuel cells, the manufacturing process of the Membrane Electrode Assembly (MEA) is highly energy intensive and difficult to manage environmentally. Other focus areas for fuel cells from an LCA perspective is to reduce the amount of PGM required in the catalyst layers and the need for materials such as Carbon Fiber Reinforced Polymer (CFRP) composite for the tank (Advanced Propulsion Centre 2021b).

Regulation centered around Tank-to-Wheel or Well-To-Wheel contributions fail to capture circular economy aspects, not drawing sufficient focus to the importance of making battery and fuel cell production more sustainable. It is also clear that more studies are needed to adequately assess the contributions from supporting infrastructure, such as the electric vehicle charging and hydrogen fueling stations.

With increasing decarbonization of the electricity grid, the case for the BEV improves—all other things being equal. Figure 2.16 shows the carbon intensity electricity grid average in different regions of the world, including future projections. As already apparent from Fig. 2.15, there is significant stratification across individual countries. Li et al. (2020) notes that the carbon intensity varies between 200 and 1,200 g CO<sub>2</sub>/kWh across the different provinces of China. Actual carbon intensities associated with BEV charging may be considerably higher than the grid average in cases of coal power being used to generate the margin electricity. Weis et al. (2016) employ a consequential life cycle approach when comparing the emissions generated

<sup>12</sup> A salar is a salt desert resulting from raw material extraction from salt water.

by different technologies in order to capture the change in power plant operations due to charging of electric and plug-in vehicles.

Disregarding any infrastructure and End-of-Life (EOL) contributions, we may express the benefit of a BEV relative to a diesel ICEV as:

$$\Delta_{CO_2} = \left[ \left( \frac{M_{CO_2}^{ICE}}{D_{FUL}} + CI_{Diesel}^{WTW} \cdot \frac{37.85}{FE_{ICEV}} \right) - \left( \frac{M_{CO_2}^{BEP}}{D_{FUL}} + CI_{EV}^{WTW} \cdot W_{EV} \right) \right] \tag{2.2}$$

where  $\Delta_{CO_2}$  is the difference in grams of CO<sub>2</sub>/mile,  $M_{CO_2}^{ICE}$  and  $M_{CO_2}^{BEP}$  are the respective amounts (grams) of CO<sub>2</sub> generated in the production of a BEV and an ICEV,  $CI_{Diesel}^{WTW}$  (g CO<sub>2</sub>/kWh) is the WTW carbon intensity of conventional diesel,  $CI_{EV}^{WTW}$  (g CO<sub>2</sub>/kWh) is the grid carbon intensity,  $D_{FUL}$  (miles) is the distance associated with vehicle Full Useful Life,  $FE_{ICEV}$  is the ICEV fuel economy (miles per U.S. gallon) and  $W_{EV}$  is the energy consumption of the BEV (kWh per mile). Table 2.2 provides some representative values to enable the BEV CO<sub>2</sub> benefit over a diesel ICEV to be calculated.

The passenger car diesel fuel economy used in this example is equivalent to 129 g CO<sub>2</sub>/km, which is consistent with the data from the European Environmental Agency for newly registered vehicles (European Environment Agency 2021). The CO<sub>2</sub> resulting from the production phase is assumed constant here, but could be expected to reduce for both the diesel ICEV as well as the BEV, as a result of energy decarbonization. Figure 2.17 uses Eq. (2.2) along with the data from Fig. 2.16 and plots the CO<sub>2</sub> benefit of the BEV relative to a diesel ICEV as a function of time and region of the world. We note that the CO<sub>2</sub> emissions of the BEV actually exceed those of a diesel ICEV in many regions of the world until at least 2025. As previously mentioned, this is based on *average* grid densities and neglects consequential charging effects. This study emphasizes the need to decarbonize the energy supply, including the electricity grid. Only then do Battery Electric Vehicles and Fuel Cell Electric Vehicles truly offer a sustainable solution. With widespread access to renewable energy and increased availability of climate-neutral fuels, such as biodiesel and e-fuels, the ICEV baseline will also improve. As an example, an ICEV running on

**Table 2.2** Carbon intensity and energy comparison between a diesel ICEV and a BEV

	Diesel ICEV	BEV
Carbon Intensity (gCO <sub>2</sub> /kWh)	330 (Ricardo 2020)	See Fig. 2.16
Fuel Economy (mpg)	60	N/A
Energy Consumption (kWh/mile)	0.63	0.29 (Electric Vehicle and Database 2021)
Production Phase CO <sub>2</sub> (kg)	8,000 (Ricardo 2020)	16,000 (Ricardo 2020)
Vehicle Full Useful Life (miles)	120,000	120,000

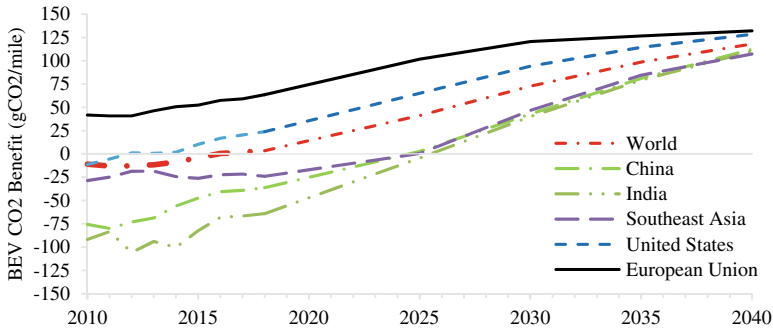


**Fig. 2.17** CO<sub>2</sub> advantage of battery electric vehicles over diesel internal combustion engines as a function of the average electricity grid carbon intensity based on Eq. (2.2)

Hydrotreated Vegetable Oil (HVO) has a carbon intensity of 31.5 g/kWh (Emission and Factors 2021), roughly one tenth of current fossil fuel based diesel.

### 2.3.3 A Global Solution to a Global Problem

As the name implies, global warming is an issue that transcends national borders. While every country has an important role to play, this does not mean the same solution will work universally. It is important to take a careful, nuanced approach that accounts for regional differences in energy supply, infrastructure and economic conditions.

It might be tempting to look to the countries primarily responsible for today's CO<sub>2</sub> emissions and argue that the lion share of the responsibility lies with them. For example, Fig. 2.18 shows that China is by far the highest emitter today with roughly 10 billion tons of CO<sub>2</sub>, representing 27% of the total global output (Ritchie and Roser 2020). However, if we instead consider cumulative emissions, the United States is by far the highest emitter (400 billion tons), followed by Europe (350 billion tons). Together, these two regions are responsible for almost 50% of the cumulative CO<sub>2</sub> emissions, historically. Clearly, the countries currently generating the bulk of the emissions do need to reduce their carbon footprint, but the developed nations have a critical role to play in transferring proven solutions, knowledge and applying lessons learned. The tremendous economic growth of the developed nations was powered by energy sources that historically produced high amounts of GHG emissions. With the threat of climate change coming into focus in these countries, important steps towards sustainability have already been taken, causing the annual CO<sub>2</sub> emissions to plateau and even decrease in the United States and Europe. While China will continue to play a key role, it is also important to recognize that over the coming decades an increasing share of the CO<sub>2</sub> emissions will come from other developing countries, as they embark on a journey towards economic prosperity.

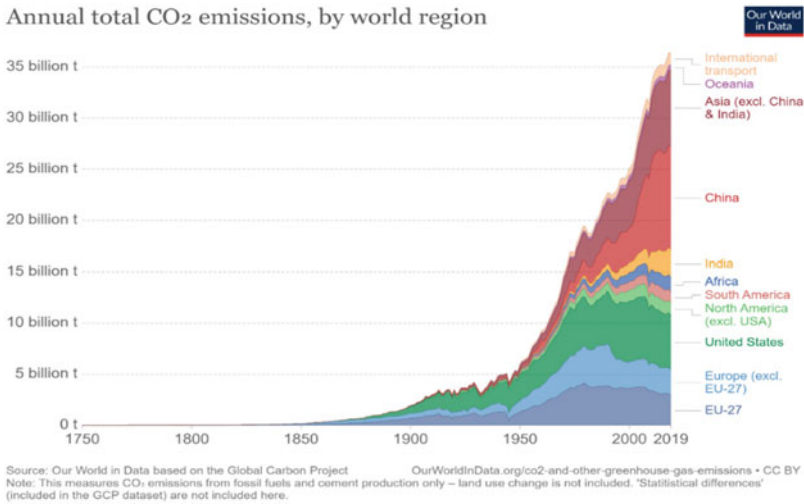


Fig. 2.18 CO<sub>2</sub> emissions by world region (Ritchie and Roser 2020)

Figure 2.19 reveals a strong correlation between CO<sub>2</sub> emissions and economic growth (Our World in Data 2021). Going forward, it is of vital importance that the developing world is able to build wealth without incurring the associated CO<sub>2</sub> emissions that accompanied economic growth in the developed nations. This is where careful consideration has to be given to prevailing local circumstances. As

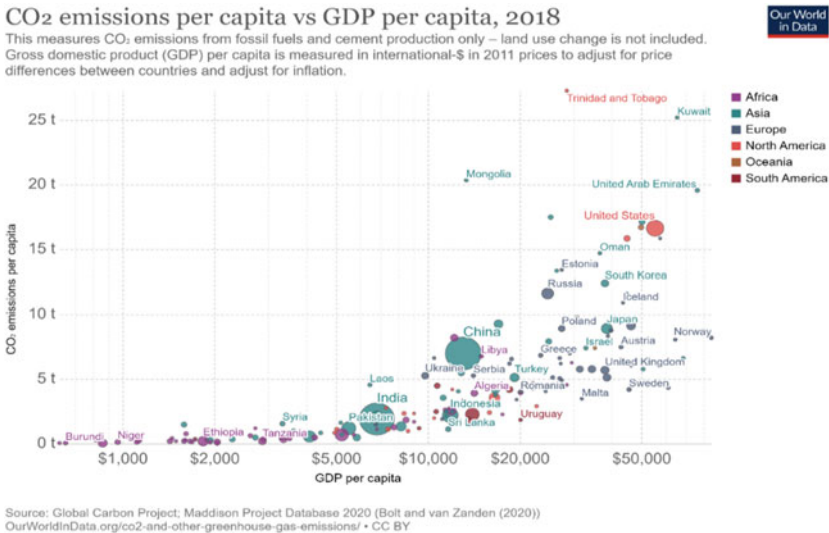


Fig. 2.19 CO<sub>2</sub> emissions per capita versus GDP per capita (2021)

an example, Africa today contributes less than 5% of total CO<sub>2</sub> output to the atmosphere. However, this number is likely to grow sharply in the future as an increasing number of people come out of poverty. The energy supply in Africa largely comes from fossil sources and biofuels (Ayompe et al. 2020). With an under developed and unreliable electricity grid, the right solution for Africa at this point in time is not widespread deployment of electric cars. A better first step would be to tighten the exhaust emissions regulations and ensure the cleanest and most efficient transport solutions are implemented in all segments of the market, removing high-polluting vehicles from the roads. This would have an immediate positive impact on carbon dioxide emissions while limiting disruption to local economies. In parallel, there needs to be a clear focus on decarbonizing the energy and electricity production. The investments associated with this are significant. Kalghatgi estimates that the world would need the equivalent of 3,100 nuclear power plants, each with an output of 3 GW, in order to replace 60% of the current fossil fuel use (Kalghatgi 2020). With the average age of vehicles being relatively high (>15 years) in many of the African countries, by far the least disruptive near-term option to reducing CO<sub>2</sub> would be drop-in biofuel and/or e-fuel replacements for regular gasoline and diesel. Incidentally, the Middle East and North Africa (MENA) region is very well suited to e-fuel production.

### ***2.3.4 One Size Doesn't Fit All***

Transportation covers a huge variety of applications which do not lend themselves equally to all technologies. Apart from the CO<sub>2</sub> emission aspects just discussed, the technologies obviously have to be economically viable. This is especially critical in commercial applications where the vehicle is a revenue generator. The reliability and durability requirements associated with commercial applications also differ significantly from automotive ones.

Using representative numbers for energy consumption, energy density and pack cost, it is straightforward to calculate the required battery capacity, weight, cost, and associated charge times for BEVs. The results of such an analysis are summarized in Table 2.3 for three different applications. For a battery electric passenger car with a range of 200 miles, the battery pack costs roughly \$8,000 and weighs about 460 kg. For many people this is considered acceptable, both from a range and cost perspective, especially when taking available incentives into account. Range/fueling anxiety, does become an issue when taking longer trips, but the majority of trips are less than 30 miles. However, let us consider a BEV that matches the range of a diesel-powered heavy-duty (HD) line-haul truck equipped with two 80-gallon (U.S.) tanks of diesel. Assuming 8 mpg, such a truck has a range of 1,280 miles. The equivalent battery electric truck would have to carry approximately 20 tons of batteries, far offsetting the weight benefit of removing the conventional powertrain, and sacrificing precious payload. Furthermore, the cost of the batteries would be around \$450,000

**Table 2.3** Battery comparison between passenger car and commercial applications

	Passenger car	MD truck	HD truck
Energy density (kg/kWh)	8	8	8
Battery cost (\$/kWh)	137	175	175
Energy Cons. (kWh/mile)	0.29	1	2
Charge rate (kW)	22	150	350
Battery capacity (kWh)	58	300	2,560
Battery cost (\$)	\$7,946	\$52,500	\$448,000
Range (miles)	200	300	1,280
Battery weight (kg)	464	2400	20,480
Charge time (h)	3	2	7

and would take around 7 hours to charge. This makes for a very challenging business proposition for heavy-duty line-haul applications to say the least.

For Medium-Duty (MD) applications with their more limited range and power requirements, there is a more attractive and nearer term business case. Depending on the assumptions made (e.g. electricity cost, annual mileage, fuel consumption and service), the medium-duty battery electric truck has the potential for a more reasonable payback.

With regards to fuel cells, a passenger car with a fuel economy of 70 miles per kg of hydrogen, achieves a range of 350 miles on a tank carrying 5 kg of hydrogen. Using the 2020 costs provided in Fig. 2.13, this results in about \$2,300 and \$14,000 for the tank and stack, respectively. Again, the heavy-duty case is very different. Using the range assumptions of Table 2.3, the hydrogen tank and stack costs would be \$75,000 and \$160,000, respectively, for a 350 kW heavy-duty truck getting 8 miles per kg of hydrogen.

Andersson and Börjesson (2021) identify a Plug-In Hybrid Electric Vehicle operating on HVO as an attractive alternative for automotive applications. The relatively small battery pack provides necessary range to comply with local zero emission regulation without generating significant CO<sub>2</sub> in the production phase.

### 2.3.5 Cause for Optimism

The task of reducing the carbon dioxide emissions in line with the Paris Agreement without stifling economic growth may seem daunting. However, as the preceding sections have shown, it is a well-defined problem for which we are looking to apply—to some extent—known solutions. The sources of the emissions are understood and we possess the tools to assess the impact of different technical solutions. Perhaps most importantly, we have a good grasp of the technologies to accomplish the task.

That said, progress relies on continued investment in research and development in all the technologies described in this chapter.

In parallel to deploying known technologies to reduce vehicle energy consumption, such as those discussed in Sect. 2.2, efforts to decarbonize the energy and electricity supply need to be aggressively pursued. Furthermore, it is important to focus on reducing the energy intensity associated with the production of batteries and hydrogen. Ample supply of renewable energy will substantially reduce the environmental impact from both conventional and electrified powertrains.

Optimized conventional powertrains are favored in developing countries, timing the introduction of battery electric and fuel cell vehicles to when coal and oil have been phased out as energy sources. The industrialized nations have a great responsibility—and opportunity—to transfer known technologies that will have an immediate impact.

CO<sub>2</sub> regulation is in place for both automotive and commercial applications in both Europe and North America. Europe's major truck manufacturers have pledged that all new trucks sold will be fossil free by 2040 with the goal of reaching carbon-neutrality by 2050 (ACEA 2020b). It also looks increasingly certain that a system will be created for emissions trading in European road transport. It is critical that the regulation be amended to capture the environmental impact over the entire product lifecycle.

There are past examples of effective global action to address environmental hazards. The agreement to curb emissions of chlorofluorocarbons<sup>13</sup> (CFCs) depleting the ozone layer is an example of swift global action. At its worst, in the late 1990s about 10% of the upper ozone layer was depleted. However, following the agreement to ban CFCs, signed by all nations in 1987, the ozone layer is expected to be fully restored by 2060. The consistent reduction in criteria pollutants from internal combustion engines over the last several decades (see Fig. 2.6), significantly contributing to reduce the smog in many major cities, is another success story demonstrating that green technologies do not have to compromise performance and economic growth.

The actions taken by the industrialized nations to curb CO<sub>2</sub> emissions have been effective and annual output is now decreasing in Europe and North America, as seen in Fig. 2.18. Global CO<sub>2</sub> emissions are expected to peak in 2035 (ExxonMobil Outlook for Energy 2019), but by quickly transferring lessons learned, we have an opportunity to accelerate the downward trend and help the developing world on their journey towards sustainable prosperity.

As we look ahead to our biggest environmental challenge yet, we would be wise to embrace a fact-driven, decisive approach, keeping multiple options open and build on past successes. Rather than betting it all on a single technology, we need to pursue a diverse mix of low-carbon technologies. In the words of Senecal and Leach (2021),

---

<sup>13</sup> Chlorofluorocarbons is a family of chemicals that has seen widespread use in refrigeration and as propellants in aerosol cans. Their role in destroying the ozone layer became widely known in the 1980s.

“the future is eclectic”. It is hard to imagine a more interesting time to be working in the transport industry.

## References

- ACEA (2020a) position paper: views on proposals for Euro 7 Emission Standard. [https://www.acea.auto/files/ACEA\\_Position\\_Paper-Views\\_on\\_proposals\\_for\\_Euro\\_7\\_emission\\_standard.pdf](https://www.acea.auto/files/ACEA_Position_Paper-Views_on_proposals_for_Euro_7_emission_standard.pdf)
- ACEA (2020b) European Automobile Manufacturers' Association: Joint Statement, The Transition to Zero-Emission Road Freight Transport
- Advanced Propulsion Centre (2021a) Electrical Energy Storage Roadmap. <https://www.apcuk.co.uk/technology-roadmaps/>
- Advanced Propulsion Centre (2021b) Fuel Cell Roadmap. <https://www.apcuk.co.uk/technology-roadmaps/>
- Aghaali H, Ångström H-E (2015) A Review of turbocompounding as a waste heat recovery system for internal combustion engines. *Renew Sustain Energy Rev* 49:813–824
- Amarkoon S, Smith J, Segal B (2013) Application of life-cycle assessment to nanoscale technology: lithium-ion batteries for electric vehicles. United States Environmental Protection Agency
- American Petroleum Institute Retail Outlet Survey (2018)
- Andersson O, Borjesson P (2021) The greenhouse gas emissions of an electrified vehicle combined with renewable fuels: life cycle assessment and policy implications. *Appl Energy*
- Anthony DW (2010) *The horse, the wheel, and language: how bronze-age riders from the Eurasian Steppes shaped the modern world*. Princeton University Press
- Ayompe LM, Davis SJ, Egoh BN (2020) Trends and drivers of African Fossil fuel CO<sub>2</sub> emissions 1990–2017. *Environ Res Lett* 15:124039
- Bannon E (2021) In cities 63% support EU ban on petrol and diesel car sales after 2030, transport & environment. <https://www.transportenvironment.org/press/cities-63-support-eu-ban-petrol-and-diesel-car-sales-after-2030>
- BloombergNEF (2018) Li-ion battery pack price outlook
- Bothe D, Steinfurt T (2020) Cradle-to-grave life-cycle assessment in the mobility sector. FVV
- BP Energy Outlook 2020 Edition, Accessed July 2021
- California Air Resources Board: Second Notice of Public Availability of Modified Text and Availability of Additional Documents: Proposed Amendments to the Heavy-Duty Engine and Vehicle Omnibus Regulation and Associated Amendments, August 2020
- Duffy MC (2010) *Electric railways, 1880–1990 (History and Management of Technology)*, Institute of Electrical Engineers
- Electric Vehicle Database (2021) Tesla model Y long range performance. Accessed July 2021
- European Environment Agency: Average CO<sub>2</sub> Emissions from Newly Registered Motor Vehicles in Europe. Accessed July 2021
- ExxonMobil (2019) *Outlook for energy: a perspective to 2040*
- Fang S, Bresser D, Passerini S (2020) Transition metal oxide anodes for electrochemical energy storage in lithium and sodium-ion batteries. *Adv Energy Mater* 10
- Floyd C (1955) *Henry's wonderful model T, 1908–1927*. McGraw-Hill, New York
- Haagen-Smit AJ (1952) Chemistry and physiology of Los Angeles Smog. *Ind Eng Chem Res* 44:1342–1346
- Hausfather Z (2018) Analysis: how much 'carbon budget' is left to limit global warming to 1.5C? Carbon Brief. <https://www.carbonbrief.org/analysis-how-much-carbon-budget-is-left-to-limit-global-warming-to-1-5c>
- Hergart CA, Louki A, Peters N (2005) On the potential of low heat rejection DI diesel engines to reduce tail-pipe emissions. SAE 2005-01-0920



- Hvolby H, Steger-Jensen K, Neagoe M, Vestergaard S, Turner P (2019) Collaborative exchange of cargo truck loads: approaches to reducing empty trucks in logistics chains. In: Ameri F, Stecke K, von Cieminski G, Kiritsis D (eds) *Advances in production management systems. Towards smart production management systems*. APMS 2019. IFIP advances in information and communication technology, vol 567. Springer, Cham. [https://doi.org/10.1007/978-3-030-29996-5\\_8](https://doi.org/10.1007/978-3-030-29996-5_8)
- International Energy Agency: Fuel cell deployment, 2017–2019, and national targets for selected countries. <https://www.iea.org/data-and-statistics/charts/fuel-cell-ev-deployment-2017-2019-and-national-targets-for-selected-countries>, June 2020
- International Energy Agency (2021) Oil Market Report. <https://www.iea.org/reports/oil-market-report-june-2021>. June 2021
- IPCC (2018) Summary for policymakers. In: *Global Warming of 1.5 °C. An IPCC Special Report on the impacts of global warming of 1.5 °C above pre-industrial levels and related global greenhouse gas emission pathways, in the context of strengthening the global response to the threat of climate change, sustainable development, and efforts to eradicate poverty* [Masson-Delmotte V, Zhai P, Pörtner H-O, Roberts D, Skea J, Shukla PR, Pirani A, Moufouma-Okia W, Péan C, Pidcock R, Connors S, Matthews JBR, Chen Y, Zhou X, Gomis MI, Lonnoy E, Maycock T, Tignor M, Waterfield T (eds.)] (In Press)
- Kalghatgi G (2019) Development of fuel/engine systems—the way forward to sustainable transport. *Engineering* 5:510–518
- Kalghatgi G (2020) Challenges of energy transition needed to meet decarbonisation targets set up to address climate change. *J Automotive Safety Energy* 11(3)
- Leach F, Kalghatgi G, Stone R, Miles P (2020) The scope for improving the efficiency and environmental impact of internal combustion engines. *Transp Eng* 1
- Li X, Chalvatzis KJ, Pappas D (2017) China's electricity emission intensity in 2020—an analysis at provincial level. In: 9th International conference on applied energy, ICAE2017
- Lindsay R (2009) Climate and earth's energy budget, NASA Earth Observatory. <https://earthobservatory.nasa.gov/features/EnergyBalance/page1.php>
- Lindsey R (2020) Climate change: atmospheric carbon dioxide. <https://www.climate.gov/news-features/understanding-climate/climate-change-atmospheric-carbon-dioxide>. Climate.gov
- Lüthi D, Le Floch M, Bereiter B, Blunier T, Barnola J-M, Siegenthaler U, Raynaud D, Jouzel J, Fischer H, Kawamura K, Stocker TF (2008) High-resolution carbon dioxide concentration record 650,000–800,000 years before present. *Nature* 453(7193):379–382. <https://doi.org/10.1038/nature06949>
- Meijer M, Grover B (2020) Development and demonstration of advanced engine and vehicle technologies for class 8 heavy-duty vehicle (SuperTruck II). DOE Annual Merit Review
- Morris CR (2012) *The dawn of innovation: the First American Revolution*, 1st edn. New York PublicAffairs
- Netherlands Green Deal Emission Factors. <https://www.co2emissiefactoren.nl/lijst-emissiefactoren/>. Accessed July 2021
- North American Council for Freight Efficiency (2019) Annual fleet fuel study
- O'Hayre R, Cha S-W, Whitney C (2016) *Fuel cell fundamentals*. Wiley
- Our World in Data: CO<sub>2</sub> emissions per capita vs. GDP per capita. <https://ourworldindata.org/grapher/co2-emissions-vs-gdp> Our World in Data. Accessed in July 2021
- Pacific Northwest National Laboratories: Battery 500. <https://energystorage.pnnl.gov/battery500.asp>. Accessed July 2021
- Posner M (2020) How Tesla should combat child labor in the democratic Republic of Congo, *Forbes*, October 2020
- Reitz RD, Ogawa H, Payri R, Fansler T, Kokjohn S, Moriyoshi Y, Agarwal AK, Arcoumanis D, Assanis D, Bae C, Boulouchos K, Canakci M, Curran S, Denbratt I, Gavaises M, Guenther M, Hasse C, Huang Z, Ishiyama T, Johansson B, Johnson TV, Kalghatgi G, Koike M, Kong SC, Leipertz A, Miles P, Novella R, Onorati A, Richter M, Shuai S, Siebers D, Su W, Trujillo M, Uchida N, Vaglieco BM, Wagner RM, Zhao H (2020) IJER Editorial: the Future of the Internal Combustion Engine 21:3–10

- Ritchie H, Roser M (2020) CO<sub>2</sub> and greenhouse gas emissions. Published online at OurWorldIn-Data.org. Retrieved from: <https://ourworldindata.org/co2-and-other-greenhouse-gas-emissions..> Accessed July 2021
- Ricardo: Determining the Environmental Impacts of Conventional and Alternatively Fueled Vehicles Through LCA, European Commission, July 2020
- Senecal K, Leach F (2021) Racing toward zero: the untold story of driving green. SAE International
- Sens M, Danzer C, von Essen C, Brauer M, Wascheck R, Seebode J, Kratzsch M (2021) Hydrogen powertrains in competition to fossil fuel based internal combustion engines and battery electric powertrains. In: 42nd International Vienna motor symposium, April 2021
- Sloan AP (1980) My years with general motors, currency
- Stanton DW (2013) Systematic development of highly efficient and clean engines to meet future commercial vehicle greenhouse gas regulations. SAE Buckendale Lecture
- Thelen W, Bubna P (2018) Battery investigation, Ricardo
- U.S. Department of Transportation (2020) Federal Highway Administration, Highway Statistics (Washington, DC: Annual issues), table HM-12. <http://www.fhwa.dot.gov/policyinformation/statistics.cfm>
- U.S. Geological Survey: Cobalt Statistics Information. <https://www.usgs.gov/centers/nmic/cobalt-statistics-and-information>. Accessed July 2021
- United Nations Economic and Social Council (2020) Proposal for a new UN regulation on uniform provisions concerning the approval of vehicles with regards to cyber security and cyber security management system
- United Nations (2015) Paris Agreement. [https://unfccc.int/sites/default/files/english\\_paris\\_agreement.pdf](https://unfccc.int/sites/default/files/english_paris_agreement.pdf)
- United States Environment Protection Agency (EPA). Global green-house gas emissions data. Available from: <https://www.epa.gov/ghgemissions/global-greenhouse-gas-emissions-data>. Accessed July 2020
- Verhelst S (2014) Recent progress in the use of hydrogen as a fuel for internal combustion engines. *Int J Hydrogen Energy* 39(2):1071–1085. <https://doi.org/10.1016/j.ijhydene.2013.10.102>
- Weis A, Jaramillo P, Michalek J (2016) Consequential life cycle air emissions externalities for plug-in electric vehicles in the PJM interconnection. *Environ Res Lett* 11:024009
- Xu B, Rathod D, Yebi A, Filipi Z, Onori S, Hoffman M (2019) A comprehensive review of organic rankine cycle waste heat recovery systems in heavy-duty diesel engine applications. *Renew Sustain Energy Rev* 107:145–170

# Chapter 3

## A Review of Emissions Control Technologies for On-Road Vehicles



Ameya Joshi

**Abstract** The year 2020 marked the 50th anniversary of the passage of the Clean Air Act in the United States. The subsequent creation of the Environmental Protection Agency (EPA) and establishment of national ambient air quality standards (NAAQS) for criteria air pollutants paved the way for increasingly stringent tailpipe emission limits for passenger cars and trucks. These limits have been met through significant advances in both engine hardware and controls, and after-treatment systems, the latter of which will be the focus of this chapter. Modern powertrains using advanced after-treatment systems can practically eliminate the harmful gases and particulates from entering the atmosphere. Three-way catalysts (TWC) can address  $\text{NO}_x$ , CO and hydrocarbons (HC) emissions from stoichiometric gasoline vehicles with near 100% efficiency when operating above the light-off temperatures. Diesel vehicles, despite the bad press in recent years, can be emitting well below the regulated limits with the adoption of the latest technologies such as selective catalytic reduction of  $\text{NO}_x$  (SCR). The key challenge in both technologies is addressing the “cold-start” emissions, which is the combination of high emissions following an engine start and after-treatment temperatures below light-off. We will review the latest options that are being pursued to address this challenge and lead to “zero-impact” emitting vehicles. Particulate filters are ubiquitous on diesel vehicles and are also making their way on to gasoline vehicles with the recent particle number regulations in Europe and China. Filtration efficiency is very high and only improves with vehicle age due to the accumulated ash layer. There is evidence that in highly polluted urban environments, the tailpipe particulate emissions can in fact be lower than the ambient concentrations. Emissions control technology is mature but still there is much more work to be done. New regulations such as Euro 7, LEV 4 and the heavy-duty low  $\text{NO}_x$  regulations in US and Europe are looking for further deep cuts in pollutant limits, regulating new species and particulates down to 10 nm, and extending the testing to include “all” driving conditions. We will review the new component technologies

---

A. Joshi (✉)

Emerging Technologies & Regulations, Environmental Technologies, Corning Inc., One Riverfront Plaza, Corning, NY 14831, USA

e-mail: [joshia@corning.com](mailto:joshia@corning.com)

and the after-treatment system layouts being developed to address these upcoming regulations.

### 3.1 Introduction

It has been fifty years since the passage of the Clean Air Act in the United States, and the ensuing standards on pollutants from vehicular tailpipes led to new technologies and significant improvements in air quality. Figure 3.1 shows a summary of ambient concentration measurements taken in Los Angeles since 1960, which show that  $\text{NO}_x$  decreased by  $\sim 75\%$ , while volatile organic compounds (VOCs) decreased by over  $95\%$  despite the large increase in the number of vehicles.  $\text{NO}_x$  and VOCs are precursors to ozone formation, which accordingly has also reduced by over  $75\%$  over this timeframe.

The tightening air quality standards have worked, and we have every reason to celebrate this success. However, there is still more work to be done. There are several regions of the world which are still highly polluted, and a recent study (Cohen et al. 2017) concluded that each year, over 4 million deaths are attributed to exposure to fine particulates ( $\text{PM}_{2.5}$  or particles below 2.5 microns) across the world. The adverse health effects are especially borne by the densely populated regions of the world which have yet to implement the latest emission standards. Moreover, the health risks persist even at low ambient pollutant concentrations achieved in advanced economies such as the US and Europe. In a recent study of Medicare data for 61 million Americans over 65 years old, Dominici et al. (2019) concluded that exposure

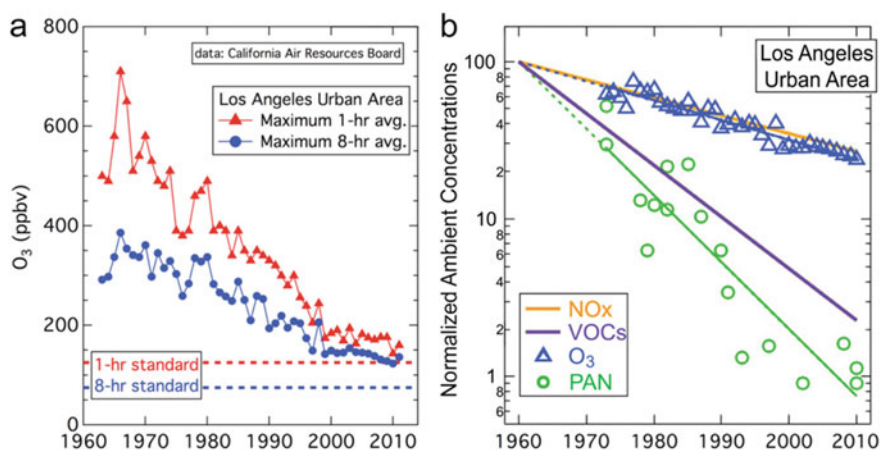


**Fig. 3.1** Progress made in the past few decades in reducing air pollution. Fifty-year history of reduction of ambient concentrations of ozone in Los Angeles (left) and several other air pollutants, normalized to 100 in 1960. Taken from Parrish and Stockwell (2015)

to PM and ozone are associated with an increase in mortality even at concentrations below the current national ambient air quality standards (NAAQS). Even as this article is being written, the US EPA is considering further lowering the NAAQS standards for fine particulates. Secondly, pollutant concentrations are known to be higher near roadside and this results in higher exposure for people living near or commuting on highways. This is especially a concern for disadvantaged communities and people of color, who disproportionately face higher levels of pollution (Tessum et al. 2021).

There is accordingly continued emphasis on tightening standards for tailpipe pollutants, especially  $\text{NO}_x$  and particulates, for both light- and heavy-duty vehicles and off-road equipment. We do not cover regulations in detail in this chapter, but ongoing discussions on the next round of regulations in Europe (Euro 7), US (LEV 4 in California) and China (China 7) are targeting steep reductions in  $\text{NO}_x$  and even particle number (PN) limits, while including particles down to 10 nm (a change from the current 23 nm cut-off) and also including limits on new species such as ammonia and nitrous oxide ( $\text{N}_2\text{O}$ ). There is a great emphasis being placed on ensuring in-use compliance over the lifetime of the vehicles and that vehicles be able to meet the limits under “all” reasonable driving conditions. Meeting these upcoming regulations will require improvements in engine technology as well as the use of advanced after-treatment systems. It is also clear that considering the tightening  $\text{CO}_2$  standards, there is little appetite for any increase in the system backpressure. In this chapter we review some of the system concepts that seem likely and review the single-component technologies, for both gasoline and diesel engines. Emissions control is a very broad and mature topic and it will be impossible to cover all of the aspects in one place, the reader is referred to recent annual reviews (Joshi 2021, 2020) which cover advances made on a wide range of technologies being developed for cleaner engines, fuels and after-treatment systems.

### ***3.1.1 After-Treatment Systems for Emissions Control: An Overview***

Modern vehicles being sold in regulated markets today have some form of after-treatment system to address gas and particulate emissions. A detailed description of the design considerations and inner workings of a modern catalytic converter are beyond the scope here and have been covered elsewhere (Heck et al. 2010). Figure 3.2 shows a high-level schematic of the two main types of components. A “flow-through” substrate is typically used for converting harmful gases such as  $\text{NO}_x$ , carbon monoxide and hydrocarbons. The catalyst is coated onto the channel walls of an inert substrate made of cordierite. As exhaust gas flows along the channels, reactants diffuse into the porous coating, where they react on active catalytic sites. A wall-flow filter, made of cordierite, aluminum titanate or silicon carbide and shown on the right, has additional plugs on alternate channels at either ends, which force

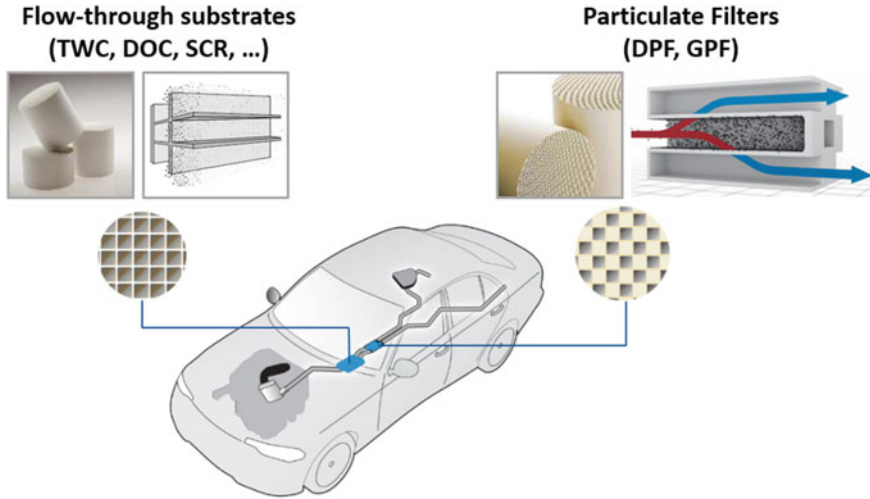


**Fig. 3.2** The after-treatment system on a modern vehicle typically consists of components to convert gases—“flow-through substrates” (left) and to eliminate particulates—“wall-flow particulate filters” (right). Inset pictures show the channel details and plugging patterns (for filters). Illustrations and images courtesy of Corning Incorporated

the flow to pass through the porous wall, on which any particles such as from soot or ash are collected. The wall may also contain a catalyst which can lend additional functionality such as for gas conversion (e.g. TWC coated GPFs; oxidation catalyst or SCR coated DPFs, to be discussed later), or assist with soot regeneration. In the following sections we will cover these various components as applied to gasoline, diesel and natural gas engines, along with some system-level considerations.

### 3.1.2 Stoichiometric Gasoline Emissions After-Treatment

Modern gasoline emissions control systems must provide the following critical improvements:

- (1) Reduction of cold-start emissions of  $\text{NO}_x$  and hydrocarbons; and
- (2) Very high particulate filtration.

Figure 3.3 shows some representative after-treatment systems that are being considered for current Euro 6/LEV III or future regulations. Vehicles in Europe and China are already equipped with three-way catalysts (TWCs) and gasoline particulate filters (GPFs). GPFs are either bare or catalyzed and can be placed either close to the engine—the so-called “close-coupled” position—or further away in the under-floor position. Electrically heated catalysts and hydrocarbon traps are being tested

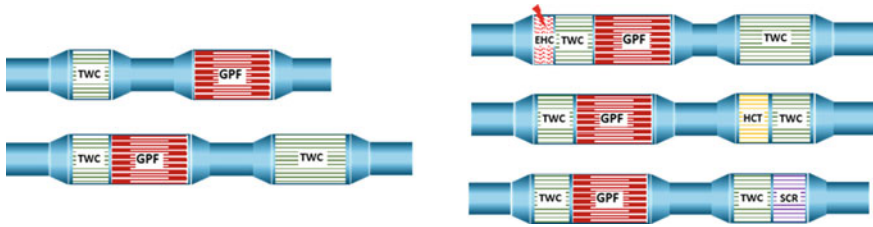


**Fig. 3.3** Representative gasoline after-treatment layouts for meeting future regulations. TWC = Three-way catalyst, GPF = Gasoline particulate filter, HCT = Hydrocarbon trap, EHC = Electrically heated catalyst, SCR = Selective catalytic reduction (of  $\text{NO}_x$ )

to reduce cold start emissions. Also foreseen is the use of a passive SCR (selective catalytic reduction) catalysts for ammonia and  $\text{NO}_x$  reductions, traditionally only used with diesel engines. The passive here refers to the lack of urea injection, which supplies ammonia as a reductant for  $\text{NO}_x$ . Instead, the ammonia is generated upstream on the TWC under rich operating conditions.

### 3.1.3 Gaseous Emissions Control

The mainstay of gaseous emissions control from a stoichiometric gasoline engine is the TWC, which is now an incredibly effective, mature technology. The TWC consists of an inert ceramic (typically cordierite) substrate made of thousands of channels, which are coated with an alumina “washcoat” containing platinum group metals (PGM) such as platinum, palladium and rhodium for the reactive sites, and components such as ceria for oxygen storage to provide a buffer during slightly lean and rich exhaust conditions. Almost full conversion of  $\text{NO}_x$ , hydrocarbons and carbon monoxide (CO) to benign water and  $\text{CO}_2$  is achieved, once the catalyst is above the “light-off” temperature. The key remaining challenge then, is to address the “cold-start” emissions, which occur in the first minute or two following the start of the vehicle till the time that the catalyst is warmed up by the exhaust gas. Here are a few of the pathways being pursued to address this problem:

1. Improved washcoat distribution: Adding PGM can provide more catalytic activity, especially improving the conversion at longer mileages when the catalysts can sinter and provide reduced surface area. However, there is a diminishing return with loading, especially if it is not accompanied with increasing dispersion, without which access to the additional sites can be limited. A better approach is to reallocate some of the washcoat to the underfloor GPF (Ball et al. 2020), which results in a net increase in residence time for the exhaust, and helps with greater conversion at high speed driving.
2. Improving catalysts: The focus here is two-fold—maximizing the low-temperature activity and PGM reduction. A systematic study (Theis et al.



- 2017) explored the impact of various aspects of catalyst design on the former target of reducing light-off temperature: catalyst preparation methods (post-impregnation was found to provide better access to PGM than catalyzed slurry), support effects (alumina found to provide high surface area and better aged performance compared to  $\text{ZrO}_2$  or  $\text{TiO}_2$ ), and Pd amount (2% found to be optimum on alumina).
3. PGM prices have increased significantly in recent years and there is increasing research being done on reducing PGM content and system cost. Research on single atom catalysts (Alcala et al. 2021) and solution-based atomic layer deposition aim to increase dispersion (Getsoian et al. 2019) towards 100% and lower the light-off temperatures to near 150 °C at a fraction of the PGM usage on commercial catalysts. Catalysts without or greatly reduced PGM content are also proposed. In one commercialized example (Hashimoto et al. 2016),  $\text{Al}_2\text{O}_3$  from the 1st layer of an underfloor TWC was replaced by  $\text{Ba/Zn/CeO}_2$  to achieve a 10% reduction in  $\text{NMOG} + \text{NO}_x$  emissions. Perovskite (Glisenti et al. 2016; Keav et al. 2014; Hanaki et al. 2016) and spinel oxide (Golden et al. 2017) based catalysts have been demonstrated to deliver good performance under lab conditions despite significantly reduced PGM content.
  4. Lower thermal mass substrates: Higher porosity substrates with low thermal mass are commercialized and heat up quickly, leading to earlier catalyst light-off. The technology offers a 10–20% reduction in  $\text{NO}_x$  and HC emissions (Warkins et al. 2020) over the already very low emissions of 30 mg/mi of combined HC +  $\text{NO}_x$  (SULEV 30 vehicles).
  5. Added external heat: With increasing availability of on-board electrical power, electrically heated catalysts (EHCs) offer an attractive solution to heat the exhaust and catalysts quickly to above light-off temperature (Bruck et al. 2020). The power demand for such heating is 2–4 kW, which can be easily met, especially when the EHC is embedded within a 48 V mild hybrid (or a full hybrid) ecosystem. Adding energy comes with a net fuel penalty, however this can be partly offset by reducing the need for traditional engine heating measures.
  6. Hydrocarbon traps: HC traps can be either a stand-alone component or applied as a dual coating below a TWC layer. A large pore zeolite is typically used to adsorb HC species at low temperatures, which are released at high temperatures when active TWC can convert them. The performance of the HCT has been shown to depend on the presence and amount of Pd, oxygen storage content, and other active metals (Lupescu et al. 2018). The benefits of HC traps in reducing cold start emissions can be substantial. One study found up to 50% reduction in HC emissions on the FTP cycle, without affecting  $\text{NO}_x$  (Xu et al. 2018a). The key challenge of HC traps is to manage the release of HC species at temperatures above the TWC light-off temperature (~300 to 350 °C). Also, current formulations are ineffective in adsorbing methane. Combining HC trapping functionality with other components is being explored. In one study (Moser et al. 2018), a HC trap was tested up to 150,000 mi with a downstream passive SCR for improved  $\text{NO}_x$  control. The HCT reduced HCs by ~5 mg/mi and  $\text{NO}_x$  by ~17 to 20 mg/mi, a significant reduction towards SULEV30 standards. In



another DOE funded project (Moses-DeBusk 2021), ongoing when this is being written, HCT coating was applied to the inlet channels of a GPF, while the outlet channels were coated with a TWC. This combination was tested on a light-duty truck on the FTP test cycle, and found to reduce total HCs by >80% during the 1st 250 s following a cold start.

### 3.1.4 *Particulate Emissions Control*

Boosted, downsized gasoline direct injected (GDI) engines have gained market share in recent years, due in part to their improved fuel economy compared to traditional port fuel injected (PFI) engines. Direct injection allows for precise control of injection timing and amount, while also enabling operation at higher compression ratios due to the reduced risk of engine knocking due to charge cooling. However, GDI engines emit more particulates, due to insufficient time for mixture preparation and fuel impingement on combustion chamber surfaces. This has prompted increased scrutiny and tighter standards on particulate emissions from gasoline vehicles across the world. Both engine and after-treatment technologies have advanced to reduce the tailpipe emissions. Multiple injections at higher pressure help to manage the fuel penetration and reduce engine out emissions. One study conducted at low ambient temperature of  $-7^{\circ}\text{C}$  (Pauer et al. 2020) showed that 6 injections at 500 bar reduced particle number (PN) emissions by 65% when compared to a reference system with 3 injections at 250 bar. Even higher injection pressure of 700 bar has been commercialized, such as on Mazda's Skyactiv-X 2.0 L engine with spark assisted compression ignition technology (Nakai et al. 2019). Still, the use of a GPF is now seen to be unavoidable for most GDI and also some PFI engines given the stringent PN limit of  $6 \times 10^{11}$  #/km in Europe and China. GPF technology is already mature, although undergoing continuous improvement, with millions of vehicles in Europe and China equipped with a GPF. All aspects of GPF design and operation are well documented (Reducing Particulate Emissions in Gasoline Engines 2018; Joshi and Johnson 2018), and we will cover some of the major considerations here.

The key performance metric is, of course, filtration efficiency. Current and upcoming regulations will require GPFs with very high filtration efficiencies in the clean state (that is, in the absence of any soot or ash layer which assists with higher filtration). Figure 3.4 below shows that the latest GPFs are delivering >90% efficiency in trapping particles, while also offering reduced soot loaded pressure drop. As shown in the left plot, the efficiency only improves with mileage, as the ash accumulation helps to form a membrane which further increases filtration (Lambert et al. 2016, 2017). The increase in filtration with ash occurs with a pressure drop penalty and the GPF must be sized appropriately to ensure adequate ash capacity for a low end-of-life pressure drop.

As this article is being written, Europe is considering further tightening the limit starting Euro 7, possibly decreasing it to  $1 \times 10^{11}$  #/km and also including particles down to 10 nm (as compared to the existing cut-off at 23 nm). This will require

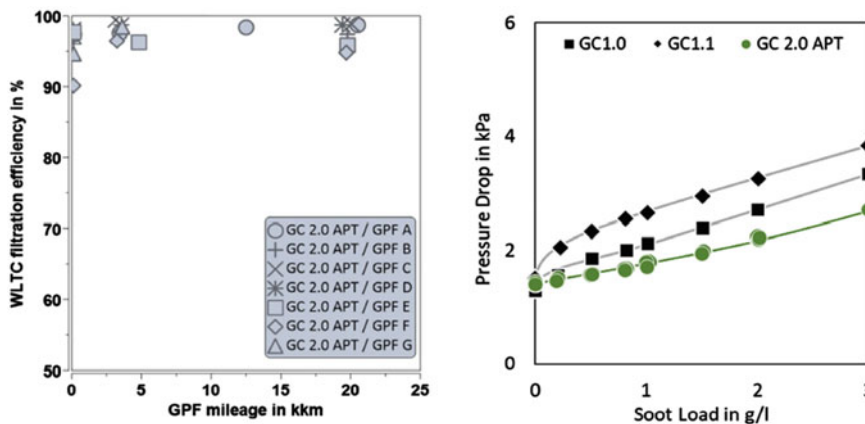


**Fig. 3.4** Filtration efficiency of an uncatalyzed GPF as tested on the World harmonized light vehicles test cycle (WLTC), as a function of mileage. Taken from Boger et al. (2021)

an increase in performance of the GPFs (filtration efficiencies of  $\geq 98\%$ ) under all driving and ambient conditions in the fresh state. There will likely be exceptions. In one study (Giechaskiel et al. 2021), a Euro 6d-Temp vehicle with a GPF was tested under real-world driving conditions covering dynamic driving, urban stop and go driving and towing a trailer uphill at 85% of maximum payload, and at ambient temperatures ranging from  $-30$  to  $50$  °C. For most of the tests, particles in the 10–23 nm range added 16–38% to the overall count compared to the 23 nm cut-off. Still, in most cases the PN emissions were an order of magnitude below the Euro 6 lab limit of  $6 \times 10^{11}$  #/km, even when counting particles down to 10 nm.

GPFs, like any after-treatment component, contribute to the system backpressure, which increases over the lifetime with ash accumulation, as noted above. Various design levers can be used to minimize the impact on fuel economy: large filter diameter, adequate length or volume for end-of-life ash capacity, good coating technology are a few examples. Also, it is to be noted that a coated GPF often replaces an existing TWC substrate, such that the incremental increase in pressure drop can be small at the system-level.

The accumulated soot needs to be regenerated to avoid an increase in pressure drop. Soot loads in gasoline engines are low (relative to diesel engines), and exhaust temperatures are high. Given this combination, soot oxidation can occur passively (Boger et al. 2015) through fuel-cut events, during which oxygen concentration is high (near ambient). Nevertheless, active soot regeneration may be considered under certain driving conditions leading to high soot loads.

Other than filtering soot, GPFs also help reduce emissions of polyaromatic hydrocarbons (PAHs), some of which are highly toxic and known carcinogens. The PAHs are adsorbed onto the soot particles and are captured along with the soot particles. The U.S. EPA is looking into this benefit closely, and recent testing showed that GPFs can reduce the toxicity of gasoline exhaust by over 99% (Bohac et al. 2021).

## 3.2 Diesel Emission Control

### 3.2.1 Diesel Oxidation Catalyst (DOC)

A DOC provides multiple functions in a diesel after-treatment system. The PGM-based catalyst helps oxidize unburnt CO and HC. Post injection of fuel and the oxidation on a DOC provides the necessary exotherm to trigger soot regeneration in the downstream DPF and for de-sulfation of the subsequent components. It also oxidizes NO to NO<sub>2</sub>, with the latter necessary to promote both passive regeneration and to promote the fast SCR reaction for NO<sub>x</sub> control. We have discussed the need for early catalyst light-off and PGM thrifiting in the TWC section, and the same considerations apply to DOC as well, perhaps with even more urgency given the low exhaust temperatures characteristic of a diesel engine. The reader is referred to a previous review (Russell and Epling 2011) to understand the design considerations for DOC PGM optimization, reaction mechanism and kinetics, deactivation and poisoning pathways.

New catalysts are being researched to improve DOC performance, with a target of 90% conversion (T90) at 150 °C. Core-shell catalysts of ZrO<sub>2</sub> on SiO<sub>2</sub> are being explored (Toops 2019), with Pt/Pd supported on the ZrO<sub>2</sub> shell. After hydrothermal aging (800 °C for 10 h), T90 for CO was measured at 175 °C and for HC at ~250 °C. DOC catalysts are also being combined with other components with an aim for system downsizing, cost reduction or faster heat up. One approach is to combine a DOC with an ammonia slip catalyst (ASC) onto the same substrate. The inner layer of catalyst provides NO oxidation, while the outer SCR coating helps with NO<sub>x</sub> conversion. The key requirement is to produce high NO<sub>2</sub> concentration for fast SCR, without generating N<sub>2</sub>O. Geisselmann et al. (2018) showed this trade-off, measuring ~40% NO<sub>2</sub>/NO<sub>x</sub> ratio at the low ammonia to NO<sub>x</sub> ratio (ANR) of 0.6, but only 25% NO<sub>2</sub> at an ANR of 1.0. Newman et al. (2018) reported on a catalyst that can generate upwards of 30% NO<sub>2</sub> at 300 °C in the presence of ammonia with no impact on N<sub>2</sub>O selectivity. Another approach is the combination of DOC with filters. For HD application (Sethuraman et al. 2019), this was shown to improve NO<sub>x</sub> conversion by 33% and allow earlier urea injection by one minute due to the reduced thermal mass.

## 3.3 DeNO<sub>x</sub> Technologies: Selective Catalytic Reduction (SCR), Lean NO<sub>x</sub> Trap (LNT), Passive NO<sub>x</sub> Adsorbers (PNA)

Selective catalytic reduction of NO<sub>x</sub> using ammonia is the leading technology for NO<sub>x</sub> control from light- and heavy-duty diesel engines. SCR catalyst can either be wash coated or extruded as a monolithic cellular structure.

A urea solution, also called a diesel exhaust fluid (DEF) is injected upstream of the catalyst which decomposes to form ammonia by the time the exhaust enters the SCR inlet. Despite the presence of abundant oxygen, the ammonia is not oxidized up to high temperatures but rather selectively reacts with and reduces  $\text{NO}_x$  (to nitrogen). An ammonia slip catalyst typically follows the SCR to oxidize any additional unreacted ammonia. Details of the reaction chemistry and a state-of-the-art for SCR technology has been reviewed recently (Selleri et al. 2021).

The SCR catalyst is typically a small-pore zeolite such as chabazite exchanged with copper or iron. Vanadium can also be effective. Copper-zeolite catalysts are the leading candidates due to their excellent conversion over a wide temperature window. Fe-zeolites offer better conversion at higher temperatures, higher resistance to sulfation and lower  $\text{N}_2\text{O}$  formation as compared to Cu-based catalysts, so that hybrid Cu-Fe-zeolite catalysts are also being pursued. One example (Pauly 2018) applied to a heavy-duty engine showed that zone coating up to 25% of the front end of the substrate with an Fe catalyst and the rest with Cu-SCR provided a good balance with low  $\text{N}_2\text{O}$  formation and high overall  $\text{NO}_x$  conversion. Vanadia catalysts also offer superior sulfur resistance and are hence preferred in markets with high sulfur fuels. For upcoming Euro 7/VII regulations, the low  $\text{N}_2\text{O}$  formation is also very attractive, shown to be over an order of magnitude lower than Cu-SCR on the HD WHTC. One of the concerns with vanadia is its sublimation and potential release at temperature greater than  $\sim 500^\circ\text{C}$ , however new catalysts are also showing improved stability with development catalysts showing no vanadia release up to  $650^\circ\text{C}$  (Nilsson et al. 2021).

The key challenge that needs to be addressed is improving low temperature SCR conversion. Uniformity of ammonia distribution is an important aspect towards maximizing the  $\text{deNO}_x$  performance. More importantly, urea cannot be dosed at temperatures below  $180\text{--}200^\circ\text{C}$  due to the risk of nitrate deposit formation, and SCR activity is also reaction rate limited at low temperatures. This leads to  $\text{NO}_x$  slip at low catalyst temperatures, which is experienced during cold starts, city driving or low load operations for heavy-duty trucks. Heated urea dosing is one option which allows for early dosing, although this still does not overcome the inherent catalyst rate limitations. For systems which deploy two SCR catalysts, one closer to the engine and another underfloor, dual dosing is being introduced with an independent dosing system for each SCR unit. This allows for improved utilization of the catalysts and net  $\text{NO}_x$  conversion (for example relying more on the underfloor catalyst to clean up the exhaust under high flow conditions characteristic of highway driving), better urea dosing control and reduced ammonia slip. Dual dosing has been commercialized on light-duty engines and will likely make its way on heavy-duty engines as well given that future systems will likely add close-coupled SCR catalysts to meet upcoming low  $\text{NO}_x$  regulations. Other novel solutions are being researched, such as additives to urea to promote urea decomposition (Hartley et al. 2019), on board conversion of urea to ammonium carbamate using waste heat, which in turn decomposes to ammonia at temperatures as low as  $60^\circ\text{C}$  (Wilson et al. 2019), and use of external heating via glow plugs (Okada et al. 2019) or heating rods in the urea tank (Larsson et al. 2019).

The performance of Cu- and Fe-zeolite catalysts is improving incrementally. On aged Cu-zeolite SCR catalysts, NO<sub>x</sub> conversion of ~75% was reported (Geisselmann and Toni 2018; Newman 2020) at 175 °C for the standard SCR reaction (NO only). Conversion increases at higher temperature and was near 100% in the 250–550 °C, after which it reduces due to ammonia oxidation. Hydrothermal stability is also an important consideration, and it was shown that the catalysts retain conversion even when aged to 900 °C. New catalyst formulations are also being explored. Zone coating with Cu/LTA zeolite and a commercial Cu/SSZ-13 was found to offer provide a good combination of both low-temperature activity and hydrothermal stability (Kim et al. 2019). Ceria-manganese/titania catalysts tested in the laboratory (Xu et al. 2018b) show >90% NO<sub>x</sub> conversion in the 140–260 °C range and also high sulfur tolerance. Hybrid metal oxide-zeolite catalysts are being developed, which can promote in-situ oxidation of NO to NO<sub>2</sub> and increase NO<sub>x</sub> conversion through the fast SCR reaction (Andana et al. 2021). In one study, the addition of 10% MnO<sub>2</sub>/ZrO<sub>2</sub> catalyst was found to increase NO<sub>x</sub> conversion by 20%, while also reducing N<sub>2</sub>O formation (Rappe et al. 2020).

Integrating the SCR catalyst with the filter can also help improve the low temperature SCR activity, and enable overall system downsizing, which is especially attractive for non-road machinery. This is already commercialized on light-duty vehicles and being explored in the heavy-duty space. The combination of SCR on filter enables early warm-up of the SCR due to proximity to the engine and urea dosing can be started earlier, reducing cold-start and low load emissions. One study (George et al. 2018) tested a US EPA 2017 engine on the NRTC (non-road transient cycle) and showed 90–140 s early urea dosing, depending on the reference DPF thermal mass. The challenge for this technology is managing the competing needs on NO<sub>2</sub> used for both passive regeneration of the soot and for the fast SCR reaction.

With SCR catalyst technology reaching maturity, attention is now also being given to improving in-use compliance over the vehicle lifetime and the slip of secondary emissions such as ammonia and N<sub>2</sub>O. Reduced deNO<sub>x</sub> activity due to aging is especially a concern for heavy-duty engines which are expected to be durable to nearly a million miles per the new California Low NO<sub>x</sub> regulation, and which are expected to require SCR catalysts in the close-coupled position before a filter leading to additional exposure to sulfur and other contaminants. Sulfur is bound to the catalyst via weak and strong interactions with copper sites, and the chemically bound sulphates must be removed by heating to temperatures >550 °C to recover the deNO<sub>x</sub> activity. This leads to a fuel penalty and moreover, even with thermal treatment, a full recovery of the catalytic activity is not guaranteed. One study points to SCR conversion dropping from 96% on a degreened catalyst to 76% on a field aged sample even after the thermal treatment (Xi et al. 2020). With limits being proposed for N<sub>2</sub>O, studies are also probing the fundamentals of the formation of this molecule (Xi et al. 2021). Advanced dosing strategies and model-based control are being implemented to minimize ammonia slip past the ammonia slip catalysts.

Passive NO<sub>x</sub> adsorbers (PNA), based on Pd/zeolites, are similar to hydrocarbon traps mentioned in previous sections, in that they adsorb NO<sub>x</sub> at low temperatures and release at higher temperatures when NO<sub>x</sub> conversion is possible. The issue with

PNA is degradation of the  $\text{NO}_x$  uptake capacity. In lab testing (Toops 2021) on a 1 wt% Pd / SSZ-13 catalyst, up to ~20% of NO uptake was found to be lost in 10 adsorption-desorption cycles. This was found to occur only when CO was present in the feed gas. Bimetallic PNAs are being investigated and a 1:1 combination of Cu and Pd is showing significant increase in the NO uptake, but also suffers from degradation after multiple cycles. This issue needs to be resolved before PNAs can be used extensively. In this same study, a physical mixture of PNA, HCT and DOC was also tested and higher conversion was measured for CO, HC and  $\text{NO}_x$  as compared to using a DOC alone.

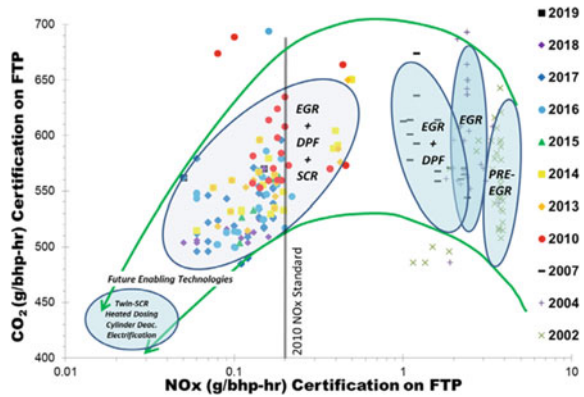
### 3.4 Emission Control Solutions for Heavy Duty Low $\text{NO}_x$

Heavy-duty vehicles and off-road equipment are also subject to ever tightening emission standards. Many of the technical advances pertinent to diesel emissions control which have been covered in the previous sections apply to heavy-duty vehicles as well. In this section we give a brief overview of the system-level approaches being pursued to meet the upcoming low  $\text{NO}_x$  standards. The need for further reductions is supported by recent field measurements (McCaffery et al. 2021) which show that trucks in use are emitting  $\text{NO}_x$  well above the regulated limit (in some cases an order of magnitude higher), especially under low load operating conditions where the exhaust temperatures fall below 200 °C or during dynamic driving including hard accelerations and stop and go urban driving which results in high engine out  $\text{NO}_x$ . California will require a 90% reduction in  $\text{NO}_x$  starting 2027 and as this is being written, the US EPA is considering aligning with this standard and Europe is also working on Euro VII standards with similar ambitions for a significant reduction in both  $\text{NO}_x$  and particle number limits. Meeting the California Low  $\text{NO}_x$  rule will require SCR efficiencies of >97% on the cold HD-FTP and >99% on the hot HD-FTP (Tennison 2019). This increase in  $\text{NO}_x$  conversion will have to be met without increasing the fuel consumption or  $\text{CO}_2$  emissions in order to also meet the equally tough GHG standards in these markets.

Can this be achieved? While past performance is no guarantee of future results, we have seen the industry successfully meet such challenges several times now. Figure 3.5 below is a summary of EPA certification data for HD engines in the past two decades (Technology Feasibility for Model Year 2024 Heavy-Duty Diesel Vehicles in Meeting Lower  $\text{NO}_x$  Standards 2019). The introduction of SCR technology has allowed a decoupling of the  $\text{NO}_x$  and fuel consumption reduction, such that both have been reducing. Advanced technology demonstrations are underway and early results show the possibility of continued progress in the coming years.

Various technologies are being considered to achieve these upcoming standards in the 2027–2030 timeframe in US, Europe and China. After-treatment improvements include advanced substrates with thinner webs, higher cell density and lower thermal mass, advanced catalysts with improved activity, selectivity and durability, very high filtration DPFs with high ash capacity, and new system architectures supported by

**Fig. 3.5** EPA certification data show that both CO<sub>2</sub> and NO<sub>x</sub> have been reducing following the introduction of deNO<sub>x</sub> technologies (Technology Feasibility for Model Year 2024 Heavy-Duty Diesel Vehicles in Meeting Lower NO<sub>x</sub> Standards 2019)



advanced urea dosing hardware and control strategies. Additional after-treatment volume, particularly for SCR may also be required. These will also be complemented with improvements on the engine and transmission side, such as through the increased use of cylinder deactivation and 48 V mild hybridization. Figure 3.6 shows some of

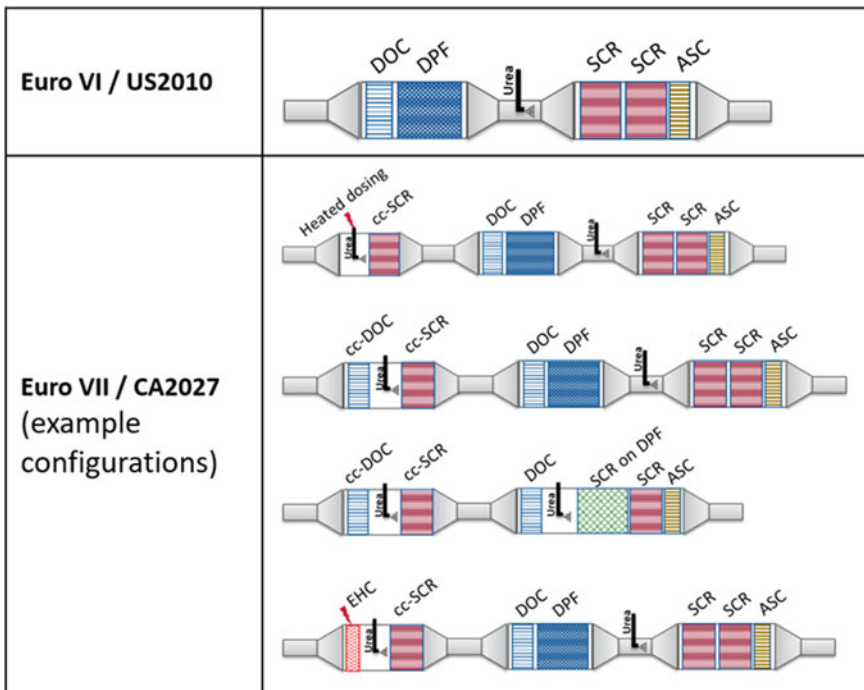


**Fig. 3.6** Representative after-treatment systems for meeting the current and upcoming low NO<sub>x</sub> regulations in US and Europe



the representative system architectures being considered. A common feature is the use of an added SCR component placed upstream of the DPF. This will allow for early light-off of the catalyst and improved low temperature deNO<sub>x</sub> conversion, critical to meet the standards under low load and urban operating conditions when temperatures can get near light-out. Other more aggressive measures such as the use of heaters is also being evaluated (Ehrly et al. 2021), while balancing the benefits with any fuel penalty.

A demonstration program was recently conducted at Southwest Research Institute, using a 2017 Cummins X15 engine (Sharp et al. 2021). Engine-out exhaust temperature was raised through engine calibration, use of cylinder deactivation, and EGR cooler bypass, enabling the turbo-out temperatures to reach 200 °C within the first 50 s. This was followed by an advanced after-treatment system consisting of a zone-coated DOC+ catalyzed filter, and two parallel banks of SCR and ASC. Emissions testing done on the HD FTP and the new low load cycle show great improvements: After accelerated aging representative of 435,000 miles, NO<sub>x</sub> emissions on the composite FTP cycle were measured at 0.020 g/bhp-h, which is right at the limit proposed for MY 2027 HD vehicles. Of course, this also highlights the challenge ahead: OEMs will target an engineering margin and would like to be lower than the limit, and this is a lab study which does not account for field aging and any deterioration due to fuel quality issues. Still, it shows that steep reductions to NO<sub>x</sub> emissions are certainly possible in the coming years. A somewhat different system is being tested in Europe. A Euro VI-C compliant truck was fitted with an advanced after-treatment system comprising of a DOC + SCR in the close-coupled position, followed by a DOC, DPF and a second SCR in the underfloor location. Hydrothermal aging of the components was done to 500,000 km and testing done on road under 4–11 °C. Initial results show that emissions were below 200 mg/kWh even at low speed driving, well below the current limit of 460 mg/kWh.

This is a very high-level description of some of the leading approaches to lower tailpipe NO<sub>x</sub> from diesel engines. Natural gas engines are already certified to ultra-low NO<sub>x</sub> standards required in 2027. These are not without their challenges either: notably methane slip and high particulate emissions. Methane is a difficult molecule to break and is converted at temperatures >350 to 400 °C. Studies continue to explore ways to reduce the light-off temperature without increasing PGM content. One recent example (Harold et al. 2020) is the use of PGM-spinel catalysts which seem to deliver improved conversion when coupled with lean-rich modulating flow.

Many other non-conventional pathways are being pursued to achieve this, such as the development of two-stroke opposed piston engines (Fromm 2021) and hydrogen-fueled internal combustion engines, which also practically eliminate particles.

### 3.5 Summary

As regulations and technologies continue to drive tailpipe emissions lower, we are now approaching the scenario where concentrations of tailpipe criteria pollutants are at similar levels as in the surrounding atmosphere. Modern catalytic converters are



extremely efficient once the catalyst is hot, so that much of the development efforts are aimed at addressing that last issue of cold start emissions. As we move towards an electrified future, there are other issues which are gaining attention. One is the “high-powered cold start” emissions associated with plug-in hybrids, which occur when the engine is suddenly turned on during a high-powered driving event, combining both high engine-out emissions and a cold catalyst. Also being addressed are emissions from full hybrids, which are very efficient and low emitting, but can suffer from multiple engine start-stop events and cooler catalysts due to the engine being turned off during low loads. Following Euro 6 and real-world driving regulations, there is evidence of greatly improved in-use compliance, but studies show that a few high emitting vehicles can offset the gains of improved engines and emissions control from the rest of the fleet. As such, there will be greater scrutiny of on-road reduction of tailpipe emissions, over the lifetime of the vehicle. New regulatory elements such as the periodic technical inspection, on-board monitoring and low load cycle for heavy-duty vehicles are some examples of the kind of tools being proposed for improving compliance.

Fuels was beyond the scope of this chapter, but new renewable and synthetic fuels promise to reduce criteria pollutants and will also lead to reduced wells-to-wheel GHG emissions.

Finally, as we are approaching very low tailpipe emissions further aided by Euro 7, LEV 4 and China 7, regulators are shifting their attention to other sources of emissions such as from brake and tire wear, signaling that the battle against tailpipe emissions is nearly won.

## References

- AE Book, Reducing particulate emissions in gasoline engines, R-471. <https://www.sae.org/publications/books/content/r-471/>
- Alcala R, DeLaRiva A, Peterson EJ, Benavidez A et al (2021) Atomically dispersed dopants for stabilizing ceria surface area. *Appl Catalysis B: Environ* 284:119722
- Andana T, Rappe KG, Gao F, Szanyi J et al (2021) Recent advances in hybrid metal oxide–zeolite catalysts for low-temperature selective catalytic reduction of NO<sub>x</sub> by ammonia. *Appl Catalysis B: Environ* 291:120054
- Ball D, Meng X, Weiwei G (2020) Vehicle emission solutions for China 6b and Euro 7. SAE Technical Paper 2020-01-0654. <https://doi.org/10.4271/2020-01-0654>
- Boger T, Glasson T, Rose D, Ingram-Ogunwumi R et al (2021) Next generation gasoline particulate filters for uncatalyzed applications and lowest particulate emissions. SAE Technical Paper 2021-01-0584. <https://doi.org/10.4271/2021-01-0584>
- Boger T, Rose D, Nicolin P, Gunasekaran N, Glasson T (2015) Oxidation of soot (Printex U) in particulate filters operated on gasoline engines. *Emiss Control Sci Technol* 1:49–63
- Bohac SV, Ludlam S, Hays MD, Preston WT (2021) Filter-collected and gas-phase PAH emissions from a cGPF-equipped light duty truck. In: Presented at the 30th CRC real world emissions workshop, March 8–11, 2021
- Bruck R, Lienou I, Schatz A, Ellmer D (2020) Unlimited clean mobility emission management for EU 7 and China 7 powertrain concepts. In: Presented at the 29th Aachen colloquium sustainable mobility

- Cohen AJ, Brauer M, Burnett R, Anderson HR, Frostad J, Estep K, Balakrishnan K, Brunekreef B, Dandona L, Dandona R, Feigin V (2017) Estimates and 25-year trends of the global burden of disease attributable to ambient air pollution: an analysis of data from the global burden of diseases study 2015. *Lancet* 389:1907–1918
- Dominici F, Schwartz J, Di Q, Braun D, Choirat C, Zanobetti A (2019) Assessing adverse health effects of long-term exposure to low levels of ambient air pollution: phase 1. Research Report 200. Health Effects Institute, Boston, MA
- Ehrly M, Dahodwala M, Xin L, Yuntao W (2021) Managing stringent ultra-low emission standards by advanced exhaust aftertreatment topologies. In: Presented at the FEV diesel powertrain 3.0 conference, June 2021
- Fromm L (2021) Achieving ultralow NO<sub>x</sub> emissions with a heavy duty diesel engine. In: Oral presentation, 2021 SAE WCX Digital Summit, April 13–15, 2021
- Geisselmann A, De Toni A (2018) Improvements in low temperature deNO<sub>x</sub> of HDD systems. In: Proceedings of the SAE HDD symposium, Gothenburg, Sweden, 16–17 October 2018
- George S, Heibel A, Beall D (2018) Next generation cordierite high porosity DPF for SCR catalyst integration. In: Presented at the SAE World Congress, Detroit, 2018
- Getsoian A et al (2019) Remarkable improvement in low temperature performance of model three-way catalysts through solution atomic layer deposition. *Nat Catal* 2:614–622
- Giechaskiel B, Valverde V, Kontses A, Melas A et al (2021) Particle number emissions of a Euro 6d-temp gasoline vehicle under extreme temperatures and driving conditions. *Catalysts* 11(5):607. <https://doi.org/10.3390/catal11050607>
- Glisenti A et al (2016) Largely Cu-doped LaCo<sub>1-x</sub>Cu<sub>x</sub>O<sub>3</sub> perovskites for TWC: toward new PGM-free catalysts. *Appl Catal B* 180:94–105
- Golden S, Nazarpour Z, Liu R (2017) TWC using advanced spinel materials and prospects for BSVI compliance. *SAE Technical Paper* 2017-26-0126. <https://doi.org/10.4271/2017-26-0126>
- Hanaki Y, Fujimoto M, Itou J (2016) Alternative technology for platinum group metals in automobile exhaust gas catalysts. *SAE Technical Paper* 2016-01-0930. <https://doi.org/10.4271/2016-01-0930>
- Harold M, Grabow L, Liu R, Epling W et al (2020) Reduced precious metal catalysts for methane and NO<sub>x</sub> emission control of natural gas vehicles. In: Presented at the 2020 DOE vehicle technology office annual merit review, June 1–4, 2020
- Hartley R, Henry C, Eakle S, Tonzetich Z (2019) Deposit reduction in SCR aftertreatment systems by addition of Ti-based coordination complex to UWS. *SAE Technical Paper* 2019-01-0313. <https://doi.org/10.4271/2019-01-0313>
- Hashimoto M, Nakanishi Y, Koyama H, Inose S et al (2016) Development of low temperature active material for three way catalyst. *SAE Technical Paper* 2016-01-0932
- Heck RM, Farrauto RJ, Gulati ST (2010) Catalytic air pollution control. <https://doi.org/10.1002/9781118397749>
- Joshi A (2020) Review of vehicle engine efficiency and emissions. *SAE Technical Paper* 2020-01-0352. <https://doi.org/10.4271/2020-01-0352>
- Joshi A (2021) Review of vehicle engine efficiency and emissions. *SAE Technical Paper* 2021-01-0575. <https://doi.org/10.4271/2021-01-0575>
- Joshi A, Johnson T (2018) Gasoline particulate filters—a review. *Emission Control Sci Technol* 4:219–239
- Keav S, Matam SK, Ferri D, Weidenkaff A (2014) Structured perovskite-based catalysts and their application as three-way catalytic converters—a review. *Catalysts* 4:226–255
- Kim PS, Kim YJ, Kim C (2019) Development of ultra-stable Cu-SCR aftertreatment system for advanced lean NO<sub>x</sub> control. *SAE Technical Paper* 2019-01-0743
- Lambert C, Bumbaroska M, Dobson D, Hangas J et al (2016) Analysis of high mileage gasoline exhaust particle filters. *SAE Int J Engines* 9(2):2016
- Lambert C, Chanko T, Jagner M, Hangas J et al (2017) Analysis of ash in low mileage, rapid aged, and high mileage gasoline exhaust particle filters. *SAE Int J Engines* 10(4)

- Larsson P, Ravenhill P, Tunestal P (2019) NO<sub>x</sub>-conversion comparison of a SCR-catalyst using a novel biomimetic effervescent injector on a heavy-duty engine. *SAE Int J Adv Curr Prac Mob* 1(1):278–283. <https://doi.org/10.4271/2019-01-0047>
- Lupescu J, Xu L, Jen H-W, Harwell A et al (2018) A new catalyzed HC trap technology that enhances the conversion of gasoline fuel cold-start emissions. *SAE Technical Paper* 2018-01-0938. <https://doi.org/10.4271/2018-01-0938>
- McCaffery C, Zhu H, Tang T, Li C et al (2021) Real-world NO<sub>x</sub> emissions from heavy-duty diesel, natural gas, and diesel hybrid electric vehicles of different vocations on California roadways. *Sci Total Env* 784:147224
- Moser DH, Nunan J, Alltizer C, Nipunage S et al (2018) Durability of an UF HC Trap/SCR catalyst system applied to a 4-cylinder PZEV calibrated vehicle. *SAE Technical Paper* 2018-01-0336. <https://doi.org/10.4271/2018-01-0336>
- Moses-DeBusk M (2021) Chemistry of cold-start emissions and impact of emissions control. In: Presented at the 2021 DOE annual merit review, held online. <https://www.energy.gov/eere/vehicles/2021-vehicle-technologies-office-amr-presentations-program>
- Nakai E, Goto T, Ezumi K, Tsumura Y et al (2019) MAZDA SKYACTIV-X 2.0 L gasoline engine. In: Presented at in the 28th Aachen colloquium automobile and engine technology
- Newman A (2020a) High-performance heavy-duty catalysts for global challenges beyond 2020. In: Proceedings of the SAE HDD symposium, Gothenburg, Sweden, 16–17 October 2018
- Newman A (2020b) High performance heavy duty catalysts for global challenges beyond 2020. In: Presented at the SAE HDD symposium, Gothenburg, Sweden, October 2018
- Nilsson M, Birgersson H, Müller W, Gabrielsson P et al (2021) Next generation global emission solution platform with dual urea dosing—meeting future emission and efficiency requirements. In: Presented at the 42nd International Vienna Motor Symposium
- Okada Y, Hirabayashi H, Sato S, Inoue H (2019) Study on improvement of NO<sub>x</sub> reduction performance at low temperature using urea reforming technology in urea SCR system. *SAE Technical Paper* 2019-01-0317. <https://doi.org/10.4271/2019-01-0317>
- Parrish D, Stockwell W (2015) Urbanization and air pollution: then and now. *Eos* 96. <https://doi.org/10.1029/2015EO021803>. Permission to use provided by D. Parrish via email on September 29th, 2021
- Pauer T, Weller H, Schunemann E, Walther J et al (2020) A gasoline powertrain with negligible influence on air quality. In: Presented at the 41st International Vienna motor symposium
- Pauly T (2018) Catalyst directions for low NO<sub>x</sub> emissions. In: Proceedings of the CLEERS 2018 Workshop, Ann Arbor, MI, USA, 18–20 September 2018
- Rappe KG, Goffe R, Webb C, Gao F, Wang Y (2020) Development and optimization of multifunctional SCRDPF after treatment for heavy-duty NO<sub>x</sub> and soot emission reduction. In: Proceedings of the 2020 DOE annual merit review, 1–4 June 2020
- Russell A, Epling WS (2011) Diesel oxidation catalysts. *Catal Rev* 53:337–423
- Selleri T, Melas AD, Joshi A, Manara D, Perujo A, Suarez-Bertoa R (2021) An overview of lean exhaust deNO<sub>x</sub> aftertreatment technologies and NO<sub>x</sub> emission regulations in the European Union. *Catalysts* 11:404. <https://doi.org/10.3390/catal11030404>
- Sethuraman S, Sitamraju S, Lopez-De Jesus YM, Markatou P (2019) Experimental and computational study of DOC on CSF for heavy duty diesel applications. *SAE Technical Paper* 2019-01-0586. <https://doi.org/10.4271/2019-01-0586>
- Sharp C, Neely G, Zavala B, Rao S (2021) CARB low NO<sub>x</sub> stage 3 program—final results and summary. *SAE Technical Paper* 2021-01-0589. <https://doi.org/10.4271/2021-01-0589>
- Technology feasibility for model year 2024 heavy-duty diesel vehicles in meeting lower NO<sub>x</sub> standards. [http://www.meca.org/resources/MECA\\_MY\\_2024\\_HD\\_Low\\_NOx\\_Report\\_061019.pdf](http://www.meca.org/resources/MECA_MY_2024_HD_Low_NOx_Report_061019.pdf)
- Tennison P (2019) A systems viewpoint and challenges to meeting ultra-low NO<sub>x</sub>. In: Presented at the ERC Symposium, Madison, WI
- Tessum CW, Paoletta DA, Chambliss SE, Apte JS, Hill JD, Marshall JD (2021) PM<sub>2.5</sub> pollutants disproportionately and systemically affect people of color in the United States. *Sci Adv* 7:eabf4491

- Theis J, Getsoian A, Lambert C (2017) The development of low temperature three-way catalysts for high efficiency gasoline engines of the future. *SAE Int J Fuels Lubr* 10(2). <https://doi.org/10.4271/2017-01-0918>
- Toops TJ (2019) Low-temperature emission control to enable fuel-efficient engine commercialization. In: Presented at in the 2019 DOE Annual merit review, Washington, DC, June 11–13, 2019
- Toops TJ (2021) Low-temperature emission control to enable fuel-efficient engine commercialization. In: Presented at the 2021 US Department of Energy annual merit review, online event, June 2021
- Warkins J, Tao T, Shen M, Lyu S (2020) Application of low-mass CorningR FLORAR substrates for cold-start emissions reduction to meet upcoming LEV III SULEV30 regulation requirement. *SAE Technical Paper* 2020-01-0652. <https://doi.org/10.4271/2020-01-0652>
- Wilson J, Hargrave G, Capper M (2019) ACCT low temperature ammonia delivery using AdBlue™. In: Presented at the integer emissions summit & AdBlue Forum Europe 2019
- Xi Y, Ottinger N, Keturakis C, Liu ZG (2020) A case study of a Cu-SSZ-13 SCR catalyst poisoned by real-world high sulfur diesel fuel. *SAE Technical Paper* 2020-01-1319. <https://doi.org/10.4271/2020-01-1319>
- Xi Y, Ottinger NA, Keturakis CJ, Liu G (2021) Dynamics of low temperature N<sub>2</sub>O formation under SCR reaction conditions over a Cu-SSZ-13 catalyst. *Appl Catal B* 294:120245. <https://doi.org/10.1016/j.apcatb.2021.120245>
- Xu L, Lupescu J, Ura J, Harwell A et al (2018a) Benefits of Pd doped zeolites for cold start HC/NO<sub>x</sub> emission reductions for gasoline and E85 fueled vehicles. *SAE Int J Fuels Lubr* 11(4):301–317. <https://doi.org/10.4271/2018-01-0948>
- Xu Q, Yang W, Cui S, Street J, Luo Y (2018b) Sulfur resistance of Ce-Mn/TiO<sub>2</sub> catalysts for low-temperature NH<sub>3</sub>-SCR. *R Soc Open Sci* 5:171846

# Chapter 4

## Opposed-Piston Engine Potential: Low CO<sub>2</sub> and Criteria Emissions



Laurence J. Fromm, Fabien Redon, and Ashwin Salvi

**Abstract** Opposed-piston (OP) engines were used in many applications in the 1930s–1960s, largely because their high thermal efficiency was important in applications that valued long-range, like aviation, marine vessels, and military vehicles. The engine architecture largely fell into disuse when modern emissions standards began in the 1960s.

Recently, OP engines have enjoyed a renaissance, driven by three primary factors:

1. The inherent efficiency of OP engines remains valuable because of concerns about climate change and energy security
2. Recent advances in design and calibration show that the OP engines can achieve near-zero levels of criteria emissions with conventional aftertreatment system configurations
3. Research and development of OP engines has yielded practical advances in cost, lower complexity, packaging, competitive oil consumption, NVH (noise, vibration, harshness), and other factors.

These factors together suggest that the OP engine is a superior architecture for providing near-zero criteria emissions and lower CO<sub>2</sub> in a cost-effective and robust manner.

This chapter provides an overview of OP engine design characteristics and summarizes recent test results for heavy-duty diesel engines. Results include:

- Peak brake thermal efficiency greater than 49%
- Engine-out soot 75% lower than a benchmark 15 L four-stroke conventional engine
- Tailpipe NO<sub>x</sub> is 96% lower than 2020 EPA regulations; 65% lower than California's 2027 ultralow NO<sub>x</sub> regulation (on the FTP cycle)
- All while using a conventional [DOC/DPF/SCR/ASC (Diesel Oxidation Catalyst, Diesel Particulate Filter, Selective Catalyst Reduction, Ammonia Slip Catalyst)] underfloor aftertreatment system.

---

L. J. Fromm (✉) · F. Redon · A. Salvi  
Achates Power, Inc., 4060 Sorrento Valley Boulevard, San Diego, CA 92121, USA  
e-mail: [Fromm@Achatespower.com](mailto:Fromm@Achatespower.com)

**Keywords** Opposed · Piston · High efficiency · Low NO<sub>x</sub> · Combustion · Climate · Transportation · Cost-effective

## 4.1 Opposed-Piston Engine Architecture

### 4.1.1 Architectural Overview

First manufactured in the 1890s, opposed-piston (OP) engines have been deployed in a variety of ground, marine, and aviation applications. Most notable were the Junkers Jumo 205 (Wilkinson 1940) and 207, German engines used before and during World War II to power planes known for their unparalleled combination of power and efficiency.

In an OP engine there are two pistons in each cylinder, with the piston crowns facing each other. In a typical configuration, the engines have two crankshafts connected by a gear train to combine torque and coordinate piston motion. The piston crowns form the combustion chamber as the pistons come together at the middle of the cylinder (Flint 2009).

Two-stroke cycles are used on most OP engines. In a two-stroke opposed-piston configuration, a set of intake ports are located at one end of the cylinder; exhaust ports are located at the other end of the cylinder. The ports are opened and closed by the motion of the pistons to enable gas exchange with efficient, uniflow scavenging. This configuration avoids the need for cylinder valves. As a result, valves, valve springs, valve keepers, camshafts, pushrods, rocker arms, and other parts used to manage breathing in conventional engines are all eliminated.

Most OP engines operate with diesel fuel and compression ignition. The majority of this chapter discusses the use of diesel fuel; at the end of the chapter, reference is made to other fuels, including JP8, gasoline, natural gas, and hydrogen.

### 4.1.2 Efficiency Advantages

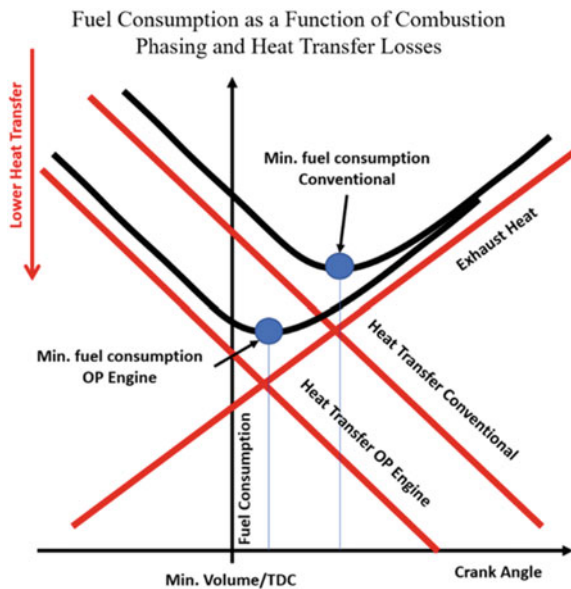
Researchers from Achates Power (Foster et al. 2011) and General Motors (Warey et al. 2016) describe the source of the OP engine efficiency advantage. There are two primary advantages:

The OP engine has lower heat rejection (approximately 30% less) than comparable four-stroke engines due to a reduced surface area/volume ratio of the combustion chamber. The OP engine does not have a cylinder head and has a long effective stroke (combining the piston motion of two converging pistons per cylinder for modest piston speed). Since cylinder heads are cooled to lower maximum temperatures than pistons, the heat transfer benefit of the OP engine arrangement improves further. An additional efficiency benefit is the reduced parasitic loss to cooling fans and improved vehicle aerodynamics due to smaller radiators.

Opposed piston engines also feature more optimally phased combustion timing. Earlier combustion (closer to top dead center or minimal volume) provides higher indicated efficiency, but if combustion is too early it can lead to increased heat transfer losses and lower efficiency. This trade-off can be seen in Fig. 4.1, where the lower surface area to volume ratio results in lower heat transfer losses in the OP engine, enabling combustion timing closer to minimum volume. This increases the effective expansion ratio and reduces fuel consumption compared to conventional engines (Salvi et al. 2018).

Combustion timing is also affected by considerations of heat rejection, noise, emissions, and other factors. Leaving the other factors the same, since the OP engine has lower heat rejection, combustion timing can be advanced to enable more efficient operation. Faster combustion also provides higher indicated efficiency but includes trade-offs. Combustion noise is highly correlated with the maximum rate of pressure rise and therefore combustion duration. For a given maximum rate of pressure rise, the OP engine can operate with shorter and more efficient combustion because it has a lower heat release density. Consider the following example. Achates Power has tested a three-cylinder (six-piston) 4.9 L (1.6 L per cylinder) engine with the same power and torque as a 6.7 L six-piston (1.1 L per cylinder) conventional engine. Since the two engines generate the same amount of power and torque, they also consume the same amount of fuel and release the same amount of heat (or energy) (since the OP engine is more efficient, it can generate the same power and torque with less fuel and heat than a conventional engine but in this example we will ignore this). But since the OP engine cylinder is 45% larger than the conventional engine cylinder (1.6 L vs. 1.1 L) it can release the heat faster at the same maximum rate

**Fig. 4.1** Lower heat transfer losses with the OP engine enables more ideal combustion phasing, minimizing fuel consumption © ASME



of pressure rise, enabling more efficient operation. Notably, the reduced heat release density also means the OP engine operates at a higher air/fuel ratio given the same boost as a conventional engine, an important factor when considering fuels that favor lean combustion, like hydrogen, as noted below.

Taken together, Warey et al. (2016) conclude “the opposed-piston diesel engine [has] about 13–15% lower CO<sub>2</sub> emissions compared to a four-stroke diesel engine”.

### 4.1.3 Emissions Advantages

The most troublesome and common criteria emissions from diesel engines are particulate matter (PM) and oxides of nitrogen (NO<sub>x</sub>). The OP engine has inherent advantages leading to low formation and reduced emissions of both.

#### Low NO<sub>x</sub> Advantages

The ability of an opposed-piston to dynamically control the scavenging ratio and, therefore, the trapped conditions of the engine lead to several of the low NO<sub>x</sub> advantages of the architecture. In a four-stroke engine, nearly all the exhaust gas is expelled during the exhaust stroke, and a full charge of new, cool gas is drawn in during the intake stroke.

By contrast, in a uniflow, two-stroke, opposed-piston engine, the engine controller manages how much exhaust gas is expelled and how much new gas is brought into the cylinder by managing the pressure differential between intake and exhaust. At high loads, the engine needs a significant charge of new gas to combine with a full fuel load. At lower loads, however, less fuel is used so less new gas is required.

As noted above, exhaust and intake ports are open when pistons travel towards the outboard ends of the cylinder. Usually, the engine is designed to have the exhaust piston slightly lead the intake piston. The exhaust ports, therefore, open first to start the blowdown process. When the intake ports are exposed—assuming the intake manifold pressure exceeds that of the exhaust manifold—scavenging begins. When the intake and exhaust ports are closed as the pistons reciprocate back towards minimum volume, scavenging ceases and compression begins. The amount of gas exchanged during the scavenging period is determined by the pressure differential between the intake and exhaust manifolds (higher pressure differential results in more gas exchange).

To create the necessary intake manifold pressure, the OP engine uses some form or combination of boosting devices that can include a turbocharger, a supercharger, a driven turbocharger, an e-turbo, and/or an exhaust gas recirculation (EGR) pump. The amount of boost can be controlled in various ways (bypass or recirculation valve, backpressure valve, continuously variable transmission, and/or electric control). Recent designs have incorporated a driven turbocharger and an EGR pump.

At low- and mid-loads the intake manifold pressure is boosted to a level to provide partial scavenging, adding enough new gas to achieve the proper air-fuel ratio for



clean and efficient combustion, but also leaving residual exhaust gas in the cylinder. Partial scavenging has numerous advantages:

1. It reduces the amount of work required to exchange gases, improving low-load efficiency. As a two-stroke engine, the OP engine does not have a pumping loop; the energy required to boost intake pressure and to facilitate exhaust gas recirculation is the only pumping work.
2. The residual exhaust gas inhibits NO<sub>x</sub> formation. EGR is a well-known and common way to reduce NO<sub>x</sub> formation and emissions. Exhaust gas in the combustion chamber dilutes the oxygen concentration thereby reducing combustion temperatures and NO<sub>x</sub> formation. Leaving exhaust gas in the cylinder avoids the work to expel and then draw in the exhaust gas.
3. It keeps low-load exhaust gas temperatures high relative to four-stroke engines.
4. It keeps high-load exhaust gas temperatures low relative to four-stroke engines. When selective catalyst reduction (SCR) catalysts are between about 250–400 °C they are highly effective in converting NO<sub>x</sub> into nitrogen and water. Higher low-load temperatures and lower high-load temperatures means the exhaust gas temperatures of the OP engine are in the optimal range for NO<sub>x</sub> conversion over most of the operating (speed and load) range of the engine, a much broader conversion range than conventional engines.
5. It enables a catalyst light-off mode (Patil et al. 2018) that generates high exhaust enthalpy to heat the SCR catalyst into the effective temperature range while simultaneously generating very low engine-out NO<sub>x</sub>. The latter feature is important because until the SCR is sufficiently hot it is not very effective at NO<sub>x</sub> conversion.

This combination of advantages makes the OP engine ideal for low NO<sub>x</sub> operation.

During the Federal Test Procedure (FTP) cycle, nearly all NO<sub>x</sub> emissions come from the first 600 seconds after a cold start, before the SCR catalyst is sufficiently warm for effective NO<sub>x</sub> conversion (Sharp et al. 2017). The catalyst light off capability of the OP engine substantially reduces both the time to activate the SCR and the cumulative engine-out NO<sub>x</sub> during the warmup period.

When the catalyst is in the optimal temperature range (250–400° C) it has a 99.7%+ conversion efficiency—the engine can have engine-out NO<sub>x</sub> as high as 3–4 g/bhp-hr and still meet the ultralow NO<sub>x</sub> goals of California and other regions. The partial scavenging ability of the OP engine enables exhaust gas temperatures in the optimal temperature range across most of the operating map of the engine, and the internal EGR capability enables attainment of the engine-out NO<sub>x</sub> goals while operating at or near peak efficiency.

When the engine is operating in low-loads or at idle, the OP engine can generate high exhaust enthalpy when needed to boost catalyst temperature while also generating low engine-out NO<sub>x</sub>. The OP engine can meet all the 2027 ultralow NO<sub>x</sub> requirements of the California Air Resources Board (CARB), including low-load

cycle and idle (Ultralow  $\text{NO}_x$  at Low Loads and Idle 2021). For example, measurements and analysis show that a 10.6 L heavy-duty OP diesel engine with only conventional underfloor aftertreatment system reduced tailpipe  $\text{NO}_x$  by 99.9% compared to CARB's current optional clean idle standard.

Importantly, the OP engine can meet the CARB 2027 ultralow  $\text{NO}_x$  requirements using only a conventional, existing underfloor aftertreatment system (Achates Power Opposed Piston Heavy Duty Diesel Engine Demonstration Performance Results 2021). Conventional engines, meanwhile, employ additional emission control devices, including electric exhaust heaters, dual DEF injectors and mixers, close-coupled SCR, dual ammonia slip catalysts, exhaust hydrocarbon injectors, heated DEF dosing, and cylinder deactivation (Hadl et al. 2021) to meet the same standards, adding significantly to the cost, complexity, and compliance risk of the engine.

### Low Soot

Particulate matter (PM) is another harmful pollutant that results from diesel combustion. PM is filterable material, typically carbonaceous solids (soot) and heavy hydrocarbons derived from uncombusted fuel and lubricating oil. Because the OP engine does not have a fixed cylinder head, the two-piston crowns can be designed to create favorable air dynamics that can minimize soot production. For example, in the Achates Power design, the combustion system design results in large stoichiometric iso-surfaces with excellent mixing and charge motion at the point of auto-ignition. These combustion system attributes are accomplished with a unique set of intake ports that provide swirl to assist in scavenging and mixing, coupled with mating converging piston crowns that create tumble motion near top dead center or minimum volume. Additionally, dual injectors with unique and proprietary nozzle design provide interdigitated fuel plumes with the appropriate flow rates and penetration to avoid contact with the piston surface as shown in Fig. 4.2, unlike conventional four-stroke engines that use the piston surface to redirect the fuel spray.

**Fig. 4.2** OP combustion chamber and fuel spray orientation ©ASME



Agglomerated fuel droplets are sheared apart by the turbulent air motion and mixed. As a result, measurements show that the 10.6 L heavy-duty OP diesel engine has just 25% of the engine out soot as comparable benchmark conventional engines. With a conventional diesel particular filter, the engine can easily satisfy the lower tailpipe PM requirements (0.005 g/bhp-hr on the FTP cycle) that are part of the CARB 2027 omnibus rulemaking while also meeting ultralow NO<sub>x</sub> and low CO<sub>2</sub> requirements.

#### 4.1.4 Mechanical Design Considerations

##### Port timing

Numerous design features determine the efficiency and effectiveness of the gas exchange process, including intake and exhaust port design (size, shape, number, and location), manifold design, and piston phasing. After combustion, an expansion cycle occurs. Exhaust pistons lead intake pistons, typically by 4°–12° crank angles. The exhaust ports, therefore, open first as the pistons continue their outward travel, and blowdown begins. During blowdown exhaust gas can only leave the cylinder via exhaust ports as the intake ports remain closed. As the intake piston continues its outward travel, the intake ports open. Fresh air starts to enter the cylinder when the cylinder pressure falls below the intake manifold pressure. Scavenging continues as long as both intake and exhaust ports are open.

##### Crank train system

A number of OP engine architectures have been developed. The dual-crankshaft, Junkers Jumo-style arrangement has several advantages, including robustness, compactness, and mechanical simplicity. A cut-away of this arrangement, created by Achates Power, and a three-cylinder representation is shown in Fig. 4.3 (Regner et al. 2013).

Most of the successful opposed-piston engines throughout history utilize the dual-crankshaft architecture that is similar to the Achates Power design, including Junkers Jumo 205 and 207, Fairbanks Morse 38D, Rolls Royce K60, Leyland L60, Kharkov Morozov, and Coventry Climax H30.

The virtues of this engine architecture include:

*Compact shape*—Compared to other opposed-piston architectures, the Jumo-style design has a thermally efficient stroke/bore ratio without excessive width or volume. Jumo-style OP engines have been designed to fit in existing passenger and commercial vehicles.

*Conventional crank-slider mechanism*—The architecture uses familiar crankshafts and connecting rods. It does not require any unusual engine mechanisms.

**Stroke-to-bore ratio.** The ratio of stroke (which is the combined stroke of the two OP pistons) to bore influences engine thermal efficiency in several ways:

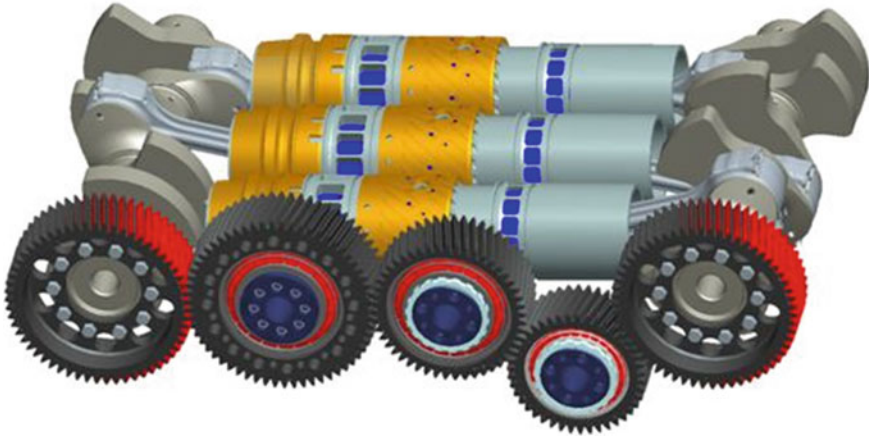


**Fig. 4.3** Cutaway of power module concept, showing internal gear train © SAE International

- The ratio of combustion chamber surface area relative to volume—highly correlated with heat rejection—decreases as the stroke/bore ratio increases. Lower heat rejection leads to higher indicated thermal efficiency. The impact is non-linear as the change in indicated thermal efficiency gets progressively worse as the stroke/bore ratio decreases.
- The scavenging efficiency increases as the stroke/bore ratio is increased. Longer stroke engines typically require less pumping work to achieve the same trapped conditions as a shorter stroked engine of the same displacement.
- Engine friction has a non-linear dependence on stroke/bore ratio. Achates Power found that for a fixed peak cylinder pressure, the crankshaft bearing friction decreases as the stroke/bore ratio increases, while the power-cylinder friction has the opposite effect. The net effect is that the friction increases when the stroke/bore ratio exceeds a value of about 2.3, although the magnitude of the effect is much smaller than the heat transfer and pumping effects.

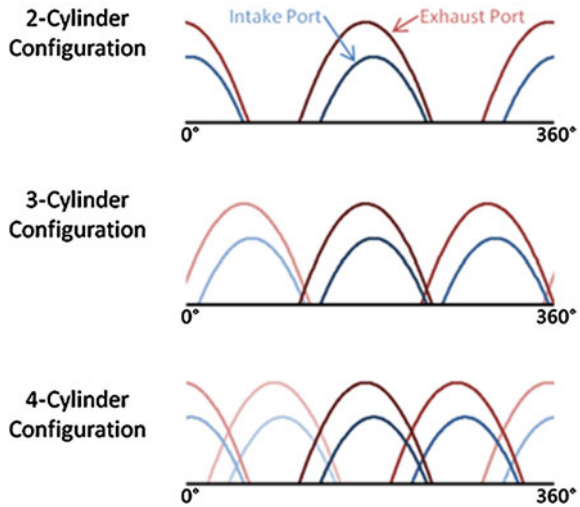
Combining these factors, indicated thermal efficiency and pumping work typically benefit from a longer stroke/bore ratio. Friction work decreases until a stroke/bore value of about 2.3 and then increases as the stroke/bore is increased further. Any OP engine with a stroke/bore below 2.0 will be compromised in efficiency.

In general, this trend is valid for all two-stroke engines, not only the opposed-piston, two-stroke engine. Conventional two-stroke engines (with one piston per cylinder) are usually designed with a stroke/bore ratio below 1.5 to avoid excessive piston speed. Any theoretical advantages of the two-stroke combustion process are overpowered by scavenging and heat transfer losses due to the low stroke/bore ratio.

### **Cylinder count**

A three-cylinder, opposed-piston engine is optimal from a gas exchange perspective compared to two-cylinder or four-cylinder versions, primarily due to gas dynamic

**Fig. 4.4** Cross-charging in a 2-stroke Engine © SAE International



effects. Figure 4.4 shows the intake and exhaust port open areas versus crank angle for two-cylinder, three-cylinder, and four-cylinder engines. The gas exchange duration is about 120° crank angle in a two-stroke, uniflow scavenged engine. In a three-cylinder design, the scavenging events are aligned in a way that they have minimal interference with each other and still keep enough mass flow going over the cycle to provide adequate energy to the turbocharger so it operates most efficiently to compress the intake air.

In a two-cylinder configuration, however, the gas-exchange events are too far separated in time, causing the turbocharger to lose energy over the cycle, resulting in a negative effect on the turbine's efficiency—especially at lower loads and engine speeds. The loss of turbocharger energy has to be compensated by additional boost elsewhere (from a supercharger, electric turbo charger, driven turbo charger, or another pumping device), which causes a reduction in brake thermal efficiency.

Conversely, in a four-cylinder configuration, the gas-exchange events overlap too much. This causes cross charging to occur at a point in time when hot exhaust gases are leaving a cylinder. The interruption of exhaust gas flow causes an increase in residual gas content and, therefore, a lower scavenging efficiency—leading to a reduction in thermal efficiency. Even with a complex design of the exhaust manifold to separate the pulses, there is still gas communication even with a twin scroll turbine housing. Separating the exhaust system into two turbochargers leads back to the two-cylinder problem with the energy flow interruption over the cycle.

Two-, four-, five-, and six-cylinder options are all viable as part of a family of engines—and indeed speak to the modularity of the design—but a three-cylinder design is optimal.

## **Fuel injection**

Modern OP engines use off-the-shelf high-pressure common rail fuel systems. Injectors, rails, and pumps are standard. Unique nozzles are created to account for the different combustion chamber geometry inherent in the OP engine. In the Achates Power designs, each cylinder contains two injectors facing each other. This proprietary design has been extensively tested.

## **Cooling System**

The consequence of high-specific power is higher thermal loading into the engine components, especially the pistons. A gallery-cooled design can be used to manage the heat going into the pistons. Dual oil cooling jets per piston can be used, if necessary, to provide the necessary oil flow to maintain acceptable piston temperatures.

Cooling circuits for the cylinder are also designed to manage high thermal loads, particularly at the center of the cylinder, where combustion occurs, and at the exhaust port bridges where hot exhaust gas exits the engine.

An important objective of cylinder cooling design and control is to maintain a uniform temperature axially along the cylinder bore to minimize bore distortion and allow the use of lower friction piston rings.

## **Wrist pin design**

It is difficult to sufficiently lubricate the wrist pin bearings of two-stroke engines because they are primarily under compressive load. Without a force reversal on the wrist pin, lubricating oil fails to migrate to all surfaces of the pin, leading to premature wear.

A biaxial bearing has been designed and developed to supply sufficient lubrication to two-stroke engine wrist pins. This bearing design uses two distinct, non-concentric journals to carry the load. The motion and geometry of the pin and carrier alternately load and unload different portions of the bearing so that the full bearing is lubricated with a squeeze-film during every engine revolution as shown in Fig. 4.5.

Achates Power has designed, built, and tested its own biaxial bearing to operate up to 230 bar peak cylinder pressures in Jumo-style engine configuration. Additionally, experimentally calibrated and proprietary analytical models have been developed to determine minimum oil film thickness, density, and film pressure of different bearing design alternatives, which enable rapid design evolution.

## **Oil Consumption and Cylinder Durability**

Ported engines have historically been known to have problems with excessive oil consumption, driven by a trade-off between low oil consumption and acceptable cylinder and piston durability. A common oil consumption goal for commercial engines is  $<0.1\%$  of fuel (fuel-specific oil consumption  $<0.1\%$ ).

Several design factors can enable excellent durability with competitive oil consumption (Chown et al. 2019; Durability Assessment of OP Engines 2021):

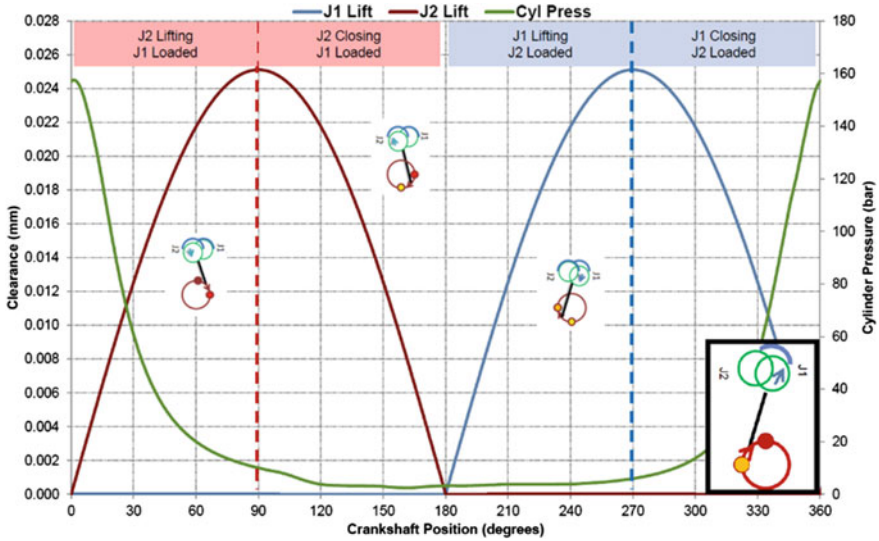


Fig. 4.5 Biaxial bearing J1, J2 loading and unloading

### Cylinder Hone Texture

The cylinder hone texture is critical for retaining oil on the cylinder wall and maintaining engine durability. Increased retention, however, generally leads to increased oil consumption. Proprietary hone patterns that selectively retain oil where needed to provide controlled lubrication can enable reduced oil consumption alongside increased durability.

### Unique OP Engine Architecture

An example opposed-piston architecture is shown in Fig. 4.6, which utilizes four piston rings, two compression (located at the top of the piston), and two oil control (located at the bottom of the piston). The compression piston rings cross the ports as the pistons open and close the intake and exhaust ports while the oil control rings always remain below the ports. This unique configuration has a few advantages.

#### *Separate lubrication circuit*

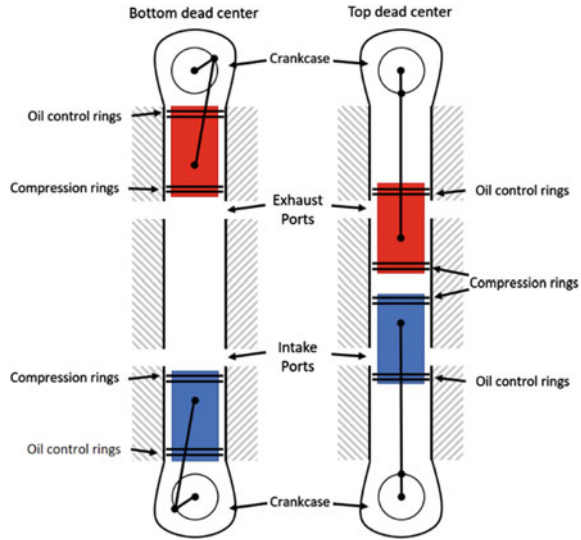
Like a conventional four-stroke engine, the closed crankcase scavenging prevents the mixture of crank oil with fresh air and eliminates the oil consumption loss mechanism that traditionally plagued two-stroke engines.

#### *Oil Control Rings Seal Oil from Manifolds*

The oil control rings prevent crankcase oil from escaping into the ports. The oil control rings remain outside the ports, sealing the crank case from the ports and manifolds.



**Fig. 4.6** OP engine schematic at bottom dead center and top dead center, not to scale



### *Reduced Thermal Distortion of Oil Control Rings*

Reduced thermal distortion of the cylinder helps maintain proper contact between piston rings and cylinder walls. The heat transfer to the cylinder walls causes thermal deformation, which can vary radially and along the length of the cylinder. If the cylinder is exposed to high thermal distortion, it may be difficult to maintain proper contact between the piston rings and the walls. This could lead to high blow-by of the trapped cylinder mass, poor oil control from the crankcase to the combustion chamber, and challenges with cylinder kit durability.

In OP engines, the cylinder wall where the oil control rings operate experiences less thermal distortion because combustion is located much further away from where the oil control rings operate and because the hot exhaust gases escape through the ports prior to interacting with the oil control ring running zone. The lower thermal distortion helps the oil rings conform to the bore surface for a given ring tension, improving the oil consumption vs. friction tradeoff. Conventional four-stroke engines have oil control rings immediately adjacent to the compression rings, which operate in a hotter environment that is more prone to greater thermal distortion near the engine head.

The oil ring configuration of an OP engine also reduces the interaction between hot exhaust gases and the oil control ring because the running zone overlap between the oil rings and compression rings are minimized.

Another benefit of this configuration is that blow by gases do not leak in the crankcase but instead exit into the intake and exhaust manifold where they are re-ingested or exhausted and processed by the aftertreatment system. This significantly reduces the dilution or contamination of the crankcase oil by fuel or soot, lowering the oil degradation rate and extending oil change intervals.



## 4.2 Performance and Emissions Results

With funding provided by the California Air Resources Board, the South Coast Air Quality Management District, the San Joaquin Air Pollution Control District, and the Sacramento Metro Air Quality Management District, CALSTART leads an industry team that created and demonstrated a three-cylinder (six-piston) 10.6 L, heavy-duty diesel engine for long haul transit.

The engine has a rated output of 300 kW (400 hp) at 1700 rpm, and peak torque of 2270 Nm at 950 rpm. The engine operating range is 550 to 2000 rpm.

Several different prototype engines were built and tested.

An early prototype was tested on a transient dynamometer at Aramco Services in Novi, MI. On the combined hot and cold FTP cycle, tailpipe NO<sub>x</sub> was measured at 0.016 g/bhp-hr, below the 2027 CARB limit of 0.02 g/bhp-hr on this test cycle. In this test, a single degreened underfloor aftertreatment system, using a diesel oxidation catalyst (DOC), selective catalyst reduction on filter (SCRoF), selective catalyst reduction (SCR), and ammonia slip catalyst (ASC) was utilized. No other aftertreatment system or emissions control technology was utilized.

Another prototype engine with additional capability was tested on a stationary dynamometer at Achates Power in San Diego, CA. This engine measured CO<sub>2</sub> of 415 g/bhp-hr on the Supplemental Emissions Test (SET) cycle, well below the 2021 limit of 447 and the 2027 limit of 432 set by the U.S. Environmental Protection Agency (EPA) Green House Gas II regulations. This engine was tested without an aftertreatment system, but with backpressure on the exhaust to simulate the aftertreatment.

Achates Power worked with a leading catalyst supplier to model tailpipe emissions on this more capable engine. In this case, a fully aged (450,000 miles) conventional one box aftertreatment system (DOC, DPF, SCR, ASC) was modelled, using measured engine out data.

The cumulative results of these tests are displayed in the tables below. Table 4.1 shows the measured and modelled results compared to the 2020 standards from

**Table 4.1** CO<sub>2</sub> and NO<sub>x</sub> comparison to 2020 standards

	Milestone 3.5 engine and BASF analysis	2020 Standard or typical	Improvement versus 2020 (%)
SET cycle	0.014 g/hp-hr NO <sub>x</sub>	0.20 g/hp-hr NO <sub>x</sub>	93
	<b>415 g/hp-hr CO<sub>2</sub></b>	460 g/hp-hr CO <sub>2</sub>	10
FTP cycle	0.007 g/hp-hr NO <sub>x</sub>	0.20 g/hp-hr NO <sub>x</sub>	96.5
	<b>465 g/hp-hr CO<sub>2</sub></b>	555 g/hp-hr CO <sub>2</sub>	16
Low load cycle	0.021 g/hp-hr NO <sub>x</sub>	1 g/hp-hr NO <sub>x</sub> <sup>1</sup>	98
Clean idle	0.02 g/hr NO <sub>x</sub>	30 g/hr NO <sub>x</sub> <sup>2</sup>	99.9

Key: **Measured from steady and transient**  
*modelled based in measured engine out*

**Table 4.2** CO<sub>2</sub> and NO<sub>x</sub> comparison to 2027 standards

	Milestone 3.5 engine and BASF analysis	2027 Regulatory Limits (CARB/EPA)	Improvement versus 2027 standards (%)
SET cycle	0.014 g/hp-hr NO <sub>x</sub>	0.020 g/hp-hr NO <sub>x</sub>	30
	<b>415 g/hp-hr CO<sub>2</sub></b>	432 g/hp-hr CO <sub>2</sub>	4
FTP cycle	0.007 g/hp-hr NO <sub>x</sub>	0.020 g/hp-hr NO <sub>x</sub>	65
	<b>465 g/hp-hr CO<sub>2</sub></b>	503 g/hp-hr CO <sub>2</sub>	8
Low load cycle	0.021 g/hp-hr NO <sub>x</sub>	0.050 g/hp-hr NO <sub>x</sub>	58
Clean idle	0.02 g/hr NO <sub>x</sub>	5 g/hr NO <sub>x</sub>	99.6

**Key: Measured from steady and transient**

*modelled based in measured engine out*

CARB and EPA (since there are no 2020 standards for low-load cycle and idle, typical figures from current engines were used). The 10.6L OP engine reduces NO<sub>x</sub> from current levels by 93–99.9%, depending on the cycle, and reduced CO<sub>2</sub> by 10–16%. Table 4.2 shows the measured and modelled results compared to the 2027 CARB and EPA requirements. In all cases, the OP engine shows evidence it can meet the future standards with a considerable margin to compliance. Since the engine utilizes only a conventional underfloor aftertreatment system, it offers a lower cost, lower complexity, and reduced compliance risk solution compared to other ultralow NO<sub>x</sub> solutions that require close-coupled and heated components.

In summary, the inherent low CO<sub>2</sub> and low NO<sub>x</sub> features of the opposed-piston engine makes it well suited to enable more sustainable transportation in a cost-effective and practical manner.

### 4.3 Alternate Fuels

In addition to diesel, OP engines operate on other fuels. The main efficiency advantage of the OP engine comes from low heat rejection due to favorable surface area to volume ratios of the combustion chamber, a feature that exists across fuel types.

Cummins worked with Achates Power to develop the Advanced Combat Engine (ACE) (Achates Power and Cummins Develop Leap Ahead Capability for the US Army Ground Combat Fleet 2021) for the U.S. Army. Operating on JP-8 fuel, the ACE engine takes advantage of low heat rejection, low fuel consumption, and high specific power to double the power pack density of combat engines.

Fairbanks Morse manufactures OP engines for power generation that operate with natural gas, with diesel pilot (Fairbanks Morse 2021). One advantage of OP engines in a dual fuel configuration is that injectors are arrayed around the circumference of the engine, offering more space for multiple injectors.

Achates Power has demonstrated a 2.7 L, three-cylinder opposed-piston engine operating with gasoline fuel using compression ignition (Salvi et al. 2018). A key

enabling feature of the OP engine for compression ignition, with low reactivity fuels, is enhanced ability to control trapped conditions, including trapped temperatures, by dynamically managing the scavenging ratio. Retaining exhaust gas at low-loads results in sufficient temperature for stable combustion across the full operating range of the engine using only compression ignition (Kalghatgi et al. 2021).

Achates Power and others have begun investigation of hydrogen combustion in an OP engine (Hydrogen Opposed Piston Engines 2021). Hydrogen combustion with an air/fuel equivalence ratio ( $\lambda$ ) of 2.2 or greater creates very little NO<sub>x</sub>. The ability to operate sufficiently lean across the operating range of the engine can result in combustion with near-zero NO<sub>x</sub>, PM, HC, and CO<sub>2</sub>. The OP engine, with its ability to operate naturally lean, is a key enabler to near-zero emissions hydrogen combustion.

## 4.4 Conclusion

While the transportation industry is making considerable effort to reduce the environmental harm caused by vehicle operation, it seems likely that internal combustion engines will be used for some time as different applications and geographies are more or less amenable to substitute technology. Since the opposed-piston engine has inherent advantages in low cost, low emissions, and high efficiency it deserves consideration for widespread commercial adoption.

## References

- Chown D, Koszewnik J, MacKenzie R, Pfeifer D, Callahan B, Vittal M, Froelund K (2019) Achieving ultra-low oil consumption in opposed piston two-stroke engines. SAE Technical Paper 2019-01-0068
- Foster D, Herold R, Lemke J, Regner G, Wahl M (2011) Thermodynamic advantages of opposed-piston, two-stroke engines. SAE International Technical Paper 2011-01-2216
- Gasoline Compression Ignition (GCI) engine technology: future prospects (2021) In: Kalghatgi G, Agarwal A, Goyal H, Houidi MB (eds). Springer
- Hadl K, Raser B, Sacher T, Graf G (2021) Solutions for lowest NO<sub>x</sub> and CO<sub>2</sub> emissions on heavy-duty engines. In: MTZ worldwide, Vol 82, Issue 03, pp 16–22  
<https://achatespower.com/wp-content/uploads/2021/06/Achates-Power-Ultralow-NOx-at-Low-Loads-and-Idle.pdf>. Last accessed 12 July 2021
- <https://achatespower.com/wp-content/uploads/2020/12/Achates-Power-Opposed-Piston-Heavy-Duty-Diesel-Engine-Demonstration-Performance-Results-Ultralow-NOx-without-additional-hardware.pdf>. Last accessed 12 July 2021
- <https://achatespower.com/wp-content/uploads/2021/02/Durability-Assessment-of-OP-Engines-Feb.2021.pdf>. Last accessed 13 July 2021
- <https://achatespower.com/achates-power-and-cummins-develop-leap-ahead-capability-for-the-us-army-ground-combat-fleet/>. Last accessed 14 July 2021
- <https://www.fairbanksmorse.com/38d-8-1/8>. Last accessed 14 July 2021

<https://achatespower.com/wp-content/uploads/2021/05/Hydrogen-Opposed-Piston-Engines.pdf>.

Last accessed 14 July 2021

- Patil S, Ghazi A, Redon F, Sharp C, Schum D, Headley J (2018) Cold start HD FTP test results on multi-cylinder opposed-piston engine demonstrating rapid exhaust enthalpy rise to achieve ultra low NO<sub>x</sub>. SAE Technical Paper 2018-01-1379
- Regner G, Johnson D, Koszewnik J, Dion E et al (2013) Modernizing the opposed piston, two stroke engine for clean, efficient transportation. SAE Technical Paper 2013-26-0114
- Salvi A, Hanson R, Zermeno R, Regner R et al (2018) Initial results on a new light-duty 2.7 L opposed-piston gasoline compression ignition multi-cylinder engine. ASME ICEF2018-9610
- Sharp C, Webb C, Neely G, Carter M et al (2017) Achieving ultra low NO<sub>x</sub> emissions levels with a 2017 heavy-duty on-highway TC diesel engine and an advanced technology emissions system—thermal management strategies. SAE Technical Paper 2017-01-095
- Waley A, Gopalakrishnan V, Potter M et al (2016) An analytical assessment of the CO<sub>2</sub> emissions benefits of two-stroke diesel engines. SAE International Technical Paper 2016-01-0659
- Wilkinson P (1940) Aircraft diesels, 1st edn. Pitman, New York

# Chapter 5

## An Overview of Hybrid Electric Vehicle Technology



Nirendra Nath Mustafi 

**Abstract** Fossil-fuel-based transportation has raised several global concerns such as ever-increasing demand for petroleum oils, their high prices and exhaustible reserves, and the associated environmental (global warming, climate change) and health degradation. Hence, the world is facing challenges to find sustainable solutions to these major issues. Adaptation of efficient, and cleaner alternative transportation systems with low to zero carbon footprint has been emphasized among the different strategies. Hybrid electric vehicle (HEV) technology has exhibited promising solutions for ensuring improvements in fuel consumption and emission rates with a performance comparable to the conventional vehicles. The performance of an HEV largely depends on the powertrain type, components configuration and its architecture, and energy management strategy (EMS). This chapter presents an overview on essential components used in HEVs including the energy storage system (i.e. the battery, super-capacitor, and fuel cell), electric motors, and dc-dc/dc-ac converters and their size/ capacity optimization. Development of an efficient EMS to harvest the benefits of HEVs without compromising vehicle performance remains a major challenge. The state-of-the-art in EMSs for efficient HEVs is presented. Furthermore, factors/ issues affecting the performance of the EMS are discussed. It is quite crucial to apply a real time control strategy for an HEV capable of coordinating the on-board power sources ensuring enhanced fuel economy and reduced emissions. However, challenges exist in developing an efficient control strategy satisfying conflicting control constraints involving fuel consumption, emissions and drivability, without over-consuming battery power at the end of a given drive cycle. A section is devoted to explore emissions performance of HEVs under actual operating conditions and the emissions management of an HEV. Finally, key issues and challenges of HEV technology are identified and discussed.

**Keywords** Hybrid electric vehicle · Battery · Super capacitors · Energy management system · Controls · Emissions

---

N. N. Mustafi (✉)  
Department of Mechanical Engineering, Rajshahi University of Engineering & Technology,  
Rajshahi 6204, Bangladesh

## 5.1 Introduction

Rapid growth of population and urbanization have led to an increased utilization of transportation, resulting in serious environmental and health hazards globally. Among the different modes, road transport alone consumes about three-quarters of the total energy consumption in this sector (Singh et al. 2019). Road transport plays a significant role in economic development of any nation by providing freedom to mobility for people, goods and services (Agarwal and Mustafi 2021). So far the vehicles predominantly run on internal combustion engine (ICE), and road vehicles account for nearly three-quarters of transport CO<sub>2</sub> emissions (IEA 2020). Furthermore, the ICE-operated vehicles fail to exhibit a good overall efficiency while running in city routes mostly at low loads, even though they are really very efficient at high load operations. The automotive industry came up with solutions to these issues by introducing full electrical vehicles (EVs) and HEVs. EVs have exhibited limited success due to its high cost, additional weight of batteries, decreased load capacity, low driving range and recharging issues. However, HEV technology has been acknowledged as a perfect transition from the full-petroleum vehicle to the full-EV. HEV technology combines two power sources—an ICE and electric motor for propulsion (Jorgensen 2008). A variety of hybrid cars are now made and marketed by the most popular manufacturers such as Audi, BMW, Chevrolet, Ford, Honda, Mercedes, McLaren, Nissan, Mitsubishi, Hyundai, Porsche, Tesla, Toyota, etc. In a HEV, the motor is driven by a rechargeable battery pack, which is usually charged by on-board generator/alternator and the regenerative braking technology. The plug-in hybrid electric vehicle (PHEV) is another version of HEV having recharging facility from external sources, such as from off-peak grid electricity. Unlike a regular HEV, PHEV relies primarily on electric motor's power with ICE as a backup source. Beyond a threshold state of charge (SoC) of the storage battery, a PHEV turns into a regular HEV and power is derived primarily from ICE (Singh et al. 2019). A PHEV can provide similar environmental benefits to EVs without abandoning the benefits of an ICE-powered vehicle. Many people in urban areas do not exceed the full-EV range in a day, thus can avoid petroleum-fuel uses completely (Amjad et al. 2010).

The automotive industry has demonstrated significant advancements in HEV technology in recent decades. The potential benefits of HEV technology lie in enhanced fuel economy while complying with stringent emission norms and drivability requirements. HEV reduces the use of ICE thus can play an important role in solving the world's environmental and energy security crises.

HEV, being a multiple energy system, faces challenges in designing appropriate powertrain control systems, which are often quite complex by nature. In general, the parameters are nonlinear and require fast response to their variations during vehicle operation. In many cases, formulation of the control design objectives becomes significantly difficult. It is a multivariable control problem with many actuators, variables, and sensors aiming to an optimization in power flow for the best fuel economy and/or minimized emissions.

This chapter has seven different major sections. After this brief introduction, Sect. 2 presents general architecture of HEVs followed by an overview on HEV components presented in Sect. 3. In Sect. 4, an overview of energy management strategies (EMS) of HEVs is portrayed. In Sect. 5, emissions performance of HEVs are reviewed in comparison to the conventional vehicles under both the laboratory and real world conditions. The key issues and challenges of HEVs are identified and discussed briefly in Sect. 6. Finally, Sect. 7 concludes the chapter.

## 5.2 General Architecture

HEV architectures are essentially divided into two categories: (i) series HEV, in which an ICE coupled with an electric machine (generator), supplies electricity to the electric motor to power the wheels of the vehicle, and to the storage batteries for recharging, (ii) parallel HEV has options of dual power supply to the vehicle’s driving wheels. Either the ICE or the electric motor—or both—can propel the vehicle. In this case power produced during regenerative braking and from the ICE (if ICE produces more power than the requirement of the vehicle) recharges the batteries via the electric motor. The third category is the combination of series and parallel HEV with an aim of harvesting benefits from both configurations. Though this system architecture is quite complicated and expensive, some modern HEVs are built on this principle using advanced control and manufacturing technologies.

### 5.2.1 Series Configuration

In a series HEV though the required power is generated by an ICE, eventually the drive wheels get power from an electric motor. Hence, a series HEV is basically an EV with an onboard electrical energy generation facility via an ICE–generator pair unit (Genset), which not only supplies power to drive wheels through an electric motor but also recharge the storage batteries (Fig. 5.1). Since the ICE and the vehicle drive train are decoupled and vehicle’s speed/acceleration depends only on stored power, the ICE can operate at optimal speeds resulting in better efficiency. Since

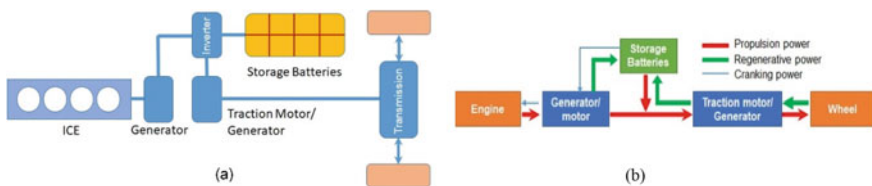


**Fig. 5.1** Rear-wheel-drive series HEV: **a** schematic diagram, **b** energy flow diagram

electric motors drive the wheels, energy gain is also possible through regenerative braking systems. A series HEV is often described as the extended range EV, which is facilitated by the Genset. Compared to parallel HEV, its control is simple. However, series configuration needs a large storage battery pack, which adds extra weight to the vehicle. Efficiency losses appear from multiple energy conversions such as mechanical—electrical—mechanical.

### 5.2.2 Parallel Configuration

In a parallel HEV configuration, an electrical powertrain system is coupled with the conventional ICE-based powertrain system through a clutch, which facilitates the vehicle to be driven by either of the power sources or both sources together (Fig. 5.2). Hence, the required power during acceleration can be shared from both sources, which makes it possible to downsize the ICE and motor as compared with a series HEV counterpart. Coupling of two power sources in a variety of powertrain configurations is possible in parallel HEVs such as post- and pre-transmission configurations, and through-the-road HEV, which combines two sources of traction forces—ICE for the front wheels and wheel-motors for the rear wheels (Xi et al. 2014; Mierlo and Hegazy 2014). The storage batteries are usually recharged using excess torque (requested by the driver) generated by ICE through motor/generator and also from regenerative braking.

Parallel HEV has flexibility in ICE operation to be turned on and off frequently as per requirements of the control strategy. Its overall powertrain efficiency is also higher than that of a series HEV for most operating conditions. In contrast to a series HEV, ICE in a parallel HEV can operate close to its optimum point only under certain conditions. The electro-mechanical system in a parallel HEV tend to be more complex, as compared to a series HEV.

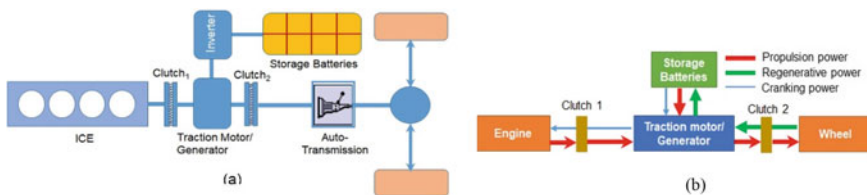
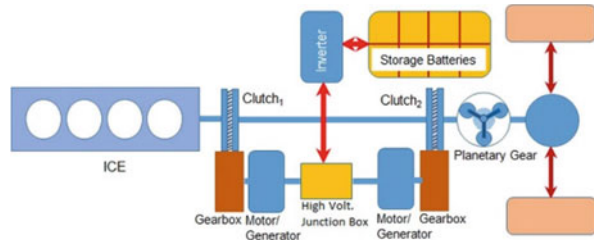


Fig. 5.2 Rear-wheel-drive parallel HEV: **a** schematic diagram, **b** energy flow diagram



**Fig. 5.3** Schematic of rear-wheel-drive series—parallel HEV



### 5.2.3 Series—Parallel Configuration

A series–parallel HEV (SP-HEV) is also known as a power-split HEV (see Fig. 5.3), as the ICE power gets divided along two paths: one heads to the generator connected to both the storage batteries as well as the electric drivetrain to drive-wheels (series path) and the other heads to drive-wheels through the conventional mechanical drivetrain (parallel path). In series path, after the generator, the electric power can either partly flow to the batteries for recharging or entirely to the wheels via the electric drivetrain. In parallel path, mechanical power of the ICE is partly or entirely transmitted to the drive-wheels. The part of mechanical power, which is not consumed by the mechanical drivetrain, produces electrical power through another motor/generator for battery recharging purpose. In the torque-assist mode of operation, the electric drivetrain can supply extra power to the drive-wheels beyond the capacity of the ICE.

The energy management system of a SP-HEV permits the electric drivetrain to adjust the ICE load for attaining the optimal fuel economy. In fact, performance of a SP-HEV depends on the fraction of power flow through the series and parallel paths. SP-HEV configuration may help to decrease the capacity of the storage battery and electric motors compared to those of a series HEV (Mierlo and Hegazy 2014), and can lower the size of ICE compared to that of a parallel HEV. In general, SP-HEVs enjoy a speed advantage, since series configuration is more efficient at low vehicle speeds (suitable for city drive) whereas parallel configuration is more efficient at high speeds (suitable for highway drive). However, the powertrain structures of SP-HEVs are complex containing two motors/generators connected to a planetary gear set and acts as a continuously variable transmission (Tran et al. 2019). Though the planetary gear set can contribute to preset power flow through the two paths, it certainly needs a sophisticated control system for power flow control to attain the best fuel economy. Hence, design of control systems for the series–parallel configuration remains the major challenge compared to that for a series or parallel configuration.

### 5.2.4 Plug-In HEV

Plug-in HEVs (PHEVs) are similar to the regular HEVs having an additional feature of recharging the storage batteries by simply plugging in an external electrical outlet.

Most PHEVs can easily be charged with a standard 120 V/240 V outlet thus providing the facility to plug in at someone's workplace or home or at the public charging stations. Hence, the battery in PHEV can be recharged through an external electric power source, regenerative braking, and by the ICE. In order to run predominantly on electric propulsion mode, PHEV uses a larger battery pack compared to a standard HEV to cover short trips in cities. For long drives, a PHEV employs ICE propulsion mode like other HEVs, which offers the desired driving range. PHEVs are generally referred to as the extended-range HEVs having driving ranges comparable to conventional petrol vehicles. Depending on the drive cycle, propulsion option (i.e. mechanical or electrical or combined) is selected for the most efficient operation as per the decision given by an onboard computer. It is possible that a person who drives less only in city areas within the all-electric range, may not use any fuel at all. In general, HEVs apply charge-sustaining control strategies while the SoC of PHEVs sustains a relatively broader range of drivability (Zhang et al. 2019).

The important attractive feature of PHEV is that the electricity required to propel the vehicle may be generated from a variety of energy sources including both conventional and renewable sources. It has been reported that considering over the whole fuel cycle, the PHEVs emit lower GHGs, compared to the conventional vehicles and HEVs (Amjad et al. 2010).

### 5.3 Basic Components of Hybrid Vehicle

Irrespective of the configuration of HEV system, its key components can be classified into four groups:

- Primary energy source/Prime mover
- Electric motors (EMs), DC-DC converter, and DC-AC inverters
- Energy storage system
- Transmissions.

#### 5.3.1 Primary Energy Source/Prime Mover

In general, the ICE (gasoline or diesel engine) acts as the prime mover or primary energy source of a hybrid electric vehicle. Fuel cells, with environmentally friendly features, are considered as the third category prime mover for HEVs. Based on the driving range, drivability requirements (i.e. light, medium or heavy duty), environmental concerns etc., an appropriate prime mover is selected. For light duty HEVs, where a wide range of vehicle operating speed is featured, a gasoline-ICE is chosen. On the other hand, for medium duty HEVs, where vehicle speed is not so important, a diesel-ICE is chosen. However, understanding of torque/power characteristics of ICEs w.r.t. speed, fuel consumption, and emissions is crucial to design an efficient hybrid system. Diesel engine operates at higher compression ratios and its

combustion temperature is also much higher compared to gasoline engines, thus provides relatively higher efficiency inherently. Diesel engines require less-frequent maintenance and exhibit a longer lifetime compared to gasoline engines counterpart. Though ICEs are widely regarded as supreme prime movers, they are strongly criticized for emitting harmful pollutions including GHGs, oxides of nitrogen ( $\text{NO}_x$ ), and particulate matter. In general, cold starting, frequent off-and-on operations, sudden acceleration, climbing hills etc. cause increased emissions from ICEs and hence their use should be minimized during such operations.

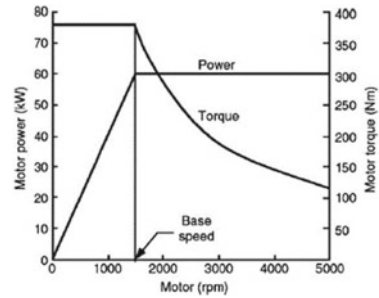
In fuel cell hybrid electric vehicles (FCHEVs) the energy fed to the EMs comes from multiple energy sources including fuel cell, batteries, and/or supercapacitors (SCs). Therefore, a fuel cell, in place of an ICE, acts as a prime mover for FCHEVs. Among the different types of fuel cells, proton exchange membrane fuel cell (PEMFC), in particular, has gained significant attention as a prime mover for fuel-cell HEVs (FCHEVs) to the automotive industries. A proton-exchange membrane fuel cell (PEMFC) uses  $\text{H}_2$  as a fuel, which instead of taking part in combustion reactions produces electrical power through electrochemical reactions and emits only water and heat. Unlike rechargeable batteries, fuel cells can operate continuously on a continuous supply of fuel ( $\text{H}_2$ ). Apart from the environmental benefits, FCHEVs demonstrate more energy efficiency compared to conventional ICEVs and HEVs. For instance, Toyota FCHV-adv has demonstrated a maximum mileage of ~830 km/~760 km based on 10–15 test cycle/JC08 test cycle per refueling (Toyota Develops Advanced Fuel Cell Hybrid Vehicle Toyota FCHV-adv 2021) and Toyota Mirai XLE 2021 has an EPA-estimated best fuel economy of 76 city/71 highway/74 combined MPGe (Miles per gallon gasoline equivalent) (EPA 2021). However, hydrogen production, storage, and refueling infrastructure, low specific power rating, use of expensive rare material catalysts, high system complexities, and the vehicle's high price are the major challenges for FCHEVs (Das et al. 2017).

### 5.3.2 *Electric and Electronic Machines*

**Electric Motors.** The electric motor is an indispensable component of electric propulsion system in HEVs. In general, EMs provide relatively higher efficiency compared to ICEs particularly at low-load range. Traction EMs require to exhibit the performance characteristics (i.e. speed-torque characteristics) close to be ideal, i.e. uniform maximum torque at low-speed operations (for vehicle's frequent starting, acceleration, climbing hills etc.) and uniform power at high-speed operations for cruising, as illustrated in Fig. 5.4 (Amjad et al. 2010; Wang et al. 2018).

Several types of EMs can be considered for HEVs application due to the expeditious advancements in power electronics and control techniques. The most preferred EMs for HEVs application include brushless DC motor (BLDC), AC induction motor, Permanent Magnet Synchronous Motor (PMSM), Switched Reluctance Motor (SRM) due to high efficiency, low cost (except PMSM) and less maintenance, better

**Fig. 5.4** Typical performance characteristics of a traction EM [adapted from Amjad et al. (2010)]



reliability and prolonged operating life. BLDC machine works on electronic commutation system instead of brushed commutation, which offers better flexibility and capabilities particularly in speed controls such as “micro stepped” operation at low speed and maintaining torque while stationary (Sharma and Kumar 2013). BLDC machines provide better torque-speed characteristics, higher efficiency with motor and power electronic devices (~78%) and higher power to weight ratios compared to DC series motor (Singh et al. 2019).

The polyphase induction motor (IM), also known as AC asynchronous motor, is extensively used in industrial applications. Particularly, squirrel-cage IMs have exhibited credentials to be used for HEV application due to their superior reliability, toughness, less maintenance requirements, low cost, and ability to operate in adverse conditions (Zeraoulia et al. 2005). IMs have a big share in commercial market for EV/HEV applications. However, important drawbacks of IMs include speed control issues, high loss, low efficiency, low power factor, and low inverter usage factor (Zeraoulia et al. 2005; Cho et al. 2000). Use of multi-phase pole-changing IMs specifically for traction application has been suggested by different researchers in order to extend the constant power zone avoiding motor oversizing (Jiang et al. 2003).

Brushless permanent magnet (PM) motors have demonstrated marked developments in power density, efficiency, and in the reduction of associated noise/vibration. In particular, permanent magnet synchronous motor (PMSMs) is preferred to use in current EVs and HEVs due to the superior qualities mentioned above along with its easy-to-cool feature. PMSMs appear to be well-suited for PHEV applications (Amjad et al. 2010). However, material costs and the availability of PM are the prime concerns of PM motors (Ishikawa 1999). Nevertheless, most of the automobile companies, such as Toyota Prius, Chevrolet Bolt EV, Ford Focus Electric, Nissan Leaf, Honda Accord, BMW i3 etc. have used PMSMs for EV/HEV applications,

In recent times, switched reluctance motors (SRMs) have gained significant interests among the researchers for HEV applications. Due to the robustness nature, SRMs are suitable for high speed applications. These machines have other merits including simple but robust construction, high fault-tolerance, and control simplicity. The torque-power characteristics of these machines exhibit a wider constant power region with high starting torque features compared to IMs and SRMs (Finken et al. 2008). Though SRMs demonstrate a cost-effective (simple construction) solution

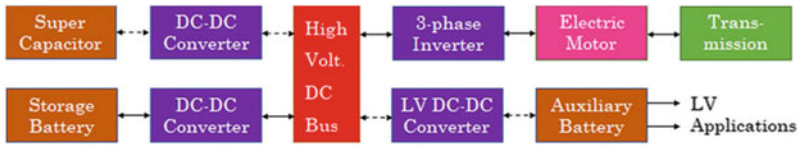


**Fig. 5.5** Typical application of different DC-DC and DC-AC converters in a HEV powertrain

for HEV applications, they have several demerits including high torque ripple, bus current ripple, medium power density, acoustic noise and electromagnetic emission (EMI) issues (Zeraoulia et al. 2005; López et al. 2019).

**DC-DC Converters.** In the HEV powertrains, electric sources (i.e., battery and/or SCs) need to be connected with DC-DC converters to step-up (boost converters) and/or step-down (buck converters) the supply DC voltage to the desired level, and with a DC-AC inverter to convert DC supply to AC via a HV DC bus (Fig. 5.5). In automotive applications, typically the voltage level for the storage battery ranges from  $\sim 250$  to  $360$  V and that for a super-capacitor varies between  $\sim 150$  and  $400$  V, which require stepping-up to match the required voltage of  $\sim 400$  to  $750$  V for driving the traction motors (Forouzesh et al. 2017). These electronic devices facilitate the effective regulation of the supply DC voltage, so that the HV AC 3-phase EM and the low voltage appliances can operate (through a low voltage (12 V) auxiliary battery) efficiently and reliably. It is imperative that these converters and inverters should have an efficiency of  $>95\%$  for HEV applications. Furthermore, these converters are required to be bidirectional in order to store the harvested regenerative energy in the electric sources (i.e. batteries and/or SCs) and to cranking the ICE.

A variety of converters and inverters have been developed for EVs and HEVs applications in the past decades to achieve the desired performance from them. According to Chakraborty et al. 2019, DC-DC converters are mainly divided into two major categories: non-isolated and isolated converters. For medium to high power HEV applications, non-isolated type DC-DC converters, such as conventional boost DC-DC converters (for  $>10$  kW capacity) are preferred (Li and He 2011; Tofoli et al. 2015) due to their low cost and simple architecture, and control strategy. Boost DC-DC converter has the capability to achieve a DC voltage gain of  $<4\%$ . The non-isolated buck-boost converter enables both voltage step-up and step-down operations. Multi-device Interleaved DC-DC Bidirectional Converter (MDIBC) is preferred for high DC voltage gain (i.e.  $>4:1$  ratio) and it exhibits several benefits including multiport inputs, reduced input current and output voltage ripples, low EMI, high efficiency and reliability.

Isolated DC-DC converters are suitable for low to medium-power ( $<10$  kW capacity) EV/HEV applications (Fernão Pires et al. 2014). An Isolated Buck DC-DC converter acts as a step-down transformer to lower the high voltage supply from the electric source to charge a 12 V auxiliary battery for running different accessories of the vehicle. The other suitable and efficient isolated converters include the Sinusoidal Amplitude Converter for reduction of voltage stress over switches, and noise-free

operation; Z-Source converter for soft switching and cold starting solutions; and the boost DC-DC converter with resonant circuit for soft switching and switching loss solutions.

Currently, Si-based semiconductors are mainly used in making the DC-DC converters for EV/HEV applications. These semiconductors exhibit a maximum efficiency of 92–93%, with a maximum switching frequency up to 30 kHz and a relatively lower power density of 3–12 W/in<sup>3</sup> (Whitaker et al. 2014; Jones et al. 2016; Liu et al. 2017). It has been reported that further improvement in performance of Si-based semiconductors may not be possible (Chin et al. 2010; Nel and Perinpanayagam 2017). In contrast, wide band gap semiconductors (WBGs) have demonstrated significant improvements in the power density (~50 W/in<sup>3</sup>) and efficiency with minimum manufacturing costs. At present, silicon carbide (SiC) and gallium nitride (GaN) semiconductors are examples of the sufficiently-matured WBG technologies (Millán et al. 2014; Shen and Omura 2007). Because of their high critical field, these devices can operate at higher voltage applications compared to the Si-based semiconductors counterpart (Shirabe et al. 2014). For high-power capacity (up to 100 kW) DC-DC converters, SiC devices and for low-power capacity (<5 kW) converters, GaN devices have proven their potentiality to be used for EV/HEV applications with desirable performance at low costs (Obata et al. 2014; Zheng et al. 2014).

**DC-AC Inverters.** DC-AC inverters are crucial electronic parts in EVs and HEVs. for DC-AC conversions with desired magnitude and frequency mainly to operate the traction AC motors. Converters/inverters use Insulated-Gate Bipolar Transistors (IGBTs) and Metal Oxide Semiconductor Field-Effect Transistor (MOSFETs) as power electronic switches, which have high efficiency and switching frequency. Switching frequency of these inverters typically varies between 5 to 20 kHz to minimize the noise generated from the motor windings (Liu 2013).

Most of the low power capacity HEVs use single-phase DC-AC inverters to power the single-phase AC traction motors, auxiliary battery, air-conditioning unit, cooling pump etc. In order to harvest regenerative power, inverters can act reversely to charge the battery. Full-bridge DC-AC inverters are of single-phase type that are frequently used in practical HEVs. Full-bridge is ranked as the most suitable converter topology because of its ability to minimize voltage and current stresses over switches and diodes, simple architecture, high efficiency and low costs (Kolli et al. 2015; Al Sakka et al. 2011). The high power EVs/HEVs commonly employ 3-phase DC-AC inverters to power a traction motor. These inverters exhibit good speed range and high efficiency. The design of the regulator is simple and multiple motors can be controlled from a single unit. The speed control of AC motors (specifically the IMs), the Current Source Inverters (CSI) are used, which can be of single-phase or 3-phase types similar to voltage source inverters.

### 5.3.3 Energy Storage System (ESS)

Onboard ESS plays a vital role in electric propulsion of HEVs. The essential features of the ESS for a HEV include high power density, high energy density, high efficiency, prolonged life cycle, compact size but light weight, reasonably safe and low cost (Khaligh and Li 2010). An HEV's performance during electric propulsion heavily relies on its ESS technology. However, vehicle configuration, drive cycle (maximum vehicle speed, accelerating pattern etc.), electric drive range/ power capability, driver's attitude in selecting operating mode also significantly influence the requirements of ESS for HEVs. The primary function of an ESS in a HEV is to store electricity generated onboard by the ICE-based generator and from regenerative braking, and externally from the standard electric outlet and to supply the electricity to meet the total electrical power demand of the vehicle. Irrespective of the generator/motor type, ESS structure of HEVs can be of single storage system or hybrid storage system (HSS). So far, battery and SCs are considered as the most widely used energy storage elements for HEVs. In a single storage system, mainly the battery system performs solely while in a hybrid system, both elements perform together enabling the vehicle to raise its power and energy density without raising size and weight. Due to the limitations of battery-based single ESS in meeting effectively all the requirements of a HEV propulsion, hybridization of both elements has become a common practice in modern HEVs. These two storage elements have complementary characteristics, which make the system more attractive, powerful and reliable. Though the battery-SC combination is most commonly used structure, adoption of fuel cell as a third element of the HSS has also been investigated in different research studies (Wu and Williamson 2007; Carter and Cruden 2008; Noumi et al. 2014).

Batteries are low energy cost devices with high energy density, which can provide enough energy during vehicle's acceleration, for instance. But they possess lower specific power, lower efficiency and shorter life cycle compared to the SCs counterpart (Wang et al. 2017).

**Batteries.** Over the past decade, tremendous efforts have been employed to develop highly efficient and cost-effective battery technologies. As a result, several high-performance batteries have been introduced in the market that are suitable for HEV applications. The list includes lead-acid batteries, nickel-cadmium (NiCd) batteries, nickel-metal hydride (NiMH) batteries, lithium-ion (Li-ion) batteries, lithium-iron-phosphate batteries. Among them the NiMH and Li-ion batteries have been widely used for HEV applications (Kurzweil and Garche 2017). Deep-cycle lead-acid battery is suitable for HEV applications due to its ability to tolerate repeated charging/discharging incidents. The nickel-cadmium (NiCd) batteries exhibit superior performance in terms of high expeditious charging/discharging capacity. NiMH batteries exhibit preferable characteristics to NiCd batteries in terms of energy density and cycle life time because of the use of metal hydride electrode. Furthermore, being Cd-free, NiMH batteries are environmentally friendly. These qualities of NiMH batteries have made them acceptable for HEV applications. In recent times, Li-ion batteries have demonstrated an expeditious penetration into the HEVs market due to



its excellent characteristics. Almost all the desired features of an ESS can be found in Li-ion batteries, which make them very attractive for HEV applications (Liu 2013). Laboratory test results for emerging Li-ion batteries have exhibited a life span of 10 years or more. High energy density and specific power of Li-ion batteries can achieve ~ 60% savings in volume and weight compared to NiMH batteries (Tarascon and Armand 2001). However, they face major safety issues related to the battery overcharging or overheating incidents. The emerging battery technology, lithium–iron–phosphate (LiFePO<sub>4</sub>) battery has provided a solution to this particular issue. A comparative picture among the different energy storage elements is illustrated in Table 5.1 (Wang et al. 2017).

**Supercapacitors.** In contrast to chemical batteries, SCs (also known as ultracapacitors) stores electrical energy directly in the form of positive and negative charges separately. Unlike a conventional capacitor, the structure of a SC consists of an electrical double-layer configuring a very large surface area, which permits to store much higher quantity of charges. Hence, the SCs are considered as electrochemical double-layer capacitors, which provide an advanced ESS having a number of attractive features including substantially high power density (by accumulating enormous quantity of charge), very long cycle life, fast charging and discharging rate, very high efficiency, environmentally friendly and reasonably safe (Simon and Gogotsi 2008; Wang et al. 2011). The double layer of a SC can be constructed with nano-porous material like activated carbon to improve its storage density.

Recently, hybrid supercapacitors have gained significant attentions as they exhibit enhanced performance compared to regular electric double layer SC. In a hybrid SC, electrodes submerged in electrolyte solution remain separated from each other through a separator, which favors electrolytic ions diffusion but prevents the direct contact of electrodes or short circuiting (Fig. 5.6). Hybrid SCs are ideal in storing the waste energy harvested by regenerative braking due to its faster charging rate thus making them as a perfect choice for HEV applications. For instance, the popular automotive manufacturers like Toyota and Mazda used hybrid SCs for their HEVs. Yaris Hybrid-R of Toyota and PSA Peugeot Citroën have used hybrid SCs for power bursts, achieving enhanced fuel economy during frequent start-and-stops, permitting sudden high accelerating capability etc. (Muzaffar et al. 2019).

However, SCs possess poorer energy density or capacity in comparison to batteries and also they suffer from high self-discharge rate (Liu 2013). The present research and development efforts are therefore directed to achieving enhanced energy density of hybrid SCs in the range of 20–30 Wh kg<sup>-1</sup> (Muzaffar et al. 2019).

### 5.3.4 Transmissions System

Transmission is one of the vital sub-systems in drivetrain, which transfers mechanical power generated by either the ICE or EM to the drive shaft, differential gearbox, and finally to drive wheels. As a result, the vehicle eventually gets mobility from



**Table 5.1** Comparative features of different energy storage elements

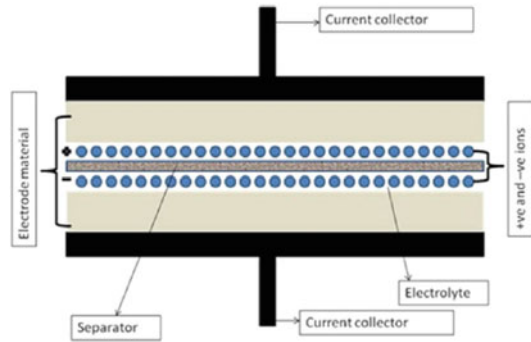
Storage type	Energy density (Wh/kg)	Power density (W/kg)	Cycle life (Times)	Charging and discharging efficiency (%)	Advantages	Disadvantages
Lead-acid battery	30–40	200–300	300–400	75	Low cost, high discharging rate and high recycling rate	High self-discharge, poor performance at low temp., short life
NiMH battery	60–80	800–1500	>1000	80	High energy density, high charging and discharging speed and long life, environmentally friendly	High self-discharge, need for cooling system and higher manufacturing cost
Lithium battery	100–120	600–2000	>1000	90	High voltage, high energy density and sp. energy, lightweight, long cycle life, low self-discharge, no pollution	Life reduce at high temp. safety concerns from overcharge/ over discharge, high security requirement
SC	4–15	1000–10,000	>100,000	85–98	Fast charging and discharging speed, wide operating temp. range, pollution-free and extremely long life	Poor energy density

Adapted from Wang et al. (2017)

stationary state and vice versa. Transmission system facilitates to achieving variation in vehicle’s torque, speed, and direction (forward or backward motion) as per requirements of the drive cycle while ensuring minimum fuel consumption and emissions. For instance, a vehicle needs high torque for starting and climbing hills or needs to disconnect the engine power from drive wheels during waiting at the traffic signals.

In comparison to the conventional vehicles, transmission system in HEVs is more complex and plays more crucial role as it has to deal with multiple motive power sources. Depending on the vehicle configuration/architecture, transmission system

**Fig. 5.6** Schematic diagram of a typical SC showing its constituents (Muzaffar et al. 2019)



in HEVs requires special care in design to provide improved drivability while maintaining fuel economy and efficient performance. Automotive manufacturers have employed varieties of transmission systems for their respective HEVs but commonly used systems include the Electric Continuous Variable Transmission (e-CVT) and Power Split Transmissions. In general, these transmission systems comprise multiple planetary gear sets which facilitate full-electric mode, full-mechanical mode, and combined mode operations as well as capturing mechanical power from regenerative braking in one vehicle. For instance, the GM Two-Mode hybrid transmission system comprising two planetary gear sets, two EMs and three clutches can provide e-CVT for high and low speed operations. Generally, two-mode operation offers increased flexibility in transmission controls, improves drivability with enhanced fuel economy and vehicle performance (Liu 2013). Further information on CVT powertrain system dedicated to commercially available HEVs are presented in Dong et al. (2011).

Dual Clutch Transmission (DCT) refers to six-speed automated manual transmission system comprising two EMs/generators connected with two shafts through reduction gearing. DCT-based hybrid powertrain can provide seven operating modes such as full-electric (only EM) mode, only ICE mode, combined mode, regenerative braking mode, power-split mode, series hybrid mode and a standstill charging mode when the vehicle remains stationary.

Renault Infinitely Variable Transmission (IVT) system consists of two EMs, two planetary gears sets, but no clutches (Villeneuve 2004). It provides infinitely variable transmission capability through effective controls of the EMs to synchronize with the vehicle speed while optimizing engine operation. However, due to the absence of clutches, the system permits only single mode of operation. An electric 4-wheel drive transmission system has been used in Toyota Highlander and Lexus hybrid vehicles, where a planetary gear-based powertrain drives the front wheels and an EM drives the rear wheels (Douglas 2006).

Zhang et al. (2018) proposed a hybrid transmission system consisting of 1-EM, 1-planetary gear set and 4- fixed gears to achieve automated manual transmission and CVT for a parallel HEV. The hybrid system had six operating modes: five mobile and one standstill mode for emergency operations. Ehsani et al. (2009) proposed a hybrid

transmission system using one EM, 3-clutches, 1-planetary gear set and 2-locks to achieve both speed coupling and torque coupling functions. However, in this system, mode transition was reported to be complicated.

## 5.4 Energy Management Strategies (EMS) of HEVs

Regardless of the configuration of HEVs, the primary objectives including maximum fuel economy and minimum emissions can only be achieved if the individual component performs efficiently and there exists a good management strategy to control their coordinating operations. Energy management strategy (EMS) of an HEV implies the carefully-designed advanced control logic that provides optimal decisions on power/energy split among ICE, EM and battery. In general, EMS remains embedded in vehicle controller and regulates the power/energy flows in the powertrains. Since EMS plays a very important role in attaining enhanced fuel economy, minimized emissions along with an extended battery cycle life, this has been extensively researched by both the academicians and industry people (Rui et al. 2018). The design and development of an effective EMS always remains a challenging job as it has to fulfil the following requirements:

- Optimization of operating points/region of ICE on the basis of engine mapping data of fuel economy and emissions reductions
- Optimization of operating points/region of EMs
- Reduction in ICE dynamics (i.e. reduction of rapid variations in speed)
- Minimization of ICE's idling operation
- Optimization of ICE's start-shut down events
- Maximization of harvesting regenerative braking energy
- Optimization of SOC operating mode of the battery
- Implementing minimum to zero-emission policy.

Over the years, many researchers have made significant contributions to developing efficient EMSs, which help to understand optimal performance characteristics of different HEVs. A number of EMSs have been proposed and implemented to attain optimal energy/power division in the HEV powertrains coping with real world drive cycles. In recent times, intelligent transportation system (ITS) has gained interests as it provides real time data through vehicle to vehicle (V2V) and vehicle to infrastructure (V2I) communications, which help to achieve enhanced overall efficiency of HEVs/PHEVs with adequate driving safety (Zhang et al. 2011). Different prevailing EMSs of HEVs/PHEVs can be categorized into two major groups: rule-based EMSs and optimization-based EMSs considering the diverse nature of control objectives and influencing factors. Intelligent based EMSs can be considered as the third branch. The detailed classification is shown in Fig. 5.7.

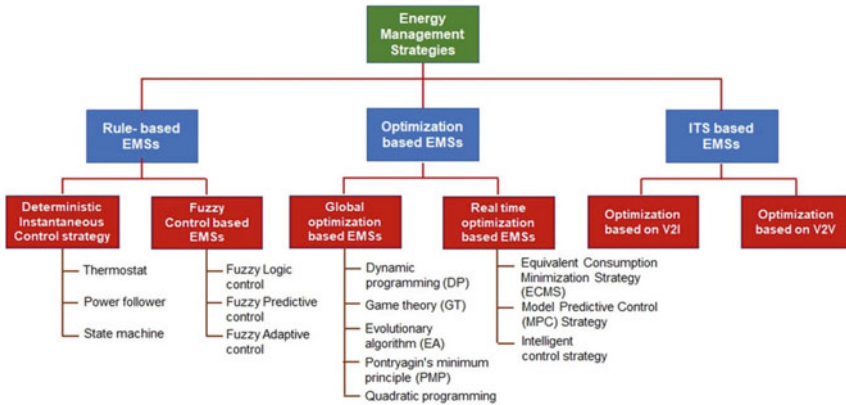


**Fig. 5.7** Energy management strategies for HEVs/PHEVs (redrawn from Yang et al. 2020a; Shen et al. 2011)

### 5.4.1 Rule-Based EMSs

Rule-based EMSs are considered as the primitive control methods generally employed in light and medium capacity HEVs applications due to its high simplicity and feasibility. Rule-based EMSs apply the control logic to make decision on power split on the basis of vehicle’s load level (Anbaran et al. 2014). There exists a logical coordination between the EM operation and ICE operation, which permits to operate the ICE as closely as possible to the optimal fuel economy and emissions region of ICE mapping. A typical rule-based EMS applied in a parallel HEV can be illustrated schematically as shown in Fig. 5.8. The rule-based EMSs can be sub-divided into two categories: deterministic instantaneous control strategy and fuzzy logic-based EMS.

Deterministic instantaneous strategy is a heuristic method and the rules for demand power split are designed based on the analysis of power flow in the drivetrain, ICE map for optimum operating conditions, and human experiences through lookup tables (Salmasi 2007). Thermostat, power follower, and state machine are the three control strategies fall under this category. The thermostat control strategy implements the decision of switching on/off of ICE based on the preset bottom and top level of

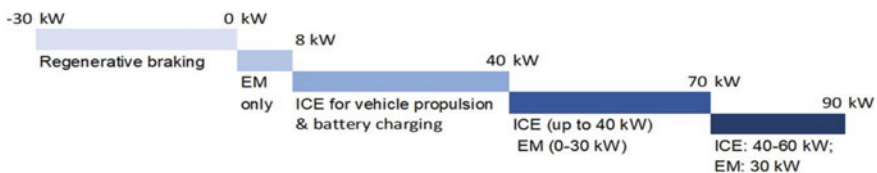


**Fig. 5.8** Schematic diagram presenting the demand power split policy based on rule-based EMS (redrawn from Liu (2013))

battery SoC respectively. Though this simple strategy fails to make decision on optimal power split covering all driving conditions, it is applicable for series HEVs that travels in a prescheduled route such as hybrid city bus. Under the power follower strategy ICE acts as the main prime mover and EM serves as an add-on power source activated when needed to generate more power by the vehicle. The rules include (i) ICE operation to its full capacity, (ii) beyond the capacity EM is switched on for additional power supply, (iii) below a minimum threshold level of power requirement, ICE shuts off, and EM starts, (iv) the EM recharges the battery by regenerative braking energy, (v) depending on battery SoC, ICE is also responsible to recharge battery via EM/generator. The major limitation of the strategy is that it fails to optimize the whole drivetrain system thus exhibits no significant improvement in overall efficiency and emissions. Even so, Toyota Prius and Honda Insight was made on the basis of power follower control strategy. Under the state machine strategy different operating modes are decided on the basis of changes in driving demand, vehicle operating condition, or on a system or a subsystem fault. Besides, dynamic control algorithms may involve in decision making in this strategy. However, implementing this control strategy, the primary goals of an HEV powertrain to achieving better fuel economy and emissions are not ensured (Salmasi 2007). The above discussion concludes that rule-based deterministic EMSs are simple and easy to develop and apply with minimum computational involvement.

However, these EMSs have not been successful in fulfilling the prime objectives of HEVs due to inability of conforming to real-time operations or dynamic changes in vehicular operations. Considering the multidisciplinary, non-linear and transient nature of energy management of HEVs under real world operating conditions, fuzzy logic-based EMS appears to be more adapting and rational tool for solving the problem.

Compared to deterministic instantaneous control strategy, fuzzy control strategy provides decisions on demand power split, which are closer to real-time and optimal. The important merits of fuzzy logic based EMS include (Salmasi 2007):

- it can tolerate inaccuracy in measurements and component variations
- it is more adapting due the high flexibility in tuning fuzzy rules as per requirements.

In order to regulate the power/energy flow in HEV drivetrain, fuzzy logic-based strategy is developed based on the following common principles (Liu 2013):

- regardless of operating condition, power demand of the vehicle is to be met at all time
- braking and acceleration actions need to be consistently taken care of
- battery SoC is to be sustained
- better overall efficiency is to be maintained during operation.

Under this EMSs, the required motor power, a function of vehicle speed, power demand and battery SOC, is determined using fuzzy logic methodology. Then this motor power is inputted to the final decision block to obtain a decision on the demand power split between the two energy sources (ICE and EM). Finally, the motor power

is recalculated by fuzzy logic so that the operation of ICE is optimized based on engine mapping for better fuel economy and emissions.

Many researchers have incorporated different optimization algorithms namely particle swarm optimization algorithm (Yang et al. 2016), genetic algorithm (Zhou et al. 2013), artificial neural network (Kamal and Adouane 2018), machine learning algorithm (Chen et al. 2008) with the fuzzy logic control rules to make the fuzzy control based EMSs more robust and adapting for HEV applications. However, akin to deterministic rule based EMSs, fuzzy control based EMSs also rely on human experiences and perception thus optimum solutions are hard to achieve by this tool.

### 5.4.2 Optimization-Based EMSs

These control strategies provide optimal decisions on demand power split of an HEV by minimizing a cost function, which commonly includes fuel consumption and exhaust emissions of ICE. As shown in Fig. 5.7, the optimization-based EMSs are commonly classified into two broad categories: global optimization-based EMSs and real-time optimization-based EMSs. Global optimization-based EMSs deal with preset drive cycles thus the obtained optimal solutions are non-casual. Though these EMSs are not applicable for real-time optimization problems, they create a basis for real-time/online optimization strategies and for quality monitoring of other EMSs. There exists a number of global optimization-based EMSs including dynamic programming (DP), game theory (GT), quadratic programming (QP), Pontryagin's minimum principle (PMP), evolutionary algorithm (EA) etc. (Yang et al. 2020b). The DP algorithm being a multistep decision tool, have been extensively employed in determining optimal EMSs for HEV/PHEV applications. DP is known to be one of the most powerful optimization tools dealing the constrained nonlinear problems, can provide the global optimal solutions (Koot et al. 2005).

DP requires breaking up of the multi-stage decision process into a series of small individual step problems. Hence, the instantaneous cost function which generally includes the fuel consumption, emissions and battery SoC is to be in discrete form representing the costs per step. In case of HEV applications, for instance, gridding of battery SoC is done over a fixed drive cycle with a time discretization step  $\Delta t$ , and thus the optimal solution is obtained only for the discrete points (SoC,  $t_i$ ). However, this approach seems to be a computational burden since computational time rises linearly with the driving cycle time. Therefore, the feasible approach is to divide the total drive cycle time into a series of time steps and obtain the optimal solution by DP for each of these steps (Shen et al. 2011; Yang et al. 2020b). The major limitation of applying DP algorithm is that it follows a preset drive cycle while the real world driving conditions can be very different. To alleviate this drawback, stochastic dynamic programming (SDP) algorithm based on Markov decision theory was employed by different researchers to develop a controller for real world applications (Lin et al. 2004; Vagg et al. 2016). Other researchers have made efforts to increase the suitability of DP algorithm for the real-time problems with reduced computational burden by

introducing different improved versions of DP algorithm such as iterative DP (Zhu et al. 2018), adaptive DP (Li et al. 2008) and so on.

Evolutionary algorithms (EAs) exhibit superior applicability for HEVs/PHEVs applications compared to other global optimization algorithms in several aspects such as EAs are easier to implement and involve less complex mathematical models; good capability of solving non-convex optimization problems having multiple local optima; high flexibility in addressing multi-objective optimization problems; ability to perform group search. Currently, there exist a number of EAs mainly include particle swarm algorithm (PSO), generic algorithm (GA), estimation distribution algorithm (EDA), simulated annealing algorithm (SA), ant colony algorithm (ACO), and so on (Yang et al. 2020b; Qi et al. 2017).

PMP is considered as a powerful tool for solving finite horizon optimization problems. The global optimal control problem, in this method, is expressed in terms of local conditions using differential equations while solving for the minimization/optimization at each time instant satisfying the given constraints (Onori et al. 2016). PMP-based control is preferable to DP approach due to its capability to provide a control input from the Hamiltonian instantaneously. The PMP optimization method is simple, less time consuming, and can provide a realization of the real-time global optimization (Zhang et al. 2017). However, optimality is ensured only when the initial condition of co-state is input accurately before starting the calculation. Since the initial condition depends on future driving schedule, PMP-based control is limited for obtaining the optimal solution under real world conditions (Kim et al. 2014).

Although the global optimization-based EMSs are capable of providing global optimal solutions, they generally incur considerable amount of computational time and most importantly, they are not applicable to real time problems. But the real time optimization is important in the sense that it ensures the least energy consumption under real time energy management. Real time optimization-based EMSs determine the instantaneous optimal working points for ICE and EMs on the basis of ICE mapping for best fuel economy, power, with improved emissions and motor speed-torque curve, which can control the state variables of HEV/PHEV influencing dynamic energy allocation. Hence, both the ICE and EMs work at their respective instantaneous optimal state points resulting in real time optimality in whole HEV drivetrain. Furthermore, real-time optimization-based strategies are not dependent on future driving information beforehand and also not confined by the specific driving cycle conditions. They are easy to implement practically and generally involve less amount of calculations. Real time optimization-based EMSs include (ECMS), model predictive control (MPC) strategy, and other intelligent control strategies. The basic concept of ECMS is that the electrical energy consumption in a HEV/PHEV can be converted into equivalent fuel consumption using an equivalence factor (EF). The actual fuel consumption of ICE as well as the equivalent fuel consumption of EM w.r.t. the battery SoC variation are the parts of the instantaneous cost function, which is minimized at each instant of the strategy. However, an appropriate estimation of EF is quite crucial since it has a great impact on the control performance of HEV/PHEV using ECMS (Jiao et al. 2018; Zhang et al. 2015). MPC strategy is a

multivariable optimization algorithm and can be suitable for energy management of HEV/PHEV. Though it provides optimal solution in the prediction domain, it exhibits potentials to operate in real time situation. According to Yang et al. (2019), MPC has three parts: predicting model, rolling optimization, and online correction. Firstly, the global optimal control problem of the whole driving cycle is converted into the local optimal control problem in the prediction horizon. Then the state of vehicle operation or its control parameters are updated for the next/future time horizon using continuous rolling optimization, and the optimal solutions are obtained while satisfying all the objective constraints.

Intelligent control strategy usually handle the control issues of complex systems, which are too hard to be solved by the conventional strategies. It is the advanced level control theory, which involves intelligent information processing, intelligent information feedback and intelligent control decision-making. The most common intelligent control strategy that has been employed for energy management applications of HEV/PHEV is machine learning algorithms mainly including artificial neural networks (ANNs) (Yang et al. 2020b).

### **5.4.3 ITS Based EMSs**

To overcome the limitations of classical EMSs in terms of inability to be implemented for real world drive cycles, ITS-based control strategies are gaining significant attentions in recent times. The V2V and V2I technologies can provide real-time traffic information and available historical data to develop EMSs for HEVs/PHEVs applications (José et al. 2008). These acquired information and data are quite crucial to precisely quantify the traffic flow and real world drive cycle parameters, which are the essential inputs for optimizing EMSs. Hence, the ITS-based control strategy is more realistic and its implementation provides enhanced overall performance of the vehicle in terms of drivability, fuel economy, exhaust emissions and safety. Lei et al. (2020) proposed a blended EMS (DP with K-means clustering algorithm) to achieve the real-time demand power split of the PHEV powertrain based on the identified driving conditions and the extracted rules including the engine starting scheme, gear shifting schedule and torque distribution strategy. Modern intelligent tools such as Global Positioning System and Geographical Information System were employed in this study to acquire the relevant information on driving conditions and the influencing parameters for the K-means clustering algorithm. Simulation results exhibited that the developed EMS could adequately address the real time variations in driving conditions thus provided substantial improvement in fuel economy with reduced computational burden.



## 5.5 Emissions Performance of HEVs

So far, HEVs have established their potentiality in reducing the consumption of petroleum fuels. Enhanced fuel economy is most commonly regarded as the major advantage of HEV technology. However, it is quite crucial to explore the emissions performance of these vehicles in comparison to the conventional vehicles (CVs). The reduction in emissions due to less fuel consumption in HEVs is easy to realize, however the variability in ICE operating conditions can significantly impact the emissions performance of the vehicle. ICE cold start, for instance, is one such operating condition, which can result in significantly high emissions. Other engine operational issues relevant to HEVs include improper engine calibration/tuning and inefficient operating conditions due to improper EMSs and inefficient operation of exhaust aftertreatment devices. Under cold start operation an ICE is not properly warmed up and usually it consumes fuel rich mixtures to overcome the in-cylinder low temperature issue to initiate combustion, and hence, the engine operates at a low efficiency leading to high rate of fuel consumption and exhaust emissions. In the case of HEV operations, a cold start event may appear when it demands for additional power, prior to which the engine has been shut down for a while. Furthermore, depending on the powertrain EMS, the frequency of ICE startup and shutdown events is relatively higher for HEV operation even within a single trip compared to CVs, which generally encounter a single cold start event at the beginning of the trip (Varella et al. 2016). According to Bagheri et al. (2021), these multiple ICE startup events are referred to as high-power cold starts since at this state the vehicle remains in motion without consuming power from the ICE and the ICE starts from its cold state to respond to the EMS's call. On the other hand, the exhaust aftertreatment systems (i.e. three-way catalytic converter (TWC)) fail to perform efficiently due to low temperatures often below their light-off temperature level. TWC plays a great role in controlling pollutant emissions from a gasoline engine and hence, gasoline HEVs can emit increased carbon monoxide (CO), unburned hydrocarbons (UHCs) and oxides of nitrogen ( $\text{NO}_x$ ) during the high power cold start events. Improper calibration/tuning of ICE may lead to non-homogenous air-fuel mixtures (especially fuel rich mixtures), and reduced thermal efficiency during restarts, which in turn, result in increased tailpipe emissions as well as particle number (PN) concentration. Bagheri et al. (2021) reviewed and analyzed 12 research studies comparing emissions performance between HEVs and CVs and the results are presented in Fig. 5.9. According to Fig. 5.9, results obtained from real driving emissions (RDE) tests were significantly different from those obtained from the chassis dynamometer (CD) tests. However, they followed a similar trend (except CO emissions) of increased emissions for HEVs compared to CVs operations. CD test results indicated that average HEV emissions increased by up to 2100%, 5783%, 24%, and 23,300% for  $\text{NO}_x$ , HCs, CO and PN compared to CVs and in one study  $\text{NO}_x$  emissions were decreased by 39%.

In contrast, results from RDE tests showed that the increment in  $\text{NO}_x$ , HCs, CO, and PN emissions ranged up to 592%, 916%, 900%, and 3285% respectively, while the decrement of  $\text{NO}_x$ , HCs, and CO emission species ranged up to 97%, 100%, and

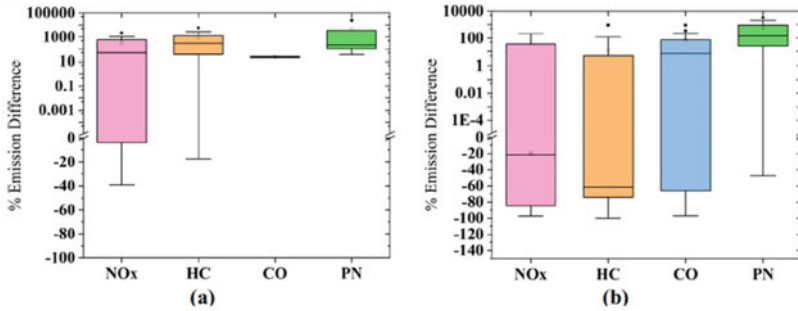


**Fig. 5.9** Percentage variation in  $\text{NO}_x$ , HC and CO emissions (in mass/distance) and PN concentration (in number/distance) between HEVs and CVs. **a** CD test results and **b** RDE test results. Positive values indicate increased emissions and the negative values indicate decreased emissions for HEVs compared to CVs. Symbol (•) indicates the maxima and minima while (□) represents mean values [adapted from Bagheri et al. (2021)]

97% respectively for HEVs compared to CVs. The researchers attributed these results of higher emissions from HEVs at high-power cold starts condition to the demand of high initial torque by the moving vehicle. Choi et al. (2021) also concluded from on-board PN measurements that PN sharply rose for 5 s after ICE restart for a GDI (gasoline direct injection) HEV. The majority of total PN concentration ( $\sim 70\%$ ) was observed during this period. The authors also concluded that optimization of combustion parameters such as injection pressure (increased), end of injection (advanced), and spark timing (retarded) could help to improve the situation.

Battery SoC has a strong influence on HEV's fuel consumption and emissions. Duarte et al. (2014), reported that fuel consumption, CO and  $\text{NO}_x$  emissions significantly increased during low-power demand operating modes (i.e. urban driving) for a battery SOC of  $<50\%$  and decreased proportionately for the battery SOC of  $>70\%$  (i.e., highway driving).

Prati et al. (2021) investigated the influence of battery SoC, hybrid mode (charge sustaining and charge depleting), road grade and vehicle air conditioning on real time emission trends of a PHEV (passenger car) using portable emission measurement system over urban, rural and motorway routes. The results revealed that battery SoC had small impact on CO and  $\text{NO}_x$  emissions, which were affected much by the vehicle driving mode particularly the ICE cold start events. Maximum CO and  $\text{NO}_x$  emissions were observed for the ICE cold start event during motorway traveling since the aftertreatment system could not perform efficiently at low temperatures (i.e.  $<$ light-off temp.). Electric powertrain was guaranteed at fully charged battery status leading to zero emissions irrespective of road gradient. However, for the same road gradient (urban strong uphill), ICE mode operation at battery depleted status caused higher CO and  $\text{CO}_2$  emissions. Benajes et al. (2018) explored the potentiality of Reactivity Controlled Compression Ignition (RCCI)- PHEV technology in emissions reduction and reported that the PHEV could exhibit the maximum benefits in terms of fuel consumption and engine-out emissions. It was demonstrated that

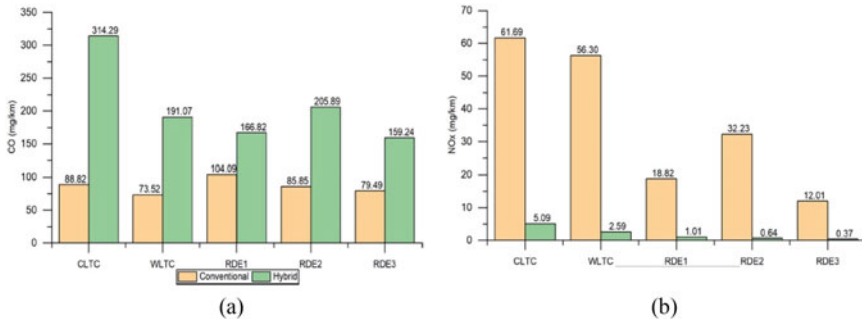


**Fig. 5.10** Comparative emission trends between conventional gasoline vehicle and its hybrid counterpart obtained for different drive cycles: CLTC, WLTC and three RDEs on CD tests: **a** CO emissions and **b** NO<sub>x</sub> emissions [adapted from Wang et al. (2020)]

PHEVs with a medium battery size (15 kWh), could attain the target CO<sub>2</sub> emission rate of 50 g/km, while NO<sub>x</sub> and soot levels complied the Euro 6 limits. Lijewski et al. (2020) experimentally compared the emissions performance between a PHEV and battery electric vehicle (BEV) fitted with a range extender (ICE operated). The results from this study also confirmed that regardless of the vehicle route, PHEV was always better in terms of engine-out emissions while complying the Euro 6 limits. Emission performance of light-duty gasoline CV and its counterpart HEV (same model) over China light-duty vehicle test cycle (CLTC), worldwide harmonized light vehicles test cycle (WLTC), and real driving emission (RDE) tests at three different routes were studied by Wang et al. (2020). Higher CO emission was recorded for HEV compared to conventional vehicle accounted for a number of issues with HEV operations including frequent re-start and longer warm-up time for the engine/catalyst, non-homogeneity in air-fuel mixture, and poor combustion, which significantly influenced CO emission. High engine speed led to instantaneous CO spikes and nearly 25% of the total CO emitted within less than 10 s of ICE startup. Results of NO<sub>x</sub> emissions revealed that HEV emitted 10% lower NO<sub>x</sub> compared to the CV irrespective of vehicle operating conditions due to lower engine load and less fuel enrichment (Fig. 5.10).

## 5.6 Critical Issues and Challenges for HEVs

HEVs are commonly regarded as the promising transport option not only for the recent times but also for the future. Over the past decade, HEV technology has gone through vigorous R&D to achieve substantial improvement. While citing many attractive benefits of HEV technology, often its limitations are forgotten. Though the recent technological advancements make the HEVs capable to perform well compared to CVs, the overall system reliability and the intelligent systems are still not up to a satisfactory level. Most importantly, the technology is not matured enough

to date and thus has several shortcomings and challenges required to be addressed to have full penetration into the current market.

*Energy storage.* Storage batteries and ultracapacitors/SCs are the main ESSs used in HEVs. Batteries have inherent shortcomings such as larger size and weight, short life cycle, regular maintenance needed, low power density, usage of toxic materials, limited recyclability, usage of earth rare materials, high costs, not environmentally friendly. Therefore, adequate R&D efforts should be continued to overcome these limitations to great extent. The technologies for SCs or hybrid SCs are still in a primitive stage. As such, it is important to develop new SC materials with various techniques to maximize their usage. The low energy density of SCs limits their use in automobiles. Other issues with SCs include losses due to resistance and current leakage.

*EMSs.* Development and implementation of most reliable and adapting EMS for HEV applications will remain ever challenging even though numerous methods have been developed and customized to meet specific requirements. Nowadays, EMSs are required to optimize the performance of the overall vehicle system through efficient coordination between multi-power sources. Several critical parameters that need special attention to implementing an efficient EMS include system stability, reliability in power supply, optimality in dynamic power source allocation, and power quality of the power sources.

*System configuration and drivetrain structure.* Each of the available HEV configurations has some specific limitations over others from the application point of view. Appropriate sizing of the HEVs based on power demand, cost and application requires further research efforts. Adoption of new and emerging technologies is also very crucial to make the system more efficient and reliable. For instance, the automotive companies are developing DC dual-voltage system especially for HEV applications. To boost system efficiency at higher power demands, automotive designers are considering to use 48 V power rails, which decreases the current needed when delivering a given amount of power. Thus a dual-voltage architecture can facilitate to provide more reliable, efficient and cost-effective power distribution.

*Power electronics.* Certainly power electronics play a great role in achieving efficient, reliable and smoother propulsion of HEVs. They are DC-DC, DC-AC converters, power switching, and any electronic device integrated with the electric devices in HEVs. Their efficient operation is so vital that any fault in them makes the system disable partially or fully. Several issues and technical challenges exist such as switching losses during on and off operations, switching frequency of PWM (pulse width modulation) operating mode, noise and EMI (electromagnetic interference) consideration, durability of the switching devices etc.

*Electric machines.* EMs are the major electric machines in EVs/HEVs, which either drive or assist to drive the vehicle. Different types of DC and AC motors are available, however their applications in HEVs have got several issues including optimal torque-speed mapping, complex speed control mechanism, expensive controllers and narrow

operating rpm band. Therefore, future direction of R&D should be in developing a compact, efficient motor having high durability, designing and developing controllers having less complexity, and capability to operate at a broader rpm band. Adopting in-wheel motor propulsion system can avoid transmission losses and can increase efficiency of electric propulsion of HEVs. Hence, designing and developing of in-wheel motor propulsion systems can be a further research area for HEV applications.

*Controls in HEV.* In general, a control system in HEVs is very complex. Efficient conversion of energy on the HEV powertrain is crucial and it mostly relies upon effective controlling of the components associated with the system. Therefore, design of efficient controller of HEV remains a great challenge. An HEV controller comprises driver command interpreter, vehicle system controller, and electronic controller. Vehicle system controller works at the decision making level whereas an electronic controller serves at the execution level. Electronic controller is composed of a variety of control units for controlling individual components including ICE, EMs, generator, regenerative braking system etc. All of these controls involve complex designs and always there are scopes of improvement.

Besides these above, there exist a number of key challenges for HEVs deployment in the current market context including,

- Low power capacity;
- Limited drivability range
- High price of HEVs;
- High maintenance costs,
- Development of refueling infrastructure particularly for electric propulsion;
- Incorporation of renewable energy source;
- Limitations associated with fuel cell application in terms of H<sub>2</sub> production, storage, refueling infrastructure;
- Downsizing, weight reduction, life cycle increasing and cost reduction of batteries;
- Emissions control of HEVs; etc.

## 5.7 Conclusions

It is believed that HEVs can fulfil the customers' demands in the current context and will successfully complete the future consumer market due to their fuel economy, and environmentally friendly features. The fundamental issue of the HEV remains in optimization of multiple energy sources to harvest maximum fuel economy with minimum emissions at low costs. This chapter has presented an overview of HEV technology focusing on configurations, architecture and major components, EMSs, and emissions performance of HEVs in comparison to CVs. Design and development of efficient EMSs as well as the controller remain the hot research areas. Global optimization EMSs are simple and can provide global optimal solutions. However, they are limited by computational burdens and real time applications. In contrast, real time optimization strategies as well as the ITS based strategies have the capability

to provide real time optimal solutions for real world applications. Though HEVs exhibit comparable or somewhat lower emissions performance compared to the CVs counterpart, more research is sought to achieve better performance. Finally, a number of key issues and challenges are identified that need sincere attention to be overcome and thus can smooth out the penetration of HEVs in current and future markets.

## References

- Agarwal AK, Mustafi NN (2021) Real-world automotive emissions: monitoring methodologies, and control measures. *Renew Sustain Energy Rev* 137:110624. <https://doi.org/10.1016/j.rser.2020.110624>
- Al Sakka M, Van Mierlo J, Gualous H (2011) DC/DC converters for electric vehicles. In: Soylu S (ed) *Electric vehicles—modelling and simulations*. <https://doi.org/10.5772/17048>
- Amjad S, Neelakrishnan S, Rudramoorthy R (2010) Review of design considerations and technological challenges for successful development and deployment of plug-in hybrid electric vehicles. *Renew Sustain Energy Rev* 14(3):1104–1110. <https://doi.org/10.1016/j.rser.2009.11.001>
- Anbaran SA, Idris NRN, Jannati , et al (2014) Rule-based supervisory control of split-parallel hybrid electric vehicle. In: *IEEE Conference on Energy Conversion (CENCON)*, pp 7–12, Johor Bahru, Malaysia (2014), <https://doi.org/10.1109/CENCON.2014.6967468>.
- Bagheri S, Huang Y, Walker PD, Zhou JL, Surawski NC (2021) Strategies for improving the emission performance of hybrid electric vehicles. *Sci Total Environ* 771:144901. <https://doi.org/10.1016/j.scitotenv.2020.144901>
- Benajes J, García A, Monsalve-Serrano J, Sari R (2018) Potential of RCCI series hybrid vehicle architecture to meet the future CO<sub>2</sub> targets with low engine-out emissions. *Appl Sci* 8(9):1472. <https://doi.org/10.3390/app8091472>.
- Carter R, Cruden A (2008) Strategies for control of a battery/supercapacitor system in an electric vehicle. In: *Proceedings on international symposium on power electronics, electrical drives, automation and motion*. IEEE, Ischia, Italy pp. 727–732. <https://doi.org/10.1109/SPEEDHAM.2008.4581315>
- Chakraborty S, Vu H-N, Hasan MM, Tran D-D, Baghdadi ME, Hegazy O (2019) DC-DC Converter topologies for electric vehicles, plug-in hybrid electric vehicles and fast charging stations: State of the art and future trends. *Energies* 12:1569. <https://doi.org/10.3390/en12081569>
- Chen Z, Abul Masrur M, Murphey YL (2008) Intelligent vehicle power management using machine learning and fuzzy logic. In: *Proceedings of IEEE international conference on fuzzy systems (IEEE World Congress on Computational Intelligence)*. IEEE, Hong Kong, China, pp 2351–2358. <https://doi.org/10.1109/FUZZY.2008.4630697>
- Chin HS, Cheong KY, Ismail AB (2010) A review on die attach materials for sic-based high-temperature power devices. *Metall Mater Trans B* 41:824–832. <https://doi.org/10.1007/s11663-010-9365-5>
- Cho CP, Wylam W, Johnston R (2000) The integrated starter alternator damper: the first step towards hybrid electric vehicles. *SAE Paper No. 2000-01-1571*
- Choi Y, Yi H, Oh Y, Park S (2021) Effects of engine restart strategy on particle number emissions from a hybrid electric vehicle equipped with a gasoline direct injection engine. *Atmos Environ* 253:118359. <https://doi.org/10.1016/j.atmosenv.2021.118359>
- Das HS, Tan CW, Yatim AHM (2017) Fuel cell hybrid electric vehicles: a review on power conditioning units and topologies. *Renew Sustain Energy Rev* 76:268–291. <https://doi.org/10.1016/j.rser.2017.03.056>
- Dong J, Dong Z, Crawford C (2011) Review of continuously variable transmission powertrain system for hybrid electric vehicles. In: *Proceedings of the ASME international mechanical engineering Congress and exposition*, vol 9: Transportation systems; safety engineering, risk analysis

- and reliability methods; applied stochastic optimization, uncertainty and probability. ASME, Denver, Colorado, USA, pp 209–219. <https://doi.org/10.1115/IMECE2011-63321>
- Douglas B, 2006 Toyota Highlander Hybrid 4WD 4dr SUV (3.3L 6cyl gas/electric hybrid CVT) review. [http://reviews.cnet.com/suv/2006-toyota-highlander-hybrid/1707-10868\\_7-31352761.html](http://reviews.cnet.com/suv/2006-toyota-highlander-hybrid/1707-10868_7-31352761.html). Last accessed 10 Aug 2021
- Duarte GO, Varella RA, Gonçalves GA, Farias TL (2014) Effect of battery state of charge on fuel use and pollutant emissions of a full hybrid electric light duty vehicle. *J Power Sources* 246:377–386
- Ehsani M, Gao Y, Emadi A (2009) Modern electric, hybrid electric, and fuel cell vehicles: fundamentals, theory, and design, 2nd edn. Power Electronics and Applications Series), CRC Press, USA
- EPA: Compare fuel cell vehicles. [https://www.fueleconomy.gov/feg/fcv\\_sbs.shtml](https://www.fueleconomy.gov/feg/fcv_sbs.shtml). Last accessed 02 Aug 2021
- Fernão Pires V, Romero-Cadaval E, Vinnikov D, Roasto I, Martins JF (2014) Power converter interfaces for electrochemical energy storage systems—a review. *Energy Convers Manag* 86:453–475. <https://doi.org/10.1016/j.enconman.2014.05.003>
- Finken T, Felden M, Hameyer K (2008) Comparison and design of different electrical machine types regarding their applicability in hybrid electrical vehicles. In: 18th International conference on electrical machines. IEEE, New York, pp 1–5. <https://doi.org/10.1109/ICELMACH.2008.4800044>
- Forouzesh M, Siwakoti YP, Gorji SA, Blaabjerg F, Lehman B (2017) Step-up DC-DC converters: a comprehensive review of voltage-boosting techniques, topologies, and applications. *IEEE Trans Power Electron* 32:9143–9178
- IEA (2020) Tracking Transport 2020, IEA, Paris. <https://www.iea.org/reports/tracking-transport-2020>. Last accessed 14 Aug 2021
- Ishikawa Y (1999) A motor-drive system design that takes into account EV characteristics. SAE Paper No. 1999-01-0739 (1999). <https://doi.org/10.4271/1999-01-0739>
- Jiang SZ et al (2003) Spectral analysis of a new six-phase pole-changing induction motor drive for electric vehicles. *IEEE Trans Industrial Electron* 50(1):123–131
- Jiao X, Li Y, Xu F, Jing Y, Zou Y (Reviewing editor) (2018) Real-time energy management based on ECMS with stochastic optimized adaptive equivalence factor for HEVs. *Cogent Eng* 5:1. <https://doi.org/10.1080/23311916.2018.1540027>
- Jones EA, Wang FF, Costinett D (2016) Review of commercial GaN power devices and GaN-based converter design challenges. *IEEE J Emerg Sel Top Power Electron* 4:707–719. <https://doi.org/10.1109/JESTPE.2016.2582685>
- Jorgensen K (2008) Technologies for electric, hybrid and hydrogen vehicles: electricity from renewable energy sources in transport. *Utilities Policy* 16(2):72–79. <https://doi.org/10.1016/j.jup.2007.11.005>
- José S, Antonio FG, Marc S (2008) Architecture and evaluation of a unified V2V and V2I communication system based on cellular networks. *Comput Commun* 31:2850–2861
- Kamal E, Adouane L (2018) Intelligent energy management strategy based on artificial neural fuzzy for hybrid vehicle. *IEEE Trans Intell Vehicles* 3:112–125. <https://doi.org/10.1109/TIV.2017.2788185>
- Khaligh A, Li Z (2010) Battery, ultracapacitor, fuel cell, and hybrid energy storage systems for electric, hybrid electric, fuel cell, and plug-in hybrid electric vehicles: state of the art. *IEEE Trans Veh Technol* 59:2806–2814. <https://doi.org/10.1109/TVT.2010.2047877>
- Kim NW, Lee DH, Zheng C et al (2014) Realization of PMP-based control for hybrid electric vehicles in a backward-looking simulation. *Int J Automot Technol* 15:625–635. <https://doi.org/10.1007/s12239-014-0065-z>
- Kolli A, Gaillard A, De Bernardinis A, Bethoux O, Hissel D, Khatir Z (2015) A review on DC/DC converter architectures for power fuel cell applications. *Energy Convers Manag* 105:716–730. <https://doi.org/10.1016/j.enconman.2015.07.060>

- Koot MJ, Kessels TBA, de Jager B, Heemels WPMH, van den Bosch PJJ, Steinbuch M (2005) Energy management strategies for vehicular electric power systems. *IEEE Trans Veh Technol* 54(3):771–782. <https://doi.org/10.1109/TVT.2005.847211>
- Kurzweil P, Garche J (2017) Overview of batteries for future automobiles. In: Lead-acid batteries for future automobiles, pp 27–96, 1<sup>st</sup> edn. Elsevier. <https://doi.org/10.1016/B978-0-444-63700-0.00002-7>
- Lei Z, Qin D, Zhao P, Li J, Liu Y, Chen Z (2020) A real-time blended energy management strategy of plug-in hybrid electric vehicles considering driving conditions. *J Clean Prod* 252:119735. <https://doi.org/10.1016/j.jclepro.2019.119735>
- Li W, Xu G, Wang Z, Xu Y (2008) Dynamic energy management for hybrid electric vehicle based on adaptive dynamic programming. In: Proceedings of the 7<sup>th</sup> World Congress on intelligent control and automation. IEEE, Chongqing, China, pp 1–6. <https://doi.org/10.1109/ICIT.2008.4608440>
- Li W, He X (2011) Review of nonisolated high-step-up DC/DC converters in photovoltaic grid-connected applications. *IEEE Trans Ind Electron* 58:1239–1250. <https://doi.org/10.1109/TIE.2010.2049715>
- Lijewski P, Kozak M, Fuć P, Rymaniak Ł, Ziólkowski A (2020) Exhaust emissions generated under actual operating conditions from a hybrid vehicle and an electric one fitted with a range extender. *Transp Res Part d: Transp Environ* 78:102183. <https://doi.org/10.1016/j.trd.2019.11.012>
- Lin CC, Peng H, Grizzle JW (2004) A stochastic control strategy for hybrid electric vehicles. In: Proceeding of American control conference. Boston, MA, USA, pp 4710–4715
- Liu W (2013) Introduction to hybrid vehicle system modeling and control. Wiley, USA
- Liu Z, Li B, Lee FC, Li Q (2017) High-efficiency high-density critical mode rectifier/inverter for WBG-device-based on-board charger. *IEEE Trans Ind Electron* 64:9114–9123. <https://doi.org/10.1109/TIE.2017.2716873>
- López I, Ibarra E, Matallana A, Andreu J, Kortabarria I (2019) Next generation electric drives for HEV/EV propulsion systems: technology, trends and challenges. *Renew Sustain Energy Rev* 114:109336. <https://doi.org/10.1016/j.rser.2019.109336>
- Van Mierlo J, Hegazy O (2014) Parallel hybrid electric vehicles (parallel HEVs). *Encycl Automot Eng*. Wiley, Chichester. <https://doi.org/10.1002/9781118354179.auto204>
- Millán J, Godignon P, Perpiñá X, Pérez-Tomás A, Rebollo J (2014) A survey of wide Bandgap power semiconductor devices. *IEEE Trans Power Electron* 29(5):2155–2163. <https://doi.org/10.1109/TPEL.2013.2268900>
- Muzaffar A, Ahamed MB, Deshmukh K, Thirumalai J (2019) A review on recent advances in hybrid supercapacitors: design, fabrication and applications. *Renew Sustain Energy Rev* 101:123–145. <https://doi.org/10.1016/j.rser.2018.10.026>
- Nel BJ, Perinpanayagam S (2017) A brief overview of SiC MOSFET failure modes and design reliability. *Proc CIRP* 59:280–285. <https://doi.org/10.1016/j.procir.2016.09.025>
- Noumi Y, Saito T, Kondo K (2014) A study on energy management controller of EDLC for batteries and capacitors hybrid electric vehicles. In: Proceedings on IECON 2014—40th annual conference of the IEEE Industrial Electronics Society. IEEE, Dallas, TX, USA, pp 2952–2957. <https://doi.org/10.1109/IECON.2014.7048929>
- Obata M, Morimoto S, Sanada M, Inoue Y (2014) Performance of PMA SynRM with ferrite magnets for EV/HEV applications considering productivity. *IEEE Trans Ind Appl* 50(4):2472–2434. <https://doi.org/10.1109/TIA.2013.2294999>
- Onori S, Serrao L, Rizzoni G (2016) Pontryagin’s minimum principle. In: Hybrid electric vehicles. Springer Briefs in control, automation and robotics series. Springer, London. [https://doi.org/10.1007/978-1-4471-6781-5\\_5](https://doi.org/10.1007/978-1-4471-6781-5_5)
- Prati MV, Costagliola MA, Giuzio R, Corsetty C, Beatrice CC (2021) Emissions and energy consumption of a plug-in hybrid passenger car in Real Driving Emission (RDE) test. *Transp Eng* 4:100069. <https://doi.org/10.1016/j.treng.2021.100069>
- Qi X, Wu G, Boriboonsomsin K, Barth MJ (2017) Development and evaluation of an evolutionary algorithm-based online energy management system for plug-in hybrid electric vehicles. *IEEE Trans Intell Transp Syst* 18(8):2181–2191. <https://doi.org/10.1109/TITS.2016.2633542>



- Rui X, Cao J, Yu Q (2018) Reinforcement learning-based real-time power management for hybrid energy storage system in the plug-in hybrid electric vehicle. *Appl Energy* 211:538–548. <https://doi.org/10.1016/j.apenergy.2017.11.072>
- Salmasi FR (2007) Control strategies for hybrid electric vehicles: evolution, classification, comparison, and future trends. *IEEE Trans Veh Technol* 56:2393–2404. <https://doi.org/10.1109/TVT.2007.899933>
- Sharma S, Kumar V (2013) Optimized motor selection for various hybrid and electric vehicles. SAE Technical Paper 2013-01-2833. <https://doi.org/10.4271/2013-01-2833>
- Shen C, Shan P, Gao T (2011) A comprehensive overview of hybrid electric vehicles. *Int J Veh Technol* 571683. <https://doi.org/10.1155/2011/571683>
- Shen Z, Omura I (2007) Power semiconductor devices for hybrid, electric, and fuel cell vehicles. *Proc IEEE* 95(4):778–789
- Shirabe K, Swamy MM, Kang JK, Hisatsune M, Wu Y, Kebort D, Honea J (2014) Efficiency comparison between Si-IGBT-Based drive and GaN-based drive. *IEEE Trans Ind Appl* 50(1):566–572. <https://doi.org/10.1109/TIA.2013.2290812>
- Simon P, Gogotsi Y (2008) Materials for electrochemical capacitors. *Nature Mater* 7:845–854. <https://doi.org/10.1038/nmat2297>
- Singh KV, Bansal HO, Singh D (2019) A comprehensive review on hybrid electric vehicles: architectures and components. *J Mod Transport* 27(2):77–107. <https://doi.org/10.1007/s40534-019-0184-3>
- Tarascon JM, Armand M (2001) Issues and challenges facing rechargeable lithium batteries. *Nature* 414(6861):359–367. <https://doi.org/10.1038/35104644> PMID: 11713543
- Tofoli FL, Pereira DdC, de Paula WJ, Júnior DdSO (2015) Survey on non-isolated high-voltage step-up dc-dc topologies based on the boost converter. *IET Power Electron* 8:2044–2057. <https://doi.org/10.1049/iet-pel.2014.0605>
- Toyota develops advanced fuel cell hybrid vehicle Toyota FCHV-adv, with new Toyota FC stack, earns vehicle-type certification. <https://global.toyota/en/detail/300475>. Last accessed 02 Aug 2021
- Tran D-D, Vafaeipour M, El Baghdadi M, Barrero R, Van Mierlo J, Hegazy O (2019) Thorough state-of-the-art analysis of electric and hybrid vehicle powertrains: topologies and integrated energy management strategies. *Renew Sustain Energy Rev* 109596. <https://doi.org/10.1016/j.rser.2019.109596>
- Vagg C, Akehurst S, Brace CJ et al (2016) Stochastic dynamic programming in the real-world control of hybrid electric vehicles. *IEEE Trans Control Syst Technol* 24:1–14
- Varella RA, Gonçalves G, Duarte G, Farias T (2016) Cold-running NO<sub>x</sub> emissions comparison between conventional and hybrid powertrain configurations using real world driving data. SAE Technical Paper 2016-01-1010. <https://doi.org/10.4271/2016-01-1010>
- Villeneuve A (2004) Dual mode electric infinitely variable transmission. SAE Technical Paper 2004-40-0019
- Wang H-W, Hu Z-A, Chang Y-Q, Chen Y-L, Wu H-Y, Zhang Z-Y, Yang Y-Y (2011) Design and synthesis of NiCO<sub>2</sub>O<sup>+</sup> reduced graphene oxide composites for high performance supercapacitors. *J Mater Chem* 21:10504–10511. <https://doi.org/10.1039/C1JM10758E>
- Wang H, Wang Q, Hu B (2017) A review of developments in energy storage systems for hybrid excavators. *Autom Constr* 80:1–10. <https://doi.org/10.1016/j.autcon.2017.03.010>
- Wang W, Fu R, Fan Y (2018) Electromagnetic parameters matching of permanent magnet synchronous motor for hybrid electric vehicles. *IFAC PapersOnLine* 51–31:407–414. <https://doi.org/10.1016/j.ifacol.2018.10.083>
- Wang Y, Hao C, Ge Y, Hao L, Tan J, Wang X et al (2020) Fuel consumption and emission performance from light-duty conventional/hybrid-electric vehicles over different cycles and real driving tests. *Fuel* 278:118340. <https://doi.org/10.1016/j.fuel.2020.118340>
- Whitaker B, Barkley A, Cole Z, Passmore B, Martin D, McNutt TR, Lostetter AB, Lee JS, Shiozaki K (2014) A high-density, high-efficiency, isolated on-board vehicle battery charger utilizing silicon

- carbide power devices. *IEEE Trans Power Electron* 29:2606–2617–88. <https://doi.org/10.1109/TPEL.2013.2279950>
- Wu D, Williamson SS (2007) Status review of power control strategies for fuel cell based hybrid electric vehicles. In: *Proceedings on IEEE Canada Electrical power conference*, pp 218–223, Canada. <https://doi.org/10.1109/EPC.2007.4520333>
- Xi J, Li M, Xu M (2014) Optimal energy management strategy for battery powered electric vehicles. *Appl Energy* 134:332–341. <https://doi.org/10.1016/j.apenergy.2014.08.033>
- Yang LH, Wang YJ, Zhu CM (2016) Study on fuzzy energy management strategy of parallel hybrid vehicle based on quantum PSO algorithm. *Int J Multimedia Ubiquit Eng* 11:147–158. <https://doi.org/10.14257/IJMUE.2016.11.5.14>
- Yang C, You S, Wang W et al (2019) A stochastic predictive energy management strategy for plug-in hybrid electric vehicles based on fast rolling optimization. *IEEE Trans Ind Electron*. <https://doi.org/10.1109/TIE.20192955398>
- Yang C, Zha M, Wang W, Liu K, Xiang C (2020a) Efficient energy management strategy for hybrid electric vehicles/plug-in hybrid electric vehicles: review and recent advances under intelligent transportation system. *IET Intell Transp Syst* 14(7):702–711. <https://doi.org/10.1049/iet-its.2019.0606>
- Yang C, Zha M, Wang W, Liu K, Xiang C (2020b) Efficient energy management strategy for hybrid electric vehicles/plug-in hybrid electric vehicles: review and recent advances under intelligent transportation system. *IET Intel Transport Syst* 14(7):702–711. <https://doi.org/10.1049/iet-its.2019.0606>
- Zeraoulia M, Benbouzid M, Diallo D (2005) Electric motor drive selection issues for HEV propulsion systems: a comparative study. In: *IEEE VPPC'05 (2005)*, Chicago, USA, pp 280–287. hal-00527584
- Zhang JP, Wang FY, Wang KF (2011) Data-driven intelligent transportation systems: a survey. *IEEE Trans Intell Transp Syst* 12(4):1624–1639. <https://doi.org/10.1109/TITS.2011.2158001>
- Zhang P, Yan FW, Du CQ (2015) A comprehensive analysis of energy management strategies for hybrid electric vehicles based on bibliometrics. *Renew Sustain Energy Rev* 48:88–104. <https://doi.org/10.1016/j.rser.2015.03.093>
- Zhang F, Hu X, Langari R, Cao D (2019) Energy management strategies of connected HEVs and PHEVs: recent progress and outlook. *Prog Energy Combust Sci* 73:235–256. <https://doi.org/10.1016/j.pecs.2019.04.002>
- Zhang Y, Mi C (2018) *Automotive power transmission systems*. Automotive series. Wiley, USA
- Zhang N, Ma X, Jin L (2017) Energy management for parallel HEV based on PMP algorithm. In: *Proceedings of the 2nd International Conference on Robotics and Automation Engineering (ICRAE)*, pp 177–182, Shanghai, China. <https://doi.org/10.1109/ICRAE.2017.8291376>
- Zheng P, Sui Y, Fu Z, Tang P, Wu F, Wang P (2014) Investigation of a five-phase 20-slot/18-pole PMSM for electric vehicles. In: *17th International Conference Proceedings on Electrical Machines and Systems (ICEMS)*. IEEE, Hangzhou, China, pp 1168–1172. <https://doi.org/10.1109/ICEMS.2014.7013664>
- Zhou ML, Lu DK, Li WM et al (2013) Optimized fuzzy logic control strategy for parallel hybrid electric vehicle based on genetic algorithm. *Appl Mech Mater* 274:345–349. <https://doi.org/10.4028/www.scientific.net/AMM.274.345>
- Zhu C, Lu F, Zhang H et al (2018) A real-time battery thermal management strategy for connected and automated hybrid electric vehicles based on iterative dynamic programming. *IEEE Trans Veh Technol* 67:8077–8084

# Chapter 6

## Life-Cycle Analysis for the Automotive Sector



Graham Conway 

**Abstract** Regulators, policymakers, environmental groups, and investors promote battery electric vehicles (BEVs) as zero-emission vehicles (ZEV). Under current regulations, emissions are measured at the vehicle tailpipe. This definition is widely accepted. However, it is misleading as emissions are still created elsewhere during the life cycle of a battery electric vehicle. For example, mining the earth for raw materials and then manufacturing them into vehicle and powertrain components create embedded emissions. In addition, the production of fuel or electricity generates emissions, and the vehicle end-of-life also impacts total emissions, depending on scrappage or recycling processes. To accurately account for these stages, a life-cycle analysis is required. In a proper life-cycle analysis, it is possible to quantify emissions at each stage of the vehicle's life to better understand cumulative emissions. Understanding cumulative emissions for different decarbonization pathways, it is possible to correctly choose the best strategy to move towards lower overall GHG emissions from transportation. LCA studies show that BEVs can lower GHG emissions, especially when charged from a renewable grid. However, alternative fuels and hybrid powertrains can have even lower life cycle GHG emissions. Therefore, LCA should be adopted as part of future policy and regulations. The main challenge with the adoption of LCA is the vast number of assumptions used. The final GHG prediction is sensitive to these assumptions and can alter the conclusion of any LCA study. This chapter will review several LCA studies and identify commonly used assumptions, variations on assumptions, and their impact on conclusions. Finally, a set of recommendations for future LCA work is presented.

**Keywords** Life-cycle analysis · Greenhouse Gas emissions · GREET

---

G. Conway (✉)  
Southwest Research Institute, San Antonio, TX 78238, USA  
e-mail: [graham.conway@swri.org](mailto:graham.conway@swri.org)

© The Author(s), under exclusive license to Springer Nature Singapore Pte Ltd. 2022  
G. Kalghatgi et al. (eds.), *Engines and Fuels for Future Transport*, Energy, Environment,  
and Sustainability, [https://doi.org/10.1007/978-981-16-8717-4\\_6](https://doi.org/10.1007/978-981-16-8717-4_6)

103

## 6.1 Introduction

Imagine you are standing in an orchard with a basket containing ten apples. Someone asked you the question, “how many apples are there?” One answer might be “ten,”—the number you hold in the basket. However, what if the person also wanted to know the number of apples on the ground around you? Or the person wants you to also count those still attached to the trees? What is the answer, then? The answer is ambiguous, as is the question. “How many apples can you hold?” or “How many apples are there in total in the orchard?” would yield a more precise answer. Choosing the right question will always give the most useful answer. Unfortunately, today in the automotive industry, we are asking the *wrong* question. We need to understand how many apples are there in the orchard, but we are asking the question, “How many apples can you hold?”

Today, there is a consensus among the scientific community that society needs to reduce artificial emissions. Reducing pollutant emissions in urban areas leads to better air quality and quality of life for those living there. In addition, greenhouse gas (GHG) emissions increase global temperatures (Cook et al. 2016). Based on a survey of 11,944 research paper abstracts, climate scientists have a 97% consensus that there is a connection between GHG emissions and global temperature increase (Cook et al. 2013). In 2019, around 6474 million tons of GHG emissions (CO<sub>2</sub> equivalent) were released from U.S. sources. The transportation sector contributed 29% of the total GHG emission and was the largest single-sector contributor to the U.S. GHG emissions (U.S. EPA 2021a). A breakdown of GHG emissions by sector can be seen in Fig. 6.1.

Greenhouse gas emissions include carbon dioxide (CO<sub>2</sub>), methane (CH<sub>4</sub>), nitrous oxide (N<sub>2</sub>O), and various hydrofluorocarbons (HFCs). The impact of each emission on “global warming” is defined by the global warming potential (GWP) of each fuel. The GWP of common GHG emissions can be seen in Table 6.1. Methane has a GWP of 25, which is 25 times more effective as a global warming gas than carbon dioxide.

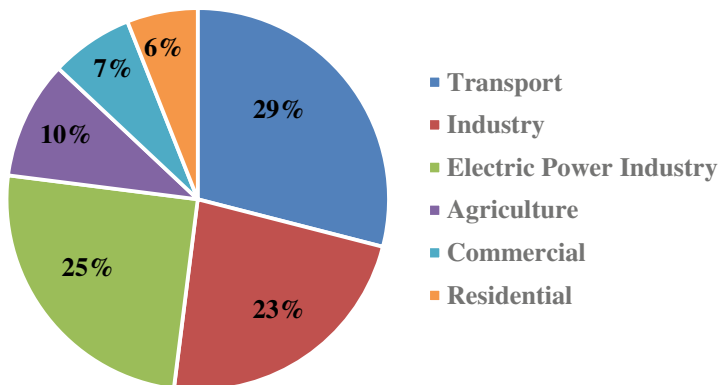


**Fig. 6.1** Share of the U.S. GHG Emissions by Sector, 2019, modified from U.S. EPA (2021a)

**Table 6.1** Commonly found greenhouse gas emissions and their respective 100-year GWP (Myhre et al. 2013)

Greenhouse gas	Chemical formula	100-year global-warming potentials
Carbon dioxide	CO <sub>2</sub>	1
Methane	CH <sub>4</sub>	25
Nitrous oxide	N <sub>2</sub> O	298
(HFC-134a) (common refrigerant)	CH <sub>2</sub> FCF <sub>3</sub>	1430

In the U.S. in 2019, 80% of GHG emissions were CO<sub>2</sub>. CO<sub>2</sub> is a product of complete combustion when a hydrocarbon fuel is burned in the air. *As more fuel is burned, more carbon dioxide is produced and vice-versa.* The EPA states that for every gallon (U.S.) of gasoline (3.78 L) burned, 19.59 lbs ((8.88 kg) of CO<sub>2</sub> is produced (U.S. EPA 2011) so a typical gasoline vehicle will produce 392 lbs (~178 kg) of CO<sub>2</sub> per full tank of fuel. A diesel produces approximately 15% more CO<sub>2</sub> per volume of fuel burned. In Fig. 6.2, we see that 82% of emissions from the transportation sector in the U.S. are generated by passenger cars (light-duty vehicles) and commercial vehicles (medium and heavy-duty vehicles). This analysis highlights the need for focusing on the transportation sector when considering GHG reduction.

To reduce the USA’s dependence on imported oil, the Energy Policy and Conservation Act of 1975 established CAFE (Corporate Average Fuel Economy) standards for passenger cars starting in 1978. These standards held automakers accountable and placed a focus on increasing fuel economy. Over time, fuel standards have become stricter despite the increase in vehicle size and power. As a result, fuel economy has improved from 15.8 mpg average in 1978 to 25.7 mpg average in 2020 (U.S. EPA

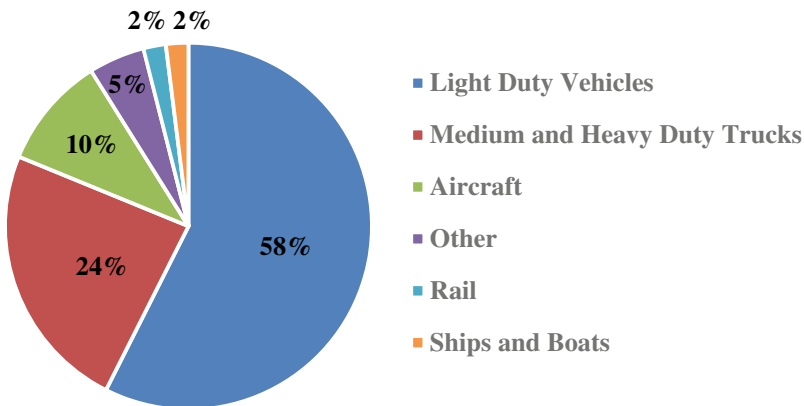


**Fig. 6.2** Share of the U.S. Transportation Sector GHG Emissions by Source, 2019 modified (U.S. EPA 2021a)

2020b)—1 U.S. mpg is around 0.425 km/liter. This corresponds to a CO<sub>2</sub> reduction from 562 g/mile in 1978 to 344 g/mile in 2020. However, it was not until December 2009 that the U.S. EPA found evidence that GHGs endanger both public health and welfare, which led to the establishment of standards for GHG emissions (U.S. Department of Energy 2021). For CAFE standards, fuel economy is measured over two pre-defined cycles under laboratory-controlled conditions. However, the fuel use is not directly measured due to transient fuel mass or volume measurement challenges. Instead, a “carbon-balance” approach is used (Lawrence 1981). In this approach, the hydrocarbon (HC), carbon monoxide (CO) carbon-dioxide (CO<sub>2</sub>), and particulate emissions are measured by inserting a probe into the tailpipe of the test vehicle (see Fig. 6.3); the test fuel is a well-defined reference fuel. The fuel economy can be calculated from the emission concentration in the tailpipe. From the fuel economy value, a g/mile CO<sub>2</sub> emission value is also calculated. For heavier vehicles, only the engine is tested but to a similar standard. This is how the industry quantifies greenhouse gas emissions from the transportation sector.

Electrified vehicles are rapidly gaining market share in major global markets (Conway et al. 2020). Electrified vehicles have some form of a hybrid system or are fully battery-electric (BEV), or are fuel-cell electric vehicles (FCV). Generally, hybrids fall into three categories: mild-hybrid (MHEV), full-hybrid (HEV), and plug-in hybrid (PHEV). Specific requirements for each category are not universally accepted. However, the following may be used for references used in this chapter.



**Fig. 6.3** Vehicle installed on a chassis dynamometer at Southwest Research Institute with exhaust emissions sampling lines and emissions sampling unit

- **ICE-only**
  - May use a start-stop system but limited to 12 V architecture.
- **MHEV**
  - Uses a 48 V e-machine of limited power (<30 kW) to assist the ICE.
- **HEV**
  - Uses a higher voltage architecture and higher power e-machine to provide more assistance to the ICE.
- **PHEV**
  - Larger battery pack and more capable electric motor. Capable of all-electric driving under many real-world conditions. It contains an onboard charger to accept electricity from an external source.
- **BEV**
  - No internal combustion engine but contains a battery pack and electric motor.
- **FCV**
  - No internal combustion engine but contains a: battery pack, electric motor, and a fuel-cell stack and hydrogen tank.

There is no measurable CO<sub>2</sub>, CO, HC, or particulate emissions created for FCVs and BEVs as there is no combustion process. However, there are processes associated with these vehicles that do release emissions, such as electricity or hydrogen generation. However, these are not measured or accounted for by our current measurement methods. Consequently, FCVs and BEVs are widely called “zero-emission” vehicles. However, as we have discussed, greenhouse gas emissions are global concerns and come from many sources. This chapter’s opening example shows that GHG emissions are the apples, so FCVs and BEVs are the baskets without apples. At the same time, an internal combustion engine (ICE) vehicle is a basket full of apples. Now, if the question asked was “which basket has more apples?” then the clear answer would have been the ICE vehicle. However, the question being asked is no longer relevant. For appropriate greenhouse gas emissions measurement, we need to be asking, “How many apples are there in the orchard?” not just “How many are in the basket?”

## 6.2 Life-Cycle Analysis

All the emissions associated with a sector or process can be quantified by Life-Cycle Analysis (LCA). Specifically for transportation topics, LCAs consider CO<sub>2</sub> emissions generated during several key phases. This work proposes six primary phases:

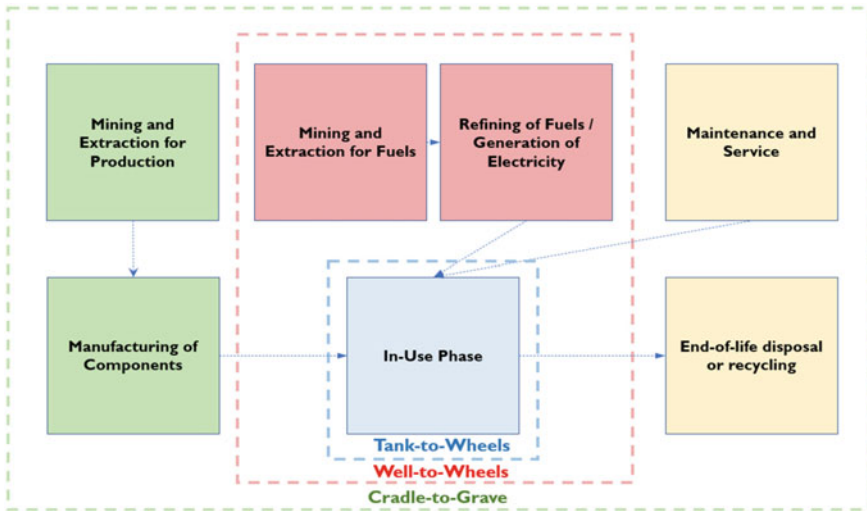


**Fig. 6.4** Framework for Life-Cycle Analysis approach to capture energy and emissions for the vehicle's life

1. Mining and extraction of the raw materials required to make the vehicle's components and fuels;
2. Manufacturing of components;
3. Refining of fuels and their transportation from refinery to refueling station and electricity generation;
4. In-use emissions generated via combustion processes;
5. Component and fluid services;
6. End-of-life disposal and recycling.

Different approaches are taken to life-cycle analysis. For example, a “tank-to-wheel” analysis considers only phase 4, a “well-to-wheel” analysis considers phases 3 and 4, while a “cradle-to-grave” analysis considers phases 1–6. See Figure 6.4 as an example framework for life-cycle analysis.

Life-Cycle Analysis (LCA) is becoming an increasingly important topic in the automotive industry due to the rise of electric and electrified vehicles and alternative fuels. These new powertrains reduce emissions generated in phase 4 and move them into other phases, thus, reducing the relevance of the current “tank-to-wheel” approach taken by regulators. A key example of why broader LCA is necessary can be seen with a simple “tank-to-wheel” approach case. A horse breathes in air and turns part of the oxygen into  $\text{CO}_2$ , which it then exhales. If the  $\text{CO}_2$  were measured from the horse, like we currently measure emissions from a vehicle's tailpipe, then it would be seen that at a 4-mph canter, a horse emits 530 g/mile  $\text{CO}_2$ , which is equivalent to a 2019 Corvette (Conway et al. 2020). Thus, under the current “tank-to-wheel” regulation, the horse is not compliant with fuel economy standards, and we would conclude



that their use should be limited. However, if a “well to wheel” approach is considered, it is possible to see that most of the fuel used in the vehicle comes from fossil sources while the energy used to power the horse comes from low carbon, biogenic sources. Biogenic CO<sub>2</sub> essentially means that at some point in the cycle, bio-matter has absorbed atmospheric CO<sub>2</sub>. In this example, the grass/hay used by the horse as its energy source absorbed CO<sub>2</sub> during its growth. This means that although the horse breathes out the same amount of CO<sub>2</sub>, it has a much lower overall carbon footprint. Furthermore, several arguments exist for a complete “cradle-to-grave” analysis due to CO<sub>2</sub> emissions associated with battery pack production, leading to a significant carbon footprint before the vehicle has driven a single mile. However, until at least a “well-to-wheel” approach is adopted in regulation, an inaccurate analysis will be performed, leading to incorrect conclusions and possible actions.

### 6.2.1 *Methods*

If all sources of GHG emitted during the life of a vehicle are considered, there are potentially thousands of pathway combinations that must be quantified. Several software programs exist which capture these pathways; the most used is the GREET® model developed by Argonne National Laboratory. The **Greenhouse gases, Regulated Emissions, and Energy use in Technologies Model** is a suite of models that simulates the energy use and emissions output of various vehicle and fuel combinations. GREET is updated annually to ensure the latest information is used (U.S. Department of Energy 2021). In addition to GHG emissions, GREET also calculates total energy consumption (non-renewable and renewable), air pollutant emissions, and water consumption. Today, GREET has more than 40,000 registered users worldwide from industry, academia, and government institutions such as the California Air Resources Board (CARB), the U.S. Environmental Protection Agency (EPA), and the International Civil Aviation Organization (Argonne National Laboratory 2020a).

When people undertake LCA studies, GHG emissions are the most researched of all the emissions. Other emissions in the life-cycle chain include air quality, total energy usage, toxicity, land use charges, water consumption, resource depletion, and costs (Hill et al. 2020). This chapter focuses on GHG emissions and often expresses total GHG emissions as CO<sub>2</sub>eq of CO<sub>2</sub>-equivalent. This term accounts for the GWP of different GHG emissions in various processes. For example, methane has a GWP of 25, and so one kg of methane is equivalent to 25 kg of CO<sub>2</sub>, i.e., 1 kg of methane can be represented as 25 kg CO<sub>2</sub>eq.

## 6.2.2 Key Considerations for Life-Cycle Analysis

### Electricity Production

A key difference between a BEV and a vehicle with an ICE is that the main source of power comes from electricity rather than a hydrocarbon fuel. The method by which the electricity is generated can significantly impact the outcome of life-cycle analysis. Some nations are heavily dependent on renewable energy sources, which have a shallow carbon footprint, such as solar, wind, geothermal and hydroelectric. In contrast, others rely on high-carbon intensity sources, including burning fossil fuels, such as lignite, hard coal, natural gas, and even oil. Nuclear is not considered renewable but has a very low carbon intensity. A summary of the global median carbon intensities for common electricity production methods can be seen in Fig. 6.5. Note that the axis is on a logarithmic scale.

There is a significant variation in how different countries generate their electricity, as seen in the electrical grid carbon intensity for various countries shown in Fig. 6.6. Norway has the highest percentage of plug-in electric vehicle sales in addition to one of the lowest carbon intensity grids in the world (Conway et al. 2020). As of 2020, Norway has 1690 hydropower plants and 53 wind farms. They account for 98% of Norway's self-produced 154.2 TWh of electricity (Energy Facts Norway 2021). Conversely, 76% of India's electricity relies on fossil fuel sources (45% coal, 5.7% natural gas, and 25.6% oil) (International Energy Agency 2020). China sells the highest volume of electric vehicles but relies on fossil-fuel sources for 88% of electricity (61.9% coal, 7.2% natural gas, and 19.1% oil) (International Energy Agency 2020). Therefore, any life-cycle analysis using a country's average grid mix will yield a large variation in life-cycle CO<sub>2</sub> results even if the vehicle type remains constant between countries.

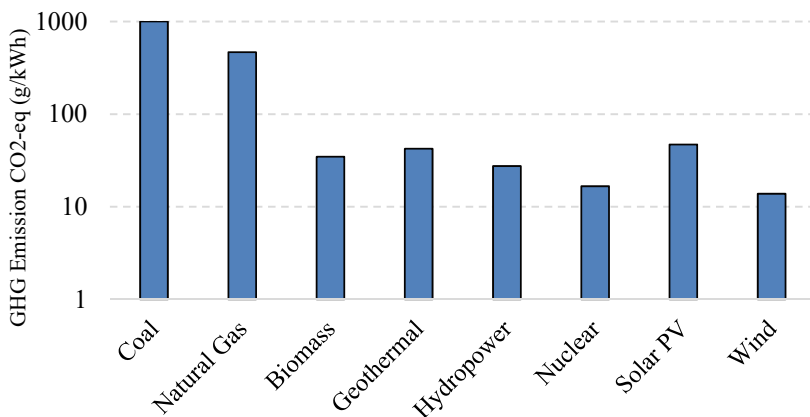


**Fig. 6.5** Global median life-cycle CO<sub>2</sub>-eq generated per kWh of electricity produced (Bruckner et al. 2014)

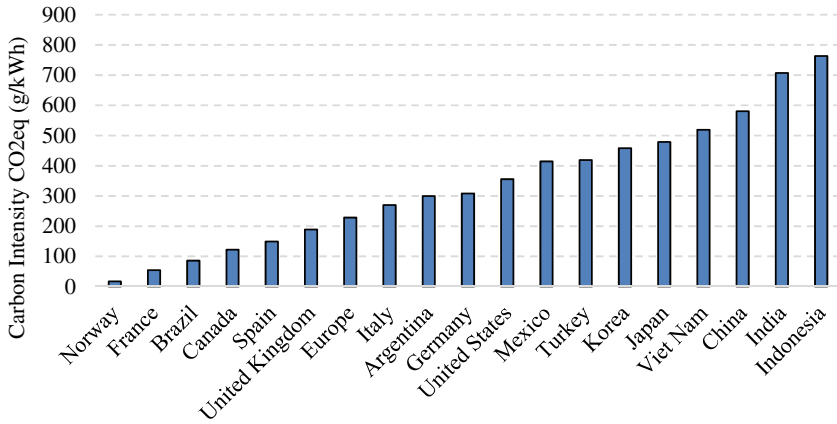


**Fig. 6.6** Electricity grid carbon intensity for various countries as of 2020 (International Energy Agency 2021b)

Southwest Research Institute study shows that an efficient BEV may have total life cycle GHG emissions equivalent to 52 g/mile in Norway. Still, if driven for the same total mileage, the same vehicle emits 240 g/mile using China’s electrical grid (Zhang et al. 2021). An LCA study states that electric vehicles are recharged from the grid using that region’s average electricity mix carbon intensity. This assumption is called the “total” or “average” energy mix approach. This approach simplifies the challenging and constantly changing real-world electricity generation situation by assuming that a region’s electricity generation has the same carbon intensity. Many life-cycle analysis studies adopt this approach due to its simplicity (Noori et al. 2015; Mayyas et al. 2017; Yang et al. 2021; Zhou et al. 2013; Gebler et al. 2020). However, there are several limitations in using the “average” approach:

1. This approach does not consider the complete picture of Norway’s electricity generation as Norway both exports and imports electricity. For example, in 2019, Norway imported around 12 TWh of electricity from neighboring countries where the average carbon intensity is higher than Norway (Statistics Norway 2021). So if an electric vehicle draws electricity from the Norwegian grid, what is the actual CO<sub>2</sub> footprint? The same electricity sharing situation occurs within and between various states within the U.S. (Burton et al. 2021).
2. As the share of electric vehicles rises, the electrical grid capacity must increase. Moreover, it must increase with a proportionally larger capacity of renewable energy sources. Otherwise, the grid will rely on fossil fuel sources to meet the extra demand. It is relatively easy to burn more coal or natural gas than increasing wind or solar output.
3. The electricity generation mix is not constant throughout any given period. Figure 6.7 shows an example of why the “average” approach can result in unrealistic results. It can be seen in the figure that California’s grid utilizes P.V. (photovoltaic) solar arrays during the day; however, in the evening, natural gas

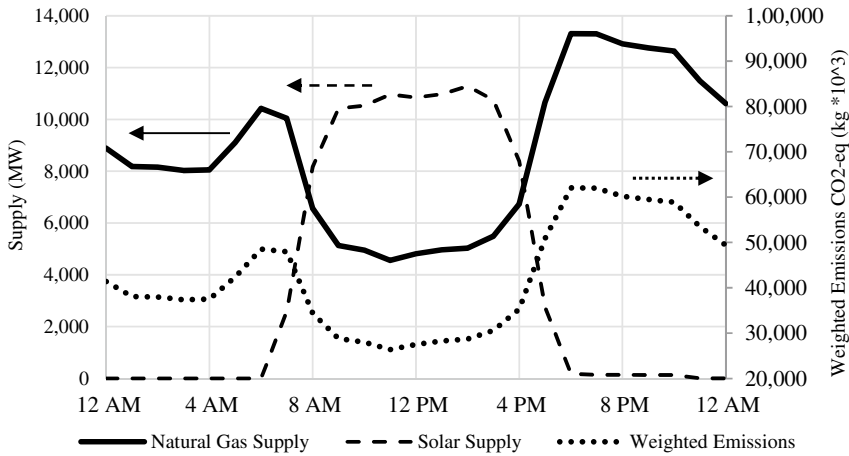


**Fig. 6.7** California Electricity Generation (03/03/2020). Figure modified from Burton et al. (2021)

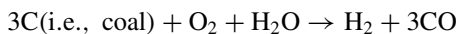
is used to buffer the deficit from reduced solar potential. Thus, depending on when people charge their vehicles, i.e., when electricity is required, there is a significant potential difference in GHG emissions produced.

A study that accounts for the transient nature of the electrical grid uses a “marginal” approach. Several life-cycle analysis studies have utilized *marginal* mix in their calculation before. However, it is not a widely adopted method due to the complexity involved. Studies that utilize a “marginal” mix often show BEV to have significantly higher emissions than when using the “average” mix (Burton et al. 2021; Ma et al. 2012; Onat et al. 2015; Garcia 2016; Samaras and Meisterling 2008).

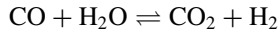
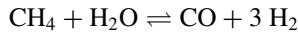
**Hydrogen Production**

Hydrogen is being discussed as a promising zero-emission technology for transportation. It can be used in a fuel cell where it reacts with oxygen to produce electricity and water, or it can be burned in an ICE to produce work, water, and oxides of nitrogen. However, like electricity, the source of hydrogen must be carefully assessed through life-cycle analysis to understand the full GHG impact of this pathway. Hydrogen is the most abundant element in the universe, accounting for around 75% of all normal matter. However, it is not easily found on earth and must be manufactured but will have a GHG emission footprint associated with each production method. There are four main methods of hydrogen production:

1. **Brown/Black Hydrogen:** Coal gasification of lignite (brown) or bituminous (black) where carbon monoxide, hydrogen, carbon dioxide, natural gas, and water vapor are produced from the incomplete combustion of coal, water, and air:



2. **Grey Hydrogen:** Endothermic steam methane reforming (a) to produce carbon monoxide and hydrogen further refined via the exothermic water–gas shift reaction (b):



3. **Blue Hydrogen:** Follows the same steps as grey hydrogen, but waste  $\text{CO}_2$  is captured via carbon capture and sequestration system (CCS).
4. **Green Hydrogen:** Splitting water into hydrogen and oxygen using an electrolyzer powered by renewable electricity.
- a. Note that an electrolyzer powered by non-renewable sources would not be economically viable as fossil fuel could just be used to produce brown/black or grey hydrogen without adding steps.

While other “colors of hydrogen” involve nuclear energy, these processes are not at scale today. Over 95% of the world’s hydrogen is Grey Hydrogen and is likely to remain at high levels into the near future. The carbon intensity of grey hydrogen has been placed at 341–365 g/kWh<sub>H<sub>2</sub></sub> (Ewing 2020b), making it less carbon-intensive per energy unit than electricity generation via natural gas but significantly higher than renewable energy sources. This assessment does not include the energy required to transport the hydrogen from the plant to the tank of the vehicle and store it on board which requires the gas to be compressed to high pressures or liquefied. This act will require additional energy. In addition, an electric vehicle is significantly more efficient than either a fuel-cell electric vehicle or hydrogen ICE vehicle. It is, therefore, difficult to justify the use of hydrogen as a “low carbon” transportation fuel while grey hydrogen is the dominant production method.

### Embedded Emissions

Producing a vehicle requires several processes. We can look at the cylinder block of an internal combustion engine as an example. If virgin aluminum is required, then the first bauxite ore would need to be mined. Next, the ore would be transported to a refining facility. It would undergo the Bayer and Hall-Heroult process to turn the bauxite ore into aluminum oxide and finally into aluminum. Next, the aluminum would likely be transported to the casting facility. It is cast into a cylinder block form before being machined, assembled into the internal combustion engine, and then installed into the vehicle. Each step of this process requires energy, and typically there will be a carbon footprint produced during each step. This carbon footprint is otherwise known as embedded emissions. These are emissions produced to get the vehicle to the showroom before driving a single passenger mile. A simple example for current U.S. vehicles can be seen in Fig. 6.8. A typical ICE US passenger vehicle’s embedded GHG emissions footprint will be approximately 6000 kg CO<sub>2</sub>-eq for a mid-sized sedan (Toyota Corolla), rising to 13,500 kg CO<sub>2</sub>-eq for a Class 2A pickup (Ford F-150). The BEV version of the sedan (Tesla Model 3 standard) and pickup

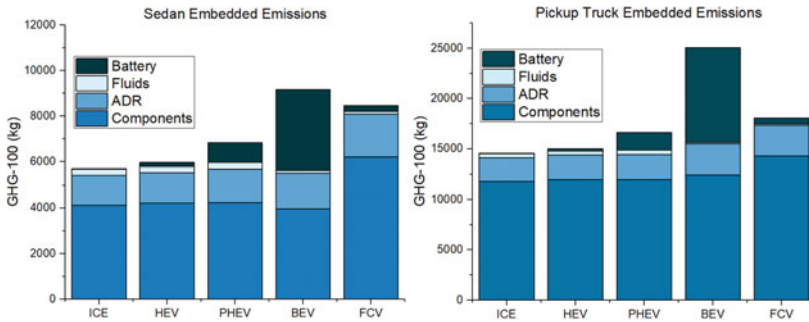


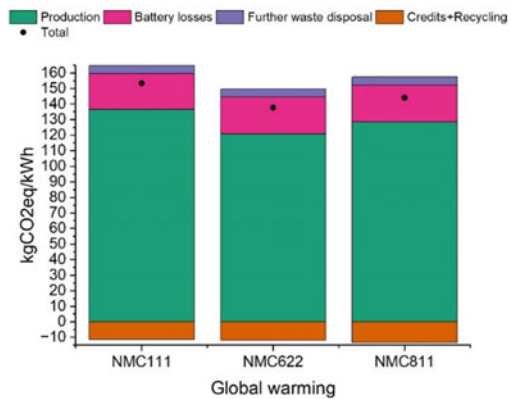
**Fig. 6.8** Embedded emissions for different powertrain types in two light-duty vehicle classes. Reproduced from data within Zhang et al. (2021)

truck have far higher embedded emissions at 9600 and 24,000 kg, respectively, mainly due to the influence of the battery pack (Zhang et al. 2021).

**Battery Pack Production**

Most LCA studies show that Hybrids, FCVs, and BEVs all have higher embedded emissions than an equivalent ICE, primarily due to the lithium-ion battery pack. This is due to the high energy requirements to make a lithium-ion battery pack, specifically the cathode production. The most common cathode chemistry used in early BEVs was NMC111—lithium-nickel-manganese-cobalt-oxide chemistry with a similar molar ratio of nickel, manganese, and cobalt (Pillot 2015). However, due to cobalt’s high cost and low availability of NMC111, cathodes have been phased out in favor of NMC622 cathode chemistries with a higher nickel content (and lower cobalt content) (Slowik et al. 2020). NMC622 batteries have a higher energy density and longer cycle life than NMC111 cells, but they also have a lower voltage. As a result, MC622 chemistry has a lower GHG footprint than both NMC111 and NMC811 chemistries, as shown in Fig. 6.9 (Accardo et al. 2021). Therefore, future BEV

**Fig. 6.9** Impacts per kWh of different NMC chemistries for the global warming potential impact (Accardo et al. 2021)



chemistry is likely to move to NMC811 cathode chemistry. Although BEVs and PHEVs move towards different cathode chemistries, graphite anodes remain the dominant choice (Slowik et al. 2020).

The most environmentally burdensome process in battery production is creating the cathode powder. NCM111 powder accounts for 36.4% of the total energy required to make the battery pack and 39.1% of the total GHG emissions. Cell production and raw aluminum used in the battery are the subsequent most energy-intensive processes, and aluminum requires 18.1% of total energy use, 17% GHG emissions. Cell production requires 19.2% of total energy use and 19% of GHG emissions. A percentage breakdown for battery production and the absolute weight, emissions, and energy required to make a 1 kWh battery are shown in Fig. 6.10.

A major challenge for people who run LCA simulations is the lack of transparent data for the latest battery chemistries. Most data has been approximated or simulated itself, and researchers must estimate energy requirements for different chemistries and processes. In a review of LCA studies, the ICCT found a large variation in report emissions for battery pack production. The least emitting battery pack production was found to be 30 kg CO<sub>2</sub>e/kWh. In comparison, the most emitting was as high as 494 kg CO<sub>2</sub>e/kWh for battery pack production emissions reported by the scientific community (The International Council on Clean Transportation 2018). Potentially this means that a long-range BEV with a 100-kWh battery pack has a carbon footprint

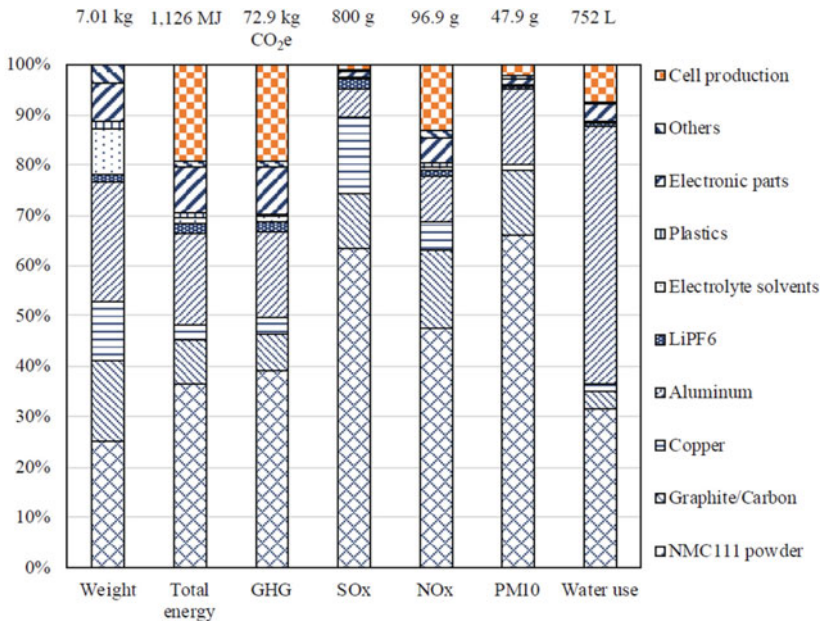


**Fig. 6.10** Breakdown of battery production energy, emissions, and weight for a 1 kWh NMC111-graphite Li-Ion battery (Dai et al. 2019)

of between 3000 kg and 49,400 kg at the start of its life, significantly higher than a non-BEV. More recent LCA studies appear to have converged on a range of between 61 CO<sub>2</sub>e/kWh to 160 CO<sub>2</sub>e/kWh. (Andersson and Börjesson 2021; Accardo et al. 2021; Emilsson and Dahllöf 2019; Dai et al. 2019; Bieker 2021). However, this still leaves a large range of battery production CO<sub>2</sub> values, which concerns those running and those reviewing or critiquing LCA studies. The range of production values can lead to a difference of 10 tons of CO<sub>2</sub> equivalent GHG emissions at the start of the vehicle's life. The major difference is attributed to the country in which the battery is produced and that countries electricity generation type. In 2020 77% of lithium-ion batteries<sup>1</sup> were produced in China, which typically has a more carbon-intensive electricity grid (Statistica 2021). Therefore, an LCA analysis should carefully consider which region is being represented by the study and choose the correct electricity mix and battery production location. It is also important to state whether the value used for battery production includes credits or recycling effects if virgin materials are not required.

Batteries will likely last longer than the vehicle's lifetime for the case of passenger cars. Despite manufacturer warranties stating around 100,000 miles, this does not indicate a replacement is necessary after this time. Suppose a second battery is required during the vehicle's lifetime. In that case, there are significant impacts on that vehicle's life-cycle GHG footprint, but this is not expected to be the typical case (Harlow et al. 2019). Battery replacements may be required for larger vehicle classes with significantly longer total mileage requirements (Vishwanathan 2020).

## Recycling

There are three potential end-of-life scenarios for an electric vehicle battery pack:

1. Retain the battery pack and repurpose it for private or commercial grid storage (provided the battery performance is still acceptable). There are numerous benefits for owners, such as cost recovery from the sale of the battery or from capturing renewable energy when there is surplus generation (Ambrose 2020).
2. Recycle the raw materials to repurpose for other uses or to create new lithium-ion batteries. The battery recycling process can be split into two parts for NMC batteries: cell and non-cell materials. Solvents can be used in pyrometallurgical and hydrometallurgical processes to recover rare-earth materials. Other components are disposed of in a landfill or by combustion (Accardo et al. 2021).
3. Disposal by landfill or combustion.

The EPA states that lithium-ion batteries and devices should not go in household garbage or recycling bins (EPA 2021c). So, the third option is extremely undesirable due to environmental damage and safety concerns with disposing of li-ion batteries. While the second option may seem attractive, there are several challenges with large-scale lithium-ion battery recycling. The toxicity of the solvents used in the recycling process is the first major challenge as well as the energy requirements for battery recycling. However, several new companies are starting to develop recycling capabilities on increasing scales. *Li-Cycle* has begun construction of the largest lithium-ion

---

<sup>1</sup> Note this includes all types of lithium-ion batteries not just those associated with electric vehicles



battery-recycling plant in North America. It plans to recover at least 95% of cobalt, nickel, lithium, and other elements and will have an input capacity of 25 metric kilotons (Kumagai 2021). As recycled batteries may reduce GHG emissions by up to 14–25%, it is a worthwhile focus for future industrial efforts (Laboratory et al. 2020c). By the time early BEVs are nearing the end of their life in 2030, there is a global potential for between 112 and 227 GWy/y second-life battery supply from recycled batteries by 2030 (Engel et al. 2019).

### FCV

The fuel cell in an FCV produces electricity which an electric motor can use to power the vehicle. Most FCVs also have a lithium-ion battery to capture braking energy and assist the fuel cell during high power demands. The size of the battery is much smaller than an FCV, the Toyota Mirai battery is just 1.24 kWh (Baldwin 2020), so the impact on embedded emissions is negligible. However, in an FCV, the hydrogen tanks have a larger GHG production footprint due to the unique materials used to withstand the 700-bar storage pressure of the onboard H<sub>2</sub>. The hydrogen tanks on the Toyota Mirai have an embedded GHG footprint of 3400 kg CO<sub>2</sub>eq (Bieker 2021). The carbon fiber reinforced plastic cannot be easily recycled either, but research efforts are ongoing to develop industry-scale recycling techniques (Karuppannan Gopalraj and Kärki 2020).

### Fuels

Combustion of a hydrocarbon fuel will always yield CO<sub>2</sub> emissions regardless of whether the fuel is a low-carbon fuel or not. A low carbon fuel meets at least one of the following criteria:

- A higher hydrogen-to-carbon ratio (H:C) than either the gasoline or diesel it replaces. As the H:C ratio increases, water–vapor product concentration increases while carbon dioxide decreases.
- Iso-octane (a surrogate for gasoline) has the chemical formula C<sub>8</sub>H<sub>18</sub> and has an H:C of 2.25. On the other hand, compressed natural gas (CH<sub>4</sub>) and methanol (CH<sub>3</sub>OH) have a theoretical H:C of 4.
- Fuels with no carbon atoms at all are considered low carbon. Two fuels commonly researched in ICE are ammonia (NH<sub>3</sub>) and pure hydrogen (H<sub>2</sub>).
- Bio-fuels are fuels that can be produced from biomass instead of fossil sources. Ethanol is a common example that can be made from corn or sugarcane. The crop absorbs atmospheric carbon dioxide as it grows. Thus, even though carbon dioxide is emitted during combustion, the net carbon dioxide emitted is lower than a fossil-derived fuel.
- Biodiesel fuel can be derived from waste cooking oil or animal fat. When combined with alcohol during transesterification, an ester will be produced.
- Renewable diesel is distinct from biodiesel. It is hydrocarbon produced through various processes, such as hydrotreating, gasification, pyrolysis, and other biochemical and thermochemical technologies.

- Synthetic or electro-fuels “E-fuels” are advanced low-carbon fuels that are manufactured. They involve creating hydrogen from water via electrolysis (using renewable electricity). CO<sub>2</sub> is also usually used and is captured from waste CO<sub>2</sub> streams, either extracted from industrial plant flue gas or the atmosphere.

We will discuss the life-cycle impacts of some of these fuels in greater detail in the following sections.

### **Fuel Production**

A typical hydrocarbon-derived fuel, i.e., gasoline or diesel, will release CO<sub>2</sub> during combustion. This “tank-to-wheel” CO<sub>2</sub> is measured by regulators and sets the efficiency of the vehicle for regulatory compliance purposes. However, it is important to recognize that the fuel also has a “well-to-tank” GHG impact due to fossil fuel extraction, refining, and transportation to the fueling station.

### **Fossil-derived Fuel Production**

Most fuels used in transportation today rely upon crude oil or fossil-fuel sources. In 2020, 90% of the total transportation sector will use petroleum products (U.S. 2021a). In the U.S., crude oil is typically delivered to a refining facility via a network of pipelines stretching across the country. Crude oil contains several molecules which are pumped or mined from underground reservoirs. Upon reaching the refining facility, the crude oil is split into several hydrocarbon molecules (each with significantly more value than the base crude oil), for example, gasoline, propane, and bitumen. Then impurities are removed so that any molecules that can cause harmful emissions during combustion are removed or significantly reduced, such as hydrotreating to reduce sulfur levels. Next, the heavier liquid from distillation goes through a ‘cracking’ process where the large molecule crude oil is broken into smaller ones. The molecules can then be combined back into larger molecules of a more desirable chemical composition. For example, propane and butane can be combined into an eight-carbon molecule suitable for gasoline blending. The following process is blending, where various grades of gasoline are produced. During the blending process, bio components can be added.

There are several steps in the production process of a crude-oil-based fuel, and of course, there are associated GHG emissions with each step. Several groups are studying LCA converge on values between 80 and 101 gCO<sub>2</sub>eq/M.J. for both production and combustion of gasoline (Hill et al. 2020; Argonne National Laboratory 2020; Yang et al. 2020; Bieker 2021). For gasoline, the production share is around 17–20% of the total GHG emissions. Of these GHG emissions, 49–63% is from crude extraction and transport, 30–44% is from the refinery process, while 5–6% is from distribution (JRC 2018; CONCAWE 2017; Hill et al. 2020).

### **Biofuels**

As introduced earlier, the term biofuels cover a wide range of fuels. With multiple different fuels and production pathways, it is impossible to cover all aspects of this chapter. The push towards alternative fuels is primarily to reduce humanity’s reliance

on fossil fuels. Several Low Carbon Fuel Standards (LCFS) have been proposed to drive industries into accepting and using biofuels, but as of 2021, there is no federal-level LCFS in the U.S. (Congressional Research Service 2021a). The most prominent LCFS standard in the U.S. is in California and is administered by The California Air Resources Board (CARB). The standard's goal is to reduce the carbon intensity of California's transportation fuels by at least 20% by 2030. A credit system is used to measure compliance. For fuels with a carbon intensity (CI) below a target, a credit is generated. A deficit is generated for those with a CI score above the target. Credits can be saved or traded for future compliance. Life-cycle analysis is a critical part of understanding a fuel's actual CI score.

For spark-ignition gasoline engines, the most appropriate biofuel to discuss is ethanol. Most ethanol in the U.S. is produced from starch-based crops by dry-or-wet-mill processing. Dry milling grinds corn into flour and ferments it into ethanol. Wet-milling plants produce corn sweeteners along with ethanol. In the U.S., most ethanol production occurs in the Midwest due to the concentration of corn production sites (U.S. EPA 2020). However, Brazil relies heavily on ethanol for transportation. Many vehicles run on 100% hydrous ethanol fuel and must contain 25% anhydrous ethanol at a minimum. The primary difference between the U.S. and Brazil (the two biggest ethanol fuel producers) is that Brazil produces ethanol from sugarcane rather than corn. Sugarcane-based ethanol has a far greater energy yield and thus requires lower operating costs and critically has a far lower GHG footprint associated with the "well-to-tank" phase.

The primary benefit of fuel like ethanol is the negative biogenic CO<sub>2</sub> emissions. These are emissions absorbed from the atmosphere as the crop grows. The overall emissions associated with ethanol are between 25 and 50% lower than fossil-derived gasoline, as shown in Fig. 6.11. The net WTW emissions are the PTW emissions plus the negative biogenic CO<sub>2</sub> emissions. LUC (land-use change) or ILUCN (indirect-use change) relates to the carbon dioxide penalty associated with repurposing land to grow crops specifically for biofuels production. A controversial part of LCA for fuels is the GHG emissions due to ILUC. There is much discussion about the ILUC penalty for various fuels and how to estimate this GHG emission penalty (Yeh 2016). A valid limitation to the total ethanol production in the U.S. is the required land space to retain our current corn crop yield for nutritional value. Interestingly no automotive LCA study found discusses LUC penalties for repurposing land for solar farms and battery factories. This is despite evidence that LUC should be a consideration for future renewable electrical grids (Ven et al. 2021).

### **Biodiesel and Renewable Diesel**

Biodiesel and renewable diesel benefits are like ethanol, where biogenic CO<sub>2</sub> can offset combustion product emissions. Biodiesel is also called fatty acid methyl ester (FAME); it is created through transesterification. This process purifies the fats and oils before being blended with crude-oil-derived diesel in a ratio of 5–20%. Renewable diesel is sometimes also called hydrotreated vegetable oil or HVO. It is produced by hydrotreating hydrogenated triglycerides (fats), removing metals and compounds containing oxygen or nitrogen. Renewable diesel can be used in 100% concentration.

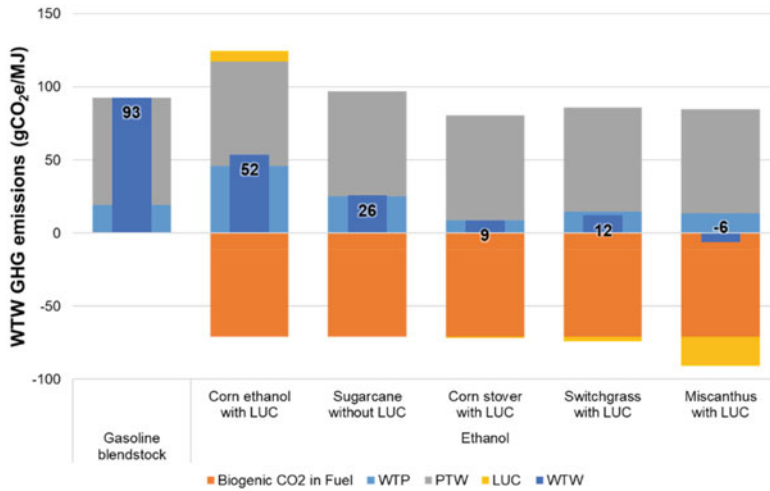


**Fig. 6.11** Well/Field-to-Wheel emissions for gasoline and five ethanol-produced fuels. PTW (Pump-to-Wheel), Biogenic CO<sub>2</sub> (absorbed by crop from the atmosphere), LUC (Land Use Change), WTP (Well-to-Pump), WTW (Well-to Wheel) (Elgowainy and Wang 2021)

It is superior to biodiesel as it generally has a higher cetane number. The capacity to generate renewable diesel is currently low. Forty-four billion gallons (166 billion liters) of diesel are consumed in the U.S. each year, while the current U.S. capacity for renewable diesel is less than 1 billion gallons per year. Many plans are in place to increase the number of production sites. If all sites came online as intended, capacity would be 5 billion gallons per year (U.S. EPA 2021b). The life-cycle benefits of biodiesel and renewable diesel, like ethanol, are significant. Biodiesel, in theory, can reduce emissions by over 70%; however, as only 20% can be blended with fossil-derived diesel, the overall benefits are much smaller (Chen et al. 2018). Renewable diesel can reduce emissions by 50- 90%, depending on the base feedstock. Tallow feedstock offers the most significant potential reduction, while rapeseed feedstock offers the slightest reduction (Natural Resources Canada 2012).

## E-Fuel

E-fuels are a relatively new area of research in the automotive sector. Some see them as a competitor to BEV and FCV technologies as they offer the potential for near-zero carbon emissions. E-fuels are sometimes referred to as power-to-x, (PtX), power-to-liquid (PtL) and power-to-gas (PtG). PtX fuels are simply either PtL or PtG fuels. The phase of the final fuel defines whether it was a PtG process or a PtL process. For example, methane is PtX and PtG, while methanol is PtX and PtL. An example of e-fuel made sustainably is methanol, and the process diagram can be seen below in Fig. 6.12.

In this process, water is split into hydrogen and oxygen via electrolysis. The electrolysis should be from renewable electricity sources. CO<sub>2</sub> is also required for

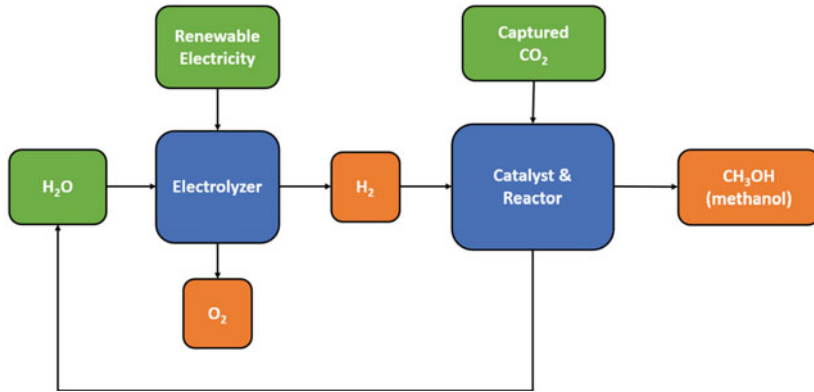


**Fig. 6.12** Process diagram showing the steps to create methanol from renewable sources

the reaction and should come from captured  $\text{CO}_2$ , either direct air capture or from waste processes such as combustion exhaust or biomass fermentation. As  $\text{CO}_2$  is a stable molecule, a large amount of heat and pressure is required to create methanol in the presence of a catalyst. One mole of  $\text{CO}_2$  and three moles of  $\text{H}_2$  are required to create one mole of methanol with one mole of water as a byproduct. The resulting methanol can be further refined into gasoline, but several additional steps are required to get to gasoline (Gitlin 2021). Thus, there is an extremely high cost and energy requirement for gasoline-like e-fuels. Automotive supplier Bosch estimates drop-in e-fuels could be as low as \$5.30/gallon by 2030 (Bosch 2020), significantly higher than regular gasoline in most U.S. states in 2021. An energy basis requires around  $5\times$  the total energy to travel one mile using an e-fuel compared to a BEV (Hill et al. 2020). Based on the high cost and poor overall efficiency, it is unlikely that fuels will replace fossil fuels or electric vehicles in the light-duty market. However, there are three potential use-cases where they may make sense:

1. Use in high-performance, low volume applications, for example, motorsport, where cost is less of a concern.
2. Use in other forms of transport where batteries are unlikely to be suitable in the foreseeable future, i.e., aviation or shipping.
3. Many renewable electricity generation methods are highly transient with environmental conditions, e.g., solar and wind, as an energy storage medium. If grid demand is lower than electricity generation, using that energy to make hydrocarbon fuels results in a high energy-density, highly usable fuel. However, it should be noted the economics of this approach are not attractive for most applications (Dahal et al. 2021).

### Life Cycle Analysis Results

BEV sales are increasing in most automotive markets (Conway et al. 2020). As of 2020, the global share of BEV sales was 3.8%, a significant increase compared to five

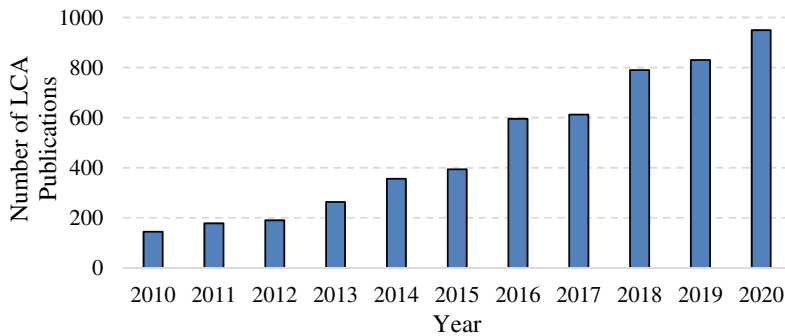


**Fig. 6.13** Number of life-cycle analysis publications per year based on three major journals

years ago, where less than 0.5% of vehicles sold globally were BEVs. Similarly, there has been a large increase in life-cycle analysis publications, as shown in Fig. 6.13. The search results for life-cycle analysis appear in *Applied Energy*, *Environmental Pollution*, and *Progress in Energy and Combustion Science* journals. The number of papers is increasing as people quantify GHG emissions from various vehicle and fuel combinations in different world regions. Many different sets of assumptions are used in LCA studies leading to a wide range of results that favor different technologies.

### 6.2.3 LCA Study Critical Review

Throughout this chapter, we have looked at the impact of various processes in a life-cycle analysis (realistically, we only touched the surface!). This section will review a recent paper at a high level to discuss their conclusions regarding different powertrain choices and some of the assumptions that contribute to the outcome. While this is an excellent example of how to perform a life-cycle analysis, there are some areas where small assumptions lead to significant changes in outcomes. Unfortunately, many peer-reviewed LCA studies are not as unbiased as this one.

#### 2021—ICCT Report

A recent, comprehensive study by ICCT (Hill et al. 2020) looked at several vehicle/powertrain/fuel combinations in different markets for a 2021 and 2030 scenario, namely, USA, Europe, China, and India, in 2019. These four markets were responsible for 70% of the total global light-duty vehicle sales (Conway et al. 2020). They considered fossil fuels, biofuels, hydrogen, e-fuels, and electricity for gasoline, diesel, natural gas, FCV, PHEV, and BEVs. Representative vehicles from each market were selected.

The study showed that in almost all scenarios, BEVs produce the lowest lifetime GHG emissions. ICE-only vehicles had similar emissions to FCVs if hydrogen is produced from coal. At the same time, PHEVs were generally better than FCV if

the hydrogen was produced from steam-reformed natural gas. Although the study does a thorough job of critically assessing all areas of current and future LCA in different markets, however, the assumptions used appear to favor a BEV outcome, for example:

- A 100% renewable electricity case was presented as a potential future option in all markets. However, a 100% biofuel scenario was not considered viable due to challenges with scaling; the study assumed that the 10% ethanol mix in fuel will not change through 2047. While there is little debate that 100% biofuel adoption is near impossible, as more people transition towards a full BEV fleet, the remaining ICE vehicles may use a higher percentage of biofuel without affecting the total biofuel requirements. Furthermore, several arguments can be made against a 100% renewable electricity scenario. A notable exception to this case would be a driver who has personal solar panels and always charges at home.
- ICE vehicle and fuel production efficiency show slight improvement between 2021 and 2030. However, the study states that manufacturers will meet 2030 fleet targets through increasing BEV and PHEV sales rather than improved ICE technologies. This ICCT study cites another ICCT report to justify this claim (Mock and Diaz 2021). Oddly, the cited report suggests a 32% fuel economy improvement moving from ICE to full hybrids by 2030. Regardless a forward-looking study attempting to determine the best engineering approach should focus on technology improvement rather than political strategies.
- The average electricity mix is used rather than the marginal electricity mix.
- E-fuels were not considered viable due to the high energy demands required to make them. However, it would be highly desirable to show the GHG potential despite this caveat.
- For U.S. biofuel-gasoline (corn-ethanol) cases, a well-to-wheel CI of 76 gCO<sub>2</sub>-eq/M.J. was used with an ILUC value of 26 gCO<sub>2</sub>eq/M.J. based on a 2010 EPA report. Since these values have been disputed, EPA has suggested more research into ILUC values (Gray and Gustafson 2016; Mueller 2016). The GREET® model assumes around 7 gCO<sub>2</sub>eq/M.J. for wet-milled corn feedstock ethanol produced in the U.S. (Argonne National Laboratory 2020a).
- Several scenarios were not presented, which would have shown that electrified ICE vehicles emit few emissions. No results were shown for biofuel PHEVs in any market. No PHEV scenarios were shown in India, presumably because there were no PHEVs available for sale in India at the time of the report. Non-plug-in hybrid vehicles were shown to offer a 20% GHG benefit in the European case, but no hybrid data was shown for other markets.

If all these challenges were considered, ICE-powered vehicles (including hybrids) might likely show lower overall GHG emissions in some markets. However, BEVs would likely continue to be superior in most markets. Critically, however, it would not suggest that BEVs are a *silver bullet* technology for all markets. Instead, different strategies would be taken by different regulators to best reduce emissions in each market. For example, data from the report has been re-plotted below in Fig. 6.14. In this figure, two additional cases have been added. An HEV has been added for the

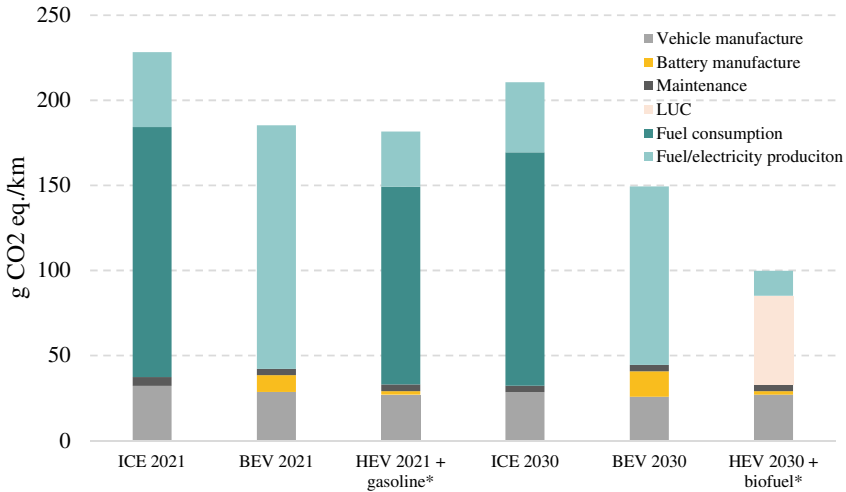


**Fig. 6.14** Future potential powertrain scenarios for the Indian market, modified from Bieker (2021) to include two new scenarios denoted by (\*)

2021 case (HEV 2021 + gasoline\*) using data from Mock and Diaz (2021) which suggests an HEV produces 21% fewer emissions in the tank-to-wheel phase vs. an ICE-only vehicle. A 2030 HEV was also added where tank-to-wheel emissions are 31% lower. The vehicle also operates on 100% molasses-based biofuel (HEV 2030 + biofuel\*) using original data. Adding in the two new datasets changes the conclusions that can be made from the study. From the original study, the conclusion would be to rapidly adopt BEV technologies and ignore improvements to HEV and ICE. A BEV push will require a significant infrastructure change. However, a move to hybrids would lower overall emissions and arguably be achievable in a shorter timeframe. A future speculative scenario that considers 100% biofuel yields significant reductions. Of course, the 100% biofuel situation is unlikely at a large scale, but it can help frame future questions engineers and regulators should be asking.

### 6.2.4 A Short Word on Regulations

Life cycle analysis regulations for transportation are currently aspirational. It is doubtful that there will be comprehensive regulations for cradle-to-grave emissions in the near term. The complexity of defining assumptions for all the cradle-to-grave processes for all types of powertrain/vehicle/fuel combinations is sizeable. Although ISO standards (14044:2006) govern life cycle assessment, these were published in 2006 and are not specifically related to the rapidly changing automotive sector. Many researchers have proposed assessment frameworks, yet there is no homogenous agreement on assumptions and methodology for LCA studies covering the entire



life (Kannangara et al. 2021). To highlight the challenge, a recent review of current global policy and regulation efforts yields the following conclusion:

Despite the prevalence of policies that encourage life cycle thinking, no lifecycle-based emissions policies for vehicles were found during this review. (Kendall 2018)

Efforts in Europe to consider LCA regulations are increasing. The E.U. Commission has set a target that by no later than 2023, they will evaluate the possibility of developing a standard Union methodology for the assessment and consistent data reporting of the total life-cycle CO<sub>2</sub> emissions of passenger cars and light commercial vehicles in the Union market ((EU)2019/631 2019).

Encouragingly similar industries have begun to implement LCA. The Civil Aviation Organization recently established the Carbon Offsetting and Reduction Scheme for International Aviation (CORSIA) to help reduce aviation GHG emissions. A methodology agreed upon by 193 ICAO members states to evaluate the life cycle GHG emissions of sustainable aviation fuels (SAFs). While this does not directly impact the automotive sector, it does suggest that policy implementation is possible. The full methodology is under embargo until August 2023, but a paper outlining some of the key points behind CORSIA is available (Prussi et al. 2021).

Despite a lack of proper evaluation and regulation behind the cradle-to-grave analysis, many governments are pushing to replace ICE vehicles with BEV and FCV alternatives. While this approach looks to be correct in the long term, other strategies which can reduce our carbon footprint in the short term are overlooked by the current definition of emissions. According to the analysis done by the International Council on Clean Transportation (ICCT), the 17 governments which have announced ICE bans account for 13% of the global light-duty vehicle sales (Wapperlhorst and Cui 2020). A list of these countries can be found in Table 6.2.

Refreshingly there are BEV manufacturers performing LCA studies to educate the public that their vehicles still have a carbon footprint. For example, in an article entitled “*Being transparent about sustainability*,” BEV manufacturer Polestar shows a significant footprint associated with their electric vehicles but that they are superior to ICE vehicles. However, it should be noted that the study did not consider hybrids (Roynes and Bolin 2021).

**Table 6.2** Target bans on the ICE were announced in various regions of the world

Year	Region
2025	Norway
2030	UK: Pure ICEs Iceland, Ireland, Israel, Netherlands, Sweden, Hainan (China)
2035	U.K.: Hybrids California (U.S.), Columbia
2040	Canada, Egypt, France, Spain, Sri Lanka, Taiwan

## 6.3 Summary and Recommendations

This chapter has reviewed several areas related to life-cycle analysis as they pertain to the transportation sector. However, many areas have not been covered in this short chapter. It covers areas relevant to LCA, such as material choices, lightweight materials, and pollutant emissions, among others. Unfortunately, these were beyond the scope of this chapter as an introduction to the topic.

The literature reviewed as part of writing this chapter highlighted several key findings:

1. There is an extremely high interest in LCA throughout the automotive industry, growing year on year.
2. This interest comes from both proponents of BEV technology as well as advocates of ICE technology.
3. The assumptions made and the methodology chosen can drastically affect the outcome of the study.
4. No globally recognized set of standards for LCA exist that could be used for regulatory purposes. Without a set of standards or a framework, the result is a wide range of LCA study conclusions.
5. Several studies appear to show that BEVs are the superior powertrain choice for the lowest GHG emissions. However, several studies reach a different conclusion, mainly that BEVs are not *always* the best choice.
6. Many studies which show BEVs to be the best choice do not fully consider the future potential of the ICE or hybrid technology.
7. Most studies use the average or total electricity mix and do not consider the impacts of marginal electrical grids.
8. Until recently, there was a large range of battery production carbon intensities in literature. More recently, the range has reduced, but it is still wide enough that the difference in starting GHG emissions from the high to the low case can be as much as 10 tons CO<sub>2</sub>-eq.
9. Biofuels offer huge potential to reduce GHG emissions on a small scale, but scaling biofuels remains a challenge globally.
10. E-fuels, including pure H<sub>2</sub>, also increase research but have several barriers to widespread adoption, mainly cost and total energy requirements.
11. FCVs do not appear to be attractive on a life cycle GHG emissions basis for light-duty vehicles.

### 6.3.1 Recommendations for LCA Study Reviewers

Proposing a framework for LCA is beyond the scope of this discussion. However, several suggestions are presented here to help LCA reviewers determine whether any bias (intentional or otherwise) exists in the analysis:

1. *Check that all assumptions are clearly stated.* This is easily the most important piece of advice for anyone reviewing an LCA study.
2. Check those assumptions are fair to both ICE and non-ICE powertrains. For example, are BEV cases only compared to gasoline or diesel vehicles? Or are they also compared to different types of hybrid? Is there a battery replacement considered just because the battery is beyond warranty?
3. Check whether the electrical grid being used is average or marginal.
4. Check the LCA author's affiliation. While an affiliation does not imply the study will be biased, it does help the reviewer consider which assumptions to interrogate.
5. Check whether a range of results is presented, which consider different assumptions that may be used.
6. Check that the study uses real-world fuel economy and electric vehicle efficiency values from independent sources, not type-approval values, which can be far lower than real-world observations.

### 6.3.2 A Final Thought

Society will continue to transition to an increasingly electrified fleet, as this is necessary to reduce our emissions footprint from transportation. However, it will take many decades before 100% of transportation, not including any form of a combustion engine; it is not clear if we will ever reach this goal. Therefore, an array of powertrain choices will be required for the foreseeable future. Only by performing proper LCA studies can we best assess each region's needs, economic position, and available resources to promote the right powertrain and fuel/electricity choices. A blanket ban on the internal combustion engine, just because it has a tailpipe, does not result in the lowest cumulative GHG emissions. Instead, it only starves the ICE of research needed to improve it with the net result of lower efficiency and higher emissions in the future.

## References

- Accardo A et al (2021) Life cycle assessment of an NMC battery for application to electric light-duty commercial vehicles and comparison with a sodium-nickel-chloride battery. *Appl Sci* 11(3). <https://doi.org/10.3390/app11031160>
- Ambrose H (2020) The second-life of used EV batteries. Union of Concerned Scientists, 27 May 2020. Available <https://blog.ucsusa.org/hanjiro-ambrose/the-second-life-of-used-ev-batteries/>. Accessed 10 Sept 2021
- Andersson Ö, Börjesson P (2021) The greenhouse gas emissions of an electrified vehicle combined with renewable fuels: life cycle assessment and policy implications. *Appl Energy* 209(116621)
- Argonne National Laboratory (2020a) Energy Systems - GREET® Model, 9 October 2020. Available: <https://greet.es.anl.gov/>. Accessed 15 Sept 2021

- Argonne National Laboratory (2020b) GREET: the greenhouse gases, regulated emissions, and energy use in technologies model, May 2020. Available: [https://www.anl.gov/sites/www/files/2020-10/GREET\\_Impact\\_Sheet.pdf](https://www.anl.gov/sites/www/files/2020-10/GREET_Impact_Sheet.pdf). Accessed 12 Sept 2021
- Argonne National Laboratory (2020c) The greenhouse gases, regulated emissions, and Energy use in Transportation Model (GREET) (Version 2020). Retrieved from <https://greet.es.anl.gov/index.php>
- Baldwin R (2020) 2021 Toyota Mirai makes a stylish play for a hydrogen future. Car and Driver, 16 December 2020. Available: <https://www.caranddriver.com/reviews/a34979927/2021-toyota-mirai-drive/>. Accessed 10 Sept 2021
- Bieker G (2021) A global comparison of the life-cycle greenhouse gas emissions of combustion engine and electric passenger cars. International Council for Clean Transportation. [https://theicct.org/sites/default/files/publications/Global-LCA-passenger-cars-jul2021\\_0.pdf](https://theicct.org/sites/default/files/publications/Global-LCA-passenger-cars-jul2021_0.pdf)
- Bosch (2020) Jumping to conclusion. Bosch, 05 July 2020. Available: <https://www.bosch.com/stories/denners-view-synthetic-fuels-and-electromobility/>. Accessed 10 Sept 2021
- Bruckner T et al (2014) 2014: Energy systems. In: Climate change 2014: Mitigation of climate change. Contribution of working group III. In: Fifth assessment report of the intergovernmental panel on climate change. Cambridge, UK, New York, NY, USA, Cambridge University Press, pp 511–597
- Burton T et al (2021) A data-driven greenhouse gas emission rate analysis for vehicle comparisons. SAE Int J Electr Vehicles JEV-2021-0039
- California ISO. Available <http://www.caiso.com/Pages/default.aspx>. Accessed 01 Oct 2020
- Chen R et al (2018) Life cycle energy and greenhouse gas emission effects of biodiesel in the United States with induced land use change impacts. *Bioresour Technol* 251:249–258
- CONCAWE (2017) Estimating the marginal CO<sub>2</sub> intensity of EU refinery products. In: CONCAWE, Brussels
- Congressional Research Service (2021a) Vehicle fuel economy and greenhouse gas standards. CRS
- Congressional Research Service (2021b) A low carbon fuel standard: in brief. CRS, Washington D.C.
- Conway G et al (2021) A review of current and future powertrain technologies and trends in 2020. *Transp Eng* 5(100080). <https://doi.org/10.1016/j.treng.2021.100080>
- Cook J et al (2013) Quantifying the consensus on anthropogenic global warming in the scientific literature. *Environ Res Lett* 8(2). <https://doi.org/10.1088/1748-9326/8/2/024024>
- Cook J et al (2016) Consensus on consensus: a synthesis of consensus estimates on human-caused global warming. *Environ Res Lett* 11(4). <https://doi.org/10.1088/1748-9326/11/4/048002>
- Dahal K et al (2021) Techno-economic review of alternative fuels and propulsion systems for the aviation sector. *Renew Sustain Energy Rev* 111564. <https://doi.org/10.1016/j.rser.2021.111564>
- Dai Q et al (2019) Life cycle analysis of lithium-ion batteries for automotive applications. *Batteries* 5(2):48. <https://doi.org/10.3390/batteries5020048>
- Elgowainy A, Wang M (2021) Transportation fuels lifecycle Greenhouse Gas (GHG) emissions: methods and challenges. Argonne National Laboratory, Presentation NASEM
- Emilsson E, Dahllöf L (2019) Status 2019 on energy use, CO<sub>2</sub> emissions, use of metals, products environmental footprint, and recycling. IVL Swedish Environmental Research Institute, Stockholm
- Energy Facts Norway (2021) Electricity production, energy facts Norway, 11 May 2021. Available: <https://energifaktanorge.no/en/norsk-energiforsyning/kraftproduksjon>. Accessed 13 Sept 2021
- Engel H, Hertzke P, Siccardo G (2019) Second-life EV batteries: the newest value pool in energy storage. McKinsey & Company
- (EU)2019/631, Regulation, Regulation (EU) 2019/631 of the European Parliament and of the Council of 17 April 2019 (EU)2019/631, Regulation, Regulation (EU) 2019/631 of the European Parliament and of the Council of 17 April 2019 setting CO<sub>2</sub> emission performance standards for new passenger cars and for new light commercial vehicles. EU Parliament, Brussels@
- Ewing M et al (2020) Hydrogen on the path to net-zero emissions: costs and climate benefits. PEMBINA institute

- Garcia R, Freire F (2016) Marginal life-cycle greenhouse gas emissions of electricity generation in Portugal and implications for electric vehicles. *Resources* 5:1–15. <https://doi.org/10.3390/resources5040041>
- Gebler M et al (2020) Life cycle assessment of an automotive factory: identifying challenges for the decarbonization of automotive production—a case study. *Clean Prod* 270. <https://doi.org/10.1016/j.jclepro.2020.122330>
- Gitlin J (2021) Porsche and Siemens energy break ground on low-carbon e-fuel plant in Chile. *ars technica*, 11 September 2021. Available: <https://arstechnica.com/cars/2021/09/porsches-new-synthetic-gasoline-may-fuel-formula-1-races/>. Accessed 20 Sept 2021
- Gray CB, Gustafson A (2016) Request for correction of information concerning the U.S. Environmental Protection Agency’s lifecycle analysis of ethanol and gasoline under the renewable fuel standard. The energy future coalition, urban air initiative and Governor’s biofuels coalition, Washington D.C.
- Harlow JE et al (2019) A wide range of testing results on an excellent lithium-ion chemistry to be used as benchmarks for new battery technologies. *J Electrochem Soc* 166(13), no. A301. <https://doi.org/10.1149/2.0981913jes>
- Hill N et al (2020) Determining the environmental impacts of conventional and alternatively fuelled vehicles through LCA. European Commission, Brussels
- International Energy Agency (2020) Data and statistics 2020. Available: <https://www.iea.org/subscribe-to-data-services/world-energy-balances-and-statistics>. Accessed 20 Sept 2021
- International Energy Agency (2021) Electricity market report. IEA, July 2021
- JRC (2018) Supporting information to the characterisation factors of recommended EF life cycle impact assessment method. JRC
- Kannangara M, Bensebaa F, Vasudev M (2021) An adaptable life cycle greenhouse gas emissions assessment framework for electric, hybrid, fuel cell and conventional vehicles: Effect of electricity mix, mileage, battery capacity and battery chemistry in the context of Canada. *J Clean Prod* 317. <https://doi.org/10.1016/j.jclepro.2021.128394>
- Karuppanan Gopalraj S, Kärki T (2020) A review on the recycling of waste carbon fibre/glass fibre-reinforced composites: fibre recovery, properties and life-cycle analysis. *Sci Nat Appl Sci* 433, no. 2(3). <https://doi.org/10.1007/s42452-020-2195-4>
- Kendall A et al (2018) Program for vehicle regulatory reform: assessing life cycle-based greenhouse gas standards. UC Davis institute of Transportation Studies, California
- Kumagai J (2021) Lithium-ion battery recycling finally takes off in North America and Europe. *IEEE Spectrum*, 05 January 2021. Available: <https://spectrum.ieee.org/lithiumion-battery-recycling-finally-takes-off-in-north-america-and-europe>. Accessed 10 Sept 2021
- Lawrence R (1981) Fuel economy measurement carbon balance method. EPA-420-D-81-103
- Ma H et al (2012) A new comparison between the life cycle greenhouse gas emissions of battery electric vehicles and internal combustion vehicles. *Energy Policy* 44:160–173. <https://doi.org/10.1016/j.enpol.2012.01.034>
- Mayyas A et al (2017) Vehicle’s lightweight design vs. electrification from life cycle assessment perspective. *J Clean Prod* 167:687–701. <https://doi.org/10.1016/j.jclepro.2017.08.145>
- Mock P, Diaz S (2021) Pathways to decarbonization: the European passenger car market in the years 2021–2035. ICCT, Washington D.C.
- Mueller S (2016) Request for correction of information concerning the U.S. Environmental Protection Agency’s lifecycle analysis of ethanol and gasoline under the renewable fuel standard. The University of Illinois at Chicago, Chicago
- Myhre G et al (2013) Anthropogenic and natural radiative forcing (Chap. 8). In: *Climate change 2013: the physical science basis: contribution of the working group I to the fifth assessment for report of the intergovernmental panel on climate change*, pp 659–740
- Natural Resources Canada (2012) Study of hydrogenation derived renewable diesel as a renewable fuel option in North America. Natural Resources Ottawa, ON, Canada

- Noori M et al (2015) Electric vehicle cost, emissions, and water footprint in the United States: development of a regional optimization model. *Energy* 89:610–625. <https://doi.org/10.1016/j.energy.2015.05.152>
- Onat N, Kuckukvar M, Tatari O (2015) Conventional, hybrid, plug-in hybrid or electric vehicles? State-based comparative carbon and energy footprint analysis in the United States. *Appl Energy* 150:36–49. <https://doi.org/10.1016/j.apenergy.2015.04.001>
- Pillot C (2015) The rechargeable battery market and main trends 2014–2025. *Avicenne Energy*
- Prussi M et al (2021) CORSIA: the first internationally adopted approach to calculate life-cycle GHG emissions for aviation fuels. *Renew Sustain Energy Rev* 111398. <https://doi.org/10.1016/j.rser.2021.111398>
- Royne F, Bolin L (2021) Life cycle assessment 2021: carbon footprint of Polestar 2 variations. Polestar. <https://www.datocms-assets.com/11286/1630409045-polestarcarapportprintkorr11210831.pdf>
- Samaras C, Meisterling K (2008) Life cycle assessment of greenhouse gas emissions from plug-in hybrid vehicles: implications for policy. *Environ Sci Technol* 42(9):3170–3176. <https://doi.org/10.1021/es702178s>
- Slowik P, Lutsey N, Hsu CW (2020a) How technology, recycling, and policy can mitigate supply risks to the long-term transition to zero-emissions vehicles. International Council on Clean Transportation. <https://theicct.org/publications/mitigating-zevsupply-risks-dec2020>
- Slowik P, Lutsey M, Hsu CW (2020b) How technology, recycling, and policy can mitigate supply risks to the long-term transition to zero-emission vehicles. International Council on Clean Transportation. <https://theicct.org/publications/mitigating-zevsupply-risks-dec2020>
- Statistics Norway (2021) Electricity, statistics Norway, 14 September 2021. Available: <https://www.ssb.no/en/energi-og-industri/energi/statistikk/elektrisitet>. Accessed 15 Sept 2020
- Statista (2021) Share of the global lithium-ion battery manufacturing capacity in 2020 with a forecast for 2025, by country, 14 July 2021. Available: <https://www.statista.com/statistics/1249871/share-of-the-global-lithium-ion-battery-manufacturing-capacity-by-country/>. Accessed 17 Sept 2021
- The International Council on Clean Transportation (2018) Effects of battery manufacturing on electric vehicle life-cycle greenhouse gas emissions. ICCT, Washington D.C.
- U.S. Department of Energy (2020) Alternative fuels data center, U.D. DOE, 2020. Available: [https://afdc.energy.gov/fuels/ethanol\\_production.html](https://afdc.energy.gov/fuels/ethanol_production.html). Accessed 21 Sept 2021
- U.S. Department of Energy (2021) Fuel economy. Available: <https://www.fueleconomy.gov/feg/>. Accessed 15 Sept 2021
- U.S. Energy Information Administration (2021a) Monthly energy review: tables 2.5, 3.8c, and 10.2b. US EIA
- U.S. Energy Information Administration (2021b) U.S. renewable diesel capacity could increase due to announced and developing projects, EIA, 29 July 2021. Available: <https://www.eia.gov/todayinenergy/detail.php?id=48916>. Accessed 10 Sept 2021
- U.S. EPA (2012) 40 CFR 600.114-12—vehicle-specific 5-cycle fuel economy and carbon-related exhaust emission calculations. 76 FR 39538, July 6, 2011, as amended at 76 FR 57379, Sept. 15, 2011,” EPA, p 919
- U.S. EPA (2021a) Fast Facts U.S. Transportation sector greenhouse gas emissions: 1990–2019. Office of Transportation and Air Quality AEPA-420-F-21-049
- U.S. EPA (2021b) The 2020 EPA Automotive trends report greenhouse gas emissions, fuel economy, and technology, Since 1975. EPA
- U.S. EPA (2021c) Used lithium-ion batteries. U.S. EPA. Available: <https://www.epa.gov/recycle/used-lithium-ion-batteries>. Accessed 05 Sept 2021
- Van de Ven DJ et al (2021) The potential land requirements and related land use change emissions of solar energy. *Sci Rep* 11 2907. <https://doi.org/10.1038/s41598-021-82042-5>
- Vishwanathan G. (2020) Decarbonization of MD-HD vehicles with propane. Propane Energy Research Council, Washington D.C.

- Wapperlhorst S, Cui H (2020) Growing momentum: global overview of government targets for phasing out sales of new internal combustion engine vehicles. ICCT, Washington D.C.
- Yang M et al (2020) Cost and life-cycle greenhouse gas implications of integrating biogas upgrading and carbon capture technologies in Cellulosic biorefineries. *Environ Sci Technol* 54:12810–12819
- Yang L et al (2021) Life cycle environmental assessment of electric and internal combustion engine vehicles in China. *Clean Prod* 285. <https://doi.org/10.1016/j.jclepro.2020.124899>
- Yeh S et al (2016) A review of low carbon fuel policies: principles, program status and future directions. *Energy Policy* 97
- Zhang L et al (2021) Light duty vehicle life cycle analysis. SAE 2021-01-0789. <https://doi.org/10.4271/2021-01-0789>
- Zhou GH et al (2013) Development of electric vehicles use in China: a study from perspective of life-cycle energy consumption and greenhouse gas emissions. *Energy Policy* 59:875–884

# Chapter 7

## Pre-chamber Combustors: An Enabling Technology for High Efficiency, Low CO<sub>2</sub> Engine Operation



Michael Bunce , Hugh Blaxill, Nathan Peters, Sai Krishna Pothuraju Subramanyam, Adrian Cooper, and Mike Bassett

**Abstract** In spark ignited engines, the efficiency of the engine is strongly influenced by the quality and duration of the combustion process as initiated by the ignition system. Jet Ignition is a concept initiated by pilot combustion in a pre-chamber connected to the main cylinder, where pilot combustion products are introduced as reactive high velocity jets. These jets initiate auto-ignition of the main fuel-air mixture, resulting in multiple distributed points of ignition. In passive jet ignition systems, this distribution leads to rapid burning, helping to mitigate knock likelihood. In active jet ignition systems, which contain auxiliary fuelling in the pre-chamber, the increased ignition energy results in the ability to operate the engine with air dilution beyond the capabilities of typical ignition systems, enabling large increases in compression ratio. Active jet ignition engines have demonstrated increases in peak and drive-cycle average thermal efficiencies of 15–25% over modern engines, representing a step change in efficiency. Pre-chamber combustors are a well-research technology, with a lineage dating back over 100 years. A wealth of research has established pre-chamber combustors as an enabling technology for high efficiency engine operation. This study will examine recent applications and benefits of pre-chambers, including knock reduction in high specific output downsized engines and lean limit extension in high efficiency engines. Fundamental barriers to pre-chamber engine adoption will be discussed: pre-chamber geometry optimization that spans the full engine map, in-pre-chamber mixture preparation, low load and idle stability, and ensuring sufficient spark retard for catalyst light-off. Pre-chamber engines can also be ideal platforms for future fuels, including low carbon fuels such as hydrogen that have highly specific operating requirements. Recent work by the authors in this area is presented. Finally, the role of the pre-chamber engine in future transport and its potential for facilitating significant de-carbonization of the sector is discussed.

**Keywords** Pre-chamber · Ignition · Lean combustion

---

M. Bunce (✉) · H. Blaxill · N. Peters · S. K. P. Subramanyam  
MAHLE Powertrain LLC, Plymouth, MI, USA  
e-mail: [mike.bunce@mahle.com](mailto:mike.bunce@mahle.com)

A. Cooper · M. Bassett  
MAHLE Powertrain Ltd., Northampton, UK



## 7.1 Introduction

The perpetual desire to conserve fuel is being coupled with an increasing awareness of the deleterious environmental impact of tailpipe emissions from the transportation sector. In response, increasingly stringent global legislation of greenhouse gas emissions will require a step change in internal combustion engine (ICE) efficiency. A method that has been explored to accomplish this goal is dilute gasoline combustion (Bunce and Blaxill 2016; Quader 1974). A major limitation in developing dilute combustion systems is the less favourable ignition quality of the mixture. This has necessitated the development of higher energy ignition sources (Ward 2001). A pre-chamber combustor is one such technology, having been researched extensively (Robinet et al. 1999; Murase et al. 1994; Toulson et al. 2010). Pre-chamber combustion concepts have demonstrated the potential for stable main chamber combustion at high levels of dilution (Attard et al. 2010).

Despite the extensive research and application history of pre-chambers, practical barriers to modern implementation of these systems in passenger car engines remain. An historic key challenge for pre-chambers has been ensuring acceptable low load, idle, and cold start performance (Cao and Li 2012). The stringency of tailpipe emissions standards has made acceptable performance at the latter conditions particularly critical. Prior research has suggested that identifying a common pre-chamber geometry that can encompass acceptable low load operation and high efficiency part load operation is a challenge.

This section examines the fundamental mechanisms that dictate pre-chamber jet ignition and determine the extent of the efficiency benefits that can be realized. With this understanding established, this section also details the considerations needed to address some of the key challenges to practical implementation of pre-chamber combustion systems in multi-cylinder production-intent engines.

### 7.1.1 Dilute SI Combustion

Dilute combustion in spark ignited (SI) engines has been proven to be one of the most effective means by which to produce substantial increases in thermal efficiency. There are typically two methods of dilution explored in SI engines: lean operation (with air dilution) and dilution through EGR. While homogeneous lean combustion necessitates the use of lean aftertreatment, the use of EGR allows the engine to maintain stoichiometric operation, thereby enabling the use of a conventional 3-way catalyst for emissions control. The key trade-off to reduced aftertreatment complexity is the reduced thermal efficiency potential of EGR compared to lean air dilution, all else being equal, resulting from the differences in the ratios of the specific heat capacities (Tang et al. 2013; Caton 2013).

Traditional centrally mounted spark plugs are typically only capable of ensuring stable dilute operation at lambda values of less than 1.6 or EGR values less than

25–30%. This limitation is manifested as misfires due to poor kernel formation and partial burning due to arrested flame development (Caton 2013). The application of pre-chamber jet ignition distributes ignition energy throughout the combustion chamber, with flame fronts that propagate from the resulting ignition points needing to traverse less physical space and individually consume less fuel in order for the combustion process to achieve completion. Active pre-chambers, those that provide an auxiliary fuelling source in the pre-chamber, enabling direct control over air-fuel ratios in both pre- and main chambers, have proven effective at expanding the dilution tolerance, particularly that of air dilution, in SI engines. The following section provides an abridged history of pre-chamber usage in SI engines.

### 7.1.2 History of Pre-chamber Combustion Systems

A pre-chamber is a chamber proportionally smaller than, and directly connected to, the main combustion chamber. Its historical uses have spanned low pressure fuel delivery, spark plug protection, and use directly as an ignition system.

Its use as an ignition system was first applied to SI engines through Sir Harry Ricardo's patent for the Ricardo Dolphin engine, on which he began development in 1903 (University of Cambridge Department of Engineering 2000). The most prominent automotive production applications of the pre-chamber concept in the latter half of the twentieth century were produced by Honda (the Compound Vortex Controlled Combustion, or CVCC, engine) (Date and Yagi 1974), Volkswagen, and Toyota (Noguchi et al. 1976). Images of the Ricardo Dolphin and Honda CVCC pre-chambers are shown in Fig. 7.1. These pre-chamber concepts initiate the combustion process in the pre-chamber, with the products of this combustion process then transferring to the main chamber and causing those contents to ignite.

The pre-chambers described above contain the spark plug and an auxiliary fuelling source, allowing for a de-coupling of the chamber air-fuel ratios. These systems

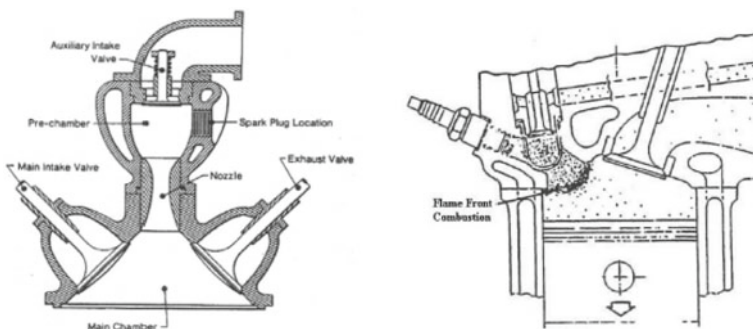


**Fig. 7.1** Two notable pre-chamber engine examples: Ricardo Dolphin (University of Cambridge Department of Engineering 2000) (left), and Honda CVCC (Date and Yagi 1974) (right)

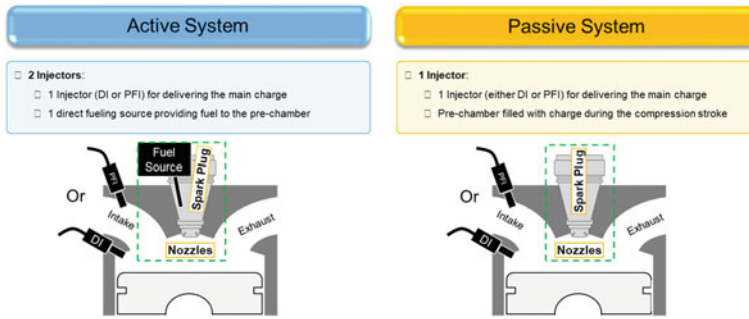


Fig. 7.2 Generalized active and passive pre-chamber configurations

are known as active pre-chambers. Some pre-chamber concepts developed subsequent to the Dolphin removed the separate pre-chamber fuelling feature (Noguchi et al. 1976; Adams 1979). In these designs, known as passive pre-chambers, fuel is injected conventionally into the main chamber and piston motion during the compression stroke forces a volume of this fuel-air mixture proportional to the pre-chamber volume to enter the pre-chamber. This type of design reduces hardware, controls, and packaging complexity, and provides a more stable combustion event compared to a conventional SI engine, though enleanment capability is limited when compared against an active pre-chamber. A comprehensive history of pre-chamber concepts is provided in Toulson et al. (2010). Generalized images of active and passive pre-chamber configurations are depicted in Fig. 7.2.

### 7.1.3 Jet Ignition

A chemical kinetically-controlled pre-chamber-based combustion mode known as jet ignition was first researched by Nicolai Semenov in the 1950s (Dainton 1986), followed shortly by pioneering research by Lev Gussak. While it retains the pre-chamber combustor, jet ignition differs primarily from its antecedent by the way combustion translates from the pre-chamber to the main chamber. Torch igniters, as exemplified by the Ricardo Dolphin and Honda CVCC, are designed to promote continuous flame front propagation from pre-chamber to main chamber via a relatively large diameter throat that separates the two chambers. With jet ignition systems the relatively large diameter throat is replaced by a nozzle containing one or more small orifices with diameters smaller than the flame quenching diameter. With this design the pre-chamber flame front is quenched and combustion is discontinuous as it translates between the chambers (Gussak et al. 1979). The primary advantage of jet ignition is the ability to distribute the ignition sites in the main chamber some distance away from the orifice exit. With a multi-orifice nozzle, the result is effectively a distributed multi-point ignition system. Increased heat losses through

the nozzle can be mitigated through precise specification of pre-chamber volume, nozzle geometry, and other features.

A major resurgence in interest in jet ignition concepts occurred primarily in academia in the 1990s (Kyaw and Watson 1992). At the time, active concepts fuelled the pre-chamber exclusively with a gaseous fuel such as vaporized gasoline or hydrogen. However gaseous fuelled passenger car sales are minimal compared to sales of vehicles that use liquid gasoline blends. Therefore, in order to develop a practical jet ignition concept for passenger car applications, a liquid gasoline injection strategy, using a common fuel for both chambers, was determined to be a necessary development step for active pre-chambers. The following sections will explore fundamental and applied jet ignition research using a system developed by MAHLE Powertrain known as MAHLE Jet Ignition (MJl)®. Active and passive MJl variants are presented.

Active MJl incorporates a direct fuel injector in the pre-chamber. This enables precise control of fuel metering and spray targeting. The latter helps to minimize particulate formation during the pre-chamber combustion event. Direct fuel injection also provides the opportunity for injection late in the cycle. A fuel injection event that occurs too early can result in “over-mixing” as seen in Fig. 7.3, producing an overly dilute mixture near the spark plug, posing a risk of misfire, despite the fact that the two scenarios depicted in Fig. 7.3 have identical fuel mass quantities. A fuel injection event late in the compression stroke is therefore desired in order to ensure an ignitable mixture near the spark plug and maximize the quantity of auxiliary injected fuel that participates in the pre-chamber combustion event. The MJl pre-chamber prototype assembly is displayed in Fig. 7.4. Figure 7.5 illustrates the importance of precise control over pre-chamber fuel quantity by displaying the sensitivity of engine efficiency to minute changes in pre-chamber injected fuel quantity.

This fuel delivery innovation to the active jet ignition concept is viewed as critical for (1) successful operation with a liquid fuel, and (2) efficient, judicious use of the pre-chamber fuel in order to preserve the system efficiency. Geometric and other performance sensitivities identified and optimized through active MJl

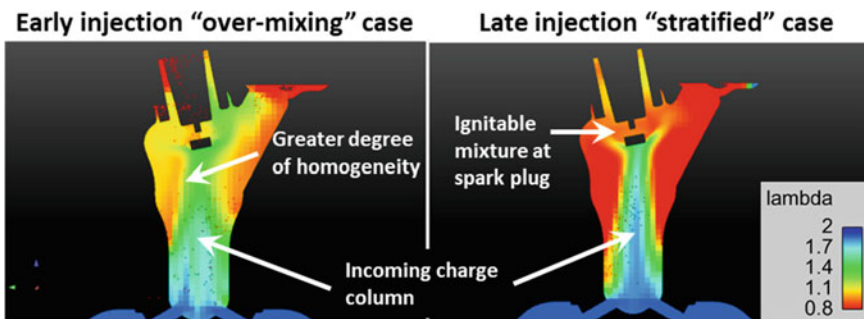


**Fig. 7.3** Mixture preparation with early (left) and late fuel injection (right) timing in the pre-chamber at time of spark with constant pre-chamber fuelling quantity

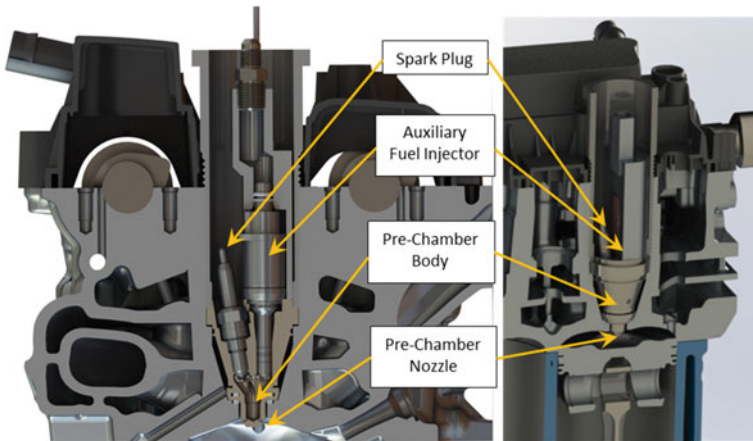


**Fig. 7.4** Cutaway of the MJI pre-chamber (left) and MJI pre-chamber assembly (right) in a typical passenger car engine

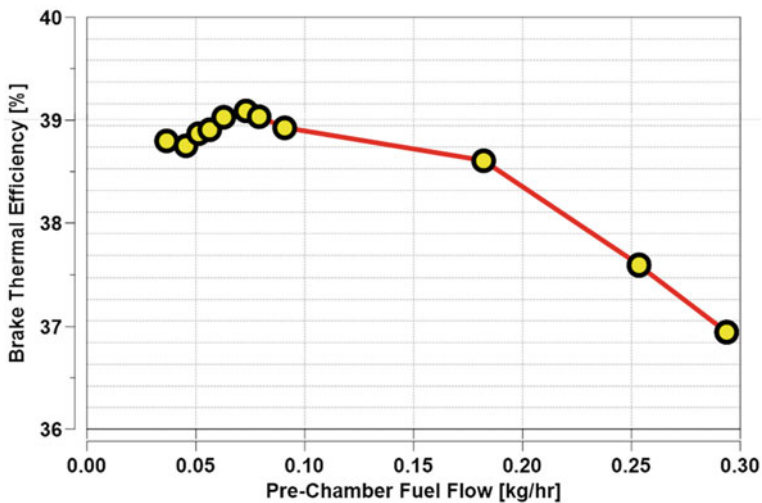


**Fig. 7.5** Brake thermal efficiency trends with pre-chamber fuel injection quantity, 1.5 L DI3, CR = 15.1, speed = 3000 rpm, BMEP = 10 bar,  $\lambda = 1.7$

research were subsequently translated to a passive MJI variant. MJI research platforms have included optical engines, single cylinders, and multi-cylinder engines, with supporting 1D and 3D analysis tools developed in parallel.

## 7.2 Fundamental Research

### 7.2.1 *Optically Accessible Engine*

High speed images acquired from an optically accessible engine qualitatively provide insight into the mechanism for main chamber ignition in jet ignition engines, regardless of dilution level or type (active or passive). Figure 7.6 illustrates jet formation and ignition for a typical active jet ignition system. The images in this figure show luminous jets, with no backlighting, emerging from the pre-chamber. No intensifying was used for these images. The false color scale indicates relative temperatures, with the white color indicative of peak flame temperatures, the red band indicative of flame front temperatures, and yellow indicative of recently burned product temperatures. The flame content in these jets is minimal. The jets subsequently create distinct ignition sites in the main chamber, visible at the leading edges of the jets, particularly in the bottom row of images. These ignition sites produce distinct flame fronts that consume the charge, eventually joining during this process. More details of this study are provided in Bunce et al. (2014).

As displayed in Fig. 7.7, average measured jet velocity correlates strongly with jet penetration prior to ignition. The higher velocity jets can penetrate farther away from the nozzle center prior to achieving conditions conducive to ignition site formation.

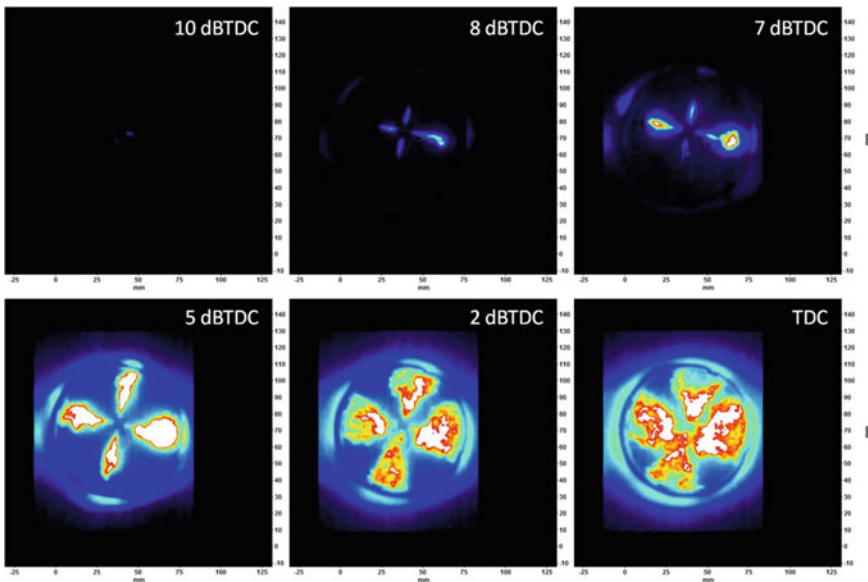
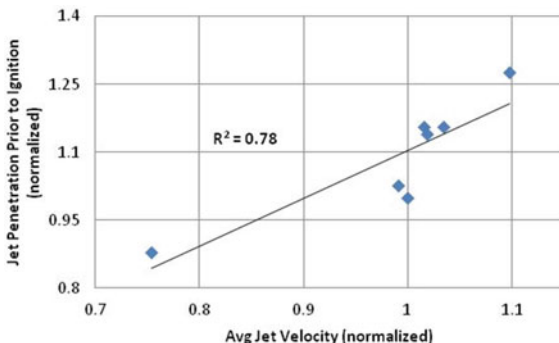


**Fig. 7.6** Chemiluminescence high speed images of the jet ignition process (Speed: 1500 rpm, gross indicated mean effective pressure: 5.5 bar,  $\lambda = 1.2$ , CR10) (Bunce et al. 2014)

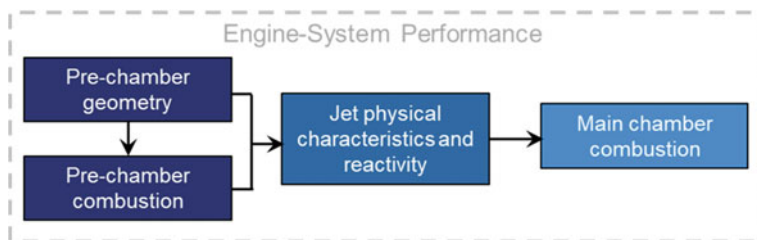
**Fig. 7.7** Jet penetration prior to ignition versus average jet velocity



### 7.2.2 Single Cylinder Engine

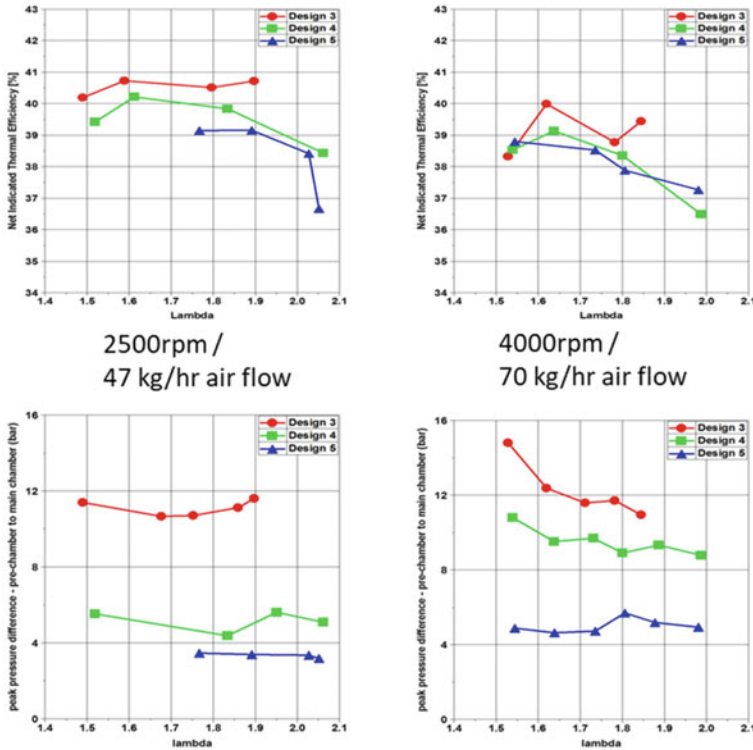
The following data is used as an example to illustrate the spectrum of jet ignition geometric sensitivities, defined here as: pre-chamber geometry—jet characteristics—engine performance. This “jet sensitivity spectrum” (Fig. 7.8) is a series of interdependencies that links in-pre-chamber mixing, pre-chamber combustion, and main chamber combustion. Detailed understanding of these mechanisms enables optimization of the entire system combustion performance.

Figure 7.9 presents trends in net thermal efficiency versus main chamber lambda ( $\lambda$ ) for two operating conditions using a single cylinder engine counterpart to the optical engine from the previous section. Three design variants (listed as 3, 4, and 5) provide nozzle orifice areas of  $1\times$ ,  $1.25\times$ , and  $2.5\times$  that of the base area. At the 2500 rpm condition, Design 3 (with the smallest orifice area) achieves a net thermal efficiency of approximately 41%, with Design 4 and Design 5 peaking at just over 40% and 39%, respectively. This trend is repeated at the 4000 rpm condition, with Design 3 peaking at 40%, and both Design 4 and Design 5 peaking at 39%. The pressure disparity between pre-chamber and main chamber during the local pressure peak encountered during the pre-chamber combustion event also scales with orifice area.



**Fig. 7.8** Graphical depiction of “jet sensitivity spectrum”





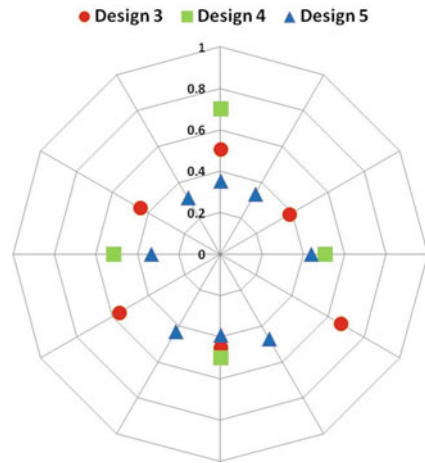
**Fig. 7.9** Net thermal efficiency and peak pre-chamber to main chamber pressure difference versus  $\lambda$ .

Single cylinder engine results indicate elevated net thermal efficiencies with designs that induce higher peak pre-chamber-to-main-chamber pressure disparities while retaining nozzle orifice diameters large enough to maintain jet reactivity in the main chamber. To explore the fundamental logic underpinning this trend, single cylinder engine data is synthesized with optical engine data, providing a more complete picture of jet effects on engine performance.

Higher velocity jets, induced by greater chamber pressure disparity, can penetrate further into the main chamber prior to creating ignition sites. This degree of penetration coupled with the ability of some or all of the jets to induce ignition sites determine the distribution of ignition energy. Figure 7.10 illustrates the site distribution differences among three designs. Design 3 combines the close coupling of Design 5 with the radial chamber coverage of the high velocity Design 4, minimizing the distance each flame front is required to travel in order to consume the charge. This more rapid combustion event results in elevated net thermal efficiency. Thermal efficiency can thus be maximized by jet velocity targeting driven by nozzle orifice area, number of orifices, and orifice diameter.



**Fig. 7.10** Ignition sites versus normalized distance from bore-center to wall for different pre-chamber and nozzle geometries



### 7.2.3 Geometry Sensitivity

The geometry of the pre-chamber and nozzle influences two critical aspects of the jet ignition process: mixture preparation inside the pre-chamber and pre-chamber combustion leading to active jet expulsion. The influence of geometry on both phases has been documented previously by the authors (Bunce et al. 2014), and a summary is provided here.

The influence of pre-chamber volume on system operation was comprehensively examined by Gussack et al. (Adams 1979), and it was this work that was responsible for the generation of the “5%” guideline, whereby the maximum pre-chamber volume should correspond to 5% of the engine’s clearance volume in order to minimize excess heat loss from the pre-chamber.

As is often cited in the development of small displacement SI engines, surface-to-volume ratio increases as combustion chamber displacement decreases. With combustion occurring in this smaller volume, there is a greater surface area through which the thermal energy generated during the combustion process can transfer resulting in increased heat losses as a percentage of fuel energy (Rittenhouse 2014). This surface-to-volume effect applies to pre-chambers as well but there is a key difference: the main system contribution of the fuel ignited in the pre-chamber is to generate thermo-chemical energy to ignite the remaining fuel in the main chamber. Because the jet expulsion event typically starts and ends during the compression stroke, fuel consumed in this process does not contribute significantly to engine torque. Therefore, a practical system optimization pathway would be to minimize the quantity of fuel that is “sacrificed” for ignition. Larger volume pre-chambers, with superior surface-to-volume ratios, require more pre-chamber fuel in order to ensure an ignitable fuel-air ratio at the spark plug. Smaller volume pre-chambers, though they experience heat loss as a higher percentage of the fuel consumed, require

less fuel in order to ensure combustion and can therefore result in higher system efficiency. An optimal pre-chamber volume can therefore be determined for each engine application that minimizes fuel required to participate in the pre-chamber combustion event but maintains a sufficiently high volume to prevent quenching of the spark kernel during the ignition event interior to the pre-chamber.

The geometry of the pre-chamber nozzle is perhaps the most impactful design optimization area. While the nominal emphasis is on generating sufficiently high jet velocity, there are physical and thermodynamic limits to the effectiveness of this approach. Here it becomes necessary to evaluate geometry sensitivities over wide areas of the engine operating map. Results from engine testing at low speed and load operation obtained from a range of nozzle geometry variants are shown in Fig. 7.11. As was demonstrated previously, a smaller orifice area produces shorter burn durations in the main chamber which contribute to increased combustion efficiency at lean conditions. Engine performance optimization clearly favors nozzle geometries that produce faster jet velocities at this part load condition.

At higher load knock limited conditions, however, this optimization trend does not hold. As is evident in Fig. 7.12, geometries with orifice areas in the middle of the range previously presented produce thermal efficiency values and stable lean limit extension superior to the previously identified small orifice area geometries. The

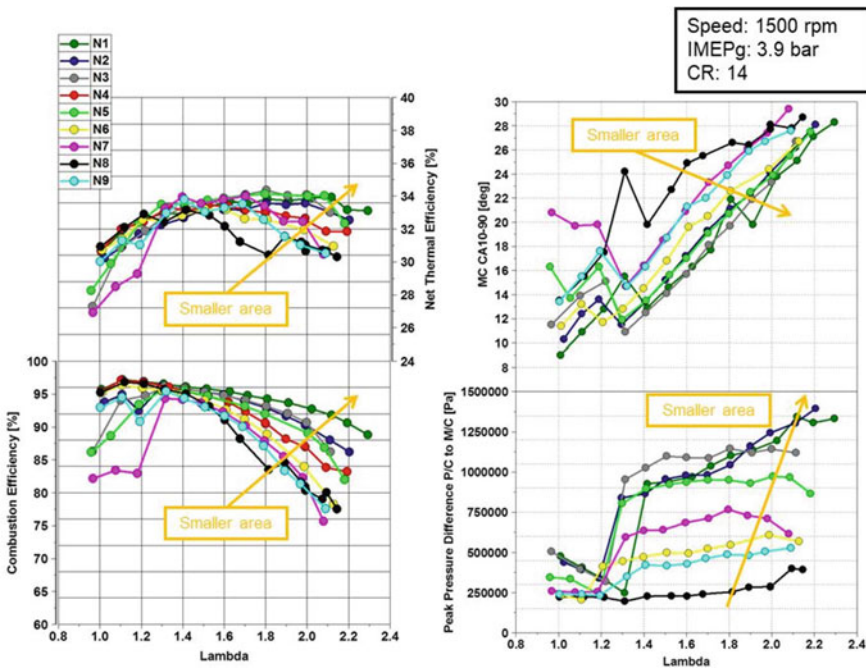


Fig. 7.11 Engine performance as a function of lambda at 1500 rpm, 3.9 bar indicated mean effective pressure (IMEPg) for a range of pre-chamber geometries

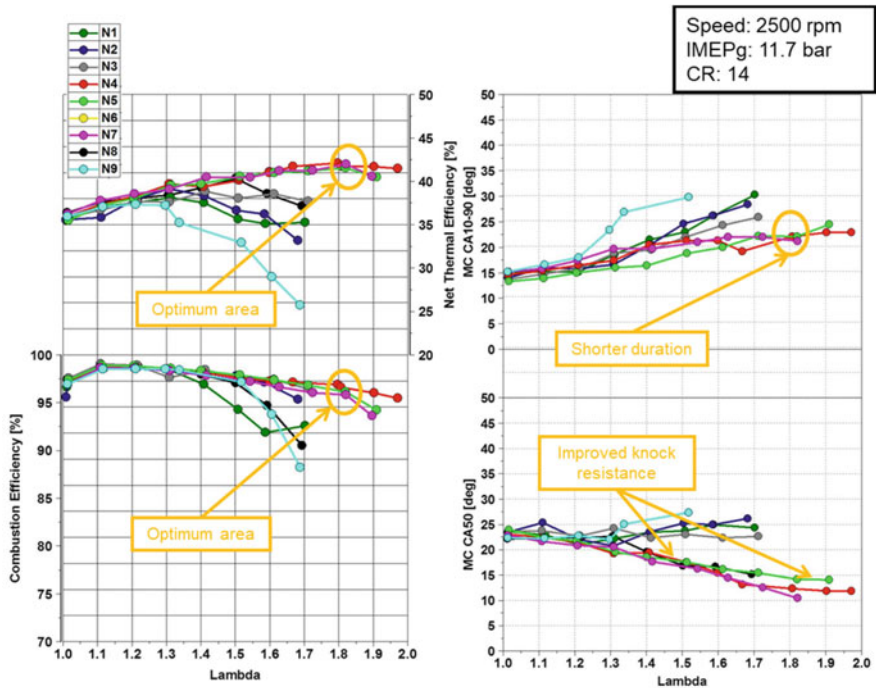


Fig. 7.12 Engine performance as a function of lambda at 2500 rpm, 11.7 bar IMEP

optimum geometry for the part load condition, N1, is among one of the least optimal geometries at the high load condition. An optimum orifice area range exists whereby knock is minimized and phasing can be advanced. The plateauing of the knock reduction potential of the small orifice area geometries is likely due to choked flow and reduced jet reactivity, a hypothesis supported by the poor lean limit extension and combustion efficiency of these designs. Conversely the large orifice area geometries produce jet velocities that are too slow to have a strong impact on end-gas knock and thus the combustion phasing is adversely affected, as is apparent from the results shown in Fig. 7.12.

Utilizing a common pre-chamber nozzle geometry that encompasses the requirements for both operating regions results in a compromise: some part load efficiency gain is sacrificed for high load knock reduction, or vice versa. In essence this is a compromise between functionality throughout the engine operating range and region-specific local peak efficiency. Ultimate selection of this pre-chamber geometry will therefore be influenced by external factors, such as intended end-use of the ICE (e.g., prime mover or hybrid). As will be seen in the section discussing low load operation, there are other regions of engine operation that have entirely different requirements for achieving even baseline functionality. All these parameters need to be considered when selecting a pre-chamber geometry that can meet the engine versatility demanded by modern engine drive cycle operation.

### 7.2.4 Pre-chamber Scavenging

Most jet ignition concepts do not include any direct introduction of oxygen, instead relying on induced gas exchange between pre-chamber and main chamber to provide sufficient oxygen for combustion. This gas exchange process is driven by pressure differentials amongst intake and exhaust ports, pre-chamber, and main chamber throughout the 4-stroke engine cycle. Understanding this process is critical to ensuring that it is not impeded, especially under heavily throttled conditions.

Figure 7.13 displays the oxygen (O<sub>2</sub>) and carbon dioxide (CO<sub>2</sub>) mass fractions inside the pre-chamber for a part load cycle. The intake valve opening event is when O<sub>2</sub> is reintroduced into the system. The O<sub>2</sub> fraction rises in the pre-chamber despite the downward motion of the piston, indicating that the pre-chamber is not bypassed by the incoming charge but rather interacts with it. The discontinuities apparent in the O<sub>2</sub> mass fraction trace correspond to intake process events, indicating that valve position and flow through the valve have a substantial influence on O<sub>2</sub> filling of the pre-chamber. With the intake valve closed and upward piston motion during the compression stroke, the remainder of the O<sub>2</sub> filling process occurs which in turn dilutes the CO<sub>2</sub> mass fraction in the pre-chamber. With sufficient O<sub>2</sub> present, fuel can then be separately added to ensure a pre-chamber lambda within the ignitability limits of the spark plug.

An experiment was undertaken to measure the residual gas fraction inside the pre-chamber and to determine what impact pre-chamber fuel injection has on residuals. A fast response CO<sub>2</sub> analyzer was used to sample contents directly from the pre-chamber. The analyzer probe was connected directly to a port at the top of the

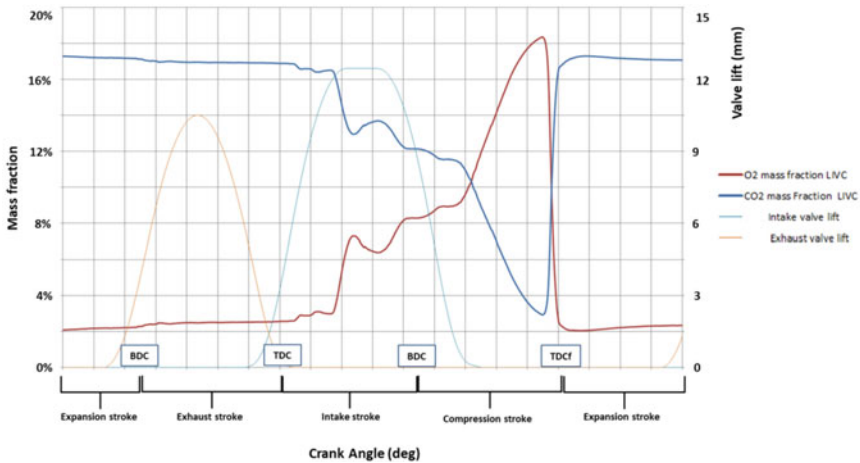


**Fig. 7.13** Representative O<sub>2</sub> and CO<sub>2</sub> mass fraction evolution in the pre-chamber versus CAD; taken from analysis

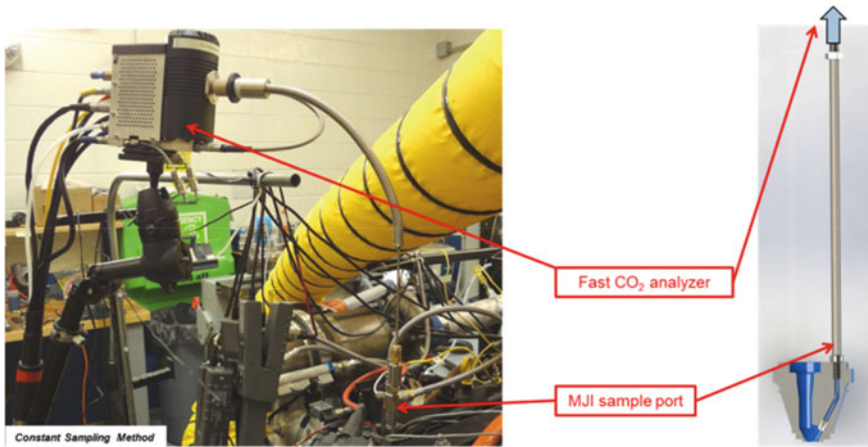


Fig. 7.14 Constant sampling method for measuring pre-chamber residual fraction

pre-chamber body. A thin capillary connected this port to the pre-chamber volume. Adequate gas flow to the analyzer for sampling was ensured (Fig. 7.14).

As is shown in Fig. 7.15, residual fraction decreases when fuel is injected directly. The residual fraction continues to decrease as the injected fuel quantity is increased. The contour plot in Fig. 7.16 shows residual fraction trends with pre-chamber fuel injection angle and quantity. The addition of the fuel mass either displaces the dominant residual content at the time of injection, or has a more a complex impact on

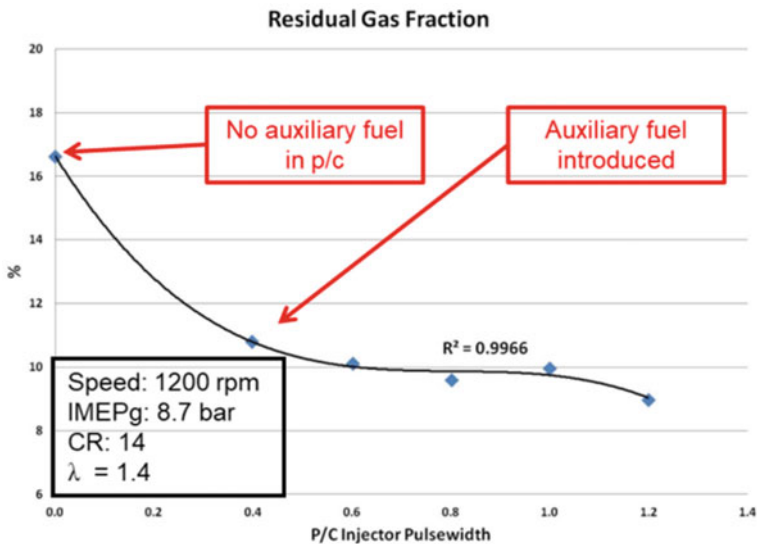
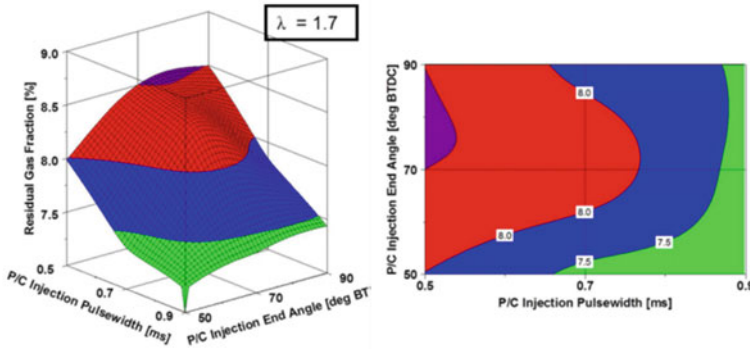


Fig. 7.15 Residual fraction trends with pre-chamber fuel quantity



**Fig. 7.16** Residual fraction trends with pre-chamber fuel quantity and end of injection angle at a representative condition; 1200 rpm, 8.7 bar IMEP,  $\lambda = 1.7$

the completeness of pre-chamber combustion that is not easily detected. Regardless of mechanism, this data suggests that the addition of pre-chamber fuel, even at a constant main chamber lambda, is an effective means by which to reduce the potentially negative impact of residual fraction on pre-chamber combustion.

### 7.2.5 Auxiliary Fuel Injection

Using a direct fuelling approach, as in MJI, that allows for precise control over auxiliary fuelling quantity and injection timing, introduces a critical avenue for system optimization. Figure 7.17 displays the effect that varying auxiliary fuel injection quantity and timing has on engine performance. At constant engine operating conditions, a late auxiliary fuel injection event reduces both main chamber CA0-10 and CA10-90 burn duration by 2 crank angle degrees (CAD). Note that spark timing is held constant to avoid combustion phasing effects. Injection timing also has a significant impact on the main chamber combustion stability, with late injection reducing the coefficient of variance (COV) by over 1.5 percentage points compared to that of the early injection case. The reductions in main chamber burn duration and COV result in an increase in net thermal efficiency of 1 percentage point.

A computational fluid dynamics (CFD) model correlated to experimental data was developed to explore the underlying causes of these sensitivities. Figure 7.18 illustrates the differences in pre-chamber and main chamber combustion pressure resulting from different auxiliary fuel injection timings. Fuelling quantities, both main chamber and pre-chamber are held constant in the simulation. The noticeable differences in main chamber peak pressure manifest as indicated mean effective pressure (IMEP) and therefore thermal efficiency differences.

Table 7.1 evaluates both overall pre-chamber  $\lambda$  and  $\lambda$  in a small area around the spark plug at time of spark. In the early injection case, both quantities are lean.



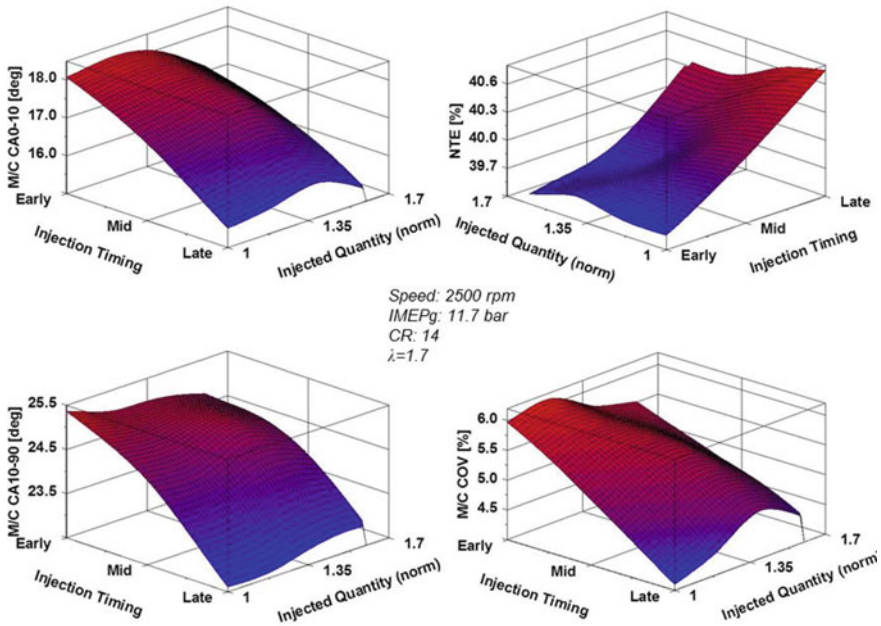


**Fig. 7.17** Main chamber (M/C) performance versus injection timing versus normalized injected quantity. Note that the net thermal efficiency (NTE) plot is rotated by 90 degrees (x and y axes are reversed) for the sake of visual clarity

In the late injection case, both values are rich despite the identical pre-chamber fuel injection quantity. A significant quantity of the auxiliary fuel (>20%) exits the pre-chamber prior to time of spark due to the low background pressure in the pre-chamber at the early injection timing. This effect, coupled with the over-mixing phenomenon described previously, results in an overly lean mixture near the spark plug which ultimately produces poor main chamber combustion, consistent with the experimentally observed phenomena.

These examples serve to illustrate engine sensitivity to effective fuel delivery and efficient fuel utilization in the pre-chamber. Though the fuel quantity is a relatively small percentage of overall system fuel, judicious utilization of this fuel, or lack thereof, has a disproportionately large influence on burn rates and thermal efficiency. Inefficient use of this pre-chamber fuel or even a poorly timed injection event could feasibly eliminate efficiency gains made with a portion of the increase in dilution ratio.

These combined elements encompass the fundamental building blocks for creating a pre-chamber jet ignition engine that can promote stable, rapid combustion: jet sensitivity spectrum, applicability of pre-chamber geometry across the engine map, intra-chamber gas exchange, and auxiliary fuel delivery. A detailed understanding of the sensitivities of these elements enables the jet ignition concept to be scaled across different engine displacements, applications, and fuels.

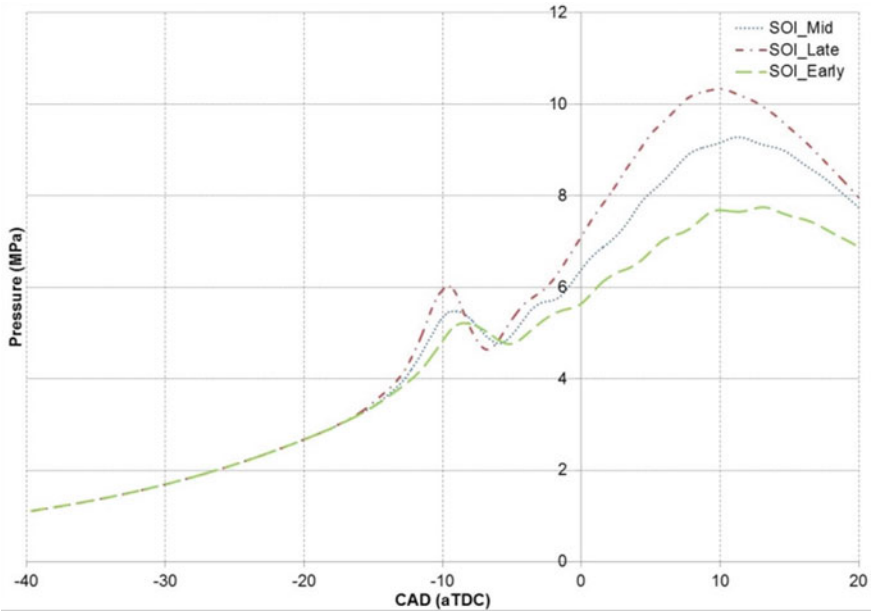


**Fig. 7.18** Cylinder pressure versus CAD, 2500 rpm, 11.7 bar IMEP, compression ratio (CR) 14:1,  $\lambda = 1.7$ , constant spark timing, constant fuel injection quantity, multiple start of injection (SOI) timings

**Table 7.1** Pre-chamber charge and combustion parameters and main chamber burn duration at 2500 rpm, 11.7 bar IMEP, CR 14:1,  $\lambda = 1.7$ , constant spark timing, constant fuel injection quantity

Injection timing	Pre-chamber $\lambda$ overall @ ST	$\lambda$ @ spark plug	Fuel efflux mass before ST (mg)	10–90% Burn duration ( $^{\circ}$ CA)
Early	1.07	>1.2	0.11	34.46
Mid	0.98	1.1	0.03	21.92
Late	0.92	0.95	0	18.34

### 7.3 Applied Research

#### 7.3.1 Multi-cylinder Jet Ignition Engine

While single cylinder experiments are important for establishing a fundamental understanding of the jet ignition combustion process, translation of these results to a multi-cylinder engine is necessary in order to address key system level challenges associated with jet ignition and dilute combustion generally. A multi-cylinder engine provides thermal conditions and a gas exchange dynamic more representative of an eventual commercial application. As has already been demonstrated, jet ignition operation is sensitive to these parameters. A multi-cylinder engine also provides



representative friction which allows reporting of brake-specific performance. Finally, a multi-cylinder engine provides the opportunity for a commercially available boost system to be fitted in order to appropriately assess air handling challenges of a dilute combustion system.

Figure 7.19 depicts the use of the different MJI engine platforms and analysis tools that were used to develop the multi-cylinder engine platform that produced the results presented in subsequent sections.

The MAHLE Di3 Downsizing demonstrator engine was selected as the basis of the dedicated MJI engine due to its robust and flexible architecture providing a good research platform representative of modern SI engines. Development of the Di3 engine is well documented (Bassett et al. 2016). Table 7.2 lists the specifications of the base Di3 engine. The engine is depicted in Fig. 7.20.

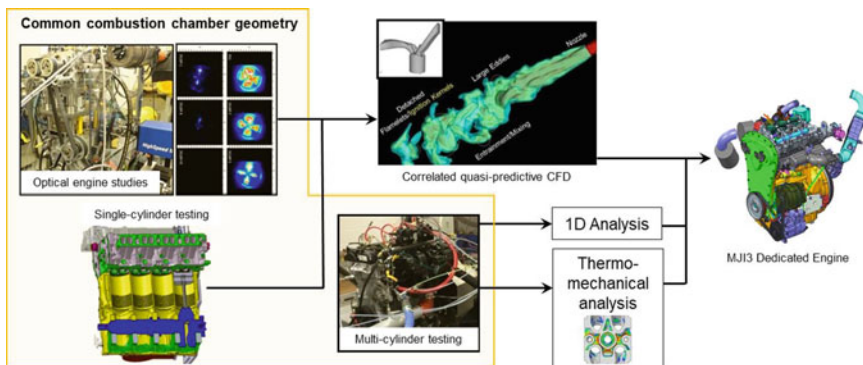


**Fig. 7.19** Flow chart of MJI research progression to dedicated multi-cylinder engine demonstration

**Table 7.2** The 1.5L MAHLE Di3 engine specifications

MAHLE Di3 Specifications	
Configuration	In-line 3 cylinder
Capacity	1497 cc
Bore	83 mm
Stroke	92.2 mm
Compression ratio	9.25:1–16:1
Peak power	141 kW ( $\lambda = 1$ )
Peak torque	334 Nm ( $\lambda = 1$ )
Variable valve timing	Inlet and exhaust with 60°CAD authority
Turbocharger	Variable geometry turbocharger

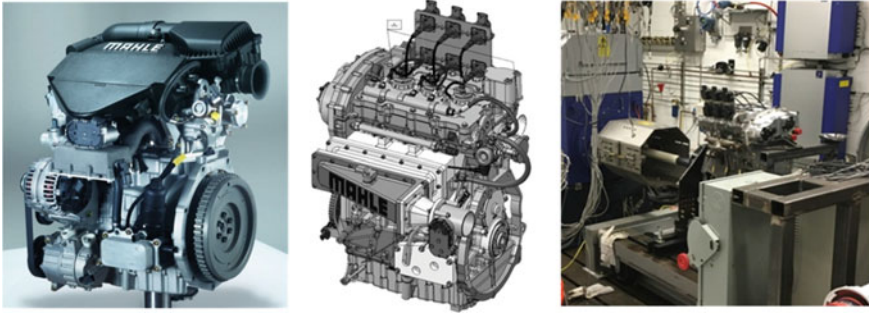


Fig. 7.20 Di3 engine images (left, center), and installed in the test cell (right)

### 7.3.2 Experimental Results

**Active System.** To fully exploit the efficiency potential of an active jet ignition system, the engine must be operated ultra-lean throughout a significant portion of the engine map. The distributed nature of ignition and the lower combustion temperatures associated with lean combustion serve to drastically reduce the likelihood of end gas knock. The knock reduction with jet ignition at  $\lambda = 1$  conditions is comparatively small but can still be leveraged to increase compression ratio. Should the engine operate exclusively at ultra-lean conditions, seldom if ever requiring a transition to high load  $\lambda = 1$  operation, then the compression ratio can be increased even further. The high compression ratio effectively penalizes active jet ignition  $\lambda = 1$  operation by extending the knock region down to lower loads compared with the baseline engine. However, with the goal of achieving the same knock limit with active ultra-lean jet ignition that is present with  $\lambda = 1$  SI operation, the compression ratio can be maximized.

Figure 7.21 demonstrates engine performance trends with increasing  $\lambda$  at a representative part load condition. While burn durations continue to increase with enleanment, these are still generally faster than the corresponding SI engine burn durations at  $\lambda = 1$ . Generally, relatively high combustion efficiency is maintained throughout the  $\lambda$  range, with deterioration near the lean limit. The two most prominent emissions constituents that determine combustion efficiency are total hydrocarbons (THC) and carbon monoxide (CO). By the nature of homogeneous lean operation, CO emissions decrease beginning in the near-lean region. Over this same period THC emissions dip in the near-lean region and then slowly increase in the ultra-lean region, resulting in a slight increase over the levels at  $\lambda = 1$ .

The decrease in engine-out nitrogen oxides ( $\text{NO}_x$ ) emissions is nearly entirely  $\lambda$  dependent and shows virtually no dependence on speed or load. This means that the observed engine-out  $\text{NO}_x$  reduction of >95% at ultra-lean conditions shown in Fig. 7.21 is consistent throughout the engine map. The remaining  $\text{NO}_x$  emissions are generated predominantly in the pre-chamber combustion event, as has been established in heavy duty pre-chamber research (Puzinauskas et al. 2000).

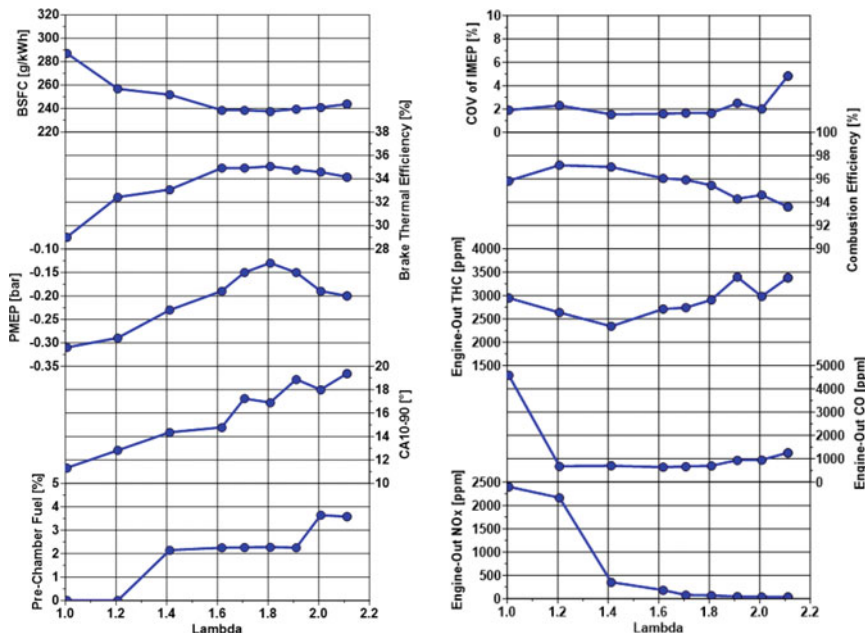


Fig. 7.21 Engine performance and emissions trends with lambda at 2000 rpm, 6 bar BMEP

Figure 7.22 compares the magnitudes of efficiency loss pathways in the baseline SI engine with those of the active jet ignition variant from  $\lambda = 1$  to the lean limit at this condition,  $\lambda = 1.9$ . The compression ratio with the base SI engine is approximately 9.25:1, and this is increased to 14:1 with the active jet ignition engine. Comparing

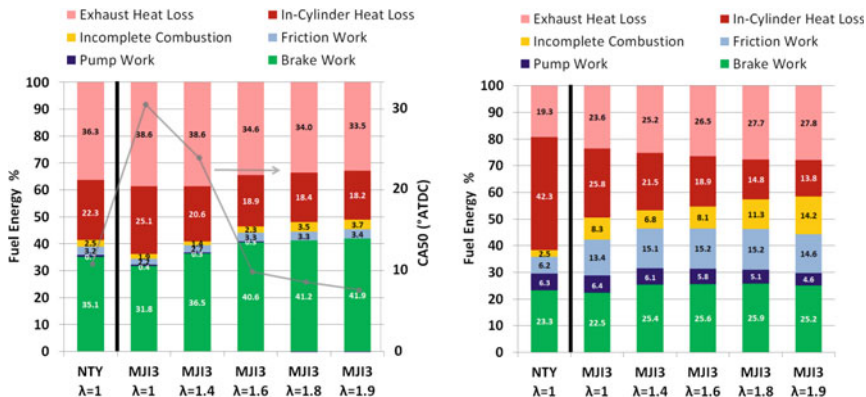


Fig. 7.22 Comparison of efficiency loss pathways between SI (NTY) and jet ignition (MJi3) at a knock limited condition (3000 rpm/12 bar BMEP, left) and a low load condition (1500 rpm/2 bar BMEP, right)

the results at  $\lambda = 1$ , the increased compression ratio produces a 3 percentage point decrease in brake work. The cause is additional heat loss, partly due to the higher mean gas temperatures induced by the increased compression ratio, but mostly due to the retarded combustion phasing necessary to avoid knock. As the jet ignition engine is enleaned at constant load, combustion phasing advances.

The incomplete combustion loss is smaller with jet ignition at  $\lambda = 1$  compared to the SI engine even though the 50% burn angle (CA50) is retarded by over 20 crank angle degrees. Indeed, the incomplete combustion loss with jet ignition only becomes equivalent to that of the SI engine at stoichiometric when the jet ignition engine achieves a  $\lambda$  of 1.6.

Ultimately the thermodynamic benefits of ultra-lean operation, further exploited through the use of a higher compression ratio, result in a brake thermal efficiency (BTE) of nearly 42% at the  $\lambda = 1.9$  condition in this engine. This represents an increase in BTE of over 19% compared to the baseline SI engine used in this experiment.

Eventually BTE reaches a plateau before decreasing slightly with further enleanment. This plateau corresponds to a “peak efficiency  $\lambda$ ” range and is dictated by a balance among efficiency loss pathways. Several optimizations can be performed in order to minimize certain emissions constituents and achieve certain target exhaust temperatures, but the optimization depicted in Fig. 7.23 maximizes BTE at each speed and load condition in the engine map. The peak efficiency  $\lambda$  distribution observed is segmented somewhat neatly by load region. The primary parameters that dictate the peak efficiency  $\lambda$  differ by these load regions as well.

The low load region experiences the least lean peak efficiency  $\lambda$ . In SI engines, combustion efficiency is typically depressed at lower loads due to the poor flame

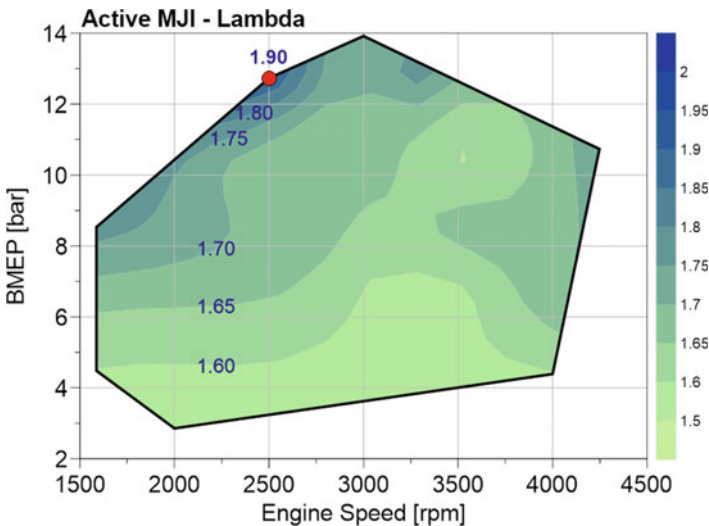


Fig. 7.23  $\lambda$  map corresponding to minimum brake specific fuel consumption (BSFC)

speeds in a low pressure, low charge density environment. At ultra-lean conditions, this issue is exacerbated as lean flame fronts are notorious for low velocity. This produces a relatively steep decline in combustion efficiency at ultra-lean conditions which is significant enough to impact the BTE trend.

At mid-load conditions, the peak efficiency  $\lambda$  shifts leaner. Here there is a complex interaction between main chamber  $\lambda$  and pre-chamber fuelling requirement. System BTE is maximized when the quantity of fuel injected into the pre-chamber is minimized. As the engine is enleaned, the pre-chamber fuelling requirement increases in order to both compensate for the leaner  $\lambda$  entering the pre-chamber from the main chamber and to create progressively more reactive radical species during pre-chamber combustion. The peak efficiency  $\lambda$  therefore favours main chamber  $\lambda$  / pre-chamber fuelling requirement combinations that maximize the efficiency benefit of the former while minimizing the negative efficiency impact of the latter.

By contrast, the selection criterion for peak efficiency  $\lambda$  is most straightforward at high load conditions. The engine favours leaner  $\lambda$  values at high load in order to reduce knock and achieve optimal phasing within combustion stability limits. The peak efficiency  $\lambda$  map presented in Fig. 7.23 produces the BSFC and BTE maps displayed in Fig. 7.24.

**Passive System.** While limited in its ability to increase dilution tolerance, the use of a passive jet ignition system provides multiple distributed ignition sites that promote significantly faster combustion within the main chamber. Figure 7.25 shows a comparison of the combustion events for a passive jet ignition system and a conventional central spark plug (CSP), at an engine speed of 4000 rpm and a load of 18 bar BMEP.

The pre-chamber combustion event is reflected in the local spike in the pre-chamber pressure trace just prior to top-dead center (TDC) firing ( $0^\circ$  crank angle). This in-turn initiates rapid combustion in the main chamber, as demonstrated by the inset heat release data also shown in Fig. 7.25 along with some of the key combustion metrics for the two cases shown in the inset table.

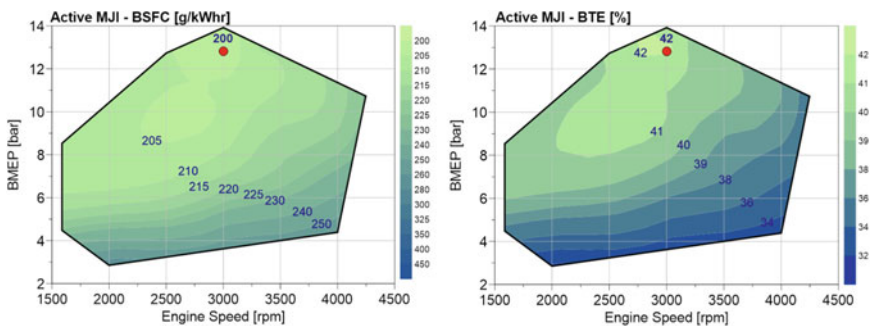


**Fig. 7.24** BSFC map (left) and BTE map (right) within stability constraint of  $COV \leq 3\%$ . US Premium Fuel; Lower Heating Value = 42.57 MJ/kg

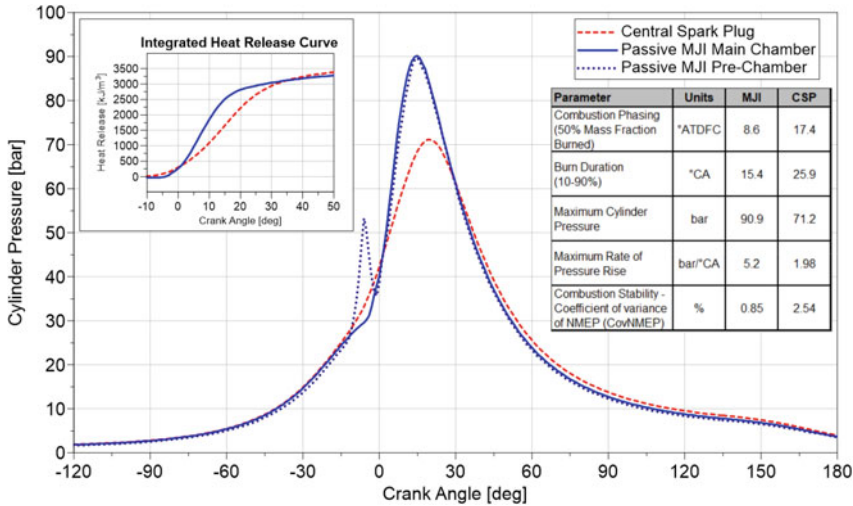


**Fig. 7.25** Comparison of passive MJI combustion to a conventional central spark plug at 4000 rpm and 18 bar BMEP

At this test condition the 10 to 90% burn duration is reduced by 40%, from 25.9 CAD to 15.4 CAD, through use of passive jet ignition, which then enables the combustion phasing to be advanced by 9 °CA before the onset of knock. As a consequence of the faster and more advanced combustion, the engine experiences higher levels of maximum cylinder pressure and the maximum rate of pressure rise.

The benefits of passive jet ignition for knock mitigation over a load sweep from 6 bar brake mean effective pressure (BMEP) up to 18 bar BMEP are shown in Fig. 7.26.

When using the CSP the engine becomes knock limited at loads about 12 bar BMEP (Fig. 7.27). At engine loads above this the combustion phasing is retarded in order to avoid knock leading to an associated increase in the 10–90% burn duration and reduced combustion stability. With the use of passive jet ignition, the maximum load that can be achieved at optimum combustion phasing increases to 16 bar, and at these loads and above the combustion phasing is improved by 8–9 CAD for this application, leading to efficiency improvements. The fast 10–90% combustion duration and improved combustion stability are maintained over the whole load range. As a consequence of the fast combustion characteristics the maximum rate of pressure rise within the cylinder is significantly increased up to a maximum of just over 5 bar/CAD. This level of pressure rise rate is at the upper limit of values typically seen in production engines, where it is limited to avoid high levels of combustion noise.

Through combining passive jet ignition with Miller-cycle operation and the addition of cooled external exhaust gas recirculation (EGR), further combustion phasing benefits can be achieved whilst also lowering the maximum rates of pressure rise.



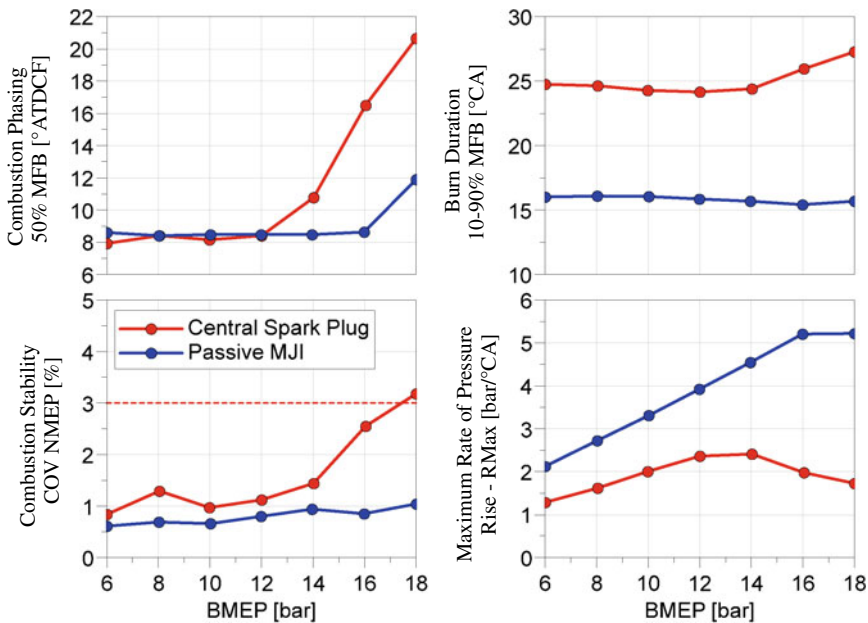


**Fig. 7.26** Comparison of passive MJI combustion to a conventional central spark plug at 4000 rpm over a load sweep from 6 to 18 bar BMEP

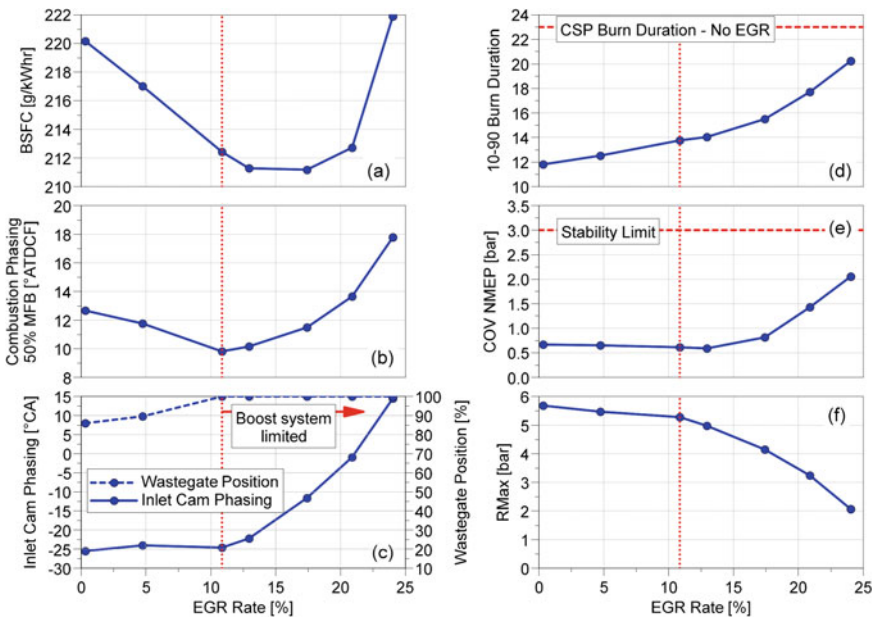


**Fig. 7.27** EGR Sweep at 3000 rpm at a load of 14 bar BMEP

Using the 1.5 L MAHLE Di3 engine, adapted for passive MJJ, operating with a high geometric compression ratio in conjunction with a PFI system and Miller-cycle intake camshaft and a low-pressure cooled external EGR system (Pre-turbine to Pre-compressor) an operating map was generated. The BSFC map for this engine is shown in Fig. 7.30.

The peak power rating for this engine is achieved under stoichiometric operating conditions with a pre-turbine temperature below 950 °C, a typical limit for turbochargers. Enrichment is typically employed by modern SI engines under high load operation in order to both increase power and keep turbine inlet temperatures below the 950 °C limit. The ability to reduce enrichment under high load operation is enabled by the faster burn duration and therefore lower exhaust temperatures associated with passive jet ignition. This lack of enrichment provides a distinct emissions advantage at these conditions. Figure 7.28 shows that a minimum BSFC value of 211 g/kWhr is achievable at an engine speed of 3000 rpm and a load of 14 bar whilst utilising simple low cost technologies.

As in active jet ignition engines, passive jet ignition engines can be optimized according to end-use application. A limited operating map hybrid powertrain offers the advantage of optimized combustion performance for a relatively narrow band of operation. Compression ratio increases can be utilized and pre-chamber geometry can be tailored due to the reduced need for pre-chamber geometry applicability across a wide operating map. Figure 7.29 shows the decrease in BSFC that can be achieved utilizing this approach (Bassett et al. 2019).

Passive jet ignition can serve as an enabler for increasing the performance achievable under stoichiometric operating conditions at lower compression ratios. In this low compression ratio configuration passive jet ignition can operate successfully

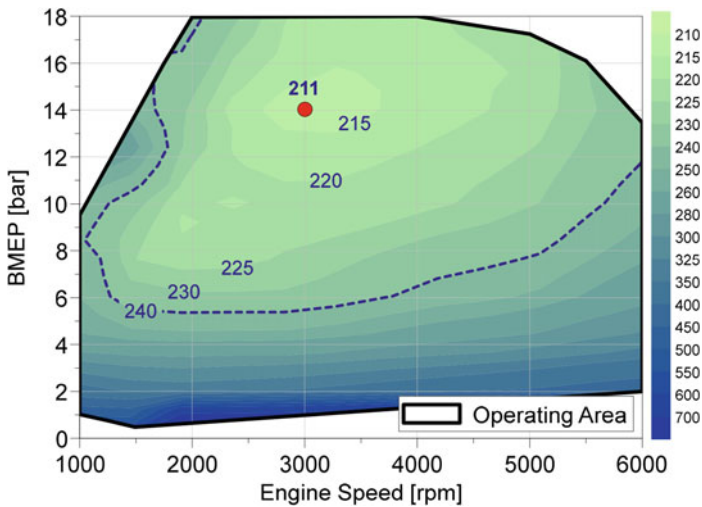
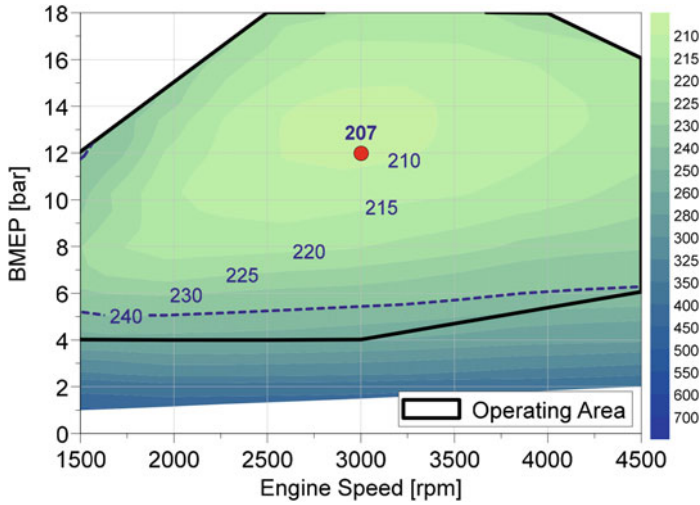


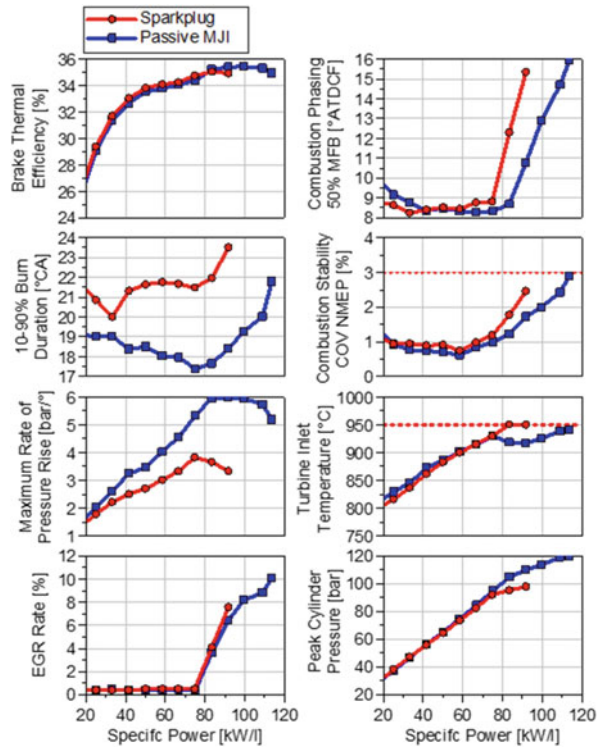
Fig. 7.28 1.5L Di3 passive MJJ whole area BSFC map. Lower Heating Value correction to 43 MJ/kg





**Fig. 7.29** Passive MJJ, dedicated hybrid engine operating map. Lower Heating Value correction to 43 MJ/kg

**Fig. 7.30** 5000 rpm load sweep for Passive MJJ compared to conventional CSP



at exceptionally high engine loads. In the case of the present engine this manifests as loads of up to 30 bar BMEP with a combustion phasing benefit of 3–4°C<sub>A</sub> compared to a conventional CSP. Using the engine in this study, passive jet ignition can operate with stoichiometric fuelling at over 100 kW/l when used in combination with moderate rates of low-pressure EGR. This is 12 kW (8 kW/l) higher than can be produced under stoichiometric operating conditions with the CSP (Fig. 7.30).

Passive jet ignition is a viable pathway for engine efficiency and performance improvements. While the efficiency and associated dilution limit extension benefits may not be as significant as those of the active system, the achievements of the passive system are produced through less complex and less costly hardware. Passive and active jet ignition systems are therefore complementary systems based on the same operating principle, and their deployment is based on the functional and performance requirements of the end-use application. The following sections detail important sensitivities that span both passive and active systems.

**Charge Motion Sensitivity.** Charge motion is typically tailored in conventional SI engines to promote fuel-air mixing. It has some secondary benefits on combustion that can be exploited. In a pre-chamber engine, interaction of charge motion with the jet ignition combustion process is more complex, as it impacts mixing dynamics and combustion in two chambers with their own interdependencies. On the multi-cylinder engine, four charge motion cases are evaluated: baseline, increased tumble, introduction of swirl, and a combination of swirl and tumble (denoted as “swumble”). Charge motion differences from the baseline are induced through the use of plate inserts into each of the intake ports (Figs. 7.31 and 7.32). The baseline configuration uses no inserts and represents a moderate tumble engine consistent with tumble levels in modern DI SI engines (a tumble ratio of approximately 3). For the tumble variant, a plate insert is used that directs flow to exit past the valve in a more severe tumble

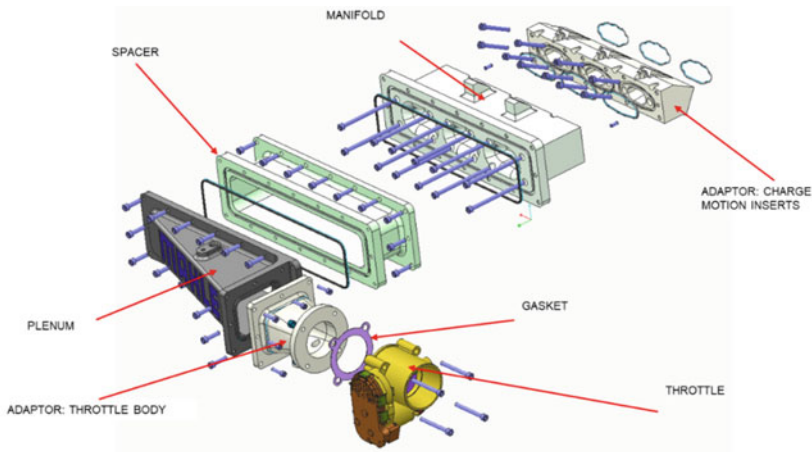
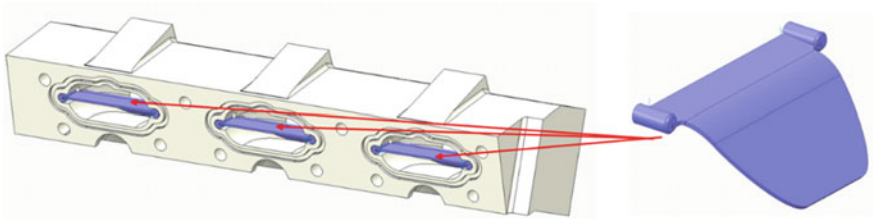


Fig. 7.31 DI3 engine air intake system—exploded view



**Fig. 7.32** Charge motion insert adaptor with tumble insert installed

**Table 7.3** Relative tumble ratio and swirl number of charge motion configurations evaluated

Configuration	Relative tumble ratio	Relative Swirl Number
Baseline	–	–
Tumble	+13%	–25%
Swirl	–39%	–1075%
Swumble	+13%	+75%

motion. For the swirl variant, a splitter plate is used with a slight incline across the diameter of the port to induce swirl. The swumble variant uses the swirl plate and tumble plate in series. The relative changes in tumble ratio and swirl number with respect to the baseline (no inserts) port are listed in Table 7.3.

The swirl variant consistently demonstrated inferior combustion stability behavior to the other variants across the full sweep of  $\lambda$  values (Fig. 7.33), showing increased

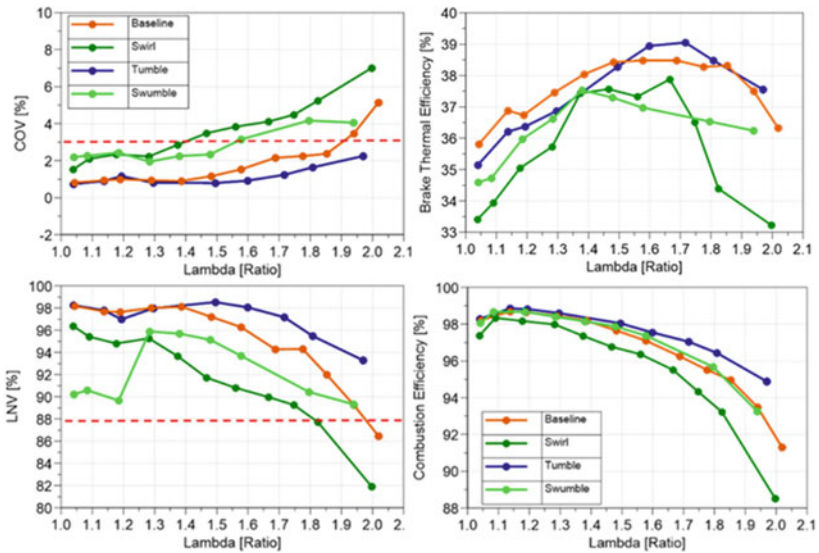


**Fig. 7.33** Combustion stability, thermal efficiency, and combustion efficiency versus  $\lambda$ .

rates of deterioration in both coefficient of variance (COV) of IMEP and least normalized value (LNV) of IMEP. This indicates both a high level of instability in the system induced by swirl motion and that the instability originates in mixture preparation in the pre-chamber, or at least it cannot be adequately mitigated through the traditional means of increasing pre-chamber fuel injection quantity. The poor stability results of the swirl charge motion variant propagate to other metrics as well, including efficiency. The introduction of increased tumble motion in the system results in superior thermal efficiency and combustion efficiency than the other variants under ultra-lean conditions. The differences in engine performance and stability induced by charge motion is not present under stoichiometric conditions. This implies that charge motion sensitivity is a key consideration for optimizing active jet ignition systems but not passive systems.

Analysis of crank-angle resolved pre-chamber pressure provides some insight into the reasons for the active jet ignition engine's affinity for tumble motion. Examination of pre-chamber behavior is confined to the portion of the pressure trace corresponding to the pre-chamber combustion event and expulsion of combustion products as reactive jets. Pre-chamber combustion behavior is described using chamber  $\Delta P$  which describes the largest measured difference between pre-chamber and main chamber pressure. Research (Bunce and Blaxill 2014) has shown that this point generally corresponds with the angle at which reactive jets first emerge from the pre-chamber.

While the magnitude of chamber  $\Delta P$  does vary somewhat amongst the four charge motion variants at common  $\lambda$  values, the standard deviation of chamber  $\Delta P$  provides the most robust indication of pre-chamber combustion stability (Peters et al. 2020). Data for all four charge motion variants was analyzed at four  $\lambda$  values: 1, 1.4, and 1.8. Figure 7.34 shows this correlation between the standard deviation of chamber  $\Delta P$  and main chamber COV for all charge motion variants. The correlation is particularly robust at the leanest conditions analyzed. Practically, this means that the variation in the peak pressure generated in the pre-chamber by the pre-chamber combustion event induces variation in main chamber combustion performance. It also means that main chamber COV, across the full  $\lambda$  range but especially under lean conditions, is primarily influenced by the degree of variation in the pre-chamber combustion event.

The relative stability of the pre-chamber combustion event influences the main chamber COV to a high degree, thereby impacting combustion efficiency at lean conditions and contributing to the peak thermal efficiency and the lean limit determination. Figure 7.34 illustrates this point, with a linear correlation between standard deviation of chamber  $\Delta P$  at the  $\lambda = 1.8$  condition and main chamber lean stability limit for the four charge motion variants. The variants with most stable lean pre-chamber combustion events, specifically stable cycle-to-cycle chamber  $\Delta P$  values, produce the most extended main chamber lean stability limits.

This result is significant because it concentrates active pre-chamber charge motion optimization to the pre-chamber combustion event itself. Active pre-chamber combustion systems generally maximize thermal efficiency when they are able to maximize the extension of the engine lean stability limit. Depending on overall engine strategy, this leaner nominal operation can enable a higher compression ratio than in

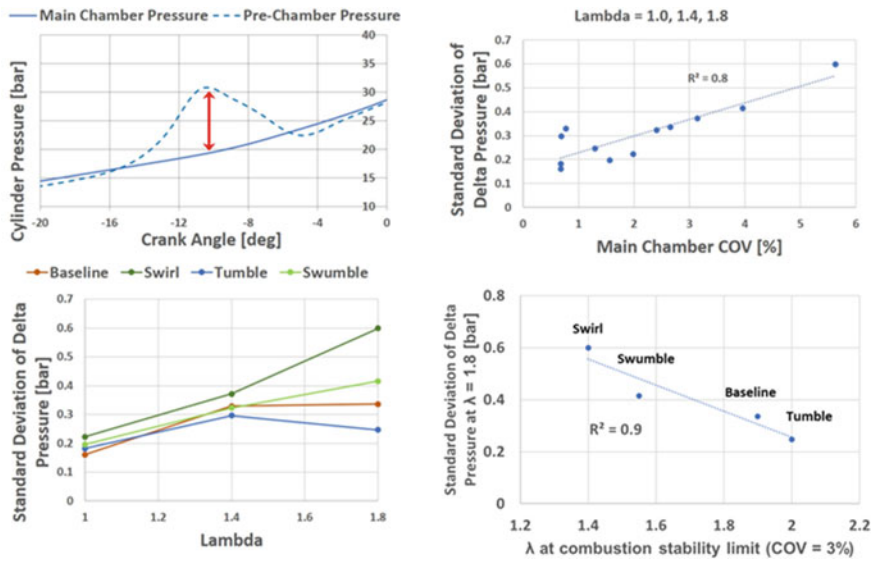


**Fig. 7.34** Pre-chamber combustion metrics: illustration of chamber  $\Delta P$  (top left); standard deviation of  $\Delta P$  versus  $\lambda$  (bottom left); standard deviation of  $\Delta P$  versus main chamber COV for  $\lambda = 1.0$ – $1.8$  (top right); main chamber lean stability limit as a function of standard deviation of  $\Delta P$  at  $\lambda = 1.8$  (bottom right)

active pre-chamber engines with less dilution tolerance, thereby further increasing both peak and cycle-average thermal efficiency potential.

### 7.3.3 Overcoming the Low Load Challenge

A well-documented (Sens et al. 2018) traditional weakness of pre-chamber concepts is operation at low loads. This issue manifests in two distinct ways: poor combustion stability at heavily throttled low loads and poor spark retard capability at loads consistent with idle and cold start spark retard (CSSR) catalyst heating operation. The efficiency benefits of both passive and active jet ignition at part load and high load cannot be practically translated to non- and mild hybrid engine applications unless a solution to the low load pre-chamber limitation is identified.

**Cold Start Spark Retard (CSSR) Operation.** The most impactful challenge posed by the low load spark retard limitation concerns the ability to heat the aftertreatment system upon cold start. Aggressive warm up of the catalyst is critical to ensuring that the vehicle can meet legislated emissions requirements. The common solution to ensure rapid heat input to the catalyst is to retard spark timing to such a degree that combustion occurs exclusively during the expansion stroke. The much later burning process results in increased exhaust enthalpy.

To properly address this issue, an examination of the failure mode is necessary. With jet ignition engines, different phases of the burn curve provide distinct information about combustion progress:

1. CA0-10 encompasses the pre-chamber combustion process from spark through time of radical jet introduction into the main chamber, as well as the ignition process in the main chamber.
2. CA10-50 encompasses the immediate post-jet ignition process and therefore still bears the influence of jet characteristics such as velocity and reactivity.
3. CA50-90 occurs long after the jet ignition process has concluded and is therefore largely uninfluenced by characteristics of pre-chamber combustion.

An examination of the different burn duration phases in Fig. 7.35 shows unbroken linear trends versus spark timing. These durations are shorter with jet ignition compared to the SI engine, which is counterintuitive to the spark retard limitation. However, inspection of the standard deviation of these burn durations indicates an increasing instability with jet ignition as spark timing is retarded, with instability is present in all three burn duration segments. The CA0-10 instability strongly implies

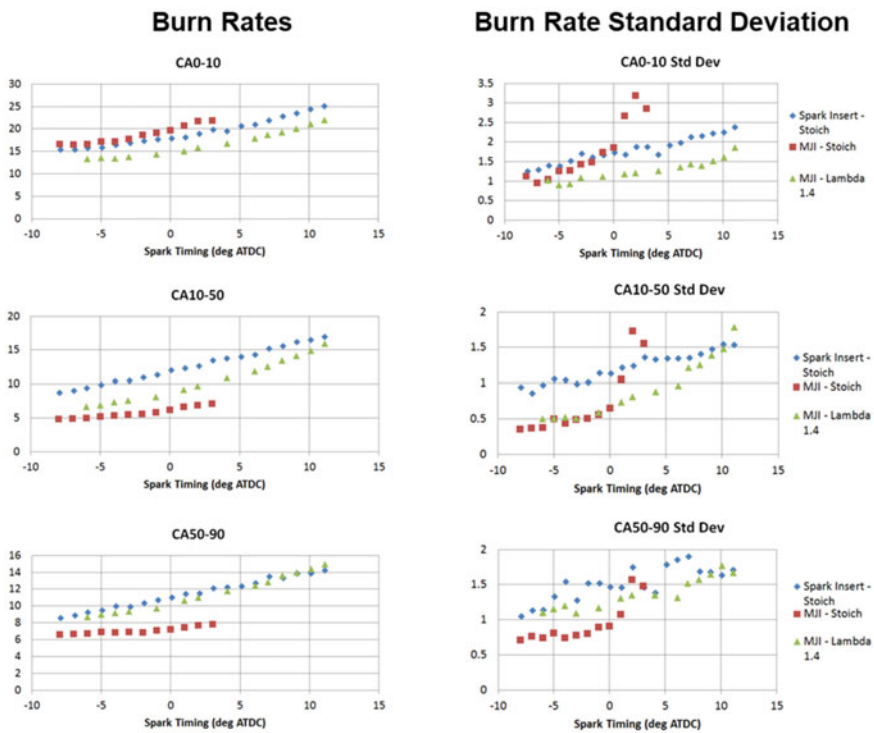


**Fig. 7.35** Engine performance as a function of spark retardation at 1500 rpm, 2 bar NMEP, 20 degree Celsius fluids

that the pre-chamber combustion event is experiencing misfires or partial burns which in turn cause the main chamber to misfire.

The ability of the active system to operate with fuel injected directly into the pre-chamber is exploited. With this approach, the jet ignition engine is able to operate at retarded spark timing identical to that of the SI engine. Notably, the combustion instability present under  $\lambda = 1$  conditions is no longer present with lean operation, indicating that by claiming direct control over pre-chamber fuel quantity and its relative location the pre-chamber combustion event is stabilized.

Lean operation is not a mechanism that can be translated easily to the passive system. Another optimization strategy or strategies must be employed that are both translatable to the passive system and also supplementary to active lean operation. The final result of a series of optimization activities is shown in Fig. 7.36, with the optimized jet ignition variant achieving spark retard nearly identical to that of the SI engine. Crucially, a common pre-chamber geometry is used to attain both successful CSSR operation and high load knock mitigation with no excessive compromise of lean limit extension or peak efficiency, as is displayed in Fig. 7.36. A single pre-chamber design coupled with a moderately featured engine is used to span the entire

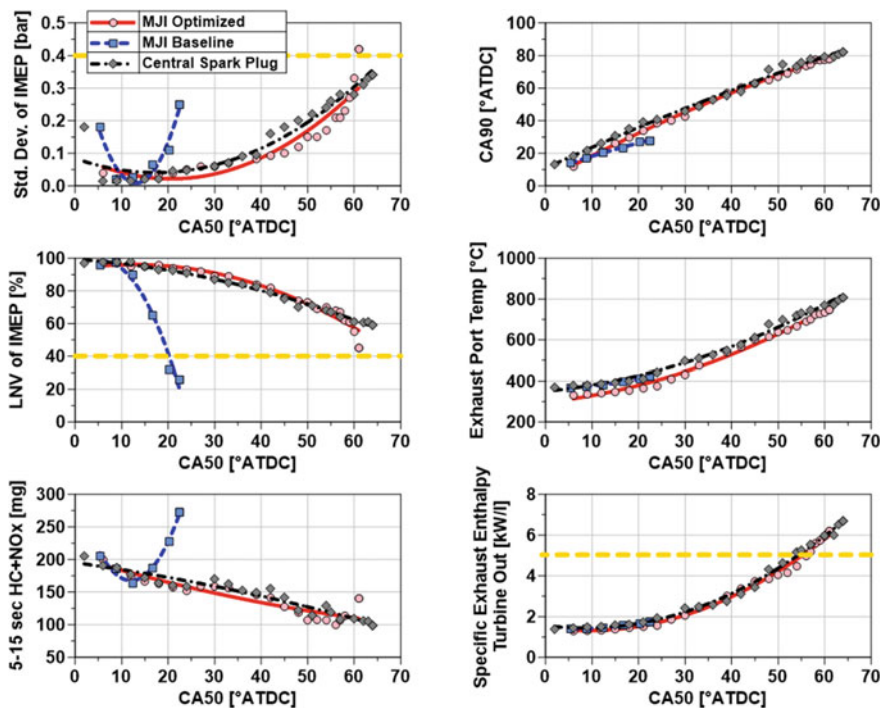


Fig. 7.36 CA50 versus Combustion Stability at 1500 rpm, 2 bar net mean effective pressure (NMEP), 20 degree Celsius fluid temperature



conventional engine operating range and can therefore be practically applied in a production context.

**Idle Operation.** Idle operation is performed at low engine speed (<1000 rpm) and low or net zero load, where the engine generates just enough load to spin itself and power the ancillary devices. A requirement for idle is retarded spark timing. At an idle condition there is an anticipation of sudden torque demand from the operator. The most rapid means by which to increase torque at this condition is to advance spark timing from a retarded location to a location in advance of top-dead center. This is due to the engine controller's ability to adjust spark timing on a cycle-by-cycle basis. Few other engine parameters can respond on such a short time basis. This rapid advancement in spark timing corresponds to a proportional increase in torque. As in the case of the CSSR condition, pre-chamber engines have historically possessed limited spark retard capability at the idle condition, limiting their ability to hold torque reserve.

The active jet ignition system carries the flexibility of operating at a relatively wide range of  $\lambda$  values at the idle condition. This capability does provide an advantage for idle operation even though it does not increase spark retard capability directly. Fuel injection quantity, like spark timing, can be adjusted by the engine controller on a cycle-by-cycle basis. However, throttle position cannot be adjusted on a cycle-by-cycle basis and throttle commands can produce a hysteresis that is impactful in this heavily throttled environment, so it is not feasible to adjust throttle and fuel quantity simultaneously to accommodate rapid torque demand and this is not attempted in production applications. However, because the active system can operate at a range of stable  $\lambda$  values at the speed and load necessary for idle,  $\lambda$  tolerance can be coupled with the existing minimal spark retard capability at these  $\lambda$  values to provide ample torque reserve (Fig. 7.37). Sudden torque demand therefore instigates both a rapid advancement of spark timing within the limited stable spark timing window and, simultaneously, a rapid increase in fuel quantity injected. The latter strategy results in rapid shifts in lean  $\lambda$  values.

Figures 7.38 and 7.39 demonstrate the adequacy of this combined spark/fuel approach to generating the torque reserve required of an idle condition. Figure 7.38 demonstrates the relationship of BMEP to CA50 retard at a constant  $\lambda$  of 1.5 in the engine. The 20 CAD range considered in these results produced a 40% reduction in BMEP. Figure 7.39 demonstrates the relationship of BMEP to enleanment at a constant air flow and a constant CA50 of 8° after TDC. Over the  $\lambda$  range considered here,  $\lambda = 1-1.8$ , BMEP reduced by 60%.

Torque reserve requirements of modern SI engines translate to approximately a 20 crank angle degree window of CA50 retard while maintaining an LNV above 70% (Cooper et al. 2020). The CA50 window for idle torque reserve is usually 10–30 dATDC. The LNV limit ensures that there are no misfires within this spark retard window. Applying this 20 CAD requirement to the trend presented in Fig. 7.38, this CA50 window corresponds to a delta of 0.4 bar BMEP, assuming the torque demand function is held to a constant engine speed. Considering only the data presented in Fig. 7.39, the CA50 retard authority present in the combined  $\lambda = 1.4-1.6$  test range



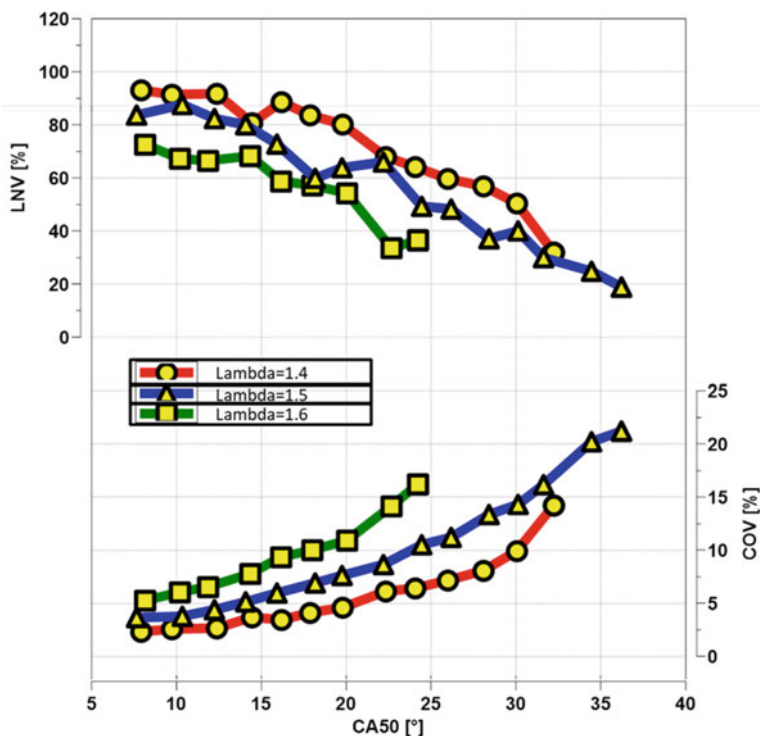


Fig. 7.37 CA50 trends with load at 850 rpm, 1 bar BMEP with a range of lean  $\lambda$  values

is 29 crank angle degrees. This corresponds to an available BMEP range of 0.58 bar. Combining these two mechanisms provides a total of 1.23 bar BMEP range, well in excess of the required 0.4 bar, verifying the validity of this  $\lambda$ -spark retard approach to accommodate torque reserve at idle.

**Low Load Operation.** A particular challenge when developing pre-chamber-based combustion systems is achieving acceptable low-load performance whilst maintaining the combustion phasing benefits at high load. This can only be achieved through careful optimization of the pre-chamber combined with management of the main-chamber conditions at these low-load operating points. Chamber air management and cam phasing can also play a role in extending low load. Under low load operating conditions, the burn durations become significantly longer and combustion stability degrades with late inlet valve closing strategies. This trend is shown in Fig. 7.40, where load sweeps, conducted at 1500 rpm, for five different inlet cam profiles are shown. During these load sweeps the inlet valve opening timing and exhaust valve overlap were held constant.

To understand the conditions within the pre-chamber that lead to this degradation in performance, with a late-inlet-valve-closing strategy, a 1D three-pressure-analysis, approach is employed. Figure 7.41 shows the spark to 10% mass-fraction-burned

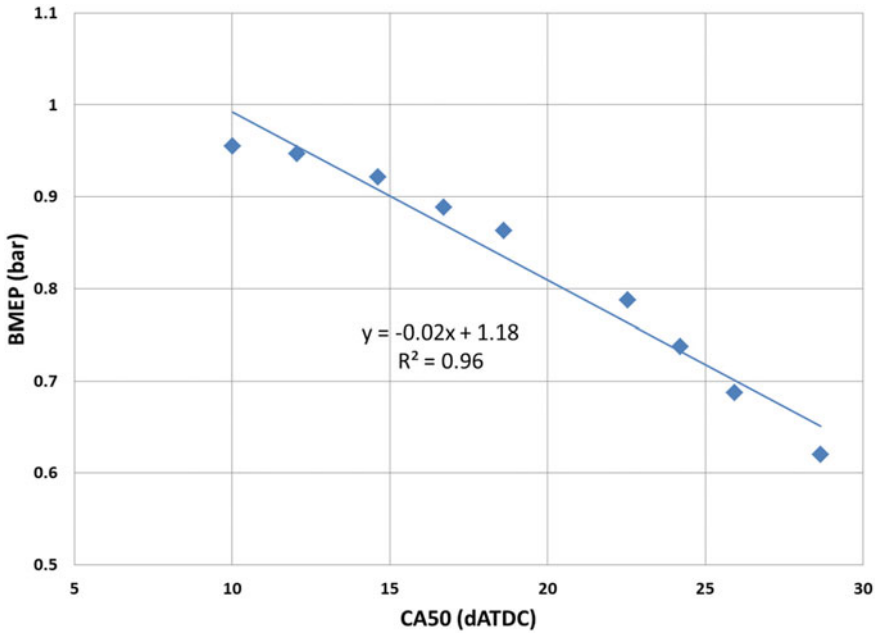


Fig. 7.38 Change in BMEP with retarding CA50 at 850 rpm,  $\lambda = 1.5$ , constant air flow

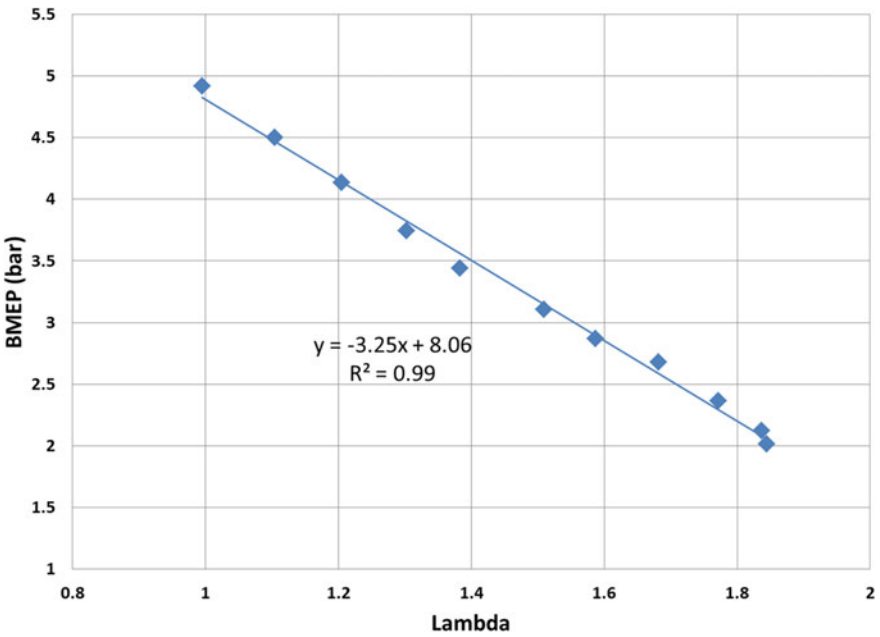


Fig. 7.39 Change in BMEP with enleanment at 850 rpm, CA50 = 8 dATDC, constant air flow

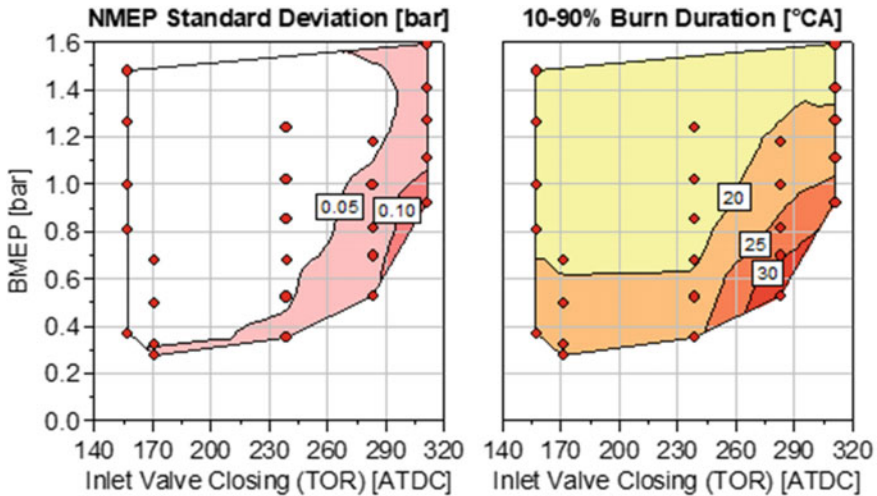


Fig. 7.40 Effect of inlet cam duration on low load stability and combustion duration

(MFB) durations and combustion stability curves for the five different inlet cam profiles measured over the same 1500 rpm load sweeps. Figure 7.41 shows that the spark to 10% MFB durations, which are indicative of the pre-chamber combustion duration, increase significantly with both the 292 °CA and 312 °CA late-closing inlet cam profiles. This increase in combustion duration also corresponds to a reduction in combustion stability. The slower pre-chamber combustion, together with the slow main chamber combustion, shown in Fig. 7.40, mean that to achieve a given 50% MFB phasing, ignition must occur earlier in the cycle.

For ignition timings earlier in the compression stroke, the pressure and therefore the mass of fresh charge in the pre-chamber is reduced. Consequently, the temperature is also reduced and the residual mass fraction is higher. All these factors lead to a weaker pre-chamber combustion event, reducing the penetration and effectiveness of the pre-chamber jets which then leads to slower main-chamber combustion. This negative cycle is initiated by the higher residual content in the main chamber and lower charge temperature, that is exacerbated by the reduced time for charge heating from the chamber walls, seen with the late-inlet-valve-closing strategies.

## 7.4 Applications

While the operating principle is the same, there are cost, complexity, and application differences between passive and active jet ignition systems. Due to its simplified componentry and synthesis with existing technologies, passive jet ignition has a relatively low implementation barrier to clear, and can be appropriate even for retrofit applications. Passive jet ignition can enable whole map  $\lambda = 1$  operation, as it does

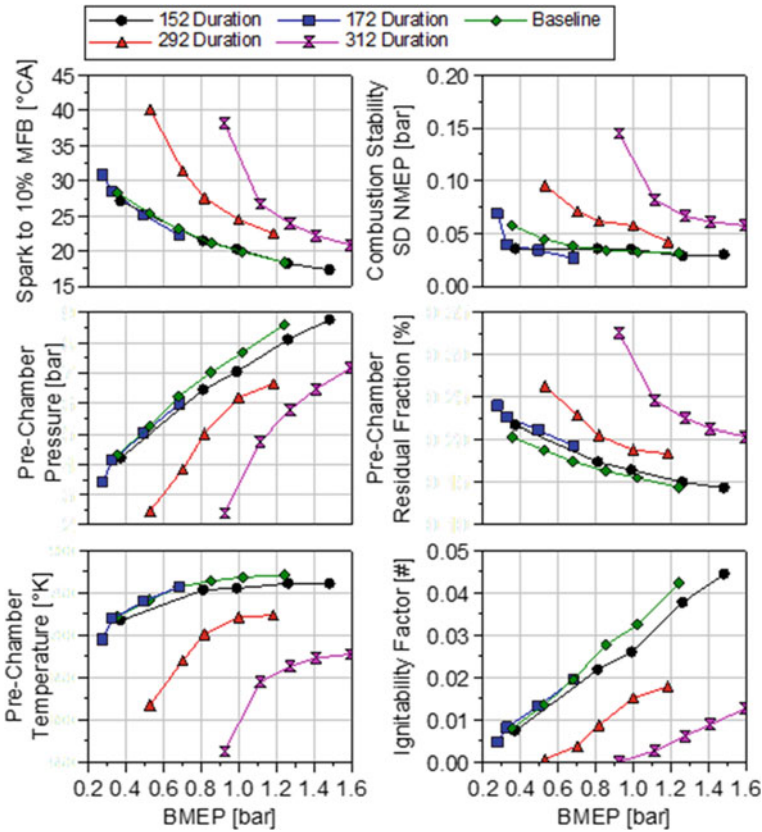


Fig. 7.41 Effect of inlet cam duration on pre-chamber conditions at the point of ignition

in this study, providing a substantial real drive cycle emissions benefit. As part of a modular powertrain, passive jet ignition is only required to span a limited operating map. With this approach, the air handling system can be further optimized to provide maximum EGR within the limited operating map, thereby providing a higher compression ratio potential. Finally, passive jet ignition can be employed as a technology to increase specific output of high performance engines. The knock reduction potential of jet ignition can be exploited in order to increase peak load and  $\lambda = 1$  operating region.

Active jet ignition has a higher technology barrier to clear than passive, both because of the additional component complexity but also because homogeneous ultra-lean operation is a fundamentally different way to operate a modern SI engine. The thermal environment is drastically different due to the reduction in temperature, the air handling system must be optimized to manage low exhaust enthalpies, and lean aftertreatment must be optimized for effective catalysis of a low  $\text{NO}_x$  output. These ancillary system changes are required regardless of which technology is used

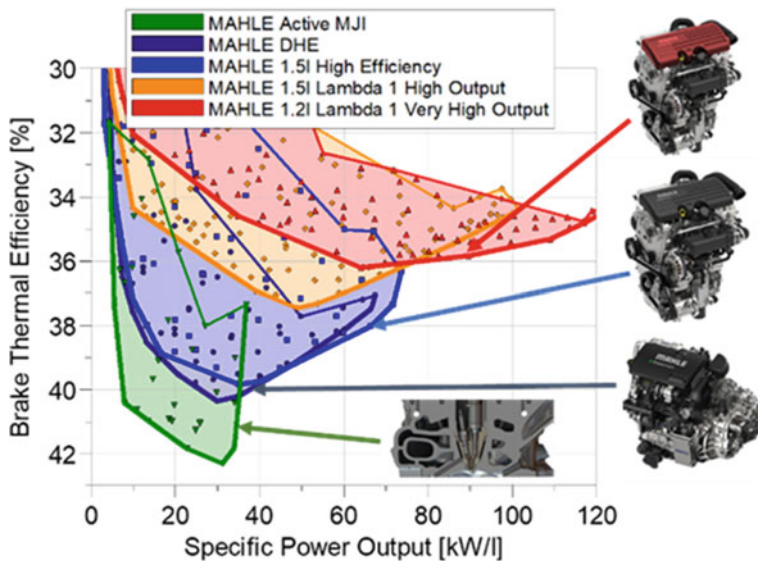


Fig. 7.42 Operating maps and BSFC of Passive and Active applications

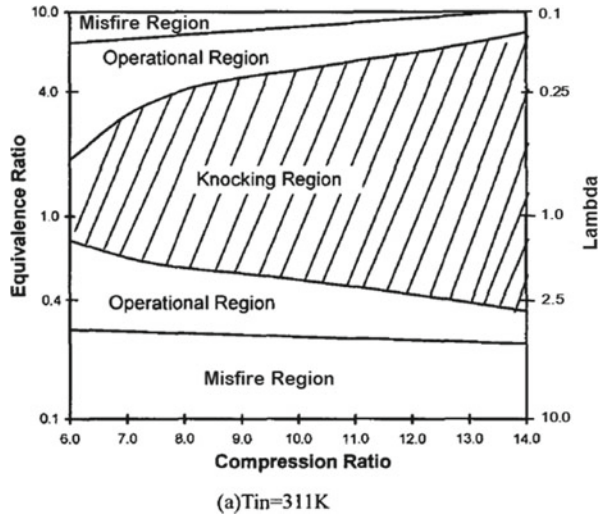
to enable ultra-lean operation. Similar to the approach with passive jet ignition, a more highly electrified powertrain engine requiring limited operating map coverage could employ a more aggressive compression ratio and other features to maximize active jet ignition efficiency, with a minimum BSFC below 195 g/kWh.

Figure 7.42 compares these different passive and active jet ignition configurations in terms of efficiency and peak power potential. The active system, defined primarily by its ability to extend the lean limit, can experience limited peak power, especially if the jet ignition engine is configured to maximize peak efficiency. Active systems do present the highest potential for increasing efficiency compared with passive systems.

Pre-chamber technologies have proven to be translatable across a wide range of engine sizes, applications, and fuel types. An emerging area of research has been the use of active jet ignition in conjunction with gaseous fuels such as natural gas and hydrogen in order to produce a high efficiency SI alternative to diesel medium and heavy duty engines. The increased ignition energy and high dilution tolerance of the active system creates a pathway for a variety of alternative fuels including propane, hydrogen, and biofuels.

Hydrogen in particular has highly specific operating requirements. Hydrogen has a high flame speed and is acutely prone to abnormal combustion such as knock and pre-ignition. To accommodate these tendencies, engine compression ratio must be lowered, which has the negative consequence of limiting peak power versus baseline diesel and natural gas engines. Operation with significant levels of air dilution is an effective method for slowing down flame speed to reduce engine mechanical limitations and for reducing abnormal combustion tendency (Fig. 7.43). Active jet

**Fig. 7.43** Variation of operational and knocking regions with compression ratio (Failed 2006)



ignition further extends the lean limit of the engine, accommodating this operational requirement. This reduction in abnormal combustion tendency provided by jet ignition-enabled enleanment also provides the opportunity to increase compression ratio, improving both power and efficiency. The improved power, efficiency, and functionality offered by the use of active jet ignition contributes to a hydrogen-fuelled ICE package with well-to-wheels CO<sub>2</sub> emissions competitive with those of a hydrogen fuel cell (Fig. 7.44). The hydrogen ICE offers a capital cost advantage versus the fuel cell, and can be an important mechanism by which to foster hydrogen infrastructure build-out and fuel system component economies of scale for eventual fuel cell deployment, while having an immediate impact on de-carbonizing the automotive sector.

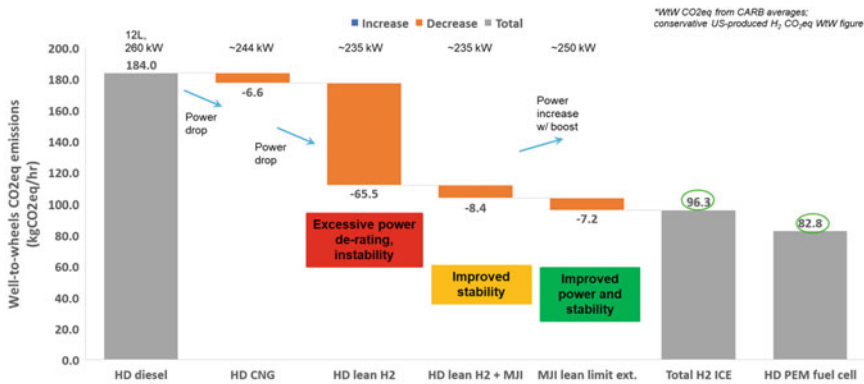


**Fig. 7.44** Well-to-wheels CO<sub>2</sub> equivalent emissions by powertrain configuration

## 7.5 Summary

Pre-chamber combustor engines have been researched extensively for their ability to increase ICE dilution tolerance and to promote rapid, stable combustion. Their effectiveness using relatively conventional components has allowed them to remain an attractive technology pathway for increasing engine efficiency and reducing CO<sub>2</sub> emissions. The intra-chamber communication introduces a degree of complexity that must be fully understood in order for systematic optimization to occur. Fundamental jet ignition engine operation can be understood through the examination of four fundamental building blocks: jet sensitivity spectrum or how pre-chamber geometry influences pre-chamber and main chamber combustion as well as the jet characteristics themselves, the applicability of a common pre-chamber geometry across the entire engine map, gas exchange between the pre-chamber and main chamber, and the intricacies of fuel delivery to the pre-chamber. A firm understanding of these concepts enables combustion system optimization to occur logically and systematically.

Jet ignition systems need to be considered from a whole engine system perspective to ensure both general functionality and that the expected efficiency benefits are realized. Considerations for boost system, cam phasing, and charge motion are necessary to ensure effective interaction between the combustion system and ancillary subsystems. Additionally, the major challenge of jet ignition engines, low load performance, requires careful optimization of pre-chamber geometry, operating strategy, and controls flexibility. Each of these optimization pathways must be also be considered in the context of end-use powertrain application. Limited operating map hybrid powertrain configurations allow for efficiency to be maximized, but the same basic technology can also be used for high performance prime mover applications, as evidenced by the recent history of pre-chamber motorsport applications. The emergence of viable low carbon fuels such as hydrogen present an opportunity for further tailoring of the jet ignition system to better meet the functional requirements of the system, specific requirements of the fuel, and the regulatory and society-driven de-carbonization requirements of future vehicles.

## References

- Adams T (1979) Torch ignition for combustion control of lean mixtures. SAE Technical Paper 790440. <https://doi.org/10.4271/790440>
- Attard W, Toulson E, Fraser E, Parsons P (2010) A turbulent jet ignition pre-chamber combustion system for large fuel economy improvements in a modern vehicle powertrain. SAE Technical Paper 2010-01-1457
- Bassett M, Hall J, Hibberd B, Borman S et al (2016) Heavily downsized gasoline demonstrator. SAE Int J Engines 9(2):729–738
- Bassett M, Reynolds I, Cooper A, Reader S, Berger M (2019) MAHLE modular hybrid powertrain. In: Proceedings from the 28th Aachen Colloquium









- Bunce M, Blaxill H (2014) "Methodology for combustion analysis of a spark ignition engine incorporating a pre-chamber combustor" SAE Technical Paper 2014-01-2603. <https://doi.org/10.4271/2014-01-2603>
- Bunce M, Blaxill H (2016) Sub-200 g/kWh BSFC on a light duty gasoline engine. SAE Technical Paper 2016-01-0709
- Bunce M, Blaxill H, Kulatilaka W, Jiang N (2014) The effects of turbulent jet characteristics on engine performance using a pre-chamber combustor. SAE Technical Paper 2014-01-1195. <https://doi.org/10.4271/2014-01-1195>
- Cao Y, Li L (2012) A novel closed loop control based on ionization current in combustion cycle at cold start in a GDI engine. SAE Technical Paper 2012-01-1339. <https://doi.org/10.4271/2012-01-1339>
- Caton J (2013) A comparison of lean operation and exhaust gas recirculation: thermodynamic reasons for the increases of efficiency. SAE Technical Paper 2013-01-0266
- Cooper A, Harrington A, Bassett M, Reader S, Bunce M (2020) Application of the passive MAHLE jet ignition system and synergies with miller cycle and exhaust gas recirculation. SAE Technical Paper 2020-01-0283
- Dainton L (1986) Nikolai Nikolaevich Semenov. 16 April 1896–25 September 1986. Biographical Memoirs of Fellows of the Royal Society 36:527–546 (CR - Copyright © 1990 The Royal Society)
- Date T, Yagi S (1974) Research and development of Honda CVCC engine. SAE Technical Paper 740605. <https://doi.org/10.4271/740605>
- Gussak L, Karpov V, Tikhonov Y (1979) The application of the lag-process in pre-chamber engines. SAE Technical Paper 790692. <https://doi.org/10.4271/790692>
- Kyaw Z, Watson H (1992) Hydrogen assisted jet ignition for near elimination of NO<sub>x</sub> and cyclic variability in the S.I. engine. In: Twenty-fourth symposium on combustion, vol 24(1), pp 1449–1455
- Li H, Karim A (2006) Hydrogen fueled spark-ignition engines predictive and experimental performance. *J Eng Gas Turbines Power* 128(1):230–236
- Murase E, Ono S, Hanada K, Oppenheim A (1994) Pulsed combustion jet ignition in lean mixtures. SAE Technical Paper 943048
- Noguchi N, Sanda S, Nakamura N (1976) Development of Toyota lean burn engine. SAE Technical Paper 760757. <https://doi.org/10.4271/760757>
- Peters N, Krishna Pothuraju Subramanyam S, Bunce M, Blaxill H, Cooper A (2020) Optimization of lambda across the engine map for the purpose of maximizing thermal efficiency of a jet ignition engine. *SAE Int J Adv Curr Prac Mobility* 2(6):3140–3150. <https://doi.org/10.4271/2020-01-0278>
- Puzinauskas P, Willson B, Evans K (2000) Optimization of natural gas combustion in spark-ignited engines through manipulation of intake-flow configuration. SAE Technical Paper 2000-01-1948. <https://doi.org/10.4271/2000-01-1948>
- Quader AA (1974) Lean combustion and the misfire limit. SAE Technical Paper 741055
- Rittenhouse J (2014) Thermal loss analysis for a small internal combustion engine. PhD Thesis, Air Force Institute of Technology, AFIT-ENY-14-M-41
- Robinet C, Higelin P, Moreau B, Pajot O, Andrzejewski J (1999) A new firing concept for internal combustion engines: "I'APIR". SAE Technical Paper 1999-01-0621
- Sens M, Binder E, Reinicke P-B, Riess M, Stappenbeck T, Woebke M (2018) Pre-chamber ignition and promising complementary technologies. In: 27th Aachen colloquium automobile and engine technology
- Tang Q, Liu J, Zhan Z, Hu T (2013) Influences on combustion characteristics and performances of EGR vs. lean burn in a gasoline engine. SAE Technical Paper 2013-01-1125
- Toulson E, Schock H, Attard W (2010) A review of pre-chamber initiated jet ignition combustion systems. SAE Technical Paper 2010-01-2263
- University of Cambridge Department of Engineering (2000) A pioneer of the internal combustion engine Sir Harry Ricardo F.R.S. <http://www-g.eng.cam.ac.uk/125/achievements/ricardo/>
- Ward M (2001) High-energy spark-flow coupling in an IC engine for ultra-lean and high EGR mixtures. SAE Technical Paper 2001-01-0548



# Chapter 8

## A Pathway to Ultra-Lean IC Engine Combustion: The Narrow Throat Pre-chamber



Manuel Alejandro Echeverri Marquez , Ponnya Hlaing ,  
Priybrat Sharma , Emre Cenker , Jihad Badra , Amer Amer,  
James W. G. Turner , Hong Im , Gaetano Magnotti ,  
and Bengt Johansson 

**Abstract** Stable internal combustion (IC) engine operation with a lean mixture allows improved thermal efficiency and reduced engine-out emissions. However, lean limits in IC engines are challenging due to poor ignitability. Narrow throat pre-chamber as an ignition source allows extending the lean limit through a robust multi-reactive jet ignition and in-cylinder turbulence generation. These benefits have revived the research interest in such narrow throat configurations of pre-chamber. Metal engine studies offer limited insights into the physics of pre-chamber combustion (PCC). However, when coupled with recent optical engine studies involving high-speed visualization and laser diagnostics, a better understanding of this combustion mode is unlocked. This work attempts to evaluate and summarise the recent advancement in PCC research.

**Keywords** Pre-chamber combustion (PCC) · Narrow-throat · Lean combustion · Jet ignition

---

M. A. E. Marquez · P. Hlaing (✉) · P. Sharma · J. W. G. Turner · H. Im · G. Magnotti  
Clean Combustion Research Centre, King Abdullah University of Science and Technology,  
Thuwal, Saudi Arabia  
e-mail: [ponnya.hlaing@kaust.edu.sa](mailto:ponnya.hlaing@kaust.edu.sa)

M. A. E. Marquez  
e-mail: [manuel.echeverrimarquez@kaust.edu.sa](mailto:manuel.echeverrimarquez@kaust.edu.sa)

P. Sharma  
e-mail: [priybrat.sharma@kaust.edu.sa](mailto:priybrat.sharma@kaust.edu.sa)

E. Cenker · J. Badra · A. Amer  
Transport Technologies Division, R&DC, Saudi Aramco, Dhahran, Eastern Province, Saudi  
Arabia

B. Johansson  
Combustion Engine Research Center (CERC), Chalmers University of Technology, Gothenburg,  
Sweden

## 8.1 Introduction

The need for decarbonization of the transport sector is well-recognized, and this is reflected by the increasingly stringent emission requirements in recent decades. Improving the energy efficiency of internal combustion engines implies improved work output from a given mass of fuel injected. Lean combustion is one of the pathways to achieve higher engine efficiency, with the added benefit of lower engine-out  $\text{NO}_x$  emissions (Dunn-Rankin et al. 2016). Ignition of a lean air-fuel mixture is a challenge for any practical combustion system. Among novel ignition technologies, the pre-chamber combustion (PCC) concept appears to be most attractive due to its simplicity in design and minimum modification required for adoption in current internal combustion engines (Biswas 2018). Moreover, the PCC concept offers additional benefits such as improved combustion stability, faster burn rates, and reduced knock propensity (Toulson et al. 2010; Alvarez et al. 2018).

A pre-chamber (PC) is a small volume accounting for a small percentages of the engine clearance volume. The PC communicates with the engine cylinder or the main chamber (MC) via nozzle holes. The combustion process initiates with the firing of the spark plug inside the PC, causing a pressure buildup which subsequently propels partially burned products into the MC in the form of jets. The pre-chamber jets constitute a source of thermal and chemical energy, which ultimately results in the ignition of the lean MC air-fuel mixture. Depending on the nozzle arrangement and the hole sizes, the jets cover a wide area of the engine combustion chamber, providing multiple ignition sites, resulting in a fast flame propagation process.

Pre-chambers can be classified based on different parameters, such as their volume and geometry. One of the main classifications is based on whether the auxiliary fuel is supplied to the pre-chamber. A passive PC lacks auxiliary fuel injection into the PC, while an active PC features a fuel injection system. Passive PCs are simpler in design, but they are restricted in the lean limit extension (Getzlaff et al. 2007; Shah et al. 2012; Yu et al. 2021). On the other hand, active PCs are more complex due to auxiliary pre-chamber fueling arrangements. Nevertheless, the air-fuel mixture in the PC can be maintained within the easily ignitable limits in an active PC regardless of the air-fuel concentration in the MC. Hence, an active PCC enables ultra-lean operation ( $\text{global-}\lambda > 2.0$ ) (Hlaing et al. 2020).

The additional space requirements of the active PCC often led to the modifications or redesigning of the cylinder head that could incur additional expense to the engine manufactures and subsequently to the end-users (Sens et al. 2020; Shapiro et al. 2019). The narrow-throat PC design has the convenience of fitting into a conventional diesel injector pocket of a heavy-duty engine while preserving a fuel delivery system and an essential spark plug. The design philosophy could probably ease the retrofitting process and help widespread adoption of the pre-chamber engines (Hlaing et al. 2019).

In the active PCC concept, the amount of fuel added into the PC is important in extending the lean limit. Gussak et al. demonstrated that the PC fuel-enrichment could extend the engine's lean operation limit compared to the pre-chamber excess

air ratio (PC- $\lambda$ ) close to stoichiometry (Gussak et al. 1979). Shah et al. reported that rich PC fueling improves engine combustion efficiency (Shah et al. 2014). Attard et al. advised that injecting 2% of the overall engine fuel consumption into the PC yielded the highest engine power output and optimal engine combustion stability (Attard and Blaxill 2012).

This manuscript presents studies on the lean limit extension capabilities of a narrow-throat PC geometry and the effect of fuel enrichment on the same. The combination of metal and equivalent optical engines experiments provides greater insight into the process associated with PCC. The metal engine experiments reveal the lean capability of the narrow-throat PC concept while detailing emission and efficiency trends. The gas exchange process between the PC and the MC is assessed using 1-D GT-Power pre-chamber engine model. The results from the model provide predictions on mixture compositions and gas temperature of the two chambers. Moreover, the optical engine experiments with high-speed imaging and laser diagnostics offer detailed insights into the pre-chamber jet ignition process and the MC combustion phenomena.

## 8.2 Pre-chamber Design and Methodology

### 8.2.1 The Narrow-Throat Pre-chamber Design

The PC body, shown in Fig. 8.1, accounts for 2.5% of the engine clearance volume. The PC volume and total nozzle opening area are selected based on the recommendations from Gussak et al., which are consistent with a later study by Shah et al. in a heavy-duty engine setting (Gussak et al. 1975; Shah et al. 2015). For the test engine of 2100 cc displacement volume, which was modified from a heavy-duty Volvo D13C500 model into a single-cylinder research engine, the actual PC volume is around 5.07 cc. The engine geometric compression ratio is 11.5. As the name suggests, the pre-chamber features a narrow and long throat with 3.3 mm in diameter

**Fig. 8.1** The internal geometry of the narrow-throat pre-chamber

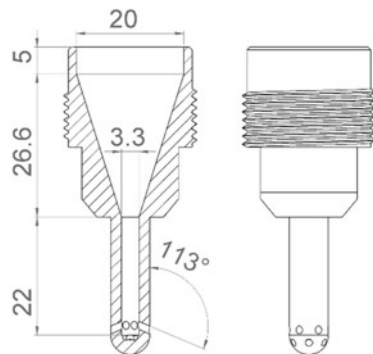


**Table 8.1** Pre-chamber geometric parameters

	Value	Unit
Pre-chamber volume	5.07	cc
Pre-chamber vol./Clearance vol	2.5	%
Number of nozzles	12	–
Nozzle diameter	1.4	mm
Nozzle area/Pre-chamber vol	0.04	cm <sup>-1</sup>
Nozzle included angle	134	deg
Throat diameter	3.30	mm
Throat length	22	mm

and 22 mm in length. Atop the throat section, the PC is in a conical shape. At the tip, which protrudes into the MC, 12 nozzle holes can be found, arranged into two layers, each consisting of 6 holes. The details of the pre-chamber internal geometry are shown in Table 8.1.

The PC body is secured into an adaptor which is a crucial part of the PCC experiments. The adaptor accommodates a spark plug, a thermocouple, a piezoelectric pressure sensor, and a gas supply channel for active PC fueling. A check valve is deform-fitted into the gas supply channel, allowing fuel to flow into the PC but checks against the PC combustion pressure. The components are shown in Fig. 8.2.

A standard clamp-down arrangement was used to secure the PC assembly inside the diesel injector pocket through a spacer that sits on top of the pre-chamber adaptor. The cross-section view of the cylinder head with the pre-chamber installed is shown in Fig. 8.3.

**Fig. 8.2** Components of the pre-chamber assembly

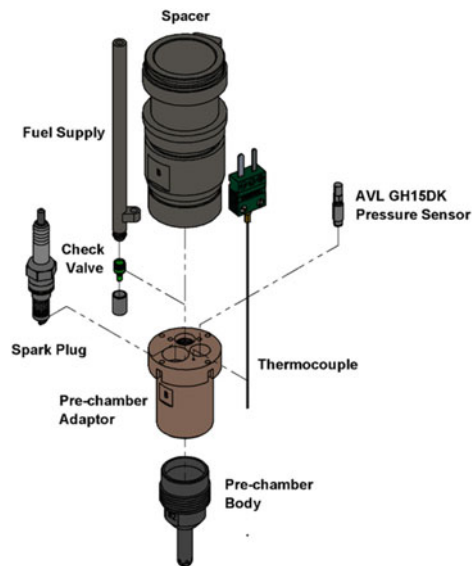
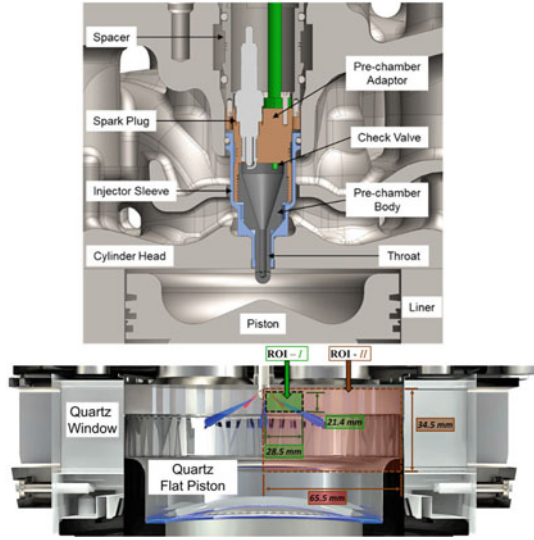


**Fig. 8.3** (Top) Cross-section view of the cylinder head with pre-chamber assembly installed and (Bottom) combustion chamber of optical engine, where ROI-I is the field of view for PIV and ROI-II for PLIF measurements



### 8.2.2 Multi-chamber Heat Release Analysis

The heat release rates in the pre-chamber and the main chamber are calculated from the measured pressure traces. The analysis method is built upon the procedure introduced by Duong et al. (2014), with modified parameters for improved accuracy. The analysis method is explained in the previous studies (Hlaing et al. 2020, 2021) and will be briefly explained here.

The main chamber rate of heat release is estimated using the expression below.

$$\frac{dQ_{MC}}{d\theta} = \frac{\gamma}{\gamma - 1} P_{MC} \frac{dV_{MC}}{d\theta} + \frac{1}{\gamma - 1} V_{MC} \frac{dP_{MC}}{d\theta} - h_{PC,MC} \frac{dm}{d\theta} \quad (8.1)$$

The first two terms of the expression are identical to conventional engine heat release calculation, while the last term refers to the enthalpy transfer between the two chambers. For the pre-chamber heat release, the term is simpler since the volume of the pre-chamber is constant.

$$\frac{dQ_{PC}}{d\theta} = \frac{1}{\gamma - 1} V_{PC} \frac{dP_{PC}}{d\theta} + h_{PC,MC} \frac{dm}{d\theta} \quad (8.2)$$

The enthalpy transfer is considered to be positive when the pre-chamber pressure is above the main chamber pressure. To calculate the enthalpy transfer, the mass flow rate between the two chambers is needed, which is estimated using the isentropic flow equation through a nozzle (Heywood 1998).

$$dm = \frac{C_d A_T P_{PC}}{\sqrt{RT_{PC}}} \left( \frac{P_{MC}}{P_{PC}} \right)^{\frac{1}{\gamma}} \left[ \frac{2\gamma}{\gamma - 1} \left( 1 - \left( \frac{P_{MC}}{P_{PC}} \right)^{\frac{\gamma-1}{\gamma}} \right) \right]^{\frac{1}{2}} \quad (8.3)$$

Estimating the mass flow rate requires information on discharge coefficient and the specific heat capacity ratio ( $\gamma$ ), which depends on the mixture composition. Depending on the flow direction, the specific heat capacity ratio of the pre-chamber and main chamber needs to be employed. The pre-chamber mixture composition needs to be estimated with sufficient accuracy to calculate the rate of heat release in the pre-chamber. For these purposes, the 1-D GT-Power model is employed. The details of the GT-Power 1-D model and the procedure was explained in a previous publication (Hlaing et al. 2021).

### 8.2.3 1-D GT-Power Simulation Setup

The single-cylinder research engine is set up in GT-Power software (Fig. 8.4). Measured pre-chamber and main chamber pressure traces, valve lift profiles, fuel flow rates, and boundary conditions from the experiments are input into the model. The pre-chamber combustion process is modeled using the SI turbulence flame combustion model, as the pre-chamber combustion process involves mainly flame propagation. For the main chamber, the jet ignition combustion model is employed, which accounts for the entrainment rate of the main chamber charge into the pre-chamber jets, similar to a diesel combustion model. The jet ignition model was developed by Wenig et al. (2019; Wenig and Roggendorf 2019).

Both chambers are simulated in “heat release-based calibration mode”, where the apparent heat release rates were extracted from the measured pressure traces and applied to the prediction of combustion progress in the two chambers. Instantaneous intake and exhaust pressure traces were also entered as model inputs to ensure that the pressure values matched the experiments and simulation during the gas exchange period. The fuel injection process into the pre-chamber is mimicked by using a check valve template. The flow rate table acquired by the manufacturer is provided to the template. The model parameters are calibrated to match the pressure traces between the simulation and experiments. The discharge coefficient through the pre-chamber nozzle is adjusted to capture the pre-chamber pressure buildup from the experiments. The model outputs, such as the mixture compositions, mass flow rate between the two chambers, and gas temperatures, are used in the heat release rate calculation, as mentioned in the previous section.

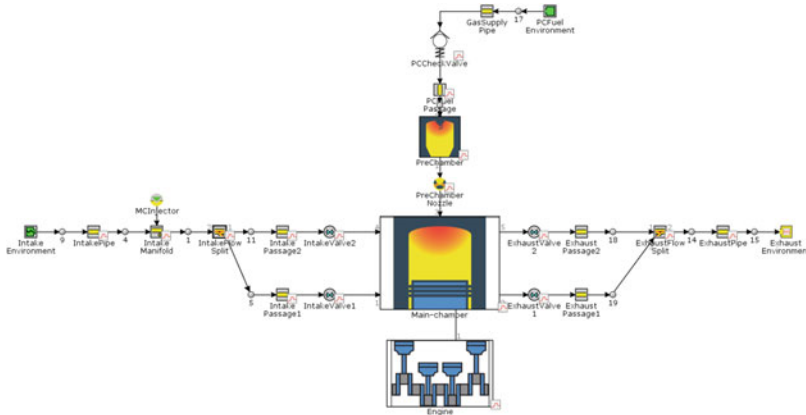


Fig. 8.4 GT-Power™ pre-chamber engine model

### 8.3 Pre-chamber Combustion

The in-cylinder process related to pre-chamber assisted combustion is complex because, in addition to the in-cylinder flow motions, thermal and fuel mass gradients across the two chambers greatly affect the ignition process. Also, the coupling between the PC and MC affects the ignition and flame propagation processes (Maurel et al. 1996). The pressure data from the PC and MC leave a lot of speculations about the coupling. Therefore, the interaction between the PC and MC is better understood using optical engine experiments. This section reports the gas exchange and dynamics of PCC using high-speed imaging and laser diagnostics.

The high-speed imaging offers a cycle resolved insight into the combustion process. At the same time, laser diagnostics-based studies allow spatially and temporally resolved visualization of in-cylinder phenomena such as velocity fields, chemical species, and combustion inside dense media like sprays or jets. The high-speed imaging measurements presented here are excited OH radical (OH\*) chemiluminescence or flame luminosity measurements. OH\* is considered representative of the in-cylinder high-temperature reaction location as it is critical intermediate species both formed and consumed during the process (Aleiferis et al. 2004). The laser-based diagnostics of the PCC concept in engines are limited to fuel tracer-based planer laser-induced fluorescence (PLIF) imaging (Müller et al. 2010; Tang et al. 2021, 2020; Sampath et al. 2020). These studies rely on the negative PLIF technique where the burning PC jets are visualized as a silhouette. This technique is used to observe PC jet interaction with unburned MC fuel. However, the internal flame structure of the jets remains unexplored, and most of the information available in the literature is based on radical imaging.

PLIF-based techniques are limited to snapshot imaging of one CAD per cycle due to the available combinations of ICCD cameras and low lasers repetition rates (10 Hz) during the experiments. The low repetition rate and high cyclic variability

of spark-initiated combustion make it difficult to follow the whole process. Particle image velocimetry (PIV) uses laser pulses (at a wavelength of 532 nm), and Mie scatters image pairs in quick succession ( $\delta t$  of 0.2 to 15  $\mu\text{s}$ ) to generate a quantitative in-cylinder velocity flow field. PIV calculates the velocity fields by correlating two Mie scatter images of particles seeded into the air inflow of the MC (Agarwal et al. 2017). Therefore, PIV captures the in-cylinder velocities, while PLIF identifies the combustion zones. The gas exchange process is best captured using PIV as combustion is not involved in the early part. The next section reports flow fields associated with PCC.

### 8.3.1 Gas/Mass Exchange—Mixture Formation Process Inside Pre-chamber

The gas/mass exchange between PC and MC involves both in and outflow of mass from the PC. Most of the studies inject fuel into PC during the intake or early compression stroke. Malé et al., in a large eddy simulation (LES) study of pre-chamber ignition, report the decrease in PC- $\lambda$  during the fuel injection followed by an increase after the injection stops (Malé et al. 2019). The studies reported in this work rely on a check valve and solenoid combination for PC fuel injection starting at 360 CAD bTDC.

The mass interaction between the PC and MC for the narrow throat PC occurs through two rows of orifices shown in Fig. 8.5. During the PC fuel injection process, the fuel moves into the MC due to the piston's downward motion or high injection pressures. This process is followed by PC mixture dilution due to the inflow of the lean MC into the PC when the piston is rising. The steps in the PC exchange process are:

- Pre-chamber fuel injection (intake stroke)
- Pre-chamber mixture dilution (compression stroke)
- Reactive jet expulsion into the main chamber (combustion in late compression stroke).

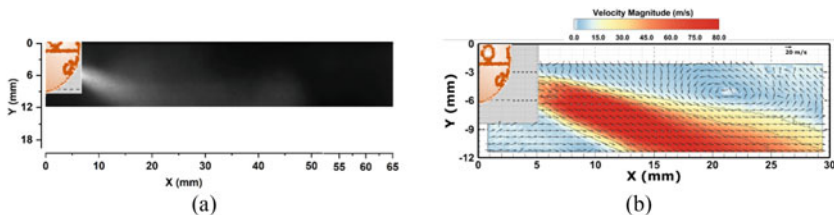


**Fig. 8.5** Shows **a** pre-chamber fuel tracer PLIF and **b** PIV ( $\delta t = 1 \mu\text{sec}$ ) images of the main chamber during the pre-chamber fuel injection process at -348 CAD aTDC



### 8.3.2 Pre-chamber Fuel Injection

The fuel injected into the PC during intake stroke leaks into the MC, and this mass exchange is driven by the pressure difference between injection pressure and the MC (Malé et al. 2019; Rajasegar et al. 2021). The fuel injected into the PC can be visualized using fuel tracer planer laser-induced fluorescence (PLIF). Acetone mixed with methane (10% n/n) is injected into the PC, and a laser sheet at the wavelength of 266 nm excites acetone in the fuel. Acetone fluorescence in the 300–500 nm range is recorded using an intensified camera (Fig. 5a). Figure 8.5a, b are PLIF and PIV measurements recorded at -348 CAD aTDC. The fuel injected into the PC appear as a jet in MC. The fuel jet mixes with the MC charge, causing enrichment of the MC.

### 8.3.3 Pre-chamber Mixture Dilution

As the piston moves towards TDC during the compression stroke, the MC charge starts to flow into the PC. The flow field measurements using PIV show that this flow occurs through the top row of nozzle orifices (Fig. 8.6). TiO<sub>2</sub> particles are seeded

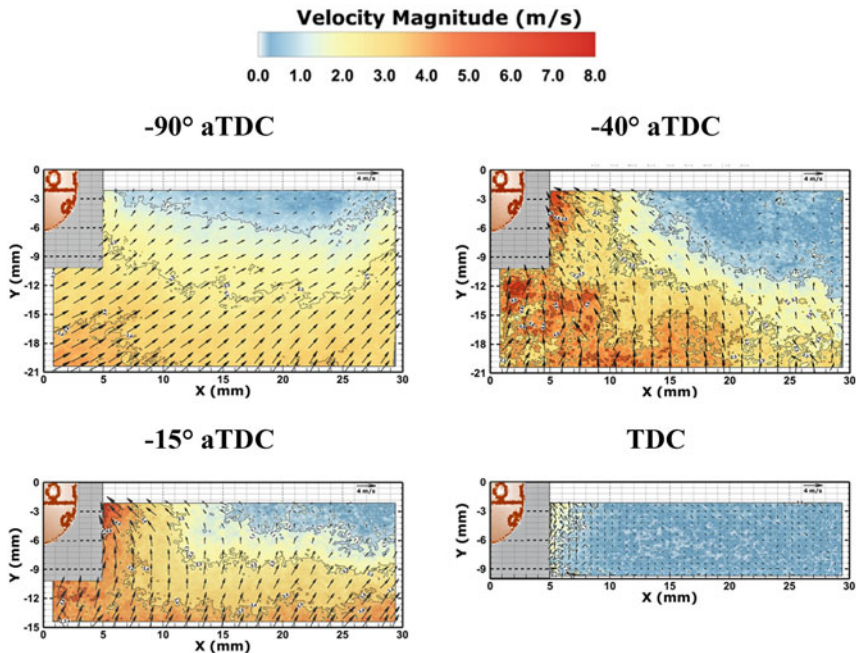
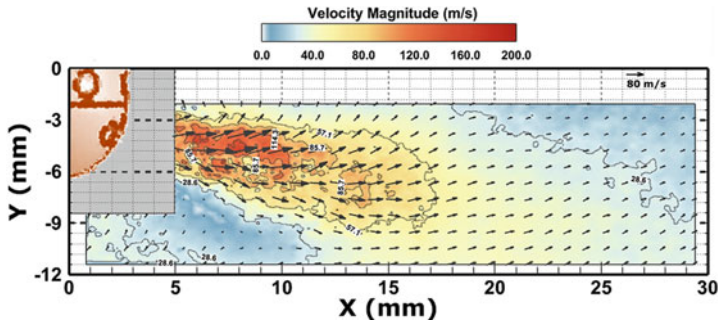


Fig. 8.6 Shows the zoomed motoring (without spark) flow field close to pre-chamber orifices measured using PIV ( $\delta t = 1 \mu\text{sec}$ )



**Fig. 8.7** Shows the pre-chamber jet velocity flow field measured ( $4^\circ$  CAD after spark) using PIV ( $\delta t = 0.3 \mu\text{sec}$ )

with a flow rate of 50 l/h at 5 bar using LaVision Particle blaster. On exposure to the laser sheet from the Litron nano PIV laser, these particles lead to Mie scattering, which is captured using the LaVision Imager ProX. The laser sheet hits directly on the PC nozzle, which produces intense scatter around the nozzle. Therefore, the flow fields closer to the PC nozzle ( $\sim 5$  mm) could not be resolved and are grayed out in the PIV images presented. The PC to MC flow velocity increases as the piston moves closed to TDC. Between  $-40$  and  $-15$  CAD aTDC, the inflow velocity is around 5 to 6 m/s. Beyond  $-15$  CAD aTDC, the velocity reduces, suggesting this flow to be directly correlated to piston speed.

### 8.3.4 Reactive Jet Expulsion into the Main Chamber

Figure 8.7 shows the typical velocity flow field of the PC jet at 4 CAD after the spark with PC only fueling. The jet is emitted from the lower PC nozzle orifices. The outer zone of the jet exhibit velocities 40 to 80 m/s, while inside the jet, velocities higher than 100 m/s are observed. The high velocities close to the nozzle orifice drop as the jet grows into the MC. The jet growth generates an entrainment motion affecting the flow field throughout the PC.

### 8.3.5 Pre-chamber Combustion Dynamics

The PCC process is driven by the PC jets that ignite the main chamber charge, and it is crucial to understand the behavior of the jets. Figure 8.8 shows the PC jets evolution without fuel addition into the MC and the respective pressure traces. The pre- and main chamber pressures were referenced to the measured absolute intake pressure at IVC. Side view images correspond to the PLIF of a fuel tracer (acetone), and the bottom view corresponds to  $\text{OH}^*$  chemiluminescence (Tang et al. 2021). The

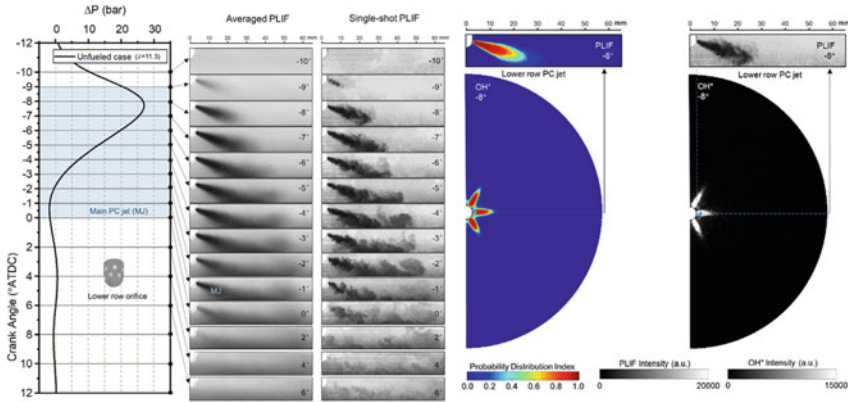


**Fig. 8.8** Pre-chamber combustion without main chamber fuel addition: Pressure difference, Averaged PLIF images (over 90 cycles), typical PLIF, and OH\* Chemiluminescence (Engine speed = 1200 rpm, Intake temperature = 30 °C, Intake pressure = 1.0 bar) (Tang et al. 2021)

pressure difference between the PC and MC ( $\Delta P$ ) increases at -12 CAD aTDC, 3 CAD after the spark timing. The first evidence of jets is at -9 CAD aTDC when a tiny jet comes out from the bottom nozzle holes. As the jet grows, the  $\Delta P$  reaches its maximum around -7.5 CAD aTDC. The PC discharge process finishes at -2 CAD aTDC, and at that point, there is still evidence of outflow from the PC. It should be stated that the first outflow from the PC is a non-reacting jet caused by the expanding gases of the combustion inside the PC that displaces the unreacted air-fuel mixture. Then, when the reacting jet comes out from the nozzle, it is shorter than the total jet, as shown in Fig. 8.8.

After studying the only PC combustion case, the entire combustion process of the narrow throat PC is described in Fig. 8.9. The reported condition corresponds to global lambda of 1.6 and 9% PCFR (Echeverri Marquez et al. 2020). The PC pressure increases around 3 CAD after spark timing, becoming higher than the main chamber pressure until its maximum pressure at -8 CAD aTDC. This process is equivalent to observations of the only PC combustion case.

The first evidence of six reacting PC jets is observed in the main chamber at -8 CAD aTDC, in terms of visible light. Those jets correspond to the bottom nozzle holes. The reacting jets grow and penetrate during the PC discharge. The growth rate of the reacting jets is bigger compared to the case without main chamber fuel. Around -5 CAD aTDC, some evidence of combustion appears at the top nozzle holes with some tiny jets. These tiny jets merge with the bottom jets and create a spherical flame front that spreads from the center. At TDC, the combustion process is mainly located in the bowl and the spherical flame front, and the reacting jets have already mixed. Then, the combustion arrives at the squish zone, and the main chamber pressure reaches its maximum. The combustion has predominant reddish and orangish tonalities, different from the early combustion stage, where the dominant color was blue.

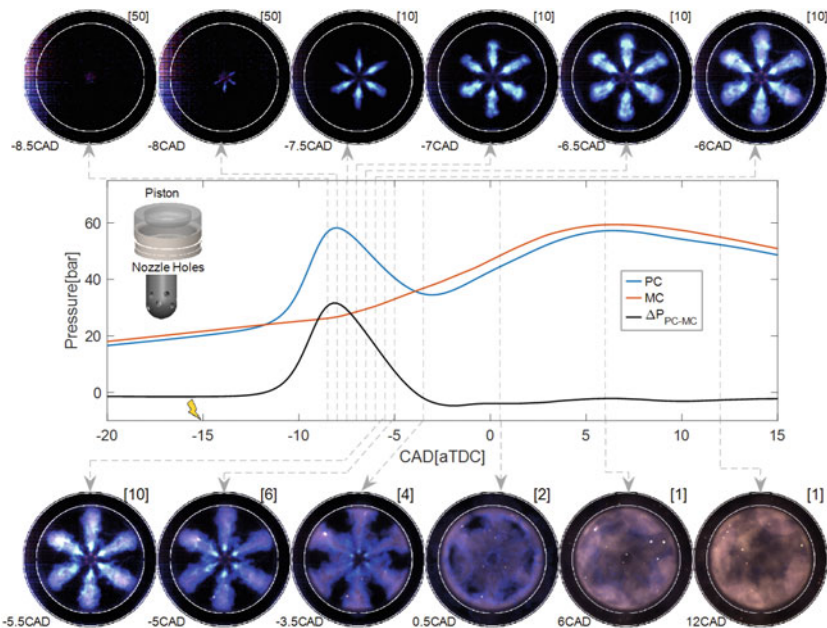


**Fig. 8.9** Evolution of a single cycle of a narrow throat active pre-chamber. Images gain have been adjusted for each image for illustration purposes, and it is reported on the right top of each image (Engine speed = 1200 rpm, Intake temperature = 30 °C, Intake pressure = 1.0 bar)

The narrow throat PC combustion in the main chamber could be schematized, as shown in Fig. 8.10. The first stage is characterized by the emergence of small jets from the bottom nozzle holes (red jets in Fig. 8.10). Those jets grow and penetrate the combustion chamber bowl. Then, tiny jets come out from the top nozzle holes (orange in Fig. 8.10). These top jets merge with the already existing bottom jets in the center, creating a spherical flame front (4 in Fig. 8.10). Finally, the bottom jets

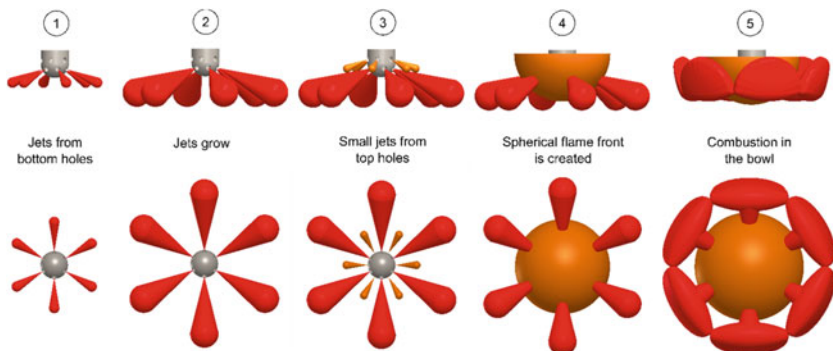


**Fig. 8.10** Combustion for narrow throat pre-chamber combustion

reach the bowl wall, and they spread out along the bowl edge at the same time. The spherical flame front grows from the center of the chamber, and together with the jets, they cover the total of the bowl and finally penetrate the squish volume.

The narrow-throat combustion process has a different development compared to other pre-chamber concepts. Rajasegar et al. observed simultaneous reacting jets from all the eight existing nozzle holes. In that case, the jets merge and create a hollow cone geometry (Rajasegar et al. 2021). Similar observations have been reported by Toulson et al. where the main chamber combustion is mainly propagated by the PC jets (Toulson et al. 2012). It is important to remember the main geometrical difference between the narrow throat PC and the PCs used by Rajasegar et al. (2021) and Toulson et al. (2012). Their geometries have a wide throat and only one row of nozzle holes. In this sense, we can conclude that the PC internal geometry has an important role in pre-chamber combustion.

## 8.4 Effect of Fuel Enrichment

The level of fuel-enrichment in the PC, indicated by the PC- $\lambda$ , is important in extending the lean limit of the engine, as mentioned in the introduction section. The effect of PC fuel enrichment was studied in metal engine experiments (Hlaing et al. 2020), and the jet characteristics were investigated in the optical PC engine (Echeverri Marquez et al. 2020).

### 8.4.1 Operating Conditions

The effect of PC- $\lambda$  is demonstrated by performing global- $\lambda$  sweeps at three different pre-chamber fuel mean effective pressure (FuelMEP) ratio, PCFR, which indicates the fraction of fuel energy injected through the PC. The PCFR is defined as follows.

$$PCFR = \frac{FuelMEP_{PC}}{FuelMEP_{PC} + FuelMEP_{MC}} \times 100\% \quad (8.4)$$

The FuelMEPs for the two chambers are calculated as below.

$$FuelMEP_{PC,MC} = \frac{mass\ of\ fuel_{PC,MC} \times LHV\ of\ Fuel}{Engine\ Displacement\ Volume} \quad (8.5)$$

The detailed engine setup and experiment conditions can be found in a previous publication (Hlaing et al. 2020). Methane (CH<sub>4</sub>) of 99.5% purity was used for both the PC and MC, and the start of fuel injection (SOI) was fixed at -360 CAD aTDC. Three levels of PCFR were assessed, and the global- $\lambda$  sweeps were performed from 1.6 until the lean limit. The lean limit is defined as the global- $\lambda$  at which the coefficient

of variation of gross indicated mean effective pressure (CoV of IMEP<sub>g</sub>) exceeds 5%. The spark timing is adjusted to provide the highest brake torque output from the engine at each operating condition.

### 8.4.2 Lean Limit Extension

Pre-chamber fuel addition is crucial for combustion stability and the lean limit extension. Therefore, a comparison of the two extreme cases, i.e., passive and active PC, explains the underlying cause of such dependence on PC fueling. Figure 8.11 presents a comparison based on the Average Flame Probability Distribution (AFPD) between an active and a passive PC. The AFPD is the spatial probability of combustion, ranging from zero to one for no combustion and combustion, respectively (Olsen and Lisowski 2009). In this case, the AFPD is calculated from the flame chemiluminescence images taken through the bottom of an optical engine combustion chamber

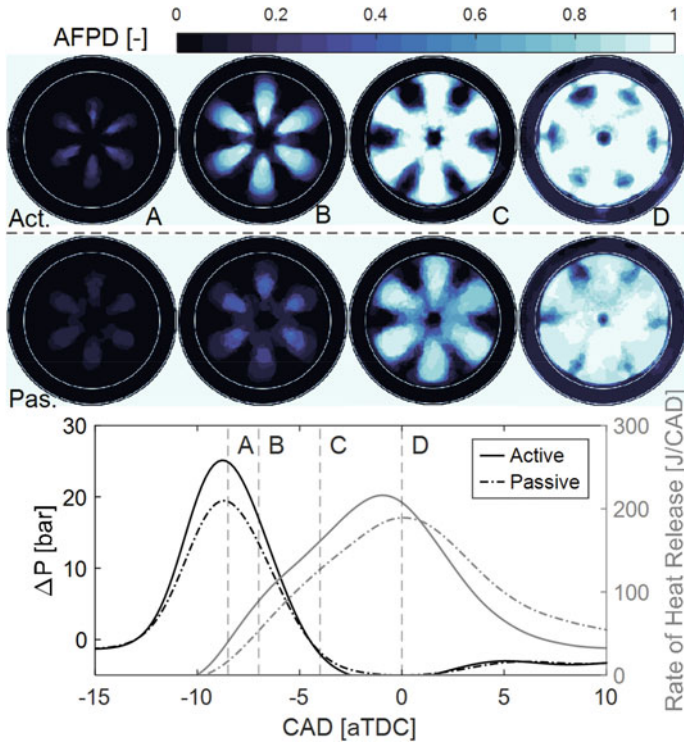


**Fig. 8.11** Average flame probability distribution for active and passive pre-chamber combustion (Engine speed = 1200 rpm, Intake temperature = 30 °C, Intake pressure = 1.0 bar, FuelMEP = 21 bar)



(Kar et al. 2010). The passive PC jets exhibit unstable behavior, which is apparent from the lower AFPD along with the PC discharge. The lower combustion zone probability in the passive PC reacting jet case leads to lower PC pressure and a consequent lower main chamber pressure.

In contrast, the active PC jets show a more homogeneous spread throughout the MC. The homogeneity of combustion in active PC leads to a larger number of ignition sites in the MC, leading to longer sustained combustion in the MC, even with lean mixtures. Therefore, the amount of fuel added to the PC determines the lean limit extension.

A more detailed study on the effect of PCFR using the metal engine strengthens the earlier conclusion that higher PCFR allows an extended lean limit (Fig. 8.12). Although the PCFR affects the maximum pressure buildup in the PC, no obvious impact on the engine gross IMEP is observed. In Fig. 12d, the PC- $\lambda$  predicted by

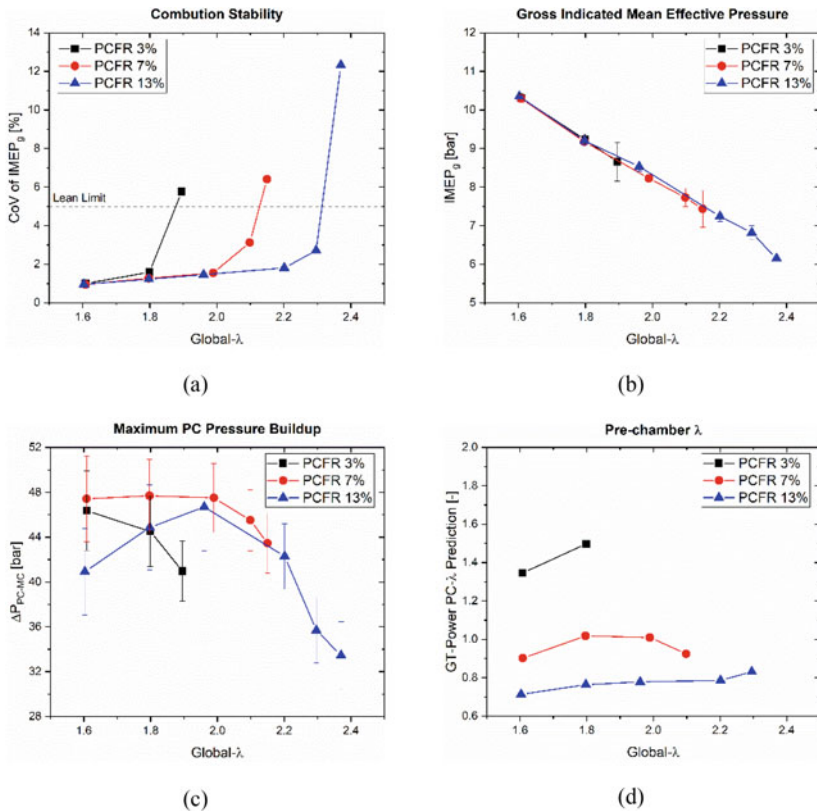


**Fig. 8.12** Effect of pre-chamber enrichment on **a** combustion stability, **b** gross IMEP, **c** maximum pressure buildup in pre-chamber, and **d** pre-chamber excess air ratio apart from the data points beyond the lean limit (Engine speed = 1200 rpm, Intake temperature = 30 °C, Intake pressure = 1.5 bar)

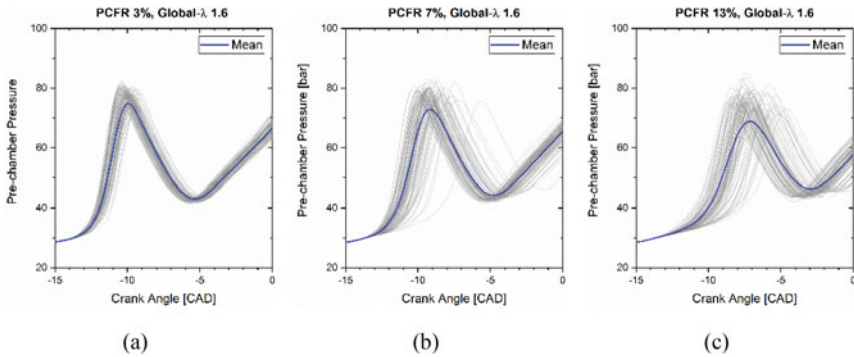


**Fig. 8.13** Pre-chamber pressure buildup for 100 cycles at global- $\lambda$  1.8 and PCFR **a** 3%, **b** 7%, and **c** 13% (Engine speed = 1200 rpm, Intake temperature = 30 °C, Intake pressure = 1.5 bar)

the GT-Power is illustrated. The predicted PC- $\lambda$  values correlate well with the pre-chamber pressure buildup as near stoichiometric pre-chamber mixtures show the highest pressure buildup.

Note that the pre-chamber pressure buildup range is 30–50 bar for the narrow-throat PC configuration, which is significantly higher than the conventional PC designs with reasonable throat diameter. In contrast, Mahle’s turbulent jet igniter shows around 20 bar pressure buildup, similar to the value that Shah et al. and Vedula et al. observed in their investigations (Bunce et al. 2014; Shah 2015; Vedula et al. 2017).

In Fig. 8.13, the mean PC pressure traces are plotted over 100-cycles data for three PCFR conditions at global- $\lambda$  1.6. The cycle-to-cycle variation of PC pressure increases with increasing PCFR. The PCFR 13% cases show the widest variation, although the instability does not affect the main chamber combustion stability, as observed in Fig. 13a.

### 8.4.3 Engine-Out Emissions and Efficiency

Figure 14a reports the specific emissions for NO<sub>x</sub>, CO, and unburned hydrocarbons. The emissions follow trends similar to gross IMEP with no discernible effect of the PC fuel enrichment. Subsequently, the efficiency parameters also do not exhibit significant dependence on PCFR, as shown in Fig. 14b.

However, reduction in global- $\lambda$  increases the specific NO<sub>x</sub> emissions, which can be attributed to higher combustion gas temperatures. In contrast, approaching the lean limit leads to excessive specific CO and HC emissions. This trend suggests a reduction in combustion efficiency due to poor utilization of injected fuel close to the lean limit. The combustion efficiency is calculated from exhaust emission analysis as follows:



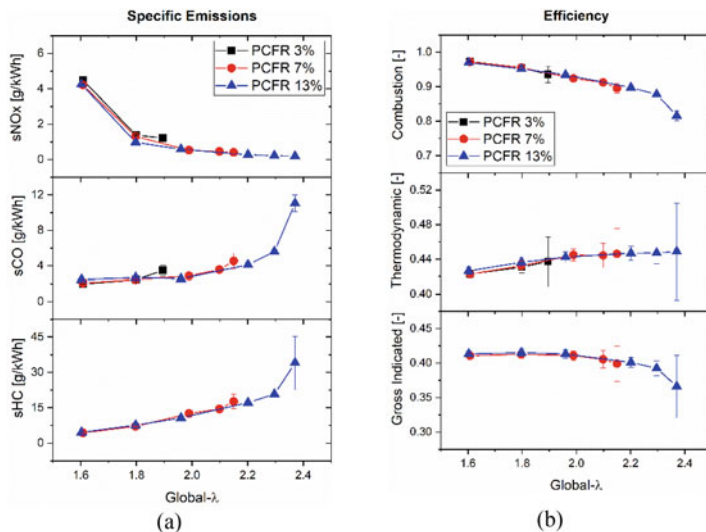


**Fig. 8.14** Engine-out emissions and engine efficiencies: **a** specific  $\text{NO}_x$ , CO, and HC emissions, and **b** combustion, thermodynamic and gross indicated efficiencies (Engine speed = 1200 rpm, Intake temperature = 30 °C, Intake pressure = 1.5 bar)

$$\eta_{comb} = 1 - \frac{m_{HC} Q_{LHV,HC} + m_{CO} Q_{LHV,CO} + m_{H_2} Q_{LHV,H_2}}{m_f Q_{LHV,f}} \quad (8.6)$$

The lower heating value (LHV) of unburned hydrocarbon emissions is assumed to be the same as the fuel injected into the engine. In the case that the MC fuel is different from PC, the mass-averaged lower heating value is used.

Operating in the ultra-lean region ( $\text{global-}\lambda > 2$ ) yields lower combustion gas temperature with less dissociation of  $\text{CO}_2$  and  $\text{H}_2\text{O}$ , which leads to a higher specific heat capacity ratio ( $\gamma$ ) (Heywood 1998). Hence, the thermodynamic efficiency improves as the  $\text{global-}\lambda$  becomes leaner, along with reduction in heat transfer losses. Peak gross indicated efficiency is observed around  $\text{global-}\lambda$  1.8. The thermodynamic and the gross indicated efficiency are calculated using the equations shown below.

$$\eta_{therm} = \frac{IMEP_g}{QMEP} = \frac{IMEP_g}{\eta_{comb} \times (FuelMEP_{PC} + FuelMEP_{MC})} \quad (8.7)$$

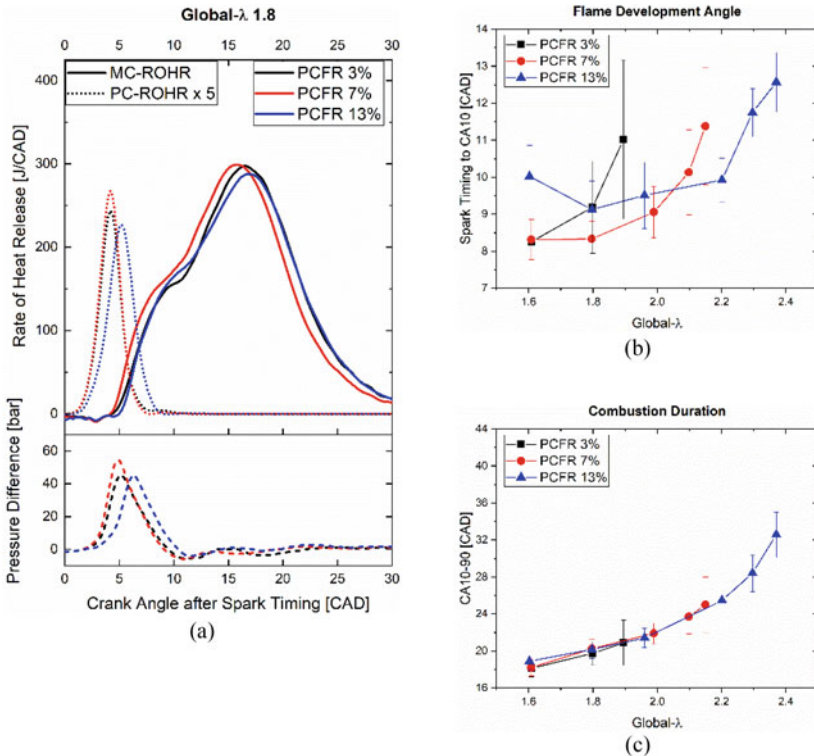
$$\eta_{gross\ indicated} = \frac{IMEP_g}{(FuelMEP_{PC} + FuelMEP_{MC})} \quad (8.8)$$

By definition, the thermodynamic efficiency ( $\eta_{therm}$ ) is a ratio between gross indicated efficiency and combustion efficiency. The efficiency is improved when the heat transfer losses and/or exhaust losses are reduced (Christensen et al. 1999; Manente et al. 2010).

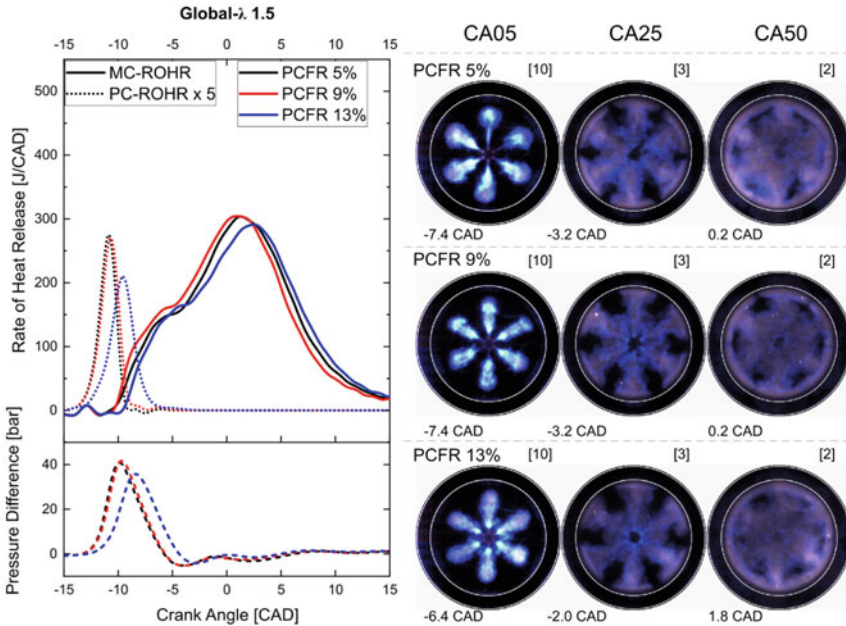
### 8.4.4 Heat Release Characteristics

Figure 8.15a shows that the PC and MC heat release rate is plotted for the global- $\lambda$  1.8 cases. The PC heat release rate profile is Gaussian in shape, while the MC heat release shows distinct two-stage heat release profiles. The PCFR 7% cases are predicted to have near stoichiometric PC- $\lambda$ . These cases show an earlier and faster rate of heat release in the PC. Consequently, the MC heat release rate rises earlier than the other cases. As shown in Fig. 8.15b, the PCFR 3% and 13% case shows a considerable delay between the spark timing and the start of heat release in the PC. Despite the delay, the MC heat release rate is comparable between the three PCFR cases, and the combustion durations are almost identical, as indicated in Fig. 15c.

An analogous study of the fuel enrichment effect in the optical engine shows a similar combustion trend. The earlier reported metal engine's study of PCFR effect on engine performance (Fig. 8.15) is re-examined optically to understand the jet behavior and its effect on MC combustion. The combustion process at PCFR 5, 9 and



**Fig. 8.15** Effect of pre-chamber enrichment on heat release characteristics: **a** rate of heat release in pre-chamber and main chamber, **b** flame development angle, and **c** combustion duration CA10-90 (Engine speed = 1200 rpm, Intake temperature = 30 °C, Intake pressure = 1.5 bar)



**Fig. 8.16** Effect of pre-chamber enrichment on heat release characteristics: rate of heat release in pre-chamber and main chamber, Pressure difference, and CA05, CA25, and CA50 images. Image gains have been adjusted for each image for illustration purposes, and it is reported on the right top of each image (Engine speed = 1200 rpm, Intake temperature = 30 °C, Intake pressure = 1.0 bar)

13% is recorded using high-speed imaging and is depicted in Fig. 8.16 along with the heat release. The spatial and temporal information about the effect of PCFR variation on the combustion process reinforces the conclusions from the metal engine study. The PC- $\lambda$  for the PCFR 9% case is slightly rich, and it presents stronger reacting jets at the early stages (CA05) of the main chamber combustion than the PCFR 5%. This observation agrees with the faster rate of heat release for that case. In this experiment, the delay of the PCFR 13% case is also present. However, this case exhibited stronger reacting jets at CA05 and an earlier appearance of the top jets. After the emergence of the PC jet, the main chamber combustion develops similarly for the three cases as it could be observed in CA25 and CA50.

### 8.4.5 Conclusions

Global parameters, such as emissions, engine performance measures, and overall combustion duration, were insensitive to PC fuel enrichment. Fuel-rich PCs tend to improve combustion stability for all tested global- $\lambda$  cases. Fuel enrichment is crucial in lean limit enhancements, and mainly, it modifies the characteristics of the jet, with

stronger jets for the richer conditions. However, near the lean limit, the unburned hydrocarbon emissions and carbon monoxide emissions became excessive, which led to a dramatic decline in combustion efficiency. The peak gross indicated efficiency is found at global- $\lambda$  1.8, which is around 41%.

## 8.5 Performance Assessment of PCC with Liquid Fuels

With the necessity of enriched air-fuel mixture in the PC being demonstrated for effective lean limit extension, the next step was to investigate the performance of PCC with different fuels. The PCC concept was proven to be suitable with various fuels, including hydrogen (Kyaw and Watson 1992), propane (Gentz and Toulson 2016; Toulson et al. 2012), natural gas (Olsen and Lisowski 2009; Wenig and Roggendorf 2019), ethanol (Bureshaid et al. 2019; da Costa et al. 2019), and conventional gasoline (Cooper et al. 2020; Zhang et al. 2020). However, injecting the liquid fuels into the PC requires a specialized injector with a sufficiently low flow rate and good fuel atomization. In the absence of such an injector, the PC was continued to be fuelled with methane.

### 8.5.1 Operating Conditions

For the most part, the operating conditions were similar to the previous experiments except that liquid fuels were injected into the MC via the air intake. An automotive fuel supply system was employed for the MC. The fuel flow rate was measured by a Coriolis mass flow meter. The engine setup, methodology, and operating conditions can be found in a previous publication (Hlaing et al. 2021).

The MC fuel injecting timing was set at 20 CAD after IVC to maximize fuel vaporization. The fuel injection, soon after the IVC, exposed the fuel to the high-temperature area of the intake valves which were closed so that the fuel was exposed to a high-temperature environment in the cylinder head. The temperature assisted in fuel vaporization before the intake valves opened again for the suction stroke. Such pre-heating of the fuel could result in improved homogeneity of the MC charge. Initial tests revealed that this method of fuel injection could dramatically reduce unburned hydrocarbon emissions.

A knock limit was set at 10 bar since excessive knock intensities were observed with some fuels. However, the experiments focused on low to mid load, which allows for a high knock limit setting to investigate the knocking process in a PCC engine. The knock intensities were calculated by the bandpass filtration of the MC pressure signal between 4 and 17 kHz. The values were cross-checked with the results from the maximum amplitude of pressure oscillations (MAPO) results. Compared to a conventional SI engine, the assigned knock intensity limit is particularly high. For fuels that are not knocked-limited, the lowest global- $\lambda$  studies were 1.6, and global- $\lambda$ .

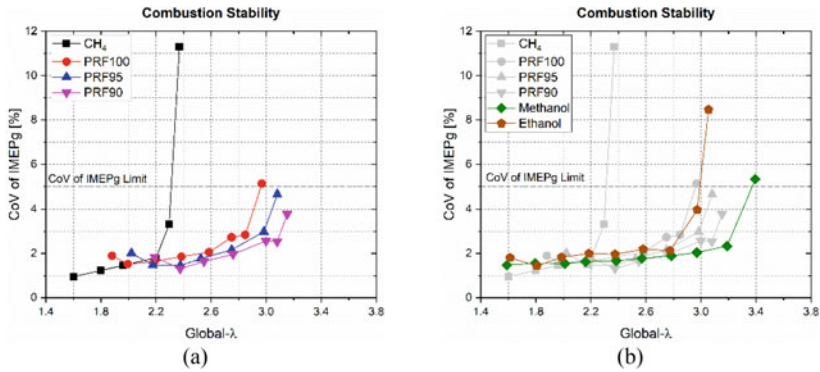


**Fig. 8.17** Combustion stability plots highlighting **a** CH<sub>4</sub> and PRFs, and **b** alcohols (Engine speed = 1200 rpm, Intake temperature = 30 °C, Intake pressure = 1.5 bar)

was increased progressively until the lean limit was reached. The PCFR was fixed at 13% throughout the studies since the highest lean limit was achieved with this PCFR.

### 8.5.2 Enhanced Lean Limit

The previous methane data is plotted along with the liquid fuel results for comparison. The graphs are divided into two groups: the first features fuels without sensitivity ( $S = RON - MON$ ) and the second, alcohols, which have fuel sensitivity.

As shown in Fig. 8.17, deploying liquid fuels in the MC shows a significantly enhanced lean operation limit at global-λ 3.0, with methanol fuel having a lean limit at global-λ 3.4. From Fig. 8.17a, operating with a lower RON fuel can improve the lean limit. The alcohols have a significantly faster laminar flame speed, which may contribute to the lean limit extension.

### 8.5.3 Excessive Knock Intensities

With the PRFs, the knock intensities were excessive, and the knock limit was reached around global-λ 2. The alcohols show considerably higher knock intensities than methane but much lower than the PRFs. Methanol and ethanol have RON values of 106 and 107, respectively. However, the knock intensities between these two fuels and the PRFs are sufficiently different to be justified solely by the difference in research octane number. Therefore, the fuel sensitivities associated with the alcohols appear to be beneficial in knock avoidance (Fig. 8.18).

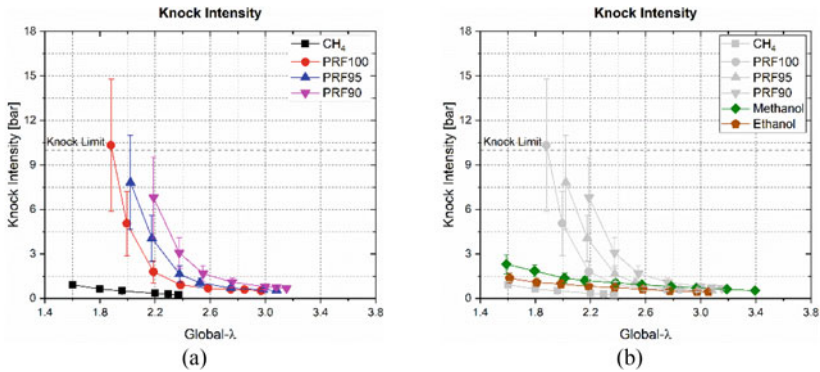


**Fig. 8.18** Knock intensities plot highlighting **a** CH<sub>4</sub> and PRFs, and **b** alcohols (Engine speed = 1200 rpm, Intake temperature = 30 °C, Intake pressure = 1.5 bar)

The heat release profiles of PRFs show a distinct end gas auto-ignition event. This is illustrated in Fig. 8.19 through PC and MC rate of heat release plots for methanol and PRF100. In addition to the two-stage MC heat release profile, PRF100 shows a significant rise in heat release rate towards the end of the combustion process. The end gas auto-ignition part declines as the global- $\lambda$  increases. On the contrary, the end

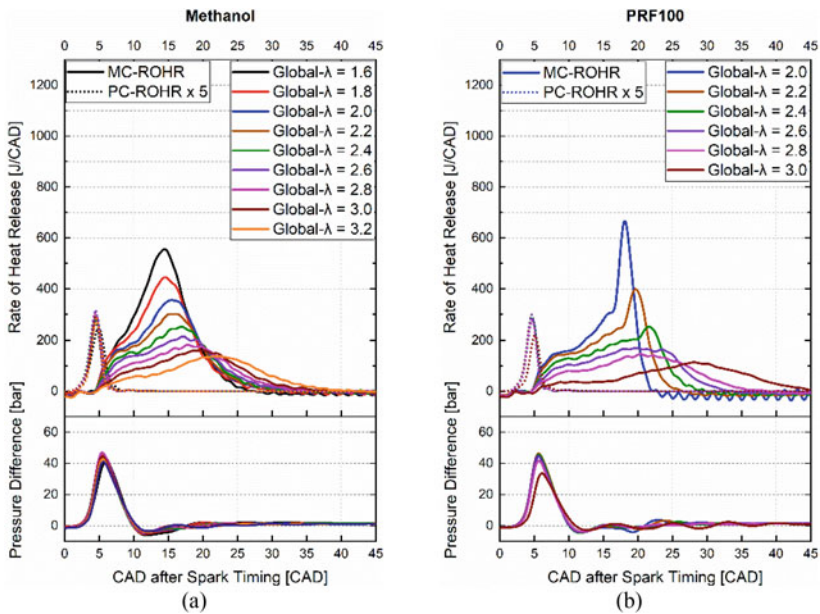


**Fig. 8.19** Rate of heat release for the main chamber, pre-chamber, along with pressure buildup in the pre-chamber: **a** methanol and **b** PRF100 (Engine speed = 1200 rpm, Intake temperature = 30 °C, Intake pressure = 1.5 bar)

gas auto-ignition part is not detected with methanol at any global- $\lambda$ , possibly due to low knock intensities of methanol.

### 8.5.4 Emissions

In general, the emission trends are similar to the methane results, with specific  $\text{NO}_x$  becoming excessive as the global- $\lambda$  is reduced and specific CO and HC emissions increase with leaner global- $\lambda$ . The alcohols have a lower calorific value than other fuels, and the mass of fuel injected is much higher. Subsequently, heightened specific HC and CO emissions for these fuels incur a combustion efficiency penalty, especially for ethanol.

Note that a FID analyzer was used for measuring the unburned hydrocarbon emissions. From the literature review, a FID underestimates the concentration of unburned fuels in the exhaust due to the presence of oxygenates when the engine is fueled with alcohol (Gabele et al. 1985; Kar and Cheng 2010). Therefore, the actual unburned hydrocarbon fuels would be expected to be higher than the FID measurements presented in Fig. 20b.

### 8.5.5 Efficiency

The combustion efficiency of liquid fuels is comparatively higher than that of methane which is a slow-burning fuel. However, combustion efficiency improvement with ethanol is scarce, while methanol maintains combustion efficiency above 90% across a wide range of global- $\lambda$ . Apart from global- $\lambda$ s close to the lean limit, the PRFs show good combustion efficiency above 95% until global- $\lambda$  2.6.

Due to excessive knock intensities, the gross indicated efficiency of the PRFs suffers near the knock limit. However, as the global- $\lambda$  increases, the heat transfer losses are reduced, and the gross indicated efficiency improves. For the PRFs, the global- $\lambda$  at which the peak gross indicated efficiency is observed becomes leaner with lower RON. Due to its high combustion efficiency, methanol achieves a gross indicated efficiency of 43%, equivalent to the peak value of the PRFs at around global- $\lambda$  2.2. Ethanol shows a considerably lower gross indicated efficiency compared to methanol due to the excessive combustion losses (Fig. 8.21).

### 8.5.6 Conclusion

The lean limit is extended to global- $\lambda$  3.0 with liquid fuels while the gross indicated efficiency is improved compared to methane, except for ethanol. For fuels with zero sensitivity, the lean limit is further extended with a lower octane rating. However,



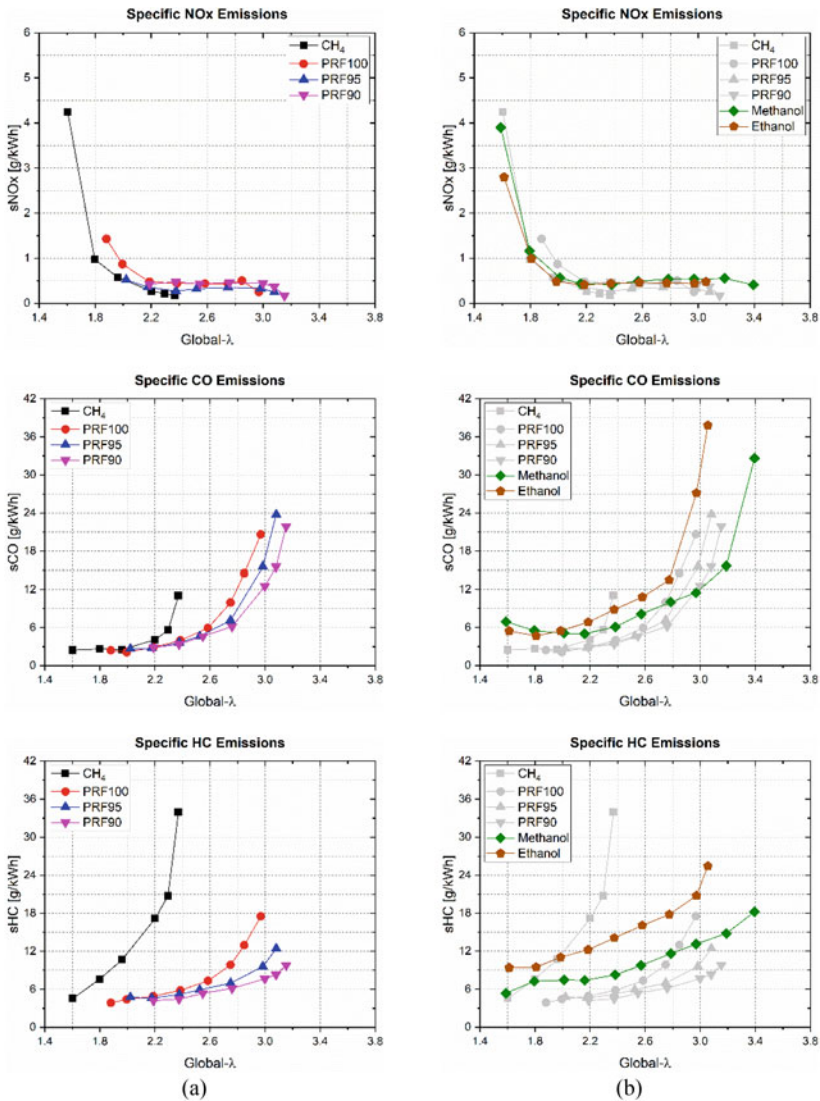


**Fig. 8.20** Specific emissions for **a** CH<sub>4</sub> and PRFs, and **b** alcohols (Engine speed = 1200 rpm, Intake temperature = 30 °C, Intake pressure = 1.5 bar)

the observation does not stand for fuels with non-zero sensitivity since methanol and ethanol exhibit a similar or higher lean limit than the PRFs, despite their RON values being higher than 100.

Moreover, excessive knock intensities are observed with the PRF fuels but not the alcohols. Inspecting the MC heat release rate in the PRFs reveals a prominent end gas auto-ignition near the combustion. For fuels showing lower knock intensity,



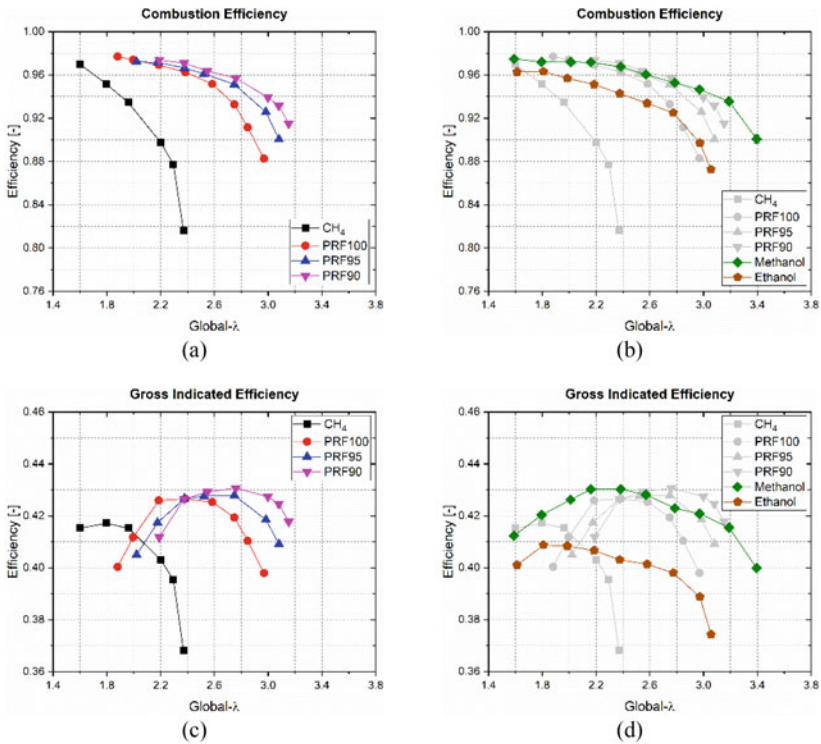


**Fig. 8.21** Efficiency: combustion efficiency for **a** CH<sub>4</sub> and PRFs, **b** alcohols, and gross indicated efficiency for **c** CH<sub>4</sub> and PRFs, **b** alcohols (Engine speed = 1200 rpm, Intake temperature = 30 °C, Intake pressure = 1.5 bar)

such as methanol and ethanol, the end gas auto-ignition part is not detected. Although the RON values of methanol and ethanol are only slightly higher than PRF100, the reduction in knock intensity is dramatic, indicating that the sensitivity of the fuel is important in knock avoidance.

The NO<sub>x</sub> emissions do not strongly depend on the MC fuel and are mostly dependent on global-λ. Ethanol shows high CO and HC emissions which led to the poor combustion efficiency of this fuel. Despite a slightly higher CO and HC emissions than the PRFs, methanol shows good combustion efficiency for a wide range of global-λ.

## 8.6 Summary

The lean limit extension capabilities of the narrow throat PC are promising in terms of both emission reduction and engine efficiency improvement. These capabilities are well showcased and established by numerous engine studies. However, the understanding of pre-chamber assisted combustion processes is still segmented with limited insight into the reacting jet—main chamber charge interaction and combustion inside the PC. Some of the key findings of the ongoing investigations are:

- The mixture formation inside the PC involves bi-directional interaction with the MC. Firstly, the fuel injected into the PC leaks into the MC enriching the MC mixture during the suction stroke. Subsequently, the MC mixture is pushed back into the PC during compression. This mixture's excess air ratio at spark timing controls the PCs' ability to ignite the lean MC mixture.
- The PC jet induces turbulence and generates multiple ignition sites in the MC. The positive difference between PC and MC pressure, generated by the PC combustion, is responsible for the jet penetration and turbulence increase. One of the major parameters controlling pre-chamber combustion is the excess air ratio at spark timing, hence the importance of the pre-chamber fuel addition and the mixing induced by the piston movement.
- There is a limited understanding of the PC jet composition as literature descriptions vary from radical to flame jet. The narrow throat PC ejects unreacted mixture initially after the start of combustion. This is followed by the shorter reacting jet appearance, which always lags the PC jet.
- The early jet behavior remains the same for MC fuelled and unfuelled cases. The jets from the six holes of the PC bottom row grow the fastest into the MC. These six jets grow wider by entraining the MC mixture and progress through the MC fast. In comparison, smaller jets from the top six holes are restricted close to the PC. Later, the jets from both rows merge circumferentially to produce an alternate spherical flame front.
- The PC fuel ratio offers a good estimate of the ignition capabilities of the PC. Fuel-rich PC leads to stable combustion even at high global- $\lambda$ . However, a more accurate estimate of mixture stratification inside the PC remains desirable.
- The emissions follow the conventional trade-off, where closer to stoichiometric global- $\lambda$  leads to high  $\text{NO}_x$  emissions, while closer to the lean limit, higher unburned HC and CO are produced due to increased quenching of the jets and ultimately, unstable combustion. The variation of the PC fueling ratio at fixed global- $\lambda$  does not show any significant response on emissions.
- The narrow throat PC can sustain controlled combustion with methane-like slow-burning fuel at global- $\lambda$  of 2.2. Even further, leaner engine operation at global- $\lambda$  of 3.4 is achievable with methanol.

- PRF fuels with PCC also exhibit an extended lean limit operation, but the excessive knock intensities are encountered even in ultra-lean operation ( $\text{global-}\lambda > 2.0$ ). Alcohols show higher knock resistance under PCC mode; methanol shows good combustion efficiencies across a wide range of  $\text{global-}\lambda$ .

**Acknowledgements** The work is supported by Saudi Aramco Research and Development Centre FUELCOM3 program under Master Research Agreement Number 6600024505/01. FUELCOM (Fuel Combustion for Advanced Engines) is a collaborative research undertaking between Saudi Aramco and King Abdullah University of Science and Technology (KAUST) to address the fundamental aspects of hydrocarbon fuel combustion in engines and develop fuel/engine design tools suitable for advanced combustion modes.

## References

- Agarwal AK, Gadekar S, Singh AP (2017) In-cylinder air-flow characteristics of different intake port geometries using tomographic PIV. *Phys Fluids* 29(9):095104. <https://doi.org/10.1063/1.5000725>
- Aleiferis PG, Hardalupas Y, Taylor AMKP, Ishii K, Urata Y (2004) Flame chemiluminescence studies of cyclic combustion variations and air-to-fuel ratio of the reacting mixture in a lean-burn stratified-charge spark-ignition engine. *Combust Flame* 136(1–2):72–90. <https://doi.org/10.1016/j.combustflame.2003.09.004>
- Alvarez CEC, Couto GE, Roso VR, Thiriet AB, Valle RM (2018) A review of prechamber ignition systems as lean combustion technology for SI engines. *Appl Therm Eng* 128:107–120. <https://doi.org/10.1016/j.applthermaleng.2017.08.118>
- Attard W, Blaxill H (2012) A lean burn gasoline fueled pre-chamber jet ignition combustion system achieving high efficiency and low  $\text{NO}_x$  at part load. <https://doi.org/10.4271/2012-01-1146>
- Biswas S (2018) Physics of turbulent jet ignition Sayan Biswas mechanisms and dynamics of ultra-lean combustion
- Bunce M, Blaxill H, Kulatilaka W, Jiang N (2014) The effects of turbulent jet characteristics on engine performance using a pre-chamber combustor. In: SAE 2014 World Congress and exhibition 1. <https://doi.org/10.4271/2014-01-1195>
- Bureshaid K, Shimura R, Feng D, Zhao H, Bunce M (2019) Experimental studies of the effect of ethanol auxiliary fueled turbulent jet ignition in an optical engine
- Christensen M, Hultqvist A, Johansson B (1999) Demonstrating the multi fuel capability of a homogeneous charge compression ignition engine with variable compression ratio. SAE Technical Papers, no. 724. <https://doi.org/10.4271/1999-01-3679>
- Cooper A, Harrington A, Bassett M, Reader S, Bunce M (2020) Application of the passive MAHLE jet ignition system and synergies with Miller cycle and exhaust gas recirculation. SAE Technical Papers 2020-April (April): 1–15. <https://doi.org/10.4271/2020-01-0283>
- da Costa RBR, Teixeira AF, Filho FAR, Pujatti FJP, Coronado CJR, Hernández JJ, Lora EES (2019) Development of a homogeneous charge pre-chamber torch ignition system for an SI engine fuelled with hydrous ethanol. *Appl Thermal Eng* 152(2018):261–74. <https://doi.org/10.1016/j.applthermaleng.2019.02.090>
- Dunn-Rankin D, Therkelsen P, Bradley D, Cheng RK, Dunn-Rankin D, Evans RL, Keller J et al (2016) Lean combustion. Lean combustion: technology and control, 2nd edn. Elsevier. <https://doi.org/10.1016/C2013-0-13446-0>
- Duong J, Andersson Ö, Hyvönen J, Álden M, Wellander R, Johansson B, Richter M (2014) High speed combustion imaging in a Large Bore Gas engine: the relationship between pre- and main

- chamber heat release. In: Heat transfer and thermal engineering, V08AT09A022, vol 8A. ASME. <https://doi.org/10.1115/imece2013-64286>
- Echeverri Marquez M, Hlaing P, Tang Q, Sampath R, Cenker E, Houidi MB, Magnotti G, Johansson B (2020) High-speed imaging of main chamber combustion of a narrow throat pre-chamber under lean conditions. In: SAE Technical Paper 2020-01-2081, vol 1. SAE International. <https://doi.org/10.4271/2020-01-2081>
- Gabele PA, Baugh JO, Black F, Snow R (1985) Characterization of emissions from vehicles using methanol and methanol-gasoline blended fuels. *J Air Pollut Control Assoc* 35(11):1168–1175. <https://doi.org/10.1080/00022470.1985.10466019>
- Gentz GR, Toulson E (2016) Experimental studies of a liquid propane auxiliary fueled turbulent jet igniter in a rapid compression machine. *SAE Int J Eng* 9(2):2016–01–0708. <https://doi.org/10.4271/2016-01-0708>
- Getzlaff J, Pape J, Gruenig C, Kuhnert D, Latsch R (2007) Investigations on pre-chamber spark plug with pilot injection 724:776–90. <https://doi.org/10.4271/2007-01-0479>
- Gussak LA, Karpov VP, Tikhonov YV (1979) The application of lag-process in prechamber engines. In: SAE Technical Papers, vol 1. SAE International. <https://doi.org/10.4271/790692>
- Gussak LA, Turkish MC, Sieglä DC (1975) High chemical activity of incomplete combustion products and a method of prechamber torch ignition for avalanche activation of combustion in internal combustion engines. In: SAE Technical Paper Series, vol 1. <https://doi.org/10.4271/750890>
- Heywood JB (1998) Internal combustion engine fundamentals. McGraw-Hill
- Hlaing P, Marquez ME, Shankar VSB, Cenker E, Houidi MB, Johansson B (2019) A study of lean burn pre-chamber concept in a heavy duty engine. SAE Tech Paper Series 1:1–13. <https://doi.org/10.4271/2019-24-0107>
- Hlaing P, Marquez ME, Burgos P, Cenker E, Houidi MB, Johansson B (2021) Analysis of fuel properties on combustion characteristics in a narrow-throat pre-chamber engine. SAE International
- Hlaing P, Marquez ME, Singh E, Almatrafi F, Cenker E, Houidi MB, Johansson B (2020) Effect of pre-chamber enrichment on lean burn pre-chamber spark ignition combustion concept with a narrow-throat geometry. SAE Technical Papers, 1–21. <https://doi.org/10.4271/2020-01-0825>
- Kar K, Cheng WK (2010) Speciated engine-out organic gas emissions from a PFI-SI engine operating on ethanol/gasoline mixtures. *SAE Int J Fuels Lubr* 2(2):91–101. <https://doi.org/10.4271/2009-01-2673>
- Kyaw ZH, Watson HC (1992) Hydrogen assisted jet ignition for near elimination of NO<sub>x</sub> and cyclic variability in the S.I. engine. In: Symposium (International) on combustion 24(1):1449–1455. [https://doi.org/10.1016/S0082-0784\(06\)80169-4](https://doi.org/10.1016/S0082-0784(06)80169-4)
- Malé Q, Staffelbach G, Vermorel O, Misdariis A, Ravet F, Poinot T (2019) Large eddy simulation of pre-chamber ignition in an internal combustion engine. *Flow Turbulence Combust* 103(2):465–483. <https://doi.org/10.1007/S10494-019-00026-Y>
- Manente V, Zander CG, Johansson B, Tunestal P, Cannella W (2010) An advanced internal combustion engine concept for low emissions and high efficiency from idle to max load using gasoline partially premixed combustion. SAE Technical Papers. <https://doi.org/10.4271/2010-01-2198>
- Maurel A, Ern P, Zielinska BJA, Wesfreid JE (1996) Experimental study of self-sustained oscillations in a confined jet. *Phys Rev E* 54(4):3643–3651. <https://doi.org/10.1103/PhysRevE.54.3643>
- Müller SHR, Böhm B, Gleißner M, Arndt S, Dreizler A (2010) Analysis of the temporal flame kernel development in an optically accessible IC engine using high-speed OH-PLIF. *Appl Phys B: Lasers Opt* 100(3):447–452. <https://doi.org/10.1007/s00340-010-4134-3>
- Olsen DB, Lisowski JM (2009) Prechamber NO<sub>x</sub> formation in low BMEP 2-stroke cycle natural gas engines. *Appl Therm Eng* 29(4):687–694. <https://doi.org/10.1016/j.applthermaleng.2008.03.049>
- Rajasegar R, Niki Y, García-Oliver JM, Li Z, Musculus MPB (2021) Fundamental insights on ignition and combustion of natural gas in an active fueled pre-chamber spark-ignition system. *Combust Flame* 232:111561. <https://doi.org/10.1016/J.COMBUSTFLAME.2021.111561>

- Sampath R, Tang Q, Marquez ME, Sharma P, Hlaing P, Houidi MB, Cenker E, Chang J, Johansson B, Magnotti G (2020) Study on the pre-chamber fueling ratio effect on the main chamber combustion using simultaneous PLIF and OH\* chemiluminescence imaging. SAE Technical Papers, no. 2020 (September). <https://doi.org/10.4271/2020-01-2024>
- Sens M, Günther M, Medicke M, Walther U (2020) Developing a spark-ignition engine with 45 % efficiency. MTZ Worldwide 81(4):46–51. <https://doi.org/10.1007/s38313-020-0194-x>
- Shah A (2015) Improving the efficiency of gas engines using pre-chamber ignition
- Shah A, Tunestal P, Johansson B (2012) Investigation of performance and emission characteristics of a heavy duty natural gas engine operated with pre-chamber spark plug and dilution with excess air and EGR. SAE Int J Engines 5(4):1790–1801. <https://doi.org/10.4271/2012-01-1980>
- Shah A, Tunestal P, Johansson B (2014) Effect of relative mixture strength on performance of divided chamber ‘avalanche activated combustion’ ignition technique in a heavy duty natural gas engine. SAE Technical Papers 1. <https://doi.org/10.4271/2014-01-1327>
- Shah A, Tunestal P, Johansson B (2015) Effect of pre-chamber volume and nozzle diameter on pre-chamber ignition in heavy duty natural gas engines. In: SAE Technical Paper Series, vol 1. <https://doi.org/10.4271/2015-01-0867>
- Shapiro E, Tiney N, Kyrtatos P, Kotzagianni M, Bolla M, Boulouchos K, Tallu G, Lucas G, Weissner M (2019) Experimental and numerical analysis of pre-chamber combustion systems for lean burn gas engines. In: SAE Technical Paper Series. <https://doi.org/10.4271/2019-01-0260>
- Tang Q, Sampath R, Marquez ME, Hlaing P, Sharma P, Houidi MB, Cenker E, Chang J, Magnotti G, Johansson B (2020) Simultaneous negative PLIF and OH\* chemiluminescence imaging of the gas exchange and flame jet from a narrow throat pre-chamber. In: SAE Technical Papers. SAE International. <https://doi.org/10.4271/2020-01-2080>
- Tang Q, Sampath R, Marquez ME, Sharma P, Hlaing P, Houidi MB, Cenker E, Chang J, Magnotti G, Johansson B (2021) Optical diagnostics on the pre-chamber jet and main chamber ignition in the active pre-chamber combustion (PCC). Combust Flame 228:218–235. <https://doi.org/10.1016/j.combustflame.2021.02.001>
- Toulson E, Huisjen A, Chen X, Squibb C, Zhu G, Schock H, Attard WP (2012) Visualization of propane and natural gas spark ignition and turbulent jet ignition combustion. SAE Int J Engines 5(4):2012-32-0002. <https://doi.org/10.4271/2012-32-0002>
- Toulson E, Schock HJ, Attard WP (2010) A review of pre-chamber initiated jet ignition combustion systems. <https://doi.org/10.4271/2010-01-2263>
- Vedula RT, Song R, Stuecken T, Zhu GG, Schock H (2017) Thermal efficiency of a dual-mode turbulent jet ignition engine under lean and near-stoichiometric operation. Int J Engine Res 18(10):1055–1066. <https://doi.org/10.1177/1468087417699979>
- Wenig M, Fogla N, Roggendorf K (2019) Towards predictive dual-fuel combustion and pre-chamber modeling for large two-stroke engines in the scope of 0D/1D simulation
- Wenig M, Roggendorf K (2019) Development of a predictive dual-fuel combustion and prechamber model for large two-stroke engines within a Fast 0D/1D-simulation environment, pp 386–397
- Yu X, Zhang A, Baur A, Engineer N (2021) The impact of pre-chamber design on part load efficiency and emissions of a Miller cycle light duty gasoline engine, pp 1–16. <https://doi.org/10.4271/2021-01-0479>. Abstract
- Zhang A, Yu X, Engineer N, Zhang Y, Pei Y (2020) Numerical investigation of pre-chamber jet combustion in a light-duty gasoline engine. In: ASME 2020 Internal combustion engine division fall technical conference, 1–15. American Society of Mechanical Engineers. <https://doi.org/10.1115/ICEF2020-2997>

# Chapter 9

## On the Use of Active Pre-chambers and Bio-hybrid Fuels in Internal Combustion Engines



Patrick Burkardt , Maximilian Fleischmann , Tim Wegmann ,  
Marco Braun , Julian Knöll , Leif Schumacher , Florian vom Lehn ,  
Bastian Lehrheuer , Matthias Meinke, Heinz Pitsch, Reinhold Kneer,  
Wolfgang Schröder, and Stefan Pischinger

**Abstract** Pre-chamber combustion systems combined with bio-hybrid fuels allow for an efficiency increase of internal combustion engines and a reduction of engine-out emissions. Experimental and numerical investigations are required to understand the combustion process and in particular the phenomena inside the pre-chamber. To this end, this study presents experimental investigations of an active pre-chamber combustion system in generic optical experiments and on a thermodynamic single-cylinder research engine. Moreover, the generic experiments are accompanied with large-eddy simulations of the single-cylinder flow field. Additional optical experiments on a rapid compression machine provide insights into both the ignition inside the pre-chamber and the subsequent combustion in the main chamber (MC) by use of the bio-hybrid fuels DEM and ethyl acetate. These fuels were also investigated on the thermodynamic single-cylinder research engine. A maximum indicated efficiency of 43% is achieved at an engine speed of 2000 1/min, an indicated mean effective pressure of 6 bar, and a relative air/fuel ratio of 2.2. A maximum relative air/fuel ratio of 2.25 is realized in the same operating point. In ongoing research,

---

P. Burkardt (✉) · M. Fleischmann · B. Lehrheuer · S. Pischinger  
Institute for Combustion Engines, RWTH Aachen University, Forckenbeckstr. 4, 52074 Aachen, Germany  
e-mail: [burkardt@vka.rwth-aachen.de](mailto:burkardt@vka.rwth-aachen.de)

T. Wegmann · M. Braun · J. Knöll · M. Meinke · W. Schröder  
Chair of Fluid Mechanics and Institute of Aerodynamics, RWTH Aachen University, Willnerstr. 5a, 52062 Aachen, Germany

L. Schumacher · R. Kneer  
Institute of Heat and Mass Transfer, RWTH Aachen University, Augustinerbach 6, 52056 Aachen, Germany

F. vom Lehn · H. Pitsch  
Institute for Combustion Technology, RWTH Aachen University, Templergraben 64, 52056 Aachen, Germany

W. Schröder  
JARA Center for Simulation and Data, RWTH Aachen University, Seffenter Weg 23, 52074 Aachen, Germany

numerical investigations of the mixture behavior after the direct fuel injection will contribute to the understanding of the combustion process in the thermodynamic single-cylinder research engine. Moreover, the findings from the numerical investigations will be validated with those of a motored optically accessible single-cylinder research engine.

**Keywords** Pre-chamber · Bio-hybrid fuels · Rapid compression machine · Single-cylinder engine · Numerical simulation

## 9.1 Introduction

Global warming as well as the limited fossil resources for fuel production lead to the research objective to design new concepts for internal combustion engines, with reduced emissions and high thermal efficiency. The greenhouse gas emissions of the transport sector is one of the main reasons for the need of improvements (Alvarez et al. 2018). The Cluster of Excellence “The Fuel Science Center (FSC)—Adaptive Conversion Systems for Renewable Energy and Carbon Sources” at RWTH Aachen University works on gaining fundamental knowledge and novel scientific methods for CO<sub>2</sub>-neutral and near-to-zero pollutant emission propulsion systems. The FSC uses sustainable technical solutions to form liquid energy carriers from renewable electricity and alternative carbon sources like biomass. The resulting fuels can be produced via several pathways and are defined as bio-hybrid fuels. These bio-hybrid fuels show high potentials for further development. In addition to the fuel production process optimization, the FSC investigates different combustion systems to maximize the efficiency and the engine-out emissions. Furthermore, the combination of bio-hybrid fuels with adjusted combustion system concepts offers a solid platform for high thermal efficiency with ultra-low emissions.

One promising combustion system is the active pre-chamber (PC) concept for spark-ignition engines. The idea is to simultaneously reduce NO<sub>x</sub> emissions and increase the engine efficiency under very lean conditions (Bozza et al. 2019). Various experimental results show a thermal efficiency increase for pre-chamber applications of up to 25% over conventional spark-ignition engine concepts (Bunce et al. 2021).

Pre-chamber concepts can be divided into passive and active pre-chamber designs. For the passive PC, the air–fuel mixture enters the pre-chamber during the compression stroke. The active pre-chamber setup has an additional injector in the pre-chamber and therefore allows ultra-lean conditions in the main chamber with stoichiometric or slightly rich conditions inside the pre-chamber to provide an air–fuel mixture within the ignition limits. Both setups include a spark plug inside the pre-chamber to ignite the air–fuel mixture (Toulson et al. 2010).

In this work, both bio-hybrid fuels and pre-chamber combustion applications are assessed in several approaches: investigations of the ignition delay time were carried out on a rapid compression machine (RCM). Additionally, the fuel injection into the pre-chamber was optically investigated. Furthermore, a variation of the relative

air/fuel ratio ( $\lambda$ ) was performed on a thermodynamic single-cylinder engine (SCE) to evaluate the combustion behavior under real-engine conditions. Numerical simulations were performed to assess both the flow field and the cycle-to-cycle variation (CCV) inside the pre-chamber during the compression stroke.

A profound outlook section presents additional experimental investigations with test facilities that are currently in construction phase. In particular, experiments with an optically accessible SCE are planned to investigate the influence of the PC and its jets on the flow field in the MC. Furthermore, optical experiments of the fuel injection and the fuel brake-up in a generic pre-chamber are in preparation. These investigations will help to thoroughly understand all details of the combustion process in the pre- and main chamber for various bio-hybrid fuels.

Finally, this work presents an outlook regarding fuel candidates and their properties for future investigations. An extensive discussion on the optimization and modelling of bio-hybrid fuels with regard to the prediction of octane numbers and laminar burning velocities is provided in Sect. 9.4.3. The aim is to co-optimize the fuel properties and the combustion processes.

## 9.2 Pre-chamber Design and Fuel Candidates

### 9.2.1 Pre-chamber Layout

Slightly different PC configurations have been investigated on the SCE and the RCM, whereas the used pre-chamber layouts for the numerical and generic investigations are applied to fulfill the corresponding requirements. The different PC layouts are depicted in Fig. 9.1.

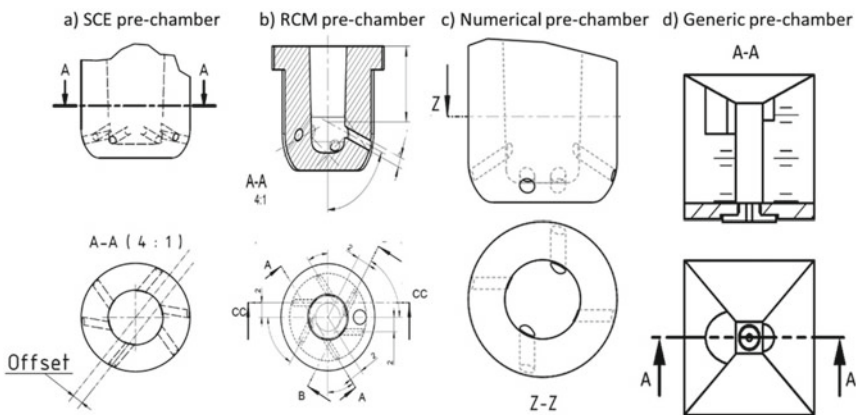


**Fig. 9.1** Pre-chamber layouts for **a** single-cylinder engine, **b** rapid compression machine, **c** numerical (Müller et al. 2020) and **d** generic pre-chamber



**Table 9.1** Pre-chamber layout specifications

	Unit	SCE	RCM	Numerical	Generic
Number of orifices	–	6	6	4	1
Orifice offset	mm	1.4	2	1.25	–
Orifice diameter	mm	0.85	0.85	2 × 0.9; 2 × 1.2	2.1
Orifice area	mm <sup>2</sup>	3.4	3.4	3.53	3.46
PC volume	mm <sup>3</sup>	1080	1380	1080	1800
PC volume to clearance volume	%	3.3	3.6	3.3	–
Orifice area to PC volume	1/mm	0.0031	0.0025	0.0033	0.002

The basic pre-chamber body was developed in a previous research project (Bozza et al. 2019; Müller et al. 2020; Serrano et al. 2019) and is used for the numerical investigations in this work (Sect. 9.3.3); however, the pre-chamber layout has been adapted for both SCE and RCM. The number of the pre-chamber orifices was increased from four to six, while the orifice diameter was adapted to achieve an orifice area comparable to the original layout. The specifications of the investigated pre-chamber layouts can be found in Table 9.1.

## 9.2.2 Fuels

The investigated active pre-chamber configurations offer the ability to independently inject different fuels in the main chamber and the pre-chamber.

In case of the SCE investigations, the pre-chamber was always fueled with ethanol while the main chamber was fueled with ethanol or methanol. Both alcohol fuels are well-suited for spark-ignition (SI) engines due to their high knock resistance. This knock resistance mainly results from the high values of the research octane number, the laminar burning velocity, and the enthalpy of vaporization, see Table 9.2. To compare the results from the SCE investigations, the SI configurations were also fueled with ethanol or methanol. Additionally, the properties of a conventional fuel RON95E10 are displayed.

The two bio-hybrid fuels diethoxymethane (DEM), as a high reactivity fuel, as well as the low reactivity fuel ethyl acetate were used in the experimental RCM investigations. A mixture consisting of ethyl acetate and air is inserted into the main chamber, whereas DEM is injected in the active pre-chamber. Both fuels are well suited for optical dual fuel pre-chamber investigations due to their low soot tendency as well as their reactivity level. Moreover, the high enthalpies of vaporization and the low adiabatic flame temperatures lead to decreased combustion temperatures and consequently to low nitrogen oxide emissions. The high oxygen content mitigates the soot production (Verhelst et al. 2019).

**Table 9.2** Fuel properties (Verhelst et al. 2019; Dahmen and Marquardt 2015, 2016; Hoppe et al. 2016a, b; Nguyen et al. 2018; Contino et al. 2011; Lehrheuer et al. 2019)

	Unit	RON95 E10	Ethanol	Methanol	DEM	Ethyl acetate
Sum formula	–	Various	C <sub>2</sub> H <sub>6</sub> O	CH <sub>4</sub> O	C <sub>5</sub> H <sub>12</sub> O <sub>2</sub>	C <sub>4</sub> H <sub>8</sub> O <sub>2</sub>
Carbon mass fraction	%	83.48	52.14	37.48	57.66	54.53
Hydrogen mass fraction	%	13.24	13.13	12.58	11.61	9.15
Oxygen mass fraction	%	3.28	34.73	49.93	30.72	36.32
Density (@ 20 °C)	kg/m <sup>3</sup>	741	787	790	831.9	897
Boiling temperature	°C	36–190	78	65	87.1	77
Vapor pressure (@ 20 °C)	kPa	–	5.8	12.8	17	12.4
Specific enthalpy of vaporization	kJ/kg <sub>air,λ=1</sub>	–	101.6	170.9	–	404
Stoichiometric air requirement	kg/kg	13.97	8.98	6.5	–	7.85
Lower heating value	MJ/kg	41.56	26.84	19.94	29.7	23.79
Laminar flame speed (@ 20 °C, 1 bar, λ = 1)	cm/s	33	38.5	40.0	–	–
Adiabatic flame temperature	K	2275	2193	2143	–	–
Research octane number	1	–	109	109	–	104.6
Centane number	1	–	–	–	39	–

## 9.3 Methodology and Results

### 9.3.1 Rapid Compression Machine

Optical investigations in a rapid compression machine (RCM) are performed to gain fundamental knowledge of the pre-chamber combustion for engine conditions. Good optical access and well defined initial and boundary conditions are the main reasons for using the RCM for the analysis of the active pre-chamber combustion. The RCM consists of high strength stainless steel for main chamber pressure up to 500 bar. The pre-chamber layout used in the RCM has a volume of 1030 mm<sup>3</sup> and is based on the SCE pre-chamber design. The active pre-chamber setup includes a single-hole

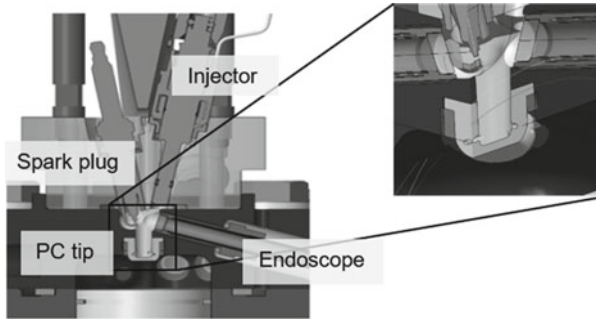


**Fig. 9.2** Optical setup with view inside active pre-chamber

injector and a conventional spark plug. Additionally, the pre-chamber tip can be exchanged and therefore the influence of different geometries can be investigated.

The RCM setup enables to investigate the properties of novel bio-hybrid fuels, which are typically available only in small quantities under engine-like conditions. Figure 9.2 shows the optical setup of the RCM design with focus on the view inside the pre-chamber with endoscopic access. All measurement results presented, were obtained for a wall temperature of  $T_{\text{wall}} = 75 \text{ }^\circ\text{C}$ . An injection pressure of  $p_{\text{inj}} = 200 \text{ bar}$  and with an injection duration of  $t_{\text{inj}} = 1 \text{ ms}$  was used.

The RCM reactor head allows simultaneous optical investigation of the combustion inside and outside the pre-chamber to analyze the PC-MC interaction. Therefore, three different cameras as well as two pressure sensors, one inside the pre-chamber and the second one for the main chamber, are installed. This enables the analysis of the PC-MC interaction with the different pressure traces as well as optical methods. The optical access inside the RCM is realized with three endoscopes, which are mainly used for the recording of the natural luminescence signal inside the active pre-chamber during injection, ignition and combustion of the bio-hybrid fuels in the pre-chamber. OH chemiluminescence measurements were performed to get further information about the pre-chamber jets entering the main chamber. In addition, natural luminosity is recorded inside the main chamber.

The optical RCM measurements with DEM and ethyl acetate including different end-of-compression pressures as well as injection and spark timings are a first proof of concept to get an impression of the pre-chamber combustion with bio-hybrid fuels. Table 9.3 displays the optical equipment used for the RCM setup.

Table 9.4 displays the operating conditions for the RCM experiments with the single-hole injector. Figure 9.3 shows the different pressure curves for the respective pressures inside the pre-chamber and the main chamber for stoichiometric (black) and lean (blue) main chamber conditions. The time line of the pressure curves is referred to the spark timing. For both measurements the end-of-compression pressure, without injection, is predefined to  $p_{\text{EOC}} = 30 \text{ bar}$ . First experimental data indicate good operation for stoichiometric as well as lean conditions for the combinations of bio-hybrid fuels with the pre-chamber combustion concept.

**Table 9.3** Optical equipment for simultaneous PC-MC investigation

Equipment	High-speed natural luminosity PC	High-speed OH-chemiluminescence MC	High-speed Natural luminosity MC
Camera	Photron Nova S12	Photron Fastcam SA1.1	Phantom V1612
Intensifier	•	LaVision IRO X	•
Filter	•	310 nm ( $\pm$ 10 nm)	•
Endoscope	Storz Endoscope visible	LaVision UV Hybrid Endoscope	Storz Endoscope visible
External light	Dolan–Jenner Mi-LED	Storz Xe-lamp	Storz Xe lamp

**Table 9.4** Operating RCM conditions

	Unit	Value
Injection pressure	bar	200
Injection duration	ms	0.5–2
Relative air/fuel ratio MC	–	1–2
End-of-compression pressure (EOC)	bar	10–35
Wall temperature	°C	75

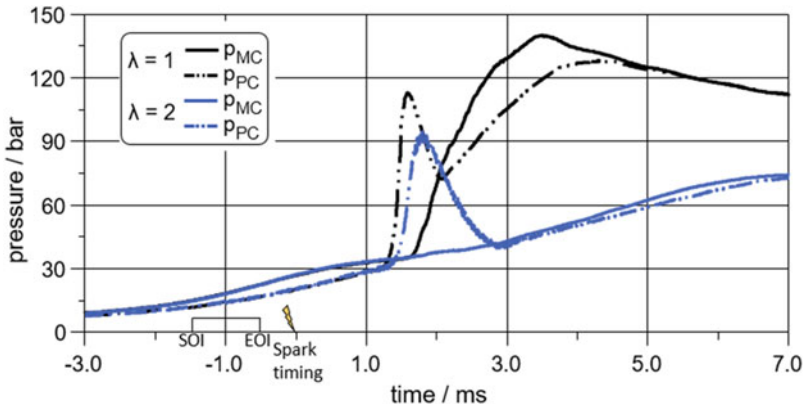


**Fig. 9.3** RCM measurements for DEM and ethyl acetate with  $\lambda_{MC}$  variation

Furthermore, the low maximum pressure as well as the slower combustion duration are a consequence of the lean air–fuel mixture inside the main chamber. Additionally, the main chamber pressure rise after the maximum pre-chamber pressure in combination with the optical measurements shows a multi ignition caused by the flames exiting the pre-chamber. A pre-chamber injection duration of  $t_{inj} = 1$  ms including start of injection (SOI) and end of injection (EOI) is realized  $t = 0.5$  ms

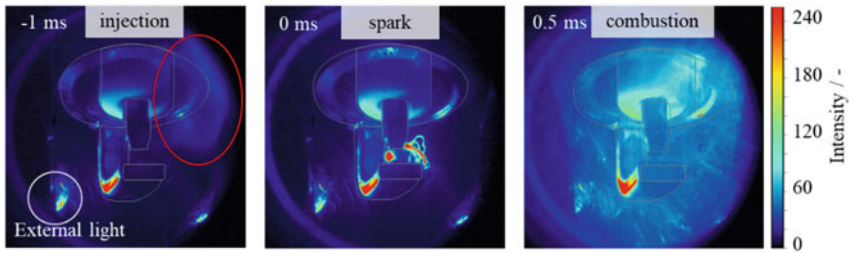


**Fig. 9.4** Natural luminosity of injection, spark, and combustion inside active pre-chamber

before the spark timing to ensure evaporation and short mixing time inside the pre-chamber. Further reduction of the mixing, which is limited by the time between injection and ignition inside the pre-chamber, leads to main chamber ignition difficulties. In this case, part of the injected fuel exits the pre-chamber and therefore, the energy of the pre-chamber jets does not reach the required ignition energy of the main chamber. The injection in addition with the ignition timing is a main aspect for the resulting pre-chamber combustion.

Figure 9.4 shows the natural luminosity of selected images from a single cycle during the injection, spark, and combustion inside the pre-chamber. The frame rate for the high-speed measurements in the active pre-chamber was 4000 frames per second. The corresponding pressure is plotted in Fig. 9.3 in black color. The images indicate the possibilities to optically investigate the injection, the spark timing, and small combustion particles inside the pre-chamber. As a conclusion, the experiments have shown comparably low luminosity. Therefore, the following adaptations for optimized optical view need to be made to analyze the charge motion as well as ongoing processes inside the pre-chamber.

For further investigations, a sodium tracer is added to the fuel injected into the pre-chamber to optimize the optical view inside the pre-chamber. During the combustion process, the sodium tracer has a natural luminosity at a wavelength of 589 nm and therefore enables a high intensity of the optical signal. Additionally, the tracer in the fuel can help to get a better understanding of the mixing process inside the pre-chamber as well as of the pre-chamber jets. On top of that an additional filter for the related wavelength offers the opportunity to investigate the fuel–air mixture with the injected fuel inside the PC. Furthermore, a UV endoscope with OH filter (310 nm) can indicate the flame propagation and charge motion inside the PC.

According to Zhao and Kaiser (2018), the aim is to get a qualitative impression of the charge motion by analyzing the combustion luminosity inside the pre-chamber. Especially the investigation of the different pre-chamber tip layouts, with varying the orifice number and design, is the main focus of future experimental measurements.

### 9.3.2 Thermodynamic Single-Cylinder Engine

The pre-chamber combustion concept has been experimentally investigated on a thermodynamic four-stroke direct-injection spark-ignition (DISI) single-cylinder engine (SCE) (Wouters et al. 2021a). The cylinder head of the SCE is capable to mount either a central spark plug or a central active pre-chamber. The fuel for the main chamber (MC) is laterally injected between the intake valves. The SCE has a compression ratio (CR) of  $CR = 16.4$  in the SI configuration. However, the CR of the PC configuration is slightly lower because the PC adds an additional volume to the clearance volume. The main engine specifications are listed in Table 9.5 and the engine PC configuration is displayed in Table 9.1.

The relative air/fuel ratio ( $\lambda$ ) of the exhaust gas was calculated from both the fuel properties and the exhaust gas composition according to the formula of Spindt (Spindt 1965) with the extension for oxygenated fuels of Bresenham et al. (Bresenham et al. 1998). The exhaust gas composition was determined from a partial exhaust gas mass flow. In particular, the measured exhaust gas components were hydrocarbons (HC), oxygen ( $O_2$ ), carbon monoxide (CO), carbon dioxide ( $CO_2$ ), and nitrogen oxides ( $NO_x$ ). Additionally, the filter smoke number (FSN) was measured as an indicator for soot emissions. The following measuring principals were used (Wouters et al. 2021b):

- HC: flame ionization detector (Rosemount NGA 2000)
- $O_2$ : paramagnetic oxygen analyzer (Rosemount NGA2000)
- CO: infrared gas analyzer (Rosemount NGA 2000)
- $CO_2$ : infrared gas analyzer (Rosemount NGA 2000)
- $NO_x$ : chemiluminescence analyzer (Eco Physics 700EL ht)
- FSN: smoke meter (AVL 415s).

**Table 9.5** Engine hardware specifications

	Unit	Value
Displacement	cm <sup>3</sup>	500
Bore	mm	75
Stroke	mm	113.2
Connecting rod length	mm	220
Valves per cylinder	–	4
Intake valve event length <sup>a</sup>	° CA	178
Exhaust valve event length <sup>a</sup>	° CA	178
Max. intake valve lift	mm	8.8
Max. exhaust valve lift	mm	8.4
Compression ratio (SI configuration)	–	16.4
Injector position MC	–	Lateral
Injector position PC	–	Central

<sup>a</sup> Referred to 1 mm valve lift

A variation of the exhaust gas  $\lambda$  at an engine speed ( $n$ ) of  $n = 2000$  1/min and an indicated mean effective pressure (IMEP) of  $\text{IMEP} = 6$  bar was performed, see Fig. 9.5. The quantity  $\lambda$  always refers to the overall value in the exhaust gas and it was not distinguished between an MC  $\lambda$  and a PC  $\lambda$ . At  $\text{IMEP} = 6$  bar, the SCE operates with the throttle in the intake line, thus, the intake pressure is lower than the ambient pressure. The exhaust pressure equals the ambient pressure.

When comparing the different fuels in equal hardware configurations, it is directly observable that the methanol-fueled configurations achieve higher lean limits and higher maximum indicated efficiencies. The main reason for the better performance of methanol is its higher laminar burning velocity compared to that of ethanol, cf. Table 9.2. Since a high laminar burning velocity results in a short burn duration, the combustion stability at high  $\lambda$  can be improved and consequently, the lean limit is extended.

When considering different hardware configurations with the same fuel, it is observable that the PC configurations achieve higher maximum indicated efficiencies compared to the SI configurations. However, among a large  $\lambda$  range the SI configurations achieve higher indicated efficiencies than their PC counterparts. Since the point where 50% mass fraction is burned is equal among the entire  $\lambda$  variation and the burn duration is more favorable in case of the PC configurations, the efficiency disadvantage of the PC configurations at low  $\lambda$  values can be attributed to increased wall heat losses. The wall heat losses became less pronounced with increasing  $\lambda$ . Thus, the benefits of a PC configuration can overcompensate for the higher wall heat losses and consequently, achieve higher maximum indicated efficiencies.

The burn delay is more pronounced for high  $\lambda$  values in case of the SI configurations than in case of their PC counterparts. To maintain a constant combustion phasing (50% mass fraction burned, MFB50) at  $\text{MFB50} = 7\text{--}8^\circ$  CA after top dead center (ATDC), the spark timing must be advanced when  $\lambda$  increases. This adjustment results in an increased burn delay. The advance of the spark timing is more pronounced in case of the SI configurations because the air-fuel mixture in vicinity to the spark plug is leaner than in an active PC. The PC configurations show, however, a rather horizontal course among the  $\lambda$  variation. This behavior has also been found by other researchers (Alvarez et al. 2018).

When comparing equal hardware configurations, the burn duration is shorter in case of the methanol-fueled applications than in the ethanol-fueled ones. This behavior results from methanol's higher laminar burning velocity compared to that of ethanol. Considering equal fuels, the PC configurations show shorter burn durations than their SI counterparts. The shorter burn durations of the PC applications compared to their SI counterparts result from the multiple distributed ignition sites inside the MC. These ignition sites lead to reduced flame distances and consequently, to decreased burn durations.

The exhaust gas temperature decreases with an increased  $\lambda$  because a high  $\lambda$  leads to a low combustion temperature. The most pronounced influence on the exhaust gas temperature resulted from the hardware configurations. Here, the PC configurations achieved lower temperatures due to their shorter burn durations. The fuel influence on the exhaust gas temperature is less pronounced. However, methanol achieves slightly

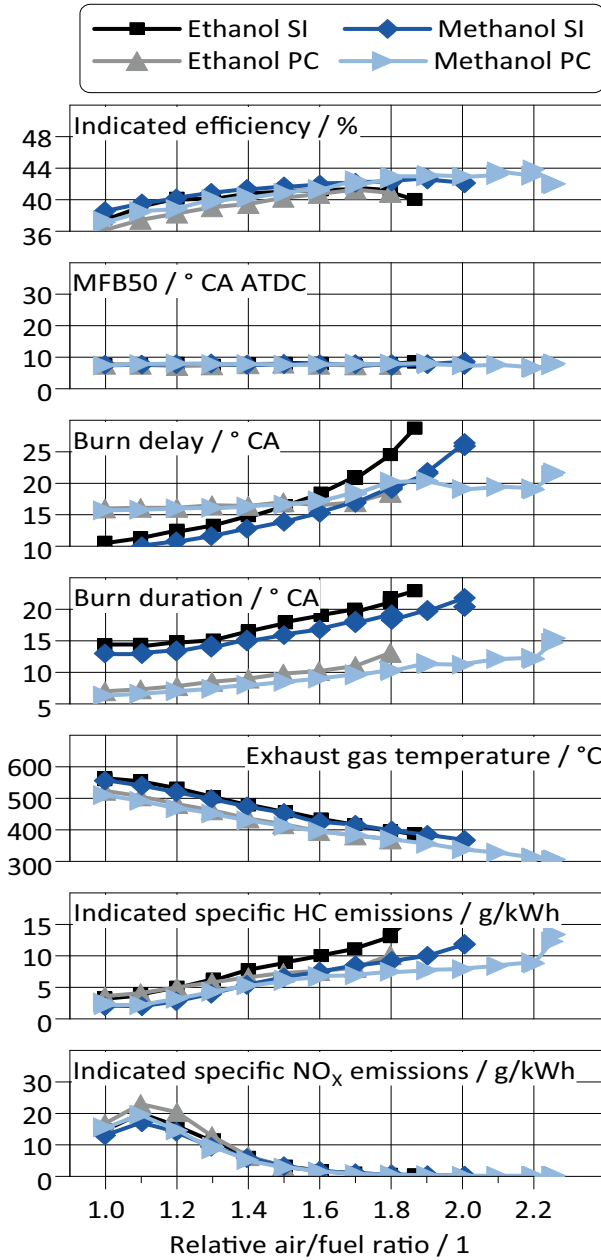


**Fig. 9.5**  $\lambda$  variation results of pre-chamber and spark ignition configurations at  $n = 2000$  1/min and IMEP = 6 bar with  $SOI_{MC} = 300^\circ$  CA BTDC,  $SOI_{PC} = 60^\circ$  CA BTDC,  $T_{intake} = 25^\circ$  C, and  $T_{coolant} = T_{oil} = 90^\circ$  C



lower temperatures than ethanol. This behavior results from both the higher enthalpy of vaporization and the lower adiabatic flame temperature of methanol compared to ethanol.

The indicated specific hydrocarbon (ISHC) emissions increase with an increase of  $\lambda$  due to the decreased combustion temperature, which leads to both increased flame quenching and decreased post oxidation. Since methanol has a shorter burn duration and consequently a reduced quenching distance than ethanol, it achieves lower ISHC emissions. Moreover, the PC combustion concepts led to short burn durations and consequently contribute to an additional decrease of the ISHC emissions.

The indicated specific nitrogen oxides (ISNO<sub>x</sub>) emissions depend on the combustion temperature. Since the combustion temperature depended on  $\lambda$ , the ISNO<sub>x</sub> emissions are also predominantly depend on  $\lambda$  rather than on the fuel or the combustion concept. Hence, the lowest ISNO<sub>x</sub> emissions are achieved by the configuration that allowed the highest lean limit, in particular, the methanol-fueled PC configuration.

### 9.3.3 Numerical Simulation

In parallel to the experimental investigations described in Sects. 3.1 and 3.2, large-eddy simulations (LES) of the same SCE with the pre-chamber configuration are conducted. The aim of these simulations is to gain further knowledge of the flow field and cycle-to-cycle variations (CCV) inside the pre-chamber during the compression stroke (Fig. 9.6). Of special interest are the gas jets entering from the MC during the compression stroke and the resulting turbulence, which drives the fuel/air mixing inside the PC. Furthermore, the influence of the MC tumble motion on the PC flow field will be investigated by comparison with an RCM setup.

Finally, the influence of the protruding PC geometry on the MC tumble flow is analyzed. The formation and break-up of the large-scale vortical flow structures, such as the tumble motion, are linked to production and convection of turbulence and significantly influence the fuel/air mixing processes inside the MC (Arcoumanis et al. 1990; Kang et al. 1997).

The CFD solver m-AIA (multiphysics Aerodynamisches Instiut Aachen) developed at the Institute of Aerodynamics, RWTH Aachen University, has been utilized for the turbulent scale resolving simulations with high mesh resolution. The code has been optimized for high-performance computing hardware and has already been successfully used for internal combustion engine applications (Schneiders et al. 2015; Berger et al. 2020). The underlying unstructured Cartesian mesh is highly suitable in this context, since it allows for automatic mesh generation, solution adaptive mesh adaptation, and dynamic load balancing. The finite volume-solver (Schneiders et al. 2016) is used for the Navier–Stokes equations formulated for compressible flows in an arbitrary Lagrangian–Eulerian formulation with a conservative sharp multiple cut-cell boundary method. The multiple level-set solver (Günther et al. 2014) allows for accurate description of independent piston and valve surface movement, including intrinsic valve opening and closing.

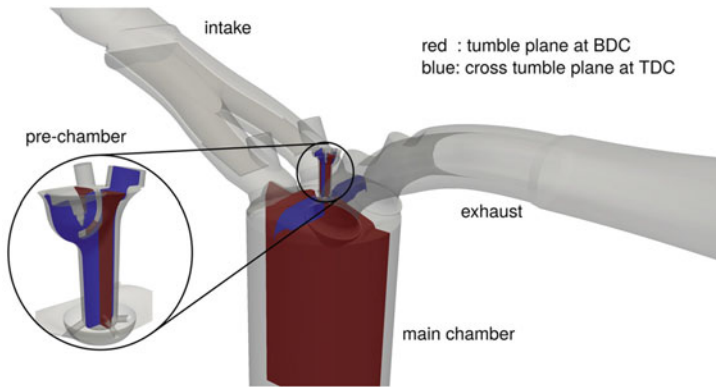


**Fig. 9.6** Illustration of the single-cylinder engine with the pre-chamber configuration used for the numerical simulation

The computational setup consists of a finite volume grid with the smallest cell length of 0.137 mm and 40 million cells at TDC and 89 million cells at BDC. Non-reflecting characteristic boundary conditions have been applied at the intake and exhaust pipes. Five consecutive cycles were conducted, and the flow data has been ensemble averaged over the last four cycles.

For all flow simulations, the operation point with an engine speed of  $n = 2000$  1/min and  $\text{IMEP} = 6$  bar has been used. First, the influence of the protruding PC geometry on the MC flow will be discussed. Second, the flow field inside the PC will be analyzed with focus on the mass flux into the PC during the compression stroke. Finally, an outlook concerning future numerical investigations will be given.

During the intake stroke, the protruding pre-chamber geometry between the intake valves reduces the effective area of the intake jets and increases the jet velocity in the valve overflow region. Thus, a 4% larger kinetic energy inside the MC compared to a conventional combustion setup featuring an Engine Combustion Network (ECN) Spray G injector can be observed in Fig. 9.7 at  $280^\circ$  crank angle (CA) before top dead center (BTDC).

A tumble break-up at earlier CA can be observed for the PC configuration during the compression stroke. Figure 9.8 shows a larger deviation from the cycle mean kinetic energy for the PC setup at  $135^\circ$  CA BTDC and a lower mean kinetic energy towards the TDC. Larger deviations from the mean kinetic energy are caused by larger turbulent fluctuations and CCVs. The larger energy deviation correlates with a more diffused tumble core in the ensemble averaged velocity field as seen in Fig. 9.8 for the protruding PC geometry at  $110^\circ$  CA BTDC.

The more diffusive vortex core for the PC yields to a weaker tumble vortex, i.e., a 15% lower vorticity at  $20^\circ$  CA BTDC compared to the G-injector setup. Previous studies (Berger et al. 2020) have shown that the shape and variance of the fuel distribution function changes significantly during the end of the compression stroke.

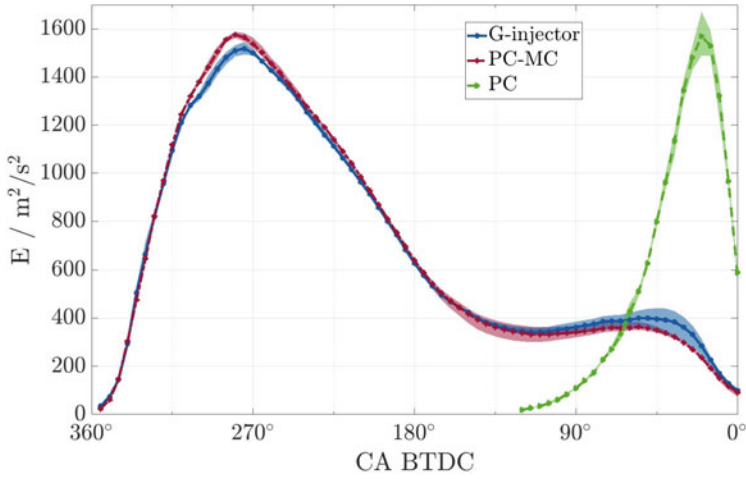


**Fig. 9.7** Volume averaged kinetic energy inside the SCE main chamber for the G-Injector (G-Injector) and pre-chamber (PC-MC) configurations and inside the pre-chamber (PC) of the pre-chamber configuration. Lines and symbols represent cycle-averaged values, and the shaded area indicates cycle minimum and maximum values

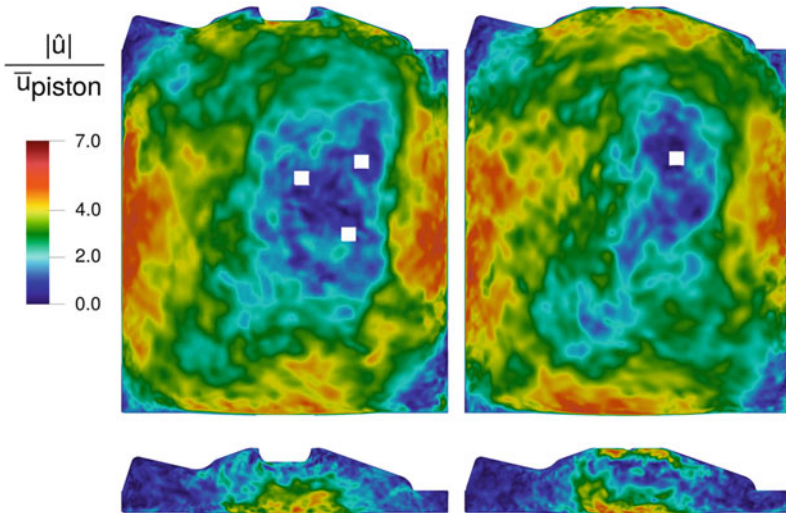


**Fig. 9.8** Comparison of the ensemble-averaged velocity magnitude normalized by the average piston velocity for the pre-chamber setup (left) and the G-injector setup (right) at 110° (top) and 20° CA BTDC (bottom) in the engine tumble plane. The white squares represent the vortex core by a local  $\Gamma$  maximum (Günther et al. 2014)

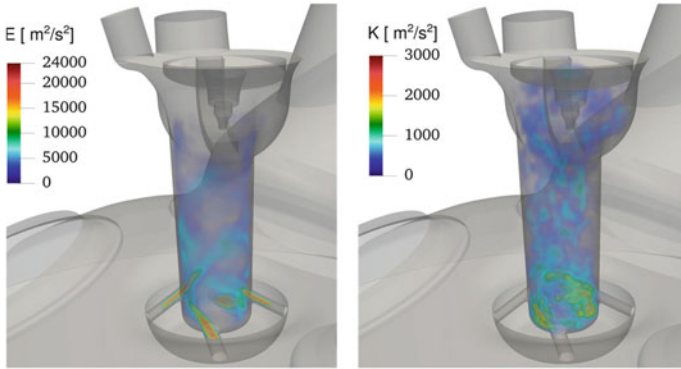


**Fig. 9.9** Volume rendering of the kinetic energy  $E$  of the ensemble-averaged flow field (left) and the turbulent kinetic energy  $K$  (right) in the pre-chamber at  $20^\circ$  CA BTDC for the SCE

Therefore, the simulation results indicate a less efficient fuel/air mixing inside the main chamber due to the protruding PC geometry.

The PC volume-averaged kinetic energy exceeds the MC energy by almost one order of magnitude near the TDC as seen in Fig. 9.9. The largest mean kinetic energy in the PC can be seen  $20^\circ$  CA BTDC with 5% cycle-to-cycle energy deviation.

Figure 9.9 shows the volume rendered energy in the PC, based on the ensemble-averaged flow field (left) and its local cycle deviation, the turbulent kinetic energy  $K$  (right).

The orifice offset and inclination of the PC orifices create a strong wall-bounded swirling motion, which can be seen in the kinetic energy field  $E$ . Inside the orifices, high values of the averaged kinetic energy but low turbulent or cycle-to-cycle variations can be seen. This indicates that the turbulent energy  $K$  is mainly produced by the interaction of the different orifice jets. The swirling motion promotes the upward transport (towards the spark plug) of the turbulent and cycle variable energy  $K$ , as shown on the right of Fig. 9.9. A preliminary comparison with simulations of an identically designed RCM has shown a comparable PC flow field and less than 5% mass flux deviation through the PC orifices.

To summarize, the protruding PC geometry has a negative effect on the MC tumble flow and might lead to less efficient fuel/air mixing. The jet and jet-wall interaction during the compression stroke significantly influences mean and turbulent energies inside the PC.

In the next step, the current simulations will be supplemented by fuel injection into the main and pre-chamber to analyze the fuel/air mixing and to optimize the fuel distribution with regard to the specific bio-hybrid fuel properties. These simulations will be further validated by experiments of the optical generic pre-chamber and the optical single-cylinder engine described in Sect. 9.4.1.

## 9.4 Ongoing Pre-chamber Investigations

### 9.4.1 Optical Single-Cylinder Engine

In addition to the adoption of molecularly controlled combustion systems and the development of novel bio-hybrid fuels, the optimization of the in-cylinder mixing process is an important prerequisite on the way to efficient combustion and low emissions. Therefore, fundamental analysis of the in-cylinder flow phenomena during the intake and the compression stroke is necessary to achieve the fundamental knowledge for further improvement of the mixture formation, especially for novel combustion systems. Due to the highly time-dependent expansion of the combustion chamber, the investigation of the in-cylinder flow is a highly three-dimensional, time-dependent problem, which requires the use of measurement techniques with high spatial and temporal resolution. Therefore, experimental investigations of a motored optical single-cylinder DISI engine are carried out at the Institute of Aerodynamics. The engine is characterized by full optical access to the combustion chamber and is manufactured in the Bowditch design, which allows access for laser optical measurement to the combustion chamber from below through a flat quartz glass piston crown. The flow velocities can be captured using different applications of particle-image velocimetry (PIV). To combine high temporal and spatial resolutions in 3D space, Braun et al. (Braun et al. 2019a, b) implemented a first high-speed tomographic PIV (HS-TPIV) setup on the optical engine that covers the entire stroke. In a subsequent publication (Braun et al. 2021), the setup was improved to an acquisition frequency of 2000 Hz while increasing the measurement volume to approx.  $50 \times 12 \times 82.5 \text{ mm}^3$ . Furthermore, the time-resolved HS-TPIV measurements were coupled with a triple-velocity decomposition method, which was developed for 3D results in Braun et al. (2021) based on a multiple snapshot proper orthogonal decomposition (POD) and a study by Vu and Guibert (2012). The results of the semi-empirical decomposition method were utilized to investigate in-cylinder velocity fluctuations from cycle-to-cycle variation (CCV) (Braun et al. 2021).

To supplement the investigations of the novel molecular combustion system featuring a pre-chamber in Sects. 9.3.1, 9.3.2 and 9.3.3, measurements of the behavior of the flow outside the pre-chamber are planned on the optical engine. For this purpose, the optical engine will be equipped with a new cylinder head, which has the same geometry and is equipped with a similar pre-chamber as the cylinder head of the fired single-cylinder engine (see Sect. 9.3.2). Furthermore, the cylinder head is designed to provide optical access to the pent roof such that the flow in proximity to the pre-chamber can be investigated.

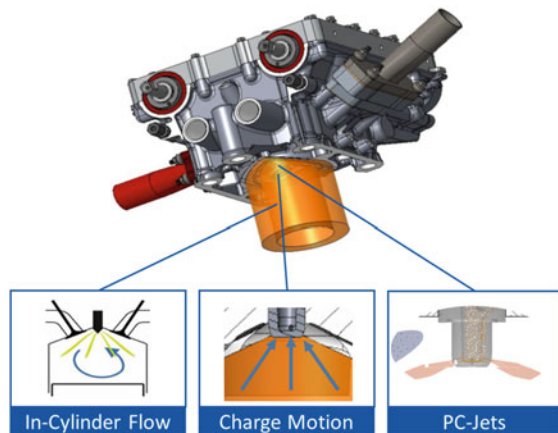
Since the optical SCE is limited to non-combustion cases, a cold gas injection system is added, allowing to mimic the flame jets penetrating from the pre-chamber into the main chamber. For the implementation of the cold gas injection system, the spark plug inside the pre-chamber is replaced by a nozzle, through which gases such as nitrogen or helium can be injected into the pre-chamber. The gas flux is controlled using a high-speed valve system, which is able to achieve the small penetration times

of the pre-chamber jets of up to 0.5 ms and can be adjusted to realize different ignition timings and durations. The requirements for the high-velocity valve system were estimated based on the experimental data of the fired engine in Sect. 9.3.2 and the numerical data obtained by simulations of the extended optical engine configuration in Sect. 9.3.3. To meet the conditions of fired operation and to set up the parameters of the valve system, a pressure transducer inside the pre-chamber is used.

By utilizing the optical access to the pent roof, it is possible to gain a deeper insight into the flow field during the end of the compression stroke. In most DISI engines the tumble vortex is the dominant large-scale flow structure and is responsible for the conservation of kinetic energy during the intake and compression strokes (Crolla et al. 2014). However, in the last part of the compression stroke, the tumble vortex breaks up and dissipates into many small-scale turbulent flow structures, which increases the turbulence level of the flow (Arcoumanis et al. 1990; Kang et al. 1997). The purpose of the tumble vortex is to generate a reliable mixture of fuel and air, and to improve the combustion process since the increased turbulence levels towards TDC raise the turbulent flame propagation speed (Chen et al. 2014). The mixture formation and turbulent flame propagation are both key parameters for a fast, efficient, and clean combustion. Based on the denoted points, three main investigation objectives can be derived regarding the mixture behavior of the new pre-chamber combustion system and the new extended field of view, which are visualized in Fig. 9.10.

First, the characteristics of the new cylinder head with regard to the turbulent structures and CCV in the main chamber are investigated. HS-TPIV measurements are performed over the entire piston stroke, similar to Braun et al. (2021). Based on existing experimental data of the optical engine with the previous setup, comparisons are evaluated concerning the turbulence level and especially the variations due to the CCV between both engine setups. This step is important to extensively investigate the development of the main chamber flow before analyzing the impact of the pre-chamber jets.

**Fig. 9.10** Main investigation objectives on the optical engine



Next, the behavior of the turbulent structures and CCV in the main chamber and close to the pre-chamber will be investigated. For this purpose, high-speed PIV measurements are performed focusing on the optically accessible pent roof. The results of this investigation will be used to estimate the volume flux from the main chamber into the pre-chamber during the compression stroke.

Finally, the influence of the jets penetrating from the pre-chamber into the main chamber will be investigated, using the cold gas injection system. The penetration depth of the jets into the main chamber as well as their influence on the turbulence level and CCV will be investigated using high-speed PIV.

The described studies will be used to extensively analyze the flow phenomena inside novel pre-chamber driven molecularly controlled combustion systems. The results with regard to turbulence levels at the point of ignition, the temporal behavior of the charge motion and the large-scale flow structures, CCV, and the interaction of the pre-chamber jets and the main chamber flow provide fundamental insight on the mixture formation and the combustion behavior of such systems, since the efficient flame propagation depends on the volume fraction of the combustion chamber that is covered by the emerging pre-chamber jets. In combination with the fired measurements in the rapid compression machine (Sect. 9.3.1) and in the single-cylinder engine (Sect. 9.3.2) and the investigations of the optical pre-chamber (Sect. 9.4.2), distinct conclusions on the combustion system's effects on the combustion efficiency, engine efficiency and soot reduction can be deduced. Finally, large-eddy simulation, similar to the investigations in Sect. 9.3.3, are able to solve problems beyond the feasibility of experiments, e.g., extensive parameter variations or engine optimization. However, such methods require extensive validation, which will be provided by measurements on the optical SCE.

#### ***9.4.2 Optical Generic Pre-chamber Experiments***

A novel transparent pre-chamber test bench is presented below. It is designed to allow laser-optical investigations of mixture formation within pre-chambers and in this way provides a fundamental understanding of the influence of a confined space on fuel injection. In particular, the spray propagation in a small volume, the formation of vortices, their influence on the fuel transportation towards the spark plug, and the spray interaction with the pre-chamber walls leading to fuel deposition (wall film formation) and consequently, to rich mixture zones, prone to increased exhaust emissions, are of interest.

The optically accessible generic pre-chamber is designed with a rectangular shape of (length 22 mm, width 7 mm, volume 1800 mm<sup>3</sup>) to ensure almost distortion-free optical visualizations of the two-phase flow (shown in Fig. 9.11). The pre-chamber itself is installed inside a high-pressure vessel to adjust the thermodynamic ambient conditions and for purging purposes. The high-pressure vessel is optically accessible from four sides via glass windows. A special window mount allows the use of microscopic lenses with a minimum working distance of 36 mm.



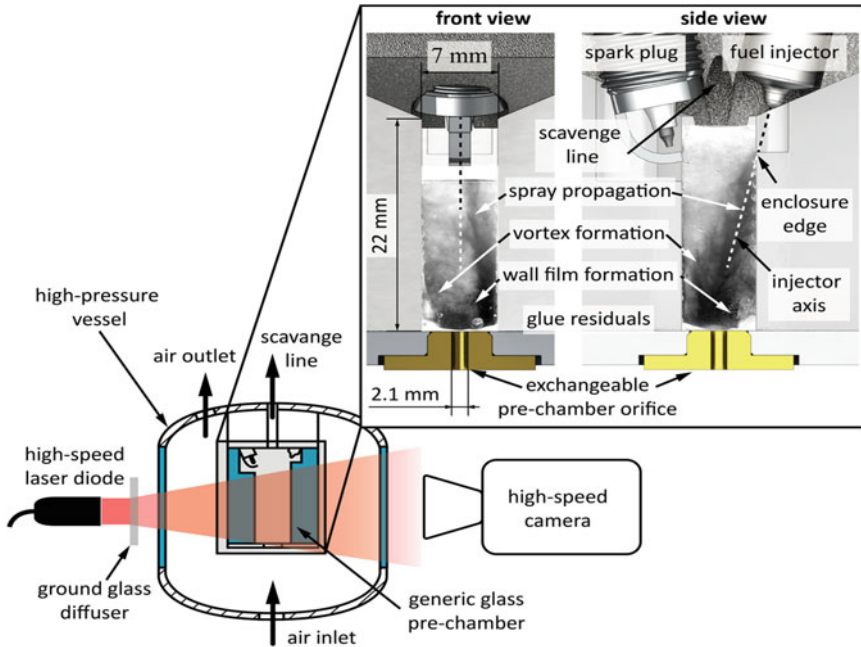


**Fig. 9.11** Overview of the generic pre-chamber test bench. The cutout shows the pre-chamber internal geometry and the location of the spark plug and the injector with an exemplary spray propagation inside the pre-chamber

The pre-chamber top holds a commercial spark plug in a round enclosure (ignition not initiated) and a single-orifice injector, with an inclination of  $12^\circ$  to the centerline of the pre-chamber (in the side view plane, see Fig. 9.11). The main axis of the nozzle orifice is in line with the injector axis. The pre-chamber orifice at the bottom is exchangeable for easy variation of the orifice geometry. A centrally located bore (between spark plug and injector, see Fig. 9.11) allows scavenging of the pre-chamber after injection to exchange the mixture with fresh air and remove residual fuel films. A pressure sensor on the scavenge line continuously monitors the pre-chamber internal pressure. The pre-chamber is mounted in a high-pressure vessel, allowing ambient pressure variations up to 60 bar.

Figure 9.12 shows the first preliminary diffused background illumination visualizations (DBI) of the pre-chamber internal mixture formation as a function of ambient pressure. In each case, Ethanol is injected with a pressure of 200 bar into the pre-chamber. The duration of injector energizing is kept constant at  $700 \mu\text{s}$  ( $250 \mu\text{s}$  holding time). A Cavitar Cavilux Smart high-speed laser diode illuminates the spray from behind, and the resulting images are recorded using a Photron Fastcam SA-X with a LAOWA 100 mm macro lens with a frame rate of 36,000 fps and a resolution of 30.4 pix/mm. Figure 9.12 shows (from left to right) exemplary images recorded



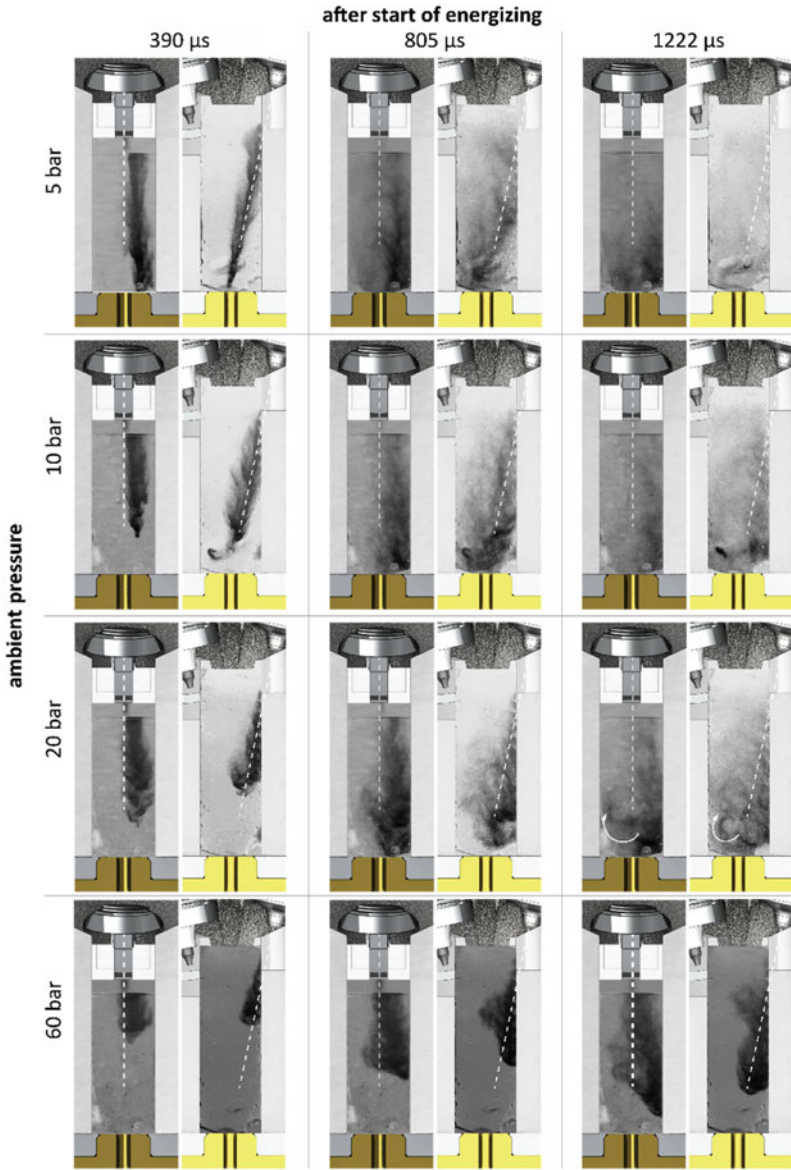


**Fig. 9.12** DBI visualizations of the spray propagation inside the pre-chamber for varying ambient pressures (vertical) and timings after the start of energizing (horizontal). Left images in each box show the front view of the spray from the direction of the spark plug, and right images are recorded perpendicular to the side. Both images are not recorded simultaneously

at 390, 805, and 1222  $\mu\text{s}$  after the start of injector energizing (ASOE) for 5, 10, 20, and 60 bar ambient pressure (from top to bottom).

For each condition, images from the front (in direction of the spark plug, left image) and side view (right image) are recorded. Front and side view are not captured simultaneously and thus are not directly comparable. Furthermore, the images show artifacts at the right, left, and bottom wall induced by glue residues from the manufacturing.

Rising ambient pressure leads to a decreasing propagation velocity and an increasing spray angle. While for an ambient pressure of 5 bar, the spray impinges onto the bottom pre-chamber wall (upper left) after 390  $\mu\text{s}$  ASOE, the spray does not hit the wall after 1222  $\mu\text{s}$  ASOE for 60 bar ambient pressure due to the increased ambient density and consequently higher drag. Increasing ambient pressure leads to an intensified deflection of the spray tip at the pre-chamber end, forming a vortex which transports droplets upstream to the spark plug (highlighted in Fig. 9.12, 20 bar, 2 images on the right).

Interestingly, the visualizations show a spray deflection towards the wall. After exiting the nozzle orifice, the spray propagates along the injector axis (dashed line in Fig. 9.12) until reaching the enclosure's edge. Further downstream, a deflection of the spray into the direction of the wall can be observed, presumably due to the Coandă effect (Wille and Fernholz 1965). Near the wall, the entrainment is hindered due to a lack of air supply, which consequently leads to a pressure drop on the wall. Consequently, the spray is deflected by the reduced pressure towards the wall and is following the wall. As already discussed in Arai et al. (1994) for diesel sprays, the spray deflection increases with increasing ambient pressure, as shown in Fig. 9.12 in the last two rows. A spray deflection to the right side is also visible in the front view (see Fig. 9.12). The spray deflection can have several reasons with mutual interaction: the Coandă effect, an undesired inclination of the nozzle orifice, or pre-chamber internal flow phenomena. Furthermore, the spray plume is widened compared to the side view. Here, the mitigation of the air entrainment due to the wall-induced Coandă effect is probably the reason. For clarification, additional investigations on unhindered spray propagation are necessary.

In summary, these qualitative measurements show interesting mixing and flow phenomena such as vortex formation and the Coandă effect, which can only be observed with the help of the described novel transparent pre-chamber concept. All these effects are strongly pressure and geometry dependent and should be considered in the design of a pre-chamber. On the one hand, an increased pressure slows down the spray propagation, respectively, the mixture formation. On the other hand, an increased pressure facilitates the vortex formation, which intensifies the fuel transportation upstream, aiming to provide an ignitable mixture in the vicinity of the spark plug. In the current configuration, the presented investigation neglects the crucial influence of fresh air flow entering the pre-chamber during the engine's compression stroke. As shown in Sect. 9.3.3, the entering gas jets are influencing the flow field inside the pre-chamber significantly and further enhanced mixing inside the pre-chamber is expected. Therefore, future investigations from the constant flow pressure vessel shall be complemented with measurements of an identical generic pre-chamber

in the rapid compression machine described in Sect. 9.3.3, since it enables consideration of the compression stroke and the entering gas jets. Comparing results from both experimental setups will help to reveal the mutual influence of ambient/injection parameters, pre-chamber geometry, the compression stroke, and finally, the ignition inside the pre-chamber and main chamber. Furthermore, complementary macroscopic and microscopic laser-optical methods will be applied (such as microscopy and laser-induced fluorescence (Schumacher et al. 2020) and allow for quantitative measurements of spray propagation, droplet size distributions, and wall-film thickness. The relative air/fuel ratio, varying ambient/injection parameters (including the ambient temperature), and different promising bio-hybrid fuels will be considered. The overall objective is to optimize the pre-chamber ignition for efficient molecularly controlled combustion systems with low emissions.

#### ***9.4.3 The Importance of Fuel Properties: Towards Co-optimization of Bio-hybrid Fuels and Engines for Ultra-high Efficiency***

In order to exploit the full potentials of novel engine combustion concepts, they should be operated with tailored fuels bearing optimal combustion properties (Burkardt et al. 2021). The degrees of freedom in the molecular fuel structure as well as the engine system thus motivate the co-optimization of fuels and engines (McCormick et al. 2017; Szybist et al. 2021; König et al. 2021; vom Lehn et al. 2021a). In order to perform such optimization, profound knowledge of the most important fuel properties affecting the engine performance is of high importance. Furthermore, in order to evaluate particular fuel components in terms of these important properties, a detailed understanding of how fuel properties depend on the molecular fuel structure is indispensable. This pertains in particular to the novel bio-hybrid fuel candidates investigated within FSC, for which detailed investigations are often lacking in the literature and pioneering work is thus needed to explore their combustion behaviors and engine application potentials. Efficient and predictive screening tools, which allow to estimate the most important combustion-relevant fuel properties, are required to streamline the process of identifying promising candidate fuels (Dahmen and Marquardt 2016).

Increasing engine efficiency is a primary target of fuel design in the context of fuel-engine co-optimization (Kalghatgi et al. 2018). As spark-ignition engine efficiency is limited by engine knock (Wang et al. 2017), the fuel knock resistance, which is commonly expressed in terms of octane numbers, is considered a major combustion property to be optimized. In addition to a high research octane number (RON), modern charged engines require a high octane sensitivity as difference of RON and motor octane number (MON) (Kalghatgi 2001; Kassai et al. 2019), meaning that low MON values are advantageous for a given RON of a fuel. Recent studies have thus been dedicated to the establishment of design rules for knock-resistant fuels

(Boot et al. 2017) and to the development of efficient quantitative structure–property relationship (QSPR) models to estimate octane numbers and octane sensitivities for fuel components of various molecular structures (Kubic et al. 2017; vom Lehn et al. 2020; Schweidtmann et al. 2020). A major limitation of these existing models, however, lies in their limited applicability and validation for many oxygenated fuel classes, owing to the fact that available octane number data are very limited for oxygenated fuels (vom Lehn et al. 2021a). An alternative to the direct use of octane numbers for such fuels lies in the determination of the derived cetane number (DCN) in combination with empirical DCN-RON correlation models (McCormick et al. 2017). First evaluations of the fuel class of cyclic acetals, which is in the focus of current FSC investigations, in terms of DCN (Idel et al. 2020) and chemical ignition delay (Wildenberg et al. 2021) measurements indicate that their reactivities are higher than for well-known octane boosters such as ethanol or methanol, indicating that their octane numbers are presumably lower. However, while the prediction of RON values from DCN data can be inaccurate, the estimation of octane sensitivities based on DCN data alone is not even possible. This motivates further research towards a more precise evaluation on the knock resistance of cyclic acetals and other novel bio-hybrid fuel molecules.

Besides RON and octane sensitivity, a number of other fuel properties impact the engine performance. Due to its charge cooling effect, a high heat of vaporization, as found, e.g., for short-chain alcohols, promotes the knock resistance of a fuel and its engine efficiency potential (Sluder et al. 2016), thus the heat of vaporization should be considered jointly with RON and octane sensitivity when designing high-efficiency fuels (vom Lehn et al. 2021a). The potentially negative impact on cold-start performance should be taken into account, though. Furthermore, the advantages of optimizing engine performance with bio-based and bio-hybrid fuel molecules come at the cost of their relatively low heating values, owing to their highly oxygenated fuel structures. This can obviously result in higher specific fuel consumptions.

In addition to the mentioned fuel properties affecting engine efficiency and/or fuel consumption, an important fuel combustion property, which has traditionally received relatively little consideration in fuel design studies, is the laminar burning velocity (LBV). While being a fundamental premixed flame property of a fuel/oxidizer mixture, the LBV magnitude can have significant impact on the combustion performance in practical engines due to its correlation with the turbulent burning velocity and its impact on flame kernel development, thus affecting burn duration, knock resistance, extinction and lean burn limits, and thus ultimately engine efficiency (Szybist et al. 2021; Cracknell et al. 2012). Very recently, a machine learning based QSPR model has been developed for the first time for the LBV prediction for various fuel classes (vom Lehn et al. 2021b). Cross-validation of the model revealed good prediction performance when applied to molecules not used for training. Hence, it can be applied for LBV assessment of novel bio-hybrid fuel candidates. Figure 9.13 shows the ranking of predicted LBV values for selected fuel compounds currently investigated in FSC. It is found that the cyclic acetals without side chains, including 1, 3-dioxolane and 1, 3-dioxane, exhibit the highest burning velocities among all considered bio-hybrid fuel compounds. More importantly, they allow for an LBV

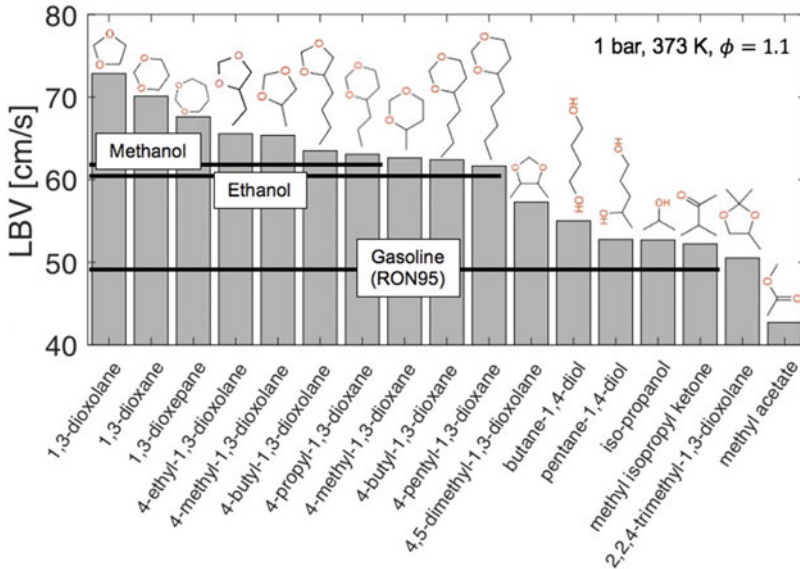


**Fig. 9.13** Laminar burning velocities of selected bio-hybrid fuels investigated within FSC (gray bars) compared with methanol, ethanol, and conventional gasoline (black horizontal lines). The pure component values are based on ANN-QSPR model predictions (vom Lehn et al. 2021b). An experimental value (Lorenzo et al. 2019) is shown for gasoline

increase of up to 50% compared with conventional gasoline and still of up to 20% compared with the well-established alternative fuels ethanol or methanol. While this flame speed enhancement is expected to be beneficial even in conventional SI combustion modes with stoichiometric operation, additional benefit may be anticipated for novel combustion modes, including ultra-lean operation. Future investigations on the engine performance with these fuels are thus of high interest.

**Acknowledgements** The authors gratefully acknowledge the funding by the Deutsche Forschungsgemeinschaft (DFG, German Research Foundation) under Germany’s Excellence Strategy—Cluster of Excellence 2186 “The Fuel Science Center” -ID: 390919832.

The authors gratefully acknowledge the Gauss Centre for Super-computing e.V. ([www.gauss-centre.eu](http://www.gauss-centre.eu)) for granting computing time on the GCS Supercomputer HAWK at Höchstleistungsrechenzentrum Stuttgart ([www.hlr.de](http://www.hlr.de)).

## References

Alvarez CEC, Couto GE, Roso VR et al (2018) A review of prechamber ignition systems as lean combustion technology for SI engines. *Appl Therm Eng* 128:107–120. <https://doi.org/10.1016/j.applthermaleng.2017.08.118>

- Arai M, Amagai K, Ebara T (1994) Attitude control of a diesel spray under the Coanda Effect. In: SAE technical paper series. SAE International400 Commonwealth Drive, Warrendale, PA, United States
- Arcoumanis C, Hu Z, Vafidis C et al (1990) Tumbling motion: a mechanism for turbulence enhancement in spark-ignition engines. In: SAE technical paper series. SAE International400 Commonwealth Drive, Warrendale, PA, United States
- Berger S, Wegmann T, Meinke M et al (2020) Large-Eddy simulation study of biofuel injection in an optical direct injection engine. In: SAE technical paper series. SAE International400 Commonwealth Drive, Warrendale, PA, United States
- Boot MD, Tian M, Hensen EJM et al (2017) Impact of fuel molecular structure on auto-ignition behavior—design rules for future high performance gasolines. *Prog Energy Combust Sci* 60:1–25. <https://doi.org/10.1016/j.pecs.2016.12.001>
- Bozza F, Bellis V de, Tufano D et al (2019) A quasi-dimensional model of pre-chamber spark-ignition engines. In: SAE Technical paper series. SAE International400 Commonwealth Drive, Warrendale, PA, United States
- Braun M, Schröder W, Klaas M (2019b) High-speed tomographic PIV measurements in a DISI engine. *Exp Fluids* 60:523. <https://doi.org/10.1007/s00348-019-2792-4>
- Braun M, Klaas M, Schröder W (2021) Analysis of cyclic variation using time-resolved tomographic particle-image velocimetry. *SAE Int J Adv Curr Prac in Mobility* 3:113–136. <https://doi.org/10.4271/2020-01-2021>
- Braun M, Klaas M, Schröder W (2019a) High-speed 3D measurements of the influence of intake pressure on the in-cylinder flow in a DISI engine. In: SAE technical paper series. SAE International400 Commonwealth Drive, Warrendale, PA, United States
- Bresenham D, Reisel J, Neusen K (1998) Spindt air-fuel ratio method generalization for oxygenated fuels. In: SAE Technical paper series. SAE International400 Commonwealth Drive, Warrendale, PA, United States
- Bunce M, Cairns A, Krishna Pothuraju Subramanyam S et al (2021) The influence of charge motion on pre-chamber and main chamber combustion in a highly dilute jet ignition engine. *Front Mech Eng* 6:884. <https://doi.org/10.3389/fmech.2020.629243>
- Burkardt P, Ottenwälder T, König A et al (2021) Toward co-optimization of renewable fuel blend production and combustion in ultra-high efficiency SI engines. *Int J Engine Res* 56:146808742110409. <https://doi.org/10.1177/14680874211040995>
- Chen H, Xu M, Hung DLS et al (2014) Cycle-to-cycle variation analysis of early flame propagation in engine cylinder using proper orthogonal decomposition. *Exp Thermal Fluid Sci* 58:48–55. <https://doi.org/10.1016/j.expthermflusci.2014.06.017>
- Contino F, Foucher F, Mounaïm-Rousselle C et al (2011) Experimental characterization of ethyl acetate, ethyl propionate, and ethyl butanoate in a homogeneous charge compression ignition engine. *Energy Fuels* 25:998–1003. <https://doi.org/10.1021/ef101602q>
- Cracknell R, Prakash A, Head R (2012) Influence of laminar burning velocity on performance of gasoline engines. In: SAE technical paper series. SAE International400 Commonwealth Drive, Warrendale, PA, United States
- Crolla D, Foster DE, Kobayashi T et al (2014) *Encyclopedia of automotive engineering*. Wiley & Sons, Ltd, Chichester, UK
- Dahmen M, Marquardt W (2015) A novel group contribution method for the prediction of the derived cetane number of oxygenated hydrocarbons. *Energy Fuels* 29:5781–5801. <https://doi.org/10.1021/acs.energyfuels.5b01032>
- Dahmen M, Marquardt W (2016) Model-based design of tailor-made biofuels. *Energy Fuels* 30:1109–1134. <https://doi.org/10.1021/acs.energyfuels.5b02674>
- Di Lorenzo M, Brequigny P, Foucher F et al (2019) Validation of TRF-E as gasoline surrogate through an experimental laminar burning speed investigation. *Fuel* 253:1578–1588. <https://doi.org/10.1016/j.fuel.2019.05.081>



- Günther C, Meinke M, Schröder W (2014) A flexible level-set approach for tracking multiple interacting interfaces in embedded boundary methods. *Comput Fluids* 102:182–202. <https://doi.org/10.1016/j.compfluid.2014.06.023>
- Hoppe F, Burke U, Thewes M et al. (2016a) Tailor-made fuels from biomass: potentials of 2-butanone and 2-methylfuran in direct injection spark ignition engines. *Fuel* 167:106–117. <https://doi.org/10.1016/j.fuel.2015.11.039>
- Hoppe F, Heuser B, Thewes M et al. (2016b) Tailor-made fuels for future engine concepts. *Int J Engine Res* 17:16–27. <https://doi.org/10.1177/1468087415603005>
- Idel J, Neumann M, Wiesenthal J, Jung C, et al (2020) Production and combustion properties of cyclic acetals as novel fuel candidates. In: 9th International conference “Fuel science—from production to propulsion”, Aachen, Germany
- Kalghatgi GT (2001) Fuel anti-knock quality—Part I. Engine studies. In: SAE technical paper series. SAE International400 Commonwealth Drive, Warrendale, PA, United States
- Kalghatgi G, Levinsky H, Colket M (2018) Future transportation fuels. *Prog Energy Combust Sci* 69:103–105. <https://doi.org/10.1016/j.peccs.2018.06.003>
- Kang K-Y, Oh S-M, Lee J-W et al (1997) The effects of tumble flow on lean burn characteristics in a four-valve SI engine. In: SAE Technical paper series. SAE International400 Commonwealth Drive, Warrendale, PA, United States
- Kassai M, Aksu C, Shiraishi T et al (2019) Mechanism analysis on the effect of fuel properties on knocking performance at boosted conditions. In: SAE technical paper series. SAE International400 Commonwealth Drive, Warrendale, PA, United States
- König A, Siska M, Schweidtmann AM et al (2021) Designing production-optimal alternative fuels for conventional, flexible-fuel, and ultra-high efficiency engines. *Chem Eng Sci* 237:116562. <https://doi.org/10.1016/j.ces.2021.116562>
- Kubic WL, Jenkins RW, Moore CM et al (2017) Artificial neural network based group contribution method for estimating Cetane and octane numbers of hydrocarbons and oxygenated organic compounds. *Ind Eng Chem Res* 56:12236–12245. <https://doi.org/10.1021/acs.iecr.7b02753>
- Lehrheuer B, Hoppe F, Heufer KA et al (2019) Diethoxymethane as tailor-made fuel for gasoline controlled autoignition. *Proc Combust Inst* 37:4691–4698. <https://doi.org/10.1016/j.proci.2018.07.063>
- McCormick RL, Fioroni G, Fouts L et al (2017) Selection criteria and screening of potential biomass-derived streams as fuel blendstocks for advanced spark-ignition engines. *SAE Int J Fuels Lubr* 10:442–460. <https://doi.org/10.4271/2017-01-0868>
- Müller C, Pischinger S, Tews S et al (2020) Analysis of experimental results with an active pre-chamber ultra-lean burn SI engine. *Int J Engine Res* 6:146808742097454. <https://doi.org/10.1177/1468087420974544>
- Nguyen D-K, van Craeynest T, Pillu T et al (2018) Downsizing potential of methanol fueled disi engine with variable valve timing and boost control. In: SAE technical paper series. SAE International400 Commonwealth Drive, Warrendale, PA, United States
- Schneiders L, Günther C, Meinke M et al (2016) An efficient conservative cut-cell method for rigid bodies interacting with viscous compressible flows. *J Comput Phys* 311:62–86. <https://doi.org/10.1016/j.jcp.2016.01.026>
- Schneiders L, Guenther C, Grimm JH et al (2015) Sharp resolution of complex moving geometries using a multi-cut-cell viscous flow solver. In: 22nd AIAA computational fluid dynamics conference. American Institute of Aeronautics and Astronautics, Reston, Virginia, p 507
- Schumacher L, Zuschlag M, Bieber M et al (2020) Planar laser-induced fluorescence for quantification of liquid removal and deposition during spray wall film interaction. *Atomiz Spr* 30:799–810. <https://doi.org/10.1615/AtomizSpr.2020034731>
- Schweidtmann AM, Rittig JG, König A et al (2020) Graph neural networks for prediction of fuel ignition quality. *Energy Fuels* 34:11395–11407. <https://doi.org/10.1021/acs.energyfuels.0c01533>
- Serrano D, Zaccardi J-M, Müller C et al (2019) Ultra-lean pre-chamber gasoline engine for future hybrid powertrains. In: SAE technical paper series. SAE International400 Commonwealth Drive, Warrendale, PA, United States

- Sluder CS, Szybist JP, McCormick RL et al (2016) Exploring the relationship between octane sensitivity and heat-of-vaporization. *SAE Int J Fuels Lubr* 9:80–90. <https://doi.org/10.4271/2016-01-0836>
- Spindt RS (1965) Air-fuel ratios from exhaust gas analysis. In: SAE technical paper series. SAE International 400 Commonwealth Drive, Warrendale, PA, United States
- Szybist JP, Busch S, McCormick RL et al (2021) What fuel properties enable higher thermal efficiency in spark-ignited engines? *Prog Energy Combust Sci* 82:100876. <https://doi.org/10.1016/j.pecs.2020.100876>
- Toulson E, Schock HJ, Attard WP (2010) A review of pre-chamber initiated jet ignition combustion systems. In: SAE Technical paper series. SAE International 400 Commonwealth Drive, Warrendale, PA, United States
- Verhelst S, Turner JW, Silgheem L et al (2019) Methanol as a fuel for internal combustion engines. *Prog Energy Combust Sci* 70:43–88. <https://doi.org/10.1016/j.pecs.2018.10.001>
- Vom Lehn F, Brosius B, Broda R et al (2020) Using machine learning with target-specific feature sets for structure-property relationship modeling of octane numbers and octane sensitivity. *Fuel* 281:118772. <https://doi.org/10.1016/j.fuel.2020.118772>
- Vom Lehn F, Cai L, Tripathi R et al (2021a) A property database of fuel compounds with emphasis on spark-ignition engine applications. *Appl Energy Combust Sci* 5:100018. <https://doi.org/10.1016/j.jaecs.2020.100018>
- Vom Lehn F, Cai L, Copa Cáceres B et al (2021b) Exploring the fuel structure dependence of laminar burning velocity: a machine learning based group contribution approach. *Combust Flame* 232:111525. <https://doi.org/10.1016/j.combustflame.2021.111525>
- Vu T-T, Guibert P (2012) Proper orthogonal decomposition analysis for cycle-to-cycle variations of engine flow. Effect of a control device in an inlet pipe. *Exp Fluids* 52:1519–1532. <https://doi.org/10.1007/s00348-012-1268-6>
- Wang Z, Liu H, Reitz RD (2017) Knocking combustion in spark-ignition engines. *Prog Energy Combust Sci* 61:78–112. <https://doi.org/10.1016/j.pecs.2017.03.004>
- Wildenberg A, Fenard Y, Carbonnier M et al (2021) An experimental and kinetic modeling study on the oxidation of 1,3-dioxolane. *Proc Combust Inst* 38:543–553. <https://doi.org/10.1016/j.proci.2020.06.362>
- Wille R, Fernholz H (1965) Report on the first European mechanics colloquium, on the Coanda effect. *J Fluid Mech* 23:801–819. <https://doi.org/10.1017/S0022112065001702>
- Wouters C, Burkardt P, Fischer M et al (2021a) Effects of stroke on spark-ignition combustion with gasoline and methanol. *Int J Engine Res* 87:146808742110396. <https://doi.org/10.1177/14680874211039685>
- Wouters C, Burkardt P, Pischinger S (2021b) Limits of compression ratio in spark-ignition combustion with methanol. *Int J Engine Res* 67:146808742110433. <https://doi.org/10.1177/14680874211043390>
- Zhao M, Kaiser S (2018) Optical Diagnostics for Knock in Compression-Ignition Engines via High-Speed Imaging. *SAE Int J Engines* 11:903–918. <https://doi.org/10.4271/2018-01-0631>



# Chapter 10

## The Use of Ammonia as a Fuel for Combustion Engines



Dong Han, Yusen Liu, and Zhen Huang

**Abstract** In the past decades, combustion engines have played an important role in addressing the transportation demands. However, emissions of greenhouse gases such as carbon dioxide (CO<sub>2</sub>) emitted by combustion engines rapidly increased, leading to climatic issues like global warming. This adverse environmental impact has been the main motivation to search for clean solutions for fossil fuel replacement. Ammonia is recognized as a promising carbon-free fuel to meet the requirement in CO<sub>2</sub> reduction. Specifically, ammonia has a higher volumetric energy density compared with Hydrogen, and it is easier to produce, store and transport in comparison to other carbon-free fuels. However, ammonia-fueled applications exhibit lower efficiency and stability compared with conventional-fueled systems, due to the lower flame speed and combustion temperatures of ammonia. In this review paper, the previous and ongoing studies exploring the potential of ammonia as an engine fuel are highlighted. The strategies to realize the usage of ammonia in combustion engines are summarized, and the future pathway to use ammonia as an engine fuel is discussed.

**Keywords** Ammonia · Combustion engines · Hydrogen · Carbon-free fuel · Dual-fuel

### 10.1 Introduction

Since the industrial revolution, burning fossil fuels has produced a number of greenhouse gases (GHG) emissions. The atmospheric concentration of carbon dioxide (CO<sub>2</sub>), a primary GHG, has been increasing from less than 300 to 408 ppm over the past two centuries (Mitchard 2018). The continually increasing GHG emissions cause the threat of global warming, evidenced by the increased global surface average

---

The original version of this chapter was revised. The word “Gasoline” in the abstract has been changed to “Hydrogen”. The correction to this chapter can be available at [https://doi.org/10.1007/978-981-16-8717-4\\_16](https://doi.org/10.1007/978-981-16-8717-4_16)

D. Han (✉) · Y. Liu · Z. Huang  
Shanghai Jiao Tong University, Shanghai 200240, China  
e-mail: [dong\\_han@sjtu.edu.cn](mailto:dong_han@sjtu.edu.cn)

© The Author(s), under exclusive license to Springer Nature Singapore Pte Ltd. 2022, corrected publication 2022

G. Kalghatgi et al. (eds.), *Engines and Fuels for Future Transport*, Energy, Environment, and Sustainability, [https://doi.org/10.1007/978-981-16-8717-4\\_10](https://doi.org/10.1007/978-981-16-8717-4_10)

temperature by approximately 1.0 °C above the pre-industrial level, according to the Intergovernmental Panel on Climate Change (Allen et al. 2019). Major risks as a result of human-induced global warming include climate and weather extremes, such as heavy precipitation, extreme heatwaves and damages to natural and human systems. To cope with the detrimental consequences of human-induced climate change, 195 countries signed the Paris Agreement (Horowitz 2016), announcing to take actions to reduce the GHG. Some major economies also set goals to achieve carbon neutrality, i.e. net-zero carbon emissions. For example, in 2019, the European Commission adopted the European Green Deal, targeting at reducing member states' carbon emissions by at least 55% by 2030, compared to 1990s levels, and realizing Europe's net-zero carbon emissions by 2050 (Mulvaney 2019). In 2020, the Chinese government committed to make the country's carbon emissions peak before 2030, and make the world's second largest economy carbon neutral by 2060 (Outline of the 14th Five-Year Plan 2021).

The transport sector is one of the primary contributors of GHG emissions, accounting for about 13% of overall GHG emissions and over 21% of the world's energy-related CO<sub>2</sub> emissions (Dulal et al. 2011). Specifically, before the second half of the twentieth century, the major contributors to the transport-related CO<sub>2</sub> emissions were Europe and the United States, which accounted for more than 85% of CO<sub>2</sub> emissions each year (Fan et al. 2018). However, in the past few decades, this percentage has declined to lower than one-third, and a significant increase in CO<sub>2</sub> emissions has been observed in the rest of the world, particularly across Asia (Solaymani 2019). To cut the greenhouse gases emissions and achieve the carbon neutrality goal in the transport sector, a significant technology transformation needs to be carried out for the powertrain or propulsion systems of the automotive and marine applications, with the low-carbon or decarbonized technologies adopted to replace the currently used fossil fuel combustion technologies. The transport applications decarbonization could be realized by utilizing battery or fuel cell propulsion systems, or by replacing the petroleum-based fuels with the carbon-free fuels, such as ammonia and hydrogen. Compared with the new-types of propulsion systems, using carbon-free fuels in combustion engines has certain advantages, including fewer modifications of the current power systems and infrastructures, and the cost competences compared to the new propulsion systems. Burning these carbon-free fuels have no direct GHG emissions, and their lifecycle GHG emissions could also be well controlled through using renewable electricity in fuel synthesis. Further, different from hydrogen, ammonia possesses merits in storage convenience and high volumetric energy density. These advantages of ammonia, particularly in the background of achieving carbon neutrality, have drawn increasing interest in using this clean fuel to power transport applications.

In this paper, we summarize the research progress and discuss the technical solutions to using ammonia as the combustion engine fuel. This chapter is organized as follows: Sect. 10.1 introduces the necessity to use ammonia in combustion engines from the perspective of achieving carbon neutrality in the transport sector. Sections 10.2 and 10.3 give an overview of the physical and chemical properties of ammonia, and the advantages and challenges of using ammonia as an engine fuel.

In Sect. 10.4, fundamental combustion characteristics and combustion kinetics of ammonia are discussed, as understanding fuel combustion fundamentals is important for engine combustion modulation. Section 10.5 provides a detailed overview of the combustion and emissions control technologies used for ammonia combustion engines, using ammonia either as a single fuel or in dual-fuel operation. Section 10.6 presents conclusions and the prospects for ammonia combustion engines.

## 10.2 Physical and Chemical Properties of Ammonia

Every year, about 200 Mt of ammonia are produced all over the world (Kobayashi et al. 2019), and are widely utilized in agriculture and industrial processes. Its large production scale makes it possible to use ammonia as a main alternative fuel. Also, ammonia can be produced from variant energy resources, including fossil fuels, biomass, solar and wind, through different conversion technologies, such as thermochemical, electrochemical, photochemical and plasma (Aziz et al. 2020). The key properties of ammonia, fossil fuels and some other alternative fuels are compared in Tables 10.1 and 10.2 (Zacharakis-Jutz 2013; Valera-Medina et al. 2018; Lesmana et al. 2019; Dasappa et al. 2003; Syed et al. 2010; Borate 2014; Lee et al. 2012; Vries et al. 2011). Compared with hydrogen, ammonia is more easily compressed into liquid, indicating that ammonia storage and transportation do not need special materials and equipment. However, ammonia has a high auto-ignition temperature and a low flame speed, and requires high ignition energy, making it more difficult to burn alone. Consequently, blending ammonia with ignition promoters, especially hydrogen, is considered in many research studies. Additionally, ammonia has a higher octane number, suggesting a better anti-knock performance. As such, ammonia engines can be operated at higher compression ratios, and the thermal efficiency of ammonia engines can be greatly promoted compared to gasoline engines by elevating the compression ratio (Grannell et al. 2008).

## 10.3 Advantages and Challenges of Ammonia as Engine Fuel

Ammonia is widely used in many fields such as chemical industry and agriculture for a long time. Therefore, there are mature systems for the production, storage, transportation and supply of ammonia, and the regulations for ammonia are more comprehensive than other alternative fuels. On the other hand, the application of ammonia in engines is technically feasible, because its high energy density makes it more suitable as a fuel than some other liquefied gases. Although ammonia is now mainly produced from fossil fuels, named grey ammonia, it can also be synthesized from renewable energy such as biomass, or solar and wind, named green ammonia. It

**Table 10.1** Characteristics of ammonia and other fuels (Zacharakis-Jutz 2013; Valera-Medina et al. 2018; Lesmana et al. 2019; Dasappa et al. 2003; Syed et al. 2010; Borate 2014; Lee et al. 2012; Vries et al. 2011)

Characteristics	Ammonia (l)	Ammonia (g)	Hydrogen (l)	Hydrogen (g)	Natural Gas (l)	Natural gas (g)
Storage temperature (K)	298 (Zacharakis-Jutz 2013)	300 (Valera-Medina et al. 2018)	20 (Zacharakis-Jutz 2013)	300 (Valera-Medina et al. 2018)	298 (Zacharakis-Jutz 2013)	300 (Valera-Medina et al. 2018)
Storage pressure (kPa)	1030 (Zacharakis-Jutz 2013)	100 (Valera-Medina et al. 2018)	24,821 (Zacharakis-Jutz 2013)	100 (Valera-Medina et al. 2018)	24,821 (Zacharakis-Jutz 2013)	100 (Valera-Medina et al. 2018)
Density (kg/m <sup>3</sup> )	602.8 (Zacharakis-Jutz 2013)	0.73 (Valera-Medina et al. 2018)	71.1 (Zacharakis-Jutz 2013)	0.08 (Valera-Medina et al. 2018)	187.2 (Zacharakis-Jutz 2013)	0.66 (Valera-Medina et al. 2018)
Latent heat of vaporization (kJ/kg)	1369 (Zacharakis-Jutz 2013)	–	446 (Zacharakis-Jutz 2013)	–	104.8 (Zacharakis-Jutz 2013)	–
Volumetric energy density (MJ/m <sup>3</sup> )	11,333 (Zacharakis-Jutz 2013)	13.7	2101 (Zacharakis-Jutz 2013)	9.6	7132 (Zacharakis-Jutz 2013)	33.1
Lower heating value (MJ/kg)	18.8 (Zacharakis-Jutz 2013)	18.8 (Valera-Medina et al. 2018)	120 (Zacharakis-Jutz 2013)	120 (Valera-Medina et al. 2018)	38.1 (Zacharakis-Jutz 2013)	50.1 (Valera-Medina et al. 2018)
Auto-ignition temperature (K)	924 (Zacharakis-Jutz 2013)	930 (Valera-Medina et al. 2018)	844 (Zacharakis-Jutz 2013)	773–850 (Valera-Medina et al. 2018)	723 (Zacharakis-Jutz 2013)	859 (Valera-Medina et al. 2018)
Adiabatic temperature (K)	1850 (Valera-Medina et al. 2018)	1850 (Valera-Medina et al. 2018)	2483 (Valera-Medina et al. 2018)	2483 (Valera-Medina et al. 2018)	2223 (Valera-Medina et al. 2018)	2223 (Valera-Medina et al. 2018)
Minimum ignition energy (mJ)	8.0 (Zacharakis-Jutz 2013)	8.0 (Zacharakis-Jutz 2013)	0.011 (Zacharakis-Jutz 2013)	0.011 (Zacharakis-Jutz 2013)	0.31 (Zacharakis-Jutz 2013)	0.31 (Zacharakis-Jutz 2013)

(continued)

Table 10.1 (continued)

Characteristics	Ammonia (l)	Ammonia (g)	Hydrogen (l)	Hydrogen (g)	Natural Gas (l)	Natural gas (g)
Flammability limits, gas in air (Vol.%)	16–25 (Zacharakis-Jutz 2013)	16–25 (Zacharakis-Jutz 2013)	4–75 (Zacharakis-Jutz 2013)	4–75 (Zacharakis-Jutz 2013)	5–15 (Zacharakis-Jutz 2013)	5–15 (Zacharakis-Jutz 2013)
Laminar flame speed (m/s)	0.15 (Zacharakis-Jutz 2013)	0.07 (Valera-Medina et al. 2018)	3.51 (Zacharakis-Jutz 2013)	3.51 (Valera-Medina et al. 2018)	–	0.38 (Valera-Medina et al. 2018)
Research octane number	110 (Zacharakis-Jutz 2013)	130 (Valera-Medina et al. 2018)	>130 (Zacharakis-Jutz 2013)	>130 (Zacharakis-Jutz 2013)	107 (Zacharakis-Jutz 2013)	120 (Valera-Medina et al. 2018)
Cetane number	–	–	–	–	–	–

**Table 10.2** Characteristics of ammonia and other fuels (Zacharakis-Jutz 2013; Valera-Medina et al. 2018; Lesmana et al. 2019; Dasappa et al. 2003; Syed et al. 2010; Borate 2014; Lee et al. 2012; Vries et al. 2011)

Characteristics	Ammonia (l)	Ammonia (g)	Gasoline	Diesel	Ethanol	Dimethyl Ether
Storage temperature (K)	298 (Zacharakis-Jutz 2013)	300 (Valera-Medina et al. 2018)	298 (Zacharakis-Jutz 2013)	298 (Zacharakis-Jutz 2013)	298 (Lesmana et al. 2019)	298 (Zacharakis-Jutz 2013)
Storage pressure (kPa)	1030 (Zacharakis-Jutz 2013)	100 (Valera-Medina et al. 2018)	101.3 (Zacharakis-Jutz 2013)	101.3 (Zacharakis-Jutz 2013)	101.3 (Lesmana et al. 2019)	500 (Zacharakis-Jutz 2013)
Density (kg/m <sup>3</sup> )	602.8 (Zacharakis-Jutz 2013)	0.73 (Valera-Medina et al. 2018)	698.3 (Zacharakis-Jutz 2013)	838.8 (Zacharakis-Jutz 2013)	790 (Lesmana et al. 2019)	668 (Zacharakis-Jutz 2013)
Latent heat of vaporization (kJ/kg)	1369 (Zacharakis-Jutz 2013)	–	71.8 (Zacharakis-Jutz 2013)	47.9 (Zacharakis-Jutz 2013)	840 (Lesmana et al. 2019)	467 (Zacharakis-Jutz 2013)
Volumetric energy density (MJ/m <sup>3</sup> )	11,333 (Zacharakis-Jutz 2013)	13.7	31,074 (Zacharakis-Jutz 2013)	36,403 (Zacharakis-Jutz 2013)	21,251	18,991 (Zacharakis-Jutz 2013)
Lower heating value (MJ/kg)	18.8 (Zacharakis-Jutz 2013)	18.8 (Valera-Medina et al. 2018)	44.5 (Zacharakis-Jutz 2013)	43.4 (Zacharakis-Jutz 2013)	26.9 (Lesmana et al. 2019)	28.4 (Zacharakis-Jutz 2013)
Auto-ignition temperature (K)	924 (Zacharakis-Jutz 2013)	930 (Valera-Medina et al. 2018)	573 (Zacharakis-Jutz 2013)	503 (Zacharakis-Jutz 2013)	636 (Lesmana et al. 2019)	623 (Zacharakis-Jutz 2013)
Adiabatic temperature (K)	1850 (Valera-Medina et al. 2018)	1850 (Valera-Medina et al. 2018)	2411 (Borate 2014)	2290 (Dasappa et al. 2003)	2355 (Borate 2014)	2227 (Lee et al. 2012)

(continued)

Table 10.2 (continued)

Characteristics	Ammonia (l)	Ammonia (g)	Gasoline	Diesel	Ethanol	Dimethyl Ether
Minimum ignition energy (mJ)	8.0 (Zacharakis-Jutz 2013)	8.0 (Zacharakis-Jutz 2013)	0.14 (Zacharakis-Jutz 2013)	–	0.65 (Lesmana et al. 2019)	0.2 (Zacharakis-Jutz 2013)
Flammability limits, gas in air (Vol.%)	16–25 (Zacharakis-Jutz 2013)	16–25 (Zacharakis-Jutz 2013)	1.4–7.6 (Zacharakis-Jutz 2013)	0.6–5.5 (Zacharakis-Jutz 2013)	3.3–19 (Lesmana et al. 2019)	3–18.6 (Zacharakis-Jutz 2013)
Laminar flame speed (m/s)	0.15 (Zacharakis-Jutz 2013)	0.07 (Valera-Medina et al. 2018)	0.58 (Zacharakis-Jutz 2013)	–	0.45 (Lesmana et al. 2019)	0.30 (Vries et al. 2011)
Research octane number	110 (Zacharakis-Jutz 2013)	130 (Valera-Medina et al. 2018)	90–98 (Zacharakis-Jutz 2013)	–	107 (Lesmana et al. 2019)	60.6 (Zacharakis-Jutz 2013)
Cetane number	–	–	–	40–50 (Lesmana et al. 2019)	–	>55 (Lesmana et al. 2019)

is predicted that the global green ammonia market will rapidly grow, at a compound annual growth rate of 7.8%, from 2021 to 2027 (Green ammonia Market 2021), which could reduce the dependence of ammonia production on fossil fuels. Although ammonia has such advantages, its application in engines still faces some safety and compatibility challenges. First, ammonia is slightly toxic, but it is fatal only when its concentration reaches 1000 times as high as the detectable concentration. Its strong pungent smell also makes it easy to detect the ammonia leak, and there are specific protective masks to avoid such poisoning. Second, the flammability limits of ammonia in the air are 16% to 25% based on the volume fraction, which is much higher than some other fuels. Third, ammonia solution is corrosive for some metals, such as copper, silver, tin, zinc and their alloys, due to its high pH number of about 11.6. However, this problem may be insignificant for its application in engines, because engines are mostly made of cast iron and steel. Reiter et al. (Reiter and Kong 2011) conducted a 40-h corrosion test on an ammonia engine, and found that the corrosiveness of ammonia has little effect on the lubrication oil. By contrast, combustion technology development is more significant in ammonia application. Ammonia has a reluctant combustion tendency and as such active pilot fuels are usually needed to maintain controllable engine combustion. Moreover, ammonia is a nitrogen-containing fuel, and its combustion could cause increased fuel-sourced  $\text{NO}_x$  emissions, and therefore effective combustion and emissions control technologies should be developed to solve this problem.

## 10.4 Ammonia Combustion Kinetics and Characteristics

Ammonia application in engines requires an understanding of its fundamental combustion behavior and combustion kinetics. Some studies in the literature have been conducted to identify ammonia flame propagation, auto-ignition characteristics and dominant chemical kinetics for its combustion behavior.

Miller et al. (1983) first established a simple model for ammonia combustion, whose prediction performance showed a good agreement with the experimentally measured flame structures and flame speeds of ammonia/oxygen and ammonia/hydrogen/oxygen flames. Further, a complete ammonia combustion kinetic model was established by Miller and Bowman (1989). After that, more research was conducted to improve model prediction performance for ammonia combustion, e.g. the models (Duynslaegher et al. 2009; Konnov 2009; Tian et al. 2009; Klippenstein et al. 2011; Song et al. 2016; Glarborg et al. 2018) developed based on the studies of Miller and Bowman (1989), Lindstedt et al. (1994) and Glarborg et al. (1994). Among these models, Konnov's model (Konnov 2009) could capture the combustion characteristics of small hydrocarbons, but it could not predict the ammonia combustion characteristics accurately under some conditions (Kumar and Meyer 2013; Xiao and Valera-Medina 2017). However, it was usually used as the base reaction set for further refinement (Nakamura et al. 2017; Duynslaegher et al. 2012), owing to a large number of species in this model. In contrast, Tian's model (Tian et al. 2009)



was more focused on ammonia oxidation at low pressures, and Song's model (Song et al. 2016) proposed and validated the main paths of ammonia combustion at high pressures. Additionally, Mathieu's model (Mathieu and Petersen 2015), developed based on Dagaut's model (Dagaut et al. 2008) by supplementing  $\text{N}_2\text{O}$ ,  $\text{NO}_2$  and  $\text{NNH}$  sub-mechanisms, was adopted by many researchers in recent years, because it could well predict ignition delay times and intermediate species characteristics (Zhang et al. 2017; He et al. 2019; Han et al. 2021). However, each model is normally developed by focusing on only one combustion target at certain conditions, without systematic characterization in fuel combustion behaviors. For instance, the models developed by Nakamura et al. (2017) and Stagni et al. (2020) have good prediction performances for ignition delay times of ammonia/air flames, but are less satisfactory when predicting  $\text{NO}_x$  emissions. The model developed by Otomo et al. (2018) was accurate in laminar flame speed prediction for ammonia/air flames at the atmospheric condition, but was unable to capture pressure effect on flame speeds (Han et al. 2020). Additionally, the combustion characteristic measurements in different studies may be discrepant, e.g. the maximum laminar flame speeds of ammonia/air mixtures measured by different groups (Mei et al. 2019; Han et al. 2019). Therefore, the development of a more accurate ammonia combustion kinetic model is still ongoing, for the more comprehensive understanding of ammonia combustion chemistry.

Besides the development of combustion kinetic models, studies on ammonia combustion characteristics have also been widely conducted in recent years. The laminar flame speed is an important target to characterize the flame propagation tendency in spark ignition (SI) engines. According to the literature, the peak laminar flame speeds of ammonia occur at around the stoichiometric ratio condition, and could be elevated with increased oxygen concentration and reduced with pressure elevation (Liu et al. 2019; Hayakawa et al. 2015). The study on the ammonia-air swirl flame showed that the blow-off of ammonia-air flame was strongly related to excessive stretch, reduced heat release rate and increased heat loss (Wei et al. 2021), and therefore the ammonia flame is usually unstable. To increase the flame speed and improve combustion stability, ammonia is always blended with active fuels, such as methane and hydrogen (Mikulčić et al. 2021; Sun et al. 2021), and the combustion characteristics of the fuel blends were also studied. The laminar flame speeds were promoted with the addition of active fuels, and it was found that the equivalence ratio where the peak laminar flame speed occurred was at around 1.1 for both the ammonia-methane and ammonia-hydrogen blends at atmospheric pressure and room temperature (Lhuillier et al. 2020a; Shu et al. 2021). However, according to Goldmann and Dinkelacker (2018), as pressure increased to 3 MPa and the initial temperature increased to 500 K, the equivalence ratio of the peak laminar flame speed was reduced to around 0.8 for the ammonia-hydrogen blends, as shown in Fig. 10.1. Moreover, the ammonia-syngas blends were also analyzed (Mei et al. 2020), and it was found that the flame speed was strongly pressure-dependent, because of the increased impacts of the three-body reaction  $\text{H} + \text{O}_2 + \text{M} = \text{HO}_2 + \text{M}$  at elevated pressures.

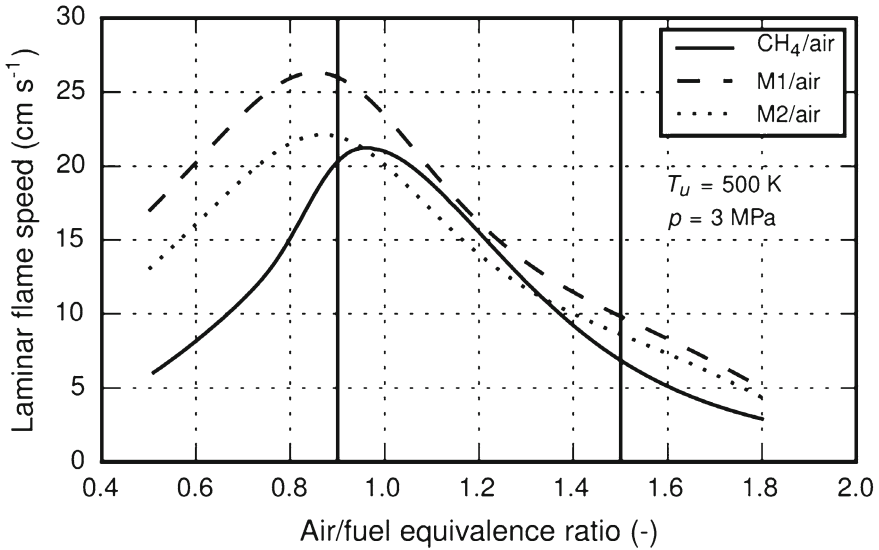


**Fig. 10.1** Laminar flame speeds of ammonia and hydrogen blends in Ref. (Goldmann and Dinkelacker 2018). (M1: 0.56 NH<sub>3</sub> + 0.44 H<sub>2</sub> and M2: 0.48 NH<sub>3</sub> + 0.39 H<sub>2</sub> + 0.13 N<sub>2</sub>)

Lean combustion is usually used in engines to achieve high combustion efficiency, and some research was conducted to identify NO<sub>x</sub> emissions characteristics in lean ammonia-methane-air combustion in a perfectly stirred reactor (PSR) (Li et al. 2019). It showed that NO<sub>x</sub> emissions were mainly produced through the HNO pathway, and were insensitive to the residence time in the PSR, indicating that shortened residence time could not effectively reduce NO<sub>x</sub> emissions. In contrast, Hussein et al. (2019) investigated emissions from ammonia-hydrogen combustion, and found that increased residence time could reduce NO emissions to a low level. In a study by Zhang et al. (2021), it was found that NO<sub>x</sub> emissions were not increased with 10% methane or hydrogen addition to ammonia. Cai et al. (2021) assessed NO emissions in a micro-combustor fueled with ammonia, and the NO<sub>x</sub> emissions could be reduced with a perforated plate design, due to the lower temperature and flame speed.

Except for the above studies, other combustion performances of ammonia and its blends were discussed, such as combustion efficiency and explosion phenomenon. Zhang et al. (2019) analyzed the energy conversion process in flames of ammonia-hydrogen blends based on the second law of thermodynamics, and revealed that the total exergy destructions in the flames decreased with hydrogen addition and pressure elevation. Li et al. (2018a, b) investigated the effects of equivalence ratios on explosion behaviors of ammonia and ammonia-hydrogen blends. They showed that the maximum explosion pressures occurred at the stoichiometric condition, and there was a positive correlation between the flame speed and explosion. The explosion limits of ammonia-hydrogen blends were also studied to reveal the responses of

critical explosion temperatures and pressures to the changed fuel components (Liu and Han 2021).

## 10.5 Combustion Engines Fueled with Ammonia

### 10.5.1 *History of Ammonia as Power*

The application of ammonia in vehicles can date back to 1822, when Gurney invented an ammonia engine to replace the steam one (Gurney et al. 1998). During World War II, it was a highlight in the history of ammonia engines. Anhydrous ammonia was utilized on motor buses to maintain public transportation in Belgium due to the lack of diesel fuel (Koch 1945), and coal gas was used as the ignition promoter for ammonia. In the 1960s, the US Army proposed the Energy Depot Concept to explore alternative fuels applied in military equipment, which caused a discussion on ammonia as fuel again. In this background, Cornelius et al. (1965), Gray et al. (1966) and Starkman et al. (1967) discussed and analyzed the possibility of ammonia application in diesel engines. They proved that pure ammonia could be used in compression ignition (CI) engines, but the compression ratio should be as high as up to 35:1. However, if some pilot fuels were used to ignite ammonia, or an SI system was adopted, the compression ratio could be reduced. Meanwhile, the National Aeronautics and Space Administration conducted the X-15 hypersonic research program (Jenkins 2007). The X-15 was powered by a rocket engine fueled with anhydrous ammonia and liquid oxygen. All of the above researches supported that ammonia could be utilized as a power fuel. Then, the research on ammonia engines suddenly decreased, with few studies published before the end of the twentieth century.

In the twenty-first century, with the increasing concerns about environmental problems, studies on ammonia engines have been increasing again. The Canadian Hydrofuel Inc. developed a multi-fuels conversion system compatible with ammonia (Chiong et al. 2021). The Marangoni presented the first racing car fueled with ammonia, GT86 ECO, in the 2013 Geneva Motor Show (Dimitriou and Javaid 2020). Additionally, the South Korean Institute for Energy Research, Xiamen University and Sturman Industries also focused on ammonia as power (Cardoso et al. 2021). Recently, explosive growth occurred in the researches for maritime engines fueled with ammonia, as the International Maritime Organization announced in 2018, that greenhouse gas emissions from shipping need to be reduced by at least 50 percent by 2050 (Joung et al. 2020). As a response, in 2019, the MAN Energy Solutions, the Shanghai Merchant Ship Design & Research Institute and the American Bureau of Shipping started a collaboration to design an ammonia-fueled container carrier of 2700 TEU capacity (Hansson et al. 2020). The Japanese shipping company NYK Line (Ayvalı et al. 2021) announced its plan to develop a series of ammonia-fueled vessels. Wartsila (Cesaro et al. 2021) also announced that they were developing the world's first full-scale four-stroke combustion engine fueled with ammonia.

### 10.5.2 Engines Fueled with Ammonia

Although ammonia was once used in power machines in the first half of the twentieth century, little test data were preserved. In the 1960s, the concept of ammonia engines was proposed again (Garabedian and Pearsall 1967; Starkman et al. 1966). In 2003, Liu et al. (2003) carried out a computational study on ammonia SI engines, and suggested that the higher compression ratio is beneficial to ammonia combustion. However, no experiments about pure ammonia in engines were conducted owing to the difficulty in pure ammonia combustion modulation. Later, Lee and Song (2018) tried to use pure ammonia in a CI engine, and the combustion strategy used in their study is described in Fig. 10.2. Specifically, due to the low ignition tendency of ammonia-air mixtures at lean conditions, some ammonia is first injected with air early in the intake process, called pilot injection, to form a homogenous mixture with equivalence ratios of 0.1–0.3. The combustion of the premixed mixture promotes the in-cylinder temperature, and as such, the main ammonia spray could be ignited more easily. Nevertheless, the range of main injection timing is very limited, because inappropriate injection tends to extinguish the pre-burn flame, resulting in unstable engine operation.

The performance of ammonia SI engines was also investigated by Lhuillier et al. (2019a). They recommended an increased intake pressure to promote ammonia combustion, and as such, the engine combustion stability and power output could be improved and become comparable to those when methane was used as the fuel. Considering that pressurization is required for liquid ammonia storage, Schonborn (2020) tried to simplify the ammonia storage by storing ammonia in water, and compared the lean combustion processes of anhydrous ammonia and 25% mass-based aqueous ammonia at different engine compressions ratios. They found that in CI modes, the minimum compression ratio to ignite pure ammonia was about 24.8, while that to ignite aqueous ammonia is 26.7. The in-cylinder combustion pressures

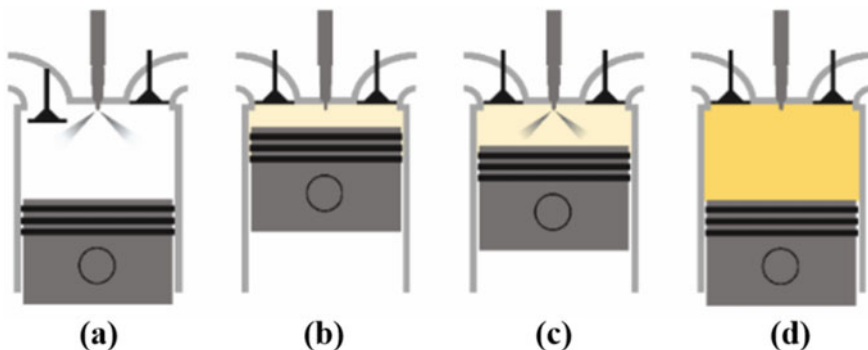


**Fig. 10.2** Combustion strategy for an ammonia engine proposed by Lee and Song (2018): **a** Pilot injection & formation of pre-mixed mixture; **b** Pre-combustion of the ammonia-air mixture; **c** Spray combustion of ammonia; **d** Expansion stroke

of the two test fuels were nearly the same, but the peak combustion temperature was reduced by about 100 K for aqueous ammonia.

### 10.5.3 Dual-Fuel Engines Fueled with Ammonia and Carbon-Based Fuels

As a result of the low reactivity of ammonia, it is difficult for engines to adopt pure ammonia. Therefore, blending ammonia with high-reactivity fuels is a reasonable solution, including gasoline, diesel, natural gas and some other low-carbon alternative fuels. Gasoline and diesel are traditional petroleum fuels, which are utilized in SI engines and CI engines, respectively. It is practical to modify a diesel or gasoline engine into a dual-fuel engine, and then the ammonia-diesel or ammonia-gasoline combustion technologies could be studied in such combustion engines.

Grannell et al. (2008) studied the application of gasoline-ammonia blends in an SI engine, and they announced that ammonia could replace most gasoline at a high load condition. They suggested a compression ratio of 10 to maintain a good thermal efficiency, which was then usually adopted by later studies (Ryu et al. 2014a; Haputhanthri et al. 2015). Meanwhile, ammonia blending suppressed knocking combustion tendency, allowing for a higher average effective intake pressure, and as such, the engine thermal efficiency at high loads is elevated. Ryu et al. (2014b) studied the effects of direct injection timing of additional ammonia in a gasoline engine. As illustrated in Fig. 10.3, the results showed that advanced injection timing and extended injection duration of ammonia could promote the engine power to 2.7 kW from the gasoline baseline power output of 0.6 kW. However, ammonia injection had insignificant impacts on the power when gasoline baseline power output was 3.0 kW. Additionally, to reduce the emissions of unburnt ammonia, hydrocarbon, CO, and NO<sub>x</sub> in the ammonia-gasoline SI engine, a three-way catalytic converter is required, and the oxygen sensor is utilized to monitor and control (Grannell et al. 2009). Niki et al. (Niki et al. 2019; Niki 2021) proposed a strategy for a diesel-ammonia dual-fuel

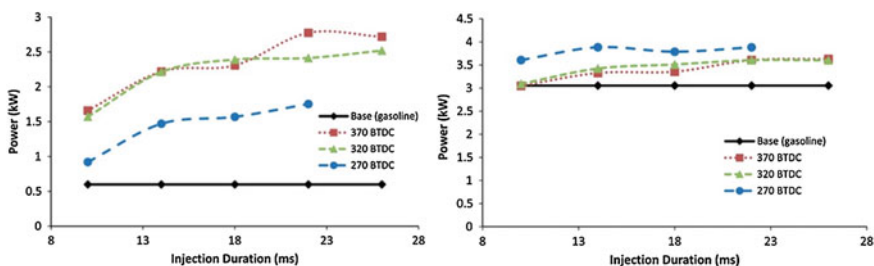


**Fig. 10.3** Engine power output comparison when using different injection timings for ammonia and gasoline. (Left: Gasoline baseline power output: 0.6 kW; Right: Gasoline baseline power output: 3.0 kW)

engine, by advancing the diesel pilot injection timing and adjusting ammonia supply flow. However, the emissions of CO, hydrocarbon, and NO<sub>x</sub> increased.

As the first-generation biomass fuel, ethanol is frequently used as an additive to gasoline in the market. Studies on the ammonia blending with gasoline and ethanol are of practical significance because ammonia has higher solubility in gasoline-ethanol blends than in pure gasoline (Haputhanthri 2014). Salek et al. (2021) numerically investigated the effects of ammonia port injection on a gasoline-ethanol SI engine. It was shown that the ammonia addition with a percentage of 10% promoted the engine power by about 1.4% at high speeds, and also increased the equivalent brake specific fuel consumption by about 3%. Moreover, the lower combustion temperature and pressure caused by ammonia addition reduced NO<sub>x</sub> emissions and knocking, but increased the carbon-containing gas emissions. To improve the performance of an ammonia-gasoline engine, Ryu et al. (2014a) adopted alumina catalyst pellets with 2% ruthenium to reform a part of ammonia into hydrogen and nitrogen, and the exhaust gas was used to heat the catalytic assembly. With the catalyst, the combustion efficiency of ammonia and gasoline was increased, the peak cylinder pressure of the dual-fuel engine was higher than that of the gasoline engine, and NO<sub>x</sub>, ammonia, CO and hydrocarbon emissions were reduced.

As for CI engines, Reiter and Kong (2011) classified the dual-fuel engine energy input into two parts, namely energy supplied by ammonia and energy supplied by diesel. It proved that the same engine torque could be reached with varied ammonia-diesel blends, and the energy supplied by ammonia could reach up to 95% at some conditions. When the energy percentage from ammonia was in the range of 40–80% of the entire engine energy, good fuel economy could be attained, as shown in Fig. 10.4. Meanwhile, NO<sub>x</sub> emissions increased with increased ammonia addition, but as long as the energy percentage from ammonia was less than 70%, NO<sub>x</sub> emissions were still lower than those when pure diesel was used. However, attention should be paid to hydrocarbon emissions with ammonia addition, due to the lower combustion temperatures of ammonia. Boretti (2017) simulated an ammonia-diesel turbocharged direct-injection engine, and reported the heat release rate and the engine efficiency were reduced with ammonia addition.

Considering the similar molecular structure of methane and ammonia, it is also possible to utilize ammonia-natural gas blends as transportation fuels. Oh et al. (2021)

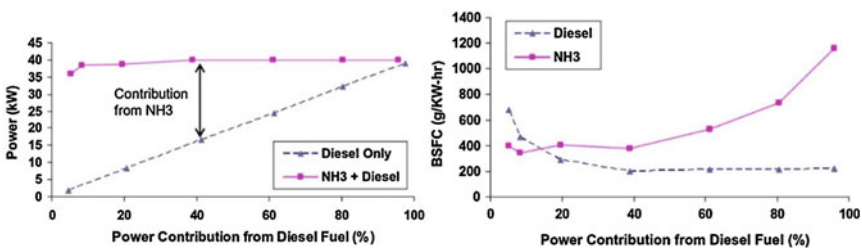


**Fig. 10.4** Engine power output and brake specific fuel consumption (BSFC) using various ammonia/diesel blends (Reiter and Kong 2011)

studied the effects of changed air–fuel ratios and ammonia blending percentage on a six-cylinder SI engine fueled with natural gas and ammonia blends. The study indicated that when the ammonia percentage exceeded 50%, CO<sub>2</sub> emissions were reduced by about 28% compared with the natural gas engine. Increased air–fuel ratio and ammonia percentage reduced flame speed and extended the combustion duration. However, the high ignition energy of ammonia caused the deteriorated combustion efficiency. In the study by Lhuillier et al. (2021), 20% methane addition to ammonia reduced the mean heat release rate in an SI engine, but did not have obvious influences on combustion duration. Oxygenated fuels were also selected by some researchers in ammonia dual-fuel engines. For example, DME has a high cetane number, indicating the potential to overcome the low auto-ignition problem of ammonia (Shikada et al. 2007). Ryu et al. (2013, 2014c) investigated fuel effects on the performances of a CI engine using different mixtures of ammonia and DME. At low loads, the engine fueled with 60% ammonia-40% DME had worse performances than that using 40% ammonia-60% DME. As shown in Fig. 10.5, increased ammonia fraction could lead to higher CO emissions, mainly due to the shorter combustion duration and lower combustion temperature. As the load increased, engine cycle fluctuation decreased, and the emissions of 60% ammonia-40% DME were lower than those of 40% ammonia-60% DME. With increased DME addition, the injection timing should be retarded to achieve the optimal torque. Compared to the engine fueled with pure DME, the engine fueled with ammonia-DME blends produced higher NO<sub>x</sub> emissions. According to the cost analysis of Gross and King (2013), although the mass-based price of DME was higher than that of ammonia, the price of 40% ammonia-60% DME was slightly lower than that of ammonia.

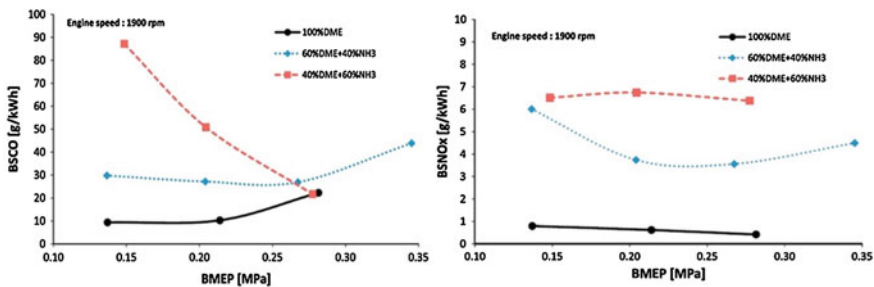


Fig. 10.5 Brake specific CO and NO<sub>x</sub> emissions from engines with ammonia-DME blends in Ryu et al. 2014c

### ***10.5.4 Dual-Fuel Engines Fueled with Ammonia and Hydrogen***

The addition of carbon fuels to ammonia has been proven to be able to improve engine performance, but it cannot completely eliminate GHG emissions. Therefore, it is believed that hydrogen is another potential fuel to mix with ammonia for engine application, because of its high mass-based energy density and carbon-free characteristic (Mansilla et al. 2018; McCay and Shafiee 2020). Although hydrogen is usually produced from carbon-based fuels, it can also be produced from renewable energy without carbon emissions (Sørensen and Spazzafumo 2018; Sørensen 2012), such as using electricity from solar and wind power plants for water electrolysis. On the other hand, hydrogen has high reactivity, high flame speed, high combustion temperature and short ignition delay, which is perfectly complementary to ammonia. As a result, the utilization of ammonia-hydrogen blends in combustion engines has been explored since a long time ago.

Due to the high octane number of ammonia-hydrogen blends, their blends are very suitable for application in SI engines (Lhuillier et al. 2019b; Frigo et al. 2012). Mørch et al. (2011) tested the ammonia-hydrogen blends with hydrogen fraction changing from 5 to 100% on a modified SI engine. They showed that the highest indicated thermal efficiency and mean effective pressure were obtained with 10% hydrogen addition, and the optimum excessive air ratio was slightly less than 1.0. Moreover, a very high hydrogen blending ratio was not recommended, because it caused reduced lower indicated efficiency and mean effective pressure. Similar observations were reported by Lhuillier et al. (2020b), as shown in Fig. 10.6, and they attributed this phenomenon to the increased heat loss caused by higher combustion temperatures of hydrogen fuel.

The ammonia-hydrogen blends can also be applied in CI engines with high compression ratios. The compression ratio selected by Pochet et al. (2017) was 16:1 to minimize the required intake temperature, and an even higher compression ratio of 22:1 was used in their recent study (Pochet et al. 2020). It showed that the IMEPs were reduced with hydrogen fractions higher than 50%, which was similarly observed in SI engines. At the compression ratio of 22:1, the IMEPs decreased by 60% from 5% hydrogen blending to pure hydrogen usage. Wang et al. (2021) numerically analyzed the equivalence ratio effects on in-cylinder combustion of a marine diesel engine fueled with hydrogen and ammonia blends, and they concluded that with the increased fuel/air equivalence ratio, the in-cylinder pressure increased and ignition delay time decreased, but higher intake temperature and pressure were preferred. When ammonia or hydrogen burns alone,  $\text{NO}_x$  emissions are significantly increased due to ammonia oxidation or high combustion temperature of hydrogen, but ammonia-hydrogen co-combustion may be a solution to  $\text{NO}_x$  emissions control. In the research by Westlye et al. (2013), they fueled an SI engine with 80% ammonia-20% hydrogen, and varied the compression ratio from 7 to 15. They showed that the NO and  $\text{NO}_2$  emissions were lower compared with gasoline at the stoichiometric condition, due to the lower combustion temperatures. However, at lean conditions,



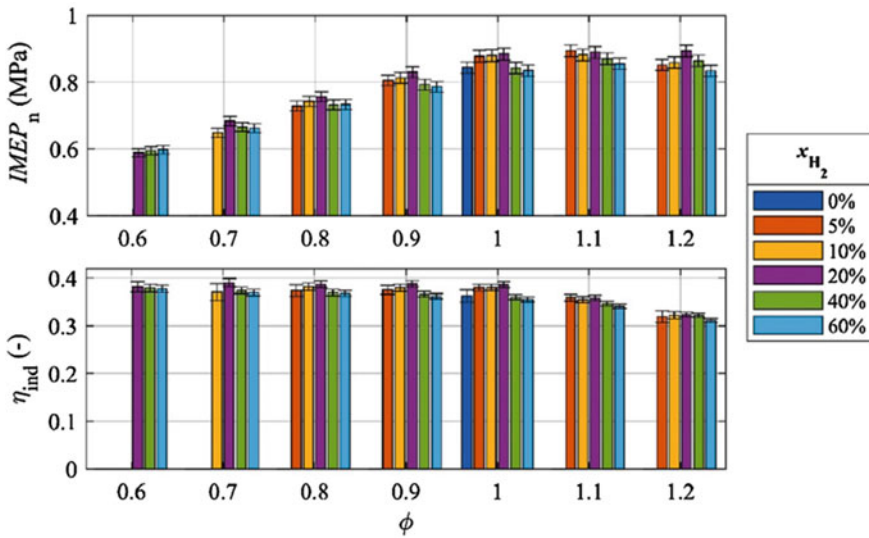


**Fig. 10.6** IMEP and indicated efficiency of an SI engine using different ammonia-hydrogen blends at changed equivalence ratios and constant intake pressure of 0.12 MPa (Lhuillier et al. 2020b)

$NO_x$  emissions were somewhat higher than gasoline combustion. Additionally, at the cold-start stage, the ammonia engine produced high unburnt ammonia emissions due to the significantly increased incomplete combustion (Koike and Suzuoki 2019). In practice, two gas tanks for ammonia and hydrogen are inconvenient for the vehicle fuel supply system design and arrangement. Comotti and Frigo (2015) adopted a hydrogen generation system (HGC) for an ammonia-fueled 4-stroke twin-cylinder SI engine, and it could supply hydrogen through ammonia reforming. Engine fuel economy was then increased and cycle fluctuation was reduced through appropriate fuel reforming intensity. Moreover, engine exhaust was used to heat HGC to optimize conversion efficiency. Further, Koike et al. (2021) studied the ammonia catalytic conversion performance of an on-board reformer at the engine cold-start process, and found that a higher air/ammonia ratio could increase the hydrogen generation, which is beneficial for rapidly achieving stable engine operation.

## 10.6 Conclusions and Prospects

Increasing concerns about GHG emissions in recent years have drawn more attention to the application of ammonia, a highly-yielded and widely-utilized carbon-free chemical, as an engine fuel. The well-developed regulations related to ammonia lay a good foundation for its application in combustion engines. In addition to the traditional chemical production way through natural gas reforming, ammonia may be

also synthesized on a large scale through renewable energy in the future, producing even less environmental impacts from the lifecycle perspective.

The application of ammonia in combustion engines behooves us to understand its fundamental combustion behaviors and kinetics, and develop special combustion technologies for ammonia engines. Combustion kinetics studies on ammonia can be dated back to decades ago, and since then many efforts have been spared to establish chemical kinetic models that could identify the key intermediate species, comprehensive chemical reaction network, and nitrogen-contained pollutants formation pathways in ammonia combustion. Fundamental flame propagation speeds and oxidation intermediate species were usually used as validation targets by researchers for their developed ammonia kinetic models. As ammonia is reluctant in fuel auto-ignition and flame propagation, a significantly increased compression ratio is required for pure ammonia engines to maintain stable in-cylinder combustion and engine operation. More literature efforts to solve the ammonia low reactivity problem and achieve stable and controllable engine operation are based on fuel blend or dual fuel combustion strategy. High reactivity fuels, including petroleum-based fuels of gasoline, diesel, natural gas, and alternative fuels of DME and hydrogen, were tried by different research groups. Air intake and fuel injection strategies were also optimized for different fuel combinations to make engine performance, efficiency and emissions in an acceptable range.

However, the application of ammonia as a large-scale practical engine fuel requires some more technical progress, and technologies focusing on fuel supply system compatibility and having the potential to satisfy increasingly stringent engine fuel economy and emissions standards should be targeted. The main technical issues needed to be resolved for ammonia engines in the future are summarized as follows.

- (1) Ammonia single fuel engine combustion technology: Ammonia has low flame propagation speeds and high auto-ignition temperatures, and these features would cause engine combustion instability and cold start problems. Dual fuel or fuel blend technology is usually used to solve this problem, commonly with petroleum-based fuels serving as the combustion promoter. However, dual fuel or fuel blend technology needs more fuel supply systems, increasing engine system complexity. Therefore, advanced combustion technologies for single-fuel ammonia engines are required, which are able to simultaneously maintain combustion stability, elevate thermal efficiency, and reduce harmful emissions.
- (2) Emissions reduction technologies for ammonia engines: Increased fuel-sourced  $\text{NO}_x$  emissions are usually found in ammonia engines. Additionally, the low combustion temperatures of ammonia are unfavorable for fuel complete oxidation, and may cause increased ammonia emissions. To control these nitrogen-contained emissions, the development of effective emissions after-treatment technologies for ammonia engines is of importance. Future studies could focus on the effectiveness assessment of existing and combination after-treatment technologies in ammonia engines emissions control, and the development of special catalysts and technologies suitable for ammonia engines emissions reduction.

- (3) Accurate and compact ammonia combustion model for engine simulation: Accurate combustion models are important in engine combustion control strategies development. Although many efforts have been spared to develop detailed ammonia combustion mechanisms, however, these mechanisms were only validated against limited fuel combustion behaviors, which were obtained at conditions different from engine operation states. Therefore, comprehensive ammonia combustion models that are able to emulate practical engine combustion behavior are highly needed. Afterward, the models need to be reduced to appropriate sizes to save computational cost, but still have acceptable calculation accuracy.

## References

- Allen M, Antwi-Agyei P, Aragon-Durand F, Babiker M, Bertoldi P, Bind M, Brown S, Buckeridge M, Camilloni I, Cartwright A, Cramer W (2019) Technical summary: global warming of 1.5° C. an IPCC special report on the impacts of global warming of 1.5° C above pre-industrial levels and related global greenhouse gas emission pathways, in the context of strengthening the global response to the threat of climate change, sustainable development, and efforts to eradicate poverty. International Institute for Applied Systems Analysis
- Ayvalı T, Tsang S, Van Vrijaldenhoven T (2021) The position of ammonia in decarbonising maritime industry: an overview and perspectives: Part I. Johnson Matthey technology review
- Aziz M, Wijayanta AT, Nandiyanto ABD (2020) Ammonia as effective hydrogen storage: a review on production, storage and utilization. *Energies* 13
- Borate N (2014) Flame temperature analysis and NO<sub>x</sub> emissions for different fuels. Michigan Technological University. Retrieved on 24th 2014
- Boretti A (2017) Novel dual fuel diesel-ammonia combustion system in advanced TDI engines. *Int J Hydrogen Energy* 42:7071–7076
- Cai T, Becker SM, Cao F, Wang B, Tang A, Fu J, Han L, Sun Y, Zhao D (2021) NO emission performance assessment on a perforated plate-implemented premixed ammonia-oxygen micro-combustion system. *Chem Eng J* 417
- Cardoso JS, Silva V, Rocha RC, Hall MJ, Costa M, Eusébio D (2021) Ammonia as an energy vector: current and future prospects for low-carbon fuel applications in internal combustion engines. *J Cleaner Prod* 296
- Cesaro Z, Ives M, Nayak-Luke R, Mason M, Bañares-Alcántara R (2021) Ammonia to power: forecasting the levelized cost of electricity from green ammonia in large-scale power plants. *Appl Energy* 282
- Chiong M-C, Chong CT, Ng J-H, Mashruk S, Chong WWF, Samiran NA, Mong GR, Valera-Medina A (2021) Advancements of combustion technologies in the ammonia-fuelled engines. *Energy Convers Manage* 244
- Comotti M, Frigo S (2015) Hydrogen generation system for ammonia–hydrogen fuelled internal combustion engines. *Int J Hydrogen Energy* 40:10673–10686
- Cornelius W, Huellmantel LW, Mitchell HR (1965) Ammonia as an engine fuel. In: 1965 International automotive engineering congress and exposition. SAE International
- Dagaut P, Glarborg P, Alzueta M (2008) The oxidation of hydrogen cyanide and related chemistry. *Prog Energy Combust Sci* 34:1–46
- Dasappa S, Sridhar HV, Sridhar G, Paul PJ, Mukunda HS (2003) Biomass gasification—a substitute to fossil fuel for heat application. *Biomass Bioenerg* 25:637–649

- de Vries J, Lowry WB, Serinyel Z, Curran HJ, Petersen EL (2011) Laminar flame speed measurements of dimethyl ether in air at pressures up to 10 atm. *Fuel* 90:331–338
- Dimitriou P, Javaid R (2020) A review of ammonia as a compression ignition engine fuel. *Int J Hydrogen Energy* 45:7098–7118
- Dulal HB, Brodnig G, Onoriose CG (2011) Climate change mitigation in the transport sector through urban planning: a review. *Habitat Int* 35:494–500
- Duynslaegher C, Jeanmart H, Vandooren J (2009) Kinetics in ammonia-containing premixed flames and a preliminary investigation of their use as fuel in spark ignition engines. *Combust Sci Technol* 181:1092–1106
- Duynslaegher C, Contino F, Vandooren J, Jeanmart H (2012) Modeling of ammonia combustion at low pressure. *Combust Flame* 159:2799–2805
- Fan YV, Perry S, Klemeš JJ, Lee CT (2018) A review on air emissions assessment: Transportation. *J Clean Prod* 194:673–684
- Frigo S, Gentili R, Doveri N (2012) Ammonia plus hydrogen as fuel in a S.I. engine: experimental results. In: 2012 Small engine technology conference & exhibition. SAE
- Pearsall TJ, Garabedian CG (1967) Combustion of anhydrous ammonia in diesel engines. In: National fuels and lubricants, powerplants, transportation meetings. SAE International
- Glarborg P, Miller JA, Ruscic B, Klippenstein SJ (2018) Modeling nitrogen chemistry in combustion. *Prog Energy Combust Sci* 67:31–68
- Glarborg P, Dam-Johansen K, Miller JA, Kee RJ, Coltrin ME (1994) Modeling the thermal DENO<sub>x</sub> process in flow reactors. Surface effects and nitrous oxide formation. *Int J Chem Kinet* 26:421–436
- Goldmann A, Dinkelacker F (2018) Approximation of laminar flame characteristics on premixed ammonia/hydrogen/nitrogen/air mixtures at elevated temperatures and pressures. *Fuel* 224:366–378
- Grannell SM, Assanis DN, Bohac SV, Gillespie DE (2008) The fuel mix limits and efficiency of a stoichiometric, ammonia, and gasoline dual fueled spark ignition engine. *J Eng Gas Turb Power* 130
- Grannell S, Assanis D, Gillespie D, Bohac S (2009) Exhaust emissions from a stoichiometric, ammonia and gasoline dual fueled spark ignition engine
- Gray JT, Dimitroff E, Meckel NT, Quillian RD (1966) Ammonia fuel—engine compatibility and combustion. In: 1966 Automotive engineering congress and exposition. SAE International
- Green ammonia Market 2020–2026 (2021) Orion Market Research Private Limited
- Gross CW, Kong S-C (2013) Performance characteristics of a compression-ignition engine using direct-injection ammonia–DME mixtures. *Fuel* 103:1069–1079
- Gurney G, Porter DH, Brack GW, Brack O Jr (1998) The life and times of Sir Goldsworthy Gurney: gentleman scientist and inventor, 1793–1875. Lehigh University Press, Bethlehem, America
- Han X, Wang Z, Costa M, Sun Z, He Y, Cen K (2019) Experimental and kinetic modeling study of laminar burning velocities of NH<sub>3</sub>/air, NH<sub>3</sub>/H<sub>2</sub>/air, NH<sub>3</sub>/CO/air and NH<sub>3</sub>/CH<sub>4</sub>/air premixed flames. *Combust Flame* 206:214–226
- Han X, Wang Z, He Y, Zhu Y, Cen K (2020) Experimental and kinetic modeling study of laminar burning velocities of NH<sub>3</sub>/syngas/air premixed flames. *Combust Flame* 213:1–13
- Han X, Lubrano Lavadera M, Konnov AA (2021) An experimental and kinetic modeling study on the laminar burning velocity of NH<sub>3</sub> + N<sub>2</sub>O + air flames. *Combust Flame* 228:13–28
- Hansson J, Brynolf S, Fridell E, Lehtveer M (2020) The potential role of ammonia as marine fuel—based on energy systems modeling and multi-criteria decision analysis. *Sustainability* 12:3265
- Haputhanthri SO (2014) Ammonia gasoline fuel blends: feasibility study of commercially available emulsifiers and effects on stability and engine performance. In: SAE 2014 international powertrain, fuels & lubricants meeting. SAE
- Haputhanthri SO, Maxwell TT, Fleming J, Austin C (2015) Ammonia and gasoline fuel blends for spark ignited internal combustion engines. *J Energy Resour Technol* 137
- Hayakawa A, Goto T, Mimoto R, Arakawa Y, Kudo T, Kobayashi H (2015) Laminar burning velocity and Markstein length of ammonia/air premixed flames at various pressures. *Fuel* 159:98–106

- He X, Shu B, Nascimento D, Moshhammer K, Costa M, Fernandes RX (2019) Auto-ignition kinetics of ammonia and ammonia/hydrogen mixtures at intermediate temperatures and high pressures. *Combust Flame* 206:189–200
- Horowitz CA (2016) Paris agreement. *Int Leg Mater* 55:740–755
- Hussein NA, Valera-Medina A, Alsaegh AS (2019) Ammonia- hydrogen combustion in a swirl burner with reduction of NO<sub>x</sub> emissions. *Energy Procedia* 158:2305–2310
- Jenkins DR (2007) X-15: extending the frontiers of flight. NASA, America
- Joung T-H, Kang S-G, Lee J-K, Ahn J (2020) The IMO initial strategy for reducing Greenhouse Gas (GHG) emissions, and its follow-up actions towards 2050. *J Int Maritime Saf Environ Aff Shipping* 4:1–7
- Klippenstein SJ, Harding LB, Glarborg P, Miller JA (2011) The role of NNH in NO formation and control. *Combust Flame* 158:774–789
- Koch E (1945) Ammonia—a fuel for motor buses. *J Inst Pet* 31:213
- Koike M, Suzuoki T (2019) In-line adsorption system for reducing cold-start ammonia emissions from engines fueled with ammonia and hydrogen. *Int J Hydrogen Energy* 44:32271–32279
- Koike M, Suzuoki T, Takeuchi T, Homma T, Hariu S, Takeuchi Y (2021) Cold-start performance of an ammonia-fueled spark ignition engine with an on-board fuel reformer. *Int J Hydrogen Energy* 46:25689–25698
- Konnov AA (2009) Implementation of the NCN pathway of prompt-NO formation in the detailed reaction mechanism. *Combust Flame* 156:2093–2105
- Kumar P, Meyer TR (2013) Experimental and modeling study of chemical-kinetics mechanisms for H<sub>2</sub>–NH<sub>3</sub>–air mixtures in laminar premixed jet flames. *Fuel* 108:166–176
- Lee D, Song HH (2018) Development of combustion strategy for the internal combustion engine fueled by ammonia and its operating characteristics. *J Mech Sci Technol* 32:1905–1925
- Lee D, Lee JS, Kim HY, Chun CK, James SC, Yoon SS (2012) Experimental study on the combustion and NO<sub>x</sub> emission characteristics of DME/LPG BLENDED FUEL USING COUNTERFLOW BURNER. *Combust Sci Technol* 184:97–113
- Lesmana H, Zhang Z, Li X, Zhu M, Xu W, Zhang D (2019) NH<sub>3</sub> as a transport fuel in internal combustion engines: a technical review. *J Energy Resour Technol* 141
- Lhuillier C, Brequigny P, Contino F, Mounaïm-Rousselle C (2021) Experimental investigation on ammonia combustion behavior in a spark-ignition engine by means of laminar and turbulent expanding flames. *Proc Combust Inst* 38:5859–5868
- Lhuillier C, Brequigny P, Contino F, Rousselle C (2019a) Combustion characteristics of ammonia in a modern spark-ignition engine. In: SAE technical paper series
- Lhuillier C, Brequigny P, Contino F, Rousselle C (2019b) Performance and emissions of an ammonia-fueled SI engine with hydrogen enrichment. In: SAE technical paper series
- Lhuillier C, Brequigny P, Lamoureux N, Contino F, Mounaïm-Rousselle C (2020a) Experimental investigation on laminar burning velocities of ammonia/hydrogen/air mixtures at elevated temperatures. *Fuel* 263
- Lhuillier C, Brequigny P, Contino F, Mounaïm-Rousselle C (2020b) Experimental study on ammonia/hydrogen/air combustion in spark ignition engine conditions. *Fuel* 269
- Li Y, Bi M, Li B, Gao W (2018a) Explosion behaviors of ammonia–air mixtures. *Combust Sci Technol* 190:1804–1816
- Li Y, Bi M, Li B, Zhou Y, Huang L, Gao W (2018b) Explosion hazard evaluation of renewable hydrogen/ammonia/air fuels. *Energy* 159:252–263
- Li S, Zhang S, Zhou H, Ren Z (2019) Analysis of air-staged combustion of NH<sub>3</sub>/CH<sub>4</sub> mixture with low NO<sub>x</sub> emission at gas turbine conditions in model combustors. *Fuel* 237:50–59
- Lindstedt RP, Lockwood FC, Selim MA (1994) Detailed kinetic modelling of chemistry and temperature effects on ammonia oxidation. *Combust Sci Technol* 99:253–276
- Liu Q, Chen X, Huang J, Shen Y, Zhang Y, Liu Z (2019) The characteristics of flame propagation in ammonia/oxygen mixtures. *J Hazard Mater* 363:187–196
- Liu Y, Han D (2021) Numerical study on explosion limits of ammonia/hydrogen/oxygen mixtures: sensitivity and eigenvalue analysis. *Fuel* 300

- Liu R, Ting DS-K, Checkel MD (2003) Ammonia as a fuel for SI engine. SAE Technical Paper
- Mansilla C, Bourasseau C, Cany C, Guinot B, Le Duigou A, Lucchese P (2018) Hydrogen applications: overview of the key economic issues and perspectives. In: Azzaro-Pantel C (ed) Hydrogen supply chains: design, deployment and operation. Academic Press, pp 271–292
- Mathieu O, Petersen EL (2015) Experimental and modeling study on the high-temperature oxidation of Ammonia and related  $\text{NO}_x$  chemistry. *Combust Flame* 162:554–570
- McCay MH, Shafiee S (2020) 22—Hydrogen: an energy carrier. In: Letcher TM (ed) Future energy: improved, sustainable and clean options for our planet, 3rd edn. Elsevier, pp 475–493
- Mei B, Zhang X, Ma S, Cui M, Guo H, Cao Z, Li Y (2019) Experimental and kinetic modeling investigation on the laminar flame propagation of ammonia under oxygen enrichment and elevated pressure conditions. *Combust Flame* 210:236–246
- Mei B, Ma S, Zhang Y, Zhang X, Li W, Li Y (2020) Exploration on laminar flame propagation of ammonia and syngas mixtures up to 10 atm. *Combust Flame* 220:368–377
- Mikulčić H, Baleta J, Wang X, Wang J, Qi F, Wang F (2021) Numerical simulation of ammonia/methane/air combustion using reduced chemical kinetics models. *Int J Hydrogen Energy* 46:23548–23563
- Miller JA, Bowman CT (1989) Mechanism and modeling of nitrogen chemistry in combustion. *Prog Energy Combust Sci* 15:287–338
- Miller JA, Smooke MD, Green RM, Kee RJ (1983) Kinetic modeling of the oxidation of ammonia in flames. *Combust Sci Technol* 34:149–176
- Mitchard ETA (2018) The tropical forest carbon cycle and climate change. *Nature* 559:527–534
- Mørch CS, Bjerre A, Gøttrup MP, Sorenson SC, Schramm J (2011) Ammonia/hydrogen mixtures in an SI-engine: engine performance and analysis of a proposed fuel system. *Fuel* 90:854–864
- Mulvaney D (2019) Green new deal. In: Solar power: innovation, sustainability, and environmental justice. University of California Press, Berkeley, pp 47–65
- Nakamura H, Hasegawa S, Tezuka T (2017) Kinetic modeling of ammonia/air weak flames in a micro flow reactor with a controlled temperature profile. *Combust Flame* 185:16–27
- Niki Y (2021) Reductions in unburned ammonia and nitrous oxide emissions from an ammonia-assisted diesel engine with early timing diesel pilot injection. *J Eng Gas Turb Power* 143
- Niki Y, Nitta Y, Sekiguchi H, Hirata K (2019) Diesel fuel multiple injection effects on emission characteristics of diesel engine mixed ammonia gas into intake air. *J Eng Gas Turb Power* 141
- Oh S, Park C, Kim S, Kim Y, Choi Y, Kim C (2021) Natural gas–ammonia dual-fuel combustion in spark-ignited engine with various air–fuel ratios and split ratios of ammonia under part load condition. *Fuel* 290
- Otomo J, Koshi M, Mitsumori T, Iwasaki H, Yamada K (2018) Chemical kinetic modeling of ammonia oxidation with improved reaction mechanism for ammonia/air and ammonia/hydrogen/air combustion. *Int J Hydrogen Energy* 43:3004–3014
- Outline of the 14th Five-Year Plan (2021–2025) for National Economic and Social Development and the Long-Range Objectives Through the Year 2035. People’s Publishing House, Beijing, China
- Pochet M, Truedsson I, Foucher F, Jeanmart H, Contino F (2017) Ammonia-hydrogen blends in homogeneous-charge compression-ignition engine. In: SAE Technical paper series
- Pochet M, Jeanmart H, Contino F (2020) A 22:1 compression ratio ammonia-hydrogen HCCI engine: combustion, load, and emission performances. *Front Mech Eng* 6
- Reiter AJ, Kong S-C (2011) Combustion and emissions characteristics of compression-ignition engine using dual ammonia-diesel fuel. *Fuel* 90:87–97
- Ryu K, Zacharakis-Jutz GE, Kong S-C (2014a) Performance enhancement of ammonia-fueled engine by using dissociation catalyst for hydrogen generation. *Int J Hydrogen Energy* 39:2390–2398
- Ryu K, Zacharakis-Jutz GE, Kong S-C (2014c) Performance characteristics of compression-ignition engine using high concentration of ammonia mixed with dimethyl ether. *Appl Energy* 113:488–499

- Ryu K, Zacharakis-Jutz G, Kong S-C (2013) Effects of fuel compositions on diesel engine performance using ammonia-DME mixtures. In: SAE technical paper series
- Ryu K, Zacharakis-Jutz GE, Kong S-C (2014) Effects of gaseous ammonia direct injection on performance characteristics of a spark-ignition engine. *Appl Energy* 116:206–215
- Salek F, Babaie M, Shakeri A, Hosseini SV, Bodisco T, Zare A (2021) Numerical study of engine performance and emissions for port injection of ammonia into a gasoline/ethanol dual-fuel spark ignition engine. *Appl Sci* 11
- Schönborn A (2020) Aqueous solution of ammonia as marine fuel. *Proc Inst Mech Eng Part M J Eng Maritime Environ* 235:142–151
- Kobayashi H, Hayakawa A, Somaratne KD, Kunkuma A, Okafor Ekenechukwu C (2019) Science and technology of ammonia combustion. *Proc Combust Inst* 37:109–133
- Shikada T, Miyoshi Y, Mogi Y, Inoue N, Ohno Y (2007) New direct synthesis technology of dimethyl ether. In: Eguchi K, Machida M, Yamanaka I (eds) *Studies in surface science and catalysis*, vol 172. Elsevier, pp 137–140
- Shu T, Xue Y, Zhou Z, Ren Z (2021) An experimental study of laminar ammonia/methane/air premixed flames using expanding spherical flames. *Fuel* 290
- Solaymani S (2019) CO<sub>2</sub> emissions patterns in 7 top carbon emitter economies: the case of transport sector. *Energy* 168:989–1001
- Song Y, Hashemi H, Christensen JM, Zou C, Marshall P, Glarborg P (2016) Ammonia oxidation at high pressure and intermediate temperatures. *Fuel* 181:358–365
- Sørensen B (2012) Hydrogen. In: Sørensen B (ed) *Hydrogen and fuel cells: emerging technologies and applications sustainable world*, 2nd edn. Academic Press, pp 5–94
- Sørensen B, Spazzafumo G (2018) 2—Hydrogen. In: Sørensen B, Spazzafumo G (eds) *Hydrogen and fuel cells: emerging technologies and applications*, 3rd edn. Academic Press, pp 5–105
- Stagni A, Cavallotti C, Arunthanayothin S, Song Y, Herbinet O, Battin-Leclerc F, Faravelli T (2020) An experimental, theoretical and kinetic-modeling study of the gas-phase oxidation of ammonia. *React Chem Eng* 5:696–711
- Starkman ES, Newhall HK, Sutton R, Maguire T, Farbar L (1966) Ammonia as a spark ignition engine fuel: theory and application. In: 1966 Automotive engineering congress and exposition. SAE International
- Starkman ES, James GE, Newhall HK (1967) Ammonia as a diesel engine fuel: theory and application. In: *National fuels and lubricants, powerplants, transportation meetings*. SAE International
- Sun Y, Cai T, Zhao D, Shahsavari M, Sun D, Sun X, Wang B (2021) RANS simulations on combustion and emission characteristics of a premixed NH<sub>3</sub>/H<sub>2</sub> swirling flame with reduced chemical kinetic model table 1. *Chin J Aeronaut*
- Syed IZ, Yeliana, Mukherjee A, Naber JD, Michalek D (2010) Numerical investigation of laminar flame speed of gasoline—ethanol/air mixtures with varying pressure, temperature and dilution. *SAE Int J Engines* 3:517–528
- Tian Z, Li Y, Zhang L, Glarborg P, Qi F (2009) An experimental and kinetic modeling study of premixed NH<sub>3</sub>/CH<sub>4</sub>/O<sub>2</sub>/Ar flames at low pressure. *Combust Flame* 156:1413–1426
- Valera-Medina A, Xiao H, Owen-Jones M, David WIF, Bowen PJ (2018) Ammonia for power. *Prog Energy Combust Sci* 69:63–102
- Wang Y, Zhou X, Liu L (2021) Theoretical investigation of the combustion performance of ammonia/hydrogen mixtures on a marine diesel engine. *Int J Hydrogen Energy* 46:14805–14812
- Wei X, Zhang M, An Z, Wang J, Huang Z, Tan H (2021) Large eddy simulation on flame topologies and the blow-off characteristics of ammonia/air flame in a model gas turbine combustor. *Fuel* 298
- Westlye FR, Ivarsson A, Schramm J (2013) Experimental investigation of nitrogen based emissions from an ammonia fueled SI-engine. *Fuel* 111:239–247
- Xiao H, Valera-Medina A (2017) Chemical kinetic mechanism study on premixed combustion of ammonia/hydrogen fuels for gas turbine use. *J Eng Gas Turb Power* 139
- Zacharakis-Jutz G (2013) Performance characteristics of ammonia engines using direct injection strategies. *Mechanical Engineering*, vol. Master of Science, p 102. Iowa State University

- Zhang Y, Mathieu O, Petersen EL, Bourque G, Curran HJ (2017) Assessing the predictions of a  $\text{NO}_x$  kinetic mechanism on recent hydrogen and syngas experimental data. *Combust Flame* 182:122–141
- Zhang M, An Z, Wang L, Wei X, Jianayihan B, Wang J, Huang Z, Tan H (2021) The regulation effect of methane and hydrogen on the emission characteristics of ammonia/air combustion in a model combustor. *Int J Hydrogen Energy* 46:21013–21025
- Zhang J, Zhong A, Huang Z, Han D (2019) Second-Law thermodynamic analysis in premixed flames of ammonia and hydrogen binary fuels. *J Eng Gas Turb Power* 141



# Chapter 11

## Ammonia as Fuel for Transportation to Mitigate Zero Carbon Impact



**Christine Mounaïm-Rousselle, Pierre Bréquigny, Agustin Valera Medina, Elena Boulet, David Emberson, and Terese Løvås**

**Abstract** The idea of using ammonia as fuel is nothing new as the first well-known Belgium use of buses fleet during World War II. Even if several studies performed during the mid-60's investigated the possibility to consider ammonia as fuel for internal combustion engines, mainly by means of CFR experiments or OD modelling, ammonia-based combustion engine fueling methods are not ready to be marketed as the use of this toxic molecule still poses major problems not only because of supply and safety issues but also because of its physical characteristics compared to conventional fuels. As function of the target, i.e. to supply ammonia either partially in standard engines to limit carbon footprint or to employ it mainly in dedicated engines to reach zero footprint, the technological challenges (dual fuel or unique fuel, SI or CI engines ...) could be different if it is as main power or auxiliary power unit (to extend battery vehicles) and as a function of the transportation type (mean duty or heavy duty engines for freight, construction, marine transportation, ...). In this chapter new results of advanced researches will be discussed in order to highlight the potential of this future green fuel.

**Keywords** Ammonia · Internal combustion engine

### 11.1 Introduction

To reach the Carbon neutrality target in 2050, many governments decided to consider clean and intermittent renewable energy resources (as wind and solar) as the main energy resources. But due to their intermittency not in phase with the demand and

---

C. Mounaïm-Rousselle (✉) · P. Bréquigny  
Univ. Orléans, INSA-CVL, PRISME, EA 4229, 45072 Orléans, France  
e-mail: [christine.rousselle@univ-orleans.fr](mailto:christine.rousselle@univ-orleans.fr)

A. V. Medina · E. Boulet  
College of Physical Sciences and Engineering, Cardiff University, Cardiff, UK

D. Emberson · T. Løvås  
Department of Energy and Process Engineering, Norway University of Science and Technology, Trondheim, Torgarden, Norway

therefore, the need to keep a secure electricity supply, the energy storage will be an integral part of the modern electricity smart grid. One way for the storage of the renewable energy excess is the water electrolysis to produce hydrogen and then to use hydrogen to fill any energy converters (for electricity, industry or transportation). Even if the technologies are making great leaps forward, until now the transportation of hydrogen includes its liquefaction (at  $-253\text{ }^{\circ}\text{C}$ ) in large scale plants or its compression to high pressures (until 700b). As one alternative hydrogen carrier, ammonia has some advantages over hydrogen as its lower cost per unit of stored energy; its higher volumetric energy density; easier and more widespread production, handling and distribution capacity, and better commercial viability; its liquid phase by compression to 0.9 MPa at atmospheric temperature; the well-established, reliable infrastructure already exists for both ammonia storage and distribution (including pipeline, rail, road, ship) as underlined Valera-Medina et al. in their accurate and comprehensive recent review (Valera-Medina et al. 2021). Ammonia has also the potential to be also an energy carrier in its own right, as it can be used directly in high temperature fuel cells, gas turbines and piston engines. It is important to emphasize that ammonia is *complementary* to the delivery of the “Hydrogen Economy”, and will participate to reach full decarbonization targets especially for heavy duty, off highway and marine engines to address the transport and storage problems. Recent studies based on global system analysis are convinced that ‘green’ ammonia has a real potential to be considered as an electro-fuel candidate with greenhouse gas emissions from an ammonia-driven vehicle lower than one third of gasoline- or diesel-driven vehicles (Angeles et al. 2018; Bicer et Dincer 2018; Zhou et al. 2019). Since the International Maritime Organization clarified its strategic roadmap to fully decarbonize this sector as soon as possible, ammonia is considered as a real candidate to reach these targets. Moreover, over the last 10 years, the potential of partial use of ammonia for stationary power units has started to be explored with various demonstrators around the planet, hence denoting the potential of this molecule.

### ***11.1.1 A Bit of History of Ammonia Fuel***

Even though at the moment there is no ship or any transport fleet operating with ammonia as fuel, the idea of using ammonia as a fuel for transportation vehicles is not so recent and its story started early during the twentieth century as recently well summarized in Sousa Cardoso et al. (2021). Briefly, after the examples during the 30 s/40 s, with the conversion of truck by Nork hydro and of bus fleet by Belgium public company during World War II (Koch 1949), 20 years later several US studies considered the possibilities to use ammonia as fuel, but no ‘real’ applications or vehicle tests were carried at this period. In 1972, a first ammonia-fueled urban vehicle built at The University of Tennessee competed in the Urban Vehicle Design Competition (Hodgson 1974). During 2010s, several retrofitted initiatives have been done to accept ammonia as fuel with gasoline or diesel as related in <https://nh3fuel.com/index.php/news/13-multimedia/20-2007-10->

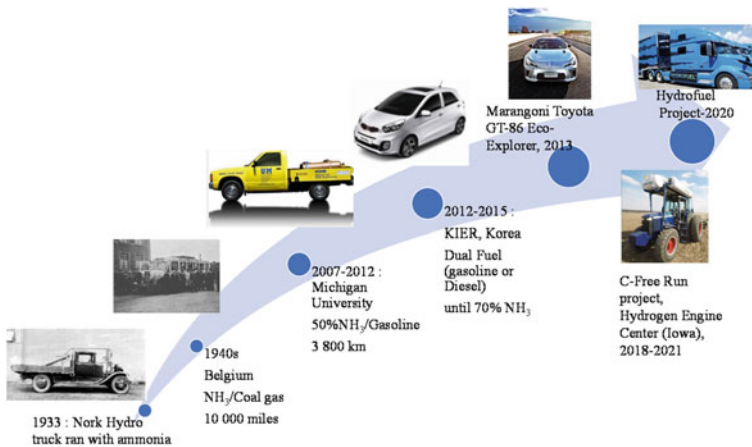
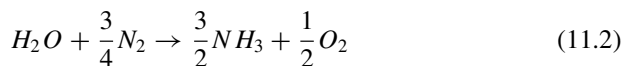
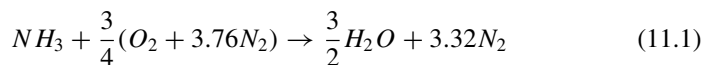


**Fig. 11.1** Summary of NH<sub>3</sub> vehicles

[16-ammonia-conference-presentation](#). Then one patent from Toyota had been done (Susumu et al. 2009) and some NH<sub>3</sub>-fueled cars have been tested during 2010–15s (as AMVEH, ECO EXPLORER MARANGONI TOYOTA or NH<sub>3</sub>car projects) as underlined in Sousa Cardoso et al. (2021) and summarized in Fig. 11.1.

### 11.1.2 Ammonia Properties and Specificities

The one-step oxidation reaction of NH<sub>3</sub> is very simple as in (11.1). If one considers the direct production pathway through water electrolysis as in (11.2), ammonia combustion is something like magical as from its production from water & air, this water & air is recovered after the energy conversion system, of course with yields and losses at different stages, but without any Carbon-type emissions.



But before considering ammonia as fuel, its main combustion characteristics need to be introduced as summarized in Table 11.1.

Its very narrow flammability limits in comparison to hydrogen can be considered as advantage as it poses much less explosive risk. But associated with high auto-ignition temperature, i.e. 1.5 that of gasoline and 3 of diesel fuel, has implications on ignition occurrence in internal combustion engines, whether the ignition types (by spark or by compression). Therefore, additional fuels and high compression ratios

**Table 11.1** Ammonia combustion properties

Fuel	Ammonia	Hydrogen	Methane	Gasoline	Diesel
Molar mass (g/mol)	17	2	16	114	167
Heat capacity ratio	1.32	1.41	1.32	1.4	1.4
Flammability limit (vol. %) (%)	15.8–28	4–76	44.7–17	1.4–7.6	1–6
Octane number	>130	>100	130	87–93	0
Auto-ignition temperature (°C)	651	530	537	440	225
stoich. Air/fuel ratio (mass)	6	34.3	17.1	15	14.6
Lower heating value (MJ/Kg fuel)	18.8	120	50.1	42.5	45
Energy content at stoich. (MJ/kg air)	3.13	3.5	2.92	2.8	3.08
% CO <sub>2</sub> emitted by stoich. combustion	0	0	9.5	12.5	12.6*
Laminar flame speed at Patm, 100 °C (m/s)	0.12	35	0.38	0.42	0.52

\* not real (lean mixture)

to promote ignition are needed to be considered to enhance both ignition delay time and auto-ignition temperature. The laminar flame speed of ammonia is lowest among most of the conventional fuels, inducing a very slow combustion process.

Hence, the reaction rates are slow, which is typically not desired for an IC engine application. This characteristic of ammonia limits also the engine operation at high regime conditions. The flame quenching distance for ammonia/air is 7 mm at stoichiometric conditions, about 10 times that of hydrogen, it signifies that the heat losses from the flame to the wall will be less in case of ammonia. The Lower heating value of ammonia is less than the half of typical engine fossil fuels. However, the stoichiometric air/fuel ratio for ammonia is also about the half of the typical fuels. This means that for a same amount of intake air, the input energy quantity will be similar, but with a double fuel consumption. Even if the adiabatic flame temperature from ammonia combustion is around 1800°C K, a bit low, it is high enough to extract work while expansion.

Ammonia is unlikely to cause engine knock under regular combustion engine conditions but as recently indicated in Mounaïm-Rousselle et al. (Mounaïm-Rousselle and Brequigny 2020; Mounaïm-Rousselle et al. 2021a), to enhance the engine optimization for spark ignited ammonia combustion might lead to operate at high compression ratios or high boosting pressures. Under these conditions the physical conditions alter and the engine knock could be relevant. The real Octane Number of ammonia is unknown but has been estimated at ~130 (Grannell et al. 2008a) which is very high and knock is therefore unlikely to happen. This property of ammonia would allow using various means to improve engine efficiency like increasing the compression ratio or to use supercharging or turbocharging without risking knock (Szybist et al. 2021; Fioroni et al. 2018). The heat of vaporization of ammonia is very high [1370 kJ/kg (Ryu et al. 2014a)], in comparison to gasoline (between 180 and 350 kJ/kg), which is one reason it is commonly used as a refrigerant. It is another advantage regarding spontaneous ignition and thus knock. But the induced reduction

of in-cylinder temperature could lead to misfires and restrict the operating conditions range in the case of direct liquid injection. As most of its properties seem to indicate that pure ammonia fuel would be knock resistant but the low flame speed and, in the case of direct liquid injection, the high heat of vaporization make stable combustion hard to achieve.

Latest researches have shown that using ammonia blends helped overcome all issues, making ammonia a suitable candidate as a carbon-free fuel for both classical engine architectures [Spark-Ignition (SI) and Compression Ignition (CI)] as reviewed in (Valera-Medina et al. 2021; Mounaïm-Rousselle and Brequigny 2020; Dimitriou and Jawad 2020). The blend of ammonia with gasoline or diesel fuel or other more usual fuels for engine can allow a fuel flexibility. But as schematized in Fig. 11.2, in order to consider ammonia as a real carbon-free fuel, fill engine with ammonia only or blended with hydrogen (on board if possible) will be the unique way to avoid CO<sub>2</sub> emissions due to the combustion itself.

The chapter will be divided in 5 sections: first one will review the latest researches in the case of SI engine fueled with ammonia fuel and identify the observed trends, the second one will focus on CI engines, the third one will be dedicated to an advanced combustion mode for low emissions engines, i.e. homogeneous combustion compression ignition engines, the fourth section will highlight the difficulties to get wide operating conditions range, especially related to cold start ones. Then, the last one will summarize the emissions problematics in the case of ammonia fuel.

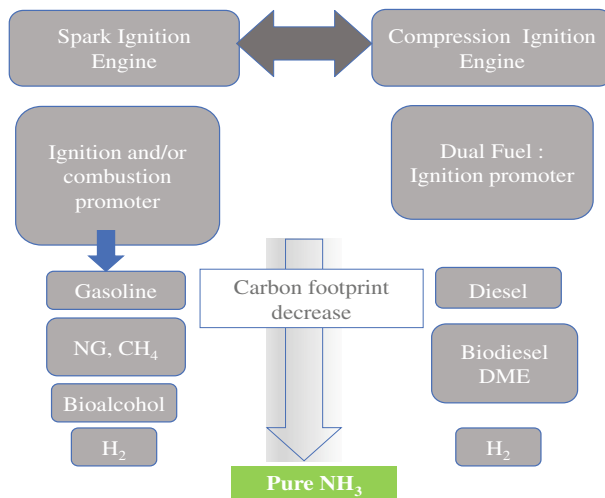


Fig. 11.2 Different technologies paths to use using ammonia as fuel for ICE

## 11.2 Ammonia SI Engine

Different practical methods for improving engine performance while burning ammonia (increase spark energy, increase compression ratio, engine supercharging, hydrogen or gasoline blend ...) have been and are still tested. The first detailed research on using ammonia in SI engines were performed in the 1960s in a one single cylinder Collaborative Research Fuel (CFR) engine. The initial study (Grannell et al. 2009) using pure ammonia showed poor performance with high ammonia slip and  $\text{NO}_x$  in the exhaust gases. The maximum indicated thermal efficiency observed was 21%, very low in comparison to gasoline performance (38%). The performance and emissions were greatly improved (close to gasoline) by implementing supercharging, or adding hydrogen to the mixtures (optimal around 2% by mass) or increasing the Compression Ratio (CR). In Mørch et al. (2011) by running at 1800 rpm with a CR of 8, 4–5% (by mass) of hydrogen was required whatever the Equivalence Ratio (ER). However, as expected high specific fuel consumption (more than twice that of gasoline) and a bad indicated output (70% lower than for gasoline) were found. Last, in Koike et al. (2012) it was concluded that  $\text{NO}_x$  emissions were much higher than for conventional fossil gasoline fuels. After this period of interest towards ammonia for SI engine, very little progress was made during 40 years. It is only in the late 2000s that it regained interest. Therefore, within the last 15 years, SI CFR as well as commercial single or multi-cylinders engines have been tested with a variety of fuel blends such as ammonia/gasoline, ammonia/methane, ammonia/alcohol and ammonia/hydrogen. An overview of all published research studies (to the knowledge of the authors) is provided in Table 11.2 and informs about different trends in their approach.

### 11.2.1 Gasoline/Ammonia Blend

All studies of gasoline/ammonia mixture revealed that the spark timing must be advanced to reach satisfying combustion (Grannell et al. 2009; Koike et al. 2012; Ryu et al. 2014b; Woo et al. 2014). While testing a Hyundai 3 cylinders, Woo et al. (2014) concluded a heat release rate about 25% lower for a blend 30% $\text{NH}_3$ /70%Gasoline than for pure gasoline. But previously, Grannell et al. (2008a, 2009) obtained good results for a blend 70% $\text{NH}_3$ /30% gasoline and recommended to improve the performance by using supercharging to take advantage of the advance spark timing. An increase in  $\text{NO}_x$  emissions was observed and seemed proportional to the amount of ammonia in the fuel blend. Haputhanthri et al. (2015) stated that using gasoline blend with 12.9% ammonia and 20% ethanol (to increase the solubility of ammonia) allowed to keep the same performance while reducing HC and  $\text{NO}_x$  emissions. Ryu et al. (2014b) suggested that the overall brake specific energy consumption was similar for the gasoline alone with ammonia/gasoline mixture tested. They also found

**Table 11.2** Main studies and literature results on the use of ammonia in SI engines

Authors	Type of engine	CD (l)	CR	Engine speed (rpm)	NH <sub>3</sub> (%vol.)	Fuel promoter
Cornelius et al. (1965)	CFR	0.44	9.4–18	800–4000	85–100	H <sub>2</sub>
Starkman et al. (1966)	CFR	0.625	6–10	1000–1800	25–100	H <sub>2</sub> *
Sawyer et al. (1968)	CFR	0.625	7 and 10	1800	25–100	H <sub>2</sub> *
Grannell et al. (2008a)	CFR	0.625	8–16	1000–1600	0–70	Gasoline
Grannell et al. (2009)			10	1000–1600	0–100	
Susumu et al. (2009)	Toyota	0.633	6.1	3600	50	H <sub>2</sub> *
Mørch et al. (2011)	CFR	0.612	6.23–13.58	1200	5–100	H <sub>2</sub>
Koike et al. (2012)	Toyota Single-cylinder	0.5	14	1200	40–90	H <sub>2</sub>
				800	0–60	Gasoline
					100	H <sub>2</sub> *
Westlye et al. (2013)	CFR	0.612	7–15	1000	80	H <sub>2</sub>
Frigo and Gentili (2012) Comotti and Frigo (2015)	Lombardini 2 cylinders	0.505	10.7	1100 2500–5000	As high as possible	H <sub>2</sub> *
Ryu et al. (2014b)	CFR	0.611	10	1800	0–80	Gasoline
Ryu et al. (2014b)					As high as possible	Gasoline + H <sub>2</sub> *
Woo et al. (2014)	Hyundai 3 cylinders	0.998	10.5	1400	0–80	Gasoline
Hapauthanthri et al. (2015)	In-line 4 cylinders	2.384	10.4	1900–5000	up to 18%	Gasoline + ethanol (0–30%)
Lhuillier et al. (2019a)	PSA 1 cylinder /4 fueled	0.4	10.5	1500	85–100	H <sub>2</sub>
Lhuillier et al. (2019b)					85–95	H <sub>2</sub>

(continued)

Table 11.2 (continued)

Authors	Type of engine	CD (l)	CR	Engine speed (rpm)	NH <sub>3</sub> (%vol.)	Fuel promoter
Lhuillier et al. (2020)					40–100	H <sub>2</sub>
Lhuillier et al. (2021)					85–100	H <sub>2</sub>
Mounaïm-Rousselle et al. (2021b)				650, 1000, 2000	85–95	CH <sub>4</sub>
					80–100	H <sub>2</sub>
Koike and Suzuoki (2019)	Single cylinder	0.5	13.8	1200	60 (%energy fraction)	H <sub>2</sub>
Koike et al. (2021)	Toyota 4 cyl	0.9	9	Cold start (from 0 to 1000 rpm)	100	H <sub>2</sub> *
Valera-Medina and Banares-Alcantara (2020)	Q3.3 TSI Engine	3.3	11.6	1500 rpm	70	H <sub>2</sub> and CH <sub>4</sub>
Oh et al. (2021)	Heavy duty 6 cyl	1.8	10.5	850 rpm	0–50	Natural gas
Salek et al. (2021)	Kia 4 cul	0.5	10.5	1000–7000	0–15	Gasoline/ethanol

CD = Cylinder Displacement, H<sub>2</sub>\* = H<sub>2</sub> introduced by means of on-board ammonia reformer



that the performance was significantly increased when a catalytic reformer to help ammonia dissociation into hydrogen.

### ***11.2.2 Methane/Ammonia Blend***

Very few recent studies (Lhuillier et al. 2021; Oh et al. 2021) have looked at the potential of mixing ammonia with natural gas as a combustion promoter but also as another way to contribute to decarbonizing if the gas comes from biomass or waste. The experiment performed by Lhuillier et al. (2021) on methane/ammonia blend showed that the energy released was much lower than expected. Especially, when the fraction of  $\text{CH}_4$  was increased, the authors observed a delay and lower and broader heat release rate. In Oh et al. (2021), low engine speed and low load were selected to evaluate the potential of ammonia/natural gas blend for possible marine application. They substituted without important issue 50% of Natural Gas, inducing a decrease of  $\text{CO}_2$  emissions by 28%. As in most of all studies about ammonia as fuel in blend for SI engine, below an ER of 0.7, the combustion is not sufficiently stable. Further tests performed by Valera-Medina et al. (2020) showed that the transition from ammonia/methane conditions due to ammonia/hydrogen had a clear, expected decline in  $\text{CO}_2$  emissions. Interestingly, high  $\text{NO}_x$  was considerably dropped in the absence of methane, a phenomenon related to the high deNO<sub>x</sub>ing potential of ammonia and the NH path to recombine with OH instead of carbon-based radicals that promote the emissions path  $\text{NH} \rightarrow \text{HNO} \rightarrow \text{NO}$ . Its narrow flammable limits range itself.

### ***11.2.3 Ammonia Helped or Not by Hydrogen***

When hydrogen was chosen as fuel promoter during experiments, it can be introduced either via another pressurized tank and flowmeter device for simplicity of the setup and the amount control or by means of a reformer or cracker, catalytic or thermal, as recently in Koike et al. (2021) to induce ammonia dissociation in  $\text{H}_2$ . Comotti and Frigo (2015) proposed that the later solution could exploit the heat of the exhaust gas to perform the dissociation, and is therefore appropriate for compact transport application as no hydrogen tank would be needed. Mørch et al. (2011) also suggested that exhaust heat could be used not only for catalytic dissociation but also more upstream to desorb ammonia stored in metal ammine complexes and then used as fuel. Like it was first identified the 1960s, the latest studies confirmed that a stable combustion in SI engine requires hydrogen in the blend. The minimum value is not universal until now as a function of the criterion: 5% of  $\text{H}_2$  by volume to avoid misfire (Mørch et al. 2011; Lhuillier et al. 2019b) or 10%  $\text{H}_2$  by volume reaching similar energy output levels comparable to conventional gasoline (Frigo and Gentili 2012; Comotti and Frigo 2015; Lhuillier et al. 2019b, 2020). At slightly boosted conditions

with 10%v/v H<sub>2</sub> or less, Lhuillier et al. (2019a) attained indicated efficiencies of minimum 37% for lean mixture close to stoichiometry. It was observed that the higher the load, the lower the hydrogen required for stable combustion (Frigo and Gentili 2012; Comotti and Frigo 2015). Moreover, satisfying combustion behavior was even achieved for 100% ammonia under very high loads (Koike et al. 2012; Mounaïm-Rousselle et al. 2021b). The highest efficiencies usually occur for ER just above one but decrease with H<sub>2</sub> content increase. Furthermore, these studies clearly conclude that a higher CR will improve a better indicated efficiency (Mørch et al. 2011; Lhuillier et al. 2019b) or some as in suggested Susumu et al. (2009) to design optimized ignition device for ammonia-fuel engine. Several studies have been focused on the cold start issues (Frigo and Gentili 2012; Mounaïm-Rousselle et al. 2021b; Koike et al. 2021) related to the difficulties to reach low load. Koike et al. (2021) explored the promising possibility of the reformer to favor the cold start of the engine before reach sufficient heating of the engine to guarantee stable operation with ammonia as fuel only. Recently, Mounaïm-Rousselle et al. (2021a) provided for the first time data about the potential of a retrofitted compression ignition engine, where a spark plug was set instead of the diesel injector. Although the in-cylinder flow-fields are not optimal for premixed combustion, increasing the compression ratio (up to 17) clearly showed the improvement in the stabilization of the operation of ammonia-only engines, especially at very low load and low speed. Similarly, Valera-Medina and Banares-Alcantara (2020) demonstrated that engines designed for natural gas could employ ammonia/hydrogen blends for powers ~20kW whilst ensuring proper combustion features. It was recognized that further improvements to the injection/ignition systems were required for optimized operation are promising and the main tendencies are highlighted in Fig. 11.3.

### 11.3 Ammonia CI Engine

In the case of Compression Ignition engine, due the auto-ignition resistance of ammonia, it requires very high Compression ratio, at least 35:1 as argued in Starkman et al. (1967); Pearsall and Garabedian 1967; Garabedian and Johnson 1966). Therefore, as summarized in Dimitriou and Jawad (2020), only a few studies can be found in world literature between the 1970s and 2010s. As for SI engine, ammonia combustion in CI engines can be promoted by mixing with other fuels to use more usual CR engines, but also with only a small quantity of reactive fuel (Grannell et al. 2008b; Kong and Gross 2012). Garabedian and Johnson (1966) concluded that conversion of CI Engines to spark ignition mode can be a good solution to lift the various barriers as ammonia has several issues related to combustion in CI mode. Recent study (Mounaïm-Rousselle et al. 2021a) improved this concept but also opened some news pathways about SACI with ammonia. Table 11.3 gives an overview of all research studies (to the knowledge of the authors).

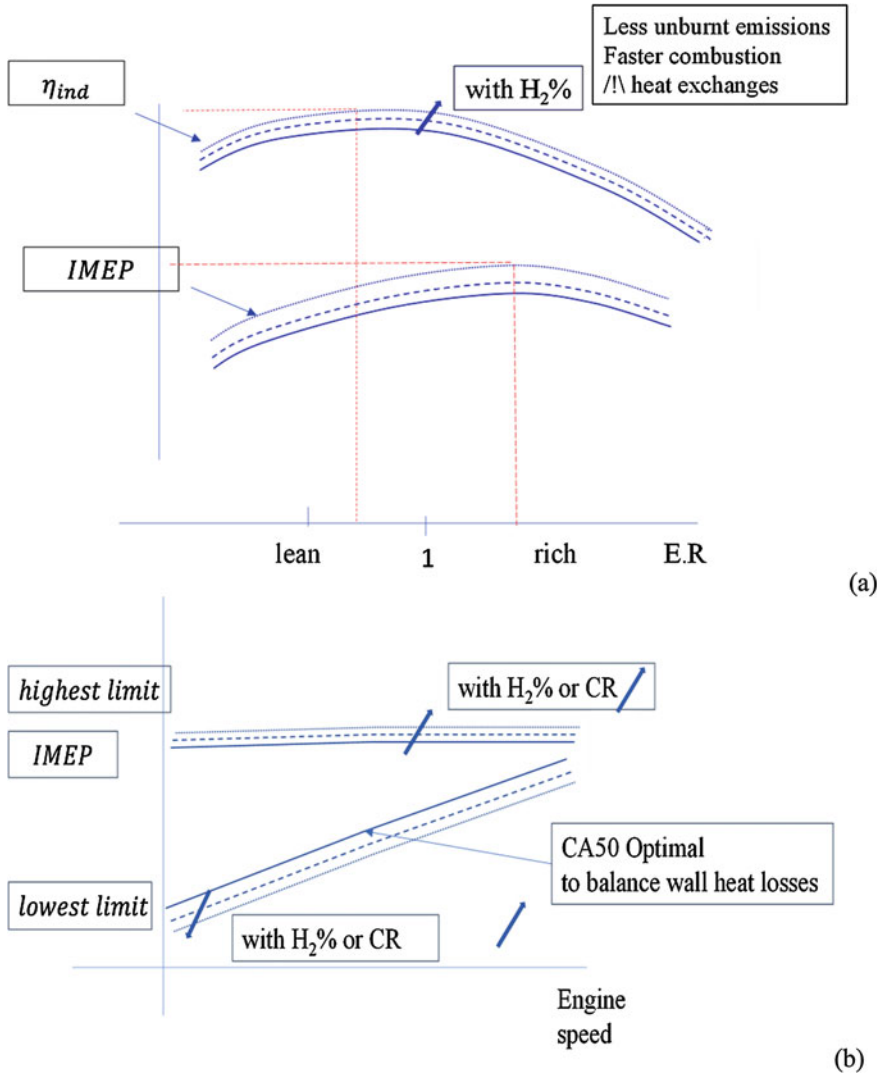


**Fig. 11.3** Main tendencies on H<sub>2</sub> addition (upt to 15%) and CR increase on thermal efficiency and IMEP (a) and on limits operating conditions (b)

### 11.3.1 100% Ammonia

Gray et al. (1967) achieved combustion of ammonia for compression ratio 35:1 with an intake air temperature above 423 K. They also found that high-temperature glow coils improved the ammonia ignition. In (Pearsall and Garabedian 1967), a first experiment with liquid ammonia direct injection was performed but due to

**Table 11.3** Main studies and literature results on the use of ammonia in CI engines

Authors	Type of engine	Cylinder volume CD (l)	CR	Engine regime (rpm)	NH <sub>3</sub> amount (%vol.)	Fuel promoter
Gray et al. (1967)	CFR	0.625	35 to 26	1000 to 1800	Up to maximum	Diesel (DI) ignition promoter (H <sub>2</sub> , hydrazine..)
Pearsall and Garabidian (1968)	CFR	0.625	20 to 25	1000 to 1800	Up to maximum	H <sub>2</sub> , acetylene, butane,
Starkman et al. (1967)	CFR	0.625	16 to 24	1000 to 1800	25 to 100	SACI
Bro and Petersen (1977)	CFR	0.625	8 to 16	1000 to 1600	0 to 70	Diesel (DI)
Ryu et al. (2014c)		0.32	20	3600	0 to 60	DME (premixed)
Reiter and Kong (2008)	JohnDeere 4 cyl	1.125	17	1000	0 to 95 (power%)	Diesel (DI)
Niki et al. (2016)				1500	100%	Diesel pilot
Sahim et al. (2018)	Palmera Single cylinder	0.21	20	2000 to 3000	2 to 10 (25%NH <sub>3</sub> + 75%H <sub>2</sub> O)	Diesel (DI)
Tai et al. (2017)	MAN 4 cylinders	0.625	18.5	2400	90 (Energy fraction)	Diesel, Diesel/Kerosene (DI)
Mounaïm-Rousselle et al. (2021a)	PSA Single cylinder engine	0.4	14 to 17	650, 1000, 2000	100	SACI
Pochet et al. (2020), Pochet (2020)	Single cylinder engine	0.5	16:1	1500	61	HCCI H <sub>2</sub>
Pochet et al. (2017)	YammarSingle cylinder engine	0.435	23:1	1500	94	HCCI H <sub>2</sub>

CD cylinder displacement

some issues are mentioned due to the ammonia vaporization before it reaches the injection nozzles. The authors used heat exchanger to cool the liquid ammonia before the injection pump. However, even after solving this problem no combustion was observed. Another attempt was conducted using port injection of gaseous ammonia along with direct injection of liquid ammonia, the ammonia combustion was occurred at 1200 rpm, but not self-sustainable beyond this value.

### ***11.3.2 Ammonia Helped by Diesel Pilot Injection***

Gray et al. (1967) also performed experiments by considering diesel as the ignition source for ammonia in dual-fuel engine. They were able to operate the engine with a compression ratio of 15.2:1 compared to 35:1 using only ammonia as a fuel. It was also found that proper combustion observed when ammonia was injected in the cylinder no later than 40 CAD (Crank Angle Degree) before the end of the diesel injection. Late injection of ammonia led to misfire. In Pearsall and Garabedian (1967) the influence of diesel cetane number was studied and the results concluded that a diesel with a 50 cetane number provided optimum performance with highest power and shortest ignition delay. The effect of diesel quantity supplied to the engine was also evaluated. In Reiter and Kong (2008) the investigation was conducted at different loads and engine regimes with an ammonia energy share ratio up to 95%. The results showed that combustion efficiency of around 95% was attained for ammonia rates between 40 and 80% and there was a reduction of NO<sub>x</sub> emissions of up to 60% as compared to diesel only operation. Niki et al. (2016) studied the influence of gaseous ammonia mixing in intake charge of CI engine. It was found that on enhancing the ammonia supply and keeping the output power constant results in lower compression and peak pressure with an increase in ignition delay with as consequence the increase of ammonia slip.

### ***11.3.3 Ammonia and Other Fuels***

From the first studies to consider ammonia as fuel for CI engine, different researches (Gray et al. 1967; Niki et al. 2016) considered different kinds of fuel to enhance the ignition as hydrogen, amyl-nitrate, dimethyl hydrazine, acetylene, or others. It was observed that ammonia combustion is highly dependent on pilot ignition source. In (Niki et al. 2016), the results showed that acetylene delivers the best performance for normal compression ratio operation but for higher compression ratio, hydrogen provides better performance. Tay et al. (2017) studied the ammonia fueled CI engine with diesel/kerosene or kerosene as a pilot fuel. The authors observed that the ignition was earlier as compared to diesel pilot fuel, with as consequence a better complete combustion of ammonia. Other studies were focused on the use of ammonia-DME mixture in CI engine (Ryu et al. 2014c). It was found that performance of the engine deteriorate when ammonia share was enhanced and beyond ammonia share (60%) results in cycle to cycle variation. The authors recommended that by using higher injection pressure, the mixing of fuel–air is increased, which results in better combustion. A recent study (Şahin et al. 2018) focused on the potential to add some ammonia solutions in Diesel CI engine to mitigate carbon emission issues but even if the performance was enhanced by ammonia solution introduction the emissions with carbon were not.

## 11.4 Ammonia for HCCI Engine

Among the potential engine technologies available to use ammonia as fuel for energy or transportation, the Homogeneous Charge Compression Ignition (HCCI) engine presents several assets. This particular engine enables a very low consumption since it operates with very lean mixture and with a high efficiency. Its major drawback lies in the difficulty of controlling the combustion phasing since the ignition of the air/fuel load is mainly driven by the chemistry thus making HCCI unsuitable for transportation. However, it could be very interesting for stationary application such as combined heat and power (CHP) plant where high efficiency is reachable.

However running HCCI engine with a high efficiency is usually limited in the search of a compromise with clean operation. As in the CI engine, a high compression ratio as well as high intake pressure and temperature conditions are required. Unfortunately, the low power output of the HCCI engine, combined with the low Lower Heating Value (LHV) of ammonia and the high intake temperature required reduce the power density of such application. Moreover, if HCCI engine is well known for its low temperature combustion (LTC) mode obtained through very lean fuel/air mixtures and leading to very low  $\text{NO}_x$  and soot levels; this remains challenging with ammonia as fuel due to its nitrogen content.

During the past years, only a few studies covered the use of ammonia in HCCI engine. Van Blarigan (2000) indeed proved the possibility to use ammonia as fuel only in HCCI mode without preheating but with a compression ratio of 40–60:1, very far from the current commercially available engines. More recently, in Pochet et al. (2020), Pochet (2020), Wang et al. (2013), different aspects of ammonia as a HCCI fuel were investigated as engine, mixing and intake conditions requirements, fundamental combustion properties, i.e. ignition delay of ammonia and ammonia/hydrogen blend in LTC conditions, CR improvements between 16:1 and 23:1 by using two different engines. Increasing the compression ratio helps to decrease the intake temperature requirement, which remains still too high in terms of heating power requirement and leads to a mixture density decrease and therefore less power output. Finally, with such intake temperature, the TDC temperature might be so high that the LTC conditions will not be met anymore leading to thermal  $\text{NO}_x$  formation and thus counteracting the benefits of the HCCI engine itself. Regarding the pressure intake condition, increasing it can surely help the process: a 2 bar intake pressure (vs. 1 bar) allows to decrease the required intake temperature by 60 K. Therefore, the difficulty of using neat ammonia as fuel in a HCCI engine with conventional compression ratio range is already highlighted. When 10% of  $\text{H}_2$  in the fuel blend at equivalence ratio 0.4, intake pressure of 2 bar and  $\text{CR} = 20:1$  results in a 100 K decrease of the intake temperature from 540 to 440 K. With 50% of  $\text{H}_2$  the required intake temperature even goes down to 400 K in same conditions.

As example, with the lowest CR and having the limits of 1.5 bar, 483 K at the intake, it was not able to run the engine with more than 61% of  $\text{NH}_3$  in  $\text{NH}_3/\text{H}_2$  fuel blend (with an 0.27 ER). The addition of ammonia in  $\text{H}_2/\text{NH}_3$  blend induced decrease of Heat Release Rate peak due to the decrease of OH, as more intermediate

species that are consuming OH are produced. Moreover, hydrogen and ammonia share their combustion radicals resulting in a damped combustion because there are simply more steps for the combustion when adding ammonia compared to pure hydrogen. To promote auto-ignition of ammonia, they tested ozone seeding as an oxidizing species to shorten the ignition delay from 0 to 140 ppm without any effect on the auto-ignition promotion.

In the other engine (highest CR), they were able to burn ammonia/hydrogen blend with ammonia content varying from 0 to 94% in the fuel blend. Due to the damping effect of ammonia on the combustion, adding ammonia in the fuel blend allows higher equivalence ratio and therefore leads to higher energy output. The obtained indicated efficiency as a function of the ammonia content was constant for the maximal energy output (about 37%). Finally, the studies conclude that to use a Diesel engine retrofitted to HCCI for ammonia requires also many optimizations in the design in terms of compression ratio, crevices, stroke-to-bore ratio as well as intake conditions (turbocharged) to well operate with high ammonia content.

## 11.5 Emissions Trends for Ammonia Engine

### 11.5.1 General Considerations

When ammonia is combusted mainly nitric oxide (NO) is formed, with small traces of nitrogen dioxide (NO<sub>2</sub>) and nitrous oxide (N<sub>2</sub>O). These molecules are precursors of acid rain, photochemical smog and greenhouse effects, especially N<sub>2</sub>O. Although NO is not hazardous at ambient level, NO<sub>2</sub> can cause allergic reactions and lung dysfunctionality until it is fatal. N<sub>2</sub>O is also an unwanted emission as its Global Warming Potential is of 300 times the one from CO<sub>2</sub>. Interestingly, environmentalists have been also studying the effect of NO<sub>x</sub> and unburned ammonia (which is also another detrimental pollutant obtained from engines running on the fuel as a consequence of inefficient combustion) on the production of fine particle matter (diameters less than 2.5 μm). The main concern of these particles is that they can pass through skin or alveoli, reaching blood streams. Ammonium nitrate (NH<sub>4</sub>NO<sub>3</sub>) and ammonium sulphate ((NH<sub>4</sub>)<sub>2</sub>SO<sub>4</sub>) are formed in the presence of ammonia, sulphates and nitrogen oxides, thus leading to particle matter.

Nitrogen oxide (NO<sub>x</sub>) emissions are inherently one of the main challenges to solve in the development of ammonia powered technologies. There are three main mechanisms for the formation of NO<sub>x</sub> in combustion systems. These mechanisms are,

- Thermal NO (Zeldovich) mechanism: the most important source of nitrogen oxides at high temperature combustion.
- Prompt NO: initiated by combination of CH<sub>n</sub>-radicals on the nitrogen molecule, leading to cyanide-nitrogen NCN formation as a precursor of the formation of nitrogen oxides.

- Fuel  $\text{NO}_x$  formation: caused by the nitrogen atom fixed into the fuel itself.

First kinetics mechanism of ammonia oxidation (Miller and Bowman 1989) already demonstrated that  $\text{NO}/\text{N}_2$  formation mainly depended on the path of  $\text{NH}_x$  radicals but in Lindstedt et al. (1994) the description of the important reactions for NO formation highlights the importance of thermal  $\text{NO}_x$  for high temperature combustion using hydrogenated blends, whilst OH plays a more crucial role with pure ammonia. From that, different improvements of these mechanisms have been and are still done. Further analyses carried out in Mendiara and Glarborg (2009) indicated that HNO from  $\text{NH}_2 + \text{O}$  reactions was the main precursor of NO formation. Moreover, when other fuels are used simultaneously with ammonia to enhance its ignition, there are some interaction between other fuels and  $\text{NH}_3$  chemistry for  $\text{NO}_x$  formation. It is clear that although researchers are getting closer to fully understand the kinetics of  $\text{NO}_x$  formation in ammonia flames, there are many complexities that need to be addressed before a “universal” model is available for the combustion of such a chemical. In Glarborg et al. (2018) a vast amount of literature on the subject of modelling nitrogen chemistry in combustion is compiled with some analyses about previous and current models. Further, fuel NO formation/reduction appears to be dependent on the O/H radical pool, which varies depending on equivalence ratio, pressure conditions and other fuel presences.

The  $\text{NO}_2$  formation reaction is shown by Eq. (11.3) but in the post-flame region,  $\text{NO}_2$  is converted back to NO, through the reaction in Eq. (11.4).



In SI Engine, as the fuel and air are premixed, the combustion chamber temperature is nearly uniform after the flame propagation in such engines, which results in  $\text{NO}_2/\text{NO}_x$  ratio less than 2%. On the other hand, in CI engine, as the combustion is mixing controlled, with a wide distribution of cool regions, it is expected an higher ratio of  $\text{NO}_2/\text{NO}_x$ .

$\text{N}_2\text{O}$  forms when  $\text{NH}_3$  is in the presence of NO and  $\text{NO}_2$  at low temperature. This formation is one part of Selective Non-Catalytic Reduction mechanism.

### 11.5.2 Exhaust Emissions in Ammonia ICE Engines

The global trend observed is that more  $\text{NO}_x$  are produced for lean combustion whereas more ammonia slip has to occur for rich mixtures due to the fuel excess itself. Because of this opposite behavior, it will be necessary to apply aftertreatment devices, even for optimized fuel blends, to ensure that emissions are below standards limits. In (Westlye et al. 2013), the comparison between convention fossil fuels indicated that even if the peak in NO is also for lean mixture in the case of ammonia combustion,



it occurs at leaner operating condition (35% excess air for ammonia/hydrogen blend instead of 10% for HC). From all previous studies in SI engines, it is also concluded that the substitution of one part of  $NH_3$  by  $H_2$  does not involve a decrease of  $NO_x$  emissions due to the decrease of nitrogenated fuel itself but increase with increase of hydrogen content. All studies concluded that  $NO$  is the major part of total  $NO_x$ . Last,  $N_2O$  emissions were always be founded at very low quantities in these studies (less than 100 ppm), which confirms the low impact of  $NH_3$  combustion in global warming. However, it must be emphasized that  $N_2O$  needs to be carefully addressed during the combustion even if as underlined in Mounaïm-Rousselle et al. (2021a), it corresponds to an equivalent quantity of ammonia blends at certain equivalence ratios, at 1.5%  $CO_2$  in emissions.

From Mounaïm-Rousselle et al. (2021a); Westlye et al. (2013); Pochet (2020), the ammonia slip is due to the crevices of combustion chamber, out of which piston top land crevice contribute more. The engine architecture (piston design, crevice, compression ratio, squish zone for CI engine...) plays an important role to ammonia slit. Therefore it is difficult to predict from any simulation tools the ammonia amount at the exhaust as it should be occurred only when ammonia is in excess. This mechanism depends on combustion characteristics of fuel, which is governed by the heat loss to combustion chamber walls also. Such mechanism describes that the fuel escaping combustion in crevices is proportional to in-cylinder pressure. When gaseous ammonia is used as a fuel, the formation of unburned ammonia is more as compared to liquid ammonia as underlined in Westlye et al. (2013). Figure 11.4 summarizes the key behaviors from the different studies. Most of previous studies with exhaust emissions measurements have been done with FTIR without considering the possible  $H_2$  emission itself. More recent studies (Mounaïm-Rousselle et al. 2021a, 2021b; Lhuillier et al. 2020, 2021) performed this measurement and conclude

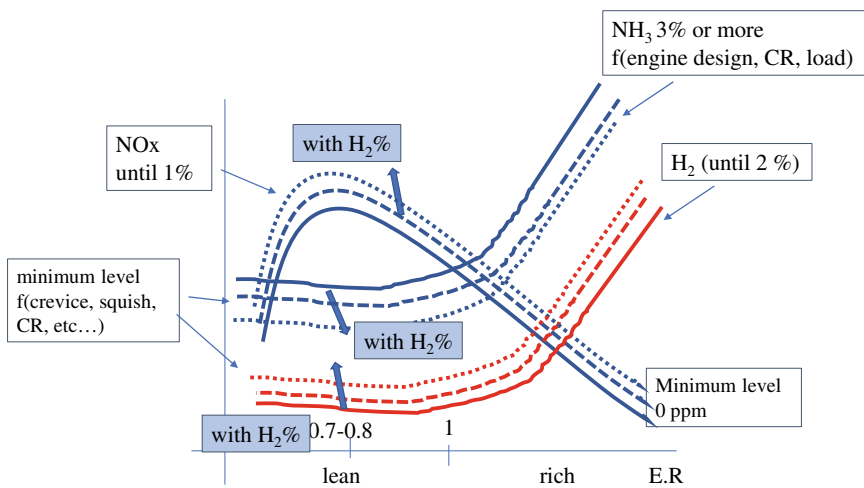
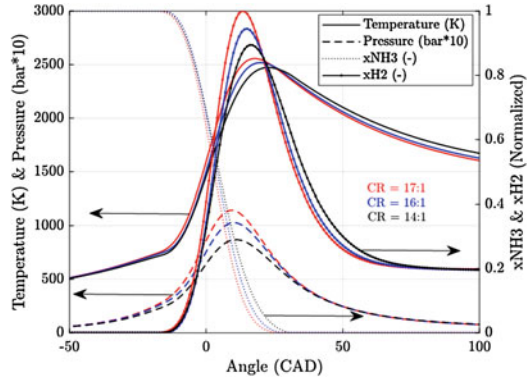


Fig. 11.4 Exhaust emissions tendency as a function of ER and %of  $H_2$  in blend

**Fig. 11.5** Example of effect of Compression Ratio on ammonia oxidation and cracking (2 zones SI engine simulation with Chemkin PRO with Stagni et al. (2020) kinetic mechanism)



that even if  $H_2$  is not until now a regulated pollutant specie, its atmosphere release is undesirable. They indicate a level of  $H_2$  at the exhaust about 1.5–2% at maximum and not only when  $H_2$  is added to ammonia at the intake. As example, by increasing the compression ratio, the cracking of ammonia to  $H_2$  inside the combustion chamber could be induced near TDC as illustrated in Fig. 11.5 where estimated  $NH_3$ ,  $H_2$  and average in-cylinder temperature from 2 zones 0D SI engine simulation (Chemkin PRO) are displayed for engine conditions presented in Mounaïm-Rousselle et al. (2021a). This needs some more dedicated studies in the future, as a function of the engine technology chosen ammonia decomposition inside the cylinder can occur and lead to this  $H_2$  emission.

### 11.5.3 $NO_x/NH_3$ Trade-Off Solution for Ammonia ICE Engines

To decrease ammonia slip and  $NO_x$ , different strategies are already considered. Recently, in Mounaïm-Rousselle et al. (2021a), the potential of intake gases dilution has been tested: a maximum of 8% of dilution can still provide stable operating conditions and can allow 40% decrease of  $NO_x$  without any  $NH_3$  emissions effect. Another classical mean is to optimise injections strategy in the case of dual-fuel engines as in Niki et al. (2018), Niki (2021), where by advancing and splitting the diesel injection lead to an increase of the combustion temperature which prevents  $N_2O$  formation as well as enhances the combustion rate of ammonia. Last one will be related to actual diesel engine: to implement selective catalytic reduction (SCR) system to mitigate as well as possible  $NO_x/NH_3$ . Even if first tests related in Mørch et al. (2011) proved that it could be efficient and to reduce emissions at same level than with gasoline, as a function of the strategy, engine operating conditions, the design of appropriate SCR will be certainly required. It is also interesting to noted that in Koike and Suzuoki

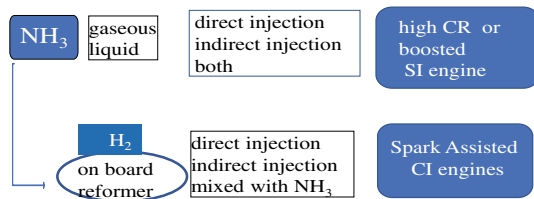
(2019, by using on-board cracker to warm the engine, nearly zero NH<sub>3</sub> emissions were achieved during cold start and fast idle by adsorbing unburned NH<sub>3</sub> only through a three-way catalyst.

### 11.6 Conclusion and Future

Figure 11.6 summarizes all potential solutions to implement ammonia IC engines. The combustion of ammonia as fuel in ICE remains very challenging even if the engine design is more and more adapted but it will contribute to reach zero-carbon emission targets. For any engine combustion modes, i.e. SI, CI or HCCI to overcome ignition difficulties, the seeding of ammonia/air mixture by H<sub>2</sub> amount is required to extend as well as possible the stable operating conditions range. From most recent studies, the improvement of ammonia engine in the case of cold start still needs to be addressed. As done in Comotti and Frigo (2015); Koike et al. (2021); Wang et al. (2013), the use of on board cracker should be a good solution especially for cold start issues and the recent studies are increasingly confident in this device, especially in the last study (Koike et al. 2021) where the potential control of ammonia combustion in engine through a thermal reformer is clearly demonstrated.

Additional technical barriers still need to be removed. First more consequent studies are required to optimize the ammonia supply of the engine itself. In most of the studies, the simple method to implement ammonia is the port fuel injection in gaseous form. However, some adverse effects can be induced as the volume efficiency reduction due to the air displacement by ammonia. Direct injection of gaseous ammonia could be an advantageous solution for maintaining global efficiency, but also to contribute to decrease ammonia slip and increase the output power. Only one study has been listed to focus on the injection and mixing characteristics of gaseous ammonia jets (Zhang et al. 2021). Due to its low energy content, the liquid direct injection could be also advantageous especially to retrofit diesel engine but its vaporization heat is so important that the decrease of in-cylinder temperature could harmful for the combustion itself. Moreover due to the specificity of its saturating vapour curve can induce fast ammonia atomisation during the injection process itself, as recently studied in Pelé et al. (2021). Last, the ammonia solubility in lubrication oil is not known until now and the contribution of ammonia slip from ammonia absorption and desorption in oil layers has to be evaluated.

**Fig. 11.6** Different technical issues for fully ammonia ICE



In view of the increasing number of announcements concerning the maritime sector in particular, a lot of work is being done in order to predict the behavior of ammonia-fuelled engines, by using modelling tools as in Wang et al. (2021); Salek et al. (2021); Hansson et al. (2020); Schönborn (2021). Even if the knowledge about ammonia oxidation is better and better, ammonia combustion in IC engines remains still far from complete as underlined in Mounaïm-Rousselle and Brequigny (2020); Mounaïm-Rousselle et al. (2021a, 2021b) and still require new studies to provide accurate data and improve the prediction of simulation tools to design and optimize future ammonia engines.

## References

- Angeles DA, Tan RR, Aviso KB, Are KRAG, Razon LF (2018) Fuzzy optimization of the automotive ammonia fuel cycle. *J Clean Prod* 186:877–882
- Bicer Y, Dincer I (2018) Life cycle assessment of ammonia utilization in city transportation and power generation. *J Clean Prod* 170:1594–1601
- Bro K, Pedersen PS (1977) Alternative diesel engine fuels: an experimental investigation of methanol, ethanol, methane and ammonia in a D.I. Diesel Engine with Pilot Injection, SAE 770794
- Comotti M, Frigo S (2015) Hydrogen generation system for ammonia–hydrogen fuelled internal combustion engines. *Int J Hydrogen Energy* 40:10673–10686
- Cornelius W, Huellmantel L, Mitchell H (1965) Ammonia as an engine fuel. In: Presented at the 1965 international automotive engineering congress and exposition, SAE Technical Paper 650052
- Dimitriou P, Jawad R (2020) A review of ammonia as a compression ignition engine fuel. *Int J Hydrogen Energy* 45(11):7098–7118
- Fioroni GM, Fouts L, Christensen E, Anderson JE, McCormick RL (2018) Measurement of heat of vaporization for research gasolines and ethanol blends by DSC/TGA. *Energy Fuels* 32:12607–12616
- Frigo S, Gentili R (2012) Analysis of the behaviour of a 4-stroke Si engine fuelled with ammonia and hydrogen. *Int J Hydrogen Energy* 38:1607–1615
- Garabedian C, Johnson J (1966) The theory of operation of an ammonia burning internal combustion engine, report 634681. Michigan, USA
- Glarborg P, Miller JA, Ruscic B, Klippenstein SJ (2018) Modeling nitrogen chemistry in combustion. *Prog Energy Combust Sci* 67:31–68
- Grannell SM, Assanis DN, Bohac SV, Gillespie DE (2008) The fuel mix limits and efficiency of a stoichiometric, ammonia, and gasoline dual fueled spark ignition engine. *J Eng Gas Turb Power* 130:042802
- Grannell SM, Assanis DN, Bohac SV, Gillespie DE (2008b) The fuel mix limits and efficiency of a stoichiometric, ammonia, and gasoline dual fueled spark ignition engine. *J Eng Gas Turb Power* 130(4):042802
- Grannell SM, Assanis DN, Gillespie DE, Bohac SV (2009) Exhaust emissions from a stoichiometric, ammonia and gasoline dual fueled spark ignition engine. In: ASME 2009 internal combustion engine division spring technical conference. ASMEDC, Milwaukee, Wisconsin, USA, pp 135–141
- Gray DS, Domke CJ, Meguerian GH, Mieville RL (1967) Ammonia application to reciprocating engines. Technical report, 5
- Hansson J, Brynolf S, Fridell E, Lehtveer M (2020) The potential role of ammonia as marine fuel—based on energy systems modeling and multi-criteria decision analysis. *Sustainability* 12:3265

- Haputhanthri SO, Maxwell TT, Fleming J, Austin C (2015) Ammonia and gasoline fuel blends for spark ignited internal combustion engines. *J Energy Resour Technol* 137:062201
- Hodgson JW (1974) Alternate fuels for transportation. Part III. Ammonia for the automobile. *Mech Eng J* 96:7  
<https://nh3fuel.com/index.php/news/13-multimedia/20-2007-10-16-ammonia-conference-presentation>. Last accessed 30 July 2021
- Koch E (1949) Ammonia as a fuel for motor buses. *J Inst Pet* 31:21–32
- Koike M, Miyagawa H, Suzuoki T, Ogasawara K (2012) Ammonia as a hydrogen energy carrier and its application to internal combustion engines. In: Sustainable vehicle technologies, pp 61–70
- Koike M, Suzuoki T, Takeuchi T, Homma T, Hariu S, Takeuchi T (2021) Cold-start performance of an ammonia-fueled spark ignition engine with an on-board fuel reformer. *Int J Hydrogen Energy* 46(50)
- Koike M, Suzuoki T (2019) In-line adsorption system for reducing cold-start ammonia emissions from engines fueled with ammonia and hydrogen. *Int J Hydrogen Energy* 44(60):32271–32279
- Kong SC, Gross CW (2012) Performance characteristics of a compression-ignition engine using direct-injection ammonia–DME mixtures. *Fuel* 103(2013):1069–1079
- Lhuillier C, Brequigny P, Contino F, Mounaïm-Rousselle C (2021) Experimental investigation on ammonia combustion behavior in a spark-ignition engine by means of laminar and turbulent expanding flames. *Proc Combust Inst* 38:5859–5868
- Lhuillier C, Brequigny P, Contino F, Rousselle C (2019) Combustion characteristics of ammonia in a modern spark-ignition engine. In: Presented at the 14th international conference on engines & vehicles, Capri, Italy, September 9, SAE Tech. Pap. 2019-24-0237 (2019)
- Lhuillier C, Brequigny P, Contino F, Rousselle C (2019b) Performance and emissions of an ammonia-fueled SI engine with hydrogen enrichment. SAE Tech. Pap. 2019-24-0137
- Lhuillier C, Brequigny P, Contino F, Mounaïm-Rousselle C (2020) Experimental study on ammonia/hydrogen/air combustion in spark ignition engine conditions. *Fuel* 269:117448
- Lindstedt RP, Lockwood FC, Selim MA (1994) Detailed kinetic modelling of chemistry and temperature effects on ammonia oxidation. *Combust Sci Technol* 99:253–276
- Mendiara T, Glarborg P (2009) Ammonia chemistry in oxy-fuel combustion of methane. *Combust Flame* 156:1937–1949
- Miller JA, Bowman CT (1989) Mechanism and modeling of nitrogen chemistry in combustion. *Prog Energy Combust Sci* 15:287–338
- Mørch CS, Bjerre A, Gøttrup MP, Sorenson SC, Schramm J (2011) Ammonia/hydrogen mixtures in an SI-engine: engine performance and analysis of a proposed fuel system. *Fuel* 90:854–864
- Mounaïm-Rousselle C, Brequigny P (2020) Ammonia as fuel for low-carbon spark-ignition engines of tomorrow's passenger cars. *Front Mech Eng* 6:70
- Mounaïm-Rousselle C, Mercier A, Brequigny P, Dumand C, Bouriot J, Houillé S (2021a) Performance of ammonia fuel in the case of spark assisted compression ignition engine, special issue on the current and future use of H<sub>2</sub> and H<sub>2</sub> based e-fuels in combustion engines and fuel cells. *Int J Engine Res* to appear
- Mounaïm-Rousselle C, Bréquigny P, Dumand C, Houillé S (2021b) Operating limits for ammonia fuel spark-ignition engine. *Energies* 14:4141
- Niki Y (2021) Reductions in unburned ammonia and nitrous oxide emissions from an ammonia-assisted diesel engine with early timing diesel pilot injection. *ASME J Eng Gas Turbines Power* 143(9):091014. <https://doi.org/10.1115/1.4051002>
- Niki Y, Yoo DH, Hirata K, Sekiguchi H (2016) Effects of ammonia gas mixed into intake air on combustion and emissions characteristics in diesel engine. *ASME Int* 10
- Niki Y, Nitta Y, Sekiguchi H, Hirata K (2018) Emission and combustion characteristics of diesel engine fumigated with ammonia. In: ASME 2018 internal combustion engine division fall technical conference, ICEF 2018, vol 1. American Society of Mechanical Engineers, p 1
- Oh S, Park C, Kim S, Kim Y, Choi Y, Kim C (2021) Natural gas–ammonia dual-fuel combustion in spark-ignited engine with various air–fuel ratios and split ratios of ammonia under part load condition. *Fuel* 290

- Pearsall T, Garabedian C (1967) Combustion of anhydrous ammonia in diesel engines. SAE Technical Paper 670947
- Pearsall TJ, Garabedian CG (1968) Combustion of anhydrous ammonia in diesel engines. SAE Transactions, pp 3213–3221
- Pelé R, Mounaïm-Rousselle C, Bréquigny P, Hespel C, Bellettre J (2021) First study on ammonia spray characteristics with a current GDI engine injector. *Fuels* 2:253–271
- Pochet M, Jeanmart H, Contino F (2020) A 22:1 compression ratio ammonia-hydrogen HCCI engine: combustion, load and emission performances. *Front Mech Eng* 6:43
- Pochet M (2020) Use of electrofuel blends in homogeneous-charge compression-ignition engines: an experimental focus on ammonia-hydrogen. Ph.D. Thesis, UC Louvain, Vrije Universiteit Brussel
- Pochet M, Truedsson I, Foucher F, Contino F, Jeanmart F (2017) Ammonia-hydrogen blends in homogeneous-charge compression-ignition engine. SAE Tech Pap (2017-24-0087)
- Reiter A.J, Kong S.C. Demonstration of compression-ignition engine combustion using ammonia in reducing greenhouse gas emissions. *Energy and Fuels*, 22(5):2963,2971, 9 (2008)
- Ryu K, Zacharakis-Jutz GE, Kong S-C (2014a) Performance enhancement of ammonia-fueled engine by using dissociation catalyst for hydrogen generation. *Int J Hydrogen Energy* 39:2390–2398
- Ryu K, Zacharakis-Jutz GE, Kong S-C (2014b) Effects of gaseous ammonia direct injection on performance characteristics of a spark-ignition engine. *Appl Energy* 116:206–215
- Ryu K, Zacharakis-Jutz GE, Kong SC (2014c) Performance characteristics of compression-ignition engine using high concentration of ammonia mixed with dimethyl ether. *Appl Energy* 113:488–499
- Şahin Z, Akcanca IZ, Durgun O (2018) Experimental investigation of the effects of ammonia solution (NH<sub>3</sub>OH) on engine performance and exhaust emissions of a small diesel engine. *Fuel* 214:330–341
- Salek F, Babaie M, Shakeri A, Hosseini SV, Bodisco T, Zare A (2021) Numerical study of engine performance and emissions for port injection of ammonia into a gasoline/ethanol dual-fuel spark ignition engine. *Appl Sci* 11:1441
- Sawyer R, Starkman E, Muzio L, Schmidt W (1968) Oxides of nitrogen in the combustion products of an ammonia fueled reciprocating engine. In: Presented at the mid-year international automotive engineering meeting. SAE Technical Paper 680401
- Schönborn A (2021) Aqueous solution of ammonia as marine fuel. *Proc Inst Mech Eng Part M J Eng Maritime Environ* 235(1):142–151
- Sousa-Cardoso J, Silva V, Rocha RC, Hall MJ, Costa M, Eusébio D (2021) Ammonia as an energy vector: Current and future prospects for low-carbon fuel applications in internal combustion engines. *J Cleaner Prod* 296
- Stagni A, Cavallotti C, Arunthanayothin S et al (2020) An experimental, theoretical and kinetic-modeling study of the gas-phase oxidation of ammonia. *React Chem Eng* 5(4). Royal Society of Chemistry (RSC):696–711
- Starkman E, James G, Newhall H (1967) Ammonia as a diesel engine fuel: theory and application. SAE Technical Paper 670946
- Susumu K, Nakamura N, Shimizu , Sugimoto T, Kim K-O (2009) Ammonia burning internal combustion engine. International Patent No WO 2010/079846 A1
- Szybist JP, Busch S, McCormick RL, Pihl JA, Splitter DA, Ratcliff MA, Kolodziej CP, Storey JME, Moses-DeBusk M, Vuilleumier D, Sjöberg M, Sluder CS, Rockstroh T, Miles P (2021) What fuel properties enable higher thermal efficiency in spark-ignited engines? *Progr Energy Combust Sci* 82:100876
- Tay KL, Yang W, Li J, Zhou D, Yu W, Zhao F, Chou SK, Mohan B (2017) Numerical investigation on the combustion and emissions of a kerosene-diesel fueled compression ignition engine assisted by ammonia fumigation. *Appl Energy* 204:1476–1488

- Valera-Medina A, Amer-Hatem F, Azad AK, Dedoussi IC, de Joannon M, Fernandes RX, Glarborg P, Hashemi H, He X, Mashruk S, McGowan J, Mounaim-Rouselle C, Ortiz-Prado A, Ortiz-Valera A, Rossetti I, Shu B, Yehia M, Xiao H, Costa M (2021) *Energy Fuels* 35(9):6964–7029
- Valera-Medina A, Banares-Alcantara R (2020) Techno-economic challenges of ammonia as an energy vector, Chapter 7, applications. pp 165–171
- Van Blarigan P (2000) Advanced internal combustion engine research. In: Proceedings of the 2000 US DOE hydrogen program review, San Ramon, California, pp 639–56 [4]
- Wang W, Herreros JM, Tsolakis A, York APE (2013) Ammonia as hydrogen carrier for transportation; investigation of the ammonia exhaust gas fuel reforming. *Int J Hydrogen Energy* 38(23):9907–9917
- Wang D, Ji C, Wang S, Yang J, Wang Z (2021) Numerical study of the premixed ammonia-hydrogen combustion under engine-relevant conditions. *Int J Hydrogen Energy* 46(2):2667–2683
- Westlye FR, Ivarsson A, Schramm J (2013) Experimental investigation of nitrogen based emissions from an ammonia fueled SI-engine. *Fuel* 111:239–247
- Woo Y, Jang JY, Lee YJ, Kim J-N (2014) Recent progress on the ammonia-gasoline and the ammonia-diesel dual fueled internal combustion engines in Korea. In: Presented at the 11th NH<sub>3</sub> fuel conference
- Zhang H, Li T, Chen R, Wang N, Wei Y, Wu D (2021) Injection characteristics and fuel-air mixing process of ammonia jets in a constant volume vessel. *Fuel* 304:121408
- Zhou M, Wang Y, Chu Y, Tang Y, Tian K, Zheng S, Chen J, Wang Z (2019) Ammonia as an environmentally benign energy carrier for the fast growth of China. *Energy Procedia* 158:4986–4991

# Chapter 12

## Methanol as a Fuel for Internal Combustion Engines



Chuntao Liu, Zhiqiang Li, Yiqiang Pei, and Yanzhao An

**Abstract** Methanol has attracted broad attention over the past few decades as an alternative fuel for diesel and gasoline for internal combustion engines. Renewable methanol has helped methanol engines achieve almost zero carbon dioxide emissions in recent years, showing greater advantages than other fuels. The development of methanol engines has undergone a long history. The revolution of methanol engines has been closely linked to the application of energies, including oil resources, and the environment. Over the last few years, a variety of proposals on the applications of methanol engines have been put forward. Methanol engines can operate with pure methanol, blended fuel, or dual fuel. In a general sense, methanol has its unique properties, such as its high oxygen content, fast laminar burning velocity, great latent heat of vaporization, and having no C–C bond, which favors its use in advanced engine technology. A detailed discussion will be made on the in-cylinder combustion process and emissions characteristics of methanol engines, as well as some typical issues found in the application in this chapter. It is hoped that some useful points can be provided for the development and study of methanol engines.

**Keywords** Methanol engine · Alternative fuel · Blended fuel · Dual fuel

### *Abbreviations*

BMBF	Biodiesel methanol blended fuel
BMDF	Biodiesel methanol dual fuel
BMEP	Brake mean effective pressure
BTDC	Before top dead center
BTE	Brake thermal efficiency
CI	Compression ignition
COV	Coefficient of variation

---

C. Liu · Z. Li · Y. Pei · Y. An (✉)  
State Key Laboratory of Engines, Tianjin University, Tianjin 300350, China  
e-mail: [yanzho\\_an@tju.edu.cn](mailto:yanzho_an@tju.edu.cn)



CR	Compression ratio
DI	Direct injection
DMBF	Diesel methanol blended fuel
DMDF	Diesel methanol dual fuel
EGR	Exhaust gas recycle
EPA	Environmental protection agency
GDI	Gasoline direct injection
GHG	Greenhouse gas
GMBF	Gasoline-methanol blended fuel
HPDI	High-pressure direct injection
HPI	Hydrogen port injection
HRR	Heat release rate
ICE	Internal combustion engine
IMEP	Indicated mean effective pressure
ITE	Indicated thermal efficiency
LBV	Laminar burning velocity
MDI	Methanol direct injection
MPI	Methanol port injection
MSR	Methanol substitution rate
PAHs	Polycyclic aromatic hydrocarbons
PM	Particulate matter
PN	Particle number
SI	Spark ignition
SOI	Start of injection
ST	Spark time
TDC	Top dead center
ULSD	Ultra-low sulfur diesel

### *Nomenclature*

CH <sub>4</sub>	Methane
CO	Carbon monoxide
CO <sub>2</sub>	Carbon dioxide
H <sub>2</sub>	Hydrogen
HC	Hydrocarbon compounds
NO	Nitrogen monoxide
NO <sub>2</sub>	Nitrogen dioxide
NO <sub>x</sub>	Nitrogen oxide
O <sub>2</sub>	Oxygen
λ	Lambda

## 12.1 Background

Human activities are estimated to have caused approximately 1.0 °C of global warming above pre-industrial levels. Until 2020, 87% of the Earth's surface is significantly warmer than the average temperature during 1951–1980 (Robert 2020), and global warming is likely to reach 1.5 °C between 2030 and 2052 at the current rate (Antoine 2021). According to data from the National Oceanic and Atmospheric Administration, the strong correspondence between the temperature and the concentration of carbon dioxide (CO<sub>2</sub>) in the atmosphere has been demonstrated during the glacial cycles over the past several hundred thousand years (Jouzel et al. 2007).

The global CO<sub>2</sub> emitted in 1950 was about 5 billion tons, but it soared to 22 billion tons in 1990, and now it maintains a level of more than 36 billion tons each year. The CO<sub>2</sub> emission from fuel combustion approximately accounts for a percentage of 34 (Hannah and Max 2021). In 2015, the climate goal of the Paris Agreement was to hold “the increase in the global average temperature to well below 2 °C above pre-industrial levels and pursue its efforts to limit the temperature increase to 1.5 °C above pre-industrial levels” (UNFCCC 2021). Following the Paris Agreement, a lot of countries show their ambitions on CO<sub>2</sub> control. The United Kingdom plans to enshrine into law a new target to slash CO<sub>2</sub> emissions 78% by 2035 (GOV.UK. 2035). China declares the aim to peak CO<sub>2</sub> emissions before 2030 and achieve carbon neutrality before 2060 (Xi 2021). In this context, a comprehensive set of measures will be attempted to implement, including expanding renewable energy usage, restricting carbon emission by introducing a carbon tax, reducing tropical deforestation, etc. (Sebastian 2018).

As shown in Fig. 12.1, the chemical storage technology has a wide range of energy capacity and a long storage period comparing with another storing technology, and methanol is one of the optimal energy carriers (Cesaro et al. 2021). Producing methanol from CO<sub>2</sub> and hydrogen (H<sub>2</sub>) makes methanol the primary substitute for fossil fuel (Jouny et al. 2018). Methanol has become an important solution to combat global warming and air pollution, especially for sectors and regions where the electrification of the powertrain is challenging.

## 12.2 Acquisition of Methanol

Methanol, as one of the most important platform chemicals, has been largely used for polymers production for many years, such as formaldehyde, acetic acid, methyl-tert-butyl ether, etc. Methanol can also be used potentially as transportation fuel alone or blended with other fossil fuels (Methanol Institute 2020). As a result of the booming construction, transportation, and electronics industries, the market of methanol is increasing continuously. The global methanol market is estimated to grow at a compound annual growth rate of 9.8% from 2019 to 2026 (see Fig. 12.2) (Polaris Market Research 2021). The global production capacity of methanol was

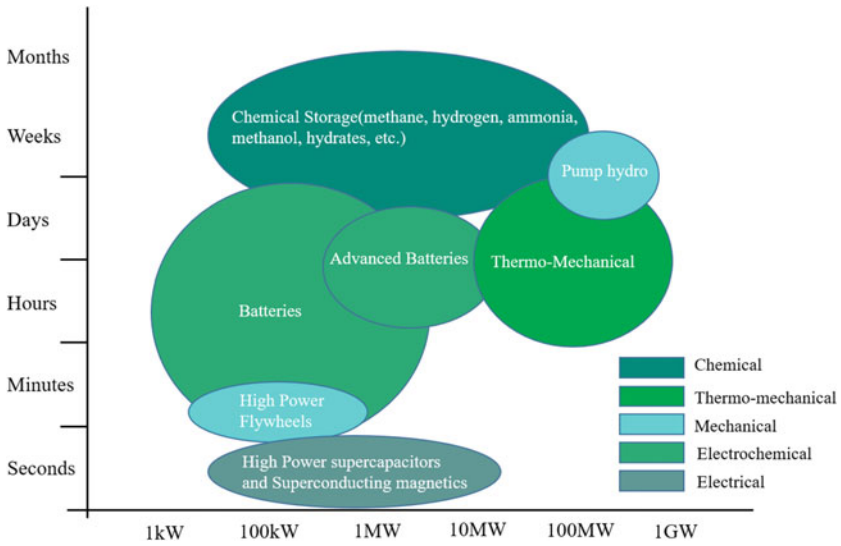


Fig. 12.1 Clean energy can be stored as methanol (Cesaro et al. 2021)

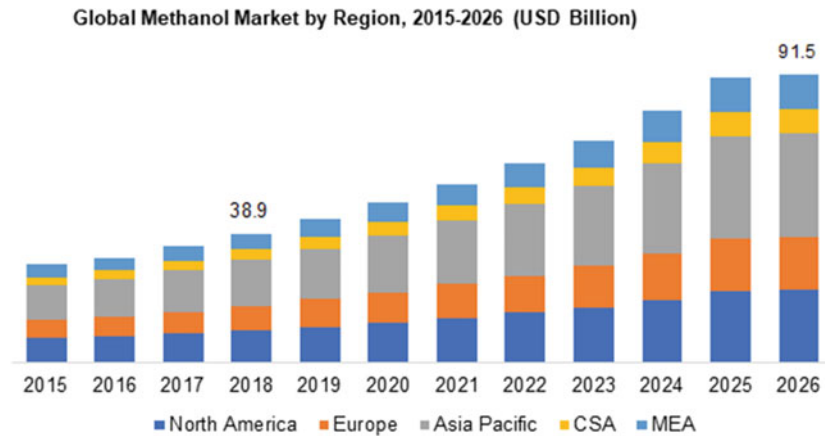


Fig. 12.2 Increase of global methanol market (Polaris Market Research 2021)

approximately 148 million metric tons in 2019, which is expected to double in 2030. This growth is attributed to the planned and announced methanol plants (Global production capacity of methanol 2021).

### 12.2.1 Development of Methanol Production

In 1861, Robert Boyle isolated the methanol via wood distillation, but Dumas and Peligot first discovered the chemical composition in 1834. Subsequently, Sabatier proposed the synthetic pathway for obtaining methanol by hydrogenating carbon monoxide (CO) (Sabatier 1926). In 1923, A synthesis gas-based methanol production process was proposed by Badische Anilin-und-Soda-Fabrik and remained the dominant technology for over 45 years. The following technology developments aimed to reduce the pressure and temperature levels to improve process economics (Bozzano and Manenti 2016). Nowadays, methanol synthesis via CO<sub>2</sub> and H<sub>2</sub> is considered a promising technology.

### 12.2.2 Process of Methanol Synthesis

Many different feedstocks can be adopted in the process of methanol synthesis, as shown in Fig. 12.3 (IRENA 2021). Commercial methanol is mostly generated from synthesis gas by the catalytic reaction of its components: H<sub>2</sub>, CO, and CO<sub>2</sub> (Garcia et al. 2021; Kattel et al. 2017), mainly from fossil fuels. In China, most methanol is produced using coal as the feedstock, whereas elsewhere in the world, it is produced using natural gas (IRENA 2021; Xu et al. 2017).

The process of methanol production from synthesis gas generally takes the following three basic steps (Tijm et al. 2001):

- Production of synthesis gas
- Conversion of the synthesis gas into methanol
- Distillation of the reactor effluent to obtain the required product specification

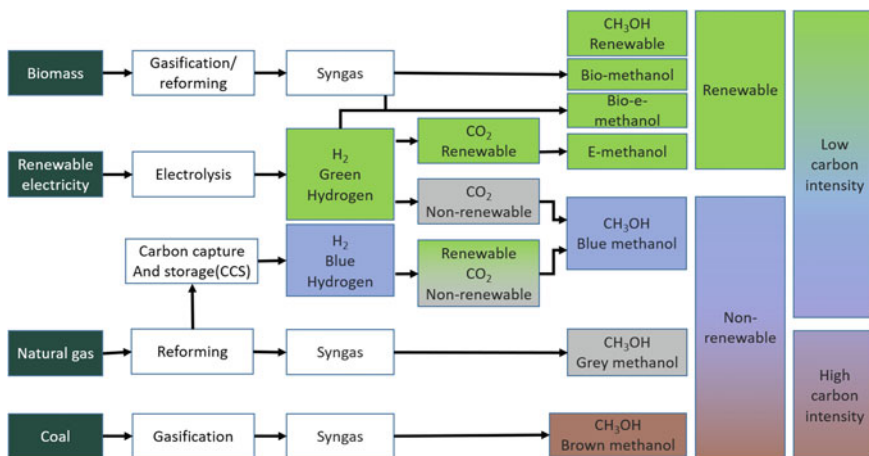


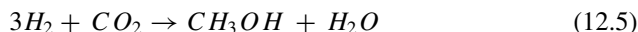
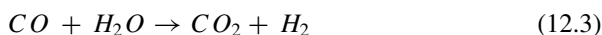
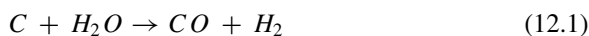
Fig. 12.3 The principal methanol production routes (IRENA 2021)

Therein the manufacturing and purification of synthesis gas are crucial parts of the overall process for methanol production (Machado et al. 2014).

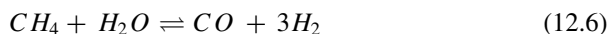
### Synthesis from Coal

Currently, coal-based methanol accounts for approximately 35% of methanol production. The synthesis gas generation can be divided into coal gasification technology and coal coking technology (Cao and Feng 2006; Li et al. 2018a).

Coal gasification is described by the reaction of coal with water steam, as shown in Eq. (12.1) (Brian 1975). This reaction is very endothermic, and the needed heat can be provided in several ways, one of which is the combustion of coal itself, as shown in Eq. (12.2). After gasification, the raw synthesis gas contains not only CO<sub>2</sub>, H<sub>2</sub>, and CO, but also H<sub>2</sub> sulfide and carbon oxysulfide. Then the purification process is needed. Another way of getting H<sub>2</sub> is through CO and water synthesis, as shown in Eq. (12.3). Methanol is then synthesized from a mixture of synthesis gas by following the reactions as shown in Eqs. (12.4) and (12.5).



For coal coking technology, the synthesis gas is coke oven gas produced during the coking process. The synthesis gas contains H<sub>2</sub>, methane (CH<sub>4</sub>), CO, and other gases. The volume percentages occupied by H<sub>2</sub>, CH<sub>4</sub>, and CO are 55–60%, 23–27%, and 5–8% respectively (Liao et al. 1998; Bermúdez et al. 2013). The synthesis gas is reformed through the reactions, as shown in Eq. (12.6). Then the methanol is synthesized by following the same reactions as shown in Eqs. (12.4) and (12.5).



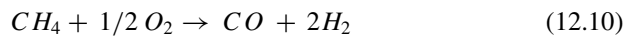
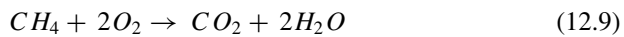
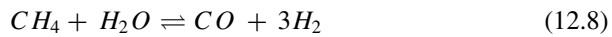
It is worth noting that the synthesis gas has an ideal H/C ratio, which can be defined through Eq. (12.7), where the ideal S is equal to 2. Due to the low S in synthesis gas from the coal, it is critical to increase the H<sub>2</sub> proportion and decrease the carbon proportion. The water–gas shift reaction is adopted to enhance the amount of H<sub>2</sub>. Meanwhile, the extra CO<sub>2</sub> must also be separated and vented to the atmosphere.

$$S = \frac{Mole_{H_2} - Mole_{CO_2}}{Mole_{CO_2} + Mole_{CO}} \quad (12.7)$$

### Synthesis from Natural Gas

Natural gas is primarily used for methanol production currently. The synthesis process of methanol involves the four basic steps: feed preparation, steam reforming, methanol synthesis, and methanol distillation, as shown in Fig. 12.4 (Bertau et al. 2014; Li et al. 2018b).

At the stage of feed preparation, the desulphurizing process of natural gas is firstly adopted to reduce the sulphury content, and then natural gas is compressed and sent into the steam reforming process. In the steam reforming process, natural gas is reformed into the synthesis gas with several reactions. The steam [see Eq. (12.8)] and auto thermal reforming [see Eq. (12.9)] are both needed. Moreover, some partial oxidation of  $\text{CH}_4$  [see Eq. (12.10)] also occurs in this process. After the distillation of crude methanol, the water is removed, and then 99% refined methanol is obtained.



Compared with the coal-based synthesis, the H/C ratio from natural gas is higher, and an ideal S is easier to reach, which means less  $\text{CO}_2$  is emitted.

### Synthesis from Biomass and Municipal Solid Waste

Renewable biomass is widely utilized in biofuel generation. It is carbon neutral because the plants absorb  $\text{CO}_2$  due to photosynthesis. Even if the biofuel is produced and burned, the  $\text{CO}_2$  emission is also offset finally. The production technology of methanol from biomass and municipal solid waste is pretty similar to that of natural gas. The entire process can also be divided into three steps: production of synthesis gas, synthesis of crude methanol, and purification of methanol. In addition, for the kraft process in the pulp and paper industry, methanol is also produced to recover the energy (IRENA 2021; Mockos et al. 2008). As biomass gasification mainly depends

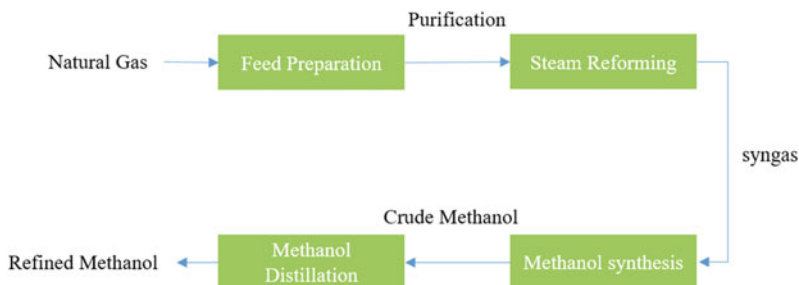


**Fig. 12.4** The synthesis process of methanol from natural gas (Bertau et al. 2014)

on partial (under stoichiometric) combustion similar to coal gasification, and the biogas reforming is identical to natural gas reforming. Hence the introduction is passed over.

### Synthesis from H<sub>2</sub> and CO<sub>2</sub>

The methanol synthesis can be formed via H<sub>2</sub> and CO<sub>2</sub>, which represents a promising environmental-friendly route for combatting CO<sub>2</sub> emissions. The basic reaction is shown in Eq. (12.11). The most efficient hydrogenation of CO<sub>2</sub> to methanol is a multi-component catalytic system (Stangeland et al. 2020).



According to the resources of H<sub>2</sub> and CO<sub>2</sub>, renewable methanol can be divided into green methanol and blue methanol. For green methanol, the H<sub>2</sub> is derived from water electrolysis via renewable electricity, such as wind electricity, solar electricity, and hydraulic electricity, while CO<sub>2</sub> is derived from capturing or biomass (Thyssenkrupp's concept of using renewable energy and waste CO<sub>2</sub> to make renewable methanol 2021). Recently, the liquid sunshine concept has been proposed in which solar energy is used to convert CO<sub>2</sub> and water to green liquid fuels (see Fig. 12.5) (Shih et al. 2018).

Up to now, due to the higher costs associated with CO<sub>2</sub> capturing and green H<sub>2</sub> production, the industrial implementation of methanol synthesis from CO<sub>2</sub> and H<sub>2</sub> has been constrained. There are also more significant thermodynamic restrictions on the conversion due to the competing reverse water–gas shift reaction, as shown in Eq. (12.12) (Andrea et al. 2017; Stangeland et al. 2018).

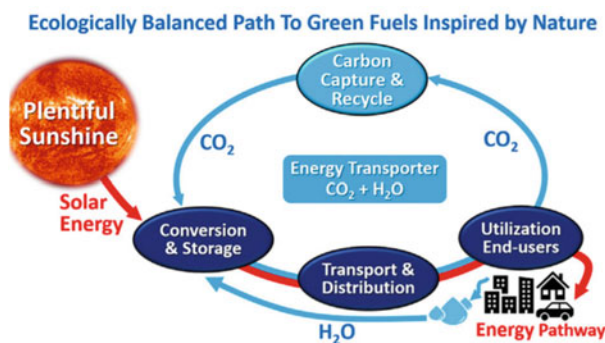


Fig. 12.5 The liquid sunshine concept (Shih et al. 2018)

## 12.3 Methanol Applications in Internal Combustion Engine

### 12.3.1 History of Methanol Engines

Methanol engines have experienced a history of more than one hundred years since their first appearance. Their evolution has been closely linked to the application of energy, especially oil resources, in addition to the environment. Several phases of growth and stagnation of methanol engines are presented in Fig. 12.6.

It should be noted that alcohol has been used as transport fuel since the beginning of the automobile industry. Automobile manufacturers have tried almost every kind of available fuel, such as alcohol, ether, ketone, esters, and other organic solvents, as long as they are ignitable and combustible. Therein ethanol was more competitive than methanol and generally became the preferred fuel option for early automobiles because it was easily distilled from fermented sugars (Gustafson 2021). Many countries poor with oil resources were particularly keen to produce ethanol fuel in their domestic agricultural sectors. An authoritative analysis of alcohol fuels from the United States Bureau of Mines showed that a gasoline engine could produce 10% more power output using alcohol fuels without any design modification. However, ethanol was no longer economically competitive due to the increasing availability of cheap gasoline, particularly in the United States, which possessed large oil resources. On the other hand, methanol engines were accompanied by various problems such as fuel system corrosion, cold start difficulty, and fuel pump liner degradation, which could not be well solved due to the limitations of the technical conditions at that time. Moreover, the powerful petroleum agencies violently opposed the further development and deployment of alcohol fuels. Consequently, automobile manufacturers were increasingly inclined to produce more engines running solely with gasoline. Thus, the research in methanol engines fell into a low tide.

Methanol raised public concern again as an alternative fuel in the 1930s. The commercially producing synthetic methanol from coal promoted the large-scale production and application of methanol. Coal-based methanol production was

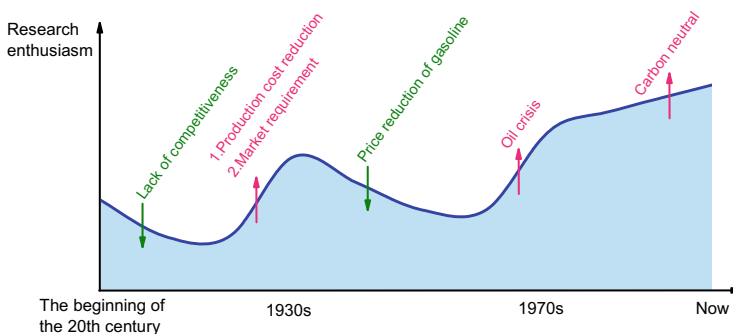


Fig. 12.6 Revolution of methanol engines



strongly intensified over several countries in Europe to achieve energy independence and military considerations. In the United States at that time, road racing entered a golden age. Methanol became the important power fuel for high-speed and highly supercharged multi-cylinder engines owing to its greater latent heat of vaporization and greater power gain. With the development of engine fuel theory, complex methanol racing fuels emerged in Europe. The addition of aromatic hydrocarbons contributed to the blending of methanol and gasoline because of their large dissolving capacity, especially in the presence of lubricating oil. Until the petroleum resources were readily and cheaply available again, the public interest in alcoholic fuels subsequently decreased. The ultimate reason for this decline of research upsurge was that the understanding and application of methanol were not mature enough. The methanol engines were designed for other fuels. Thereby the advantages of methanol fuels could not be fully utilized.

The oil crisis in the 1970s made automotive engineers and petroleum chemists realize the decline of world oil reserves and the effects of industrial byproducts on the pollution to ecosystems, which accelerated the searching for alternative fuels in the countries which were too dependent on it. Then the public interest in alcohol fuels was aroused again around the world. In the United States, a methanol fuel project was proposed and then went through a long period, aiming to achieve national energy security and improved air quality. However, it ended resulting from the appearance of reformulated gasoline at the beginning of the twenty-first century. What should be pointed out was that the problem of methanol corrosion was thoroughly solved with methanol compatible material. Meanwhile, the National Proalcohol Program was put forward in Brazil to replace gasoline with ethanol. By 1984, Brazilian sales of ethanol-powered cars accounted for 95% of all vehicle sales. In the second decade of the twenty-first century, Israel launched a ten-year national plan called the Fuel Choices Initiative, which aimed to explore competitive fuels, reduce dependence on oil and reduce greenhouse gas (GHG) emissions. The greatness of this plan was to reduce both domestic and global dependence on oil. In 2012, China began the methanol vehicle pilot project to solve the dilemma of more coal, less oil, and less gas and improve energy security. In China, methanol production and sales were largely controlled by state-owned enterprises or local governments, which established a favorable political base for promoting methanol as a kind of alternative fuel.

Undoubtedly, the global energy crisis and environmental pollution accelerate the application of methanol engines. Renewable methanol does not depend on biomass resources but relies on the capture and chemical recycling of CO<sub>2</sub>. Figure 12.7 illustrates the respective well-to-wheels GHG emissions of all investigated renewable methanol (CO<sub>2</sub> capture and recycling) and comparative fossil and biofuel pathways (Chaplin 2013). It can be seen that the renewable methanol pathway only accounts for very marginal GHG emissions and, in this regard, is superior to fossil and bio-methanol pathways.

In the more than 100 years of development and application of methanol engines, especially in recent decades, methanol has been used as fuel in various ways. Next, the classification of methanol engines will be introduced.

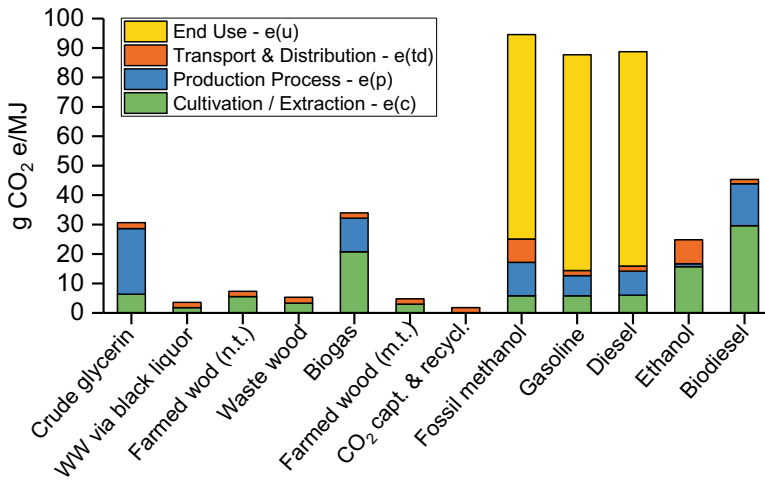


**Fig. 12.7** Well-to-wheels GHG emissions of renewable methanol pathways (g CO<sub>2</sub> e/MJ) (Chaplin 2013)

### 12.3.2 Classification of Methanol Engines

Methanol engines have been widely applied in road vehicles and marine shipping (Wang et al. 2020). They can be simply divided into three types (see Table 12.1) depending on how to combine methanol with other fuels.

#### (1) Engine Fueled with Pure Methanol

As described above, methanol is easily ignited and thereby can be directly used in engines. Principally methanol is suitable for premixed combustion and spark ignition (SI) engines due to its high autoignition resistance. Generally, methanol engines' compression ratio (CR) is greater than that of gasoline engines due to their excellent knock resistance and great latent heat of vaporization.

**Table 12.1** Classification of methanol engines

Type	Details
Engine fueled with pure methanol	Pure methanol as fuel
Engine fueled with traditional fuels and methanol	Traditional fuels include gasoline and diesel
Engine fueled with alternative fuels and methanol	Alternative fuels include biodiesel, H <sub>2</sub> , natural gas, etc.

## (2) Engine Fueled with Traditional Fuels and Methanol

With the help of a cosolvent, methanol can be used as a fuel additive to traditional fuels such as gasoline and diesel to improve the fuel economy and decrease pollutant emissions of base engines.

## (3) Engine Fueled with Alternative Fuels and Methanol

There are many alternative fuels besides methanol. Methanol can be combined with these alternative fuels to form a new kind of alternative fuel. The available alternative fuels include biodiesel,  $H_2$ , natural gas, etc. For liquid fuels, like biodiesel, the methanol can either be used as an additive or be injected independently. For gaseous fuels, like natural gas, dual-injection is the most suitable mode.

A brief introduction is given to the classification of methanol engines in this section. The combustion and emission characteristics of methanol engines will be described in detail for specific engine types in the next section.

## 12.4 Characteristics of Different Methanol Engines

### 12.4.1 Engine Fueled with Pure Methanol

The properties of methanol, such as its high oxygen content, fast laminar burning velocity (LBV), great latent heat of vaporization, and having no C–C bond, favor its use in advanced engine technology. In particular, it is possible to improve CR, downsize engine outline, and thus improve thermal efficiency and reduce pollutant emissions (Verhelst et al. 2019).

#### (1) Thermal Efficiency

Methanol is more suitable for SI engines owing to its low cetane number. Previous studies on compression ignition (CI) engines have demonstrated that combustion is very sensitive to the engine's operating boundary, and any little cyclic variation of the air–fuel mixture during the compression stroke may lead to a significant variation of combustion and engine performance (Zhang and Wu 2016). The high-octane number indicates that methanol has excellent knock resistance, and the great latent heat of vaporization allows for further raising the CR, which is beneficial to improve the engine's thermal efficiency. The higher CR does not always mean better thermal efficiency. A test performed on a stratified-charge direct injection (DI) SI methanol engine showed that too high CR could not improve the engine brake thermal efficiency (BTE) at low load conditions (Gong et al. 2016, 2020a) (see Fig. 12.8).

Some studies have proven that the BTE of methanol engines is higher than that of gasoline engines (Balki and Sayin 2014; Wu et al. 2016). The high flame-diffusion velocity of methanol can improve the homogeneity of the air–fuel mixture and reduce the chance of misfire and partial burning. For a DISI methanol engine, it was proved that stable combustion could be achieved when the global equivalence ratio was

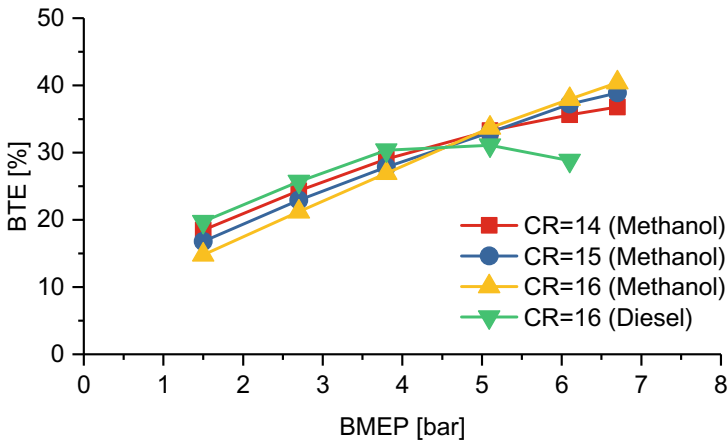


Fig. 12.8 Effect of CR on BTE (Gong et al. 2016)

greater than 0.4 (Gong et al. 2017), which created favorable conditions for improving thermal efficiency. Meanwhile, the experimental studies carried out by the United States Environmental Protection Agency (EPA) demonstrated the BTE of methanol engine was better than that of turbocharged diesel engine, and a broader high efficiency operating range was achieved from methanol engine as shown in Fig. 12.9 (Brusstar et al. 2002; Brusstar and Gray 2007). Some researches referring to DI methanol engines have indicated that the BTE could be further improved if adopting high-energy multi-spark ignition (Gong et al. 2011a).

(2) Engine-out Emissions

i. Nitrogen Oxide (NO<sub>x</sub>) Emission

NO<sub>x</sub> is generated in the areas of combustion with a high temperature and substantial excess air. The lower combustion temperature of methanol engines yields lower NO<sub>x</sub> emissions than that of gasoline engines, as

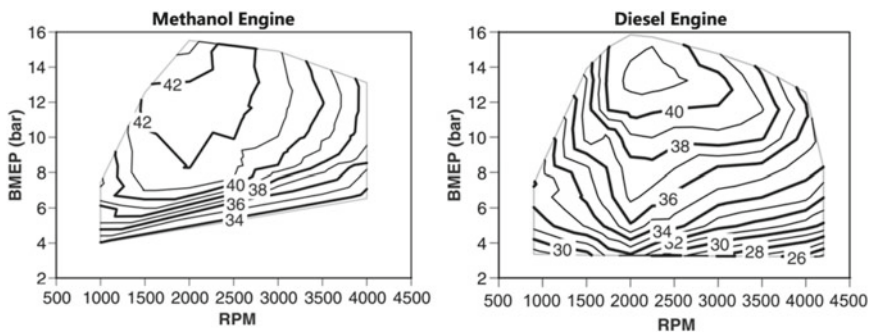
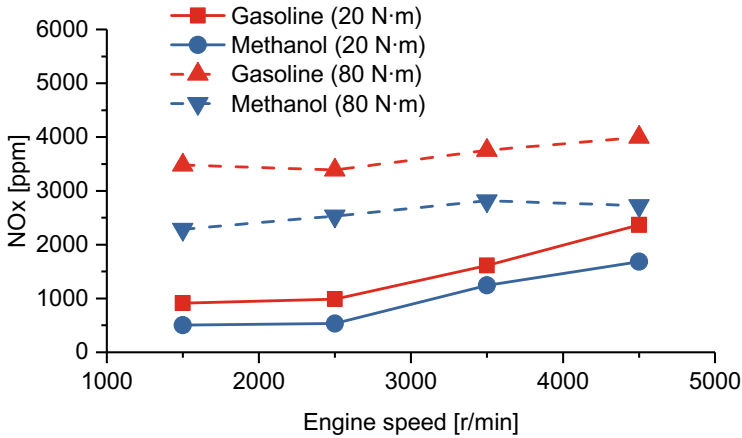


Fig. 12.9 BTE comparison between methanol engine and diesel engine (Brusstar et al. 2002)



**Fig. 12.10**  $\text{NO}_x$  emissions comparison between methanol engine and gasoline engine (Vancoillie et al. 2012)

shown in Fig. 12.10. It is worthy to note that the vacuum in the intake due to the reason that throttling is quite considerable at low loads, hence internal exhaust gas recycle (EGR) level can be expected to be important. But at high loads, the internal EGR level is low, which explains the higher  $\text{NO}_x$  emissions of methanol engines (Vancoillie et al. 2012). Inspired by it, external EGR is widely used to reduce further  $\text{NO}_x$  emissions of methanol engines, particularly at high loads (Zhen et al. 2020a).

ii. CO and Hydrocarbon compounds (HC) Emissions

In principle, CO indicates the completeness of combustion and is primarily controlled by the equivalence ratio. The sources of HC emissions fall into four pathways: flame quenching near the cold wall, the unburned mixture owing to the crevice effect, the unburned mixture from the lubricant oil, and incomplete combustion with partial cycle (Heywood 1988). Compared with gasoline and diesel, the oxygen-containing nature of methanol makes it easier to complete combustion. A mass of studies has shown that methanol fuel can significantly reduce CO and HC emissions (Balki and Sayin 2014; Wu et al. 2016; Vancoillie et al. 2012; Tian et al. 2020; Balki et al. 2016). Surely, incomplete combustion with flame extinction at low load may increase HC emissions. Some researches referring to DI methanol engines have shown the CO and HC emissions can be further reduced by adding more nozzle holes at the sacrifice of  $\text{NO}_x$  emissions at high load (Gong et al. 2011b).

iii.  $\text{CO}_2$  Emission

Each fuel produces a fixed amount of  $\text{CO}_2$  per unit of heat when it burns. As shown in Table 12.2, the  $\text{CO}_2$  produced by burning methanol is lower than that of gasoline and diesel, which means methanol is more

**Table 12.2** Comparison of CO<sub>2</sub> emissions (Brusstar and Gray 2007)

Fuel	Methanol	Gasoline	Diesel
CO <sub>2</sub> emission [g/MJ]	69.8	74.2	74.1

effective in reducing CO<sub>2</sub> than gasoline and diesel (Brusstar and Gray 2007).

iv. Unregulated Emissions

According to United States EPA's assessment, the volatile organic compounds emissions from all mixtures of methanol and gasoline were lower than that of gasoline engines. Even those vehicles with higher HC emissions contributed less to ozone destruction than gasoline vehicles. The experimental results from the Southwest Research Institute showed that although methanol engines emitted more aldehydes than gasoline and diesel engines, current technology could reduce the aldehydes to the level of conventional vehicles (Cheung et al. 2009). It was measured that formaldehyde emission from methanol engines far outweighed that from diesel engines, especially at low atmospheric temperature and at low load. It might be ascribed to low combustion temperature and less effective oxidation catalyst. Therefore, the formaldehyde emission may be a limiting factor for the achievable methanol fraction at low loads (Cheung et al. 2009; Wei et al. 2015).

(3) Challenge

i. Cyclic Variation

The coefficient of variation of indicated mean effective pressure (COV<sub>IMEP</sub>) is an important factor affecting the operation of SI engines by combustion instability and misfire (Bode et al. 2019; Chen et al. 2017a), particularly in the conditions of low flame speed with a lean mixture (see Fig. 12.11) (Chen et al. 2019a). The evaporative cooling effect of methanol is the most probable cause for ignition site quenching and it may be responsible for the observed increase in cyclic variation associated with spray-driven methanol combustion (Gong et al. 2011c). In recent years, with the progress of combustion theory and control methods, some efforts have been made to improve the cyclic variation of methanol engine, and the technical methods include increasing in-cylinder turbulent flow, improving fuel physicochemical properties, optimizing injection timing and ignition timing, etc. (Gong et al. 2011c; Wang and Ji 2012).

ii. Corrosivity

Generally, methanol is corrosive with copper, rubber, aluminum, brass, and many plastics. Therefore, additives are typically used, on the fuel side, to improve the fuel's lubricity, reduce carbon residues, enhance anti-corrosion and anti-rust properties, and protect certain metals. In addition, methanol possibly causes shrinkage, swelling, hardening, or softening of

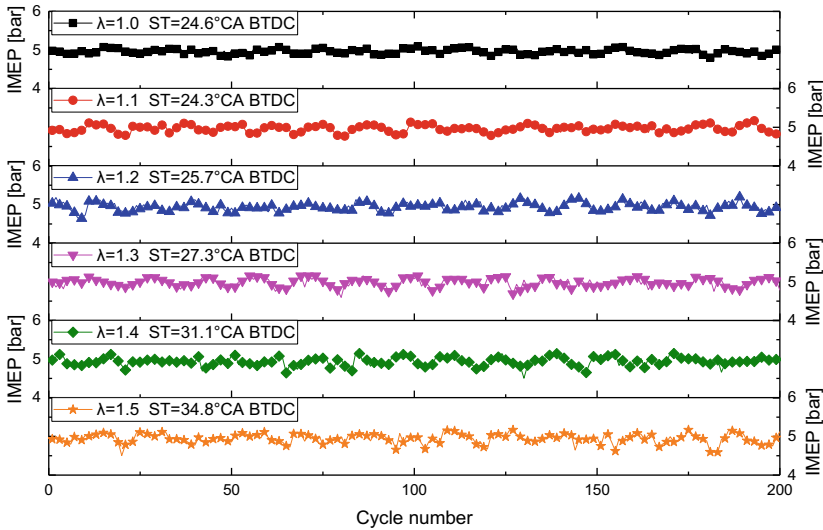


Fig. 12.11 COV<sub>IMEP</sub> with various  $\lambda$  for methanol engine (Chen et al. 2019a)

elastomers in the fuel system, especially for a higher methanol concentration. Therefore, alcohol-compatible elastomer classes such as fluorocarbon elastomers or nitrile butadiene rubbers are necessary for fuel systems (Yuen et al. 2010; Turner et al. 2012).

iii. Rubbing Wear

Compared to gasoline or diesel engines, the cylinder liner and valves of methanol engines are prone to wear issues, which is attributed to the smokeless combustion (the soot helps in lubricating the friction interfaces). Consequently, these in-cylinder friction interfaces, especially valves, should be manufactured with special materials.

iv. Cold Start

Cold start is a huge challenge for methanol engines. Many reasons lead to this issue: firstly, the lower vapor pressure and higher boiling point of methanol compared to gasoline may result in difficulties in the mixture preparation and ignition at low ambient temperature (Gong et al. 2018); secondly, more fuel needs to be injected due to low energy density of methanol, which, in turn, will further reduce in-cylinder gas temperature because of high latent heat of methanol vaporization; thirdly, the low flammability limit of methanol indicates that a higher concentration of fuel is necessary before ignition. Many efforts have been made to solve the above difficulties, such as heating charge to raise the mixture temperature, optimizing control strategy to improve spray atomization and vaporization, adding volatile additives to expand flammability limit, and increasing the number of spark plugs number to strengthen ignition energy.

v. Toxicity and Safety

Methanol has gained a negative reputation when it comes to its toxicity to human health and the environment. The results of animal tests to determine the toxicity of various fuels by inhalation, oral and dermal contact have proven that the toxicity of alcohol fuels is comparable, and in many cases better than that of gasoline or diesel (Bromberg and Cheng 2010). Methanol released from automobiles is usually related to the refueling and cold-start process, which shall be given special consideration. But it may be noted that during the Californian M85 trial, which lasted for several years and involves over 15 000 gasoline methanol blended fuel vehicles being used by the general public without special training in refueling, not a single issue of toxicity was reported (Ward and Teague 1996). Furthermore, methanol is readily degraded by photo-oxidation and biodegradation with no evidence of bioaccumulation in the environment. Thus, the accidental release of methanol into the environment during its production, transportation, or storage, although possible, will cause less damage than a corresponding crude oil or gasoline spill. Moreover, methanol has shown clear advantages over gasoline because it is not readily ignitable below 10 °C. To say the least, even if methanol fire occurs, it can be extinguished with water thanks to its good miscibility. A significant hazard is that methanol flame is practically invisible in sunlight, but this can be addressed through additives or the use of gasoline-methanol blends.

### ***12.4.2 Engine Fueled with Traditional Fuels and Methanol***

As an alternative fuel, methanol can either completely replace traditional fuel or be blended with traditional fuel. In recent years, methanol has been studied more widely as a blending fuel.

#### **Engine Fueled with Gasoline and Methanol**

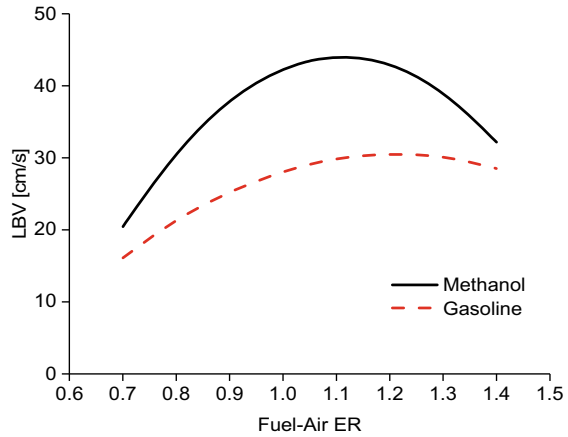
Methanol and gasoline can be either injected independently or injected as a blended fuel. The effects of these two modes are similar because both mixtures are composed of methanol, gasoline, and air before ignition due to the longer preparation time of the mixture.

(1) Thermal Efficiency

In recent years, a large number of tests have proven that the thermal efficiency of gasoline engines, including two-stroke engines (Obulesu et al. 2021), would be improved after methanol adding in (Agarwal et al. 2014; Elfasakhany 2017). One of the important reasons for this phenomenon is the fast LBV of methanol (see Fig. 12.12), which represents the heat release rate (HRR) of combustion (Brusstar 2005; Wei et al. 2021a).



**Fig. 12.12** LBV comparison between methanol and gasoline (Brusstar 2005)



The reasons why methanol accelerates the combustion process can be explained like that, with the pre-reaction of methanol, the combustion phases are advanced due to the chain branching reaction ( $CH_2O + O_2 = CHO + HO_2$ ) to produce two radical species, which speed up the combustion. In addition, the ignition of methanol is mainly controlled by the six chemical reaction paths, which are closely inter-related with the generation and consumption of OH. With the initial temperature increasing, methanol shortens the ignition delay of the gasoline methanol blended fuel (GMBF) engine (Wang et al. 2009). Considering the simple chemical reaction path of methanol, the long ignition delay at low temperature is the result of the requirement of higher activation energy, as shown in Fig. 12.13, while it leads to shorter ignition delay and faster heat release when the temperature goes above 1000 K (Wei et al. 2021a; Liu et al. 2019).

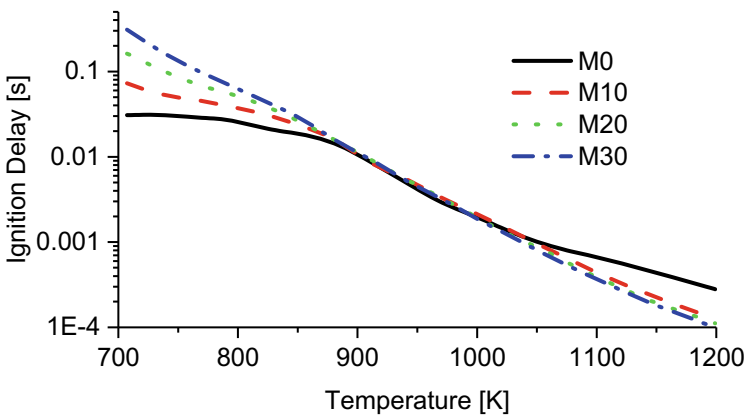


**Fig. 12.13** Variation of ignition delay with methanol substitution rate (MSR) for GMBF engine (Wei et al. 2021a)

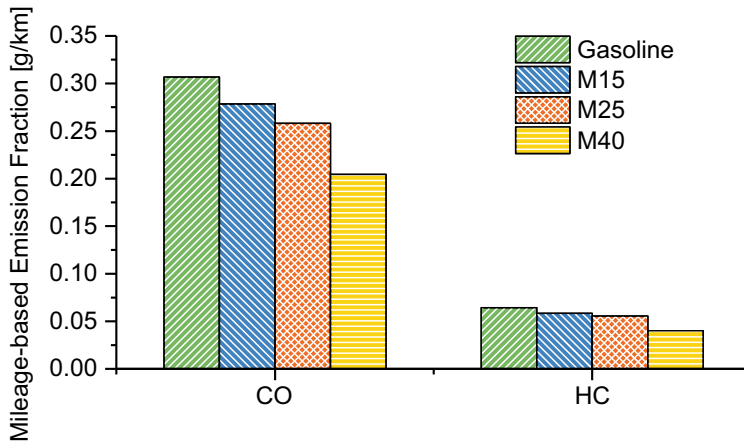


**Fig. 12.14** Variations of CO and HC emissions with MSR for GMBF engine (Wang et al. 2015a)

## (2) Engine-out Emissions

### i. $\text{NO}_x$ Emissions

Relatively low adiabatic flame temperature and high evaporation heat value of methanol contribute to yield lower  $\text{NO}_x$  emissions. However, the addition of methanol can also drive the in-cylinder air–fuel mixture to the slightly lean side and significantly accelerate the production of  $\text{NO}_x$  (Wang et al. 2015a). Therefore, the addition of methanol may have competing effects on  $\text{NO}_x$  emissions. The results are closely related to the engine configuration, control strategy, and even additives.

### ii. CO and HC Emissions

A decrease in CO and HC emissions is found with an increase in methanol concentration in the blend (Canakci et al. 2013), as shown in Fig. 12.14. When methanol is used as a partial alternative fuel, the demand for oxygen in the combustion chamber is reduced due to the lower stoichiometric air/fuel ratio and C/H ratio of methanol, which is beneficial to prevent in-cylinder fuel-rich zones and alleviates incomplete combustion. These effects are especially meaningful during acceleration and high-speed operating conditions. No C–C bond in methanol also helps to restrict the formation of incomplete resultants (Wang et al. 2015a).

### iii. Particulate Matter (PM) Emission

Because methanol is a kind of oxygenated fuel and no C–C bond exists in its chemical structure, the thermal pyrolysis route within fuel-rich zones forming CH radicals and polycyclic aromatic hydrocarbons (PAHs) is effectively restrained (Hong et al. 2018). Both CH radicals and PAHs are the key precursors for PM formation in the combustion chamber. Besides, burning methanol in gasoline direct injection (GDI) engines can reduce the dependence upon configurations of fuel supply

systems. Extra O and OH radicals derived by methanol are also conducive to consume carbonaceous in-cylinder particles (Wang et al. 2015a). The mileage-based mass and number of PM shown in Fig. 12.15 demonstrate that, with the addition of methanol, the mass of PM is reduced while a slight increment of particulate number is noticed with the rise of MSR.

iv. Unregulated Emissions

The main unregulated emissions from the engines fueled with gasoline-methanol blend are methanol and formaldehyde. It was reported that the formaldehyde emission increased in the exhaust gas with the increase in MSR (Zhao et al. 2009).

(3) Challenge

i. Knock

Usually, knock resistance is improved with the addition of methanol because its lower intensity of chemical reactions and low in-cylinder temperature reduce the interaction between pressure waves and the flame front as well as put off the onset of knock. However, it was found that the knock intensity increased with the methanol content increasing in an iso-octane/methanol blend under known knock combustion, and the onset of knock was also advanced. Hence, when applying methanol in gasoline SI engines, not only its antiknock effect as well as the ability of knock enhancement due to its high temperature reactions should be considered (Feng et al. 2019).

ii. Miscibility

Considering the poor miscibility of methanol and gasoline, higher alcohol additives need to be added into gasoline-methanol blends to avoid phase separation and enhance the stability of the blended fuel. Though these additives only share a small percentage in mass or in volume, the way

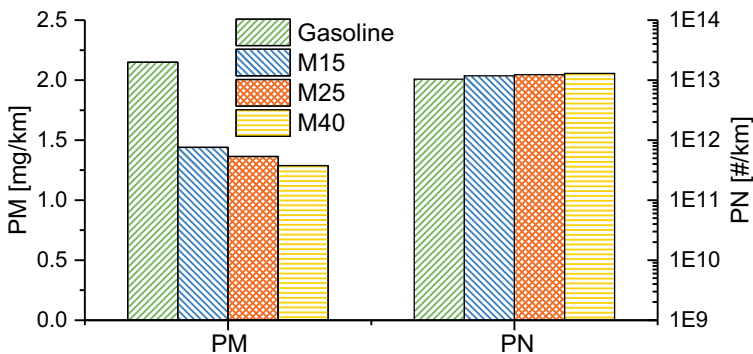


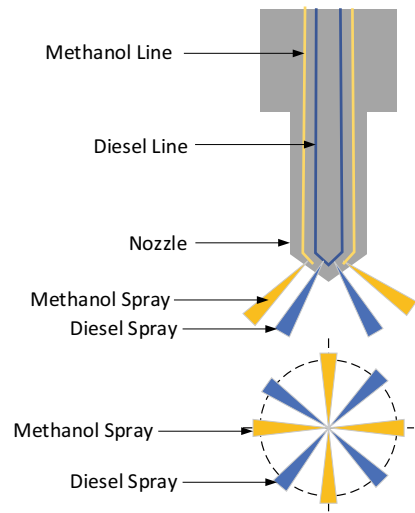
**Fig. 12.15** Variations of PM and particle number (PN) emissions with MSR for GMBF engine (Wang et al. 2015a)

they react in burning, particularly during the warm-up phase of the three-way catalyst, have vital impacts on  $\text{NO}_x$  and HC emissions (Wang et al. 2015a; Jin et al. 2020).

### Engine Fueled with Diesel and Methanol

The combination of diesel and methanol is mainly divided into two modes: diesel methanol blended fuel (DMBF) and diesel methanol dual fuel (DMDF). For DMBF, only one fuel injection system is installed. Diesel and methanol are fully blended before injection (Fan et al. 2021). For DMDF, two independent fuel injection systems are installed, one for methanol injection and the other for diesel injection. Usually, methanol is injected into the intake manifold with low pressure during the intake process, and diesel is directly injected into the cylinder around the top dead center (TDC) of the piston (Wei et al. 2021b). There are also few reports of both methanol and diesel being injected into the cylinder. Recently, an M-D-M mode, in which methanol was injected once before and once after the diesel injection, has been proposed and shows good fuel economy and low emissions at both low and high loads (Li et al. 2021a, 2020). Also, the M-D-D mode, where diesel is divided into pre-injection and main-injection, could be adopted to optimize the engine performance and pollutant emissions (Li et al. 2021b). Another approach of DMDF is that methanol is introduced into the cylinder through a high-pressure direct injection (HPDI) system (see Fig. 12.16), along with a pilot injection of diesel. Diesel pilot injection initiates the combustion first, and then methanol is injected into the burning diesel pilot flames (Kumar et al. 2021). Since the last approach is less commonly applied, it will not be described in detail here.

**Fig. 12.16** HPDI system for DMDF engine (Kumar et al. 2021)



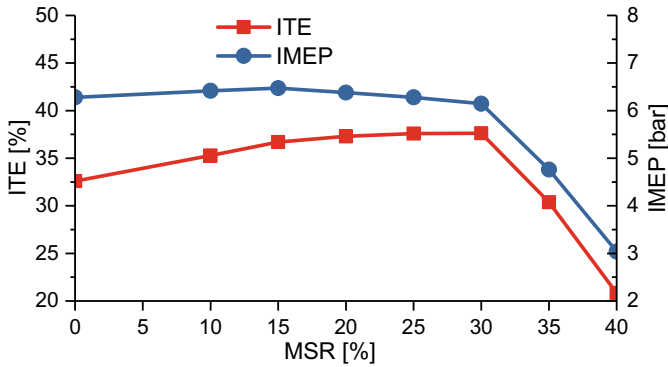


**Fig. 12.17** Variations of indicated thermal efficiency (ITE) and IMEP with MSR for DMBF engine (Jamrozik 2017)

### (1) Thermal Efficiency

For a DMBF engine, with the rise of MSR, the thermal efficiency shows a trend of increasing first and then decreasing (Jamrozik 2017) (see Fig. 12.17). Even an insignificant addition of methanol has a positive effect on the combustion of the diesel fuel as the major portion of the energy is supplied to the engine. The increase in the methanol content in the blend supplies more chemically active oxygen to the combustion chamber and thus leads to the rise of the temperature in reaction zones at the beginning of the combustion process, with more simultaneous ignition spots. The positive effects of methanol vaporization and fast burning lead to a substantial reduction of the heat losses from the combustion chamber. The increase in efficiency of an engine fueled with methanol is likely to be caused by low pumping loss and increased charging efficiency due to the high latent heat of evaporation of methanol.

Generally, DMDF combustion worsens the BTE of an engine at low loads, while boosting it at medium and high loads. At low load, the decrease in BTE is caused by the deteriorated combustion mainly due to the low heat value and great latent heat of vaporization of methanol, which decreases the in-cylinder temperature and exhaust temperature. Experimental results have demonstrated that the exhaust temperature of a DMDF engine decreases with the rise of MSR. However, under medium to high load operating conditions, the rich mixture and high in-cylinder temperature cause better combustion and shortened burning duration, resulting in higher BTE (Wang et al. 2015b). Some researchers have noted that, for a DMDF engine, a small amount of unburned methanol might directly escape into the exhaust gas during the valve overlap period, giving rise to the decrease of BTE (Cheung et al. 2009; Ning et al. 2020a). It was reported that the addition of nanoparticles, such as silica, alumina, and ceria, with all dosages, resulted in an improvement in BTE and braked specific fuel consumption, which was attributed to the catalytic effect and the high energy surface of nanoparticles for improving combustion and the most obvious improvement occurred at high load regardless of MSR (Wei et al. 2021b, 2021c). In addition, relevant investigations revealed that the BTE at low load could be improved

significantly by raising the intake air temperature and advancing the injection timing of diesel.

## (2) Engine-out Emissions

### i. PM Emission

A large number of studies have demonstrated that both DMBF and DMDF have great potential to reduce the PM emission of diesel engines due to methanol's intrinsic properties (Chen et al. 2020a; Wei et al. 2021d, 2020; Duraisamy et al. 2020; Ning et al. 2020b). The impacts of methanol on sooting tendency, soot structure, and soot emissions have been deeply researched (Catapano et al. 2019; Yan et al. 2019; Dong et al. 2020; Ying and Liu 2021; Fan et al. 2021). The explanations of why the methanol application achieves a reduction of PM emission can be grouped into three categories: (1) low carbon fraction in methanol avoids aromatic generation and thus lessens soot formation; (2) low cetane number of methanol leads to long ignition delay, which yields more premixed fuel vaporization, and then reduces the local rich combustion zones, finally decreases the soot formation; (3) high oxygen content in component provides more oxygen available for promotion of combustion and carbon oxidation. It is worthy to notice that some kinds of cosolvents, added into DMBF to improve their indissolubility, can also contribute to the variations in fuel burning and soot formation. To exclude the influence of the cosolvent, some novel methods such as mixer stirring, magnetic stirring, and homogenizing machines have been applied to prepare the DMBF with no or tiny amount of solvent (Wei et al. 2020; Jamrozik 2017). It also should be noted that with the increase in intake air temperature, auto-ignition of methanol-air mixture might make diesel be injected into the burning mixture. Then high in-cylinder gas temperature and less air might cause the fuel pyrolysis, which increased PM emission (Xu et al. 2014).

It is worthy to note that the influence of PM on the environment and human health also depends on its mass concentration as well as its number concentration and size distribution. Relevant investigations showed that PM mass concentration and the total number of particles at low and medium loads were both reduced for DMDF. However, it also led to a shift of the particles towards a smaller geometrical mean diameter, as shown in Fig. 12.18, especially at a high load. The rise of nano-sized particles could have a serious impact on human health (Cheng et al. 2008a).

### ii. NO<sub>x</sub> Emissions

For diesel engines, combustion usually occurs with excess air, which is conducive to nitrogen oxide generation. The rise of MSR in the blend leads to an increase in NO<sub>x</sub> emissions. The rise of the NO<sub>x</sub> content in the exhaust gas is connected with the accelerated burning rate and HRR of the DMBF engine. Unlike the DMBF engine, there are two possible trends in NO<sub>x</sub> emissions for the DMDF engine. On the one hand, the high latent heat of vaporization and the low heat value contribute to the decrease of

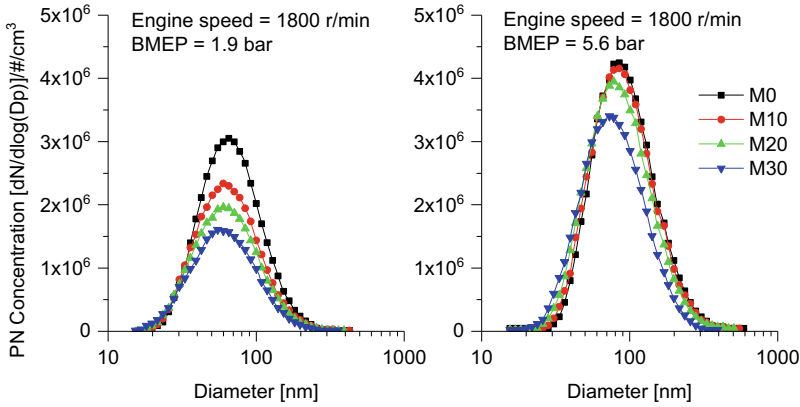


**Fig. 12.18** Variation of PN concentration with MSR for DMDF engine (Cheng et al. 2008a)

in-cylinder gas temperature, and rapid heat release shortens the duration of high temperature in-cylinder, which weakens the high temperature environment and help to reduce NO<sub>x</sub> generation. On the other hand, low intake temperature increases the charging coefficient and creates an oxygen-rich environment. Moreover, methanol prolongs ignition delay and accelerates heat release, resulting in more premixed combustion and higher combustion temperature (Ning et al. 2020b; Park et al. 2017), as shown in Fig. 12.19. Therefore, the variation trend of NO<sub>x</sub> emissions depends on the interactions of these factors according to the specific operating conditions.

In an attempt to reduce smoke and NO<sub>x</sub> emissions from diesel engines, the diesel methanol compound combustion system, in which the single diesel fuel mode was applied for cold start, and low load and dual fuel mode was applied for medium to high load after the engine warmed up, was proposed and showed a good effect

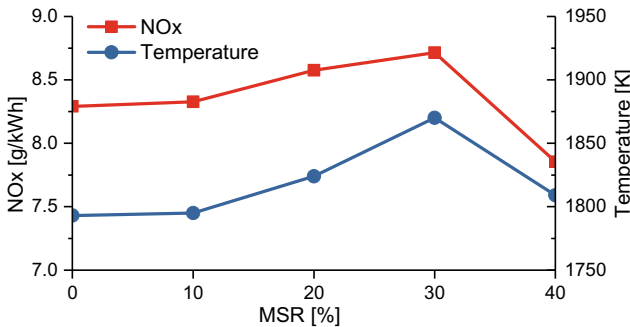


**Fig. 12.19** Variation of NO<sub>x</sub> emissions with MSR for DMDF engine (Ning et al. 2020b)

on reducing emissions of  $\text{NO}_x$  and PM (Wei et al. 2017). Exhaust gas recirculation (EGR) and swirl, the conventional method to reduce  $\text{NO}_x$  emissions of diesel engines, can also be applied to DMBF and DMDF engines (Wang et al. 2019a). Recently, a water nanoemulsion method has been proposed for a DMBF engine which showed better effects than EGR and swirl. Moreover, it did not require any modification to the base engine and could be mixed easily with a diesel-methanol blend by using a suitable emulsifier (Soni and Gupta 2017).

It's important to note that many researchers have discovered that the addition of methanol or other oxygenated fuels dramatically increases the nitrogen dioxide ( $\text{NO}_2$ ) emission, as shown in Fig. 12.20, which leads to a higher  $\text{NO}_2/\text{NO}$  ratio than that of a diesel engine (Pan et al. 2015; Wei et al. 2015). As is well known,  $\text{NO}_2$  plays an important role in the passive regeneration of diesel particulate filters due to its strong oxidation characteristics, and the  $\text{NO}_2/\text{NO}$  ratio can effectively affect the selective catalytic reduction efficiency. Hence, the investigation of formation characteristics and influence factors of  $\text{NO}_2$  emission in a DMDF system is crucial. Some researchers have suggested that the increase in  $\text{NO}_2$  lies in the  $\text{HO}_2$  free radicals produced from methanol reactions, and adjusting the formation and conservation of  $\text{NO}$  and  $\text{HO}_2$  radicals through regulating combustion temperature enables the control of  $\text{NO}_2$  emission (Lu et al. 2019).

### iii. CO and HC Emissions

CO generation has a great relationship with insufficient atomization and vaporization of fuel and insufficient mixing of fuel and air at low temperature diffusion combustion stage. Figure 12.21 presents the unit emission of CO for a DMBF engine. The rise of MSR causes a reduction of CO emission resulting from a greater amount of available oxygen and lower carbon component in the fuel. HC contained in the exhaust gas is generated due to incomplete or partial combustion of the fuel. These compounds also result from the partial decomposition of hydrocarbons during chain reactions during the combustion process. Figure 12.21 also shows the unit HC emissions for a DMBF engine.

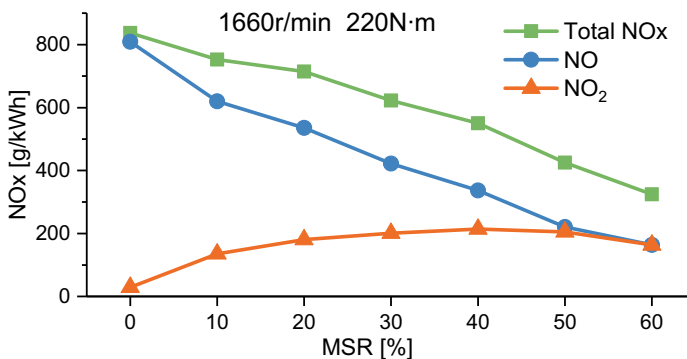
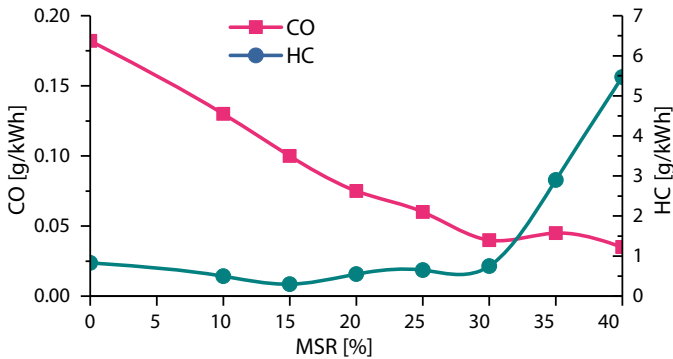


Fig. 12.20 Variation of  $\text{NO}_2$  emission with MSR for DMDF engine (Lu et al. 2019)





**Fig. 12.21** Variations of CO and HC emissions with MSR for DMBF engine (Jamrozik 2017)

The rise of MSR until exceeding the critical value does not lead to substantial variations in HC emissions, and the HC emissions would noticeably rise once MSR exceeds the critical value resulting from leaner combustible mixtures and a decline in the combustion process temperature.

When engines operate with DMDF, the homogenous methanol-air mixture and low in-cylinder gas temperature, similar to an SI engine, tend to produce more unburned CO and HC emissions. The engine-out emissions of CO and HC increase with the rise of MSR. It should be noted that the catalytic efficiency is very low until the exhaust gas temperature exceeds the light-off temperature of the oxidation catalyst. It is reported that the addition of nanoparticles, such as silica, alumina, and ceria, to methanol could significantly reduce CO and HC emissions, as shown in Fig. 12.22. The reason was that the catalytic action of nanoparticles could reduce the combustion activation temperature of carbon to promote combustion, and the additional oxygen molecules provided by the nanoparticles helped convert CO molecules into CO<sub>2</sub> molecules (Wei et al. 2021b).

### (3) Challenge

#### i. Miscibility

The introduction of a large methanol quantity for DMBF is limited because of its poor miscibility with diesel. To overcome the phase separation issues, different additives such as cosolvents or emulsions are introduced in diesel-methanol blends to ensure adequate miscibility of the constituents.

#### ii. Toxicity and Corrosivity

Usually, additives are necessary for DMBF due to the indissolubility between methanol and diesel. However, these cosolvents are typically composed of nitrogen-containing compounds such as octyl nitrate and tetrahydrofurfuryl nitrate, many of which are toxic and or carcinogenic. It is necessary to ensure that they have been completely converted before they are released into the environment. For all engines with methanol in

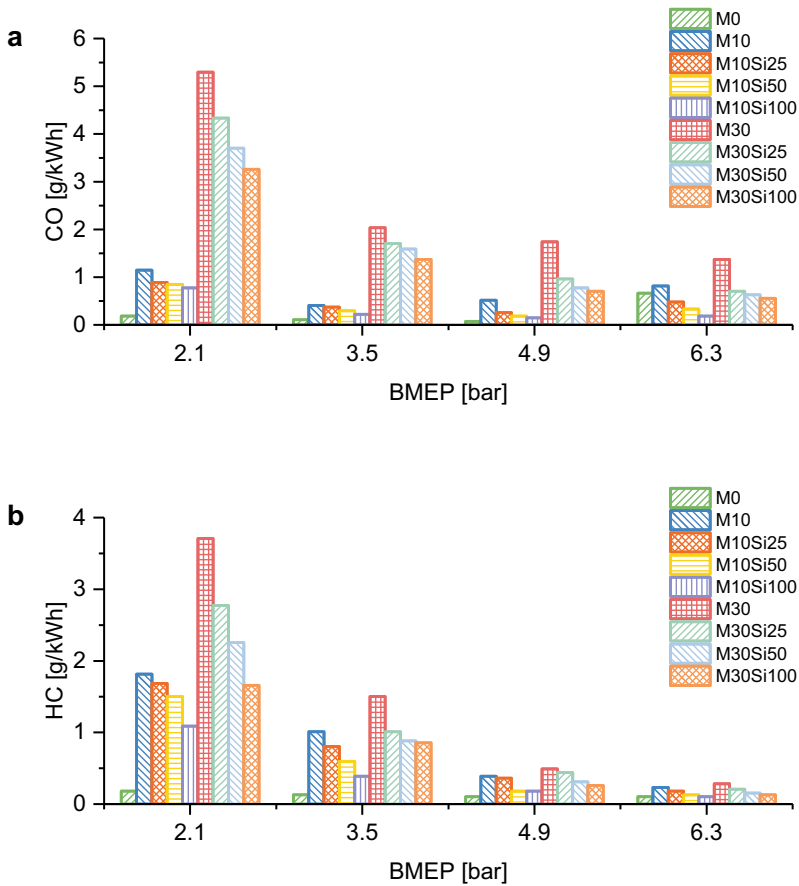


**Fig. 12.22** Variations of CO and HC emissions with MSR for DMDF engine (Wei et al. 2021b)

the fuel, especially for DMDF mode, special materials like Teflon should be used, which could also avoid the corrosive problem of methanol.

iii. Cyclic Variation

Figure 12.23 presents the  $COV_{IMEP}$  with MSR for a DMBF engine. The  $COV_{IMEP}$  is lower than 10% as the MSR does not exceed 30%, which suggests proper and steady engine operation (Jamrozik 2017).

The  $COV_{IMEP}$  of a DMDF engine at high loads is comparable with that of a diesel engine. But the magnitude of cyclic variation increases at low load and is more sensitive to MSR (see Fig. 12.24) (Wang et al. 2016). The cylinder-to-cylinder variation reflects the evenness degree of each engine cylinder. It is reported that the unevenness degree of an engine

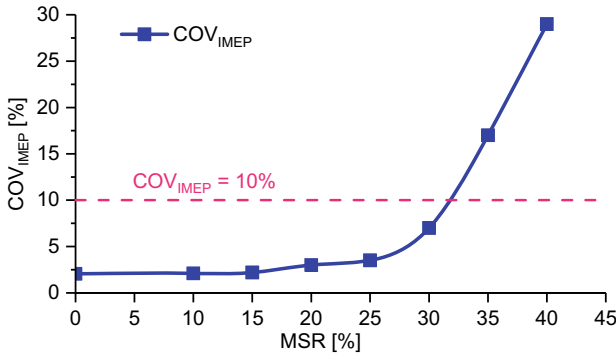


Fig. 12.23 COV<sub>IMEP</sub> with MSR for DMBF engine (Jamrozik 2017)

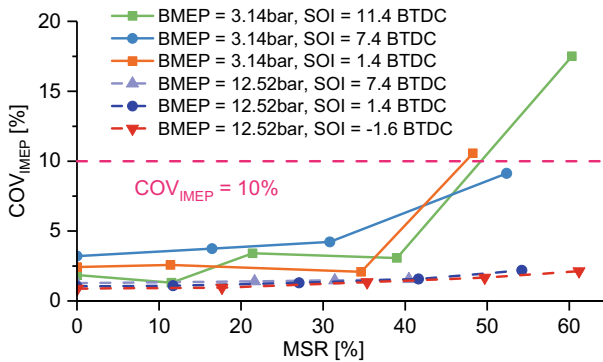


Fig. 12.24 COV<sub>IMEP</sub> for DMBF engine (Wang et al. 2016)

is enhanced with the rise of MSR, especially at high load. The cylinder-to-cylinder variation is also related to the engine speed, intake air temperature, and injection timing (Chen et al. 2016, 2017b).

### 12.4.3 Engine Fueled with Alternative Fuels and Methanol

#### Engine Fueled with Biodiesel and Methanol

Biodiesel has received wide attention as an alternative fuel due to its advantages such as the abundance, renewability, and cleanliness of raw materials, better engine performance, and fewer GHG emissions (Ogunkunle and Ahmed 2019). Previous investigations have shown that burning biodiesel in diesel engines could reduce HC, CO, and PM emissions, but NO<sub>x</sub> emissions might increase. The increase in NO<sub>x</sub> emissions serves as biodiesel’s major impediment to widespread use (Cheng

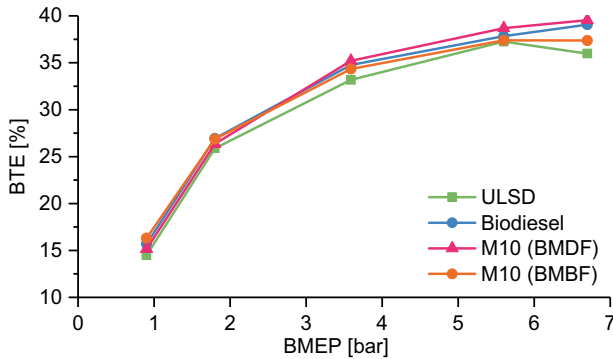


**Fig. 12.25** Variations of BTE with brake mean effective pressure (BMEP) for BMBF and BMDF engines (Cheng et al. 2008b)

et al. 2008b), and this provides an opportunity for the combination of methanol and biodiesel.

### (1) Thermal Efficiency

Generally, the thermal efficiency of a biodiesel engine is lower than that of a diesel engine due to its lower energy density (Seesy et al. 2021). But there was reported that the BTE of a biodiesel engine was higher than that of an ultra-low sulfur diesel (ULSD) engine, and with the addition of methanol, the BTE was further improved (Kakati et al. 2021). The reasons why methanol improves BTE can be summarized as that the lower viscosity of methanol reduces the overall viscosity of the blended fuel and the higher oxygen content of methanol helps the blended fuel to burn more efficiently (An et al. 2015). Of the operations involving biodiesel with or without methanol, the blending mode gives better efficiency at low engine load while dual fuel mode gives better efficiency at high engine load (Cheng et al. 2008b), as shown in Fig. 12.25. At low loads, the mixture formed by the pre-injected methanol and intake air is too lean to support complete combustion, resulting in deterioration of combustion efficiency. However, at medium to high engine loads, the mixture gets rich enough, resulting in better combustion because the mixture burns in premixed mode (Cheng et al. 2008b).

### (2) Engine-out Emissions

#### i. PM Emission

The oxygen content of biodiesel helps reduce the formation of PM, while the higher oxygen content of methanol will further do that (see Fig. 12.26). For blending mode, more fuel is burned in the premixed mode which is conducive to reduce PM emission. Moreover, PM concentration is known to be influenced by fuel viscosity. Therefore, more high viscosity fuel leads to poor atomization during injection and consequently, larger particles are present in the exhaust gas (Salmani et al. 2015). Relevant simulation

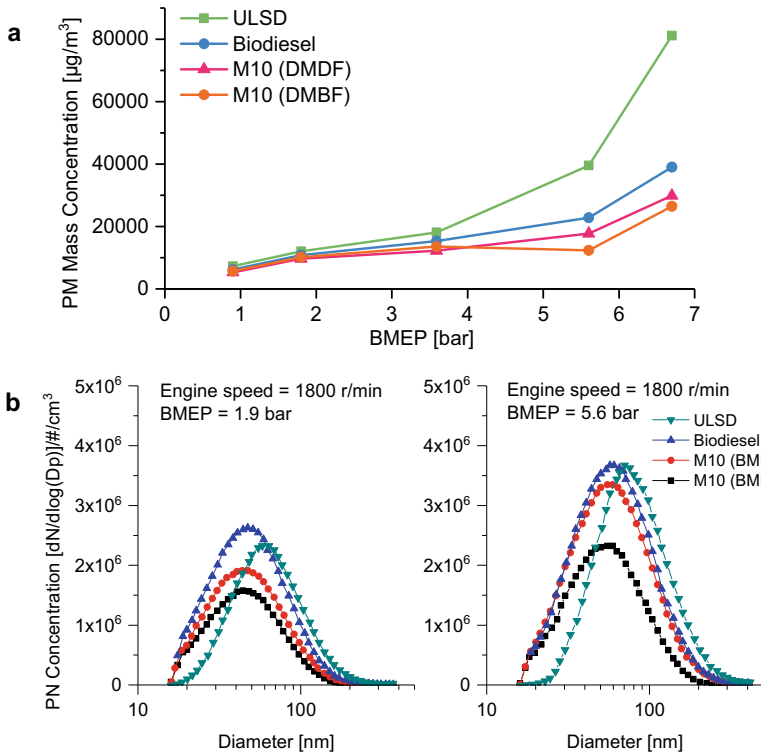


**Fig. 12.26** Variations of PM and PN with BMEP for BMBF and BMDF engines (Cheng et al. 2008b)

results showed that the soot in the cylinder was mainly concentrated near the injector nozzle, where there was a higher percentage of poorly mixed fuel, leading to rich burn and more soot formation (Yang and Yang 2019). It is worthy to note that the particles get smaller when engines operate with biodiesel, with or without methanol in combination, meanwhile fewer particles are produced.

ii.  $\text{NO}_x$  Emissions

Compared with diesel engines or biodiesel engines,  $\text{NO}_x$  emissions decrease when engines operating with methanol in both modes, especially at light engine load, as shown in Fig. 12.27. However, the higher oxygen content of methanol and the increase in fuel burned in the premixed mode may lead to an increase in  $\text{NO}_x$  emissions. The cooling effect of the methanol is more dominating (Cheng et al. 2008b; Kakati et al. 2021). It was noticed that, similar to diesel, there is a significant increase in  $\text{NO}_2$  emission when biodiesel burns with methanol, particularly in dual fuel mode.

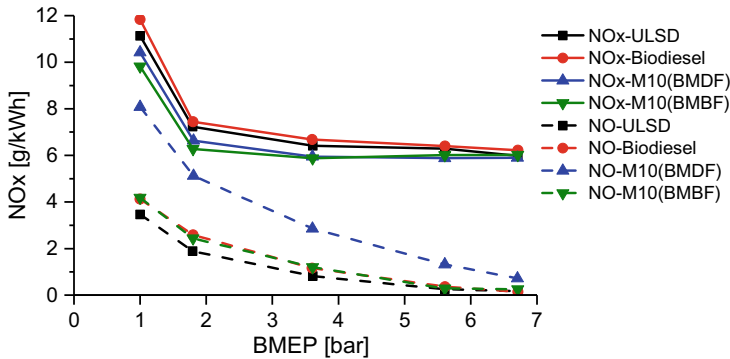


**Fig. 12.27** Variations of NO<sub>x</sub> emissions with BMEP for BMBF and BMDF engines (Cheng et al. 2008b)

iii. CO and HC Emissions

Both CO and HC are products of incomplete combustion. At a high engine load, the higher combustion temperature promotes combustion and hence yields less CO and HC emissions. It was reported that a decrease of CO and HC emissions would be obtained if replacing diesel with biodiesel, but only a little variation of CO and HC emissions was observed when replacing biodiesel with blended fuel, and both rise (Thiyagarajan et al. 2020) and decline (An et al. 2015) of CO and HC emissions have been reported. This might be related to the control strategy and operating conditions of the engine. However, when the engine operated in dual fuel mode, the CO and HC emissions were much higher than pure biodiesel, especially at low engine load, as shown in Fig. 12.28 (Cheng et al. 2008b; Huang et al. 2020). Some researchers have suggested that split injection

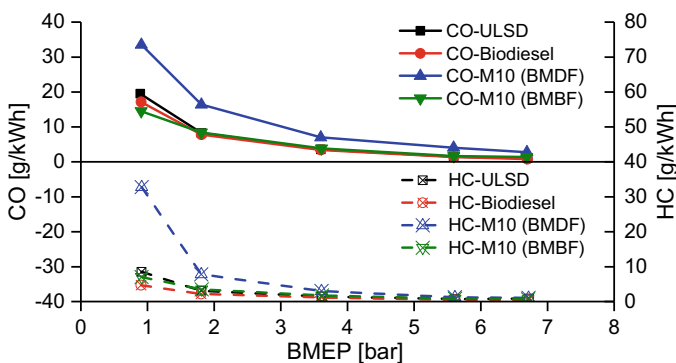


**Fig. 12.28** Variations of CO and HC emission with BMEP for BMBF and BMDF engines (Cheng et al. 2008b)

of fuel with a low swirl ratio could improve combustion and reduce CO and HC emissions (Zehni et al. 2020; Panda and Ramesh 2021).

### (3) Challenge

Mutual solubility between biodiesel and methanol is quite difficult because of methanol's polarity. From the existing literature pertinent to biodiesel-methanol blends, it was observed that the maximum methanol participation in such dual fuel operations was only 10–15% on a volume basis (Kakati et al. 2021). Therefore, a cosolvent, like n-octanol, is necessary to improve the stability of the blends (Xuan et al. 2021).

## Engine Fueled with H<sub>2</sub> and Methanol

As mentioned before, it is difficult in mixture preparation and ignition at low ambient temperature for methanol SI engine due to its low vapor pressure and high flash point. H<sub>2</sub>-methanol dual-fuel, including hydrogen and methanol dual-port injection (HPI + MPI) and hydrogen port injection with methanol direct injection (HPI + MDI) (Gong et al. 2019a), provides a workable way to resolve this issue. H<sub>2</sub> has the characteristics of wide lean burn, small ignition energy demand, and rapid flame propagation, which are beneficial to extend the lean-burn limit, reduce cyclic variation, improve fuel economy and eliminate knocking (Bhasker and Porpatham 2017).

### (1) Thermal Efficiency

There are many reports on adding H<sub>2</sub> to a methanol engine to improve thermal efficiency, and some experiments have demonstrated that H<sub>2</sub> addition to methanol could accelerate combustion and shorten combustion duration, especially under lean-burn conditions (Gong et al. 2018, 2019a, 2020b; Ji et al. 2016) (see Fig. 12.29). Meanwhile, COV<sub>IMEP</sub> is reduced with the increase in H<sub>2</sub> addition (Zhang et al. 2015). The result can be ascribed to the fact that adding H<sub>2</sub> increases the LBV and the resistance of the flame to strain-induced extinction and enlarges the operating window of stable combustion (Sarli 2014).

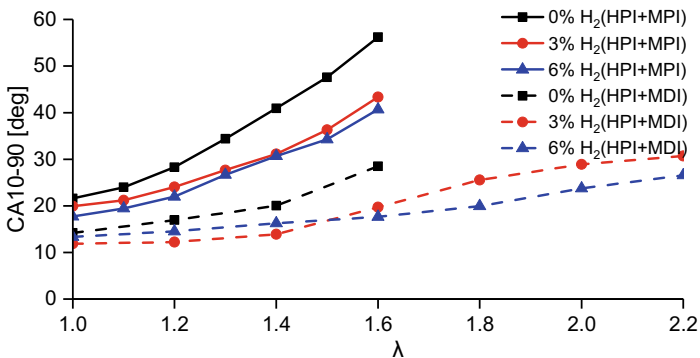


Fig. 12.29 Combustion during comparisons with different H<sub>2</sub> proportions (Gong et al. 2019a)

## (2) Engine-out Emissions

i.  $\text{NO}_x$  Emissions

The addition of  $\text{H}_2$  can reduce  $\text{NO}_x$  emissions when  $\lambda$  is small, as shown in Fig. 12.30. This may be due to lower volumetric efficiency and incomplete combustion at richer mixtures with  $\text{H}_2$  addition (Zhen et al. 2020b). However,  $\text{H}_2$  addition increases  $\text{NO}_x$  emissions once  $\lambda$  exceeds a critical value for both an HPI + MPI engine and an HPI + MDI engine. These results from  $\text{H}_2$  addition increasing the burning rate of lean mixtures. Furthermore,  $\text{NO}_x$  emissions of an HPI + MDI engine are lower than that of an HPI + MPI engine because the latent heat of evaporation of methanol is high, and the maximum combustion temperature in the cylinder is greatly reduced due to late injection (Gong et al. 2019a).

## ii. CO and HC Emissions

$\text{H}_2$  can widen the dilute combustion limit of the mixture. However, the CO emission increases rapidly, for rich burn, with the addition of  $\text{H}_2$ , as shown in Fig. 12.31. It is possibly because  $\text{H}_2$  has a much higher stoichiometric ratio than methanol and the combustion of  $\text{H}_2$  added to methanol leads to a lack of oxygen to create an inhomogeneous fuel–air mixture that affects the oxidation of CO to  $\text{CO}_2$  (Gong et al. 2020c). But for lean burning, it is found that CO emission decreases with more  $\text{H}_2$  addition at different engine speeds (Gong et al. 2019b; Zhang et al. 2014). The addition of  $\text{H}_2$  has an obvious effect on the reduction of HC emissions, especially for the HPI + MDI engine (Gong et al. 2019a; Nuthan Prasad et al. 2021) (see Fig. 12.32). This is caused by the partial replacement of carbon-based fuel by cleaner  $\text{H}_2$  fuel and complete combustion due to  $\text{H}_2$  (Gong et al. 2020d).

## (3) Challenge

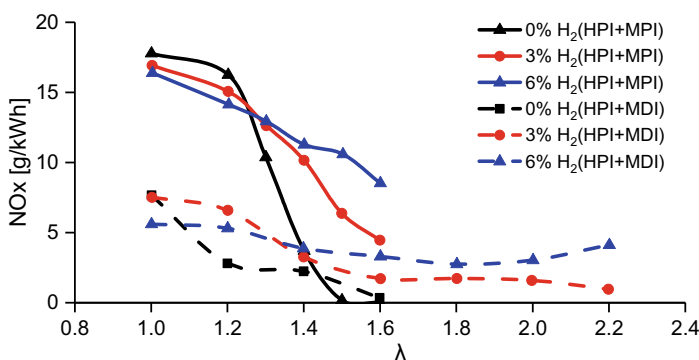


Fig. 12.30 Variations of  $\text{NO}_x$  emissions with  $\lambda$  at different  $\text{H}_2$  proportions (Gong et al. 2019a)



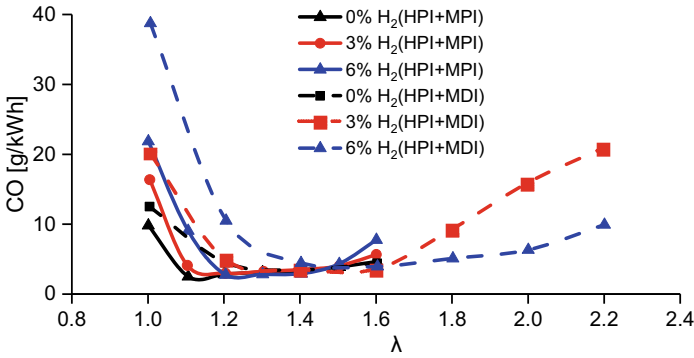


Fig. 12.31 Variations of CO emission with  $\lambda$  at different H<sub>2</sub> proportions (Gong et al. 2019a)

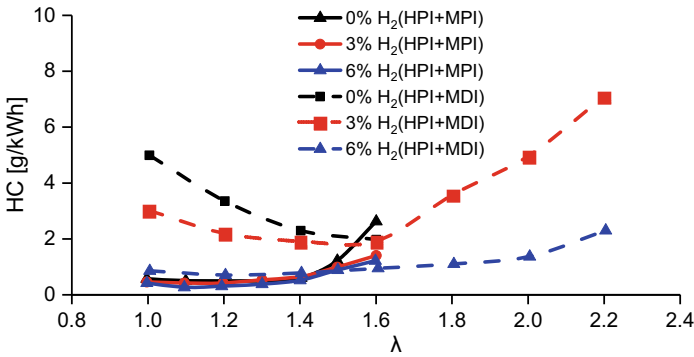


Fig. 12.32 Variations of HC emission with  $\lambda$  at different H<sub>2</sub> proportions (Gong et al. 2019a)

The core issues limiting the large-scale application of H<sub>2</sub> are storage, price, and especially safety. Safety issues are exacerbated even when a small amount of H<sub>2</sub> is used for fuel enrichment (Salzano et al. 2012). The cost of producing H<sub>2</sub> is another factor restricting its large-scale application. The other issues mentioned for a pure methanol engine will not be repeated here.

### Engine Fueled with Natural Gas and Methanol

Natural gas is considered to be the most promising alternative fuel due to its low emissions feature. Special attention has been focused on natural gas-methanol dual fuel because both of them are regarded as green fuels to reduce CO<sub>2</sub> emissions compared with conventional fuels potentially. On the one hand, the enrichment with methanol can improve the degree of completeness of natural gas combustion and reduce HC emissions, especially at light load. On the other hand, the addition of natural gas can eliminate the difficulty of cold start with methanol fuel. However, owing to the

different physical states of natural gas and methanol at standard conditions, these two kinds of fuels must be injected separately (Chen et al. 2019b).

### (1) Thermal Efficiency

A mass of studies has demonstrated that increasing the MSR of a natural gas-methanol dual-fuel engine contributes to the improvement of BTE (Chen et al. 2019c; Wang et al. 2019b), as shown in Fig. 12.33. It can be explained from two aspects. Firstly, during the dehydrogenation process of methanol oxidation, numerous hydroxyl activities are produced, which accelerates the oxidation of natural gas (Chen et al. 2020b). The more concentrated heat release rate leads to more isochoric combustion and increases heat utilization (Chen et al. 2019d). Secondly, the exhaust temperature is reduced with the rise of MSR, which decreases the heat loss from the exhaust gas. Thus, the BTE is improved due to the increase in heat utilization and the decrease in heat loss.

### (2) Engine-out Emissions

#### i. $\text{NO}_x$ Emissions

It was found that the spark timing significantly affected the  $\text{NO}_x$  emissions (see Fig. 12.34a). Methanol has two effects on  $\text{NO}_x$  emissions. On the one hand, the high LBV and oxygen content of methanol increases the in-cylinder pressure and temperature. On the other hand, fast burning shortens the combustion duration. These two effects have opposite effects on thermal  $\text{NO}_x$  production; thus, the final  $\text{NO}_x$  emissions depend on their competition. The published

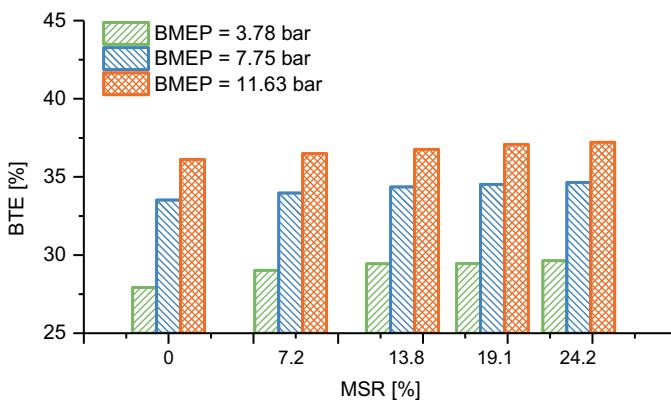
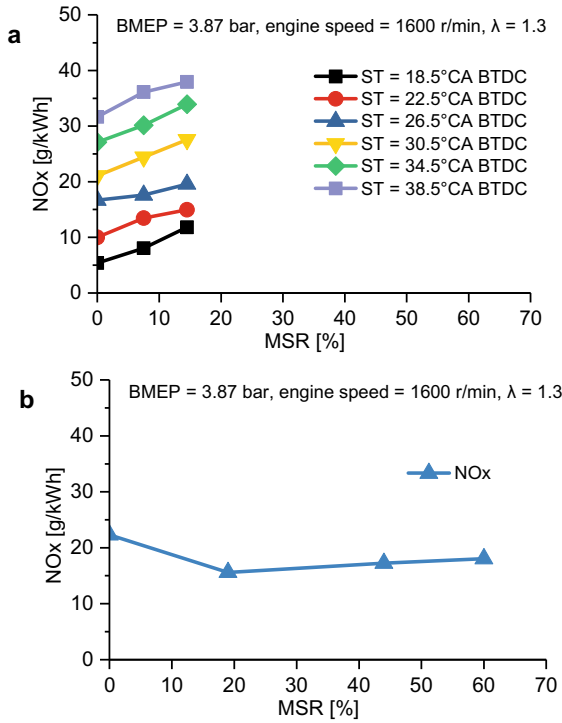


Fig. 12.33 Effects of MSR on BTE (Chen et al. 2019d)



**Fig. 12.34** Effects of MSR on the NO<sub>x</sub> emissions (Chen et al. 2019b, c)

results suggest that both outcomes are possible (Chen et al. 2019b, 2019c; Wang et al. 2019b), as shown in Fig. 12.34.

ii. CO and HC Emissions

On the one hand, methanol has a greater oxygen content than natural gas. Thus, the natural gas-methanol mixture is more likely to achieve a higher degree of completeness of combustion, which reduces CO emissions. On the other hand, methanol is easy to deteriorates the combustion due to its high latent heat of vaporization. Normally the variation in the CO is negligible with an increase of MSR at a specific BMEP, as shown in Fig. 12.35. For a natural gas engine, it has been reported that the main constituent of HC emissions is unburned CH<sub>4</sub>, which has been one of the most important GHG in the past decades. The addition of methanol can decrease the HC emissions of a natural gas engine, and the greater the MSR, the less the HC emissions. These results can be attributed to the reduction of unburned CH<sub>4</sub> and unburned air–fuel mixture.

In addition to the binary fuels mentioned in this book, there are many combinations of methanol and other fuels, including the ternary fuel, quaternary fuel, and even more (Gong et al. 2019c; Somasundaram et al.

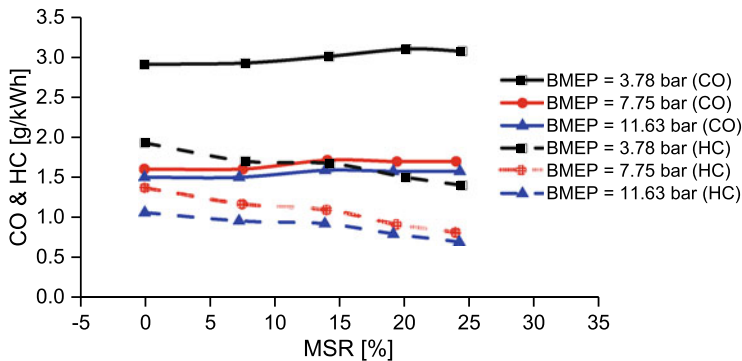


Fig. 12.35 Effects of MSR on CO and HC emissions (Chen et al. 2019d)

2017; Thiyagarajan et al. 2020; Jiao et al. 2019; Kumar et al. 2019; Sarıkoç 2021; Zhao et al. 2020; Chen et al. 2021; Yılmaz and Taştan 2018). Because the relevant research is diverse and the groups of researchers are small, they will not be covered in detail in this chapter.

## 12.5 Conclusion

The methanol engine has experienced a history of more than one hundred years since its first appearance and has undergone several phases of growth and stagnation. Every revolution of the methanol engine has been closely linked to the application of energies, including oil resources, in addition to the environment.

Methanol has its properties, such as its high oxygen content, fast LBV, high latent heat of vaporization, and having no C–C bond, which makes methanol to be used in various ways. According to the existing research, both pure methanol and combined fuel approaches have the potential to improve internal combustion engines' performance, but the extent of improvement depends largely on specific configurations of engines and control strategies. However, advantages are normally accompanied by disadvantages. Methanol engines also encounter some problems in their application, such as toxicity, corrosivity, rubbing wear, weak cold start, and miscibility with other fuels. Fortunately, there have been good solutions to these problems. As the current large-scale demonstrations around the globe indicate, there are no technical or safety-related reasons for discarding methanol as a viable transportation fuel.

Admittedly, most experimental results are obtained in the laboratory, and more road testing would be helpful. Some relatively mature technologies employed in traditional fueled engines such as stratified combustion, highly flexible valvetrains, and variable geometry turbines can also be applied on methanol engines. Also, thermochemical recuperation (fuel reforming using waste heat) is worth applying to explore potential efficiency benefits.

## References

- Agarwal AK, Karare H, Dhar A (2014) Combustion, performance, emissions and particulate characterization of a methanol-gasoline blend (gasohol) fuelled medium duty spark ignition transportation engine. *Fuel Process Technol* 121:16–24
- An H, Yang WM, Li J (2015) Numerical modeling on a diesel engine fueled by biodiesel-methanol blends. *Energy Convers Manage* 93:100–108
- Andrea A, Atul B, Urakawa A et al (2017) Challenges in the greener production of formates/formic acid, methanol, and DME by heterogeneously catalyzed CO<sub>2</sub> hydrogenation processes. *Chem Rev* 117:9804–9838
- Antoine DSE (2021) Global warming of 1.5 °C. <https://www.ipcc.ch/sr15>. Accessed 6 June 2021
- Balki MK, Sayin C (2014) The effect of compression ratio on the performance, emissions and combustion of an SI (spark ignition) engine fueled with pure ethanol, methanol and unleaded gasoline. *Energy* 71:194–201
- Balki MK, Sayin C, Sarıkaya M (2016) Optimization of the operating parameters based on Taguchi method in an SI engine used pure gasoline, ethanol and methanol. *Fuel* 180:630–637
- Bermúdez JM, Arenillas A, Luque R et al (2013) An overview of novel technologies to valorise coke oven gas surplus. *Fuel Process Technol* 110:150–159
- Bertau M, Wernicke HJ, Schmidt F (2014) Methanol utilization technologies in methanol: the basic chemical and energy feedstock of the future. Berlin, Germany, Springer, pp 1–677
- Bhasker JP, Porpatham E (2017) Effects of compression ratio and hydrogen addition on lean combustion characteristics and emission formation in a compressed natural gas fuelled spark ignition engine. *Fuel* 208:260–270
- Bode J, Schorr J, Krüger C et al (2019) Influence of the in-cylinder flow on cycle-to-cycle variations in lean combustion DISI engines measured by high-speed scanning-PIV. *Proc Combust Inst* 37:4929–4236
- Bozzano G, Manenti F (2016) Efficient methanol synthesis: perspectives, technologies and optimization strategies. *Prog Energy Combust* 56:71–105
- Brian MH (1975) Methanol from coal—a step toward energy self sufficiency. *Energy Sour* 2(3):233–249
- Bromberg L, Cheng W (2010) Methanol as an alternative transportation fuel in the US: options for sustainable and/or energy-secure transportation. Tech. Rep. Massachusetts Institute of Technology. [http://www.afdc.energy.gov/pdfs/mit\\_methanol\\_white\\_paper.pdf](http://www.afdc.energy.gov/pdfs/mit_methanol_white_paper.pdf). Accessed 6 June 2021
- Brusstar M (2005) Sustainable technology choice for alternative fuels. In: ISAF XV international symposium on alcohol fuels, San Diego, USA, 26–28 Sept 2005
- Brusstar M, Gray C (2007) High efficiency with future alcohol fuels in a stoichiometric medium duty spark ignition engine. SAE Technical Paper 2007-01-3993
- Brusstar M, Stuhldreher M, Swain D et al (2002) High efficiency and low emissions from a port-injected engine with neat alcohol fuels. SAE Technical Paper 2002-01-2743
- Canakci M, Ozsezen AN, Alptekin E et al (2013) Impact of alcohol-gasoline fuel blends on the exhaust emission of an SI engine. *Renew Energy* 52:111–117
- Cao K, Feng X (2006) Energy analysis and comparison of methanol synthesis processes using different feedstocks. *Chem Ind Eng Prog* 25(12):1461–1466
- Catapano F, Iorio SD, Luise L et al (2019) Influence of ethanol blended and dual fueled with gasoline on soot formation and particulate matter emissions in a small displacement spark ignition engine. *Fuel* 245:253–262
- Cesaro Z, Nayak-Luke RM, Bañares-Alcántara R (2021) Techno-economic challenges of green ammonia as an energy vector. Academic Press, pp 15–26
- Chaplin AG (2013) Renewable methanol. Dissertation, Aalborg University
- Chen ZF, Yao CD, Wang QG et al (2016) Study of cylinder-to-cylinder variation in a diesel engine fueled with diesel/methanol dual fuel. *Fuel* 170:67–76

- Chen Y, Wang Y, Raine R (2017a) Correlation between cycle-by-cycle variation, burning rate, and knock: a statistical study from PFI and DISI engines. *Fuel* 206:210–218
- Chen ZF, Yao CD, Yao AR et al (2017b) The impact of methanol injecting position on cylinder-to-cylinder variation in a diesel methanol dual fuel engine. *Fuel* 191:150–163
- Chen ZM, Wang L, Zeng K (2019b) A comparative study on the combustion and emissions of dual-fuel engine fueled with natural gas/methanol, natural gas/ethanol, and natural gas/n-butanol. *Energy Convers Manage* 192:11–19
- Chen ZM, Wang L, Zhang QG (2019c) Effects of spark timing and methanol addition on combustion characteristics and emissions of dual-fuel engine fuelled with natural gas and methanol under lean-burn condition. *Energy Convers Manage* 181:519–527
- Chen ZM, Wang L, Yuan XN (2019d) Experimental investigation on performance and combustion characteristics of spark-ignition dual-fuel engine fueled with methanol/natural gas. *Appl Therm Eng* 150:164–174
- Chen H, He JJ, Chen ZM et al (2021) A comparative study of combustion and emission characteristics of dual-fuel engine fueled with diesel/methanol and diesel-polyoxymethylene dimethyl ether blend/methanol. *Process Saf Environ* 147:714–722
- Chen ZM, Wang L, Zeng K (2019a) Comparative study of combustion process and cycle-by-cycle variations of spark-ignition engine fueled with pure methanol, ethanol, and n-butanol at various air-fuel ratios. *Fuel* 254:115683
- Chen C, Yao AR, Yao CD et al (2020a) Experimental study of the active and passive regeneration procedures of a diesel particulate filter in a diesel methanol dual fuel engine. *Fuel* 264:116801
- Chen ZM, Chen H, Wang L, Zhang QG (2020) Parametric study on effects of excess air/fuel ratio, spark timing, and methanol injection timing on combustion characteristics and performance of natural gas/methanol dual-fuel engine at low loads. *Energy Convers Manage* 210:112742
- Cheng CH, Cheung CS, Chan TL et al (2008a) Experimental investigation on the performance, gaseous and particulate emissions of a methanol fumigated diesel engine. *Sci Total Environ* 389:115–124
- Cheng CH, Cheung CS, Chan TL et al (2008b) Comparison of emissions of a direct injection diesel engine operating on biodiesel with emulsified and fumigated methanol. *Fuel* 87(10–11):1870–1879
- Cheung CS, Zhang ZH, Chan TL et al (2009) Investigation on the effect of port-injected methanol on the performance and emissions of a diesel engine at different engine speeds. *Energy Fuel* 23(11):5684–5694
- Dong X, Jia M, Chang Y et al (2020) Kinetic modeling study of polycyclic aromatic hydrocarbon formation and oxidation for oxygenated fuels including methanol, n-butanol, methyl butanoate, and dimethyl ether. *Energy Fuel* 34(4):4882–4898
- Duraisamy G, Rangasamy M, Govindan N (2020) A comparative study on methanol/diesel and methanol/PODE dual fuel RCCI combustion in an automotive diesel engine. *Renew Energy* 145:542–556
- Elfasakhany A (2017) Investigations on performance and pollutant emissions of spark-ignition engines fueled with n-butanol-, isobutanol-, ethanol-, methanol- and acetone-gasoline blends: A comparative study. *Renew Sust Energy Rev* 71:404–413
- Fan CY, Wei JJ, Huang HZ et al (2021) Chemical feature of the soot emissions from a diesel engine fueled with methanol-diesel blends. *Fuel* 297:120739
- Feng HQ, Wei JN, Zhang J (2019) Numerical analysis of knock combustion with methanol-isooctane blends in downsized SI engine. *Fuel* 236:394–403
- Garcia G, Arriola E, Chen WH et al (2021) A comprehensive review of hydrogen production from methanol thermochemical conversion for sustainability. *Energy* 217:119384
- Global production capacity of methanol 2018–2030. <https://www.statista.com/statistics/1065891/global-methanol-production-capacity>. Accessed 6 June 2021
- Gong CM, Huang K, Jia JL et al (2011a) Improvement of fuel economy of a direct-injection spark-ignition methanol engine under light loads. *Fuel* 90:1826–1832

- Gong CM, Huang K, Jia JL et al (2011b) Regulated emissions from a direct-injection spark-ignition methanol engine. *Energy* 36:3379–3387
- Gong CM, Huang K, Chen YL et al (2011c) Cycle-by-cycle combustion variation in a DISI engine fueled with methanol. *Fuel* 90:2817–2819
- Gong CM, Liu FH, Sun JZ et al (2016) Effect of compression ratio on performance and emissions of a stratified-charge DISI (direct injection spark ignition) methanol engine. *Energy* 96:166–175
- Gong CM, Peng LG, Liu FH (2017) Modeling of the overall equivalence ratio effects on combustion process and unregulated emissions of an SIDI methanol engine. *Energy* 125:118–126
- Gong CM, Li ZH, Li D et al (2018) Numerical investigation of hydrogen addition effects on methanol-air mixtures combustion in premixed laminar flames under lean burn conditions. *Renew Energy* 127:56–63
- Gong CM, Li ZH, Chen YL et al (2019b) Influence of ignition timing on combustion and emissions of a spark-ignition methanol engine with added hydrogen under lean-burn conditions. *Fuel* 235:227–238
- Gong CM, Liu ZL, Su H et al (2019c) Effect of injection strategy on cold start firing, combustion and emissions of a LPG/methanol dual-fuel spark-ignition engine. *Energy* 178:126–133
- Gong CM, Li ZH, Yi L et al (2019a) Comparative study on combustion and emissions between methanol port-injection engine and methanol direct-injection engine with H<sub>2</sub>-enriched port-injection under lean-burn conditions. *Energy Convers Manage* 200:112096
- Gong CM, Yi L, Zhang ZL et al (2020a) Assessment of ultra-lean burn characteristics for a stratified-charge direct injection spark-ignition methanol engine under different high compression ratios. *Appl Energy* 261:114478
- Gong CM, Li ZH, Yi L et al (2020b) Research on the performance of a hydrogen/methanol dual-injection assisted spark-ignition engine using late-injection strategy for methanol. *Fuel* 260:116403
- Gong CM, Li ZH, Yi L et al (2020c) Experimental investigation of equivalence ratio effects on combustion and emissions characteristics of an H<sub>2</sub>/methanol dual-injection engine under different spark timings. *Fuel* 262:116463
- Gong CM, Li ZH, Sun JZ et al (2020d) Evaluation on combustion and lean-burn limit of a medium compression ratio hydrogen/methanol dual-injection spark-ignition engine under methanol late-injection. *Appl Energy* 277:115622
- GOV.UK (2021) UK enshrines new target in law to slash emissions by 78% by 2035. <https://www.gov.uk/government/news/uk-enshrines-new-target-in-law-to-slash-emissions-by-78-by-2035>. Accessed 6 June 2021
- Gustafson C (2021) History of ethanol production and policy. <http://www.ag.ndsu.edu/energy/biofuels/energy-briefs/history-of-ethanol-production-and-policy>. Accessed 6 June 2021
- Hannah R, Max R (2021) Global CO<sub>2</sub> emissions. <https://ourworldindata.org/co2-emissions>. Accessed 6 June 2021
- Heywood JB (1988) *Internal combustion engine fundamentals*. McGraw-Hill, New York
- Hong W, Yuan C, Xie FX et al (2018) Particulate matter and particle-bound PAHs emissions from gasoline direct injection (GDI) engine with methanol-gasoline blended fuel during start. *Int J Auto Tech-Kor* 19(4):717–72
- Huang JQ, Xiao HL, Yang XL et al (2020) Effects of methanol blending on combustion characteristics and various emissions of a diesel engine fueled with soybean biodiesel. *Fuel* 282:118734
- IRENA (2021) *Innovation outlook: renewable methanol*. <https://www.irena.org/publications/2021/Jan/Innovation-Outlook-Renewable-Methanol>. Accessed 6 June 2021
- Jamrozik A (2017) The effect of the alcohol content in the fuel mixture on the performance and emissions of a direct injection diesel engine fueled with diesel-methanol and diesel-ethanol blends. *Energy Convers Manage* 148:461–476
- Ji CW, Yang JX, Liu XL et al (2016) A quasi-dimensional model for combustion performance prediction of an SI hydrogen-enriched methanol engine. *Int J Hydrogen Energy* 41(39):17676–17686

- Jiao YF, Liu RL, Zhang ZJ et al (2019) Comparison of combustion and emission characteristics of a diesel engine fueled with diesel and methanol-Fischer-Tropsch diesel-biodiesel-diesel blends at various altitudes. *Fuel* 243:52–59
- Jin C, Zhang X, Han W et al (2020) Macro and micro solubility between low-carbon alcohols and rapeseed oil using different co-solvents. *Fuel* 270:117511
- Jouny M, Luc W, Jiao F (2018) General techno-economic analysis of CO<sub>2</sub> electrolysis systems. *Ind Eng Chem Res* 57:2165–2177
- Jouzel J, Masson-Delmotte V, Cattani O et al (2007) Orbital and millennial antarctic climate variability over the past 800,000 years. *Science* 317(5839):793–797
- Kakati D, Biswas S, Banerjee R (2021) Parametric sensitivity analysis of split injection coupled varying methanol induced reactivity strategies on the exergy efficiency enhancement and emission reductions objectives in a biodiesel fuelled CI engine. *Energy* 225:120204
- Kattel SR, Pedro J, Chen JG et al (2017) Active sites for CO<sub>2</sub> hydrogenation to methanol on Cu/ZnO catalysts. *United States: N. p* 2017. Web. <https://doi.org/10.1126/science.aal3573>
- Kumar C, Rana KB, Tripathi B (2019) Effect of diesel-methanol-nitromethane blends combustion on VCR stationary CI engine performance and exhaust emissions. *Environ Sci Pollut R* 26:6517–6531
- Kumar D, Valera H, Gautam A et al (2021) Simulations of methanol fueled locomotive engine using high pressure co-axial direct injection system. *Fuel* 295:120231
- Li CH, Bai HT, Lu YY et al (2018a) Life-cycle assessment for coal-based methanol production in China. *J Clean Prod* 188:1004–1017
- Li J, Ma X, Liu H et al (2018b) Life cycle assessment and economic analysis of methanol production from coke oven gas compared with coal and natural gas routes. *J Clean Prod* 185:299–308
- Li ZY, Wang Y, Geng HM et al (2020) Investigation of injection strategy for a diesel engine with directly injected methanol and pilot diesel at medium load. *Fuel* 266:116958
- Li ZY, Wang Y, Yin ZB et al (2021a) Effect of injection strategy on a diesel/methanol dual-fuel direct-injection engine. *Appl Therm Eng* 189:116691
- Li YY, Chen H, Zhang CH et al (2021b) Effects of diesel pre-injection on the combustion and emission characteristics of a common-rail diesel engine fueled with diesel-methanol dual-fuel. *Fuel* 290:119824
- Liao H, Li B, Zhang B (1998) Pyrolysis of coal with hydrogen-rich gases. 2. Desulfurization and denitrogenation in coal pyrolysis under coke-oven gas and synthesis gas. *Fuel* 77(14):1643–1646
- Liu Q, Liu Z, Ren X et al (2019) Study on sensitivity differences of critical spontaneous ignition temperature between alcohol and hydrocarbon fuels based on reaction pathway. *Energies* 12(3):1–16
- Lu H, Yao AR, Yao CD et al (2019) An investigation on the characteristics of and influence factors for NO<sub>2</sub> formation in diesel/methanol dual fuel engine. *Fuel* 235:617–626
- Machado CF, Medeiros JL, Araújo OF et al (2014) A comparative analysis of methanol production routes: synthesis gas versus CO<sub>2</sub> hydrogenation. In: *Proceedings of the 2014 international conference on industrial engineering and operations management, Bali, Indonesia*, pp 7–9
- Methanol Institute (2020) 16th annual state of the energy industry forum 23 Jan 2020, Washington, DC Singapore
- Mockos GR, Smith WA, Loge FJ et al (2008) Selective enrichment of a methanol-utilizing consortium using pulp and paper mill waste streams. *Appl Biochem Biotechnol* 148(1–3):211–226
- Ning L, Duan QM, Kou HL et al (2020a) Parametric study on effects of methanol injection timing and methanol substitution percentage on combustion and emissions of methanol/diesel dual-fuel direct injection engine at full load. *Fuel* 279:118424
- Ning L, Duan QM, Chen ZM et al (2020b) Comparative study on the combustion and emissions of a non-road common rail diesel engine fueled with primary alcohol fuels (methanol, ethanol, and n-butanol)/diesel dual fuel. *Fuel* 266:117034
- Nuthan Prasad BS, Pandey JK, Kumar GN (2021) Effect of hydrogen enrichment on performance, combustion, and emission of a methanol fueled SI engine. *Int J Hydrogen Energy* (In Press). <https://doi.org/10.1016/j.ijhydene.2021.05.039>



- Obulesu P, Kumar RS, Ramanjaneyulu B (2021) A experimental test on 2-stroke spark ignition engine with gasoline and methanol-gasoline blends using brass coated piston. *Mater Today Proc* 39:590–595
- Ogunkunle O, Ahmed NA (2019) A review of global current scenario of biodiesel adoption and combustion in vehicular diesel engines. *Energy Rep* 5:1560–1579
- Pan W, Yao CD, Han GP et al (2015) The impact of intake air temperature on performance and exhaust emissions of a diesel methanol dual fuel engine. *Fuel* 162:101–110
- Panda K, Ramesh A (2021) Diesel injection strategies for reducing emissions and enhancing the performance of a methanol based dual fuel stationary engine. *Fuel* 289:119809
- Park S, Cho J, Park J et al (2017) Numerical study of the performance and NO<sub>x</sub> emissions of a diesel-methanol dual-fuel engine using multi-objective Pareto optimization. *Energy* 124:272–283
- Polaris Market Research 2019–03. <https://www.polarismarketresearch.com>. Accessed 6 June 2021
- Robert R (2021) Global temperature report for 2020. <http://berkeleyearth.org/global-temperature-report-for-2020>. Accessed 6 June 2021
- Sabatier P (1926) How I have been led to the direct hydrogenation method by metallic catalysts. *Ind Eng Chem* 18(10):1005–1008
- Salmani MH, Rehman S, Zaidi K et al (2015) Study of ignition characteristics of microemulsion of coconut oil under off diesel engine conditions. *Corros Eng Sci Technol* 18(3):318–324
- Salzano E, Cammarota F, Benedetto AD et al (2012) Explosion behavior of hydrogen methane/air mixtures. *J Loss Prev Process Ind* 25:443–447
- Sarıkoç S (2021) Effect of H<sub>2</sub> addition to methanol-gasoline blend on an SI engine at various lambda values and engine loads: a case of performance, combustion, and emission characteristics. *Fuel* 297:120732
- Sarli VD (2014) Stability and emissions of a lean pre-mixed combustor with rich catalytic/ lean-burn pilot. *Int J Chem React Eng* 12:77–89
- Sebastian CP (2018) Reduction of CO<sub>2</sub> to chemicals and fuels: a solution to global warming and energy crisis. *ACS Energy Lett* 3:1557–1561
- Seesy AIE, Waly MS, He ZX et al (2021) Influence of quaternary combinations of biodiesel/methanol/n-octanol/diethyl ether from waste cooking oil on combustion, emission, and stability aspects of a diesel engine. *Energy Convers Manage* 240:114268
- Shih CF, Zhang T, Li JH et al (2018) Powering the future with liquid sunshine. *Joule* 2:1925–1949
- Somasundaram S, Mohanraj T, Raju SP et al (2017) Operating characteristics of multi-cylinder petrol engine using LPG with methanol. In: *Innovative design and development practices in aerospace and automotive engineering*. Springer Singapore, Singapore, pp 507–516
- Soni DK, Gupta R (2017) Application of nano emulsion method in a methanol powered diesel engine. *Energy* 126:638–648
- Stangeland K, Li H, Yu Z (2018) Thermodynamic analysis of chemical and phase equilibria in CO<sub>2</sub> hydrogenation to methanol, dimethyl ether, and higher alcohols. *Ind Eng Chem Res* 57:4081–4094
- Stangeland K, Li H, Yu Z (2020) CO<sub>2</sub> hydrogenation to methanol: the structure-activity relationships of different catalyst systems. *Energy Ecol Environ* 5:272–285
- Thiyagarajan S, Sonthalia A, Geo VE et al (2020) Effect of manifold injection of methanol/n-pentanol in safflower biodiesel fuelled CI engine. *Fuel* 261:116378
- Thyssenkrupp's concept of using renewable energy and waste CO<sub>2</sub> to make renewable methanol. <https://www.thyssenkrupp.com>. Accessed 6 June 2021
- Tian Z, Zhen XD, Wang Y et al (2020) Comparative study on combustion and emission characteristics of methanol, ethanol and butanol fuel in TISI engine. *Fuel* 259:116199
- Tijm PJA, Waller FJ, Brown DM (2001) Methanol technology developments for the new millennium. *Appl Catal Agen* 221:275–282
- Turner JWG, Pearson RJ, Harrison P et al (2012) Evolutionary decarbonization of transport: a contiguous roadmap to affordable mobility for everyone using sustainable organic fuels for transport. In: *Sustainable vehicle technologies*, Gaydon, UK, pp 71–88
- UNFCCC (2021) Adoption of the Paris Agreement. Report No. FCCC/CP/2015/L.9/Rev.1. <http://unfccc.int/resource/docs/2015/cop21/eng/l09r01.pdf>. Accessed 6 June 2021

- Vancoillie J, Demuynck J, Sileghem L et al (2012) Comparison of the renewable transportation fuels, hydrogen and methanol formed from hydrogen, with gasoline-Engine efficiency study. *Int J Hydrogen Energy* 37(12):9914–9924
- Verhelst S, Turner JWG, Sileghem L et al (2019) Methanol as a fuel for internal combustion engines. *Prog Energy Combust Sci* 70:43–88
- Wang S, Ji C (2012) Cyclic variation in a hydrogen-enriched spark-ignition gasoline engine under various operating conditions. *Int J Hydrogen Energy* 37:1112–1119
- Wang G, Liao SY, Liu XB (2009) Numerical study on ignition delay period of methanol-isooctane/n-heptane blended fuel. *Vehicle Engine* 4:7–15
- Wang X, Ge YS, Liu LL et al (2015a) Evaluation on toxic reduction and fuel economy of a gasoline direct injection- (GDI-) powered passenger car fueled with methanol-gasoline blends with various substitution ratios. *Appl Energ* 157:134–143
- Wang QG, Wei LJ, Wang P et al (2015b) Investigation of operating range in a methanol fumigated diesel engine. *Fuel* 140:164–170
- Wang QG, Wang B, Yao CD et al (2016) Study on cyclic variability of dual fuel combustion in a methanol fumigated diesel engine. *Fuel* 164:99–109
- Wang H, Yao AR, Yao CD et al (2020) Investigation to meet China II emission legislation for marine diesel engine with diesel methanol compound combustion technology. *J Environ Sci* 96:99–108
- Wang B, Yao AR, Chen C et al (2019a) Strategy of improving fuel consumption and reducing emission at low load in a diesel methanol dual fuel engine. *Fuel* 254:115660
- Wang L, Chen ZM, Zhang TC et al (2019b) Effect of excess air/fuel ratio and methanol addition on the performance, emissions, and combustion characteristics of a natural gas/methanol dual-fuel engine. *Fuel* 255:115799
- Ward P, Teague J (1996) Fifteen years of fuel methanol distribution. In: Paper presented in the 11th conference on alcohol fuels, Sun City, South Africa, pp 1–12
- Wei LJ, Yao CD, Wang QG et al (2015) Combustion and emission characteristics of a turbocharged diesel engine using high premixed ratio of methanol and diesel fuel. *Fuel* 140:156–163
- Wei HY, Yao CD, Pan W et al (2017) To meet demand of Euro V emission legislation urea free for HD diesel engine with DMCC. *Fuel* 207:33–46
- Wei JJ, Fan CY, Qiu L et al (2020) Impact of methanol substitute fuel on oxidation reactivity of soot emissions from a modern CI engine. *Fuel* 268:117352
- Wei JN, Feng HQ, Liu HF et al (2021) Analysis of knocking combustion with methanol/iso-octane and ethanol/isooctane blends in a spark-ignition engine. *Fuel* 284:118979
- Wei JJ, He CJ, Lv G et al (2021b) The combustion, performance and emissions investigation of a dual-fuel diesel engine using silicon dioxide nanoparticle additives to methanol. *Energy* 230:120734
- Wei JJ, He CJ, Fan CY et al (2021c) Comparison in the effects of alumina, ceria and silica nanoparticle additives on the combustion and emission characteristics of a modern methanol-diesel dual-fuel CI engine. *Energy Convers Manage* 238:114121
- Wei JJ, Yin ZH, Wang CM et al (2021d) Impact of aluminium oxide nanoparticles as an additive in diesel-methanol blends on a modern DI diesel engine. *Appl Therm Eng* 185:116372
- Wu B, Wang LJ, Shen XW et al (2016) Comparison of lean burn characteristics of an SI engine fueled with methanol and gasoline under idle condition. *Appl Therm Eng* 95:264–270
- Xi JP (2021) Statement by H.E. Xi Jinping President of the People's Republic of China at the General Debate of the 75th Session of The United Nations General Assembly. [https://www.fmprc.gov.cn/mfa\\_eng/zxxx\\_662805/t1817098.shtml](https://www.fmprc.gov.cn/mfa_eng/zxxx_662805/t1817098.shtml). Accessed 6 June 2021
- Xu GL, Yao CD, Rutland CJ (2014) Simulations of diesel-methanol dual-fuel engine combustion with large eddy simulation and Reynolds-averaged Navier-Stokes model. *Int J Engine Res* 15:751–769
- Xu XY, Liu Y, Zhang F et al (2017) Clean coal technologies in China based on methanol platform. *Catal Today* 298:61–68

- Xuan TM, Sun ZC, Seesy AIE et al (2021) An optical study on spray and combustion characteristics of ternary hydrogenated catalytic biodiesel/methanol/n-octanol blends; part II: Liquid length and in-flame soot. *Energy* 227:120543
- Yan F, Xu L, Wang Y et al (2019) On the opposing effects of methanol and ethanol addition on PAH and soot formation in ethylene counterflow diffusion flames. *Combust Flame* 202:228–242
- Yang WM, Yang M (2019) Phi-T map analysis on RCCI engine fueled by methanol and biodiesel. *Energy* 187:115958
- Yilmaz I, Taştan M (2018) Investigation of hydrogen addition to methanol-gasoline blends in an SI engine. *Int J Hydrogen Energy* 43(44):20252–20261
- Ying Y, Liu D (2021) Soot properties in ethylene inverse diffusion flames blended with different carbon chain length alcohols. *Fuel* 287:119520
- Yuen P, Villaire W, Beckett J (2010) Automotive materials engineering challenges and solutions for the use of ethanol and methanol blended fuels. SAE Technical Paper 2010-01-0729
- Zehni A, Balazadeh N, Hajibabaei M et al (2020) Numerical study of the effects of split injection strategy and swirl ratio for biodiesel PCCI combustion and emissions. *Propul Power Res* 9(4):355–371
- Zhang CH, Wu H (2016) Combustion characteristics and performance of a methanol fueled homogenous charge compression ignition (HCCI) engine. *J Energy Inst* 89(3):346–353
- Zhang B, Ji CW, Wang SF et al (2014) Idling performance of a hydrogen-blended methanol engine at lean conditions. *Energy Procedia* 61:331–334
- Zhang B, Ji CW, Wang SF (2015) Combustion analysis and emissions characteristics of a hydrogen-blended methanol engine at various spark timings. *Int J Hydrogen Energy* 40(13):4707–4716
- Zhao F, Zhang X, Shuai SJ et al (2009) Unregulated emissions and combustion characteristics of low-content methanol-gasoline blended fuels. *Energy. Fuel.* 24:1283–1292
- Zhao LF, Wang DF, Qi WQ et al (2020) Particulate matter (PM) emissions and performance of bio-butanol-methanol-gasoline blends coupled with air dilution in SI engines. *J Aerosol Sci* 145:105546
- Zhen XD, Li XY, Wang Y et al (2020a) Effects of the initial flame kernel radius and EGR rate on the performance, combustion and emission of high-compression spark-ignition methanol engine. *Fuel* 262:116633
- Zhen XD, Li XY, Wang Y et al (2020b) Comparative study on combustion and emission characteristics of methanol/hydrogen, ethanol/hydrogen and methane/hydrogen blends in high compression ratio SI engine. *Fuel* 267:117193

# Chapter 13

## Technologies for Knock Mitigation in SI Engines—A Review



Cinzia Tornatore , Luca Marchitto , and Gerardo Valentino 

**Abstract** Design trend in spark ignition (SI) engines aims to improve power density and efficiency to ensure that regulated emissions levels are minimized. From a thermodynamic point of view this involves increased in-cylinder pressure and local mixture conditions that promote autoignition of the end gas, leading to knock. In order to prevent knock, the commonly used technique consists in retarding spark timing and combustion phasing, which results in a lower thermodynamic efficiency and higher exhaust temperature. A delayed spark timing is frequently coupled with over-fueling that allows to reduce the exhaust temperatures as well as knock tendency. This strategy clearly results in worsened fuel economy and increased emissions levels. At present time knock represents a limiting factor for a further development of new generation of high performance spark ignition engines and a number of technological solutions have been proposed by the scientific community and OEMs to overcome the limitations connected to this phenomenon. New engine architectures with optimized combustion chamber geometry shapes and combination of methodologies have been proposed for a reduced combustion time to enhance high-performance engines. Changes in the engine cooling systems have been applied to enhance end gas cooling leading to knock suppression effect. Other favorable options proposed for knock mitigation are water injection and cooled exhaust gas recirculation. Moreover, attention is also paid on renewable alcohol fuels with a research octane number higher than gasoline. This contribution aims to review some of the recent progresses in this topic with detailed analyses of current and promising future technologies to avoid knock and enable the development of future high efficiency SI powertrains with low impact on emissions.

**Keywords** Spark ignition engines · Knocking · Knock mitigation

---

C. Tornatore (✉) · L. Marchitto · G. Valentino  
STEMS, Italian National Research Council, Via Marconi 4, 80125 Napoli, Italy  
e-mail: [cinzia.tornatore@stems.cnr.it](mailto:cinzia.tornatore@stems.cnr.it)

© The Author(s), under exclusive license to Springer Nature Singapore Pte Ltd. 2022  
G. Kalghatgi et al. (eds.), *Engines and Fuels for Future Transport*, Energy, Environment,  
and Sustainability, [https://doi.org/10.1007/978-981-16-8717-4\\_13](https://doi.org/10.1007/978-981-16-8717-4_13)

325

### 13.1 Knocking Phenomenon and Limitations in Spark Ignition Engines Optimization

The future of automotive mobility will be characterized by a mix of technologies, involving full electric (BEV) and hybrid vehicles (PHEV), fuel cell electric vehicles (FCEV) and conventional internal combustion engines vehicles (ICV), depending on consumer acceptance and future emissions legislation. In this scenario, the internal combustion (IC) engine will still play a crucial role, whether used for power generation or for operating the vehicle itself, even in electrified powertrain configurations such as hybrids. For this reason, the scientific community is still very involved in improving the thermal efficiency of IC engines without significant penalties in operating costs in the short-to-medium term (Reitz et al. 2020).

At present, there are more than one billion passenger cars and commercial vehicles in use worldwide and more than 60% of them are equipped with spark ignition (SI) engines.

Compared to compression ignition engines, SI engines can meet stringent emissions regulations using the inexpensive three-way catalytic converter system. However, their efficiency is still to be significantly increased to comply with the future CO<sub>2</sub> regulations. One of the main obstacles for new generation SI engines optimization is their tendency to knocking (Konig and Sheppard 1990).

The SI normal combustion event starts from the spark discharge between the electrodes during the compression stroke: a spherical flame front propagates from the spark plug throughout the combustion chamber with a speed from 15 to 30 m/s. During the flame propagation, three different zones can be distinguished: the thin flame front zone, a fully burned zone behind the flame and the unburned fuel-air mixture zone ahead of the flame front, called the end-gas region.

Due to the piston movement, flame front spreading towards the combustion chamber walls and radiation phenomena the end gas pressure and temperature increase. In some locations in the end gas, fuel and air can react spontaneously with heat release in the absence of flame. This phenomenon is known as autoignition.

At this point the pressure and temperature sharply increase due to a sudden release of chemical energy in the rest of the end gas. Pressure waves generated by sequential autoignitions propagate, hit the chamber wall vibrating back and forth across the cylinder, generating pressure oscillations which cause a pinging sound (Cho et al. 2021). Velocities reached during this phase are between 300 and 1000 m/s.

This abnormal combustion event induced by auto-ignition, occurring in the end gas and featuring a pinging noise, is called knocking.

The harmful effects of knocking are: noise and roughness, mechanical damages, carbon deposits, increase in heat transfer due to the higher maximum temperature and the cleaning of protective layer of inactive stagnant gas on the cylinder walls due to pressure waves, decrease in power output and efficiency, local overheating that can lead to pre-ignition phenomena.

Therefore, knock occurrence in SI engines must be avoided during engine operation, representing the main limitation of increasing the compression ratio for developing high-efficiency engines.

In this chapter, the main technologies proposed by the scientific community and OEMs for knock mitigation in SI engines are forward-looking reviewed. In details the following topics are examined: engine control strategies to reduce knocking (retarding spark timing and enriching the mixture), combustion chamber geometry optimization, enhanced engine cooling, water injection, cooled exhaust gas recirculation and use of anti-knock fuels.

For each selected topic, the main principles and fundamentals are outlined, major findings by researchers and engineers in the relevant areas are presented and discussed as well the prospective of engineering application is provided. The chapter is intended to be useful for readers who wish to undertake the investigation of pathways to mitigate knocking in engine experiments for improved engine design and control.

It is worth pointing out that highly turbocharged (downsized) gasoline engines, in the low-speed and high-load regime, are also challenged by the occurrence of a new engine knock mode, called super-knock. The major difference between super-knock and conventional knock is the value of the pressure increase at the start of the event: in the case of super-knock this value is more than an order of magnitude higher. Super-knock mainly derives from pre-ignition and its control cannot be obtained applying common knock suppression methods that will be discussed in this review chapter.

## 13.2 Engine Control Strategies to Reduce Knocking

Conventional knock is a race between the flame propagation in the cylinder and the thermal auto-ignition of the unburned “end gas” (Heywood 1988). For avoiding engine knock, the time of flame propagation to the end gas ( $\tau_1$ ) needs to be lower than the time of the end-gas auto-ignition ( $\tau_2$ ) (Wang et al. 2017).

In order to control engine knock, it is necessary to intervene on the parameters that influence  $\tau_1$  and  $\tau_2$ .

In commercial engines, the commonly applied approach consists in retarding the spark timing, moreover, in boosted engines, the spark retarding is usually coupled with the fuel enrichment that allows further reducing knock tendency and the temperature at the exhaust.

### 13.2.1 Retarding Spark Timing

Maximum Brake Torque (MBT) timing is the optimal timing for best allowed thermal efficiency, nevertheless, knock tendency may preclude such an advanced timing. When knock occurs, a knock sensor installed on the combustion chamber detects the

pressure oscillations and sends to the Electronic Control Unit (ECU) a signal based on the intensity of the vibrations. In this case, the spark timing is retarded by the ECU until the pressure oscillations are reduced to an adequate level.

The reasons why retarding the spark timing mitigates knock (Russ 1996), can be summarized as follows:

Delaying combustion by retarding spark timing causes ignition to take place at a higher in-cylinder temperature and pressure: this causes the flame to develop more quickly (reduction in  $\tau_1$ ).

Retarding the ignition timing reduces the peak pressure and temperature achieved in the cylinder, due to un-optimized combustion phasing. This will cool the end gas and reduce its pressure thereby prolonging the ignition delay (increase in  $\tau_2$ ).

In (Ayala et al. 2006) tests were carried out to determine the correlation between spark timing and engine output under a variety of conditions in a single cylinder 4-valve spark-ignition research engine. The experiments confirmed that a late combustion reduces the work output because of the decrease in the cylinder peak pressure, as well as the volume ratio and the temperature ratio through which the gases expand.

When choosing the spark advance for a certain engine operating condition, knock needs to be avoided but occasional occurrence is acceptable. Thus, to attain the highest achievable fuel economy, SA is kept at the borderline value that assures a knock probability below a predetermined level. This value is too conservative in many situations, in Shen et al. (2017a), a spark advance self-optimization strategy was implemented for a SI engine operating in lean-burn mode. The strategy aimed at tuning combustion phase in order to achieve high efficiency under a probability constraint of knocking events. This type of optimization can mitigate the drop in thermal efficiency but the method of ignition delaying inherently maintains this drawback.

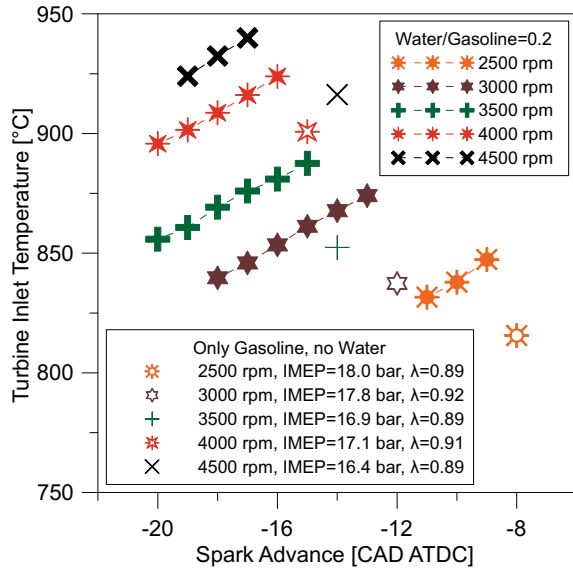
This method has another drawback: with a delay in spark advance, the combustion event starts later. Since the exhaust valve opening time remains unchanged, short time passes between completion of combustion process and exhaust valve opening. This leads to an increase in exhaust gas temperature that can be detrimental to the life of the exhaust valve with potential damage of turbine in the case of turbocharged engines.

The increase in the exhaust temperature has been largely addressed by the scientific community and some solutions have been proposed. Among all, the enriching of the mixture, reported in detail in the following subsection, is widely used for this purpose.

In (Tornatore et al. 2017), the effect of spark advance (coupled with water injection) on turbine inlet temperature (TIT) was presented. Tests were performed on a twin-cylinder turbocharged SI engine, water and gasoline were port injected with two different injection systems. Figure 13.1 shows the turbine inlet temperature without water injection (star symbols) in rich conditions and with water injection (represented as colored continuous lines), in stoichiometric conditions. A water to gasoline fraction of 0.2 by volume was considered.

Switching from the reference-rich to stoichiometric condition, even with water injection, an increase in TIT was measured. By advancing the spark timing, under stoichiometric/water injection conditions, the turbine inlet temperature was reduced

**Fig. 13.1** Turbine Inlet Temperature against the spark advance in the interval of engine speed from 2500 to 4500 rpm. Redrawn from Tornatore et al. (2017)



for all the engine speeds. The WI allowed to run the engine at stoichiometric condition with TIT values below the threshold limit ( $<950\text{ }^{\circ}\text{C}$ ), at the same indicated mean effective pressure.

### 13.2.2 Enriching the Mixture

This paragraph assesses the over-fueling methodology currently used at high engine load conditions to avoid knock and control the turbine inlet temperature in turbocharged engines (Ratcliff et al. 2018). Usually the resulting mixture is characterized by a lambda value (air/fuel ratio divided by stoichiometric ratio) in a range from 0.89 to 1.

There are mainly two phenomena connected to mixture enrichment that allow knocking suppression:

1. Reduction in fuel–air mixture temperature through evaporative cooling.

Fuel enrichment in SI engines has a very significant effect on charge cooling, since the excess fuel injected in the combustion chamber (DI) or in the intake manifold (PFI) reduces the charge temperature due to the latent heat of evaporation. Even if evaporative cooling is more significant in DI engines due to the fuel phase change directly in the combustion chamber, this phenomenon is still relevant in PFI engines since fuel is injected close to the inlet valve and the evaporation leads to a considerable reduction of the charge temperature.



## 2. Increase in specific heat of the charge.

In the case of a rich mixture, the excess quantity of fuel, compared to the stoichiometric one, will not completely burn due to the insufficient amount of air available. Some excess fuel can be partly oxidized, forming intermediate products like CO, other fuel remains unburned. The unburned fuel acts as an inert diluent, absorbing part of the energy released by combustion, and thus helping to contain the temperature rise. In other words, the excess fuel changes the specific heat of the charge. Three main sources of end-gas can be recognized: heat transfer, compression of the end-gas and heat release from chemical reactions. When the mixture composition of the charge is altered, the heating by compression considerably changes because of the different specific heat of the charge. A fuel rich mixture is heated less by compression than a lean mixture (Grandin et al. 2002).

These mechanisms prolong the time to end-gas auto-ignition and finally suppress the onset of knocking combustion.

On the other side, there are two mechanisms for rich mixtures competing with the previous ones. The first competing mechanism is related to the increase in auto-ignition tendency for rich mixtures. In (Stapf and Reis 2015), it has been reported that under rich conditions, for iso-octane and heptane, the auto-ignition delay time is reduced. At high levels of enrichment this mechanism cannot be revealed since the cooling effect dominates and knock intensity decreases as a result (Cairns and Koupaie 2017). The second competing mechanism is the chemical heat release increase as the mixture is enriched. This leads to an increased temperature of the end-gas.

To resume, when enriching the mixture, the effect obtained is the result of a balance between increased temperature from chemical reactions and, on the other side, the combined cooling effect of fuel evaporation and decreased temperature of the end gas during isentropic compression.

In (Singh and Dibble 2018) the effectiveness of several enrichment strategies on knock suppression was evaluated in a gasoline spark ignition. Multiple options for fuel injection were tested, including a direct injector and a port-fuel injector: enrichment was achieved via DI at varying start of injection and injection quantities.

When a very small amount of fuel was injected before the spark timing, knock intensity increased. Small addition to stoichiometric mixture increased the in-cylinder temperature, and hence the end-gas was more prone to auto-ignite earlier. Moreover, the end-gas was also less resistant to auto-ignition. This led to an increase in knock intensity. However, as the enrichment quantity increased, the charge cooling effect arising from the latent heat of vaporization started to be dominant and the knock intensity decreased. This work demonstrated that using enrichment to suppress knock in an engine is not always trivial and in some conditions a compromise is needed between increased knock from lower amount of fuel injection and misfires from too much fuel enrichment.

In conclusion, fuel enrichment at high load is a technique to suppress knock that does not require changes in the engine architecture and the slightly rich combustion may help maximize full load output. In addition, excess fuel is also helpful at higher speeds and loads to limit exhaust gas temperatures and protect the exhaust components.

On the other side, the condition of fuel enrichment comes with its drawbacks. The first one is certainly the reduced fuel consumption efficiency. Moreover, a rich combustion induces an increase in HC and CO emissions, and the three-way catalyst conversion efficiency is very low in non-stoichiometric conditions. This leads to increased engine out emissions. Such strategy is clearly not sustainable to comply with the future emission standards, particularly in light of the real-world driving cycles currently being proposed within the EU, and elsewhere, to cover a wider area of engine operation (Vafamehr et al. 2016).

In this context, stratified combustion modes have been proposed in DI SI engines to suppress knocking: these strategies take advantage of fuel enrichment, but only in a limited part of the combustion chamber: i.e. near the spark plug. Stratified (Bai et al. 2010) and partially stratified fuel combustion strategies (Tornatore and Sjöberg 2021) allow to operate the engine with an overall lean (even  $\lambda$  higher than 2) or stoichiometric air/fuel ratio, while a rich mixture formed near the spark plug, by a late fuel injection, induces an increase in flame propagation speed and a local reduction in charge temperature. At the same time, the lean mixture in the end gas suppresses auto ignition phenomena. The overall air/fuel ratio can be kept stoichiometric meeting the requirements of the three way catalysts (TWC) solving the emissions problem, or lean to gain benefits in terms of fuel consumption.

In conclusion, the fuel stratification can suppress knocking with a lower power output loss compared to the method of retarding spark timing and has better fuel economy and less gaseous emissions than the method of over-fueling. However, stratified combustion has several drawbacks (Johansson et al. 2013). The main challenges are the reduction in combustion stability and the tendency to produce high particulate emissions: the latter is mostly due to the diffusive flames caused by fuel wetting on some surfaces of the combustion chamber such as the piston top.

### 13.3 Combustion Chamber Geometry Optimization

Many studies have been carried out with the aim of minimizing knocking through combustion chamber geometry optimization. More in details, the scientific literature often reports that such optimization should be aimed at reducing the combustion duration: this allows the air-fuel mixture in the end-gas region to be burned by the propagating flame front before the in-cylinder temperature and pressure reach autoignition conditions.

The main changes in engine geometry that allow the reduction in combustion duration deal with intensified turbulence: increasing turbulence intensity leads to fast combustion, this is usually achieved through increased tumble and squish motion.

Tumble is large-scale organized flow with its rotation plane perpendicular to the cylinder axis. A controlled and coherent tumble motion during the intake stroke is an effective method of enhancing turbulence intensity before the ignition timing, thereby accelerating the burn rates. Squish is a radial organized flow that takes place at the end of the compression stroke towards the center-line of the cylinder. As the piston reaches TDC, the squish flow produces a secondary tumble flow, where rotation occurs near a circumferential axis close to the outer edge of the piston cavity. At the end of the compression stroke, this large scale of organized flows breaks down into small scale eddies and turbulence level is enhanced. Thanks to the squish flow, the flame is fed with fresh mixture coming from the combustion chamber periphery obtaining a more homogeneous air-fuel mixture before ignition (Kaplan 2019). The squish flow control is a key technology for improving the knock limit in spark ignition engines (Ueda et al. 1999).

Modifications of inlet ducts and piston design are performed in order to increase tumble and squish inside the cylinder (Zaccardi et al. 2010). Changes can concern, for example, the shape of the combustion chamber, the diameters of the valves, the lift of the valves, the design of the ports, the position of the spark plug and the shape of the piston crown, where it is possible to create compression zones (squish) to intensify turbulence levels at the end of the compression stroke.

Many research papers report the influence of piston crown shape alterations on knock. In (Fujimoto et al. 2002) the geometry of the piston crown was physically modified to compare the behavior of the air flow for different combustion chamber shapes. Particle image velocimetry (PIV) allowed a comparison between the tumble and squish-generated flow velocity distributions when the squish area was located at the intake valve and at the exhaust valve side. High heat release was realized at late stage combustion with a simultaneous decrease in cyclic variation of initial burn. Consequently, knocking was controlled compared with a flat piston. In (Radwan et al. 2007) a study was carried out on the influence of induction manifold angles on turbulence generation and the effects on detonation and preignition in a spark-ignition engine. Tumbling motion was generated using variable intake manifold angles in addition to the original one. Using manifold angles of  $40^\circ$  or  $50^\circ$  made the engine less prone to detonation or preignition in comparison with the conventional angle of  $90^\circ$  at all speeds, loads, ignition timings and inlet air temperatures.

In (Matsuo et al. 2016), through the optimization of intake port geometry, the tumble ratio of a dedicated engine for the Toyota Prius hybrid increased from 0.8 (of the previous 2ZR-FXE model) to 2.8 (of the ESTEC 2ZR-FXE model). Introduction of high tumble-induced-high-turbulence leads to low tendency to knock.

In (Hwang et al. 2016) to Kappa 1.6 L GDI engine: the optimized intake port, combustion chamber and piston induced significant fast burn rate. More in details, straightened intake port with sharp edge was applied and valve seat cutter was optimized to increase the tumble flow to improve intake air flow. Moreover, intake port was designed to avoid the decrease in flow coefficient. Also, optimizing piston bowl shape enhanced mixture flow in the combustion chamber. An eccentric bowl shape increased tumble ratio and turbulent kinetic energy. Also the effect of squish in

combustion chamber was analyzed by flow simulation: an open type squish was applied to improve combustion burn rate.

On the other side, some authors reported that increasing flame speed shows a negative impact on knock mitigation. According to this theory, in-cylinder low flow speed and low turbulence could induce a slow combustion that gives a longer residence time for end-gas auto-ignition occurrence, thus knock is intensified (Mahendar et al. 2018; Gómez Montoya and Amell Arrieta 2019). I.e., Yue and Som (2021) found that increasing flame speed shows a negative impact on knock mitigation, but provides improvement on thermal efficiency by shortening the combustion duration.

This contrast demonstrates that the underlying mechanism of the effects of flame propagation speed on auto-ignition is not completely clear (Zhou et al. 2020) and dedicated studies should be carried out in each condition in order to find the best piston combustion chamber design for knocking mitigation, achieving high thermal efficiency at the same time.

## 13.4 Enhanced Engine Cooling

Another advantageous technique that has been proposed for knock mitigation is to improve engine cooling (Cho et al. 2021; Pang and Brace 2004): enhanced cooling reduces in-cylinder end gas temperature during compression, thereby preventing the unburned mixture from reaching auto ignition conditions. However, excessive cooling can lead to an increase in heat loss and thus a worsening of combustion efficiency.

In the scientific literature there are different approaches to enhance end gas cooling, here the most relevant ones are resumed.

### 13.4.1 Dual Cooling System

In dual cooling systems the cylinder head and the cylinder block of the SI engine are cooled by independent circuits. Each cooling circuit operates with a different temperature set point and this allows each section of the engine to operate at its optimum temperature, maximizing the overall effect of the cooling system on engine performance.

One of the first studies of dual cooling systems was carried out in Kobayashi et al. (1984). The authors implemented a dual circuit cooling system in a 1.3 L four-cylinder engine with a compression ratio of 9.0. It was found that the reduction in the temperature of cylinder head coolant influenced the degree of knock mitigation more than the reduction in the liner coolant temperature. The reason, in the authors' opinion, is that head coolant temperature reduction probably causes a better cooling of end gas region during flame propagation, due to the larger decrease in the combustion chamber wall temperature.

Split cooling system was also implemented in production engines. More in details, in Hwang et al. (2016) engine cooling system was optimized to improve Kappa 1.6 L GDI engine knocking characteristics. The split cooling system allowed to separately control coolant temperature for block and head: to reduce piston friction losses, a higher coolant temperature was set in the block (100–105 °C) while the head coolant temperature was set a lower value of 90 °C. Thanks to the split cooling and semi-cross flow, knock was effectively suppressed and spark timing could be advanced by 1–3CA at 8 test points.

### ***13.4.2 Evaporative Cooling System***

The principle behind evaporative cooling is to take advantage of the noteworthy heat transfer rates caused by the liquid–vapor phase change that occurs during boiling (Jafari et al. 2017). Heat from the engine is absorbed by using the latent heat of vaporization of the coolant. This provides a significant improvement over traditional engine cooling systems based on liquid single-phase convective heat transfer.

Over the past century, evaporative cooling has been widely studied for application to thermal management of internal combustion engines for automotive. Even if many system concepts have been proposed (Porot et al. 1997), patented (Tilton and Tilton 1993; Pautsch 2003), analyzed, prototyped and, in some cases, implemented, none has been adopted by vehicle manufacturers for serial production.

In order to allow the application of this technology, some research questions need to be addressed. From the basic research point of view, it is mandatory to improve the knowledge on physics of vapor formation in the presence of vibrations and agitating boundaries typical of internal combustion engines.

Moreover, it is necessary to identify a durable coolant not suffering from deterioration due to repeated evaporation and condensing maintaining anti-corrosion/erosion cooling system standards.

Finally, the problem of evaporative cooling control needs to be addressed in order to guarantee adequate stability under all operating conditions with cost-effective control sensing and control actuation.

### ***13.4.3 Precision Cooling System***

In SI engines, the heat flows are generally high in the areas close to the exhaust valve seats and they decrease towards the cylinder walls. Ideally, the heat transfer coefficient on the coolant-side of a combustion chamber should match the heat flow levels on the gas side. Precision cooling system consists in directing the flow of coolant to achieve an optimized temperature distribution (Robinson et al. 1999).

This results in lower temperatures in the upper portion of the cylinders, more uniform temperatures throughout the engine, and a lower average temperature.

The effects of precision cooling systems have been investigated in automotive engines. The studies reported in the literature (Finlay et al. 1988) demonstrated the effectiveness of precision cooling system in allowing ignition timing advance by reducing the chamber wall temperatures. The majority of work with precision cooling has focused on convective only heat transfer, but the precision cooling advantages can be combined with evaporative cooling ones.

#### ***13.4.4 Piston Cooling***

Traditionally, an oil spray jet is directed towards the bottom of the piston for its cooling: even if this technique is simple and effective, the achievable temperature reductions on the piston top-land are often insufficient.

Currently, cooling galleries inside the piston head are adopted to optimize heat exchange. They consist in hollow annular cooling channels filled with oil through a nozzle installed in the crankcase. The high-speed collision of engine oil on gallery surfaces enhances the heat transfer capacity through the impinging effect induced from reciprocating motion.

In (Reyes Belmonte et al. 2015) an original aluminum piston was considered and an oil cooling gallery was introduced near the piston crown to allow a temperature reduction on the top land and a more uniform temperature distribution across the crown. The numerical investigation allowed to conclude that placing a cooling gallery near the top land induces temperature reductions between 30 and 50 °C.

Also in Hwang et al. (2016) piston cooling gallery was found to be an effective technique to suppress knocking. With piston oil gallery, hot spot temperature of the piston crown was reduced of 17 °C. In this way, 2–3CA spark timing advance was allowed and BSFC in detonation border line zone was improved of 0.3–0.5%.

#### ***13.4.5 Increased Heat Transfer at Exhaust Valve***

Heat energy produced by the flame in the combustion chamber is transferred through bottom surface and neck area of the exhaust valve and released through contact with the valve seat insert and the valve guide. Thus, in order to reduce the temperature of the exhaust valve, it is necessary to increase the rate of heat release on the exhaust valve, valve seat insert and valve guide.

In (Hwang et al. 2016) a sodium-filled exhaust valve and a copper alloy valve guide were applied to Kappa 1.6 L GDI engine. Through thermal analysis it was found that the temperature of exhaust valve decreased up to 128 °C, at neck of it, and 83 °C at the side of combustion chamber face. As a result, it was possible to anticipate the ignition time by 1–2 CA and achieve 0.3% of BSFC improvement.

### 13.4.6 Nano-fluids

Nano-Fluids have been used both in cooling water and oil in order to enhance end gas cooling. Nano-fluids are colloidal suspension into a conventional base fluids of nanoparticle: particles of different materials (metals, metal oxides, organics, carbon, etc.) with a size in the range 1–100 nm. Nano-fluids show higher heat diffusion coefficient if compared with the baseline fluid. This is the main reason why they represent ideal coolants that increase heat transfer efficiency.

In (Kumar and Subudhi 2019) a comprehensive review on nanofluids use, as a coolant in the vehicle engine cooling system, is reported. The review paper compared the convective heat transfer in the radiator for various nanofluids. The improvements in the heat transfer ranged from about 15–20% to a maximum about 193%.

In (Teodosio et al. 2019) the effects of alumina nanofluid coolant on the performance of a spark ignition engine were analyzed by 1D and 3D models. Investigations revealed a fuel consumption benefit ranging from 2% up to 5.4% at full load, mainly arising from decreased knock tendency and reduced mixture over-fueling.

In (Peng et al. 2014) a numerical simulation was carried out on the flow and heat transfer process of nanofluids (copper/diamond nanoparticles) inside a piston cooling gallery. The results showed large improvements in thermal conductivity, and small deteriorations in viscosity and specific heat with the increase of nanoparticle volume fraction.

The results reported in the scientific literature on this topic, indicate that nanofluids are promising for enhanced heat transfer application in internal combustion engines. On the other hand, some drawbacks connected to the use of nanofluids should be highlighted and faced by the scientific community to allow this technology to be eligible for commercial applications. First of all, particles can accumulate or sediment if the fluid is in a state of stagnation for a long time. Moreover, the costs of suspended nanoparticles and surfactants is usually high. Finally, nanofluids can cause damage due to higher corrosivity.

The availability of modern tools such as CFD are suited to help exploit the advantages of cooling by offering solutions to highly complex three dimensional heat flow and coolant flow problems.

## 13.5 Water Injection

Among different methodologies, water injection is recognized as a robust alternative to replace conventional knock mitigation techniques aiming at lowering air/fuel charge temperature or thermal capacity.

Introducing liquid water in the combustion chamber results in a considerable charge cooling due to the high latent heat of evaporation. Further, when vaporized, water works as a thermal diluent during the combustion process with benefits similar to ones of a cooled EGR (Zhu et al. 2019). As a result, water injection lowers

in-cylinder and exhaust temperature, prevents knock and pre-ignition phenomena, reducing also  $\text{NO}_x$  emissions.

First studies concerning the use of water injection in internal combustion engines date back to the end of 20s (Mason and Flath 1925). In 1925 Mason et al. investigated the influence of water injection in the intake manifold of a spark ignition engine on the power output and fuel consumption. They demonstrated the feasibility of water injection as an effective technique to reduce fuel consumption and to extend the engine compression ratio with further advantages on the power output. Similar studies were conducted by Ricardo in 1931, with the aim of suppressing knock in high-speed ICEs (Ricardo 1931). Then, with the implementation of the intercooler system the interest in water injection as knock mitigator gradually diminished.

More recently, between the end of 90s and begin of 2000s, the growing attention paid to the use of hydrogen in internal combustion engines has triggered a new interest for the water addition. Hydrogen is carbon free, it has a wide range of flammability and high flame speed allowing for a more efficient combustion even at lean mixture conditions. On the other hand, the higher burning velocity increases the in-cylinder pressure peaks and rises the rate, promoting the formation of  $\text{NO}_x$  emissions and pre-ignition (Verhelst et al. 2006). Introducing water in the intake manifold is a solution widely adopted to control pressure rise and to prolong combustion duration, lowering  $\text{NO}_x$  emissions and preventing hydrogen pre-ignition and backfire (Subramanian et al. 2007).

In the last decade, the continuous demand for reducing  $\text{CO}_2$  emissions has fostered the development of small displacement, turbocharged engines with the aim of reducing part load throttling and preserving high specific power at high loads. However, this solution faces high pressure and temperature conditions which increase the knock tendency at high load and speed (Morganti et al. 2017). Therefore, to control knock tendency the spark advance is delayed and the engine is operated with richer mixture to reduce exhaust temperature and preserve the turbocharger integrity. This strategy causes a detriment in performance, consumption and emissions. For this reason, water injection is investigated as it can eliminate the fuel enrichment. Due to the high latent heat of vaporization (2250 kJ/kg), about 6 times higher than RON 95 gasoline (397 kJ/kg), introducing water into the cylinders cools the intake charge, reduces the knock tendency and the exhaust gas temperature.

Experimental tests on production vehicles equipped with a secondary water PFI system highlighted a reduction in fuel consumption up to 13% when suppressing fuel enrichment, and up to 4% in the reference homologation cycle (NEDC) (Brooke 2015). Tornatore et al. found similar results on a downsized port fuel injection (PFI) twin-cylinder turbocharged spark ignition engine, with an improvement in fuel efficiency up to 12% at full load conditions when over-fueling was eliminated (Tornatore et al. 2017). In order to reduce the refill of water thank many technologies are under investigation to develop on-board water recovery, mainly from exhaust and air conditioning systems. Depending on the different solutions, the water temperature and pressure conditions can largely change. This impacts on the vaporization process and, in turn, on the cooling efficiency.



Besides the vaporization, additional benefits on the charge cooling are given by the higher specific heat capacity of water compared to air. In (Hoppe et al. 2016) a numerical study has been performed to define the relative weight of water vaporization and specific heat capacity on the end gas cooling.

Isooctane was considered as gasoline surrogate and a direct water injection system was adopted. When vapor is injected, the cooling effect is only due to the difference in heat capacity: compared to reference case the temperature trend is almost overlapped along the compression stage while a slight difference is found at the spark timing with a reduction in charge temperature of about 7 °C. As a direct water injection system is considered, the vaporization of liquid water occurs in the cylinder, producing a reduction in air-fuel mixture temperature with a drop of about 34 °C compared to the reference case. This outcome indicates that the evaporation may be considered the main trigger of charge cooling. From the analysis of physical-chemical properties the advantages of direct water injection compared to port water injection are significant: introducing water directly in the combustion chamber allows taking full advantage of water vaporization. On the other hand, drawbacks must be considered because the adoption of a secondary direct injection system that increases the complexity and costs.

Hunger et al. performed a numerical analysis on the influence of injection timing on the water evaporation in the cylinder of an engine equipped with a direct water injection system (Hunger et al. 2017). They found a correlation between the start of injection and water evaporation: evaporated mass reduced with advancing the injection timing. At first stage of compression the temperature and pressure conditions are not suitable for water evaporation, hence, when the injection is too early part of the water impinges on the cylinder walls. As the piston approaches the TDC the liquid water evaporates partially subtracting the heat from combustion chamber walls, reducing the charge cooling efficiency. Further, an estimation of water thermal efficiency, defined as the ratio between the effective temperature reduction of end gas and maximum temperature reduction theoretically achievable, highlighted a maximum efficiency of about 36%.

One of the main drawbacks to be overcome, before making water injection a standard on production vehicles, is the water supply. Depending on the engine characteristics and vehicle class, the water request over a WLTP cycle is between the 30% and 50% of fuel amount (Xiao et al. 2018). For this reason, different solutions for on-board water recovery technologies are under investigation with the aim of avoiding continuous refilling of water reservoir by drivers. Even if water recovery from the air conditioning system is the most easily accessible way, as it does not involve complex filtering processes, the dependence of water amount on the season makes this solution unsuitable for granting the total request. Several studies indicate water recovery from exhaust gas as a viable source to satisfy the water demand. In (Sun et al. 2018) different types of water separation systems were proposed to separate condensate from flow stream. For two of them the water amount collected at the exhaust exceeds the water injection demand over a WLTP driving cycle.

## 13.6 Cooled Exhaust Gas Recirculation

Cooled Exhaust Gas Recirculation (EGR) is a well-known technique to reduce knock propensity in spark ignition engines. In the recent past, charge dilution was mainly adopted in Diesel Engines, with the aim of reducing combustion temperature and  $\text{NO}_x$  formation. First application of EGR for knock mitigation in spark ignition engines dates back 1920, when Ricardo (1920) proposed the introduction of “a small proportion of cooled exhaust gas into the cylinder of the supercharging engine along with the fuel and air through the main inlet valve” to suppress knock. More recently, EGR in spark ignition engines has been adopted to reduce fuel consumption and  $\text{NO}_x$  emissions (Tornatore et al. 2019). Firstly, the charge dilution allows reducing pumping losses at part load: as the engine is operated at stoichiometric conditions, the introduction of the exhaust gases in the inlet limits the oxygen amount; hence, a reduction in valve throttling is required to compensate the air mass drop with benefits on fuel economy and  $\text{NO}_x$  emissions. At high load, charge dilution is a viable and relatively low-cost way to mitigate knock. Depending on the system architecture, exhaust gas recirculation can provide different effects on engine performance and efficiency: hot EGR increases the intake temperature improving thermal efficiency and reducing cycle-to-cycle variability at part load; cooled exhaust gas increases its density and thus the volumetric efficiency while reducing the end gas temperature and knock propensity at high load (Shen et al. 2017b). The general trend for spark ignition engines is the adoption of boosted, high specific power engines, equipped with variable valve timing. In these conditions, internal exhaust gas recirculation is operated by means of negative valve overlap. Further, the pumping losses are minimized since the load regulation is mainly carried out by the intake valve lift rather than the throttle. Therefore, the advantages of external exhaust gas recirculation are limited at part load (Conway et al. 2018). Reversely, at full load, cooled EGR can replace fuel enrichment in knock mitigation. Compared to hot EGR, cooled EGR provides higher charge density, improving the volumetric efficiency. Two different technical solutions are available for realizing cooled external EGR, low pressure (LP) EGR and high pressure (HP) EGR. In the first case the exhaust gases are intercepted downstream of the turbine and catalyst, cooled and mixed with fresh air upstream of the compressor. In the HP EGR, the exhaust gases are intercepted before the turbine inlet and mixed to the compressed fresh air downstream the intercooler. When LP EGR is adopted the exhaust gas can corrode compressor and intercooler (Wei et al. 2012). On the other hand, using HP EGR introduces some limitations, mainly at low engine speed, related to the reduced difference between the exhaust gases pressure and intake pressure which restricts the maximum allowable EGR rate (Fischer et al. 2017). In (Potteau et al. 2007) a comparison between LP and HP EGR on a 2 l turbocharged spark ignition engine highlighted a significant difference in BSFC advantages at high load condition. When HP EGR was applied an improvement of 6.6% in fuel efficiency was found, less than half of 13.6% obtained with LP EGR at the same operating condition. This behavior was attributed to the lower advance in KLSA involved with HP EGR compared to LP EGR. In fact, due to the low difference

between HP exhaust gas and boost pressure, the EGR amount was limited and knock suppression effect was lowered.

Knock occurs when the end gas faces temperature and pressure conditions for autoignition. EGR has two opposite effects on the in-cylinder temperature: as a thermal diluent it increases the charge mass, prolongs the combustion duration and reduces the in-cylinder peak. On the other hand, the ratio of specific heats ( $\gamma$ ) increases, due to the reduction in specific heat capacity, with an opposite effect on the temperature and pressure at the end of compression (Parsons et al. 2015). Obviously, the increase in  $\gamma$  improves the thermal efficiency but it also limits the potential of EGR as knock mitigator. Based on these considerations, the role of intake pressure and temperature is apparent in the effectiveness of EGR as knock mitigator. Szybist et al. (2017) investigated the influence of cooled EGR on the knock propensity of a boosted spark ignition engine, at varying the boost pressure. They conducted a numerical and experimental study to correlate the charge dilution with the autoignition delay of unburned gas and, in turn, with knock propensity. In Fig. 13.2 the simulation of pressure-temperature traces of end gas at different intake pressures (color lines) is overlapped to 8 ms autoignition delay contours, for three different EGR levels: 0% (solid line), 10% (dashed line) and 20% (dotted line).

In a first stage (indicated with 1 in the figure), the autoignition delay curve is almost vertical, indicating a strong sensitivity to the temperature; with increase in end gas temperature, a second stage (indicated with 2 in the figure) highlights a dominant influence of pressure with an almost horizontal trend; finally, a third stage

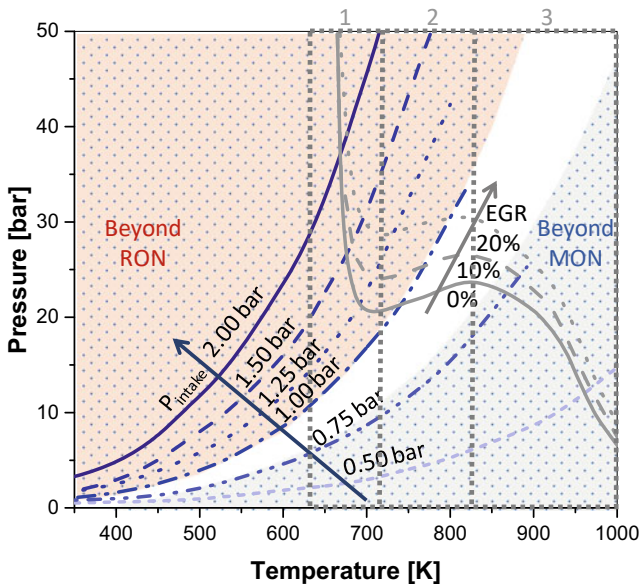


**Fig. 13.2** Pressure-temperature trend of end gas at different intake pressure overlapped to 8 ms autoignition delay contours for three different EGR levels. Redrawn from Szybist et al. (2017)

(indicated with 3 in the figure) at end gas temperature between 850 and 1000 K, is sensitive to both pressure and temperature change.

As apparent in the figure, the first stage of autoignition delay curve is almost independent on the EGR rate, while the charge dilution is strongly effective in the second stage. Looking at unburned gas curves, it can be noted that knock conditions, under engine boost operation, move from pressure sensitive region to temperature sensitive region, where the EGR influence is limited. Similar results were found at different autoignition delay values. Therefore, Szybist concluded that EGR is an effective solution for knock mitigation at aspirated or low boost condition, allowing compression ratio increase for efficiency improvement. As concerns the high boosted pressure engines, the knock propensity is only slightly reduced with exhaust gas recirculation. The high pressure and relatively low combustion chamber temperature typical of end gas knocking autoignition occurrence in such engines prevent a consistent increase of autoignition time by means of EGR. Similar consideration was done by Conway et al. (2018) who studied the influence of a cooled low pressure EGR system on a 1.6 l turbocharged GDI engine with a compression ratio (CR) of 10.5:1 successively increased to 12:1. They found an increase in fuel efficiency over the whole engine map by using LP-EGR on 10.5:1 CR with maximum advantages at high load due to the better combustion phasing involved with knock mitigation. When CR was increased to 12:1, similar results were at part-medium load, while, at high load, the advance in spark timing due to the LP-EGR application did not result in a corresponding advantage on combustion center, thus increasing combustion instability. For this reason, high/full load operations were possible only without EGR.

### 13.7 Use of Anti-knock Fuels

Engine knock is strongly dependent on fuel composition and properties. Currently, fuels anti-knock quality is defined by Research Octane Number (RON) and Motor Octane Number (MON). These parameters have been adopted for gasoline fuels since the 1920s (ASTM International 2012). They are measured by comparing the gasoline with blends of iso-octane and n-heptane, known as primary reference fuels (PRF) in a CFR (Cooperative Fuels Research) engine according to test procedures set by ASTM (American Society for Testing and Materials).

The two main differences between the RON and MON tests are engine speed and intake air temperature: the temperature for a given unburned mixture pressure is higher in the MON test compared to the RON test (Mittal and Heywood 2008).

For practical fuels, RON is higher than MON and their difference is referred as octane sensitivity ( $S = RON - MON$ ): this parameter indicates how fuel's octane rating is "sensitive" to engine speed and intake air temperature. Both, a high RON and a high sensitivity, have been shown to be directionally important with regards to the present evolution of SI engines towards 'beyond RON' operation.

An octane index (OI), has been defined as:  $OI = RON - K \times S$  in Kalghatgi (2001). It represents an effective octane rating, correlating RON and MON values

of a fuel to its knock-limited spark advance (KLSA).  $K$  depends on the pressure-temperature history of the unburned gas, and thus it depends on the engine operating condition.  $K$  is not a fuel property, it can be estimated from experimental data using a multiple linear regression approach that ideally requires a large set of fuels where RON and  $S$  are not correlated (Ratcliff et al. 2018).

It is noted that neither RON nor MON can accurately represent the anti-knock quality of fuels under modern engine conditions.

Practical gasolines contain aromatics, olefins and oxygenates which respond very differently in chemical kinetic terms to increasing pressure compared to PRF which are used to define the RON and MON scales (Leach et al. 2020).

In (Kalghatgi et al. 2014) it is proposed to replace the octane scale, based on primary reference fuels, with a scale based on toluene/n-heptane mixtures (TRF, toluene reference fuels) for ranking practical fuels. The fuel would be tested in the RON test and assigned a toluene number, TN, the volume percent of toluene in the TRF that matches it for knock. In this way, a single number (TN) can specify the anti-knock quality of the fuel at different conditions better than RON or MON. If PRF are used as surrogates, information on RON, MON and the  $K$  value is needed. Moreover, using TN, practical fuels such as ethanol mixtures, which are more resistant to autoignition than iso-octane ( $\text{RON} > 100$ ) can be rated within the scale and matched to an actual rating fuel rather than through extrapolation.

The increase in anti-knock quality of gasolines will be mandatory in the next future: (Kalghatgi 2019) by 2040 all gasoline in the U.S. will possible have  $\text{RON} > 98$  whereas currently the most commonly used gasoline in U.S, has a RON of around 92. Moreover, the importance of high-octane alternative fuels such as alcohols (mainly ethanol, methanol and butanol), MTBE, di-isobutylene will also increase as gasoline additives and/or as pure fuels.

Octane/Toluene numbers indicate the chemical resistance to knock, another fundamental fuel property that can help reducing the knock tendency is the heat of vaporization (HOV), that is the quantity of heat needed for liquid to vapor conversion.

When the fuel is injected in the intake manifold (port fuel injection), the evaporation energy is subtracted both from the engine structure and from the air/fuel mixture entering the combustion chamber. In the case of direct injection, the energy for fuel evaporation is mainly extracted from the mixture with an enhanced cooling effect.

In both cases, fuel evaporation causes charge cooling, proportional to fuel's heat of vaporization. Thus, a reduction in the temperature is achieved in the charge at end of compression, and presumably in the end gas, increasing the autoignition resistance.

In (Stein et al. 2009) the authors studied the effect of injection system on the knock resistance of different ethanol-gasoline blends. Three injection systems were tested in a single cylinder engine: upstream, prevaporized fuel injection; port-fuel injection and direct injection. The results showed that chemical and evaporative charge cooling anti-knock effect were of comparable importance with direct injection. For port-fuel injected engines, the cooling effect was considerably smaller.

Nevertheless, according to the scientific literature, the factor  $K$ , previously introduced, accounts for this effect. The lower temperature achieved at a given pressure

**Table 13.1** Main properties of alcohols, typical gasoline and iso-octane (Verhelst et al. 2019)

	Isooctane	Gasoline (typical)	Methanol	Ethanol	1-Butanol
Chemical formula	C <sub>8</sub> H <sub>18</sub>	Various	CH <sub>3</sub> OH	C <sub>2</sub> H <sub>5</sub> OH	C <sub>4</sub> H <sub>9</sub> OH
Heat of vaporization [kJ/kg]	270	180–350	1100	838	585
Adiabatic flame temperature [K]	2276	2275	2143	2193	2262
Autoignition temperature [K]	690	465–743	738	698	616
Research Octane Number	100	95	109	109	94
Motor Octane Number	100	85	92	98	81
Sensitivity (RON-MON)	0	10	17	11	13

results in lower  $K$ , thus, fuels with higher HOV, such as ethanol blends, will therefore have lower values of  $K$ , all other factors being equal (Ratcliff et al. 2018).

Considering the previously introduced characteristics, among the main fuels that have been regarded as knock suppressors, the ones deserving a specific discussion are Alcohols. The interest in these fuels comes from their benefiting physical-chemical properties when used as fuel for SI engines and from the possibility to produce them from renewable sources, with a reduction in petroleum dependence and net CO<sub>2</sub> emissions.

Table 13.1, extracted from Verhelst et al. (2019), resumes the main alcohols properties in comparison with typical gasoline ones and with the reference iso-octane fuel, more in details, methanol, ethanol and 1-butanol are considered.

Compared to gasoline, alcohol fuels allow achieving a lower temperature throughout the engine cycle thanks to the higher heat of vaporization and to a lower adiabatic flame temperature of alcohol-air mixtures. As widely described before, lower in-cylinder temperatures indicate an improving in the resistance to engine knock.

Besides the capacity of inducing lower in-cylinder temperature, alcohols show high autoignition temperatures that indicate also a high chemical resistance to knocking.

Finally, as widely reported in the scientific literature, alcohol-air mixtures have a higher laminar burning velocity than gasoline: a faster flame propagation allows consuming the end-gas before it can get to autoignition conditions.

Table 13.1 also reports RON, MON and sensitivity. It is worth noting that the effect of charge cooling affects the evaluation of the octane number of alcohols according to common methods. In (Yates et al. 2010), the authors concluded that several values for RON and MON of alcohols, reported in the scientific literature, are biased by the evaporative cooling effect. In this light, they selected values of RON and MON

from researches where the intake charge temperature was controlled regardless of the evaporation effect. The selected numbers are reported in Table 13.1.

Recently, double injection strategies have been investigated and developed in order to realize octane-on-demand concept (Morganti et al. 2016). Two injection systems have been applied on the engine: one for standard gasoline and one for the high octane fuel. They can operate both PFI and DI or PFI + DI (Daniel et al. 2012). The engine is normally fueled with gasoline at low and middle load conditions, while the high octane rating fuel is introduced at higher engine loads where knock mitigation is needed. It is clear that the use of alcohol fuels, directly injecting them in the combustion chamber, allows exploiting also their potential of charge cooling. This system provides flexibility in actively dynamic control of the engine knock (octane rating) (Zhuang et al. 2017).

## 13.8 Conclusions

In recent years, different technologies have been developed in order to overcome the limitations connected to knocking tendency in the new generation of high-performance spark ignition engines. This paper aimed at providing an overview of the different ways for suppressing knock, paying particular attention to the most effective in fuel efficiency improvements. The most important results of this review paper are summarized as follow:

- The conventionally adopted methodology consisting in retarding the spark advance and enriching the air/fuel charge is no longer sustainable in the view of an optimization of internal combustion engines in terms of emissions and fuel consumption. Even though fuel enrichment is adopted in limited regions of engine maps, the growing need for reducing greenhouse gases emissions makes necessary to find alternative solutions with the aim of limiting overfueling at high loads, without penalizing performances.
- Stratified and partially stratified injection can be used to suppress knocking. In these strategies, the mixture enrichment is produced only near the spark plug, taking advantage of the local cooling effect and of a fast flame front propagation associated to rich mixtures. At the same time, the overall air/fuel ratio keeps stoichiometric to solve the emissions problem using TWC, or lean reducing the overall fuel consumption. Stratified operation seems to be promising even if its actuation and control is onerous.
- Combustion chamber geometry optimization and enhanced engine cooling result to be significant for knock mitigation. The advantages of these techniques can be exploited using modern tools for simulation. Utilizing suitable fuel mechanisms, flame and heat transfer models, auto-ignition could be captured ahead of the flame though 3D Computational Fluid Dynamics (CFD) modeling, this could allow to test different combustion chamber geometries to mitigate knock tendency. Finite Element Method (FEM) coupled with CFD can allow a simplified evaluation of



the advantages of engine cooling methods on knock tendency, offering solutions to highly complex three dimensional heat flow and coolant flow problems.

- Cooled exhaust gas recirculation is a powerful technology to mitigate knock in naturally aspirated and lightly boosted engines, but its effectiveness is strongly reduced when applied in high power density engines that utilize higher boost levels. This makes cooled EGR less attractive for modern turbocharged spark ignition engines, working with high boost pressure and compression ratio. Further, even if the EGR implementation can be carried out with relatively minor modifications, some challenges need to be addressed such as misfire, combustion stability and EGR metering.
- Water injection has proven to be a valuable technique of knock mitigation in SI engines. However, significant difficulties need to be overcome before this technology could be extensively adopted. From a consumer point of view, the most relevant problem is the rather large amount of on-board water required and thus the need to often filling up a water tank (roughly every fuel stop) (Xiao et al. 2018). Through the development of suitable methodologies on board water recovery can be a method to overcome the refilling inconvenience.
- With regards to fuels, gasoline with higher octane number will probably be required in the next future to enable higher efficiency in SI engines. A more flexible control of knock tendency could be obtained through octane on demand injection systems: using direct injection of a second fuel, such as alcohol.

The integration of different technologies limiting SI engines knocking tendency may allow obtaining a new class of high-efficiency and low-environmental impact engines, essential to improve the sustainability of the transport sector. It is necessary to keep in mind that every change in engine architecture needs to result in a positive balance with the cost of additional hardware and the complexity for engine management.

## References

- ASTM International (2012) Annual book of ASTM standards 05.01-05.05. West Conshohocken, PA
- Ayala FA, Gerty MD, Heywood JB (2006) Effects of combustion phasing, relative air-fuel ratio, compression ratio, and load on SI engine efficiency. SAE Technical Paper 2006-01-0229. <https://doi.org/10.4271/2006-01-0229>
- Bai Y, Wang Z, Wang J (2010) knocking suppression using stratified stoichiometric mixture in a DISI engine. SAE Technical Paper 2010-01-0597. <https://doi.org/10.4271/2010-01-0597>
- Brooke L (2015) Bosch developing new water-injection system for production engines, SAE automotive engineering magazine. <https://www.sae.org/news/2015/05/bosch-developing-new-water-injection-system-for-production-engines>, last accessed 15 July 2021
- Cairns A, Koupaie MM (2017) The competing chemical and physical effects of transient fuel enrichment during heavy knock in an optical SI engine using ethanol blends. SAE Technical Paper 2017-01-0665. <https://doi.org/10.4271/2017-01-0665>
- Cho S, Song C, Kim N, Oh S, Han D, Min K (2021) Influence of the wall temperatures of the combustion chamber and intake ports on the charge temperature and knock characteristics in



- a spark-ignited engine. *Appl Therm Eng* 182:116000. <https://doi.org/10.1016/j.applthermaleng.2020.116000>
- Conway G, Robertson D, Chadwell C, McDonald J, Kargul J, Barba D, Stuhldreher M (2018) Evaluation of emerging technologies on a 1.6 L turbocharged GDI engine. SAE Technical Paper 2018-01-142. <https://doi.org/10.4271/2018-01-1423>
- Daniel R, Wang C, Xu H, Tian G (2012) Dual-injection as a knock mitigation strategy using pure ethanol and methanol. *SAE Int J Fuels Lubr* 5(2):772–784. <https://doi.org/10.4271/2012-01-1152>
- Finlay IC, Gallacher GR, Biddulph TW, Marshall RA (1988) The application of precision cooling to the cylinder-head of a small, automotive, petrol engine. SAE Technical Paper 880263. <https://doi.org/10.4271/880263>
- Fischer M, Günther M, Berger C, Troeger R, Pasternak M, Mauss F (2017) Suppressing knocking by using CleanEGR—better fuel economy and lower raw emissions simultaneously. In: International Conference on Knocking in Gasoline Engines. Springer, Berlin, Germany, pp 363–384. [https://doi.org/10.1007/978-3-319-69760-4\\_21](https://doi.org/10.1007/978-3-319-69760-4_21)
- Fujimoto M, Iwai K, Kataoka M, Tabata M (2002) Effect of combustion chamber shape on tumble flow, squish-generated flow and burn rate. *JSAE Rev* 23(3):291–296. [https://doi.org/10.1016/S0389-4304\(02\)00201-1](https://doi.org/10.1016/S0389-4304(02)00201-1)
- Gómez Montoya JP, Amell Arrieta AA (2019) Effect of the turbulence intensity on knocking tendency in a SI engine with high compression ratio using biogas and blends with natural gas, propane and hydrogen. *Int J Hydrogen Energy* 44(33):18532–18544. <https://doi.org/10.1016/j.ijhydene.2019.05.146>
- Grandin B, Denbratt I, Bood J, Brackmann C, Bengtsson PE, Tunér A, Mauss F, Sun-den B (2002) Heat release in the end-gas prior to knock in lean, rich and stoichiometric mixtures with and without EGR. SAE Technical Paper 2002-01-0239. <https://doi.org/10.4271/2002-01-0239>
- Heywood J (1988) Internal combustion engine fundamentals. McGraw-Hill Education, New York, NY, USA
- Hoppe F, Thewes M, Baumgarten H, Dohmen J (2016) Water injection for gasoline engines: potentials, challenges, and solutions. *Int J Engine Res* 17(1):86–96. <https://doi.org/10.1177/1468087415599867>
- Hunger M, Böcking T, Walther U, Günther M, Freisinger N, Karl G (2017) Potential of direct water injection to reduce knocking and increase the efficiency of gasoline engines. In: International Conference on Knocking in Gasoline Engines. Springer, Berlin, Germany, pp 338–359. [https://doi.org/10.1007/978-3-319-69760-4\\_20](https://doi.org/10.1007/978-3-319-69760-4_20)
- Hwang K, Hwang I, Lee H, Park H et al (2016) Development of new high-efficiency Kappa 1.6 L GDI engine. SAE Technical Paper 2016-01-0667. <https://doi.org/10.4271/2016-01-0667>
- Jafari S, Dunne JF, Langari M, Yang Z, Pirault JP, Long CA, Thalackottore Jose J (2017) A review of evaporative cooling system concepts for engine thermal management in motor vehicles. *Proc IMechE Part D J Automobile Eng* 231(8):1126–1143. <https://doi.org/10.1177/0954407016674606>
- Johansson A, Hemdal S, Dahlander P (2013) Experimental Investigation of soot in a spray guided single cylinder GDI-engine operated in a stratified mode. SAE Technical Paper 2013-24-0052. <https://doi.org/10.4271/2013-24-0052>
- Kalghatgi G (2001) Fuel anti-knock quality—Part I. Engine studies. SAE Technical Paper 2001-01-3584. <https://doi.org/10.4271/2001-01-3584>
- Kalghatgi G (2019) Development of fuel/engine systems—the way forward to sustainable transport. *Engineering* 5(3):510–518. <https://doi.org/10.1016/j.eng.2019.01.009>
- Kalghatgi G, Head R, Chang J, Viollet Y, Babiker H, Amer A (2014) An alternative method based on toluene/n-heptane surrogate fuels for rating the anti-knock quality of practical gasolines. *SAE Int J Fuels Lubr* 7(3):663–672. <https://doi.org/10.4271/2014-01-2609>
- Kaplan M (2019) Influence of swirl, tumble and squish flows on combustion characteristics and emissions in internal combustion engine-review. *Int J Automotive Eng Technol IJAET* 8(2):83–102. <https://doi.org/10.18245/ijaet.58258>

- Kobayashi H, Yoshimura H, Hirayama T (1984) A study on dual circuit cooling for higher compression ratio. SAE Technical Paper 841294. <https://doi.org/10.4271/841294>
- König G, Sheppard CGW (1990) End gas autoignition and knock in a spark ignition engine. SAE Trans 99:820–839
- Kumar A, Subudhi S (2019) Preparation, characterization and heat transfer analysis of nanofluids used for engine cooling. Appl Therm Eng 160:114092. <https://doi.org/10.1016/j.applthermaleng.2019.114092>
- Leach F, Kalghatgi G, Stone R, Miles P (2020) The scope for improving the efficiency and environmental impact of internal combustion engines. Trans Eng 1:100005. <https://doi.org/10.1016/j.treng.2020.100005>
- Mahendar S, Erlandsson A, Adlercreutz L (2018) Challenges for spark ignition engines in heavy duty application: a review. SAE Technical Paper 2018–01–0907. <https://doi.org/10.4271/2018-01-0907>
- Mason HW, Flath EH (1925) Effects of water injection with increased compression in the internal combustion engine. Doctoral dissertation, Georgia Institute of Technology
- Matsuo S, Ikeda E, Ito Y, Nishiura H (2016) The new Toyota inline 4 cylinder 1.8L ESTEC 2ZR-FXE gasoline engine for hybrid car. SAE Technical Paper 2016-01-0684. <https://doi.org/10.4271/2016-01-0684>
- Mittal V, Heywood J B (2008) The relevance of fuel RON and MON to knock onset in modern SI engines. SAE Technical Paper 2008-01-2414. <https://doi.org/10.4271/2008-01-2414>
- Morganti K, Viollet Y, Head R, Kalghatgi G, Al-Abdullah M, Alzubail A (2017) Maximizing the benefits of high octane fuels in spark-ignition engines. Fuel 207:470–487. <https://doi.org/10.1016/j.fuel.2017.06.066>
- Morganti K, Abdullah M, Alzubail A, Viollet Y (2016) Improving the efficiency of conventional spark-ignition engines using octane-on-demand combustion. Part I: engine studies. SAE Technical Paper 2016-01-0679. <https://doi.org/10.4271/2016-01-0679>
- Pang HH, Brace CJ (2004) Review of engine cooling technologies for modern engines. Proc Inst Mech Eng Part D J Automobile Eng 218(11):1209–1215. <https://doi.org/10.1243/0954407042580110>
- Parsons D, Akehurst S, Brace C (2015) The potential of catalysed exhaust gas recirculation to improve high-load operation in spark ignition engines. Int J Engine Res 16(4):592–605. <https://doi.org/10.1177/1468087414554628>
- Pautsch GW (2003) Spray evaporative cooling system and method. US Patent No. 6, 646, 879
- Peng W, Jizu L, Minli B, Yuyan W, Chengzhi H, Liang Z (2014) Numerical simulation on the flow and heat transfer process of nanofluids inside a piston cooling gallery. Numer Heat Transf Part A Appl 65(4):378–400. <https://doi.org/10.1080/10407782.2013.832071>
- Porot P, Menegazzi P, Ap N (1997) Understanding and improving evaporative engine cooling at high load, high speed by engine tests and 3D calculations. SAE Technical Paper 971792. <https://doi.org/10.4271/971792>
- Potteau S, Lutz P, Leroux S, Moroz S, Tomas E (2007) Cooled EGR for a turbo SI engine to reduce knocking and fuel consumption. SAE Technical Paper 2007-01-3978. <https://doi.org/10.4271/2007-01-3978>
- Radwan MS, Helali AHB, Elfeky SM, Attai YA (2007) An investigation on knock and pre-ignition with tumble induced turbulence. SAE Technical Paper 2007-01-3557. <https://doi.org/10.4271/2007-01-3557>
- Ratcliff MA, Burton J, Sindler P, Christensen E et al (2018) Effects of heat of vaporization and octane sensitivity on knock-limited spark ignition engine performance. SAE Technical Paper 2018-01-0218. <https://doi.org/10.4271/2018-01-0218>
- Reitz RD, Ogawa H, Payri R et al (2020) IJER editorial: the future of the internal combustion engine. Int J Engine Res 21(1):3–10. <https://doi.org/10.1177/1468087419877990>
- Reyes Belmonte M, Copeland C, Hislop D, Hopkins G et al (2015) Improving heat transfer and reducing mass in a gasoline piston using additive manufacturing. SAE Technical Paper 2015-01-0505. <https://doi.org/10.4271/2015-01-0505>

- Ricardo HR (1920) Some experiments on supercharging in a high-speed engine. *Proc Inst Automobile Eng* 15(1):717–770
- Ricardo HR (1931) *The High-Speed Internal-Combustion Engine*. Blackie & son limited
- Robinson K, Campbell NAF, Hawley JG, Tilley DG (1999) A review of precision engine cooling. SAE Technical Paper 1999-01-0578. <https://doi.org/10.4271/1999-01-0578>
- Russ S (1996) A review of the effect of engine operating conditions on borderline knock. SAE Technical Paper 960497. <https://doi.org/10.4271/960497>
- Shen X, Zhang Y, Shen T, Khajorntraidit C (2017a) Spark advance self-optimization with knock probability threshold for lean-burn operation mode of SI engine. *Energy* 122:1–10. <https://doi.org/10.1016/j.energy.2017.01.065>
- Shen K, Li F, Zhang Z, Sun Y, Yin C (2017b) Effects of LP and HP cooled EGR on performance and emissions in turbocharged GDI engine. *Appl Therm Eng* 125:746–755. <https://doi.org/10.1016/j.applthermaleng.2017.07.064>
- Singh E, Dibble R (2018) Effectiveness of fuel enrichment on knock suppression in a gasoline spark-ignited engine. SAE Technical Paper 2018-01-1665. <https://doi.org/10.4271/2018-01-1665>
- Stapf KG, Reis B (2015) Simulation of auto-ignition behaviour for varying gasoline engine operating conditions. In: *Proceedings of the 2nd conference on engine processes*. Berlin, Germany
- Stein RA, House CJ, Leone TG (2009) Optimal use of E85 in a turbo-charged, direct injection engine. SAE Technical Paper 2009-01-1490. <https://doi.org/10.4271/2009-01-1490>
- Subramanian V, Mallikarjuna JM, Ramesh A (2007) Effect of water injection and spark timing on the nitric oxide emission and combustion parameters of a hydrogen fuelled spark ignition engine. *Int J Hydrogen Energy* 32(9):1159–1173. <https://doi.org/10.1016/j.ijhydene.2006.07.022>
- Sun Y, Fischer M, Bradford M, Kotrba A, Randolph E (2018) Water recovery from gasoline engine exhaust for water injection. SAE Technical Paper 2018-01-0369. <https://doi.org/10.4271/2018-01-0369>
- Szybist JP, Wagnon SW, Splitter D, Pitz WJ, Mehl M (2017) The reduced effectiveness of EGR to mitigate knock at high loads in boosted SI engines. *SAE Int J Engines* 10(5):2305–2318
- Teodosio L, Bozza F, Berni F (2019) Effects of nanofluids contaminated coolant on the performance of a spark ignition engine. In: *AIP conference proceedings* 2191:020147. <https://doi.org/10.1063/1.5138880>
- Tilton DE, Tilton CL (1993) High heat flux evaporative spray cooling. US Patent No. 5, 220, 804
- Tornatore C, Sjöberg M (2021) Optical investigation of a partial fuel stratification strategy to stabilize overall lean operation of a DISI engine fueled with gasoline and E30. *Energies* 14(2):396. <https://doi.org/10.3390/en14020396>
- Tornatore C, Siano D, Marchitto L, Iacobacci A, Valentino G, Bozza F (2017) Water injection: A technology to improve performance and emissions of downsized turbocharged spark ignited engines. *SAE Int J Engines* 10(5):2319–2329. <https://doi.org/10.4271/2017-24-0062>
- Tornatore C, Bozza F, De Bellis V, Teodosio L, Valentino G, Marchitto L (2019) Experimental and numerical study on the influence of cooled EGR on knock tendency, performance and emissions of a downsized spark-ignition engine. *Energy* 172:968–976. <https://doi.org/10.1016/j.energy.2019.02.031>
- Ueda T, Okumura T, Sugiura S, Kojima S (1999) Effects of squish area shape on knocking in a four-valve spark ignition engine. SAE Technical Paper 1999-01-1494. <https://doi.org/10.4271/1999-01-1494>
- Vafamehr H, Cairns A, Sampson O, Koupaie MM (2016) The competing chemical and physical effects of transient fuel enrichment on heavy knock in an optical spark ignition engine. *Appl Energy* 179:687–697. <https://doi.org/10.1016/j.apenergy.2016.07.038>
- Verhelst S, Turner JW, Sileghem L, Vancoillie J (2019) Methanol as a fuel for internal combustion engines. *Prog Energy Combust Sci* 70:43–88. <https://doi.org/10.1016/j.pecs.2018.10.001>
- Verhelst S, Sierens R, Verstraeten S (2006) A critical review of experimental research on hydrogen fueled SI engines. SAE Technical Paper 2006-01-0430. <https://doi.org/10.4271/2006-01-0430>
- Wang Z, Liu H, Reitz RD (2017) Knocking combustion in spark-ignition engines. *Prog Energy Combust Sci* 61:78–112. <https://doi.org/10.1016/j.pecs.2017.03.004>

- Wei H, Zhu T, Shu G, Tan L, Wang Y (2012) Gasoline engine exhaust gas recirculation—a review. *Appl Energy* 99:534–544. <https://doi.org/10.1016/j.apenergy.2012.05.011>
- Xiao G, Yang Z, Isenstadt A (2018) Fuel-efficiency technology trend assessment for LDVs in China: advanced engine technology. International council on clean transportation. [https://theicct.org/sites/default/files/publications/PV\\_Tech\\_Trend\\_Engine\\_20180917.pdf](https://theicct.org/sites/default/files/publications/PV_Tech_Trend_Engine_20180917.pdf)
- Yates A, Bell A, Swarts A (2010) Insights relating to the autoignition characteristics of alcohol fuels. *Fuel* 89(1):83–93. <https://doi.org/10.1016/j.fuel.2009.06.037>
- Yue Z, Som S (2021) Fuel property effects on knock propensity and thermal efficiency in a direct-injection spark-ignition engine. *Appl Energy* 281:114221. <https://doi.org/10.1016/j.apenergy.2019.114221>
- Zaccardi J-M, Laget O, Pagot A, Mokhtari S, Leone T (2010) Investigations on the effects of in-cylinder charge motion and injection mode on pre-ignition in highly boosted spark ignition engines. In: 19th Aachener Kolloquium Fahrzeug-und Motorentechnik. Aachen, Germany, pp 1323–1349
- Zhou L, Zhang X, Zhong L, Yu J (2020) Effects of flame propagation velocity and turbulence intensity on end-gas auto-ignition in a spark ignition gasoline engine. *Energies* 13:5039. <https://doi.org/10.3390/en13195039>
- Zhu S, Hu B, Akehurst S, Copeland C, Lewis A, Yuan H, Kennedy I, Bernards J, Branney, C (2019) A review of water injection applied on the internal combustion engine. *Energy Convers Manag* 184:139–158. <https://doi.org/10.1016/j.enconman.2019.01.042>
- Zhuang Y, Qian Y, Hong G (2017) The effect of ethanol direct injection on knock mitigation in a gasoline port injection engine. *Fuel* 210:187–197. <https://doi.org/10.1016/j.fuel.2017.08.060>

# Chapter 14

## Explicit Equations for Designing Surrogate Gasoline Formulations Containing Toluene, n-Heptane and Iso-pentane



Roger F. Cracknell, Jack Scrutton, and Sandro Gail

**Abstract** Simple surrogate formulations for gasoline are useful for modelling purposes and for comparing experimental results using a carefully designed fuel. The most common approach is to start with Primary Reference Fuels (PRF)—i.e., isooctane and n-heptane. These have the disadvantage that they cannot replicate the octane sensitivity (RON-MON) of a real fuel, and so it is common to add toluene to make a Toluene Primary Reference Fuel (TPRF) surrogate. The vapour pressure of TPRFs is much lower than a real fuel, and so the flash boiling behaviour of a real fuel cannot be properly replicated. To overcome the volatility challenges, an alternative to TPRF is advocated which involves replacing some or all the isooctane by isopentane. In the event of total replacement, a three-component “THIP” (Toluene, n-Heptane, Iso-Pentane) surrogate fuel is produced. It is shown that by adding isopentane it is possible to have a simple surrogate that can reproduce the lower part of the distillation curve of a real fuel. Explicit equations are presented that allow THIP surrogates to be created based on a desired RON, MON and DVPE (Research Octane Number, Motor Octane Number, Dry Vapour Pressure Equivalent).

**Keywords** RON · MON · Fuel sensitivity · Surrogate gasoline · Modelling · IDT · DVPE

### 14.1 Introduction

The main classes of hydrocarbon components in gasoline are Paraffins, Isoparaffins, Olefins, Naphthenes, and Aromatics (PIONA), and an analysis of the hydrocarbon content by Gas Chromatography (GC) frequently summarises the content according

---

R. F. Cracknell (✉) · J. Scrutton  
Shell Global Solutions (UK), Shell Centre, London SE1 7NA, United Kingdom  
e-mail: [roger.cracknell@shell.com](mailto:roger.cracknell@shell.com)

S. Gail  
Shell Global Solutions GmbH, Hohe-Schaar Straße 36, D-21107 Hamburg, Germany

J. Scrutton  
University of Bath, Claverton Down, Bath BA2 7AY, United Kingdom

to the PIONA classes. Market gasolines also frequently contain oxygenated species such as ethanol.

It is often desirable to create simplified surrogate fuels which can emulate a number of the key features of real fuels: the simplified composition enables experiments to be more easily compared as well as enabling faster or simpler chemical kinetic modelling, including incorporation into full chemistry Computational Fluid Dynamics (CFD) models.

The simplest surrogate fuels are usually based on the gasoline Primary Reference Fuels (PRFs), isooctane and n-heptane, which are used within the Research Octane Number (RON) and Motor Octane Number (MON) tests on a Cooperative Fuel Research (CFR) Engine (ASTM international 2012; ASTM 2011). Since PRFs provide the octane standard, then by definition the RON and MON of a given PRF blend must be identical, for example a mixture containing 95% by volume of isooctane and 5% by volume of n-heptane must have, by definition, both a RON and MON of 95. However, the RON of a real fuel is typically around 10 units higher than its MON because PRF blends tend to show more low temperature reactivity than real fuels. The difference between RON and MON is commonly referred to as octane sensitivity (S). Toluene is frequently added to a PRF mixture to make a Toluene Primary Reference Fuel (TPRF) with a realistic octane sensitivity and is in a sense used to be representative of all species that suppress Low Temperature Heat Release (LTHR), such as olefins and ethanol, even though it may mean that the surrogate has a higher aromatic content than a normal gasoline (Westbrook et al. 2017). For this reason, TPRFs are widely studied (Morgan et al. 2010; Kalghatgi et al. 2015; Knop et al. 2014; Ghosh et al. 2006; Singh and Sarathy 2021; Singh et al. 2017; Javed et al. 2016; Lorenzo et al. 2019; Hoth et al. 2018). For the purposes of nomenclature, the terms Toluene Primary Reference Fuel, Toluene Reference Fuel (TRF) and Toluene Standardisation Fuel (TSF) are treated in this work as equivalent and interchangeable, although we note that the TSF plays a special role in validating RON and MON tests as per ASTM D2699 and D2700.

There is always a balance between the chemical simplicity of a gasoline surrogate, and the ability to match the features of a real fuel. Some approaches result in increasing the number of components, to more accurately represent the chemical and physical properties of the gasoline. Alternative methods have been proposed which focus on the elementary molecular parameters in the target fuel, rather than on broad molecular classes, such as the minimalist functional group (MFG) approach in which Jameel et al. (2018) considered an implicit methodology by emulating the target fuel's H/C ratio and Derived Cetane Number (DCN). Alternatively, in the Hybrid Chemistry (HyChem) model of Wang et al. (2018), and other related methods (Zhang et al. 2021), in which empirical lumped kinetic parameters are used to model thermal and oxidative pyrolysis. An overview of different approaches to gasoline surrogate formulation is given in a recent review by Sarathy et al. (2018).

Distillation properties, particularly the vapour pressure, play a significant role in spray development, with spray penetration in gasoline direct injection systems being strongly influenced by the flash boiling behaviour of the lighter components (Romunde et al. 2007). The vapour pressure of a market gasoline is usually quantified

in terms of the Dry Vapour Pressure Equivalent (DVPE) which normally ranges from 40 to 110 kPa (Richards 2014). Higher values of DVPE are normally preferred in the winter to ensure easy starting, while lower values are preferred in the summer to limit evaporative emissions. A deficiency of the TPRF surrogate approach is the inability to represent the volatility of real gasoline fuels: TPRF surrogates typically have DVPEs between 7 and 12 kPa—a value which is roughly an order of magnitude lower than the typical range of commercially available gasolines.

An approach which has been developed in two recent publications (Gail et al. 2021a, 2021b) is to replace the iso-octane with isopentane in a TPRF surrogate. Isopentane has a RON of 93.2, and a MON of 90.8, but is much more volatile than iso-octane (Gary et al. 2007), thereby enabling a surrogate fuel to be developed with a much more realistic DVPE. From the practical standpoint of making a surrogate containing a volatile component, it is much easier to use isopentane which is liquid at room temperature and pressure, than. We have adopted the term “isopentane containing surrogate” for a surrogate in which some of the iso-octane has been replaced. When iso-octane is completely replaced by isopentane in a TPRF, a new three-component surrogate we term “THIP” (Toluene, n-Heptane, Iso-Pentane) is obtained.

This paper is structured as follows: In the next section, we summarise some of our key findings from recent work on surrogate blends containing isopentane, illustrating how they can be used to match the properties and behaviour of market gasolines. In the following section, we provide a guide as to how THIP surrogates can be designed, given a target RON, MON and DVPE.

## 14.2 Properties of Isopentane-Containing Surrogates

Table 14.1 and Fig. 14.1 show an example of 3 THIP formulations and one TPRF formulation designed to match the properties of a 95 RON market gasoline fuel. All of the surrogates are able to approximately match the RON, MON and sensitivity of the reference fuel. However, the presence of the isopentane means that a THIP surrogate can represent the DVPE and density of a market fuel more accurately than is possible with a TPRF surrogate. THIP blends B and C span the reference fuel in terms of the lower part of the distillation curve. It is not possible to replicate the upper part of the distillation curve with an isopentane containing surrogate unless heavier species are present. This could be important, for example, when investigating the particulate forming tendency of fuels.

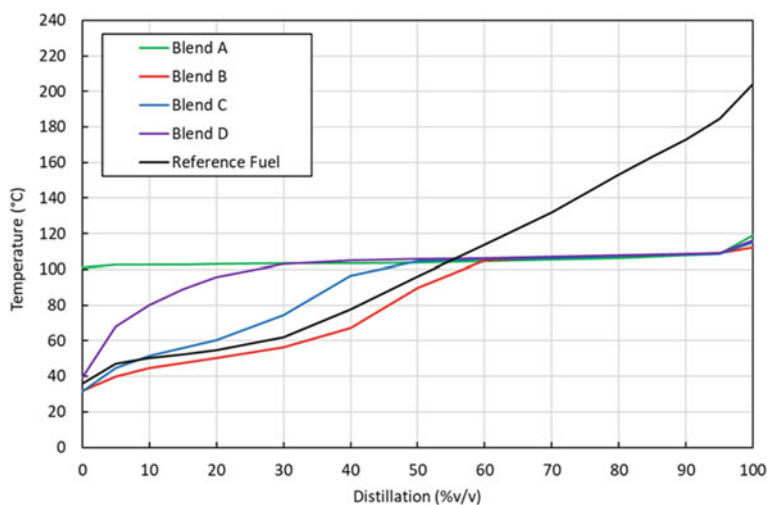
The THIP surrogates agree reasonably well in ignition delay time (IDT) measured on a rapid compression machine with the reference fuel, as shown in Fig. 14.2. The TPRF surrogate (Blend A) is also shown for completeness. Pentane isomers have been the subject of detailed investigation (Bugler et al. 2015), and chemical kinetic mechanisms are available which include isopentane (Sarathy et al. 2016). Figure 14.3 shows the simulated IDT for fuel B plotted against the data from Fig. 14.2 using



**Table 14.1** TPRF and THIP surrogates formulated to match the properties of a 95 RON market gasoline

	Unit	TPRF blend A	THIP blend B	THIP blend C	THIP blend D	Reference fuel
Isooctane	%vol	15.0	0.0	0.0	0.0	EN228 compliant composition
Isopentane		0.0	45.0	32.0	14.0	
n-Heptane		20.0	10.0	13.0	18.0	
Toluene		65.0	45.0	55.0	68.0	
RON	–	95.4	94.8	95.4	95.6	95.8
MON	–	84.8	86.3	85.4	84.7	85.0
DVPE	kPa	11.9	71.9	56.2	32.4	59.4
Density	kg/m <sup>3</sup>	808.4	745.4	770.2	804.6	756.8
Sensitivity = RON–MON	–	10.6	8.5	10.0	10.9	10.8

Data from Gail et al. (2021a)

**Fig. 14.1** Measured distillation curves (DIN EN ISO 3405) of TPRF and THIP Surrogates formulated to match the properties of a 95 RON market gasoline (redrawn from Gail et al. 2021b)

the mechanism in Bugler et al. (2015), suggesting that existing chemical kinetic mechanisms are able to adequately represent THIP surrogates.

In a separate piece of work, an isopentane containing surrogate was produced to match the RON and MON of premium gasoline (RON 98). Table 14.2 shows the properties of the surrogate and the reference premium gasoline (RPG) to which it is matched. It also shows the properties of another 98 RON gasoline, which is labelled as “Development Fuel” with a slightly different RON and MON to the RPG.



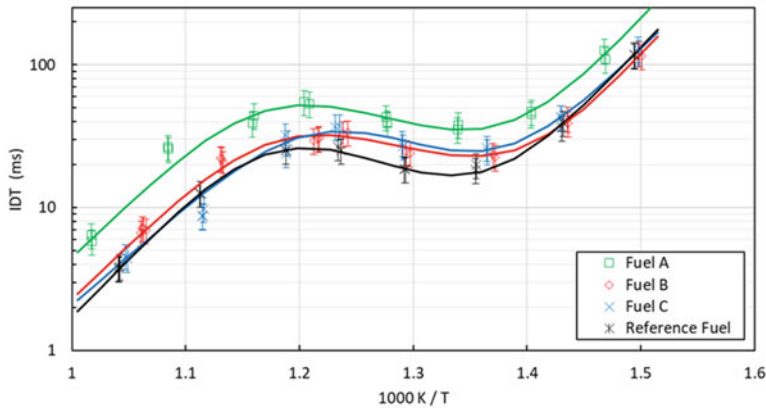


**Fig. 14.2** Ignition Delay Time measured in a rapid compression machine at RWTH Aachen for two THIP surrogates and the reference fuel ( $P_c = 15$  bar,  $\phi = 1$ ). Data from Gail et al. (2021b)

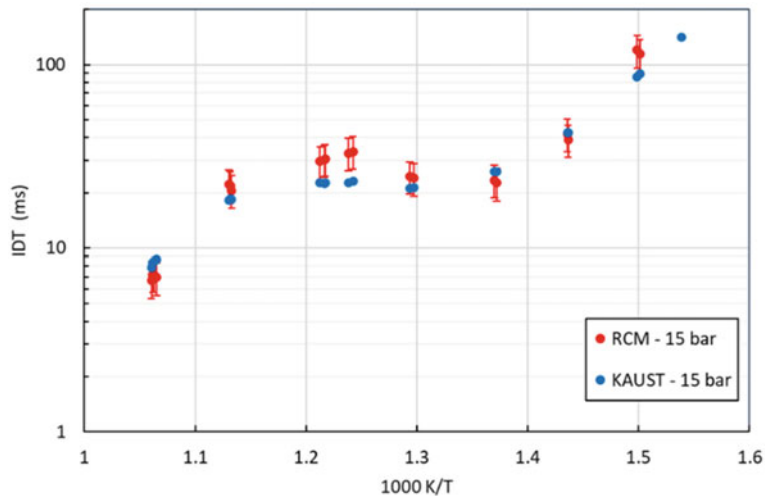


**Fig. 14.3** Comparison of IDT curves between experimental and simulation results for a THIP surrogate composition using the KAUST 2016 mechanism (Gail et al. 2021b) ( $P_c = 15$  bar,  $\phi = 1$ )

Using the “Development Fuel” allowed assessment of the repeatability of the engine knock measurements.

As reported in Gail et al. (2021a), the three fuels described in Table 14.2 were run in a V8 turbocharged DI engine and the knocking characteristics of the three fuels determined as a function of the 50% mass fraction burned point (MFB50). Two different metrics were used to quantify the knocking behaviour—firstly the maximum amplitude of the pressure oscillation (MAPO), and the knock frequency. Figure 14.4 shows the 99.5 percentile value of MFB50 which exceed the threshold MAPO value

**Table 14.2** Properties of an isopentane-containing surrogate matched to 98 RON Reference Premium Gasoline

Fuel description	Reference premium gasoline (RPG)	Surrogate for RPG	Development fuel
Density at 15 °C (kg/m <sup>3</sup> )	738.0	729.5	754.5
DVPE (kPa)	87.9	85.1	57.3
RON	98.0	97.9	98.7
MON	87.9	88.0	86.7
IBP (°C)	22.4	28.0	31.4
E70 (%vol)	32.0	52.3	23.9
Composition	Full boiling range premium gasoline	1.1 vol% isooctane 4.16 vol% n-heptane 40.14 vol% toluene 54.6 vol% isopentane	Full boiling range premium gasoline, with a slightly different RON and MON to RPG

Data from Gail et al. (2021a)

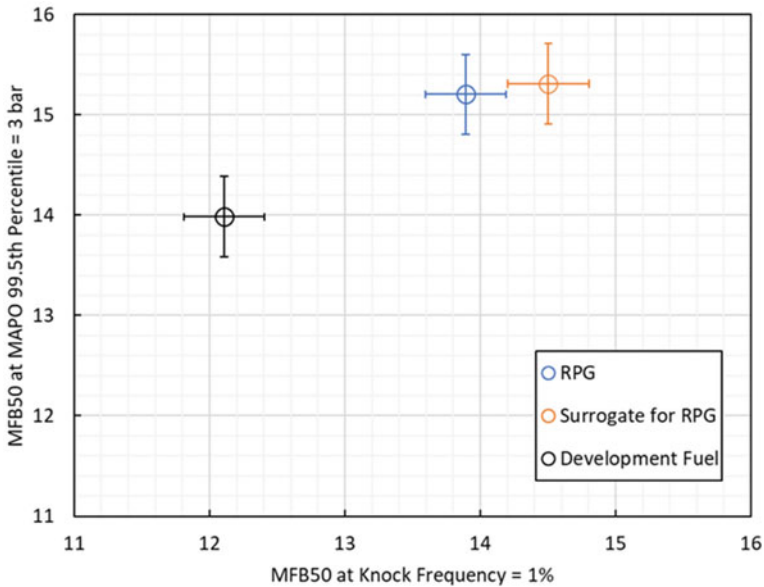


**Fig. 14.4** Comparison of knock limit combustion phasing for the reference premium gasoline fuel (RPG), and isopentane containing surrogate designed to match the RPG, and a third fuel (development fuel) with a marginally different RON and MON. Redrawn from Gail et al. (2021a)

of 3 bar plotted against the MFB50 at which 1% of the cycles are knocking. The error bars are determined by the repeatability of results for the development fuel. The RPG fuel and the isopentane-containing surrogate behave in a very similar fashion in terms of their knocking behaviour, whereas the development fuel with a marginally higher RON and octane sensitivity is able to operate between 1 and 2 crank angle degrees of more advanced combustion to achieve the same knocking behaviour.

### 14.3 Defining Surrogate Compositions

A range of empirical equations and mathematical models exist for predicting TPRF composition based on a given RON and MON. Morgan et al. (2010) developed a non-linear-by-liquid-volume model from experimentally determined RON and MON values of TPRF surrogates. Kalghatgi et al. (2015) developed a method which uses coefficients derived from the octane number of a PRF and the toluene mass fraction to calculate the RON and sensitivity of the TPRF. Knop et al. used a linear-by-mole method based on the pure components' RON and MON values (Knop et al. 2014).

These methods define required TPRF compositions to match a given RON and MON. Although the main benefit of using THIP surrogates is their much-improved ability to replicate gasoline properties other than octane number, matching the RON and MON of a real gasoline whilst achieving this is very much desired. Therefore, this section aims to develop an equivalent method to those described above for THIP surrogates.

In order to define a THIP composition for a target RON and MON, equations mapping composition into RON and MON space are first required. A second order non-linear-by-liquid-volume (nLbV) model was initially chosen due to the success of this approach in modelling TPRF surrogates by Morgan et al. (2010). This is represented by

$$\begin{aligned}
 RON = & a_{tol}v_{tol} + a_{iP}v_{iP} + a_{nH}v_{nH} + a_{tol,iP}v_{tol}v_{iP} + a_{iP,nH}v_{iP}v_{nH} \\
 & + a_{tol,nH}v_{tol}v_{nH} + a_{tol,iP,nH}v_{tol}v_{iP}v_{nH}
 \end{aligned}
 \tag{14.1}$$

$v_{tol}$ ,  $v_{iP}$ ,  $v_{nH}$  represent the volume fraction of toluene, iso-pentane and n-heptane, respectively.  $a_{tol}$ ,  $a_{iP}$  and  $a_{nH}$  represent the coefficients for toluene, iso-pentane and n-heptane, respectively.  $a_{tol,iP}$ ,  $a_{iP,nH}$  and  $a_{tol,nH}$  represent the coefficients for the binary interaction terms.  $a_{tol,iP,nH}$  represents the coefficient for the ternary interaction term. The equivalent equations for MON and sensitivity are of the same form, with different coefficient values.

An experimental matrix, which was designed to give maximum coverage of the range of THIP compositions, is shown in Table 14.3, along with the RON, MON and DVPE of each blend, measured in a CFR engine at the Shell Technology Centre in Hamburg (STCHA). "N/A" denotes where accurate measurements could not be made. The MON of pure isopentane could not be measured due to the volatility of

**Table 14.3** Experimental matrix of THIP surrogates. RON and MON measurements were made in a CFR engine at Shell Research and technology Centre Hamburg. DVPE measurements were made using DIN ISO 13016-1

Blend	Isopentane	n-Heptane	Toluene	RON	MON	DVPE
	%vol					kPa
a	100.0	0.0	0.0	92.4	90.8	135.7
b	0.0	0.0	100.0	113.8	106.0	7.3
c	50.0	50.0	0.0	N/A	N/A	83.6
d	50.0	0.0	50.0	102.1	91.3	79.4
e	0.0	50.0	50.0	65.0	58.0	10.5
f	33.3	33.3	33.3	75.3	69.0	58.7
g	66.7	16.7	16.7	83.6	79.4	100.9
h	16.7	66.7	16.7	N/A	N/A	N/A
i	16.7	16.7	66.7	96.8	85.7	35.1
j	75.0	12.5	12.5	86.3	82.7	111.9
k	12.5	75.0	12.5	N/A	N/A	37.4
l	12.5	12.5	75.0	101.2	89.9	29.3
m	68.0	5.0	27.0	94.8	88.0	106.9
n	62.0	3.0	35.0	97.8	89.1	101.1
o	59.0	1.0	40.0	97.8	89.4	98.9

MON data for blend a is from Gail et al. (2021b)

isopentane, therefore a value of 90.8 has been used here (Gary et al. 2007). This dataset was used as the training dataset for a least-squares technique, performed using the R programming language, the output of which is the values for each of the coefficients in the above equation. The coefficients of the 2nd order model are shown in Table 14.4. By definition, a coefficient for the sensitivity equation is equal to the difference between the corresponding RON coefficient and MON coefficient.

The performance of the model was tested on the three THIP blends which were investigated in a previous study by the authors (Gail et al. 2021a), blends B, C and D in Table 14.1. The compositions of these blends are used as the model input to predict the RON and MON for each. The sum of squared errors (SSE) is then calculated using

**Table 14.4** Coefficients for the non-linear-by-volume model equations

Coefficient	$a_{tol}$	$a_{iP}$	$a_{nH}$	$a_{tol,iP}$	$a_{iP,nH}$	$a_{tol,nH}$	$a_{tol,iP,nH}$
RON	113.8	92.5	0.0	-6.2	8.0	32.4	131.3
MON	105.7	91.1	0.0	-26.7	36.9	20.0	-13.1
Sensitivity	8.2	1.4	0.0	20.5	-28.9	12.4	144.4

$$SSE = \sum_{i=1}^N (\text{RON}_{\text{expt},i} - \text{RON}_{\text{calc},i})^2 \quad (14.2)$$

With the coefficients for the 2nd order RON and MON equations calculated, it is now possible to determine the required THIP composition for a target RON and MON. First, a new variable,  $z$ , must be introduced, defined as

$$z = v_{iP} / (v_{iP} + v_{nH}) \quad (14.3)$$

After substitution, this allows Eq. 14.1 to be rewritten as

$$\begin{aligned} \text{RON} = & a_{\text{tol}}v_{\text{tol}} + a_{iP}z(1 - v_{\text{tol}}) + a_{\text{tol},iP}v_{\text{tol}}z(1 - v_{\text{tol}}) + a_{iP,nH}z(1 - z)(1 - v_{\text{tol}})^2 \\ & + a_{\text{tol},nH}v_{\text{tol}}(1 - z)(1 - v_{\text{tol}}) + a_{\text{tol},iP,nH}v_{\text{tol}}z(1 - z)(1 - v_{\text{tol}})^2 \end{aligned} \quad (14.4)$$

Since the equivalent equation can also be written for the MON, these two equations can be solved simultaneously, using a tool such as MATLAB, to determine  $v_{\text{tol}}$  and  $z$ . These two values can then be used to calculate  $v_{iP}$  and  $v_{nH}$ , since  $v_{\text{tol}}$ ,  $v_{iP}$ , and  $v_{nH}$  must sum to 1.

It was decided to also to develop a mole-based model, equivalent to that developed by Knop et al. (2014) for TPRF surrogates, to investigate how this would compare to the full 2nd order non-linear-by-volume model. For the RON, this is described by

$$\text{RON} = a_{\text{tol}}x_{\text{tol}} + a_{iP}x_{iP} + a_{nH}x_{nH} \quad (14.5)$$

where  $x_{\text{tol}}$ ,  $x_{iP}$  and  $x_{nH}$  represent the mole fractions of toluene, isopentane and n-heptane in the surrogate, respectively.

Since the RON and MON of n-heptane both equal zero, there is no contribution to the surrogate RON and MON from n-heptane, therefore the equation is reduced to

$$\text{RON} = a_{\text{tol}}x_{\text{tol}} + a_{iP}x_{iP} \quad (14.6)$$

Using the same set of data to train the model, a linear least squares technique was used to determine the coefficients  $a_{\text{tol}}$  and  $a_{iP}$ , for both the RON and MON equations, shown in Table 14.5. The RON and MON model equations can then be solved simultaneously to determine  $x_{\text{tol}}$  and  $x_{iP}$  for a target RON and MON.

**Table 14.5** Coefficients for the mole-based model equations

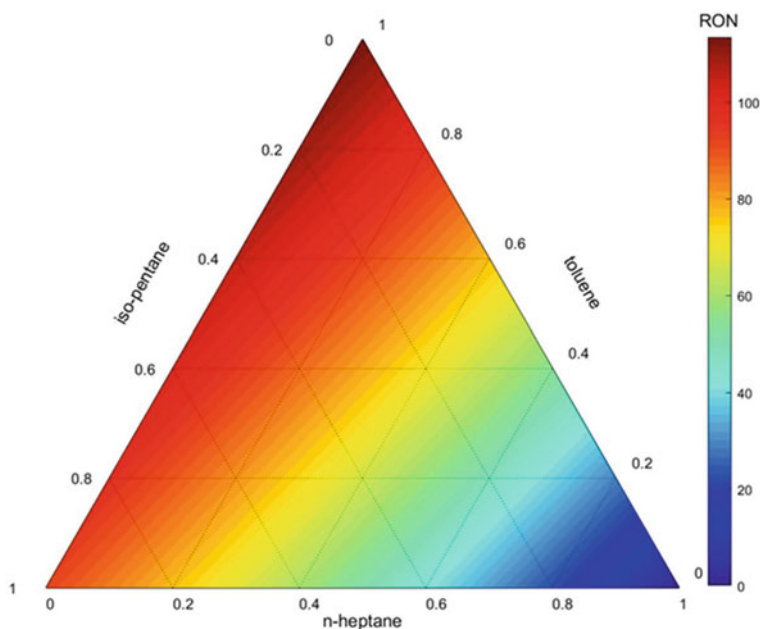
Coefficient	$a_{\text{tol}}$	$a_{iP}$	$a_{nH}$
RON	113.5	91.7	0.0
MON	101.3	87.8	0.0
Sensitivity	12.2	3.9	0.0

**Table 14.6** SSE analysis of the two models

	nLbV	Mole-based
RON	3.8	0.6
MON	1.1	4.6
Sensitivity	6.9	5.5
Total	11.8	10.7

Once again, the model's performance was tested by calculating the sum of squared errors for blends B, C and D in Table 14.1. The SSE analysis of both the 2nd order non-linear-by-volume model and the mole-based model is summarised in Table 14.6. The mole-based model has the lowest SSE for the RON measurements, and the 2nd order non-linear-by-volume (nLbV) model has the lowest SSE for the MON measurements. Due the total SSE being lowest when using the mole-based model, this was used in the subsequent part of the investigation. The ternary plots of RON, MON and sensitivity against composition, for the mole-based model, are shown in Figs. 14.5, 14.6, and 14.7, respectively.

The mole-based model predictions plotted against the measured values of RON and MON for both the training data (in Table 14.2) and the three blends used to test the model (from Table 14.1) are shown in Figs. 14.8 and 14.9, respectively. The line  $y = x$ , which would represent a perfect model, is also plotted.

**Fig. 14.5** Ternary plot for the RON of THIP surrogates predicted by the mole-based model

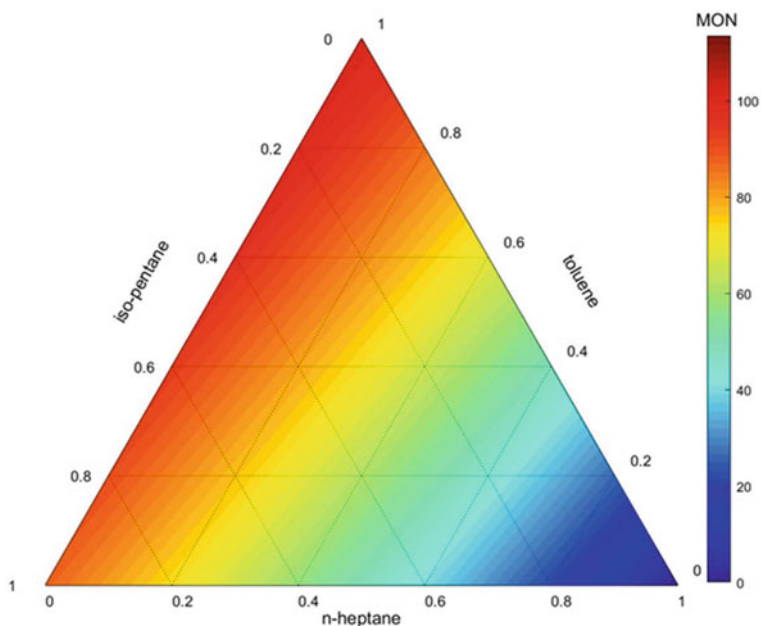


Fig. 14.6 Ternary plot for the MON of THIP surrogates predicted by the mole-based model

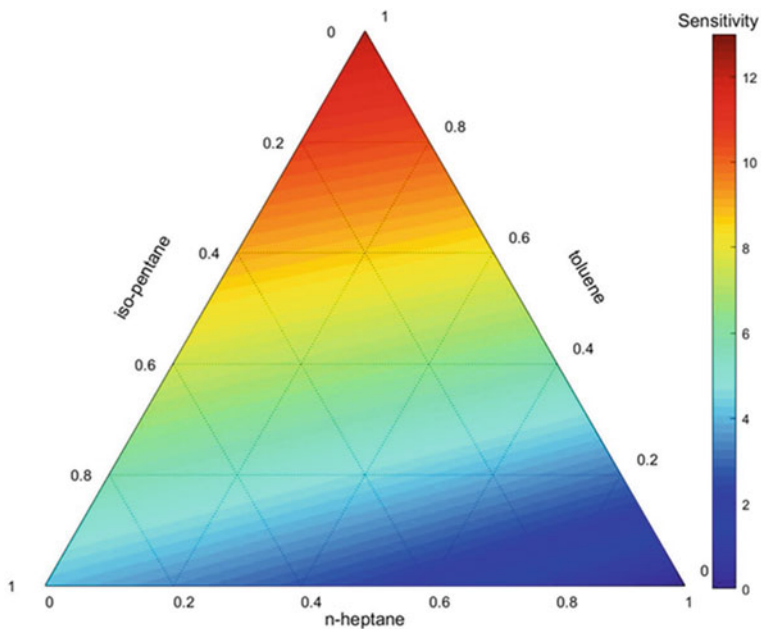


Fig. 14.7 Ternary plot for the sensitivity of THIP surrogates predicted by the mole-based model

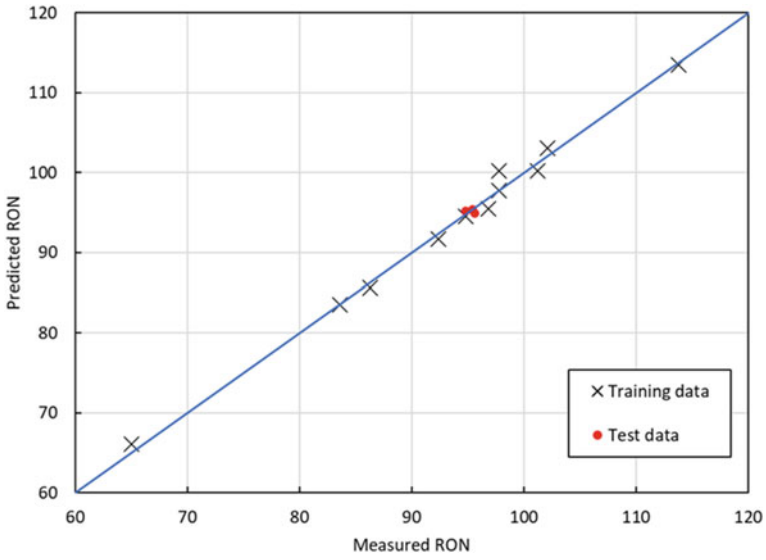


Fig. 14.8 RON measured in the CFR engine against RON predicted by the mole-based model

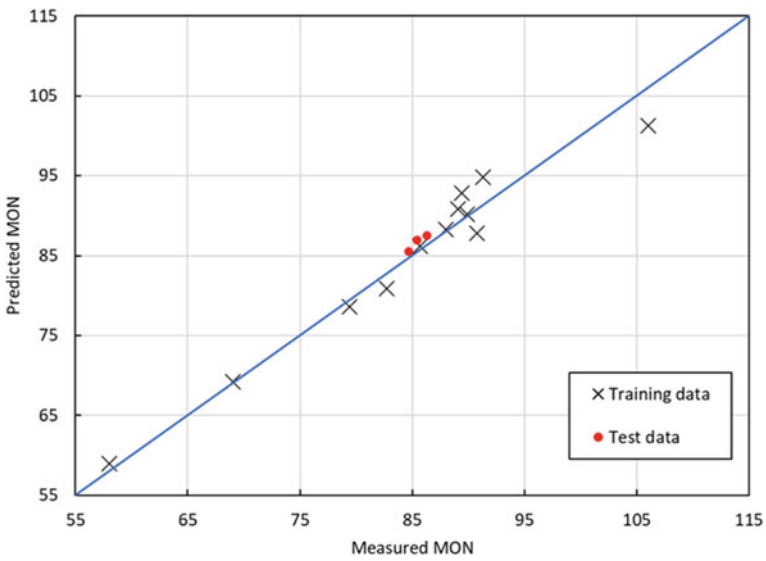


Fig. 14.9 MON measured in the CFR engine against MON predicted by the mole-based model



A further aim was to define the surrogate composition to match a target DVPE as closely as possible, as well as the octane numbers. The DVPE was modelled using the Chevron equation (Gary et al. 2007), described by

$$DVPE_{blend} = \left( \sum_{i=1}^N v_i DVPE_i^{1.32} \right)^{1/1.32} \quad (14.7)$$

The Chevron coefficient was optimised to 1.32 using the measured DVPE values for each of the blends in Table 14.2. The ternary plot for the DVPE against composition using this model is shown in Fig. 14.10. Since matching the surrogate to target RON, MON and DVPE exactly is very rarely possible, it was decided to generate the composition required to match the RON and MON to within 1 unit of each, and then within these boundaries, to optimise the DVPE to be as close to the target as possible. To achieve this, the mole-based model equations are solved to generate a range of solutions that give a RON and MON within 1 unit of the targets. Each of these compositions generated are used as the input to Eq. 14.7, and the composition with the closest DVPE to the target is selected.

For example, if the target RON and MON are set at 95 and 85 (the predicted RON must be between 94 and 96, and predicted MON must be between 84 and 86), then the model produces solutions which have predicted DVPEs in the range 8.4–61.4 kPa. Since the EN228 fuel specification for DVPE is 45–60 kPa for summer,

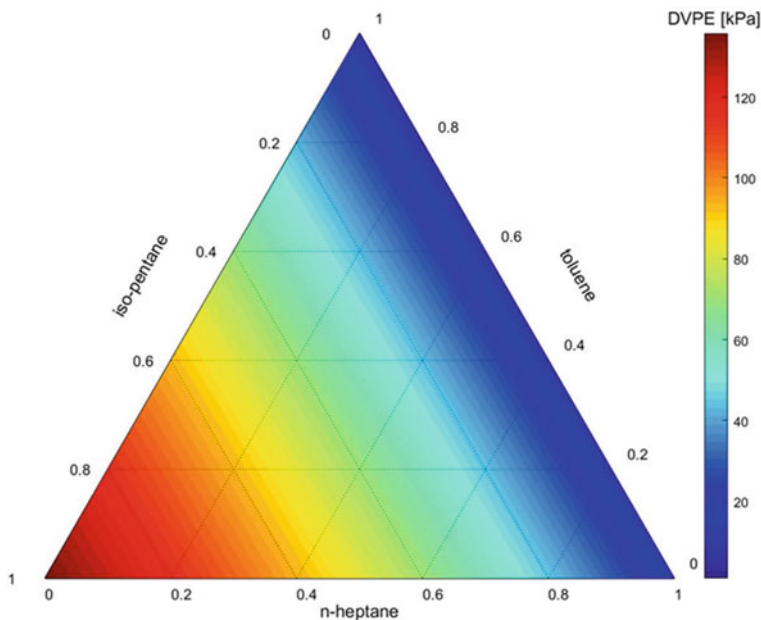


**Fig. 14.10** Ternary plot for the DVPE of THIP surrogates predicted using the Chevron method

and 70–100 kPa for winter (Richards 2014), then any DVPE within the summer specifications can be closely matched for this RON and MON. If a DVPE of 60 kPa is chosen, the required composition, by % volume, is 53.3% toluene, 32.4% isopentane, and 14.3% n-heptane, which gives a predicted RON and MON of 94.08 and 85.84, respectively.

It is of course possible to alter the acceptable deviation from the target RON and MON, depending on the importance of matching particular properties. Using the example of a 95 RON and 85 MON fuel as above, solving the equations to give RON and MON values within 0.5 units of each produces solutions which have predicted DVPEs in the range 8.4–39.5 kPa. This reduced range of DVPEs illustrates the trade-off that must be made when designing surrogates to match multiple properties.

A further benefit of using THIP surrogates is that lower densities are achievable when compared to using TPRF surrogates (Gail et al. 2021b). Figure 14.11 illustrates the ternary plots for density at 15 °C calculated using a linear by volume method. EN228 specifications state that the density of gasoline must lie in the range 720–775 kg/m<sup>3</sup> at 15 °C (DIN EN228 2017). The scale has been adjusted on Fig. 14.12 in order to easily view the range of THIP compositions that have a density within EN228 specifications. This range of compositions highlighted can be placed as a further constraint on the mole-based model when designing THIP surrogates.

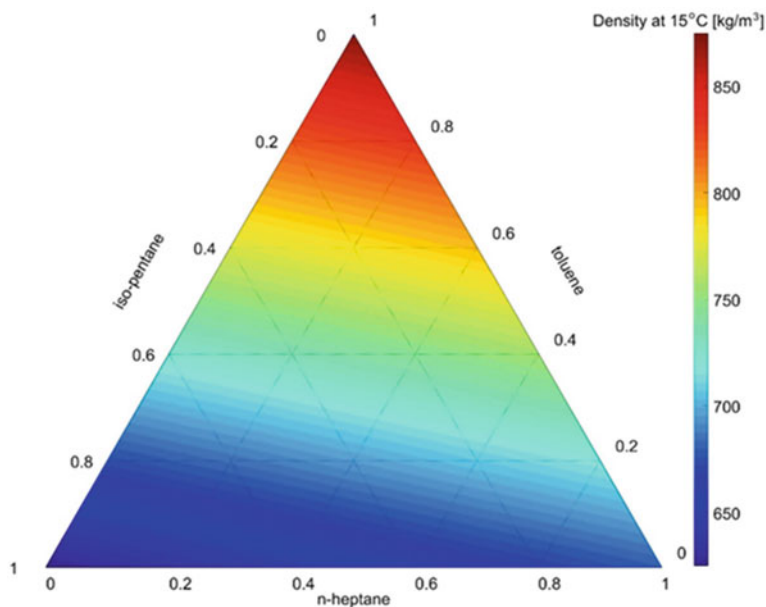


**Fig. 14.11** Ternary plot for the density (at 15 °C) of THIP surrogates

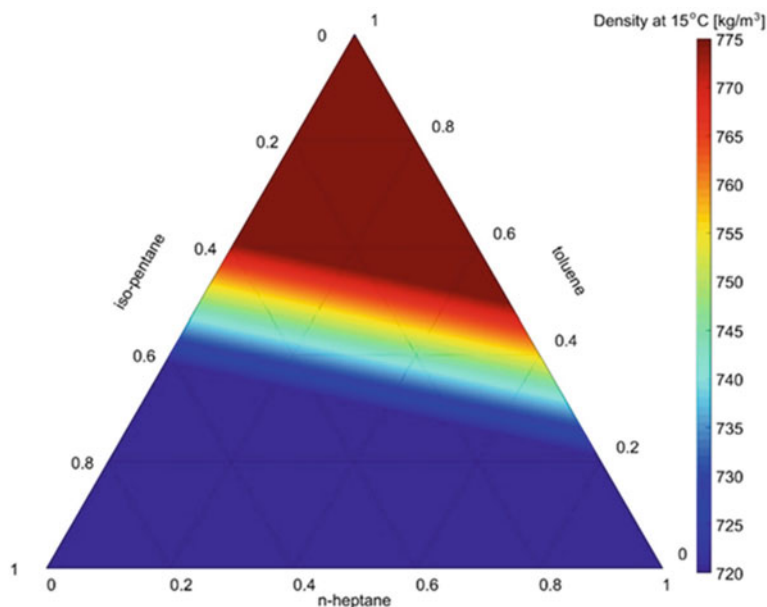


Fig. 14.12 Ternary plot for the density (at 15 °C) of THIP surrogates with an adjusted scale

## 14.4 Conclusions

Surrogate formulations for gasoline, with a limited number of components are useful for modelling purposes and for comparing experimental results using a carefully controlled fuel. A three-component surrogate based on toluene, n-heptane and isooctane (TPRF) is often employed that can match the RON and MON of actual gasoline fuels. In a series of recent papers we have advocated the use of an alternative surrogate formulation in which the isooctane is partially or wholly replaced by isooctane. In the event of total replacement of iso-octane, a 3-component surrogate is produced containing toluene, n-heptane and isopentane (THIP).

Replacement of isooctane with isopentane in surrogate formulations gives the following advantages:

- Unlike TPRF surrogates, isopentane containing surrogates can more accurately represent the DVPE and other volatility parameters, and more accurately represent the density of real gasoline fuels. Like TPRF surrogates, the absence of heavier components means they cannot replicate the upper part of the distillation curve.
- Like TPRF surrogates, they can capture the RON, MON, and sensitivity of real gasoline fuels. They can also give good agreement with ignition delays measured on a rapid compression machine. It has been shown that they can replicate the knocking behaviour on a performance engine of a real fuel with the same RON and MON.

- Suitable kinetic models exist which can model the ignition delay of isopentane containing surrogates, and we strongly encourage further work in this area.

In order to facilitate the use of isopentane containing surrogates, a method has been developed to predict THIP formulations given the RON and MON as an input. Two techniques were tested, a non-linear by volume method that was previously used by Morgan et al. (2010) and a mole-based technique. By analysing the sum of the squares of the errors, the mole-based technique is found to be preferable. By allowing the RON and MON to be within  $\pm 1$  unit of the target values, it is shown that THIP surrogates can be formulated with a wide (and realistic) range of DVPEs.

## References

- ASTM (2011) Standard test method for motor octane number of spark ignition engine fuel. ASTM D2700-18
- ASTM international (2012) Standard test method for research octane number of spark-ignition engine fuel. ASTM D2699-12
- Bugler J, Somers KP, Silke EJ, Curran HJ (2015) Revisiting the kinetics and thermodynamics of the low-temperature oxidation pathways of alkanes: a case study of the three pentane isomers. *J Phys Chem A* 119(28):7510–7527
- Di Lorenzo M, Brequigny P, Foucher F, Mounaïm-Rousselle C (2019) Validation of TRF-E as gasoline surrogate through an experimental laminar burning speed investigation. *Fuel* 253:1578–1588
- DIN EN 228 (2017)—Automotive fuels—Unleaded petrol—Requirements and test methods
- Gail S, Cracknell RF, Corrigan D, Festa A, Shankar V, Poulet B, Lovett G, Büttgen RD, Heufer KA, Mortellaro F (2021a) Evaluating a novel gasoline surrogate containing isopentane using a rapid compression machine and an engine. *Proc Combust Inst* 38(4):5643–5653
- Gail S, Cracknell RF, Poulet B, Lovett G, Festa A, Shankar V, Büttgen RD, Heufer KA (2021b) THIP: a new TPRF-like fuel surrogate development approach to better match real fuel properties. *Fuel* 286:119395
- Gary JH, Handwerk JH, Kaiser MJ, Geddes D (2007) *Petroleum refining: technology and economics*. CRC Press
- Ghosh P, Hickey KJ, Jaffe SB (2006) Development of a detailed gasoline composition-based octane model. *Ind Eng Chem Res* 45(1):337–345
- Hoth A, Kolodziej CP, Rockstroh T, Wallner T (2018) Combustion characteristics of PRF and TSF ethanol blends with RON 98 in an instrumented CFR engine (No. 2018-01-1672). SAE Technical Paper
- Jameel AGA, Naser N, Issayev G, Touitou J, Ghosh MK, Emwas AH, Farooq A, Dooley S, Sarathy SM (2018) A minimalist functional group (MFG) approach for surrogate fuel formulation. *Combust Flame* 192:250–271
- Javed T, Lee C, AlAbbad M, Djebbi K, Beshir M, Badra J, Curran H, Farooq A (2016) Ignition studies of n-heptane/iso-octane/toluene blends. *Combust Flame* 171:223–233
- Kalghatgi G, Babiker H, Badra J (2015) A simple method to predict knock using toluene, n-heptane and iso-octane blends (TPRF) as gasoline surrogates. *SAE Int J Engines* 8(2):505–519
- Knop V, Loos M, Pera C, Jeuland N (2014) A linear-by-mole blending rule for octane numbers of n-heptane/iso-octane/toluene mixtures. *Fuel* 115:666–673
- Morgan N, Smallbone A, Bhave A, Kraft M, Cracknell R, Kalghatgi G (2010) Mapping surrogate gasoline compositions into RON/MON space. *Combust Flame* 157(6):1122–1131
- Richards P (2014) *Automotive fuels reference book*, vol 297. SAE Technical Paper

- Sarathy SM, Kukkadapu G, Mehl M, Javed T, Ahmed A, Naser N, Farooq A (2016) Compositional effects on the ignition of FACE gasolines. *Combust Flame* 169:171–193
- Sarathy SM, Farooq A, Kalghatgi GT (2018) Recent progress in gasoline surrogate fuels. *Prog Energy Combust Sci* 65:67–108
- Singh E, Sarathy SM (2021) The role of intermediate-temperature heat release in octane sensitivity of fuels with matching research octane number. *Energy Fuels* 35(5):4457–4477
- Singh E, Badra J, Mehl M, Sarathy SM (2017) Chemical kinetic insights into the octane number and octane sensitivity of gasoline surrogate mixtures. *Energy Fuels* 31(2):1945–1960
- Van Romunde Z, Aleiferis PG, Cracknell RF, Walmsley HL (2007) Effect of fuel properties on spray development from a multi-hole DISI engine injector. *SAE Trans* 1313–1331
- Wang H, Xu R, Wang K, Bowman CT, Hanson RK, Davidson DF, Brezinsky K, Egolfopoulos FN (2018) A physics-based approach to modeling real-fuel combustion chemistry-I. Evidence from experiments, and thermodynamic, chemical kinetic and statistical considerations. *Combust Flame* 193:502–519
- Westbrook CK, Mehl M, Pitz WJ, Sjöberg M (2017) Chemical kinetics of octane sensitivity in a spark-ignition engine. *Combust Flame* 175:2–15
- Zhang X, Yalamanchi KK, Sarathy SM (2021) A functional-group-based approach to modeling real-fuel combustion chemistry-I: prediction of stoichiometric parameters for lumped pyrolysis reactions. *Combust Flame* 227:497–509

# Chapter 15

## Prediction of Ignition Modes in Shock Tubes Relevant to Engine Conditions



Minh Bau Luong and Hong G. Im

**Abstract** A theoretical prediction of ignition modes in shock tubes relevant to engine conditions is proposed and validated with a wide range of shock tube experiment data. The predictive Sankaran number,  $Sa_p$ , is adapted to distinguish between the weak and strong ignition modes. The non-ideal temperature and pressure rise inherently occurring in combustion devices is considered in the formulation of  $Sa_p$ . The  $Sa_p$  criterion is then validated by the experimental data in shock tubes for a number of fuels exhibiting negative temperature coefficient (NTC) and non-NTC behavior. It is demonstrated that the  $Sa_p$  criterion can accurately predict the weak and strong ignition modes regardless of the NTC and non-NTC fuels over a wide range of pressure and temperature.  $Sa_p = 1$  serves as a reliable marker to delineate the boundary between the strong ignition ( $Sa_p < 1$ ) and weak ignition ( $Sa_p > 1$ ). As inspired by the newly-developed  $Sa_p$  criterion in shock tube, it strongly suggests that the sensitivity of ignition delay variation in non-constant volume reactors such as the polytropic compression/expansion heating effect in an internal combustion engine and in a rapid compression machine (RCM) should be incorporated in evaluating an ignition criterion to better predict the ignition modes.

**Keywords** Preignition · Shock tube · Ignition regime · Ignition criteria · Strong/weak ignition · Ethanol · Methanol · *n*-hexane · Negative temperature coefficient (ntc)

### 15.1 Introduction

Preignition is an undesired phenomenon that has been observed in different apparatus (Davidson and Hanson 2009; Hanson and Davidson 2014; Goldsborough et al. 2017; Wang et al. 2017; Kalghatgi and Bradley 2012; Kalghatgi 2015) when they are

---

M. B. Luong (✉) · H. G. Im  
Clean Combustion Research Center, King Abdullah University of Science and Technology,  
Thuwal, Saudi Arabia  
e-mail: [minhbau.luong@kaust.edu.sa](mailto:minhbau.luong@kaust.edu.sa)

© The Author(s), under exclusive license to Springer Nature Singapore Pte Ltd. 2022  
G. Kalghatgi et al. (eds.), *Engines and Fuels for Future Transport*, Energy, Environment,  
and Sustainability, [https://doi.org/10.1007/978-981-16-8717-4\\_15](https://doi.org/10.1007/978-981-16-8717-4_15)

369

operated under extreme conditions of high load. Once preignition occurs, it induces adverse effects on the performance of the combustion apparatus, i.e., reduced thermal efficiency in practical combustion devices such as internal combustion engines (Wang et al. 2017; Kalghatgi and Bradley 2012; Kalghatgi 2015; Luong et al. 2013, 2014, 2015, 2017a, b, c, 2019, 2021a, b, ; Dai et al. 2015; 2017; Yu and Chen 2015; Terashima et al. 2017; Pan et al. 2017, 2016; Wei et al. 2018; Sow et al. 2019; Kim et al. 2015; Ali et al. 2018), or affecting the accuracy of the acquired quantities in the experimental apparatus such as rapid combustion machines (RCM) (Pan et al. 2020, 2021), and shock tubes (Javed et al. 2017; Figueroa-Labastida et al. 2018, 2021a, b; Luong et al. 2021). Irregular preignition is typically initiated by uncontrolled ignition sources such as hot spots and oil droplets. The mechanism and the source of such irregular preignition events are still not well understood. Therefore, a reliable criterion to predict irregular preignition phenomena is needed (Meyer and Oppenheim 1971; Lutz et al. 1989; Kalghatgi and Bradley 2012; Im et al. 2015; Luong et al. 2020, 2021a, b; Towery et al. 2020; Figueroa-Labastida et al. 2021b).

Among various experimental apparatus, shock tubes are typically used to provide experimental data of temperature, pressure and species concentration histories over a wide range of conditions, thereby allowing cross validation of experimental data with chemical kinetic models (Davidson and Hanson 2009; Hanson and Davidson 2014; Goldsborough et al. 2017). In an ideal shock tube experiment, the test gas is uniformly distributed, heated by the reflected shock wave, and after a certain ignition delay time,  $\tau_{ig}$ , the autoignition is expected to occur volumetrically throughout the reactor. For conditions that require a long measurement time window (on the order of a few ms), the non-ideal effects in shock tubes such as facility-dependent non-idealities in gas dynamics, incident shock attenuation, reflected shock bifurcation, and wall heat transfer naturally developed in a shock tube, cause pressure and temperature rise over time before the main ignition (Petersen and Hanson 2001; Davidson and Hanson 2009; Hanson and Davidson 2014; Goldsborough et al. 2017; Yamashita et al. 2012; Lamnaouer et al. 2014; Grogan and Ihme 2015; Hargis and Petersen 2015; Nativel et al. 2020; Pryor et al. 2017. Such pressure and temperature rise,  $dP/dt$  and  $dT/dt$ , is usually modeled by the isentropic  $T - P$  relation (Davidson and Hanson 2004; Chaos and Dryer 2010) to match the predicted and the measured ignition delay times (Davidson and Hanson 2004; Li et al. 2008; Chaos and Dryer 2010).

However, the isentropic model for  $dP/dt$  is insufficient for a strong preignition process as illustrated in Fig. 15.1 that is typically seen in the mixtures with high fuel loading (Pang et al. 2009; Hanson and Davidson 2014; Javed et al. 2017; Figueroa-Labastida et al. 2018, 2021a, b). The non-ideal facility-dependent effects induce not only the temporal evolution of  $dP/dt$  and  $dT/dt$ , but also spatial non-uniformities in temperature that significantly enhance the preignition propensity in a highly reactive test gas, leading to a localized ignition process in shock tubes (Davidson and Hanson 2004; Li et al. 2008; Chaos and Dryer 2010; Javed et al. 2017; Figueroa-Labastida et al. 2018, 2021a, b). For example, Figueroa-Labastida et al. (2018, 2021a, 2021b) studied the ignition modes of ethanol, methanol and *n*-hexane and found that higher fuel concentration mixture is more susceptible to exhibit early localized ignition kernels, subsequently leading to an inhomogeneous ignition process. The

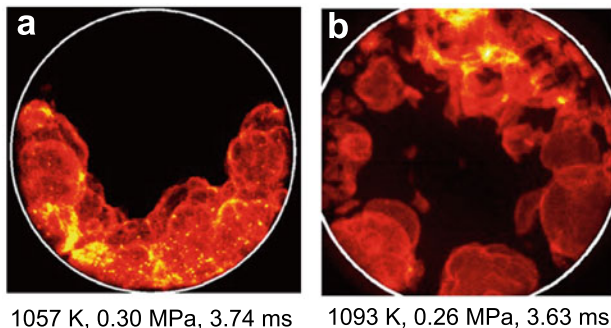


**Fig. 15.1** The inhomogeneous ignition of the *n*-heptane mixture, 21% O<sub>2</sub> /Ar,  $\phi = 0.5$ , acquired **a** after three consecutive experiments were performed without cleaning, and **b** after the shock tube was cleaned. The initial reflected shock temperatures and pressures were labeled for each experiment (taken from Ref. Troutman et al. 2016)

presence of localized preignition significantly shortens the measured  $\tau_{ig,m}$ , approximately by an order of magnitude shorter than ideal homogeneous ignition results (Pang et al. 2009; Hanson and Davidson 2014; Javed et al. 2017; Figueroa-Labastida et al. 2018, 2021a, b). Note that the measured  $\tau_{ig,m}$  suffering from a strong preignition process is not suitable to be utilized in the development of kinetic models. Therefore, an accurate criterion to predict preignition events *a priori* is necessary to avoid prevent the experiments from exhibiting the non-ideal behaviors leading to a high uncertainty in the measurement of  $\tau_{ig,m}$ . This chapter attempts to provide an overview of theoretical framework to predict ignition characteristics in a nearly uniform reactant mixture in the presence of temperature inhomogeneities (Sankaran et al. 2005; Im et al. 2015, Luong et al. 2019, 2020; Figueroa-Labastida et al. 2021b).

In the following, a theoretical background to predict the preignition propensity encountered in combustion devices (Zeldovich 1980; Sankaran et al. 2005; Im et al. 2015; Luong et al. 2020) is briefly reviewed, followed by a refined predictive criterion applied to shock tubes presented in the subsequent sections. An extensive dataset published in the recent studies (Javed et al. 2017; Figueroa-Labastida et al. 2018, 2021a, b) showing different degrees of the preignition propensity over a wide range of conditions is utilized to access the predictive accuracy of the criterion.

## 15.2 Theoretical Background

This section reviews the ignition criterion to predict the preignition propensity *a priori* in the shock tubes. This refined criterion is a variant of the Sankaran number (Sankaran et al. 2005; Im et al. 2015; Luong et al. 2020) which is derived from the Zeldovich's theory, briefly summarized as flows.



### 15.2.1 Ignition Regime Criterion

According to Zeldovich's theory (Zeldovich 1980), the spontaneous propagation speed of an ignition front,  $S_{sp}$ , is determined as

$$S_{sp} = |\nabla\tau_{ig}|^{-1}, \quad (15.1)$$

where  $\tau_{ig}$  is the homogeneous ignition delay time at a local mixture condition. Based on  $S_{sp}$ , Zeldovich (1980) identified different ignition modes in a thermally stratified mixture. In the presence of large spatial variations in  $\tau_{ig}$ , local ignition establishes a deflagration front (weak ignition). For a mixture with a smaller level of  $\tau_{ig}$  variations, the mixture ignites sequentially, and  $S_{sp}$  exhibits a rapid ignition front propagation (strong ignition). If  $S_{sp}$  is sufficiently large and comparable to the speed of sound,  $S_{sp} \approx a$ , the combustion wave coupled with the acoustic wave leads to a rapid pressure rise, and may result in detonation development characterized by extremely high amplitudes of pressure oscillations. In the asymptotic limit of zero gradient,  $S_{sp}$  becomes infinity, resulting in the purely homogeneous ignition mode.

Based on Zeldovich's theory and validated by high-fidelity DNS data, Sankaran et al. (2005) proposed a criterion to predict the weak or strong ignition modes, so-called the Zeldovich-Sankaran number (Sa), referred to as the Sankaran number herein for brevity, which is based on the ratio of laminar flame speed to the ignition front speed.

$$Sa = \beta \frac{S_L}{S_{sp}}, \quad (15.2)$$

where  $\beta$  is an empirical factor set to be 0.5 to account for some delay in developing a deflagration from the ignition kernel due to the interactions of thermal and radial diffusion between the neighboring regions.  $Sa = 1$  serves as the boundary between the homogeneous/strong ( $Sa < 1$ ) and the inhomogeneous/weak ( $Sa > 1$ ) ignition.

### 15.2.2 Prediction of Ignition Regimes in Turbulent Conditions

In practical combustion devices, the detailed spatially-resolved information of the scalar fluctuations is not available, and thus the prediction should be made based on the statistical quantities such as the mean and variance of fluctuations in RANS or LES simulations for prediction in real engines. To leverage these quantities, Im et al. (2015) conducted a theoretical scaling analysis to build the ignition regime diagram that classifies the combustion modes a priori of a homogeneous reactant mixture with temperature fluctuations and turbulence. The resulting *predictive* Sa criterion is written in the following form Im et al. (2015), Luong et al. (2020)

$$\text{Sa}_p = \beta S_L \left| \frac{d\tau_{\text{ig}}}{dT} \right|_{|\widehat{\nabla T}|} = \beta S_L \left| \frac{d\tau_{\text{ig}}}{dT} \right|_{\frac{T'}{l\text{Re}_l^{-0.5}}}, \quad (15.3)$$

where  $d\tau_{\text{ig}}/dT$  represents the ignition delay sensitivity to temperature, and  $\nabla T$  is the temperature gradient of the bulk mixture (Im et al. 2015; Pal et al. 2017; Luong et al. 2020), which is approximated by the statistical mean temperature gradient,  $|\widehat{\nabla T}|$ .  $T'$  is the variance of the temperature of the bulk mixture.  $\text{Re}_l = u'l/\nu$  is the turbulent Reynolds number,  $\nu$  is the kinematic viscosity of the bulk mixture gas,  $u'$  is the root mean square (RMS) turbulent velocity fluctuation, and  $l$  is the integral scale of velocity field.

The *predictive*  $\text{Sa}_p$  criterion was further extended to account for temperature and concentration fluctuations by Luong et al. (2019, 2020). The criterion was then applied to negative temperature coefficient (NTC) and non-NTC fuels. The ignition modes of these fuels can also be predicted by  $\text{Sa}_p$  regardless of the NTC and non-NTC characteristics of fuels over a wide range of initial mean temperatures and different fluctuation levels.

### 15.2.2.1 Prediction of Ignition Regimes in Shock Tube Conditions

Note that in the previous studies (Im et al. 2015; Pal et al. 2017; Luong et al. 2015, 2019, 2020, 2021a, b; Meyer and Oppenheim 1971; Sankaran et al. 2005; Strozzi et al. 2012; Walton et al. 2007; Mansfield and Wooldridge 2014; Mansfield et al. 2015),  $\tau_{\text{ig}}$  and  $d\tau_{\text{ig}}/dT$  were evaluated in a adiabatic constant-volume condition, i.e., by an ideal constant-UV reactor. However, the measured  $\tau_{\text{ig,m}}$  in shock tubes is much shorter than the ideal  $\tau_{\text{ig}}$  computed by the ideal constant-UV reactor, especially with increasing test time  $\gtrsim O(1)$  ms. It is attributed to the inherent facility-dependent effects of the non-ideal gas dynamics behind the reflected shock wave (Petersen and Hanson 2001; Nativel et al. 2020; Davidson and Hanson 2004) (i.e., shock attenuation, boundary layer growth, and shock-wave/boundary-layer interactions), leading to the pressure and temperature rise during the test time. Therefore, when computing the ignition delay time sensitivity to temperature,  $d\tau_{\text{ig}}/dT$ , it is necessary to account for the non-ideal pressure and temperature rise.

To account for these non-ideal effects, a linear time-varying pressure rise,  $dP/dt$ , in the unit of %/ms where  $P$  is normalized by the initial pressure, together with associated temperature rise approximately deduced from the *isentropic* pressure-temperature relation (Petersen and Hanson 2001; Li et al. 2008; Chaos and Dryer 2010; Figueroa-Labastida et al. 2021b) is incorporated into the UV reactor after each time-step iteration to compute  $\tau_{\text{ig}}$ , denoted herein as  $\tau_{\text{ig,i}}$ .  $\tau_{\text{ig,m}}$  denotes the measured ignition delay time in shock tubes to differentiate from  $\tau_{\text{ig,i}}$ . The  $dP/dt$  effect significantly shortens  $\tau_{\text{ig,i}}$ , and greatly affects the magnitude of the ignition delay sensitivity to temperature,  $d\tau_{\text{ig,i}}/dT$ , that will be further elaborated in Sect. 15.3.2.

The *predictive* Sankaran number applied to shock tubes is written as Troutman et al. 2016; Donovan et al. 2004; Figueroa-Labastida et al. 2021b; Luong et al. 2021):

$$Sa_p = \beta S_L \left| \frac{d\tau_{ig,i}}{dT} \right| \frac{T'}{l_T Re_T^{-0.5}}, \quad (15.4)$$

where  $\beta$  is an empirically weighting factor of 0.5 Sankaran et al. (2005),  $S_T$  is the laminar flame speed computed based on the initial composition and conditions of  $P$  and  $T$  of the bulk mixtures after the reflected shock wave.  $Re_T$  is roughly estimated as  $Re_T = T' l_T / \alpha$ , in analogy with  $Re_l = u' l / \nu$  for the velocity field, to include the effect of thermal diffusivity,  $\alpha$ , of the initial bulk mixture.  $l_T$  and  $T'$  are the characteristic length scale, and the RMS fluctuation of temperature field, respectively, that is naturally developed between the boundary layer and the core gas.  $T'$  of 2 K and  $l_T$  of 1 mm are chosen, which are comparable to those typically observed in shock tubes (Troutman et al. 2016; Donovan et al. 2004; Figueroa-Labastida et al. 2021b; Luong et al. 2021).

The significance of  $Sa_p$  is that  $Sa_p = 1$  serves as the boundary between the strong ( $Sa_p < 1$ ) and the weak ( $Sa_p > 1$ ) ignition (Sankaran et al. 2005; Luong et al. 2015, 2019, 2020; Figueroa-Labastida et al. 2021b).  $Sa_p \gg 1$  indicates a dominant weak ignition such that the measured  $\tau_{ig,m}$  is much shorter than the modelled  $\tau_{ig,i}$  with the  $dP/dt$  correction,  $\tau_{ig,m} \ll \tau_{ig,i}$ .  $Sa_p \sim 1$  indicates a transition between weak and strong ignition such that the measured  $\tau_{ig,m}$  is not significantly affected by non-homogeneous ignition, i.e., it is still comparable with  $\tau_{ig,i}$ ,  $\tau_{ig,m} \sim \tau_{ig,i}$ . These ignition characteristics will be elaborated further in the following sections.

## 15.3 Results and Discussion

### 15.3.1 Description of Selected Mixtures

In the subsequent analysis, the experimental data of three fuels (i.e., methanol, methanol, and *n*-hexane) featuring different degrees of preignition propensity are utilized to validate the predictive accuracy of the  $Sa_p$  criterion (Javed et al. 2017; Figueroa-Labastida et al. 2018, 2021a, b). The composition of all the selected mixtures are described in Table 15.1. The methanol and ethanol mixtures exhibit a single-stage ignition, while the *n*-hexane mixtures exhibit a strong NTC behavior. The preignition propensity for each mixture is described in conjunction with the assessment of the  $Sa_p$  criterion in the subsequent sections.

Among several factors, a specific value of  $dP/dt$  is highly dependent on the inner diameter of shock tubes, the test time, and the value of  $T_5$  &  $P_5$ , together with bath gas being used (Petersen and Hanson 2001; Davidson and Hanson 2004, 2009; Hanson and Davidson 2014; Nativel et al. 2020). For example, the KAUST shock tube with an inner diameter  $\sim 14$  cm typically induces a  $dP/dt \sim 1\text{--}3$  %/ms for a test time of a few milliseconds (Javed et al. 2017; Figueroa-Labastida et al. 2018, 2021a, b). Note that the  $dP/dt$  values discussed herein are used to account for the non-ideal facility effects without considering the pressure rise due to the

**Table 15.1** Compositions of the studied fuel mixtures

Fuel	Mixture	$X_{\text{Fuel}}$ (%)	$X_{\text{O}_2}$ (%)	$X_{\text{Ar}}$ (%)	$X_{\text{N}_2}$ (%)	$\phi$
Methanol (Figueroa-Labastida et al. 2018)	M1	5.7	8.6	85.7		1.0
	M2	5.0	15.0	80.0		0.5
	M3	12.3	18.4	69.3		1.0
	M4	12.3	18.4		69.3	1.0
Ethanol (Figueroa-Labastida et al. 2018, 2021b)	E1	5.0	15.0	80.0		1.0
	E2	5.0	15.0		80.0	1.0
	E3	5.0	30.0	65.0		0.5
	E4	5.0	30.0		65.0	0.5
	E5	2.9	17.4	79.7		1.0
	E6	2.9	8.8	88.3		0.5
<i>n</i> -Hexane (Javed et al. 2017; Figuroa-Labastida et al. 2021a)	Hex 1	5.0	47.5	47.5		1.0
	Hex 2	1.0	9.5	89.5		1.0

energy release induced by premature combustion. To keep consistency in this study unless otherwise specified,  $dP/dt$  of 2%/ms is used, which is found to be reasonable to discern the inhomogeneous and homogeneous ignition for the experimental data measured by a KAUST shock tube (Figueroa-Labastida et al. 2021b; Luong et al. 2021).

### 15.3.2 Effects of $dP/dt$ on $d\tau_{\text{ig},i}/dT$

A crucial factor to improve the predictive accuracy of  $Sa_p$  for the ignition modes in shock tubes is the consideration of the  $dP/dt$  effect in evaluating the ignition delay sensitivity to temperature,  $d\tau_{\text{ig},i}/dT$ . By accounting for the  $dP/dt$  effect in evaluating  $d\tau_{\text{ig},i}/dT$ , it is generally found that  $d\tau_{\text{ig},i}/dT$  is approximately an order of magnitude smaller than that predicted without the pressure correction. Consequently, without accounting for the  $dP/dt$  effect, the traditional  $Sa_p$  under a constant-volume assumption is subjected to significant errors in predicting the combustion modes in the non-constant volume devices such as shock tubes. This point is quantitatively assessed in the following discussion.

The  $dP/dt$  effect on the magnitude of  $\tau_{\text{ig},i}$  and  $|d\tau_{\text{ig},i}/dT|$  is examined in Fig. 15.2 for the ethanol E5 mixture exhibiting a homogeneous ignition. A few noticeable points are made from Fig. 15.2. First, the ratio of  $\tau_{\text{ig},i}$  to  $\tau_{\text{ig}}$  decreases significantly with either increasing  $dP/dt$  or decreasing temperature. Overall,  $\tau_{\text{ig},i}$  with  $dP/dt = 2\%/ms$  is approximately in one order of magnitude smaller than  $\tau_{\text{ig}}$  of the ideal UV

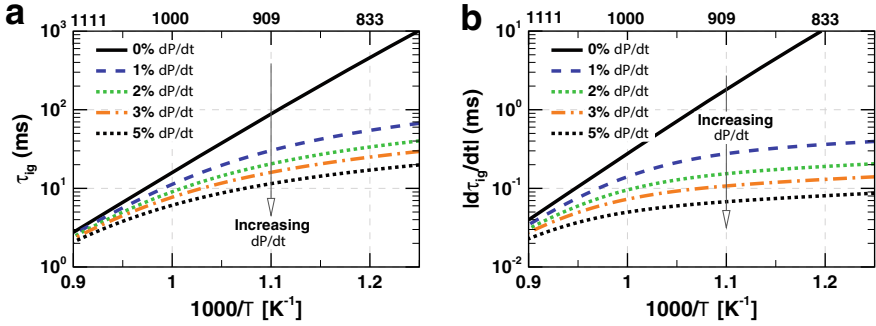


**Fig. 15.2** The ignition delay time,  $\tau_{ig,i}$ , with varied  $dP/dt$  and its corresponding absolute gradient with respect to temperature,  $|d\tau_{ig,i}/dT|$ , as a function of  $1000/T$  at 2 bar for the ethanol E5 mixture (Figueroa-Labastida et al. 2021b) (taken from Ref. Luong et al. 2021)

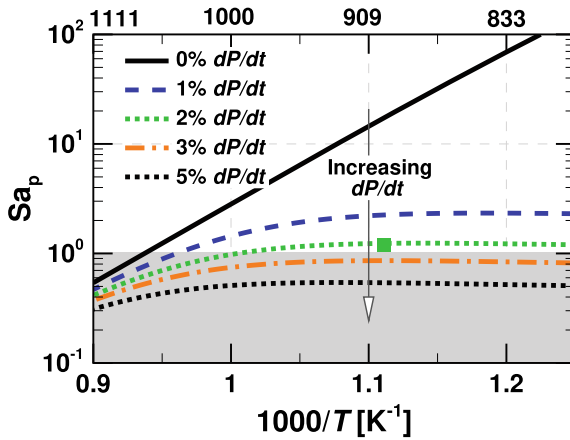


**Fig. 15.3** The predicted Sankaran number,  $Sa_p$ , with varied  $dP/dt$  as a function of  $1000/T$  at 2 bar for the ethanol E5 mixture (Figueroa-Labastida et al. 2021b) (taken from Ref. Luong et al. 2021). The grey shaded area in the figure denotes the region with  $Sa_p < 1$ , predicting that the mixture is likely to be a homogeneous ignition dominance. The square denotes the lowest temperatures experimentally tested where no pronounced preignition was observed

reactor ( $dP/dt$  of 0 %/ms) at  $T < 950$  K. More specifically,  $\tau_{ig,i}$  with  $dP/dt = 2$  %/ms is smaller than  $\tau_{ig} \sim 4.5$  times at 900 K, and  $\sim 14.5$  times at 830 K. Second, the ratio of  $|d\tau_{ig,i}/dT|$  to  $|d\tau_{ig}/dT|$  decreases even more pronounced as compared to the ratio of  $\tau_{ig,i}$  to  $\tau_{ig} \cdot |d\tau_{ig,i}/dT|$  with  $dP/dt$  of 2 %/ms is smaller than  $|d\tau_{ig}/dT| \sim 12$  times at 900 K, and  $\sim 56$  times at 830 K. This difference is also reflected into their corresponding  $Sa_p$  shown in Fig. 15.3.

As readily seen in Fig. 15.3, the  $Sa_p$  values are much greater than unity, i.e.,  $Sa_p = 14.5$  at 900 K and  $Sa_p = 68.8$  at 830 K with  $dP/dt$  of 0%/ms while at this low temperature regime,  $Sa_p \lesssim 1$  with  $dP/dt$  of 2%/ms. Without the consideration

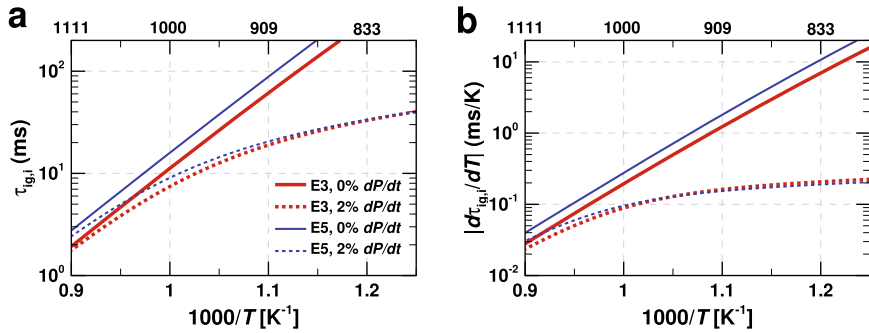


**Fig. 15.4** Comparison between E3 and E5 mixtures for the ignition delay time,  $\tau_{ig,i}$ , with  $dP/dt = 2$  %/ms, and its corresponding absolute gradient with respect to temperature,  $|d\tau_{ig,i}/dT|$ , as a function of  $1000/T$  and  $dP/dt$  at 2 bar, Figueroa-Labastida et al. (2021b).  $\tau_{ig}$  of the ideal UV reactor with  $dP/dt$  of 0 %/ms is also plotted for direct comparison

of the  $dP/dt$  effect,  $dP/dt = 0$ , the ethanol E5 mixture is predicted to experience a weak ignition dominance as suggested by  $Sa_p \gg 1$  at  $T < 950$  K, which is incorrect—inconsistent with the experimental observations of a strong ignition dominance (Figueroa-Labastida et al. 2018). On the contrary, by applying the correction of  $dP/dt = 2$  %/ms in computing  $|d\tau_{ig,i}/dT|$ , the dominant strong ignition mode is accurately predicted for E5 as dictated by  $Sa_p \lesssim 1$ , which is quantitatively consistent with the experimental data—no pronounced preignition was observed at low temperature up to 934K for E5 (Figueroa-Labastida et al. 2018).

Two representative ethanol mixtures with high- and low-fuel loading, E3 and E5, exhibiting two distinct modes of inhomogeneous and homogeneous ignition, respectively, are chosen to elaborate further the  $dP/dt$  effect.  $\tau_{ig,i}$ ,  $d\tau_{ig,i}/dT$ , and  $Sa_p$  with and without the  $dP/dt$  correction are shown in Figs. 15.4 and 15.5 for these two mixtures. As readily seen in Fig. 15.4b, the difference between  $|d\tau_{ig,i}/dT|$  and  $|d\tau_{ig}/dT|$  of the E5 mixture with low-fuel loading is greater than that of the E3 mixture with high-fuel loading. It is generally found that  $|d\tau_{ig,i}/dT|$  of a mixture with low-fuel loading is more affected by the  $dP/dt$  effect, rendering it more apt to exhibit a strong ignition (Figueroa-Labastida et al. 2021b; Luong et al. 2021).  $Sa_p$  of E3 is much greater than unity, accurately suggesting that E3 is prone to preignition at the low temperature regime,  $T < 1050$  K.

As also revealed in Fig. 15.4, with the  $dP/dt$  correction of 2%/ms,  $|d\tau_{ig,i}/dT|$  of E3 is nearly identical to that of E5 despite the difference in the ideal constant-UV  $\tau_{ig}$  between E3 and E5; however,  $Sa_p$  of E3 is approximately two times larger than  $Sa_p$  of E5. It is attributed to their difference in the laminar flame speed that also directly reflects into the magnitude of  $Sa_p$  (see Eq. 15.4). Note that except the difference in  $S_L$ , other parameters of E3 and E5 in Eq. 15.4 are nearly identical (Figueroa-Labastida et al. 2021b).

Generally, decreasing the fuel concentration decreases the flame speed while it increases the laminar flame thickness. As representatively shown in Fig. 15.6,

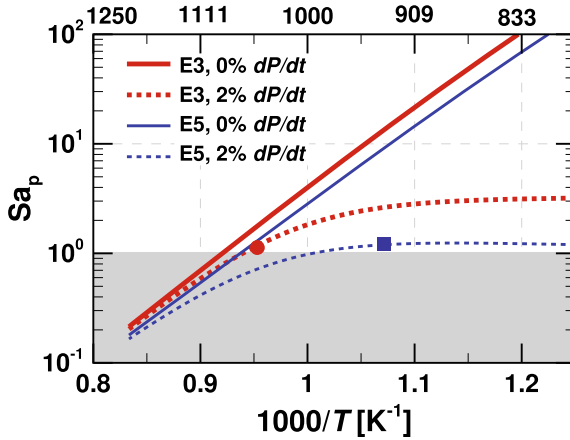


**Fig. 15.5** Comparison between E3 and E5 mixtures for the predicted Sankaran number,  $Sa_p$ , as a function of  $1000/T$  at 2 bar for the ethanol mixtures, E3 and E5, Figueroa-Labastida et al. (2021b). The grey shaded area in the figure denotes the region with  $Sa_p < 1$ , predicting that the mixture is likely to be a homogeneous ignition dominance. The circle denotes the transition temperature delineating the homogeneous and non-homogeneous ignition. The square denotes the lowest temperatures experimentally tested where no pronounced preignition was observed (taken from Ref. Luong et al. 2021)

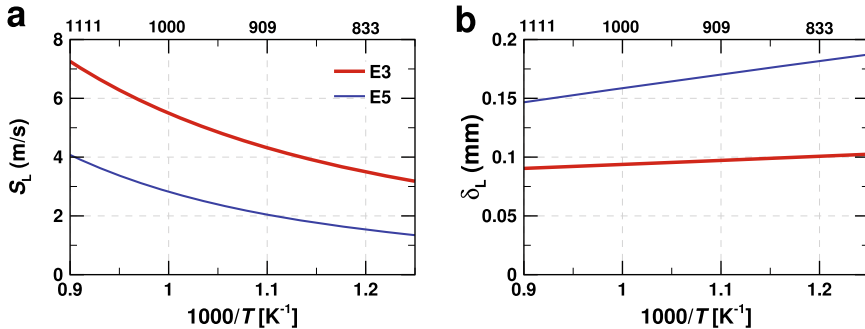


**Fig. 15.6** The flame speed and the flame thickness as a function of  $1000/T$  at 2 bar for the ethanol mixtures, E3 and E5, Luong et al. (2021)

the flame speed (flame thickness) of E3 with high-fuel loading is approximately two times greater (smaller) than that of E5 with low-fuel loading. Laminar flame thickness was suggested by Kalghatgi and Bradley (2012) as an indicator to predict preignition tendency of a mixture. The smaller the flame thickness of a mixture, the higher the preignition tendency. However, a specific threshold of the flame thickness to determine the temperature at which the onset of preignition would occur for a mixture is ambiguous. Unlike the flame thickness, the non-dimensional  $Sa_p$  number

can rigorously discern the combustion modes in shock tubes, i.e.,  $Sa_p = 1$  delineates the boundary between the strong ( $Sa_p < 1$ ) and the weak ( $Sa_p > 1$ ) ignition.

In summary, incorporating the  $dP/dt$  effect in evaluating  $|d\tau_{ig,i}/dT|$  allows  $Sa_p$  to better predict the combustion modes in shock tubes as further demonstrated in the following sections.

### 15.3.3 Preignition Tendency of Ethanol Mixtures

The prediction of ignition modes for six ethanol mixtures, E1–E6 are shown in Fig. 15.7. Overall, the prediction is found to be consistent with the observed preignition propensity for these ethanol mixtures as selectively shown in Figs. 15.8, 15.9, 15.10, 15.11 and 15.12.

According to the experimental data, no pronounced preignition was observed for the E5 and E6 mixtures with low-fuel concentration (see Fig. 15.8) (Figueroa-Labastida et al. 2018, 2021b) while the E1, E3, and E4 mixtures with high-fuel concentration experienced weak ignition at low temperature (see Figs. 15.9, 15.10, 15.11 and 15.12). As shown in Fig. 15.8, a good match between the measured  $\tau_{ig,m}$  and the modelled  $\tau_{ig,i}$  indicates no noticeable preignition activities occurred for E5 and E6. In contrast to E5 and E6, a large discrepancy between  $\tau_{ig,m}$  and  $\tau_{ig,i}$  was observed for E1, E3, and E4 at the low temperature regime (see Fig. 15.9b and Figs. 15.10 and 15.12). It was also found that for the mixtures with a comparable mass and reactivity, the Ar-containing mixtures exhibit a higher preignition propensity than the  $N_2$ -containing mixtures (see Fig. 15.9b) (Figueroa-Labastida et al. 2018, 2021b).

Recently, Figueroa-Labastida et al. (2021b) found that the primary reason for the higher preignition propensity of the Ar-containing mixtures stems from the heat

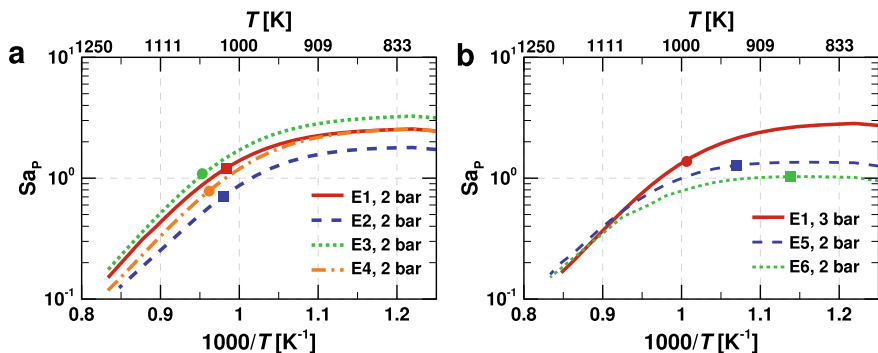


**Fig. 15.7** The predicted Sankaran number,  $Sa_p$ , as a function of  $1000/T$  for the ethanol mixtures. Circles denote the transition temperature delineating the homogeneous and non-homogeneous ignition. Squares denote the lowest temperatures experimentally tested where no preignition has been observed (taken from Ref. Figueroa-Labastida et al 2021b)



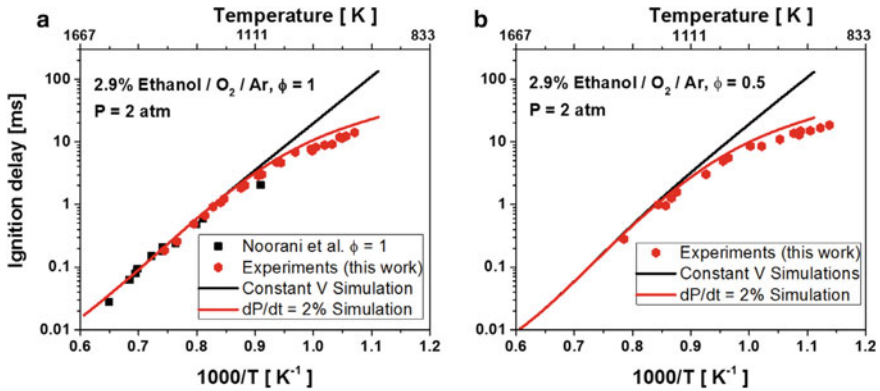


**Fig. 15.8** Comparison between the measured  $\tau_{ig}$  (symbols) and the computed constant-volume  $\tau_{ig}$  (lines). Black and red lines are for constant volume simulations, and 2% dP/dt simulations, respectively. The test mixtures: **a** 2.9% ethanol/8.7% O<sub>2</sub>/Ar,  $\phi = 1$ ; and **b** 2.9% ethanol/17.4% O<sub>2</sub>/Ar,  $\phi = 0.5$  (taken from Ref. Figueroa-Labastida et al. 2018)

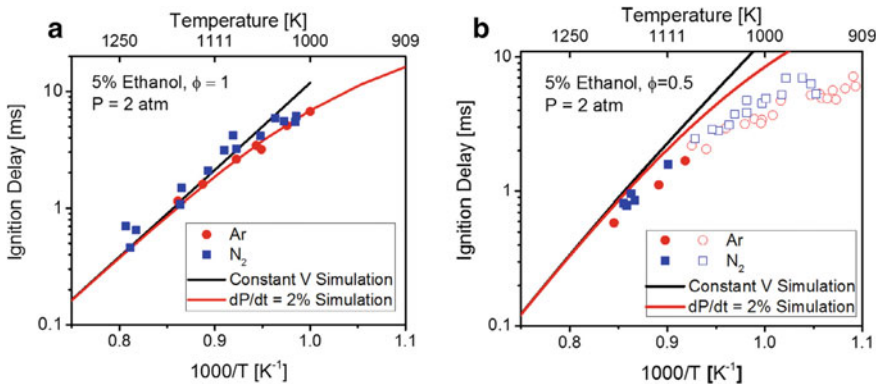


**Fig. 15.9** Comparison between the measured  $\tau_{ig}$  (symbols) and the computed constant-volume  $\tau_{ig}$  (lines). Black and red lines are for constant volume simulations, and 2% dP/dt simulations, respectively. The test mixtures: **a** 5% ethanol/15% O<sub>2</sub>/Ar and 5% ethanol/15% O<sub>2</sub>/N<sub>2</sub> at  $\phi = 1$ ; and **b** 5% ethanol/30% O<sub>2</sub>/Ar and 5% ethanol/30% O<sub>2</sub>/N<sub>2</sub> at  $\phi = 0.5$ . Closed symbols denote the measurements with homogeneous ignition while open symbols denote the measurements with nonhomogeneous ignition (taken from Ref. Figueroa-Labastida et al. (2018))

capacity difference between Ar and N<sub>2</sub>, i.e., the Ar-containing mixtures with a lower heat capacity facilitate the earlier development of premature deflagrations from ignition kernels (Luong et al. 2019; Figueroa-Labastida et al. 2021b). It is also found that in contrast to a low-fuel-concentration mixture, the ignition process of a high-fuel-concentration mixture is significantly affected by premature deflagration fronts that induce much higher pressure rise rate attributed to its faster laminar flame speed and higher cumulative energy release (Figueroa-Labastida et al. 2021b). Consequently, the ignition delay time of the main ignition of the high-fuel concen-

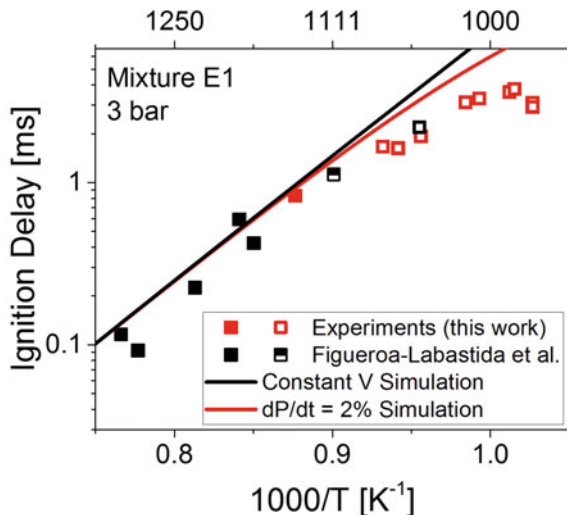


**Fig. 15.10** Comparison between the measured  $\tau_{ig}$  (symbols) and the computed constant-volume  $\tau_{ig}$  (lines) for the ethanol E1 mixture of 5% ethanol/15% O<sub>2</sub>/Ar with  $\phi = 1$ . Black and red lines are for constant volume simulations, and 2% dP/dt simulations, respectively (taken from Ref. Figueroa-Labastida et al. (2018))

tration mixture is significantly shortened. Note that the E1 mixture, with  $\phi = 1$  and high-fuel concentration, was initially reported to exhibit no noticeable preignition (Figueroa-Labastida et al. 2018); however, as suggested by  $Sa_p$  (Figueroa-Labastida et al. 2021b) further conducted more experiments at a lower temperature, and found that E1 also exhibited pronounced preignition as shown in Fig. 15.11.

In a good agreement with the experimental results, E5 with  $Sa_p \sim 1$ , and E6 with  $Sa_p \lesssim 1$  in the low-temperature regime are predicted to experience a strong ignition, i.e., E5 and E6 exhibit a strong ignition at low temperature up to 934K and 870 K, respectively (see Fig. 15.8).

Unlike E5 and E6, E1–E4 with high fuel concentration are predicted to exhibit inhomogeneous ignition at the low-temperature range at which  $Sa_p \geq 1$ . As shown in Fig. 15.7, the Ar-containing mixtures, E1 and E3, are predicted to show preignition tendency at temperature  $< 1040$  K and  $< 1050$  K, respectively. As representatively shown Figs. 15.11 and 15.12, E1 experienced an intermediate ignition at temperature of 974 K and pressure of 3.1 bar while E3 exhibited a weak/inhomogeneous ignition process at low temperature of 898 K and pressure of 1.7 bar. The preignition propensity of the two cases is well-predicted by the  $Sa_p$  criterion. The corresponding  $Sa_p$  values of two cases are 1.6 and 2.9.

For the N<sub>2</sub>-containing mixtures, E2 and E4, the temperature showing preignition tendency is predicted to occur at a slightly lower temperature,  $< 980$  K and  $< 1020$  K, respectively. It was experimentally observed that the temperature transition between the weak and strong ignition for E3 and E4, marked by circles in Fig. 15.7, are

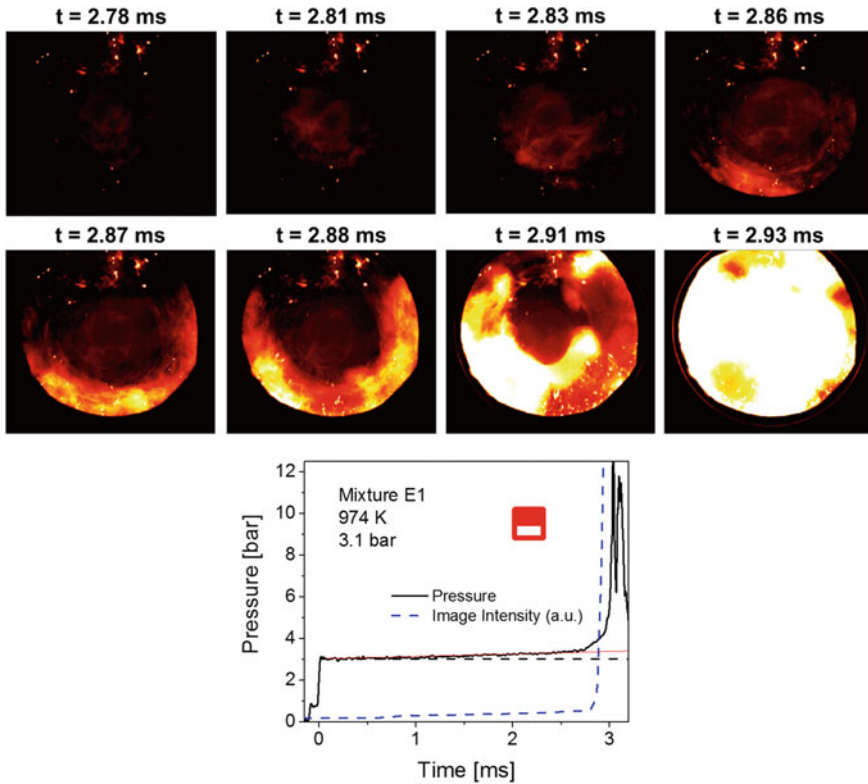


**Fig. 15.11** Imaging of the intermediate ignition process (mixed inhomogeneous/homogeneous ignition) of the ethanol E1 mixture, 5%  $C_2H_5OH/15\%$   $O_2/Ar$ ,  $\phi = 1$  at 974 K, and 3.1 bar, with  $Sa_p = 1.6$ . The red line describes the pressure rise due to the  $dP/dt$  effect, and the dashed blue line is the image intensity recorded from the high-speed camera (taken from Ref. Figueroa-Labastida et al. 2021b)

consistent with the predicted temperatures. For E2, its lowest temperature test marked by squares in Fig. 15.7 still shows a strong ignition behavior, which is correctly predicted by  $Sa_p$ . The preignition tendency for E1 is predicted to occur at the slightly lower temperature of 1030 K as pressure increases from 2.0 to 3.0 bar. The predicted temperature for the occurrence of an intermediate ignition for E1 at 3 bar is close to the value of the experimental observations as marked by circles in Fig. 15.7, while a strong ignition was still observed at the lowest tested temperature of 1017 K for E1 at 2 bar as also accurately predicted by  $Sa_p$ .

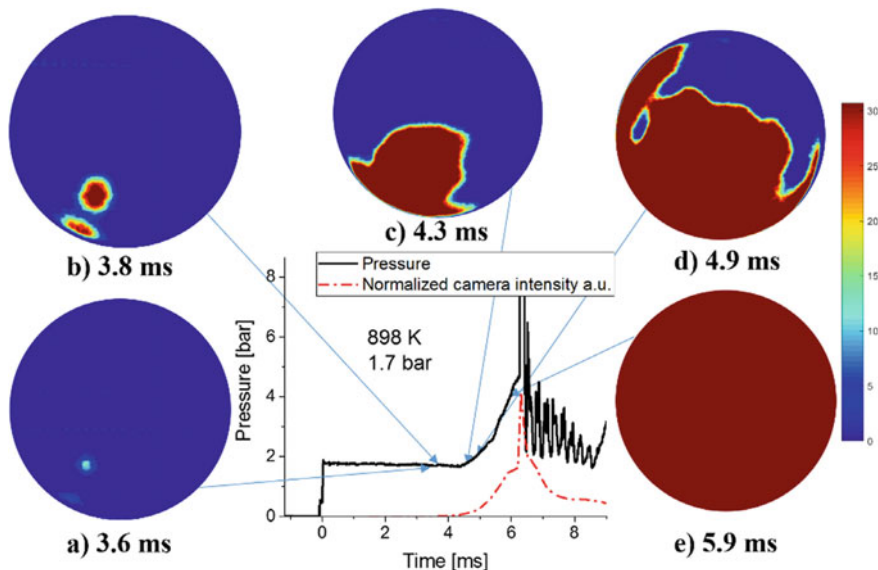


**Fig. 15.12** Imaging of the inhomogeneous ignition process of the ethanol E3 mixture, 5% ethanol/30% O<sub>2</sub>/Ar, at 898 K and 1.7 bar, with  $Sa_p = 2.9$  (taken from Ref. Figueroa-Labastida et al. 2018)

### 15.3.3.1 Preignition Tendency of Methanol Mixtures

Figures 15.13 and 15.14 show the measured  $\tau_{ig,m}$  in comparison with the computed  $\tau_{ig,i}$  for the methanol mixtures. M1 and M2 with low-fuel concentration exhibit a homogeneous ignition mode (see Fig. 15.13), while M3 and M4 with high-fuel concentration exhibit an inhomogeneous ignition mode at the low-temperature region (see Fig. 15.14).

Figure 15.16 shows the high-speed imaging sequences observed in shock tube experiments for two methanol cases with the measured  $\tau_{ig,m} \approx 5$  ms exhibiting three representative distinct behaviors of strong, intermediate, and weak ignition modes. As shown in Figs. 15.16 and 15.15, the methanol M3 mixture at 880 K and 2.4 bar developed two localized ignition kernels noticeably at early time of 3.1 ms, evolving into low-speed deflagration-like fronts that steadily propagate at the speed approximately of 45 m/s, and gradually consume the entire unburnt mixture for a long time interval approximately of 2 ms. This case serves as a representative example of a pronounced preignition with noticeable pressure rise due to premature deflagrations. The preignition severely affects the measured  $\tau_{ig,m}$  such that  $\tau_{ig,m}$  is much shorter than the modelled  $\tau_{ig,i}$  as readily seen in Fig. 15.14.

On the contrary, the methanol M1 mixture at 1004 K and 1.8 bar exhibits a homogeneous ignition, featured by a spontaneous ignition process with a short combustion duration approximately of 0.15 ms (see Fig. 15.16). The methanol M3 mixture at 1007 K and 1.8 bar is classified as a mixed combustion mode of weak and strong igni-

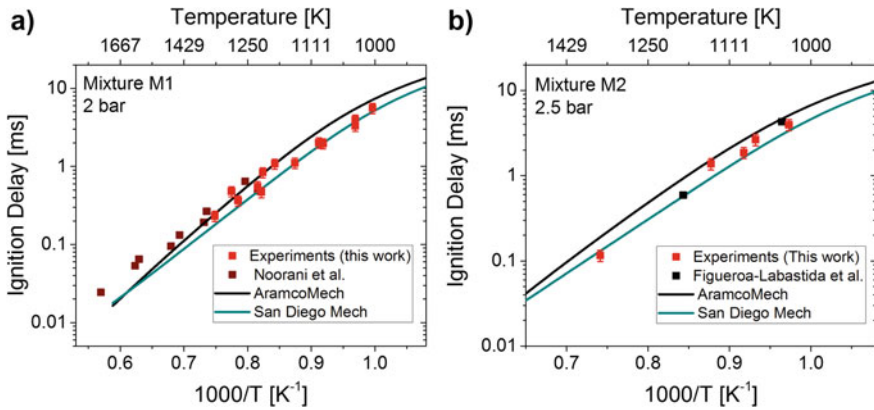


**Fig. 15.13** Comparison between the measured  $\tau_{ig}$  (symbols) and the computed  $\tau_{ig,i}$  (lines) with  $dP/dt = 3\%/ms$  for the methanol M1 and M2 mixtures. The test mixtures: **a** M1 with 5.7% methanol/8.6%  $O_2/Ar$  at  $\phi = 1$  and 2 bar; and **b** M2 with 5.0% methanol/15%  $O_2/Ar$  at  $\phi = 0.5$  and 2.5 bar (taken from Ref. Figueroa-Labastida et al. 2021b)

tion, featured by many localized ignition kernels developed shortly prior to the main ignition occurring nearly homogeneously. Consistent with the experimental results, the  $Sa_p$  criterion can accurately capture the ignition modes of these mixtures. Particularly, the corresponding  $Sa_p$  values for three cases from top to bottom in Fig. 15.16 are 0.6, 1.0, and 2.8, respectively, indicating strong ( $Sa_p < 1$ ), intermediate ( $Sa_p \sim 1$ ), and weak ignition modes ( $Sa_p \gg 1$ ), respectively.

The  $Sa_p$  as a function of temperature for the methanol mixtures is plotted in Fig. 15.17. The values of  $Sa_p$  consistently capture the experimental results in Figs. 15.13 and 15.16. Particularly, the M1 and M2 mixtures with  $Sa_p < 1$  are predicted to exhibit a homogeneous ignition at high temperatures ( $T > 950$  K). At the low-temperature regime,  $T < 950$  K, the M1 and M2 mixtures are predicted to experience a mixed mode of homogeneous and inhomogeneous ignition mode as dictated by  $Sa_p \sim 1$ . Unlike the M1 and M2 mixtures exhibiting a dominant strong ignition, the M3 and M4 mixtures are predicted to exhibit a pronounced preignition as dictated by  $Sa_p > 1$  at  $T \ll 1020$  K for M3, and at  $T \ll 980$  K for M4. The prediction for the M3 mixtures are found to be consistent with the experimental observations in Figs. 15.14, 15.16 and 15.15.

### 15.3.4 Preignition Tendency of *n*-Hexane Mixtures

In recent work (Javed et al. 2017; Figueroa-Labastida et al. 2021a), it was found that the *n*-hexane mixture, Hex 1, with high-fuel concentration, i.e., 5% *n*-heptane and  $\phi = 1$  exhibited a strong preignition while Hex 2 with low-fuel concentration, i.e., 1% *n*-heptane and  $\phi = 1$ , exhibited a homogeneous ignition. As seen in Figs. 15.18

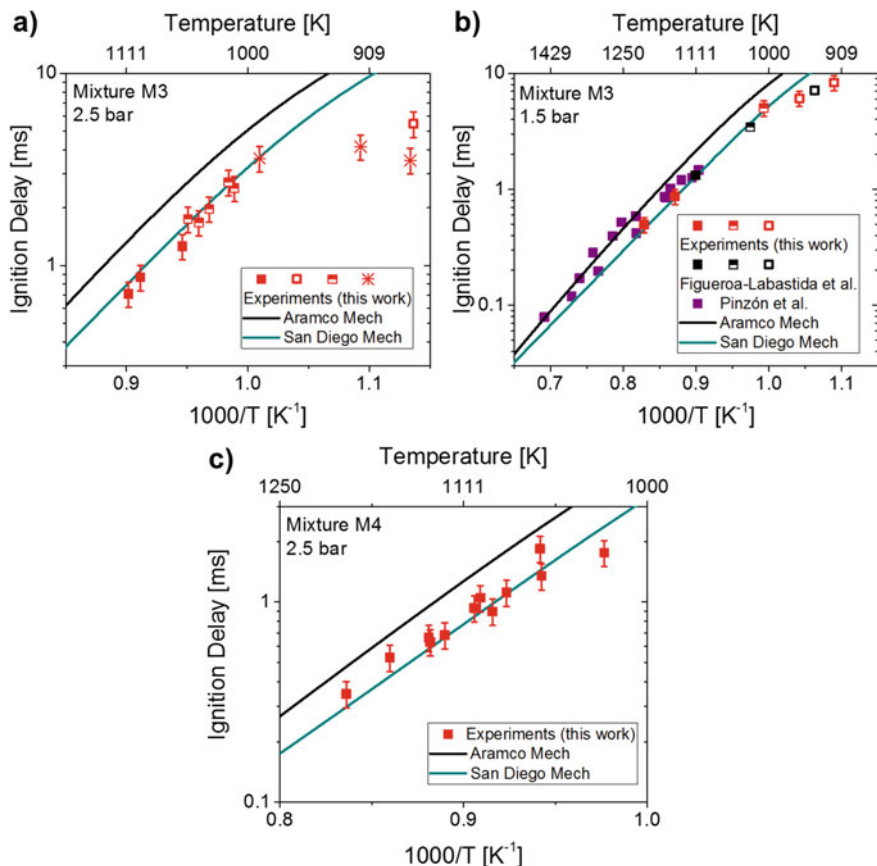


**Fig. 15.14** Comparison between the measured  $\tau_{ig}$  (symbols) and the computed  $\tau_{ig,i}$  (lines) for the methanol M3 and M4 mixtures. The test mixtures: (a-b) M3 with 13.2% methanol/18.4%  $O_2/Ar$ ,  $\phi = 1$ , at (a) 2.5 bar with  $dP/dt = 3$  %/ms, and (b) 1.5 bar with  $dP/dt = 2$  %/ms; and (c) M4 with 12.3% methanol/18.4%  $O_2/N_2$ ,  $\phi = 1$ , at 2.5 bar with  $dP/dt = 3$  %/ms. Closed symbols denote the measurements with homogeneous ignition while open and semi-filled symbols denote the measurements with nonhomogeneous ignition (taken from Ref. Figueroa-Labastida et al. 2021b)

and 15.19, a large difference between  $\tau_{ig,m}$  and  $\tau_{ig,i}$  was observed for Hex 1 due to the development of preignition kernels envolved into deflagrations that gradually consume the test mixture as representatively shown in Fig. 15.20.

The prediction of combustion modes for the  $n$ -hexane mixtures is shown in Fig. 15.21. In general, the prediction by the  $Sa_p$  criterion quantitatively agrees with the observed preignition tendency of the  $n$ -hexane mixtures regardless of the non-monotonic profile of the measured  $\tau_{ig,m}$  caused by the NTC regime. Particularly, Hex 2 with low-fuel concentration is predicted to experience a homogeneous/strong ignition,  $Sa_p \leq 1$  at  $\sim T > 720K$ , which is consistent with the experimental obser-

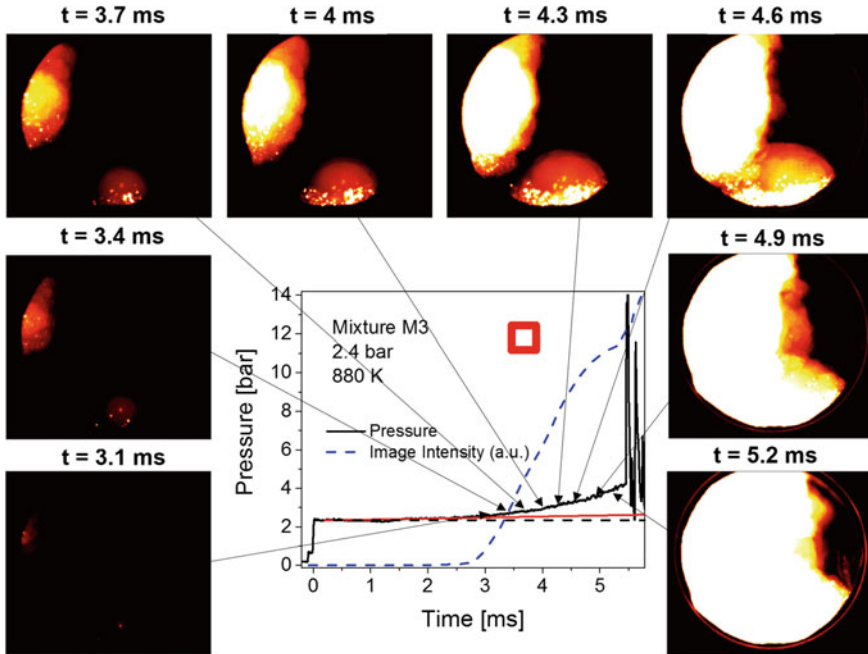


**Fig. 15.15** Imaging of the temporal inhomogeneous ignition process of the methanol M3 mixture, 12.3%  $\text{CH}_3\text{OH}/18.4\%$   $\text{O}_2/\text{Ar}$ ,  $\phi = 1$  at 880 K and 2.4 bar, with  $\text{Sa}_p = 2.8$ . The red line describes the pressure rise due to the  $dP/dt$  effect, and the dashed blue line is the image intensity recorded from the high-speed camera (taken from Ref. Figueroa-Labastida et al. 2021b)

vations that no noticeable preignition was observed for this range of temperature. On the contrary, Hex 1 with high-fuel concentration at the temperature range  $\sim 1050 \text{ K} < T < 850 \text{ K}$ , which were experimentally observed the strong preignition activities, are also well captured by  $\text{Sa}_p \gg 1$ . In the lower-temperature regime,  $700\text{--}750 \text{ K}$ ,  $\text{Sa}_p \sim 1$  indicates the transition of weak-to-strong ignition mode for Hex 1. Therefore, the measured  $\tau_{ig}$  is expected to be comparable with  $\tau_{ig}$  with  $dP/dt$  correction.

For the test time is in the order of  $\gtrsim 20 \text{ ms}$  at temperature,  $T < 700 \text{ K}$ , the effect of thermal diffusivity becomes important (as quantified by the Damköhler number in Refs. Figueroa-Labastida et al. 2021b; Javed et al. 2017; Im et al. 2015) to dissipate the thermal gradients. The effect of thermal diffusivity significantly homogenizes the thermal fluctuations in the test gas. As such, a dominant homogeneous ignition is expected for a mixture with nearly uniform thermal gradients, i.e., with a negligible  $T'$ , instead of  $T' \sim 2 \text{ K}$  chosen to compute  $\text{Sa}_p$  in this study, and thereby reducing  $\text{Sa}_p \ll 1$ . A consistent prediction by  $\text{Sa}_p$  is also achieved for *n*-heptane mixtures with both low- and high-fuel concentration (Luong et al. 2021).

In a separate study (Luong et al. 2021), we are conducting more comprehensive validations with experimental data for many fuels (i.e.,  $\text{N}_2$ , syngas, both non-NTC and NTC fuels) under a wider spectrum of different initial conditions and  $dP/dt$ . We



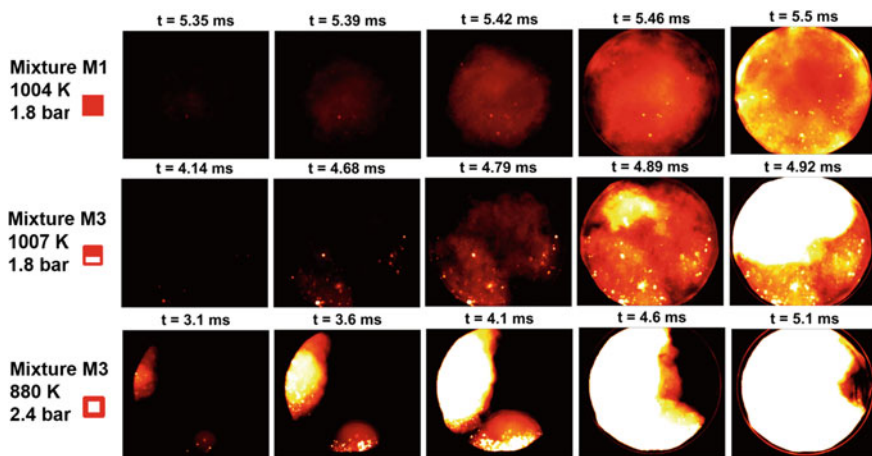


**Fig. 15.16** Comparison of the ignition modes of the methanol mixtures: first row—strong homogeneous ignition of M1, 5.7% CH<sub>3</sub>OH/8.6% O<sub>2</sub>/Ar,  $\phi = 1$  at 1004 K and 1.8 bar; second row – intermediate ignition mode (mixed inhomogeneous and homogeneous ignition) of M3, 12.3% CH<sub>3</sub>OH/18.4% O<sub>2</sub>/Ar,  $\phi = 1$  at 1007 K and 1.8 bar; third row—weak inhomogeneous ignition of M3 at 880 K, and 2.4 bar (taken from Ref. Figueroa-Labastida et al. 2021b). The  $Sa_p$  values of three cases from top to bottom are 0.6, 1.0, and 2.8, respectively

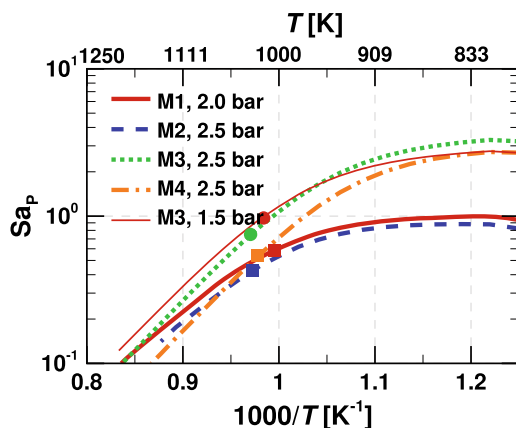


**Fig. 15.17** The predicted Sankaran number,  $Sa_p$ , as a function of  $1000/T$  for the methanol mixtures. Circles denote the transition temperature delineating the homogeneous and non-homogeneous ignition. Squares denote the lowest temperatures experimentally tested where no preignition has been observed (taken from Ref. Figueroa-Labastida et al. 2021b)



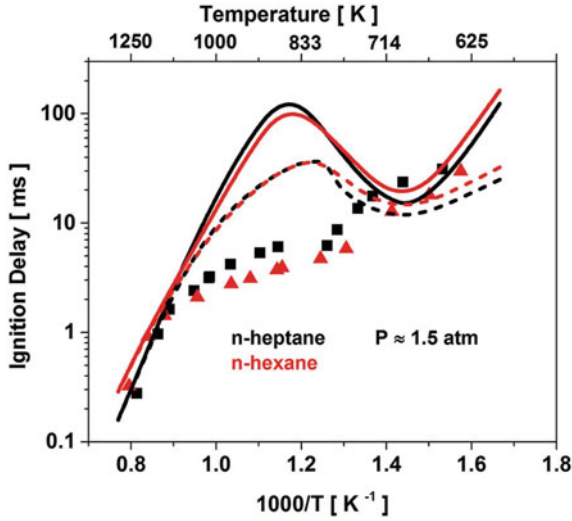


**Fig. 15.18** Comparison between the measured  $\tau_{ig}$  (symbols) and the computed constant-volume  $\tau_{ig}$  (lines). Solid and dashed lines are for constant volume simulations, and 3% dP/dt simulations, respectively. The test mixtures: 2% *n*-heptane/44% O<sub>2</sub>/Ar with  $\phi = 0.5$ , and 5% *n*-hexane/44% O<sub>2</sub>/Ar with  $\phi = 1$  (Hex 1) (taken from Ref. Javed et al. 2017)

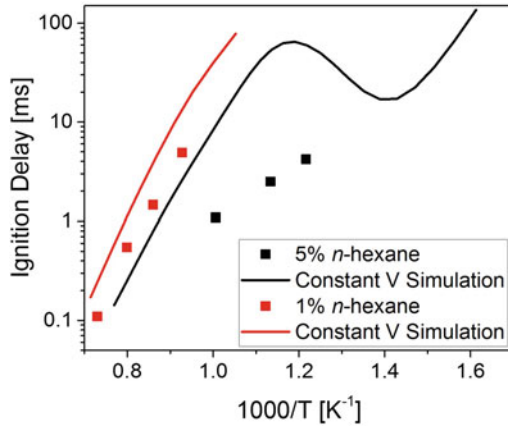


**Fig. 15.19** Measured ignition delay time of 5% *n*-hexane/47.5% O<sub>2</sub>/Ar, and 1% *n*-hexane/9.5% O<sub>2</sub>/Ar, Hex 1 and Hex 2. Solid lines depict constant-volume simulations (taken from Ref. Figueroa-Labastida et al. 2021a)

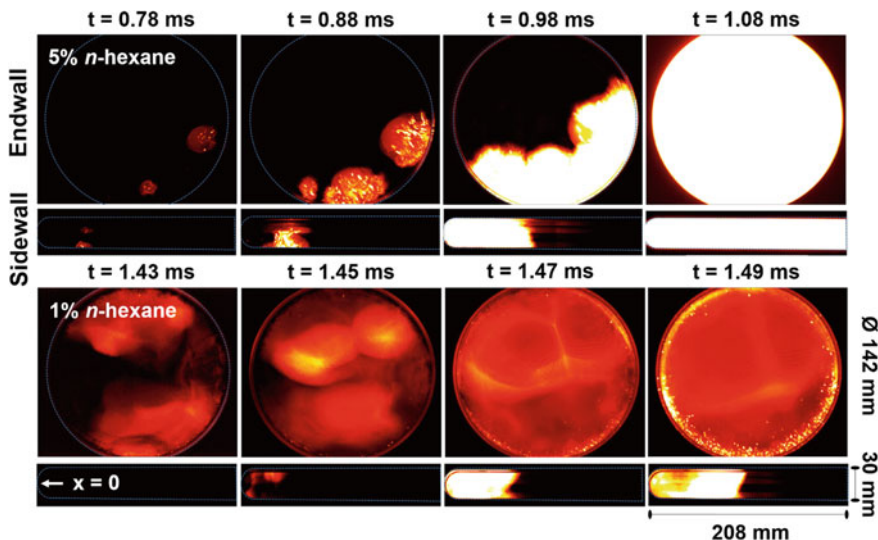


**Fig. 15.20** Simultaneous endwall and sidewall imaging of the ignition process of the *n*-hexane mixtures: Hex 1, 5% *n*-C<sub>6</sub>H<sub>14</sub>/47.5% O<sub>2</sub>/Ar,  $\phi = 1$  at 994 K and 2.4 bar (top row, inhomogeneous ignition with  $Sa_p = 3.7$ ), and Hex 2, 1% *n*-C<sub>6</sub>H<sub>14</sub>/9.5% O<sub>2</sub>/Ar,  $\phi = 1$  at 1163 K, and 2.4 bar (bottom row, homogeneous ignition with  $Sa_p = 0.4$ ).  $x = 0$  denotes the endwall on the left side of the images (taken from Ref. Figueroa-Labastida et al. 2021a)

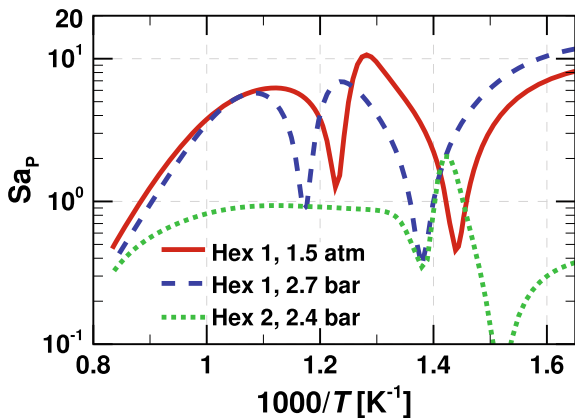


**Fig. 15.21** The predictive Sankaran number,  $Sa_p$ , as a function of  $1000/T$  for three *n*-hexane mixtures: Hex 1 (5% *n*-C<sub>6</sub>H<sub>14</sub>/47.5% O<sub>2</sub>/47.5% Ar,  $\phi = 1$ ) at 1.5 atm and 2.7 bar, and Hex 2 (1% *n*-C<sub>6</sub>H<sub>14</sub>/9.5% O<sub>2</sub>/89.5% Ar,  $\phi = 1$ ) at 2.4 bar (Javd et al. 2017; Figueroa-Labastida et al. 2021a) (taken from Ref. Luong et al. 2021). The *n*-heptane detailed mechanism v3.1 (Mehl et al. 2011) and  $dP/dt$  of 2%/ms were used to compute  $Sa_p$

are also performing multi-dimensional direct numerical simulations under shock tube and internal combustion (IC) engine conditions that accounts for the  $dP/dt$  effect. From the results of these ongoing studies, we find a consistent predictive accuracy of  $Sa_p$  for the observed combustion modes. The good predictive accuracy demonstrated by the newly-developed  $Sa_p$  criterion in shock tube strongly suggests that the sensitivity of ignition delay variation,  $d\tau_{ig}/dT$ , in non-constant volume reactors such as the polytropic compression/expansion heating effect in an internal combustion engines and in a rapid compression machines (RCM) should be incorporated in formulating an ignition criterion that allows better prediction of the ignition modes. This is of strong practical significance and is currently being investigated further by large scale simulations.

## 15.4 Summary

Recent developments in the theoretical framework to predict preignition development in shock tubes were summarized. A brief review was given on the theoretical background of ignition regimes, starting from the original Zeldovich (1980) theory (Zeldovich 1980), and followed by the predictive ignition criteria by Sankaran et al. (2005) and Im et al. (2015), Luong et al. (2020). The newly-developed predictive Sankaran criterion,  $Sa_p$ , was proposed to predict the preignition propensity in shock tubes. The key idea behind the newly-developed predictive  $Sa_p$  criterion is the consideration of the non-ideal temperature and pressure rise over time in evaluating the ignition delay sensitivity to temperature that allows  $Sa_p$  to better predict the combustion modes in shock tubes.

An extensive dataset of three fuels (i.e., methanol and ethanol mixtures exhibiting a single-stage ignition, and *n*-hexane mixtures exhibiting a strong NTC behavior) taken from the recent studies (Javed et al. 2017; Figueroa-Labastida et al. 2018, 2021a, b) showing different degrees of the preignition propensity over a wide range of conditions is adopted to verify the predictive accuracy of the newly-developed criterion. It is demonstrated that the  $Sa_p$  criterion can accurately predict the weak and strong ignition modes in shock tubes regardless of the NTC and non-NTC fuels over a wide range of pressure and temperature.  $Sa_p = 1$  serves as a reliable marker to delineate the boundary between the strong ignition ( $Sa_p < 1$ ) and weak ignition ( $Sa_p > 1$ ).

Stochastic and undesired preignition events also occur in other combustion devices such as IC engines and rapid combustion machines (RCM) that significantly degrades their operating performance. The combustion process in these devices undergoes even a much stronger non-constant volume ignition than that in shock tubes. As demonstrated in shock tubes, it is therefore crucially important to account for the non-ideal pressure and temperature rise when computing the ignition delay time sensitivity to temperature,  $d\tau_{ig}/dT$ , that improves the predictive accuracy of  $Sa_p$ . This is of strong practical significance and is currently being investigated further by large scale simulations.

**Acknowledgements** This work was sponsored by King Abdullah University of Science and Technology and used the resources of the KAUST Supercomputing Laboratory.

## References

- Ali MJM, Luong MB, Sow A, Hernández Pérez FE, Im HG (2018) Probabilistic approach to predict abnormal combustion in spark ignition engines. SAE paper (2018) 2018-01-1722
- Chaos M, Dryer FL (2010) Chemical-kinetic modeling of ignition delay: considerations in interpreting shock tube data. *Int J Chem Kinet* 42:143–150
- Dai P, Chen Z, Chen S, Ju Y (2015) Numerical experiments on reaction front propagation in n-heptane/air mixture with temperature gradient. *Proc Combust Inst* 35:3045–3052
- Dai P, Qi C, Chen Z (2017) Effects of initial temperature on autoignition and detonation development in dimethyl ether/air mixtures with temperature gradient. *Proc Combust Inst* 36:3643–3650
- Davidson DF, Hanson RK (2004) Interpreting shock tube ignition data. *Int J Chem Kinet* 36:510–523
- Davidson DF, Hanson RK (2009) Recent advances in shock tube/laser diagnostic methods for improved chemical kinetics measurements. *Shock Waves* 19:271–283
- Donovan MT, He X, Zigler BT, Palmer TR, Wooldridge MS, Atreya A (2004) Demonstration of a free-piston rapid compression facility for the study of high temperature combustion phenomena. *Combust Flame* 137:351–365
- Figueroa-Labastida M, Badra J, Elbaz AM, Farooq A (2018) Shock tube studies of ethanol preignition. *Combust Flame* 198:176–185
- Figueroa-Labastida M, Badra J, Farooq A (2021) Dual-camera high-speed imaging of the ignition modes of ethanol, methanol and n-hexane in a shock tube. *Combust Flame* 224:33–42
- Figueroa-Labastida M, Luong MB, Badra J, Im HG, Farooq A (2021b) Experimental and computational studies of methanol and ethanol preignition behind reflected shock waves. *Combust Flame*
- Goldsborough SS, Hochgreb S, Vanhove G, Wooldridge MS, Curran HJ, Sung C-J (2017) Advances in rapid compression machine studies of low- and intermediate-temperature autoignition phenomena. *Prog Energy Combust Sci* 63:1–78
- Grogan KP, Ihme M (2015) Weak and strong ignition of hydrogen/oxygen mixtures in shock-tube systems. *Proc Combust Inst* 35:2181–2189
- Hanson R, Davidson D (2014) Recent advances in laser absorption and shock tube methods for studies of combustion chemistry. *Prog Energy Combust Sci* 44:103–114
- Hargis JW, Petersen EL (2015) Methane ignition in a shock tube with high levels of CO<sub>2</sub> dilution: consideration of the reflected-shock bifurcation. *Energy Fuels* 29:7712–7726
- Im HG, Pal P, Wooldridge MS, Mansfield AB (2015) A regime diagram for autoignition of homogeneous reactant mixtures with turbulent velocity and temperature fluctuations. *Combust Sci Technol* 187:1263–1275
- Javed T, Badra J, Jaasim M, Es-Sebbar E, Labastida MF, Chung SH, Im HG, Farooq A (2017) Shock tube ignition delay data affected by localized ignition phenomena. *Combust Sci Technol* 189:1138–1161
- Kalghatgi GT (2015) Developments in internal combustion engines and implications for combustion science and future transport fuels. *Proc Combust Inst* 35:101–115
- Kalghatgi GT, Bradley D (2012) Pre-ignition and ‘super-knock’ in turbo-charged spark-ignition engines. *Int J Engine Res* 13:399–414
- Kim SO, Luong MB, Chen JH, Yoo CS (2015) A DNS study of the ignition of lean PRF/air mixtures with temperature inhomogeneities under high pressure and intermediate temperature. *Combust Flame* 162:717–726
- Lamnaouer M, Kassab A, Divo E, Polley N, Garza-Urquiza R, Petersen E (2014) A conjugate axisymmetric model of a high-pressure shock-tube facility. *Int J Numer Method H* 24:873–890

- Li H, Owens ZC, Davidson DF, Hanson RK (2008) A simple reactive gasdynamic model for the computation of gas temperature and species concentrations behind reflected shock waves. *Int J Chem Kinet* 40:189–198
- Luong MB, Desai S, Hernández Pérez FE, Sankaran R, Johansson B, Im HG (2019) Prediction of ignition regimes in DME/air mixtures with temperature and concentration fluctuations. *AIAA SciTech 2019 Forum*. <https://doi.org/10.2514/6.2019-2241>
- Luong MB, Figueroa-Labastida M, Farooq A, Im HG (2021) Prediction of preignition tendency in shock tubes. *Combust Flame* (in preparation)
- Luong MB, Figueroa-Labastida M, Tingas E-A, Sow A, Pérez FEH, Badra J, Farooq A, Im HG (2019) Prediction of ignition modes of NTC-fuel/air mixtures with temperature and concentration fluctuations. *ICDERS2019 Paper* 297
- Luong MB, Luo Z, Lu T, Chung SH, Yoo CS (2013) Direct numerical simulations of the ignition of lean primary reference fuel/air mixtures with temperature inhomogeneities. *Combust Flame* 160:2038–2047
- Luong MB, Lu T, Chung SH, Yoo CS (2014) Direct numerical simulations of the ignition of a lean biodiesel/air mixture with temperature and composition inhomogeneities at high pressure and intermediate temperature. *Combust Flame* 161:2878–2889
- Luong MB, Yu GH, Lu T, Chung SH, Yoo CS (2015) Direct numerical simulations of ignition of a lean *n*-heptane/air mixture with temperature and composition inhomogeneities relevant to HCCI and SCCI combustion. *Combust Flame* 162:4566–4585
- Luong MB, Yu GH, Chung SH, Yoo CS (2017) Ignition of a lean PRF/air mixture under RCCI/SCCI conditions: a comparative DNS study. *Proc Combust Inst* 36:3623–3631
- Luong MB, Yu GH, Chung SH, Yoo CS (2017) Ignition of a lean PRF/air mixture under RCCI/SCCI conditions: chemical aspects. *Proc Combust Inst* 36:3587–3596
- Luong MB, Sankaran R, Yu GH, Chung SH, Yoo CS (2017) On the effect of injection timing on the ignition of lean PRF/air/EGR mixtures under direct dual fuel stratification conditions. *Combust Flame* 183:309–321
- Luong MB, Hernández Pérez FE, Im HG (2020) Prediction of ignition modes of NTC-fuel/air mixtures with temperature and concentration fluctuations. *Combust Flame* 213:382–393
- Luong MB, Desai S, Hernández Pérez FE, Sankaran R, Johansson B, Im HG (2021a) A statistical analysis of developing knock intensity in a mixture with temperature inhomogeneities. *Proc Combust Inst* 38:5781–5789
- Luong MB, Desai S, Hernández Pérez FE, Sankaran R, Johansson B, Im HG (2021) Effects of turbulence and temperature fluctuations on knock development in an ethanol/air mixture. *Flow Turbul Combust* 106:575–595
- Lutz AE, Kee RJ, Miller JA, Dwyer HA, AK (1989) Oppenheim, Dynamic effects of autoignition centers for hydrogen and *c*<sub>1,2</sub>-hydrocarbon fuels. *Symp (Int) Combust* 22:1683–1693
- Mansfield AB, Wooldridge MS (2014) High-pressure low-temperature ignition behavior of syngas mixtures. *Combust Flame* 161:2242–2251
- Mansfield AB, Wooldridge MS, Di H, He X (2015) Low-temperature ignition behavior of iso-octane. *Combust Flame* 139:79–86
- Mehl M, Pitz WJ, Westbrook CK, Curran HJ (2011) Kinetic modeling of gasoline surrogate components and mixtures under engine conditions. *Proc Combust Inst* 33:193–200
- Meyer JW, Oppenheim AK (1971) On the shock-induced ignition of explosive gases. *Symp (Int) Combust* 13:1153–1164
- Nativel D, Cooper SP, Lipkowitz T, Fikri M, Petersen EL, Schulz C (2020) Impact of shock-tube facility-dependent effects on incident- and reflected-shock conditions over a wide range of pressures and mach numbers. *Combust Flame* 217:200–211
- Pal P, Valorani M, Arias PG, Im HG, Wooldridge MS, Ciottoli PP, Galassi RM (2017) Computational characterization of ignition regimes in a syngas/air mixture with temperature fluctuations. *Proc Combust Inst* 36:3705–3716
- Pan J, Wei H, Shu G, Chen Z, Zhao P (2016) The role of low temperature chemistry in combustion mode development under elevated pressures. *Combust Flame* 174:179–193

- Pan J, Wei H, Shu G, Chen R (2017) Effect of pressure wave disturbance on auto-ignition mode transition and knocking intensity under enclosed conditions. *Combust Flame* 185:63–74
- Pan J, Hu Z, Wei H, Wang L, He Y, Wang X (2020) Forced turbulence affected auto-ignition and combustion modes under engine-relevant conditions. *Appl Energy Combust Sci* 1–4:100015
- Pan J, Zheng Z, Wei H, Pan M, Shu G, Liang X (2021) An experimental investigation on pre-ignition phenomena: Emphasis on the role of turbulence. *Proc. Combust. Inst.* 38:5801–5810
- Pang GA, Davidson DF, Hanson RK (2009) Experimental study and modeling of shock tube ignition delay times for hydrogen-oxygen-argon mixtures at low temperatures. *Proc Combust Inst* 32:181–188
- Petersen EL, Hanson RK (2001) Nonideal effects behind reflected shock waves in a high-pressure shock tube. *Shock Waves* 10:405–420
- Pryor O, Barak S, Koroglu B, Ninnemann E, Vasu SS (2017) Measurements and interpretation of shock tube ignition delay times in highly CO<sub>2</sub> diluted mixtures using multiple diagnostics. *Combust Flame* 180:63–76
- Sankaran R, Im HG, Hawkes ER, Chen JH (2005) The effects of non-uniform temperature distribution on the ignition of a lean homogeneous hydrogen-air mixture. *Proc Combust Inst* 30:875–882
- Sow A, Lee BJ, Hernández Pérez FE, Im HG (2019) Detonation onset in a thermally stratified constant volume reactor. *Proc Combust Inst* 37:3529–3536
- Strozzi C, Mura A, Sotton J, Bellenoue M (2012) Experimental analysis of propagation regimes during the autoignition of a fully premixed methane-air mixture in the presence of temperature inhomogeneities. *Combust Flame* 159:3323–3341
- Terashima H, Matsugi A, Koshi M (2017) Origin and reactivity of hot-spots in end-gas autoignition with effects of negative temperature coefficients: Relevance to pressure wave developments. *Combust Flame* 184:324–334
- Towery CAZ, Poludnenko AY, Hamlington PE (2020) Detonation initiation by compressible turbulence thermodynamic fluctuations. *Combust Flame* 213:172–183
- Troutman VA, Strand CL, Campbell MF, Tulgestke AM, Miller VA, Davidson DF, Hanson RK (2016) High-speed OH\* chemiluminescence imaging of ignition through a shock tube end-wall. *Appl Phys B* 122:56
- Walton SM, He X, Zigler BT, Wooldridge MS, Atreya A (2007) An experimental investigation of iso-octane ignition phenomena. *Combust Flame* 150:246–262
- Wang Z, Liu H, Reitz RD (2017) Knocking combustion in spark-ignition engines. *Prog Energy Combust Sci* 61:78–112
- Wei H, Chen C, Shu G, Liang X, Zhou L (2018) Pressure wave evolution during two hotspots autoignition within end-gas region under internal combustion engine-relevant conditions. *Combust Flame* 189:142–154
- Yamashita H, Kasahara J, Sugiyama Y, Matsuo A (2012) Visualization study of ignition modes behind bifurcated-reflected shock waves. *Combust Flame* 159:2954–2966
- Yu H, Chen Z (2015) End-gas autoignition and detonation development in a closed chamber. *Combust Flame* 162:4102–4111
- Zeldovich YB (1980) Regime classification of an exothermic reaction with nonuniform initial conditions. *Combust Flame* 39:211–214

# Correction to: The Use of Ammonia as a Fuel for Combustion Engines



Dong Han, Yusen Liu, and Zhen Huang

**Correction to:**  
**Chapter 10 in: G. Kalghatgi et al. (eds.), *Engines and Fuels for Future Transport, Energy, Environment, and Sustainability*,**

[https://doi.org/10.1007/978-981-16-8717-4\\_10](https://doi.org/10.1007/978-981-16-8717-4_10)

In the original version of this chapter, the author mistakenly included the word “Gasoline” instead of “Hydrogen” in the abstract.

The correction chapter has been updated with the change.

---

The updated version of this chapter can be found at  
[https://doi.org/10.1007/978-981-16-8717-4\\_10](https://doi.org/10.1007/978-981-16-8717-4_10)